

Development of a Micro and Nano Cavity Microfluidic-SERS Platform



A thesis submitted to Dublin City University for the award of PhD

By

Aurélien V. Gimenez

Under the supervision of Prof. Tia E. Keyes

School of Chemical Sciences,
Dublin City University, Glasnevin, Dublin 9

September 2020

Declaration

I hereby certify that this material, which I now submit for assessment on the programme of study leading to the award of PhD. is entirely my own work, and that I have exercised reasonable care to ensure that the work is original, and does not to the best of my knowledge breach any law of copyright, and has not been taken from the work of others save and to the extent that such work has been cited and acknowledged within the text of my work.

Signed: _____

ID No.: _____ **13211145** _____

Date: _____

Acknowledgements

First and foremost, I would like to thank my supervisor Prof. Tia E. Keyes for giving me this incredible opportunity. Her endless knowledge, encouragement, time and most of all patience over the years have been invaluable.

I would like to extend my gratitude to the staff of the Dept. of Chemical Sciences, including PI's for the useful discussions about my work, Julie for her assistance in administrative tasks but more particularly to the technical staff, Aisling, Veronica, Vinny, Ambrose, Damian and John and also from the NRF Maurice, Lorcan, Úna, Barry and Josephine for their help and support regarding experiments I undertook during my PhD. A particular thank you to Mr. Christopher Crouch from the department of Mechanical and Manufacturing Engineering to grant me access to equipment for measurements of material properties and to Mr. Conor Murphy from the National Centre for Plasma Science Technology for his assistance with the Plasma etcher.

Within DCU I got the opportunity to work and socialize with people in a multi-cultural community and this has been a really enriching experience. Thank you all for this. I cannot mention everyone but I'm thinking of few of you with who I had long chats, lunches or nights out, Colm, Liam, Suzanne, Laura, Samantha, Keriling, Sara, Teresa and Mohammad.

Cheers also to Tia Keyes' group members both past (Gavin, Ciaran, Aaron, Vinnie, Sean, Siva, Aisling, Darragh, Agata) and present (David, Karmel, Rokas, Nirod, Shane, John, Jack) who contributed in any way to my work and development, even just through a chat. A particular recognition to 3 exceptional lab-mates who made this adventure unforgettable.

First, a big thank you to Dr. Kiang Wei Kho. I hope you don't get offended by my French humour as I have a huge and deep respect for you. I am really grateful for your guidance and theoretical explanations regarding the Physics I came across during my PhD. You are one of the smartest colleagues I got the chance to work and collaborate with and I really admire your professionalism and dedication. Bear in mind wherever you are "I see you...".

Next is Dr. Christopher De Búrca. Despite our speciality in the research group being totally different, you have always been a trustful and faithful PhD. companion from

beginning to end, able to listen and put yourself at your interlocutor level. Thank you also for becoming a friend, for all the great moments, for correcting my English, listening to my rants and my Latino music in loop in the lab and introducing me to craft beers... Still need to try those Wexican Rissoles though!

Finally, to Guilherme Batista Tartaro Berselli. Thank you for being yourself, spontaneous, record man of the most nonsenses told per hour to make people smile. I will always remember the joy you brought to the lab, particularly all the nervous and stupid laughs we had during the down moments when experiments were not working... - "On va juger les morts... Je veux en finir... C' est la castagne...". Merci Lopez Joe.

Outside DCU, I would like to first thank my Volleyball and Beach Volleyball friends who allowed me to free my mind during tough study times through fun sessions, trainings, matches and parties, particularly to my teammates and close friends Simeon and Marcin. You guys share good values and know how to have fun, especially outside court! Also thank you to my best friends back home, especially Lucy, Mélanie and Mickaël. Thanks for being always present despite the distance. We don't meet or chat very often, but I know we'll always be there for each other. I cannot forget to express my gratitude to "auntie" Fiona and "uncle" Gamel without whom this would not have happened. Thank you for your hospitality and giving me the opportunity to come to Ireland to improve my English, initially scheduled for 3 months (lol).

Last words will be for those closest to me, my family. I would like to thank my parents, Brigitte and Christian, in French. Maman, Papa, merci pour votre amour, support et patience. Ma réussite d'aujourd'hui est le fruit de votre travail de parents. Vous pouvez être fier de vous, de l'éducation que vous m'avez apportée ainsi que des valeurs que vous m'avez inculquées. Vous avez toujours été là pour moi, dans les bons moments mais aussi les plus difficiles et j'espère pouvoir un jour vous rendre la pareille.

Finally and above all, I would like to thank my partner, Lucia, in Italian. Tesoro mi'. Grazie per il tuo tempo e la tua presenza. Virginia Woolf evocando il successo di un uomo cita: «Dietro un grande uomo c'è una grande donna». Non avrei mai la pretesa di dire di essere un grand'uomo ma posso affermare che invece tu sei una grande donna. Grazie per essere ogni giorno al mio fianco. Hai saputo sostenermi, incoraggiarmi e credere in me nei miei momenti di dubbio. Sei il mio orgoglio. Ti amo!

Table of contents

Declaration	iii
Acknowledgements	v
Table of contents	vii
Abbreviations	xiii
Abstract	xix
1 Chapter 1: Literature survey	1
1.1 Introduction.....	2
1.2 Raman spectroscopy and Surface Enhanced Raman Spectroscopy.....	3
1.3 Strong electric field location at metallic nanostructures.....	5
1.4 Reproducibility issues in SERS.....	8
1.4.1 SERS mechanism influencing factors.....	8
1.4.2 Substrates structural factors influencing reproducibility.....	9
1.4.3 Influencing factors coming from molecule	11
1.4.4 Optical system parameters influence	12
1.5 SERS substrates.....	12
1.5.1 Metal nanoparticles in suspension	13
1.5.1.1 Physical method.....	13
1.5.1.2 Chemical method.....	13
1.5.2 Nanoparticles immobilised on solid substrates	16
1.5.3 Direct nanolithography or template-based substrates.....	17
1.5.3.1 Nanovoids platforms for SERS.....	19
1.6 Lipid bilayers models	27
1.6.1 Black Lipid Membranes.....	27
1.6.2 Liposomes.....	28
1.6.3 Supported Lipid Bilayers.....	29
1.6.4 Pore suspended Lipid Bilayers	31
1.7 Lipid bilayers in microfluidic devices	34
1.7.1 Supported lipid membranes	34
1.7.2 Suspended lipid membranes	35
1.7.3 Alternative lipid membranes microsystems.....	35
1.8 SERS of lipids.....	36
1.9 SERS in microfluidic devices.....	39
1.9.1 Metal colloids-based microfluidics-SERS platform.....	40
1.9.2 Nanostructured solid substrate microfluidics-SERS platform.....	42
1.9.2.1 In-situ fabrication	42
1.9.2.2 Integrated substrates.....	43

1.10	Conclusions.....	47
1.11	References	49
2	Chapter 2: Fabrication of a FLIM/FCS optically transparent microfluidic device for micropore arrays.....	59
2.1	Introduction.....	60
2.2	Experimental.....	62
2.2.1	Microfluidic device manufacturing and operational principle	62
2.2.2	Fabrication of a PMMA substrate for Cavity Supported Lipid Bilayers.....	64
2.2.2.1	Method A: Hot embossing cavities using a silicone-based master.....	64
2.2.2.1.1	Fabrication of a Gold microcavity array negative mould.....	64
2.2.2.1.2	Silicone based embossing master casting.....	66
2.2.2.1.3	Hot embossing microcavities on a PMMA substrate.....	69
2.2.2.2	Method B: Hot embossing cavities using an Si beads/Au-Si wafer based master	71
2.2.2.2.1	Fabrication of a Gold-Silica based embossing master	71
2.2.2.2.2	Thiolation of Si beads.....	72
2.2.2.2.3	Hot embossing microcavities on a PMMA substrate.....	73
2.2.3	Lipid bilayer formation	74
2.2.3.1	Plasma cleaning	74
2.2.3.2	Preparation of Small Unilamellar Vesicles.....	74
2.2.3.3	Formation of monolayer by Langmuir-Blodgett technique	75
2.2.3.4	Microfluidic device assembling.....	76
2.2.4	Material and instrumentation.....	76
2.2.4.1	Device manufacturing.....	76
2.2.4.1.1	CO ₂ laser	76
2.2.4.1.2	Cutting plotter	77
2.2.4.2	Cavities substrate manufacturing and characterisation.....	77
2.2.4.2.1	Plasma cleaner.....	77
2.2.4.2.2	Contact angle analyser.....	78
2.2.4.2.3	Silicone master	79
2.2.4.2.4	Hot embosser	79
2.2.4.2.5	Shore A Durometer.....	82
2.2.4.2.6	Compressive strength analyser.....	82
2.2.4.3	Scanning Electron Microscopy	83
2.2.4.4	Atomic Force Microscopy	84
2.2.4.5	Lipid bilayer characterisation by Fluorescence Correlation Spectroscopy.....	85
2.3	Results and discussions	88
2.3.1	Microfluidic device testing	88

2.3.2	Fabrication of a PMMA substrate for Supported Lipid Bilayers.....	90
2.3.2.1	Method A: Hot embossing cavities using a silicone-based master	91
2.3.2.1.1	Hardness optimisation of the silicone based embossing master	91
2.3.2.1.1.1	Study of the curing temperature.....	93
	Hardness shore A measurements.....	93
	Compressive strength measurements	96
2.3.2.1.1.2	Study of the impact of the ratio silicone elastomer base vs. curing agent on Elastosil® RT607	98
	Hardness shore A measurements.....	98
	Compressive strength measurements	101
2.3.2.1.2	Importance and characterisation of gold microcavities dimensions	106
2.3.2.1.3	Characterisation of positive features of the embossing master	110
2.3.2.1.4	Optimisation of hot embossing parameters.....	112
2.3.2.1.5	Characterisation of the PMMA embossed cavities	115
2.3.3	Method B: Hot embossing cavities using an Si beads/Au-Si wafer based master	118
2.3.3.1.1	Thiolation of the silica spheres to improve adhesion to the gold embossing master.....	119
2.3.3.1.2	Hot embossing with thiolated silica microspheres/Au-Si wafer based embossing master	123
2.3.3.2	Supported Lipid Bilayer formation and characterisation	124
2.3.3.2.1	Diffusion study of Supported Lipid Bilayers on planar PMMA for material compatibility check.....	124
2.3.3.2.2	Diffusion study of Supported Lipid Bilayers on PMMA cavities	128
2.4	Conclusions	132
2.5	References	135
3	Chapter 3: Optimized fabrication of uniform gold cavity arrays of controlled dimension over extended (cm²) surfaces and angle dependent SERS.....	139
3.1	Introduction.....	140
3.2	Experimental	142
3.2.1	Easy and robust fabrication of large uniform well-ordered gold nano and micro cavity arrays for SERS applications	142
3.2.1.1	Large uniform assembly of a hexagonally close packed monolayer of polystyrene spheres onto a gold-silicon wafer	142
3.2.1.2	Fabrication of hemisphere gold cavities by controlled electrodeposition up to the equator	142
3.2.1.3	Assessment of the fabrication method reproducibility by electrochemically active area determination	143
3.2.1.4	Characterisation of optimised gold micro and nano cavity arrays...	143
3.2.2	FDTD simulations.....	144

3.2.3	Selective modification of the array for angle dependence study of SERS signal from molecules adsorbed at the gold surface.....	144
3.2.4	Angle dependence set up and measurements.....	145
3.2.5	Angle Dependent Raman Measurements of a DOPC lipid bilayer suspended at a gold nano cavity array	148
3.3	Results and discussion	150
3.3.1	Optimisation of the gold micro and nano cavity arrays fabrication.....	150
3.3.1.1	Optimisation of the PS spheres arrangement at the gold surface	150
3.3.1.1.1	Simple drop casting.....	150
3.3.1.1.2	Vertical dry out in oven.....	153
3.3.1.1.3	Inverted dip-coating.....	154
3.3.1.1.4	Approaches to overcome the “coffee ring” effect for horizontal drop casting.....	156
3.3.1.1.5	Convective assembly on tilted stage.....	158
3.3.1.1.6	Extrapolation to 2 μm , 1 μm , 510 nm diameter PS spheres	163
3.3.1.2	Model study for a reproducible growth of gold cavities at and above the equator.....	164
3.3.2	Assessment of the new fabrication method by comparison to the standard one.....	171
3.3.3	Characterisation of optimised gold micro and nano cavity arrays	173
3.3.4	Angle dependence of SERS signal at gold cavity arrays	176
3.3.4.1	FDTD simulations	176
3.3.4.2	Polarisation angle of laser on Raman spectrometer.....	191
3.3.4.3	Angle dependence study of SERS signal from molecules adsorbed on selectively modified gold cavity arrays.....	193
3.3.4.4	Angle dependence study of a DOPC lipid bilayer suspended at a gold nano cavity array.....	200
3.4	Conclusions.....	204
3.5	References	207
4	Chapter 4: Fabrication of nano sub-structures towards enhancement of in-cavity signal	211
4.1	Introduction.....	212
4.2	Experimental.....	215
4.2.1	Fabrication of nano substructures within gold cavity (Au-cav) array using a top-down approach	215
4.2.2	Sputtered gold thickness study.....	216
4.2.2.1	Gold sputter coating	216
4.2.2.2	Profilometry	216
4.2.3	Diffuse reflectance.....	216
4.2.4	SEM and FESEM characterisation	217

4.2.5	FDTD simulations.....	217
4.2.6	SERS and MEF measurements	217
4.3	Results and discussion.....	219
4.3.1	Air bubble as a method for nano particles formation.....	219
4.3.2	Cavity sub-nanostructure development using plasma etching.....	223
4.3.2.1	Control on SAM formation kinetic	223
4.3.2.2	Influence of etching parameters on nano structures' shape.....	227
4.3.2.3	Optimisation of nanostructures based on SERS signal	233
4.3.2.4	Gold coating thickness optimisation.....	236
4.3.3	Characterisation.....	239
4.3.3.1	FESEM.....	239
4.3.3.2	Diffuse reflectance characterisation	243
4.3.3.3	FDTD simulations.....	247
4.3.3.4	Influence of medium on SERS signal: air vs. water measurements..	249
4.3.3.5	Optimised cavity / nano particle sizes for SERS measurements	252
4.3.3.6	Impact of nanoparticle modified cavities on luminescence	262
4.3.3.6.1	Concentration dependence study on NPs in 1 μ m cavities using [Ru(bpy) ₃]Cl ₂ probe	262
4.3.3.6.2	MEF characterisation of different sizes of cavity / NPs.....	265
4.4	Conclusions	274
4.5	References	276
5	Chapter 5: Towards a microfluidic platform based on gold micropore arrays lipid membrane supports	279
5.1	Introduction.....	280
5.2	Experimental.....	281
5.2.1	Electrochemical measurements.....	281
5.2.1.1	EIS trials on Au-Si electrodes for microfluidic device	281
5.2.1.2	Electrochemical compatibility of new gold electrodes on PET.....	281
5.2.1.3	Contact angle measurement.....	281
5.2.2	SEM characterisation.....	281
5.2.3	Choice of material for electrode substrate.....	282
5.3	Results and discussions.....	283
5.3.1	Working electrode for microfluidic device	283
5.3.2	Alternative design of the device.....	291
5.3.2.1	Choice of material as electrode substrate	291
5.3.2.2	Design towards a substrate for lipid membranes study from PET...292	
5.3.2.2.1	Electrodes size and shape	293
5.3.2.2.2	Device design.....	295

5.3.2.3	Assembly and leakage test.....	296
5.3.3	Electrochemical compatibility.....	296
5.3.4	Cavity array and nano substructuring.....	299
5.4	Conclusion.....	302
5.5	References.....	303
6	Chapter 6: Conclusions and future work.....	305
6.1	Conclusions.....	306
6.2	Future work.....	310
6.3	References.....	312
Appendices.....		313
Appendix A.	Hardness optimisation of the silicone based embossing master - Study of the curing temperature – Hardness Shore A measurements	A-0
Appendix B.	Hardness optimisation of the silicone based embossing master - Study of the impact of the ratio silicone elastomer base vs. curing agent on Elastosil® RT607 – Hardness Shore A measurements.....	B-0
Appendix C.	Hardness optimisation of the silicone based embossing master - Study of the impact of the ratio silicone elastomer base vs. curing agent on Elastosil® RT607 – Compressive strength measurements.....	C-0
Appendix D.	Thesis Outputs: Publications and Conferences	D-0

Abbreviations

α	Polarizability / Surface density
$\Delta\nu$	Raman shift
$(d\sigma/d\Omega)$	Differential Raman cross-section per molecule
η	Overall efficiency of the detection system
λ	Wavelength
v_c	Formation rate of PS sphere monolayer at a vertical surface
μ	Fluid dynamic viscosity at 25 °C
ρ_p	Particle density
ρ_f	Fluid density
a	Diameter of cavity aperture
A	Area
AC	Alternating Current
AFM	Atomic Force Microscopy
Ag	Silver
AgFON	Silver Film-Over-Nanospheres
ALD	Atomic Layer Deposition
anti-HBsAg	Hepatitis monoclonal antibody
APTMS	(3-aminopropyl) trimethoxysilane
ATR	Attenuated Total Reflectance
Au	Gold
Au-cav	Gold cavity
bkg	Background
BLM	Black Lipid Membrane
BSA	Bovine Serum Albumin
BSE	Back Scattered Electrons
CCD	Charge-coupled device
CNC	Computer Numerical-Controlled
COC	Cyclic Olefin Copolymer
COP	Cyclic Olefin Polymer
CPE	Constant Phase Element
CTAB	Cetyl Trimethyl Ammonium Bromide or Cetrimonium bromide
Cu	Copper

CV	Coefficient of variation
d	Diameter
D_{dn}	Average diffusion coefficient of probe molecule at day “n”
DI	Deionized
DIB	Droplet-interface-bilayer
DMA	Dynamic Mechanical Analysis
DNA	Deoxyribonucleic acid
DOPC	1,2-dioleoyl-sn-glycero-3-phosphocholine
DOPE	1,2-dioleoyl-sn-glycero-3-phosphoethanolamine
DPDS	Diphenyl disulphide
DSC	Differential Scanning Calorimetry
E	Electric field / Electric potential
$E(r)$	Electric field at a given point
$E_0(r)$	Electric field of the incident laser
EBL	Electron beam lithography
EC-SERS	Electrochemical Surface Enhanced Raman Spectroscopy
EDC	1-Ethyl-3-(3-dimethylaminopropyl)carbodiimide
EF	Enhancement Factor
EIS	Electrochemical Impedance Spectroscopy
ELISA	Enzyme-Linked Immunosorbent Assay
F	Faraday’s constant
FCS	Fluorescence Correlation Spectroscopy
FDTD	Finite-Difference Time Domain
FEM	Finite Element Method
FESEM	Field Emission Scanning Electron Microscopy
FIB	Focused Ion Beam
FLIM	Fluorescence-lifetime imaging microscopy
FRAP	Fluorescence recovery after photobleaching
FTIR	Fourier-transform infrared spectroscopy
FTO	Fluorine doped Tin Oxide
g	Acceleration due to gravity (9.8 m/s ²)
g^4	Electromagnetic enhancement
GUV	Giant Unilamellar Vesicle
h	Height

HAZ	Heat Affected Zone
HBsAg	Hepatitis B virus surface antigen
I	Intensity / Current
I_{SERS}	Intensity of the signal obtained during SERS measurements
icNP	In-cavity nanoparticle
IPA	Isopropyl alcohol
IR	Infrared
LAH	Lithium Aluminium Hydride
LB	Langmuir-Blodgett
LS	Langmuir-Schaefer
LSPR	Localized Surface Plasmon Resonance
LUV	Large Unilamellar Vesicle
MDAI	5,6-methylenedioxy-2-aminoindane
MDMA	3,4-Methylenedioxymethamphetamine
MEF	Metal Enhanced Fluorescence
MLV	Multilamellar vesicle
MPTMS	(3-mercaptopropyl) trimethoxysilane
MSLB	Microcavity-Supported Lipid Bilayer
n	Number of moles of deposited species during electrodeposition
N_x	Number of scattering molecules in the SERS volume
N.A.	Numerical Aperture
NHS	N-hydroxysuccinimide
NIL	Nanoimprint lithography
NP	Nanoparticle
NSL	Nanosphere lithography
P	Dipole moment
P_L	Incident laser power
PBS	Phosphate-buffered saline
PC	Polycarbonate
PDMS	Polydimethylsiloxane
PEG	Polyethylene-glycol
PET	Polyethylene terephthalate
PETG	Polyethylene terephthalate glycol
PGA	Poly- γ -D-glutamic acid

PMMA	Poly(methyl methacrylate)
PS	Polystyrene
PSA	Pressure-sensitive adhesive
PSPR	Propagating Surface Plasmon Resonance
PVC	Polyvinylchloride
Q	Cumulative charge passed through the electrochemical cell
r	Radius
R	Resistance
RF	Radio Frequency
RIE	Reactive-ion etching
R6G	Rhodamine 6G
SAM	Self-assembled monolayer
SE	Secondary Electrons
SEM	Scanning Electron Microscopy
SERS	Surface Enhanced Raman Spectroscopy
SERRS	Surface Enhanced Resonance Raman Spectroscopy
Si	Silicon
SLB	Supported Lipid Bilayer
SH-PEG-SH	α - ω -dimercapto polyethylene glycol
SOP	Standard Operating Procedure
SPP	Surface Plasmon Polariton
SPR	Surface Plasmon Resonance
SUV	Small Unilamellar Vesicle
t	Time
TDDFT	Time Dependent Density Functional Theory
TERS	Tip-enhanced Raman Spectroscopy
T_g	Glass transition temperature
THF	Tetrahydrofuran
TMA	Thermal Mechanic Analysis
UV	Ultraviolet
V	Volume
V_s	Settling velocity of PS spheres in water
z	Number of electrons involved in a redox equation
4-ATP	4-Aminothiophenol

4,4'-BPY	4,4'-Bipyridine
$\%OG_{gold}$	Relative overgrown volume of gold after passing the equator
$\%OG_{height}$	Relative height overgrowth after passing the equator
$\%OG_Q$	Relative charge needed in the overgrowth after passing the equator

Abstract

Aurélien V. Gimenez

Development of a Micro and Nano Cavity Microfluidic-SERS Platform

Substrates for Surface Enhanced Raman Spectroscopy (SERS) that combine high enhancement with low-cost, reproducible fabrication are an important challenge. In particular substrates that enable multimodal methods such as SERS with Fluorescence Correlation Spectroscopy (FCS) or Electrochemical Impedance Spectroscopy (EIS) and amenable to microfluidic assembly are attractive but also challenging to implement.

This thesis explored novel methods for reproducible fabrication of pore array substrates for application in fluorescence correlation and in particular, for surface enhanced spectroscopy, with the underlying aim of developing microfluidic platforms that can ultimately be applied to study of microcavity supported lipid bilayers.

Chapter 2 describes two new ways of hot embossing 3 μm diameter cavity arrays onto an optically transparent PMMA substrate for implementation in a microfluidic device, using positive embossing masters made of hardened silicone and silica beads chemically bonded onto an Au-Si wafer.

Chapter 3 optimizes sphere lithography methods to achieve outstanding pore-array packing over 1 cm^2 gold surface. This was accomplished by correlating electrodeposition i-t curve with electron imaging data to identify a reproducible point at which deposition has reached the equator of the sphere template, independent of the sphere/electrode dimensions. These advances dramatically improve the electroactive area variability between batches of cavity arrays used as electrodes and SERS reproducibility.

Finite-Difference Time Domain (FDTD) simulations and experiments designed to study the angle dependence of incident light on the SERS signal from the improved arrays confirmed that distribution and intensity of the field at the cavity surface could be tuned by tilting the substrate over controlled angles.

Chapter 4 describes novel methods to confine and improve the electric field distribution at the bottom of the cavity by nano sub-structuring four different diameter voids ranging from 510 nm to 3 μm diameter using oxygen plasma etching. A robust and efficient fabrication technique provided plasmonic nano sub-structured arrays which showed consistently higher intensities of SERS and Metal Enhanced Fluorescence (MEF) signal than their unstructured equivalents and better variability of results intra and inter samples, particularly for small size cavities.

Finally, chapter 5 describes implementation of the optimized arrays into a PET/PMMA-based two-channel microfluidic device designed to host up to four different lipid membrane compositions.

1 Chapter 1: Literature survey

1.1 Introduction

This thesis focusses on the development of low-cost and reproducible methods for fabrication of pore arrays and their implementation in simple microfluidic flow-through sample dispensing devices. The project constitutes part of a broader project with the aim of using such devices for the development and study of microcavity supported lipid bilayers. Our purpose herein is to develop arrays and platform that are suitable for study by multimodal analytical modalities such as FCS, EIS and Raman spectroscopy. The pore array has applications beyond the bilayer and as later chapters described we focus here on new or improved methods for preparation of reproducible and robust micropore array SERS platforms and implementation into devices that permit reagent to be introduced to the array via flow channels.

In the present chapter, the theoretical background regarding SERS, the main analytical technique used in this thesis is described. An overview of typical, SERS substrates is provided including the origin of the Raman signal enhancement at metallic surfaces. For analytical applications, using arrayed substrates, the reproducibility of SERS response, batch to batch and across a substrate is very important and often a balance must be met between magnitude of SERS response and fabrication reproducibility. These issues are discussed along with recent advances in the fabrication and use of such substrates, with a particular emphasis on nanovoid platforms.

In the context of the final application intended for the device developed in this thesis for lipid membranes study, we briefly introduce the topic of biophysical lipid membrane models and describe how some groups implemented such model into microfluidic devices. There are few examples of microfluidic SERS platforms for lipid bilayers so, separately we briefly describe how SERS structures have been applied to lipid study.

Finally, we review the area of SERS in microfluidic devices, which has shown an increasing interest in the last decade due to the advantages in combining these two techniques.

1.2 Raman spectroscopy and Surface Enhanced Raman Spectroscopy

Raman spectroscopy is a vibrational spectroscopy technique named after Professor C.V. Raman who, along with K.S. Krishnan, first experimentally established the phenomenon of inelastic scattering of light in 1928.¹ When a sample is irradiated with light, photons may be absorbed leading to promotion of molecules to a higher energy excited state. Alternatively, photons can be scattered with the same frequency of incident light or with additional or less energy than the incident photons. The latter two phenomena are the basis of Raman spectroscopy, where a single frequency of radiation is used to irradiate the sample and the shift in frequency between incident and scattered photons is measured.²

Figure 1 provides a simple energy level diagram illustrating the origin of the Raman effect. This effect is described by the nature of the polarizability (α) of a molecule. When a molecule is placed in an electric field (E), it suffers distortion since the positively charged nuclei are attracted toward the negative pole, and electrons toward the positive pole.³ This charge separation produces an induced dipole moment (P) described by $P = \alpha \cdot E$.

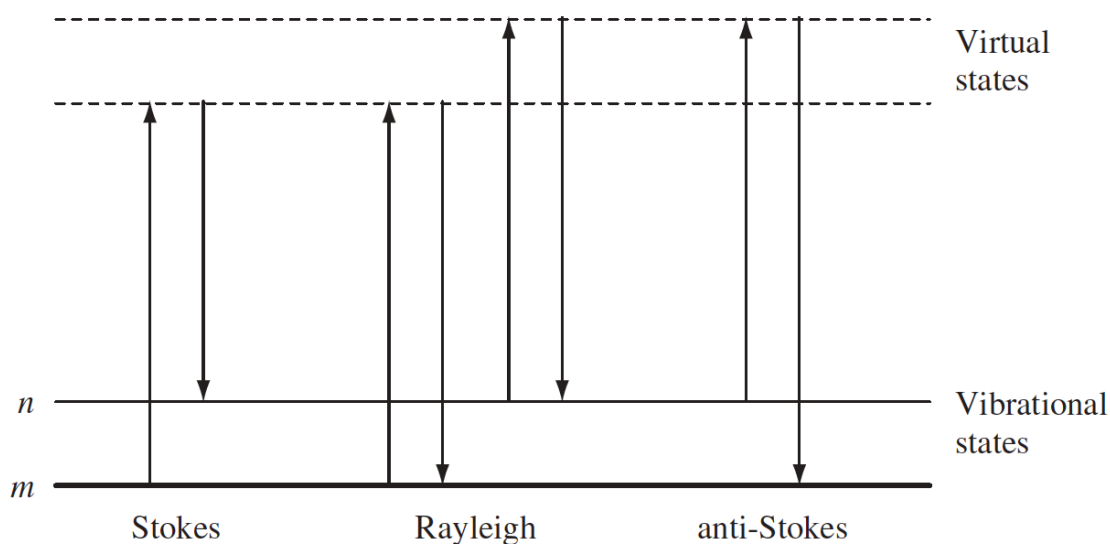


Figure 1 : Diagram of the Rayleigh and Raman scattering processes. Figure reproduced from reference.²

Under intense laser irradiation, most of the light is scattered from the sample by Rayleigh scattering, (i.e. with the same frequency as the incident light) but one in 10^6 to 10^8 photons are inelastically scattered (Raman scatter), which makes Raman a

weak process.- However, incident laser light promotes the molecule to a very short lived “virtual state” from where the molecule relaxes almost instantaneously to a vibrational level higher (Stokes) or lower (anti-Stokes) than the vibrational state the molecule originated from. The energy difference between the initial and the final vibrational levels $\Delta\nu$, also called Raman shift, follows Equation 1, where $\lambda_{\text{incident}}$ and $\lambda_{\text{scattered}}$ are the wavelength of the incident and the inelastically scattered photon respectively.

Equation 1 : Equation for the calculation of the Raman shift.

$$\Delta\nu = \frac{1}{\lambda_{\text{incident}}} - \frac{1}{\lambda_{\text{scattered}}}$$

To compensate for this weak process, high power lasers are usually used, though a drawback is that this can lead to other processes such as sample degradation and fluorescence, which can perturbate the Raman measurement.

In Surface Enhanced Raman Spectroscopy, the two mechanisms which have been proposed to account for the SERS effect are an electromagnetic and a chemical enhancement mechanism.

Electromagnetic Enhancement (surface plasmon) is the strongest contribution to SERS enhancement and can reach values up to 10^{10} . It originates from the localization of light at the surface substrate and is independent of the type of molecule analysed and is attributed to plasmonic field.⁴ Electromagnetic enhancement occurs when the wavelength of the incident laser is close in energy to the plasma wavelength of the metal. Molecules adsorbed or in close proximity to the surface (1 to 10 nm) experience then an augmented electromagnetic field.

In the Chemical Enhancement, 10^2 to 10^4 enhancement occurs and is thought to be attributed to the formation of a charge-transfer complex between the surface and analyte molecule leading to electronic transitions between adsorbate and surface states, the mechanism is somewhat similar to resonance Raman. The incident radiation striking the roughened metallic surface excites a photon within the metal to higher energy level. From this excited state, a charge transfer process promotes the electron to a vibrational level of the same energy within the target analyte. Then transfer of a photon of different frequency (due to vibrational transition) to the metallic energy

levels occurs from the molecule which is returned to the ground state. For the chemical mechanism, intimate contact between substrate and analyte is required.

Electromagnetic Enhancement is a major contributor to the observed enhancement however Chemical Enhancement also plays a significant role. Combined, both mechanisms result in then enhanced signal produced, although determination of extent to which each actually contributes is difficult to assess.

1.3 Strong electric field location at metallic nanostructures

Surface enhanced techniques such as SERS or MEF are enabled by metal nanostructures supporting plasmons. However, the various surfaces morphologies of such structures lead to differences of enhancement in signal intensity. In fact, some regions can contribute significantly to the enhancement of the signal due to the presence of highly localized intense plasmonic field at the nanostructures surface, also called “hot spots”. Significant investigation regarding the distribution of the electromagnetic field around plasmonic systems has been carried out to understand the kinds of structures that promote these “hot spots”.

In the case of isolated metallic nanoparticles (NPs), the electric field amplitude depends strongly on the structure size and shape, but also on the incident light wavelength and polarization. Across the nanostructure, the electric field is not uniform and strongest field can generally be found at sharp edges or tips as illustrated in Figure 2, therefore anisotropic structures usually to achieve larger field enhancement factors than isotropic spherical particles. Hao et al. calculated field enhancement factors for similar sized silver nanoparticles of different shapes.⁶ The maximum electric field value for a 20 nm diameter spherical particle was obtained with a 700 nm incident light and was calculated to be 14 times the applied field. The field enhancement factor was then calculated under the same conditions for nanoprisms, nanorods and nanospheroids. These anisotropic structures showed greater values than for spherical particles, estimated as equal to 59.1, 67 and 68.5 respectively.

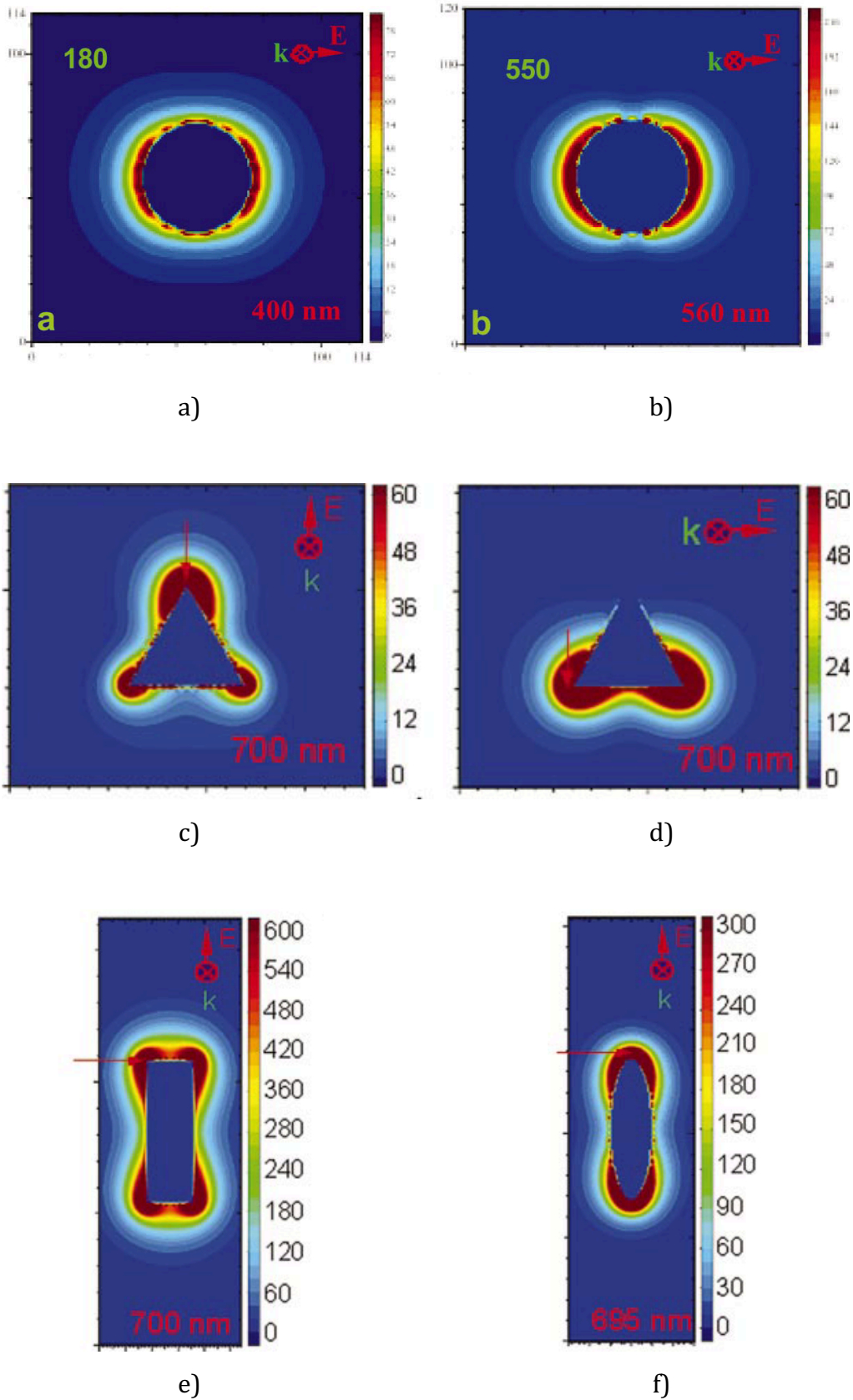


Figure 2 : Electromagnetic field enhancement contours external to silver nanoparticles with different shapes, including (a) nanosphere, (b) nanodisk, (c) and (d) triangular nanoprism polarized along two different axes, (e) nanorod and (f) nanospheroïd polarized along their long axes. Figure adapted from references.^{6,7}

In the case of dimers and aggregates, the strongest electric fields are typically observed at the nanogap between structures when the NPs are brought in close proximity to each other with a separation much smaller than the wavelength of light. Under these circumstances their transient dipoles couple and strong electromagnetic fields interfere coherently forming the “hot spots”.⁸ The enhanced field extends well beyond the surface of the NP, creating a sensing volume in which molecules can be detected. Significantly larger Raman signal enhancements are observed for NP aggregates in comparison to individual NPs and such configurations can even allow for single molecule measurements using SERS spectroscopy as reported for the first time by Kneipp et al., who managed single molecule detection of crystal violet molecule using aqueous colloidal silver solution.^{9,10} More recently, Zhan et al. fabricated gold bowtie structures with nanoscale precision using a DNA origami-based bottom-up assembly strategy, as bowtie type structures are reported to generate field enhancement several orders of magnitude higher than ones for gold nanosphere dimers.¹¹ They demonstrated the remarkable plasmonic coupling and field enhancement properties of the bowtie nanostructures achieving single molecules SERS detection at the nanogap, including measurement with low laser power (μW range) of an alkyne which usually require high laser power (mW range).

With growing understanding of the electromagnetic field distribution enabled by experiment combined with calculation, maximising the SERS signal intensity can be achieved by nano structuring, which generates strong fields on a highly localized area. Multiplying the number of hot spots in the detection volume can also further improve the signal intensity as more molecules would be under influence of the strong electric fields. However, another parameter to consider alongside these elements is the reproducibility of the measurement. This is important if SERS is to find application in analytical methods but particularly in using chemical means of growing nanostructures this can be difficult to control.

1.4 Reproducibility issues in SERS

From a fundamental and practical point of view, researchers are interested in high SERS signal intensity but also its high reproducibility. However, it seems difficult to combine those two criteria simultaneously. Despite managing to enhance drastically the signal of the weak Raman process, which makes SERS a highly specific and sensitive technique, SERS measurements often suffer low reproducibility, in terms of enhancement. This fluctuation in Raman signal intensity from spot to spot and/or from sample to sample has historically slowed down its application into commercial market, despite the technique being an attractive tool for sensing and identifying molecules in trace amounts as it has the advantage to give intensity/concentration as well as fingerprint data. These fluctuations can be attributed to the design and quality of the SERS substrate, but can also originate from the measurement conditions.¹² This section of the literature review presents different factors that influence the reproducibility of SERS intensity and that should be considered from the development to the SERS measurement itself.

Electric field enhancement through the plasmonic fields of metallic nanostructures is the main origin of enhancement of the Raman signal in SERS. Therefore, it is first important to understand what the influencing factors are in the SERS mechanism. Secondly, SERS substrates structural factors will be described. Finally, other factors such as number of molecules involved, and instrumental setup in promoting SERS will be discussed.

1.4.1 SERS mechanism influencing factors

Intensity of the signal obtained during SERS measurements (I_{SERS}) can be estimated by Equation 2, where N_x is the number of scattering molecules in the SERS volume, $(d\sigma/d\Omega)$ is the differential Raman cross-section per molecule, g^4 is the electromagnetic enhancement, P_L is the incident laser power, A is the area of the focus, and η is the overall efficiency of the detection system including the collection efficiency of scattered light, transmission efficiency of the spectrograph and photon detection efficiency.¹³

Equation 2 : Equation for the estimation of the intensity of SERS signal.

$$I_{SERS} = N_x \left(\frac{d\sigma}{d\Omega} \right) g^4 \frac{P_L}{A} \eta$$

From this equation, it can be understood that achieving a high uniformity and reproducibility of the SER signal is challenging as it involves controlling several factors of influence such as the number of molecules, their orientation at the metallic surface, the enhancement factor, the laser power and the efficiency of the optical system.

Experimentally, the parameter the most difficult to control is the number of molecules at the metallic surface and their precise location in the detection volume. This will be discussed *vide infra*. Notwithstanding this, the SERS signal intensity depends drastically on the enhancement factor and the wavelength of incident light. Indeed, considering several approximations^{14,15}, the SERS enhancement factor (*EF*) can be estimated with Equation 3, where $E(r)$ is the electric field at a given point and $E_0(r)$ the electric field of the incident laser. This equation allows one to understand that the reproducibility of the SERS signal intensity is highly influenced by the electric field.

Equation 3 : Equation for the approximation of SERS enhancement factors.

$$EF \approx \left| \frac{E(r)}{E_0(r)} \right|^4$$

Therefore, to obtain reproducible signal intensity during SERS measurements, parameters such as structures size, shape and distribution and interparticle spacing should be controlled as much as possible during the fabrication of the SERS substrates as they affect strongly the amplitude and distribution of the electric field.¹⁶

1.4.2 Substrates structural factors influencing reproducibility

A lot of effort has been applied during the last two decades toward developing physical or chemical techniques to produce uniform nanoparticles and arrays.¹⁷⁻¹⁹

Improvements regarding the synthesis of colloidal metallic nanoparticles with a better monodispersity has led to less fluctuation in the SERS signal measured compared to work previously published and should facilitate self-assembly of clusters with uniform optical resonance properties.^{20,21} Several scientific reviews have been published regarding the improvement of metallic nanoparticle size and shape and their properties.²²⁻²⁵ Despite managing uniform fabrication of particles of similar size, small changes to shape of the structure influences strongly the intensity of the SERS signal as reported by McLellan et al. and Fang et al.^{26,27} For example, Figure 3 illustrates the

variation in SERS intensity obtained for 1,4-benzenedithiol adsorbed at the surface of four individual silver particles of similar size but different morphology. Right bipyramids (A) are common side products (up to 10%) in a typical synthesis of silver nanocubes (B). Truncated cubes (C and D) were obtained in the same batch by further etching of the silver nanocubes.

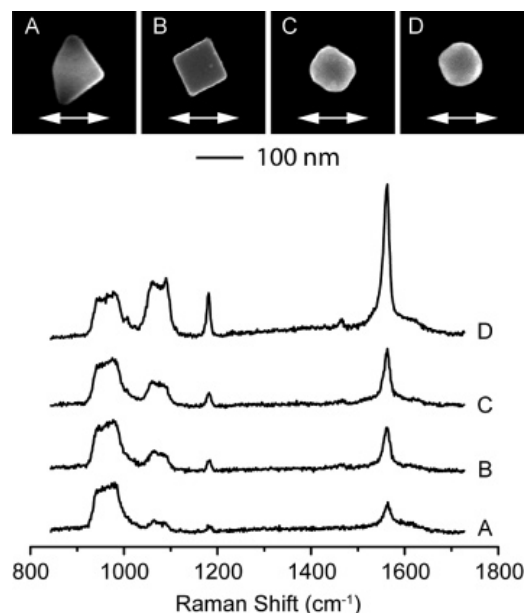


Figure 3 : Comparison of SERS spectra of 1,4-benzenedithiol adsorbed on single Ag nanoparticles with different morphologies: (A) right bipyramid, (B) cube with sharp corners, and (C,D) truncated cubes, as shown in the accompanying SEM images. Figure reproduced from reference.²⁶

Despite endeavours toward the improvement of the fabrication process, size and shape still vary to a certain extent within a single batch of nanoparticles that can lead to reproducibility issues in the SERS measurements.

Regarding arrays on substrates, well-ordered periodic metallic nanoparticle arrays of different morphologies can now be produced by many techniques including sphere lithography, beam lithography, vacuum specific deposition such as atomic layer deposition, or electrodeposition.

The formation of nanoparticle arrays from solution remains the most straightforward way to fabricate an effective substrate for SERS and methods have been reviewed by Brown and Milton.²⁸ However, slight variation within the array such as size and shape of individual structures, but also size distribution, interparticle spacing and aggregation state of the positive or negative nanostructures resulting from

the particles in solution can lead to differences in SERS intensity across a substrate, making it difficult to obtain good reproducibility of SERS signal. For example, Gopinath et al. studied the effect of nanocylinder diameters on the Raman enhancement for periodic and aperiodic arrays with a fix interparticle separation and show that SERS performance can be improved by tuning the particle radius.²⁹

To realize the potential of SERS for the trace analysis and detection, it is necessary to engineer the substrate to maximize signal strength whilst ensuring reproducibility of the surface plasmon resonances of the substrate. Therefore, in parallel with SERS experiments, characterization of the nanostructures with analytical and numerical methods are essential for a better understanding of the structural parameters influencing the electromagnetic field and thus the fluctuations in SERS signal intensity. Finite Element Method³⁰, Rigorous Coupled Wave Analysis³¹ or more commonly used Finite Difference Time Domain (FDTD)³² can be used both for simple and also more complex structures.

1.4.3 Influencing factors coming from molecule

As mentioned previously, the molecule factor is an experimental parameter difficult to control, but of high influence on the reproducibility of the SERS signal. The intensity of the signal is function of the molecules adsorbed at the metal substrate, therefore the quality of the self-assembled monolayer (SAM) is of key importance and adsorption efficiency should be considered during the assembly process. However, this is not the only influencing parameter.

The relative number of molecules present in regions of high electromagnetic field will also play a major role in the intensity of the signal, particularly at low concentration. Indeed, not all the molecules adsorbed at the metal surface can generate a signal, due to the highly localized strong electromagnetic field around the nanoparticle. Molecules diffusing in and out of the "hot spot" regions will lead to spectral fluctuations as illustrated in Figure 4. Based on Hao and Schatz work³³, Halvorson and Vikesland presented the expected SERS spectra for pyridine as a function of the electromagnetic field strength the molecule is exposed to, when adsorbed at silver nanoparticles and dimers.³⁴ Size and shape, but also orientation of the metallic nanoparticle influenced the distribution and intensity of the

electromagnetic field at their surface, and the relative location of the single pyridine molecule affects the intensity of the SERS signal.

Raman cross-section and orientation of the molecules with respect to the metallic surface also impacts the reproducibility of the SERS signal.^{35,36}

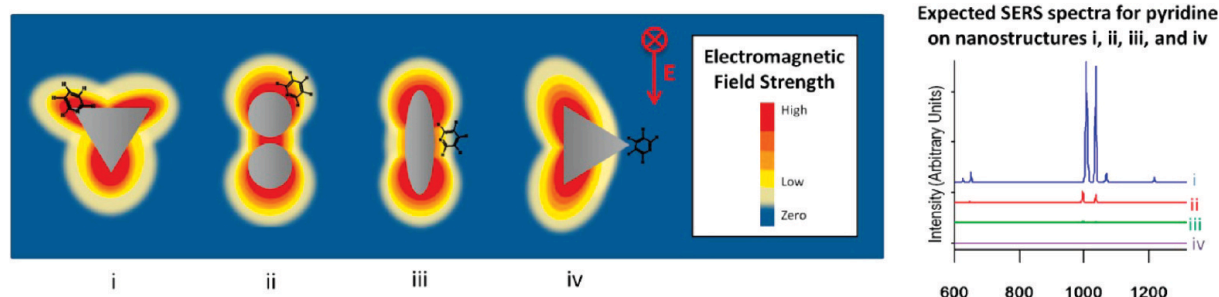


Figure 4 : Silver nanoparticle and its electromagnetic field (Left). Expected SERS spectra for pyridine on the corresponding nanostructures (Right). Figure reproduced from reference.³⁴

1.4.4 Optical system parameters influence

Finally, experimental conditions regarding the optical system used for SERS measurement are also important to control as they can play a significant role in the reproducibility of the signal.

To limit fluctuations, excitation and detection conditions should remain as constant as possible during individual and across replicate measurements. Etchegoin et al. showed that laser power can dramatically influence the enhancement factor value, showing discrepancies in the order of 10^2 to 10^3 depending on the incident power, arising from the photostability of the SERS probe used.³⁷ Alignment-dependent spot size of the laser focus, excitation and transmission efficiency of the spectrograph, and temperature variation that impacts the detection efficiency of charge-coupled device (CCD), are other parameters that can affect the intensity of the Raman signal, therefore these elements of the Raman system should be kept as stable as possible.

1.5 SERS substrates

Since the first observation of SERS by Fleischmann and co-workers in 1974, at electrochemically roughened silver,³⁸ a wide range of SERS substrates have emerged and are reported in the literature. This section aims at presenting a non-exhaustive list of SERS structures possibilities used in the scientific community, going through their fabrication, advantages and applications, and classified in three main categories. Metal

nanoparticles in suspension presenting different geometries, particles immobilised on solid substrates and substrates with nanostructures fabricated by direct nanolithography or template based are reviewed.

1.5.1 Metal nanoparticles in suspension

1.5.1.1 Physical method

One way to produce metal nanoparticle suspensions is through use of physical methods such as pulsed laser ablation of noble metals in liquid medium. Neddersen et al. first introduced this method and managed the fabrication in water and methanol of stable gold, silver and platinum nanoparticles.³⁹ Focusing the laser pulses on the immersed target, a plasma plume is generated and atomized material is removed from the target, creating nanoparticles in solution. The size of the produced nanoparticles can be modified by changing process conditions such as ablation time and pH of the solution.^{40,41} Usually, smaller particles are obtained by increasing the ablation time. More recently, Vinod and Gopchandran used a similar method to fabricate highly monodisperse gold (Au) and silver (Ag) nanoparticles.⁴² They then studied the SERS properties of the monometallic colloidal solutions but also of their mix in different ratio and found that the plasmon characteristics are strongly influenced by the laser fluence used during the synthesis. Varying the Au:Ag concentration ratio of the mixed solutions, they observed best SERS signal intensities for Au:Ag colloids compared to monometallic solutions, probably due to the tendency of the particles to aggregate in these solutions as observed by Scanning Electron Microscopy (SEM), creating localized “hot spots” at their junctions.

This physical fabrication method has the advantage of eliminating some of the problems associated with chemical techniques, as except for the solvent no other chemical is used, resulting in particles free of potentially interfering ionic and organic species.

1.5.1.2 Chemical method

Chemical methods, such as wet chemical synthesis, are also applied for the fabrication of metallic nanoparticles solutions, more commonly than physical methods. One of the widely spread technique consists in reducing gold or silver ions in aqueous solution with reducing and capping agent. Reducing agents change the metal ion in solution into a solid particle while capping agents bind at the particles' surface and

prevent aggregation by repulsive or steric forces, such as sodium citrate, NaBH₄ or hydroxylamine. Reducing agent commonly found in the literature are sodium citrate, dodecanethiol, thiol polyethylene-glycol (PEG), cetrimonium bromide (CTAB), tannic acid, hydroxylamine hydrochloride and polyvinylpyrrolidone.

More than 60 years ago, Turkevich et al. published a method for the synthesis of gold nanoparticles using sodium citrate as reducing and capping agent.⁴⁴ Silver nanoparticles were later synthesized by Lee and Meisel on the same basis.⁴⁵ However, as the original method led to irregularly shaped nanoparticles, several groups implemented since modifications to improve size and shape of the nanostructures.⁴⁶⁻⁴⁸ Strength and concentration of the reducing agent are influencing strongly the size of the particles with weak reducing agent such as sodium citrate leading to larger particles while strong reducing agents such as sodium borohydride lead to smaller ones. Size distribution can be adjusted during the two-step process nucleation/growth. During the nucleation, metal atoms combine to form clusters and finally crystal nuclei. The crystal nuclei, or “seeds”, grow in size to form nanoparticles. The shape of the final nanoparticle can be altered during the growing process by using surfactant that will cause a change in surface energy and control particle aggregation. Stabilizing then specific crystal planes in the growing nanostructure, controlled growth of that plane is then possible.⁴⁹ Combination between different surfactants and particle material allowed to create a wide variety of nanoparticles shapes including nanospheres^{44,50}, nanorods^{51,52}, nanocubes⁵³, nanotriangles^{50,54}, nanowires⁵³, nanostars^{50,55,56}, nanoplates⁵³, nanoflowers^{57,58} and nanodendrites.⁵⁹⁻⁶²

The SERS performances of colloidal solutions is affected by the particle size, but also, as described earlier, strongly by the shape of the nanoparticles as illustrated by Tian et al. who compared SERS efficiencies of gold nanoparticles of similar size but different shapes.⁵⁰ Figure 5 presents SEM images of the three types of particles studied and the corresponding SERS spectra of Rhodamine 6G (R6G) used as SERS probe in the different colloidal solutions. They observed that SERS intensity was increasing in the sequence nanospheres < nanospheres aggregates < nanotriangles < nanostars due to the increase in number and strength of local field hotspots at the nanoparticles' sharp edges and tips.

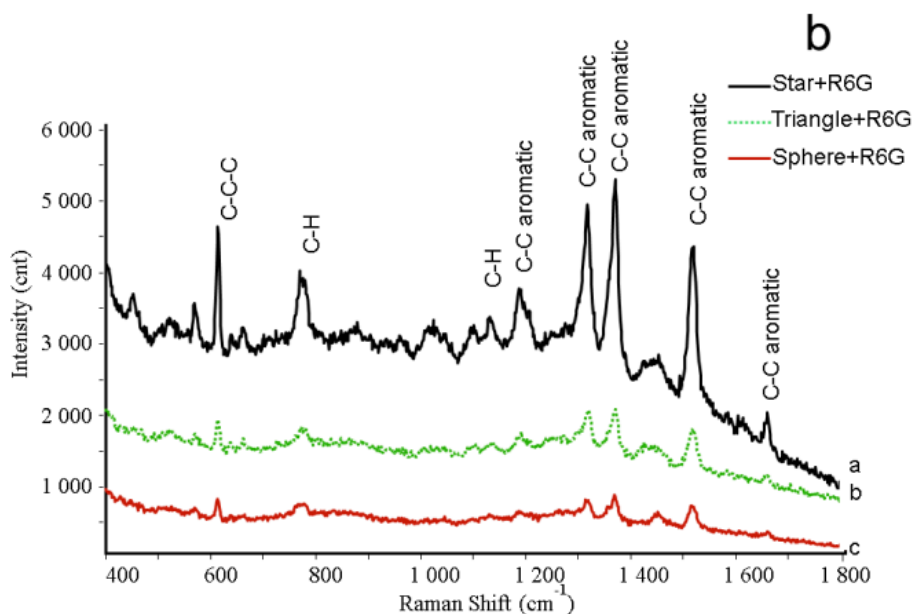
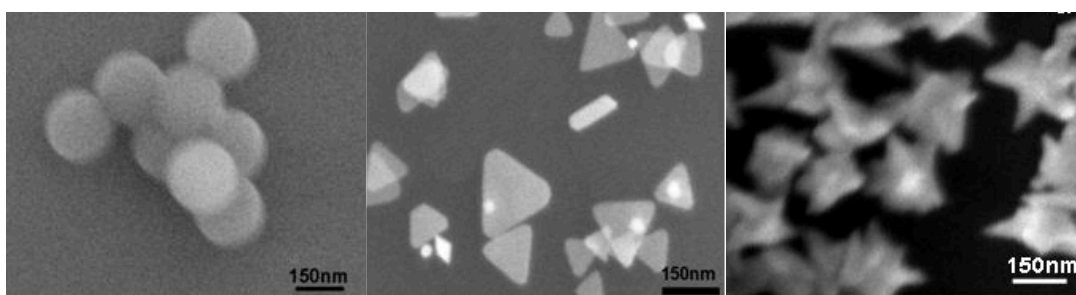


Figure 5 : SEM images of gold nanospheres (top left), nanotriangles (top middle) and nanostars (top right) synthesized to study the effect of particle shape on SERS efficiency. (Bottom) Corresponding SERS spectra of 5 μM R6G in solutions of gold nanostars (black), nanotriangles (green) and aggregated nanospheres (red) at a concentration of 3×10^9 particles/mL. Figure adapted from reference.⁵⁰

Metallic colloidal suspensions have been used in analytical measurements for the detection of aromatic compounds such as drugs, as they exhibit strong Raman scattering cross sections. For example, Alharbi et al. synthesized silver colloids by reducing silver nitrate with a solution of trisodium citrate and used it for the detection of nicotine and its metabolite cotinine and trans-3'-hydroxycotinine.⁶³ They noticed that best SERS intensities were respectively obtained for different pH depending on the analyte. They managed to simultaneously and accurately quantify the three analytes for concentrations ranging from 10^{-7} to 10^{-5} M without recourse to lengthy chromatography.

More recently, the same group used silver hydroxylamine colloid to detect and quantify the opioid tramadol in artificial urine.⁶⁴ They observed that no aggregating agent or pH modification was necessary as the complexity of the medium rich in salt allowed for particles aggregation, increasing thus the SERS efficiency. They estimated the limit of detection to be 2.5×10^{-6} M, which is close to the levels typically found in individuals who use tramadol for pain relief.

SERS using silver nanoparticles in solution has also been used to detect derivatives of banned substances such as 5,6-methylenedioxy-2-aminoindane (MDAI), which is a cheaper alternative to the illegal 3,4-Methylenedioxymethamphetamine (MDMA).⁶⁵

As mentioned previously, metallic colloidal solutions of particles with varied shape and size obtained by physical or chemical methods can be used for SERS application in solution by adding directly the sample to be studied to the colloidal suspension and focus the laser spot inside the suspension. However, they can also be immobilised onto metallic or non-metallic surfaces to form another type of SERS substrate.

1.5.2 Nanoparticles immobilised on solid substrates

Immobilizing nanoparticles on solid substrates is a means to promote aggregation of the particles to achieve improved SERS properties as previously described. Different means have been reported in the literature to concentrate metallic particles on substrates of different types.

One simple, physical way that has been explored is the use of filters such as alumina or paper. Walsh and Chumanov used the properties of an alumina filter silver coated by vapor deposition to preconcentrate dilute analytes at the platform surface for SERS measurements.⁶⁶ Colloidal solutions of nanoparticles can also be impregnated into filter paper as reported by He et al.⁶⁷ or can be drop cast onto flexible adhesives as described lately by Chen et al.⁶⁸ in their work on rapid detection of pesticides residues in fruits and vegetables, facilitating their use for swabbing samples and increase their collection efficiency comparatively to rigid substrates. Another physical way has been developed recently by McCann et al. who described a novel technique to deposit gold nanoparticles onto Cyclic Olefin Polymer (COP).⁶⁹ The technique based on pulsed laser deposition in ambient pressure conditions leads to the deposition of nanostructured

films on the substrate, for which plasmonic properties can be tuned when changing the laser parameters such as laser fluence and scan speed during the ablation process.⁷⁰

Metal nanoparticles can also be strongly immobilized at solid substrates using a chemical tether. This technique has been widely used to bind gold and silver nanoparticles to quartz or metal substrates and several examples are available in the literature with technique differing depending on the substrate to be bonded to. For example, di-mercapto compounds have been used to bind metallic nanostructures directly to metal surfaces such as described by Bibikova et al. who used α - ω -dimercapto polyethylene glycol (SH-PEG-SH) to immobilize gold nanostars at a silicon substrate via a thin layer of gold.⁷¹ Binding nanostructures to silicon based substrates without intermediate metallic layer was also achieved with the intermediate of organosilane compounds such as (3-mercaptopropyl) trimethoxysilane (MPTMS) or (3-aminopropyl) trimethoxysilane (APTMS) that can bind on silica through silanization and to metallic nanoparticles by the other end directly or after conjugation, as described by Kamińska et al. in their work using SERS to study protein interaction or by Péron et al. in the fabrication of such substrate for the detection of polycyclic aromatic hydrocarbon compounds in artificial sea-water.^{72,73} However, the chemistry in these approaches can sometimes yield undesirable spectral background.

The different unordered arrays reported generally show very high Raman enhancement but often suffer from a lack of reproducibility in the SERS signal within a single substrate and between substrates fabricated following the same procedure which is a significant limitation.

1.5.3 Direct nanolithography or template-based substrates

Directly fabrication processes for SERS substrates, such as nanolithography techniques, can yield highly ordered substrates. These top-down approaches have the advantage they can reproduce a large range of desired morphologies. For example, Chirumamilla et al. used Electron beam (e-beam) Lithography (EBL) and reactive-ion etching (RIE) to fabricate 3D Nanostar Dimers with a Sub-10-nm Gap for single/few-molecule SERS.⁷⁴ Figure 6 illustrates the remarkable nanostructures that can be fabricated as an array. Gopalakrishnan et al. used similar structures in a ring cavity for the detection of rhodamine and adenine at extremely low density up to the limit of few molecules.⁷⁵ Through excellent hot spot localisation and homogeneity they could reach enhancement factor of the order of 4×10^{10} with SERS signal deviating from no more

than 10 % among a same sample reused several times. However, despite presenting the strong ability to control size and shape of the fabricated nanostructures, such fabrication techniques among with Focused Ion Beam (FIB) lithography for example are of very high-cost and time-consuming.

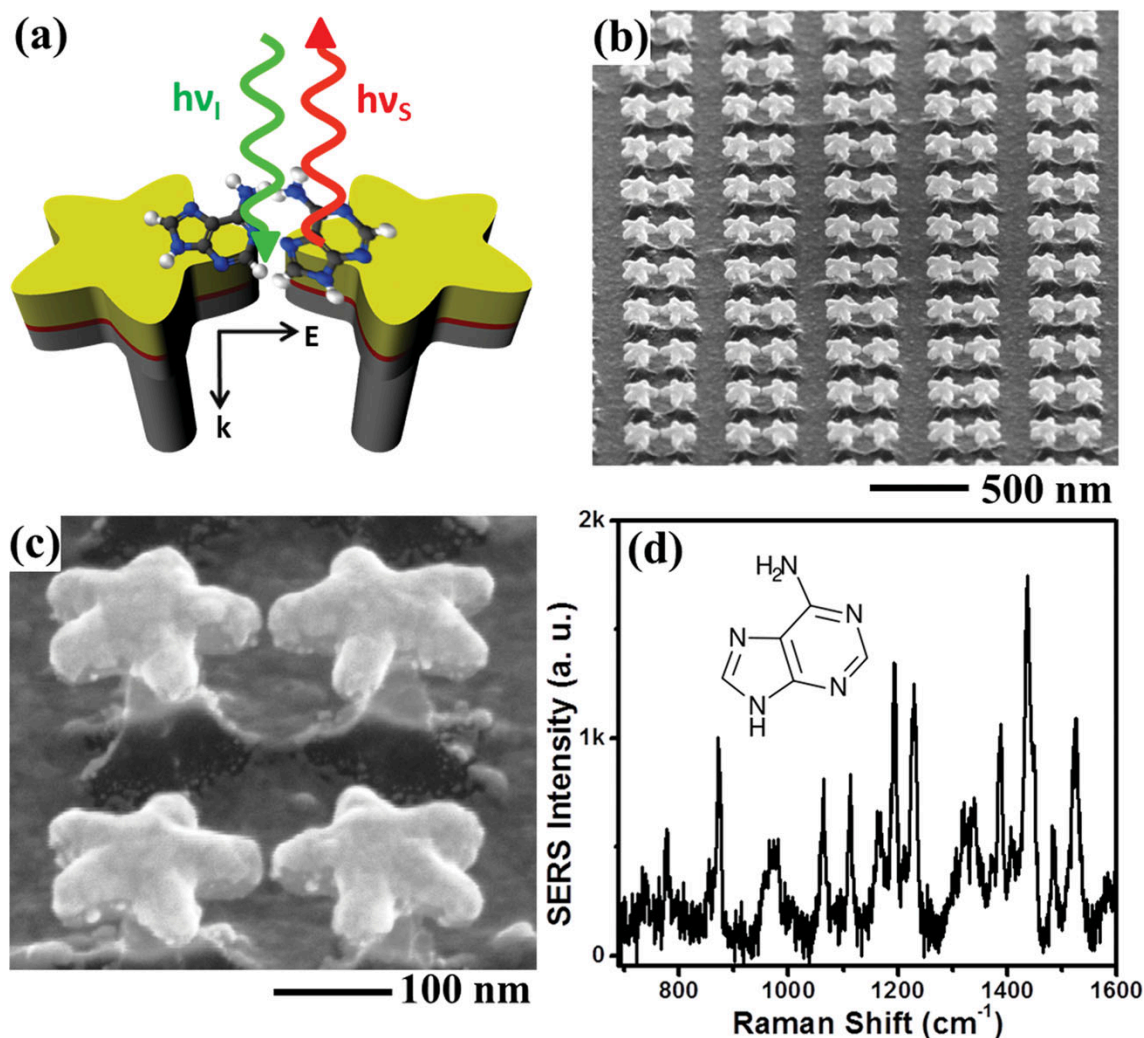


Figure 6 : a) Illustration of the SERS working principle for a free-standing 3D nanostar dimer. E and k are the electric field and wavevector, respectively. $h\nu_i$ and $h\nu_s$ represent the incoming and scattered photon energy, respectively. b,c) SEM images at a 52° tilted view of the nanostar on silicon pillar dimers with a 6-nm inter particle spacing and 150-nm Si pillar height. d) Raman spectrum recorded from adenine that was chemisorbed from a solution at 1 pM concentration. The k in the intensity scale denotes 1000. Insert: chemical structure of adenine. Figure reproduced from reference.⁷⁴

An alternative to those techniques is Nanoimprint lithography (NIL) and Nanosphere lithography (NSL) described more in details in the next section regarding nanovoids platforms for SERS. These methods allow for a higher throughput, as less

time consuming and more cost effective than EBL or FIB, still allowing for fabrication of nanostructures in periodic arrays with good SERS properties. For example, Wang et al. used NSL and wet etching to fabricate pyramid, ridged-hexagon and quasi-triangle nanostructures generating enhancement factor of the order of 10^6 to 10^7 with good reproducibility.⁷⁶

1.5.3.1 Nanovoids platforms for SERS

This section of the literature review focuses on fabrication and work done regarding nanostructured surfaces with similar morphologies to the ones used in this thesis. Keyes group have used such arrays in recent works for the assessment of artificial lipid membranes.⁷⁷⁻⁷⁹ Indeed, spherical pore array substrates are used as support in the formation of pore-suspended bilayers, creating a cell-membrane like environment for transmembrane proteins with liquid media on either side of the lipid bilayer as explained in section 1.6.4..

Surfaces with negative curvature are relatively less commonly applied to SERS than particles and are reported in literature under different names such as nanocavities, nanoholes, nanowells or nanovoids and are getting increasing attention due to their plasmonic properties similar to metal nanoparticles, but with the added advantage that their porous nature offers a capture volume for analyte. Different lithography techniques have been employed in the last decades to control the geometry of highly ordered negative features, such as NSL⁸⁰, soft NIL⁸¹, EBL^{82,83} or FIB milling.⁸⁴

Brolo et al. used FIB to fabricate 200 nm diameter hole arrays onto a glass substrate presenting a gold film of 100 nm thickness and illustrated in Figure 7.⁸⁴ High reproducibility of substrate architecture is enabled in such arrays due do the highly specialized equipment which allow a good control of the periodicity of the pattern. The same research group used such substrates to do SERS measurement of oxazine 720 adsorbed at the gold nanohole array and reported strong enhancement of the SERS signal for this molecule, attributed to surface plasmon resonance of the nanohole array combined with internal electronic resonance from the adsorbed molecules.⁸⁵ However, Raman signal intensity from R6G and pyridine adsorbed at similar arrays was found to be very weak, indicating that electronic resonance from the molecule probed is needed, and that nanostructures alone were not sufficient to obtain high enhancement of

Raman signal, thus narrowing down the panel of molecules that could be studied at those arrays.

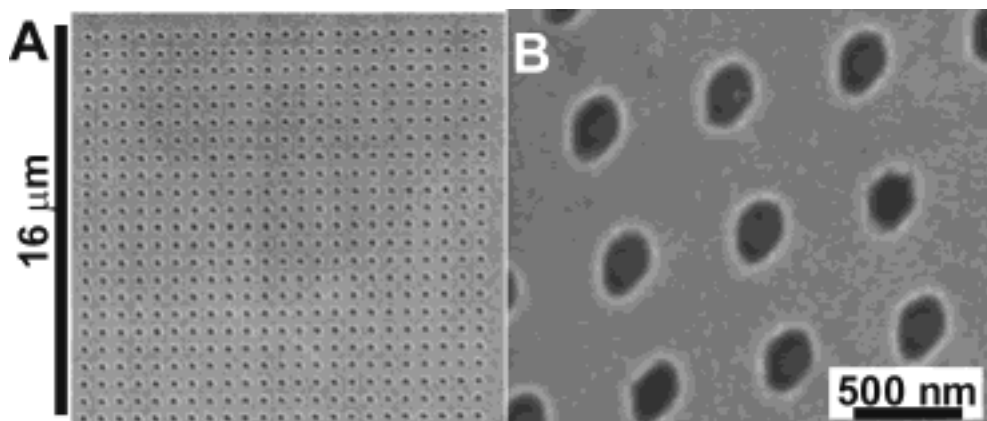


Figure 7 : SEM image of 200 nm diameter hole array onto a glass substrate presenting a 100 nm thick gold film. Array was patterned using focused ion beam milling technique. Figure reproduced from reference.⁸⁴

EBL was also used to fabricate arrays with similar topology. Yue et al. studied the dependence effects on edge-to-edge distance on gold nanoholes.⁸⁶ Arrays were fabricated by spin coating a 150 nm thick layer of PMMA onto a silicon wafer. After e-beam writing, the pattern was developed, and a 30 nm layer of gold was evaporated onto the substrate surface with an electron beam evaporator. The SERS performance of the fabricated arrays was assessed using 4-Mercaptopyridine adsorbed at their surface. Nanohole diameter was kept constant at 85 nm and edge-to-edge distance was varied from 55 nm to 205 nm in 50 nm increments. It was found that the enhancement factor increased exponentially when the edge-to-edge distance decreases, probably due to the strengthened electric field across the edges through coupling between adjacent nanostructures.

More recently, Wu and Lin assessed arrays fabricated in a similar manner with 4-mercaptobenzoic acid as SERS probe, but varied both diameter of the nanoholes and the structures spacing.⁸⁷ Gold nanohole arrays were here fabricated on a Fluorine doped Tin Oxide (FTO) glass substrate with a ZEP-520 thickness of 300 nm as positive electron beam resist, and uniformly coated 50 nm thin gold film. Despite the fact that the arrays were of different dimensions compared to Yue et al., consistent observation of dependence effect on edge-to-edge distance was observed with enhancement factor increasing as nanoholes became closer at a constant diameter. However, enhancement

factor increased considerably, going from 10^4 to 10^6 , when increasing the diameter of the nanohole from 125 nm to 562 nm while keeping the edge-to-edge distance constant, as illustrates the SERS spectra in Figure 8. Here, this observation could be explained by a larger SERS-active area for bigger diameter nanoholes combined to Surface Plasmon Resonance (SPR) red shifting as the diameter increases and matching progressively the excitation wavelength.

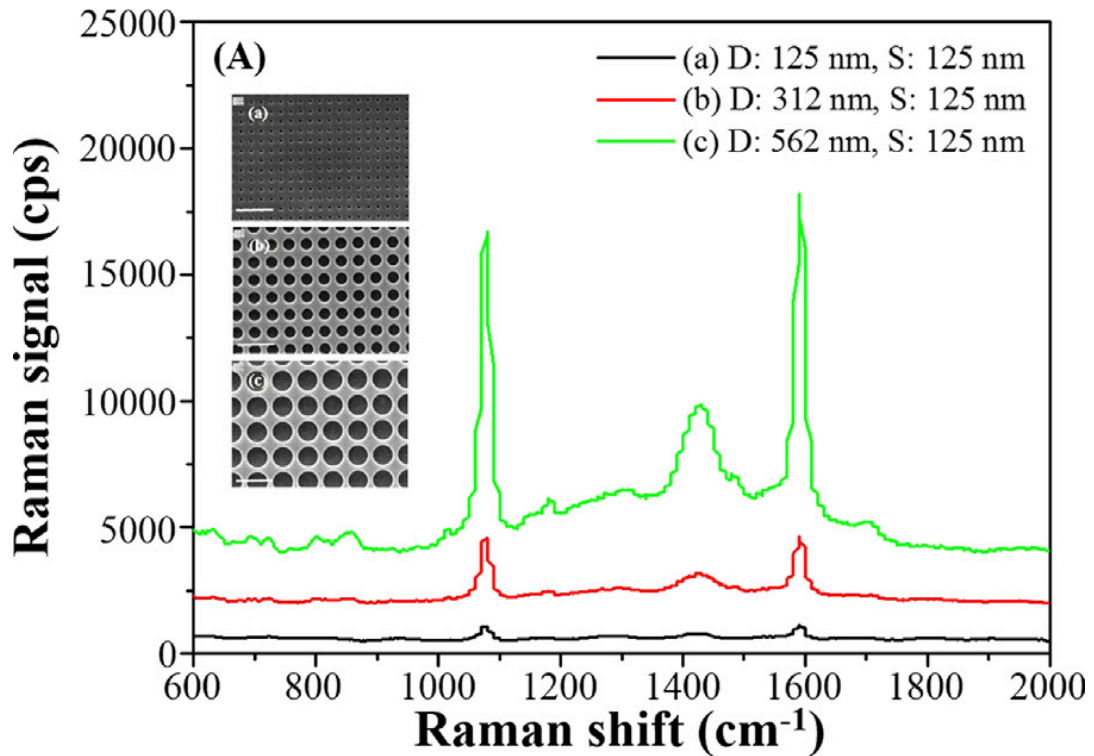


Figure 8: SERS spectra of 4-Mercaptobenzoic acid adsorbed at gold nanohole arrays with different structures diameter D and a constant edge-to-edge distance of 125 nm. SEM images of the tested arrays are displayed on the figure (top: $D = 125$ nm; middle: $D = 312$ nm; bottom: $D = 562$ nm). Figure reproduced from reference.⁸⁷

With a higher throughput, NIL has been used to pattern materials at the nanoscale over large areas.⁸⁸ This technique allows the replication of features on a hard or soft stamp in a thermoplastic or UV-curable polymeric material by embossing or moulding. Depositing a metal film on the resulting polymeric replicas produces plasmonic structures useful for chemical and biosensing applications. Baca et al. fabricated nanowells in a layer of photocurable epoxy SU8 and evaporated a 40 nm layer of gold onto the substrate giving it plasmonic properties, as illustrated in Figure 9.⁸¹ Those substrates were assessed using benzene thiol as SERS probe adsorbed at the

gold surface and showed stable SERS response over a long period with high reproducibility of signal intensity and enhancement factor ranging from 10^4 to 10^5 .

More recently, Ding et al. developed an aluminium spherical-shaped nanovoid array substrate by combining nanoimprint lithography of etched polymer/silica opal films with electron beam evaporation.⁸⁹ The resulting structures were used for the detection of the DNA base adenine in aqueous solution by UV-SERS and showed enhancement of the Raman signal by more than three orders of magnitude compared to planar substrates.

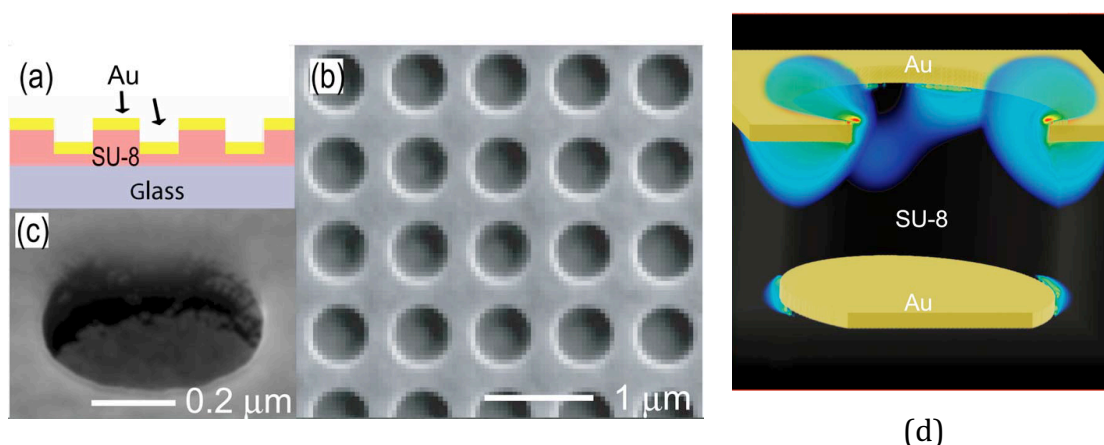


Figure 9: (a) Schematic cross-sectional view of a molded plasmonic crystal for use as SERS substrate. (b) SEM image of a representative plasmonic nanoarray ($D = 0.514 \mu\text{m}$, $P = 0.760 \mu\text{m}$, and a depth of $0.360 \mu\text{m}$). (c) High resolution SEM image of a single nanohole. (d) Calculated electric field intensity at 821 nm for $D = 0.514 \mu\text{m}$ and $P = 0.760 \mu\text{m}$. Figure adapted from reference.⁸¹

Finally, although presenting different morphology than the nanostructured substrates presented in this section, plasmonic well-ordered inverted pyramids could also act as liquid reservoir in a similar way to spherical cavities. However, regarding our intended application to a suspend lipid membrane at its aperture, a question remains about the square edges that might not be suitable and hinder the stability of the bilayer, if ever it manages to form. Figure 10 illustrates the commercially available inverted pyramid array in Klarite™ from Mesophotonics, Ltd.⁹⁰ Pyramidal shaped pits are etched into silicon with dimensions calculated to generate localized plasmons and thus show SERS properties once coated with gold. Such plasmonic substrates present both Propagating Surface Plasmon Resonance (PSPR) and Localized Surface Plasmon Resonance (LSPR) and have demonstrated good SERS detection capability. Botti et al.

recently used it to detect nitro-based explosives, providing reproducible detection limits of tens of picograms with enhancement factor in the range of 10^6 for trinitrotoluene.⁹¹

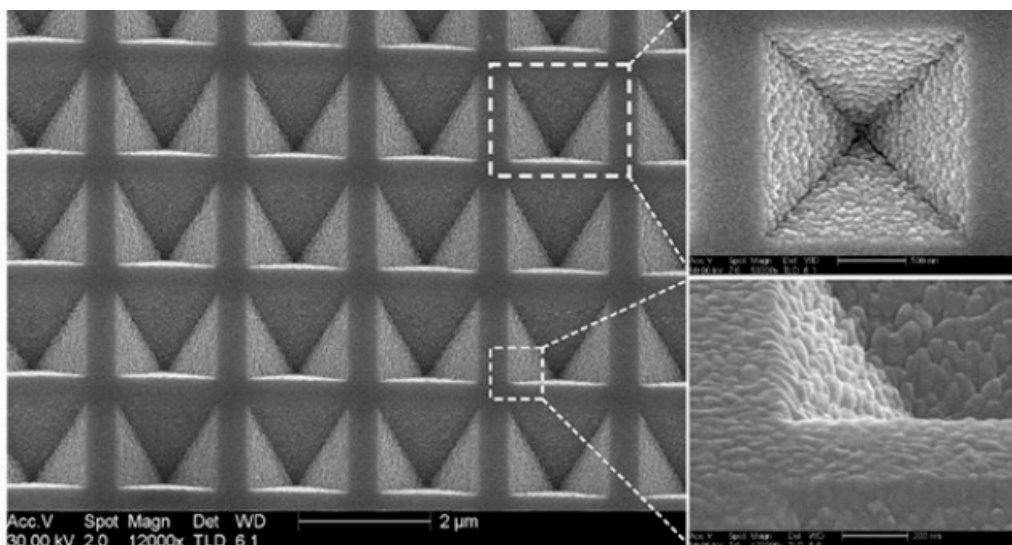


Figure 10 : SEM image illustrating the well-ordered inverted pyramids in Klarite™ substrates from Mesophotonics, Ltd. Figure adapted from reference.⁹⁰

Among all these techniques, NSL remains a technique widely used due to its simplicity, low cost and very high throughput compared to other lithographic methods previously described. This versatile hybrid bottom-up procedure has been employed to fabricate periodic spherical nanovoids by several groups. As described in this thesis, with careful optimization it is possible to make ordered arrays that extend over tens of millimetres on rigid or flexible substrates and that have SERS reproducibility sample to sample and across a sample to rival platforms prepared using expensive electron beam lithographic methods. Flexible arrays have been produced combining soft lithography and nanosphere lithography. A colloidal solution of polystyrene (PS) nanosphere is left to dry onto a solid surface substrate such as glass and Polydimethylsiloxane (PDMS) is subsequently poured and cured on top of the sphere template. After chemically removing of the spheres from the cured polymer, a thin metal layer is sputtered on top of the bowl-shaped nanovoids, making the substrate SERS active. Kahraman et al. studied the optical properties of such substrates by tuning the diameter and depth of the voids using different sizes of PS spheres.⁹² They showed that SERS enhancement factors of 10^6 magnitude could be reached and were dependent on the plasmon absorption wavelength and laser wavelength used during

the experiments, as the position of the surface plasmon absorption varied with the nanostructures' dimensions. Lately, our group showed that controlling size but also shape of the surface features could affect the optical properties of the array.^{93,94} Stretching the flexible polymer template lead to cuboidal voids, with absorbance maxima shifted compared ones for the spherical cavities.

Rigid arrays are nevertheless more reported in the literature, probably due to their ease to be tuned in term of size and shape of the wells. As in the fabrication method described for the flexible arrays, the general procedure is to first drop coat a colloidal solution of PS spheres as described by Bartlett et al.⁹⁵ or SiO₂ spheres as described by Xu et al.⁹⁶ of desired diameter at the surface of a conductive substrate. The nanospheres self-assemble in an ordered pattern and metal can then be electrodeposited around the spheres template. After dissolution by sonication in a suitable solvent, spheres are removed from the template and lead to the SERS active periodic nanovoid substrate. The size, shape and spacing of the wells can be controlled through the choice of the sphere used as a mask and the thickness of the metal film deposited, and thus can be tuned to obtain optimized plasmonic properties. Bartlett and co-workers are probably the group that has conducted the most extensive study regarding the optical properties of such metallic nanocavity arrays. They reported that for a single size of sphere used, varying the film thickness allows to tune the plasmon and thus modify the SERS properties of the array as illustrated in Figure 11.⁹⁷ For example, best enhancement of 3×10^6 for a monolayer of benzenethiol adsorbed at the gold nanocavity array surface was obtained for a thickness of gold of $\approx 0.6d$, with d being the diameter of the template sphere of 900 nm., when excited under 1064 nm light. They also conducted deep theoretical studies regarding the presence of different surface plasmons mode on gold nanocavity arrays with different thicknesses and reported the presence of both Bragg and Mie plasmons at the array surface.⁹⁸

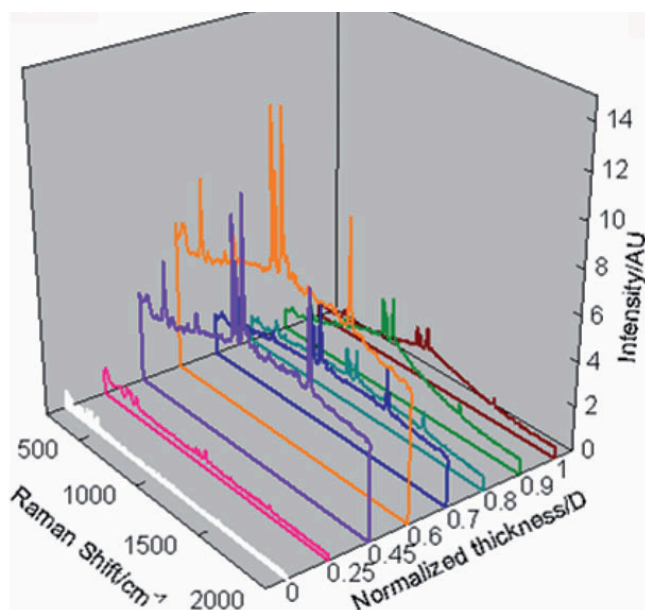


Figure 11 : Raman spectra of a benzenethiol monolayer adsorbed at gold cavity arrays made with template sphere of 900 nm diameter and presenting different film thicknesses. Figure adapted from reference.⁹⁷

Overall, diverse techniques have been reported for the fabrication of SERS substrates, each with respective advantages and drawbacks. In their review, Brown and Milton compared the relative performance of different types of SERS structures in terms of characteristics essential for useful scientific and commercial applications. This summary is presented in Table 1. They conclude that in general, structured NPs provide higher enhancement than structured surfaces, but structured surfaces show greater reproducibility both within and between structures. It seems then that NSL seems a good compromise to more expensive and lower throughput lithographic techniques such as EBL or FIB to achieve good SERS intensity and reproducibility.

Table 1 : Comparison of the relative performance of the types of structures in terms of characteristics essential for useful scientific and commercial applications. All the columns are of relevance with respect to the utility of structures in industrial applications, whereas the five columns on the right-hand side are of most importance for scientific research. Estimated performance with respect to each characteristic decreases in the order: ✓✓ > ✓ > ✓/x > x > xx. Table reproduced from reference.²⁸

Approach	Method	Performance characteristic							
		Ease of preparation	Cost of preparation	Ease of use	Large substrate sizes possible	Spot-to-spot reproducibility	Substrate-to-substrate reproducibility	Enhancement factor	Stability
Structured nanoparticles	Free nanoparticles	✓✓	✓✓	✓✓	xx	xx	✓/x	✓✓	✓/x
	Clustered nanoparticles in liquid phase	✓	✓✓	✓✓	✓	xx	✓/x	✓	✓/x
	Templated nanoparticles	✓	✓✓	✓	✓	x	✓	✓	✓/x
	Structured array of nanoparticles	✓/x	✓	✓/x	✓✓	✓/x	✓	✓	✓
	Structured (multi-)layers of tethered nanoparticles	✓/x	✓	✓/x	✓	✓	✓	✓	✓
Structured surfaces	Unstructured metal surface	✓✓	✓✓	✓✓	✓✓	xx	xx	x	✓✓
	Chemically roughened metals surface	✓✓	✓✓	✓✓	✓✓	✓/x	✓/x	✓/x	✓
	Electro-chemically roughened metal surface	✓	✓✓	✓✓	✓✓	✓/x	✓	✓	✓/x
	Lithographically produced surfaces	x	x	✓	✓/x	✓✓	✓✓	✓✓	✓✓
	3D structured surfaces	x	✓/x	✓/x	✓	✓	✓✓	✓✓	✓

1.6 Lipid bilayers models

As the key focus of this work is the assembly of a bilayer containing microfluidic device, the state of the art of model membranes is briefly outlined here.

1.6.1 Black Lipid Membranes

In the early 1960's, Mueller et al. reported the first single black lipid membrane model in aqueous solution and studied its electrical and optical properties.⁹⁹ After extracting lipid membranes from ox brain in a chloroform-methanol mixture, the membrane solution was painted under water over a 1mm diameter hole of a polyethylene substrate, forming interference colours visible under reflected light with a microscope. Thinning of the painted lipid membrane by evaporation or diffusion of the organic solvent lead to the appearance of black areas attributed to a single bilayer membrane, which is the origin of their name: Black Lipid Membranes (BLM). The membrane formation method used by Mueller has been used since without major modification and BLMs are still widely formed by painting a solution of phospholipids (1%-2%) dissolved in an organic solvent, such as n-decane, over a Teflon or polyethylene aperture smaller than 1mm diameter and filled with an aqueous solution, as illustrated in Figure 12.

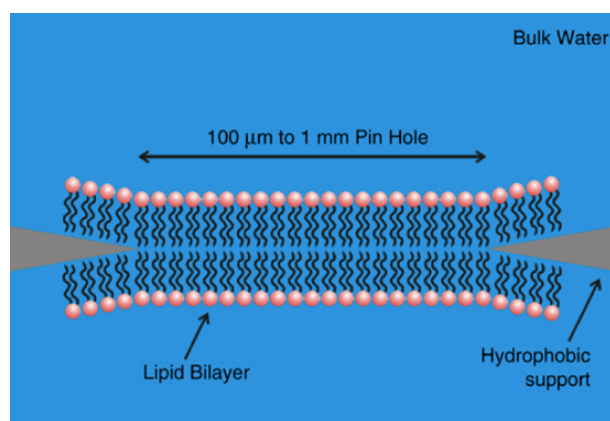


Figure 12 : Schematic of a Black Lipid Membrane painted over a 100 μm to 1 mm aperture of a hydrophobic substrate. Image reproduced from reference.¹⁰⁰

Disadvantages include their poor inherent stability, the use of organic solvent which is impossible to completely eliminate from the layer the fact that BLMs tend

to be multilayers rather than true bilayers. The latter two dramatically reduce their biomimicry.

Lately Zhu et al.¹⁰¹ studied the stability of BLMs over different pores sizes using EIS. His group proved that BLMs formed over smaller aperture pores (200nm diameter) were more stable than over larger apertures (700nm diameter) bringing its lifetime to at least 6 days, however the incorporation of more complex structures within the bilayer such as gramicidin was reducing drastically the lifetime of the membrane to a single day.

1.6.2 Liposomes

Liposomes can be described as closed bilayer vesicles, which spontaneously form during the dispersion of phospholipids in water. They can be classified by their size and the number of bilayers constituting a single vesicle, also called lamellarity.¹⁰²

Multilamellar vesicles (MLVs) are usually ranging between 0.2 and 50 μ m diameter and can contain up to 20 concentric bilayers. Therefore, they are not constituting a good cell membrane model as their structure can prevent molecular binding and sees interaction of the inner bilayers. By sonicating or extruding MLVs through a polycarbonate membrane of a specific porosity, unilamellar vesicles can be obtained.¹⁰³ Small Unilamellar Vesicles (SUVs) with diameter up to 100nm and Large Unilamellar Vesicles (LUVs) and ranging from 100nm up to few μ m can be distinguished by their size. Those liposomes present an asymmetry in their structure due to the nature of their curvature, as the inner leaflet present less lipids. One drawback in the formation process of SUVs and LUVs is their polydispersity below the size of the pores of the membrane used, which can potentially affect experimental results. SUVs tends to be more stable than LUVs due to their small sizes.

Another type of liposomes ranging from 10 to 100 μ m diameter can be formed by electroformation.¹⁰⁴ Those Giant Unilamellar Vesicles (GUVs) have been widely used a model membranes system as they are of similar size range as cells and are free of any sort of supporting surface. However due to their size they present a poor stability and are limited in their composition due to non-possibility to make them asymmetric.¹⁰²

1.6.3 Supported Lipid Bilayers

SLBs, or solid-Supported Lipid Bilayers (SLBs) are defined as a continuous lipid bilayer on a planar substrate. SLBs are typically true bilayers, simple to prepare, and have dramatically improved stability compared to BLMs. The success in forming SLBs over flat surfaces is mainly dependant on the characteristics of the substrate as it must be hydrophilic, be smooth and clean. Widely reported substrates are silica, borosilicate glass or mica¹⁰⁵⁻¹⁰⁷, as they allow the easily formation of SLBs over a thin water layer at their surface (10-20Å).¹⁰⁰

Three general methods can be used to form SLBs as illustrated in Figure 13:

- Langmuir-Blodgett (LB) method (lower leaflet) followed by the transfer of a second monolayer (upper leaflet) by Langmuir-Schaefer (LS) method.
- Or (b) adsorption and fusion of SUVs from an aqueous suspension onto the surface of the substrate.^{108,109}
- The third method (c) is a combination of the above two previous method, consisting of forming the lower leaflet of the bilayer by Langmuir-Blodgett method followed by vesicles disruption to form the upper leaflet.¹¹⁰

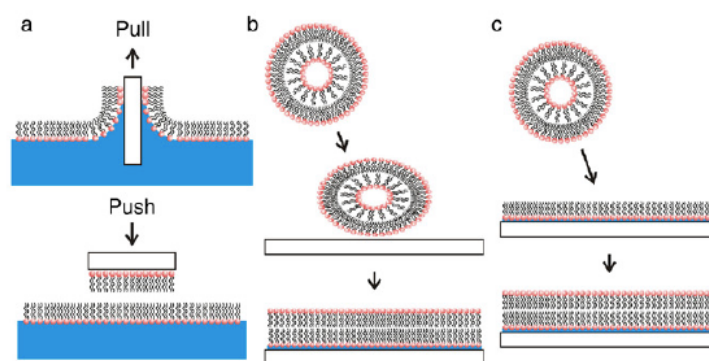


Figure 13 : Schematic illustrating the general techniques for the formation of supported lipid bilayers. (a) Langmuir-Blodgett / Langmuir-Schaefer; (b) Adsorption and vesicles fusion; (c) Langmuir-Blodgett / Vesicles fusion. Image reproduced from reference.¹⁰⁰

Although SLBs are robust and stable due to the proximity of the lower leaflet of the bilayer to the substrate (typically 2.5 to 5 nm water intervenes), the lipid bilayer tends to interact with the support.

This interaction dramatically reduces lipid mobility (at both leaflets) compared with liposomes and generally makes SLBs unsuitable for reconstitution of transmembrane proteins, as there is insufficient volume below the bilayer to enable cytoplasmic tails to assume proper orientation within the membrane leading also to immobility and conformational loss due to surface interactions.

Two approaches have been explored to increase volume between the bilayer and the substrate:

- Polymer cushioned lipid bilayers

Polymer spacers are used between the membrane and the solid support to increase the distance between them and prevent immobilisation or denaturation of transmembrane proteins, as illustrates Figure 14. Different types of polymer have been explored to decouple membrane proteins from the underlying solid substrate, such as dextran on Si/SiO₂ surfaces¹¹¹, cellulose on Indium-Tin-Oxyde electrodes¹¹² or chitosan onto glass substrates.¹¹³ Despite preventing interaction between the membrane and the substrate, it has been noticed that the polymer used as a cushion could have interactions with the membrane, which could be a limitation to their use.

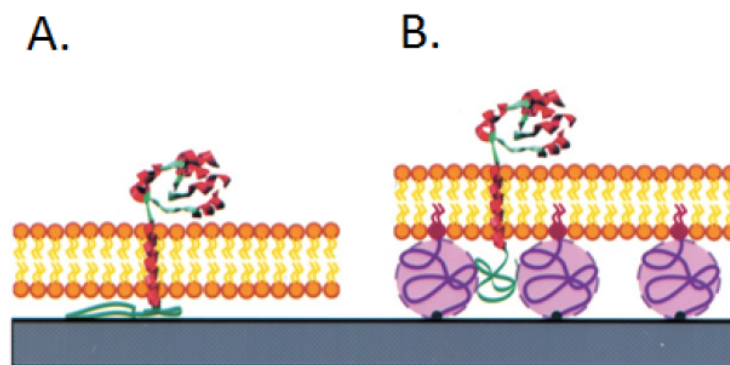


Figure 14 : Schematic representation of a trans-membrane protein into supported lipid bilayer without (a) and with polymer cushion (b). Image reproduced from reference.¹¹⁴

- Tethered lipid bilayers

Another approach with the same final aim has also been developed as an alternative route to polymer cushion lipid bilayer. This method consists to covalently tether the lipid to the supporting substrate by the intermediate of a self-assembled monolayer, for example thiolated compounds on gold^{115,116} or silanes on silicon.

1.6.4 Pore suspended Lipid Bilayers

Pore suspended lipid bilayers are a potentially powerful approach to yield useful artificial cell membranes. Our group and others have demonstrated that lipid membranes suspended over cavities can overcome many of the drawbacks of SLBs and BLMs while keeping their advantages in terms of versatility and stability in the case of SLBs.

Microcavity-Supported Lipid Bilayers (MSLBs) have the advantage of eliminating the interaction of the bilayer with the underlying support while conserving the stability and robustness of the membrane, which are critical parameters. A free-standing membrane over aqueous pores permits the reconstitution of transmembrane proteins while allowing retention of lateral mobility. Whereas many prior reports have focussed on nanopores and on solvent free systems, our group have focussed on SLBs over micron dimensions pores that are buffer filled. With apertures greater than 1 μm diameter, this facilitates the use of optical techniques and permits the studies of membrane transporter proteins as the system gives access to the buffer either side of the bilayer, which allows a more representative natural environment of the cell.^{77-79,117,118}

Such a model has been reported by Osborn and Yager, with monolayers transferred to a grid by Langmuir-Blodgett method. More recently, Heinemann and Schwille described a technique that consists in electrostatically enhance bursting of GUVs over a functionalised silicon grid with pores of 2.5 μm diameter apertures.

Table 2 summarizes the most commonly used membrane models with their controllable parameters, their advantages and drawbacks.

Table 2 : Overview of the most commonly used membrane model system. (Adapted from reference¹⁰²)

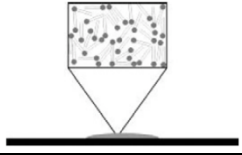
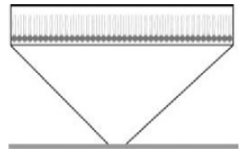
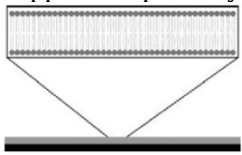
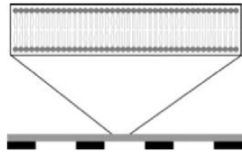
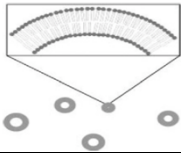
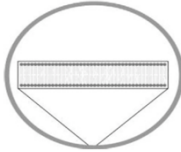
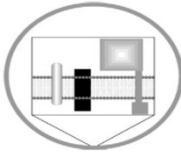
Experimental approach	Controllable parameters	Major advantages	Major disadvantages
Protein-lipid overlay 	<ul style="list-style-type: none"> - lipid composition 	<ul style="list-style-type: none"> - fast and easy to perform - relative high throughput 	<ul style="list-style-type: none"> - lipid presentation in non-physiological context - difficult to quantitate - variable deposition efficiency - susceptibility to removal during the incubation and wash cycles
Monolayers 	<ul style="list-style-type: none"> - lipid composition - tunable lateral pressure 	<ul style="list-style-type: none"> - defined geometry of lipid assembly (flat membrane) - homogeneity of the system - accessibility to fluorescence (confocal) microscopy, FCS, Brewster angle microscopy, AFM (after transfer to support) 	<ul style="list-style-type: none"> - single leaflet presentation - requirement for relatively large amount of protein. - restricted to planar lipid monolayers
Supported lipid bilayers 	<ul style="list-style-type: none"> - lipid composition - incorporation of integral proteins/compounds - membrane curvature/patterning 	<ul style="list-style-type: none"> - flat geometry - asymmetric lipid distribution is amenable - accessibility to broad range of biophysical methods (e.g. AFM, TIRF, SPR) - accessibility of both leaflets (polymer-cushioned systems) 	<ul style="list-style-type: none"> - interactions with support may result in restricted fluidity of lipids and segregation between the leaflets (partially overcome in polymer-cushioned systems) - possible defects within a bilayer
Pore-suspending membranes 	<ul style="list-style-type: none"> - lipid composition - incorporation of integral proteins/compounds 	<ul style="list-style-type: none"> - flat geometry - asymmetric lipid distribution is amenable - suitable for broad range of biophysical methods (particularly for conductance measurements, fluorescence microscopy) - accessibility of both leaflets 	<ul style="list-style-type: none"> - reduced stability comparing to SLB - presence of residual organic solvents (primarily in BLMs)

Table 2 : Continued.

<p>Liposomes</p> 	<ul style="list-style-type: none"> - lipid composition - membrane curvature/lipid packing (vesicle size-dependent) - incorporation of integral proteins/compounds 	<ul style="list-style-type: none"> - simple preparation procedure - free-standing membrane - compatibility with multiple methodical approaches 	<ul style="list-style-type: none"> - possible polydispersity in terms of size and multilamellarity - symmetric lipid distribution - size below optical resolution - only one leaflet accessible
<p>GUVs</p> 	<ul style="list-style-type: none"> - lipid composition - membrane tension - membrane deformation can be induced (deflation, tubulation) - incorporation of integral proteins/compounds 	<ul style="list-style-type: none"> - micrometer-scale structure - free-standing membranes - microscopically accessible - compatibility with multiple methodical approaches 	<ul style="list-style-type: none"> - heterogeneity in lipid composition at the individual specimen level - increased fragility compared to SUVs and LUV
<p>Giant Plasma Membrane Vesicles (GPMVs)</p> 	<ul style="list-style-type: none"> - protein content by overexpression 	<ul style="list-style-type: none"> - relatively high population homogeneity - micrometer-scale structure - free-standing membranes - complex lipid and protein composition - microscopically accessible 	<ul style="list-style-type: none"> - undefined lipid and protein composition - chemically induced crosslinking of lipids and proteins - possible depletion of specific lipid classes

1.7 Lipid bilayers in microfluidic devices

Platforms that permits study of the biophysical behaviour of the cell membranes away from the complexity of the cell will give a better understanding of the cell environment, in particular they can be used to understand interactions of the cell membrane with molecular and larger species which gain entry to the cell through the membrane including drugs, drug delivery vehicles and pathogens. Robust models' membrane will benefit health research. Indeed, the development of complex artificial lipid bilayer on chip, integrating protein membranes, represents a highly sensitive molecular sensor and drug screening application.¹¹⁹

Trying to reproduce artificially a simplified model of the cell environment in a microfluidic device is a significant challenge as the implementation of the bilayer, which is fluidic and an inherently fragile structure, is critical, but doable if few parameters are considered, such as the material used and the structure of the device. Although relatively early in the development over past two decades, standard laboratory procedures described previously have been implemented in microfluidic devices to attempt artificial reproduction of the cell membrane. This review presents the three main strategies found in the literature.

1.7.1 Supported lipid membranes

Several research groups have managed to form and study supported lipid membranes in microfluidic devices. A key objective in reported work, as an attempt to overcome their drawbacks described previously, is forming them for example onto gel substrates that would act as an ion reservoir. Ide et al.^{120,121} reported the formation of a lipid bilayer over an agarose layer allowing simultaneous optical and electrical recording of single molecule bonding to single channel proteins.

Other techniques have been reported into microfluidic devices using the principle of tethered lipid bilayers by creating on the substrate a self-assembled monolayer of molecule such as thiolipids used by Dorvel et al.¹²² on gold surfaces. The molecule assembled at the surface of the substrate will bind to the lipid molecules or to the ion channel within the membrane, anchoring the lipid bilayer to the substrate and improving thus its stability.

1.7.2 Suspended lipid membranes

As described previously in section 1.6.4, suspended lipid membranes have an advantage over supported lipid membranes, which is the accessibility of the fluidic environment either sides of the bilayer. Most improvements in the last decade regarding those type of membranes were done to prevent manual intervention for painting BLM using the classic method and trying to form BLM following automatable procedures as described for example by Suzuki et al.¹²³ Various approaches have been developed and improved to date to perform the formation of such lipid membranes. To overcome the drawback of the presence of solvent in BLMs described previously, liposomes have been commonly used and vesicles were disrupted over aperture of porous membranes.¹¹⁹ However, such systems show their limits for electrical study as the electrical seal between the solvent-free membrane and the porous support is poor leading to higher level of electrical current leakage compared to solvent containing membranes. Finally, another atypical procedure was recently proposed by Malmstadt et al.¹²⁴ using the porous properties of PDMS to absorb solvent from a lipid-solvent mixture through the wall of the microfluidic device. Thinning of the solvent layer from the mixture trapped between two aqueous solutions was performed by bringing in contact two lipid monolayer and forming thus a solvent free lipid bilayer anchored at the PDMS walls.

1.7.3 Alternative lipid membranes microsystems

Alternative techniques to supported and suspended lipid membranes have also been developed based on droplet manipulation. Funakoshi et al.¹²⁵ proposed two PMMA based microfluidic devices, where droplet-interface-bilayers (DIBs) are formed by contacting two monolayers assembled at the interface between water and an organic solvent. However, optical studies of those droplet-based lipid bilayers are challenging due to their vertically aligned formation in the microfluidic devices, as illustrated in Figure 15.

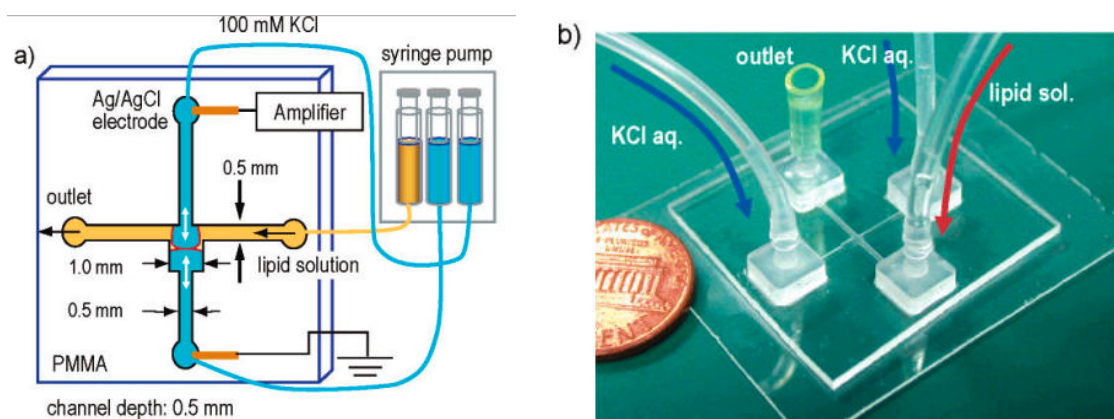


Figure 15 : Schematic (a) and photograph (b) of a PMMA based microfluidic device proposed by Funakoshi et al. where a droplet-based lipid bilayer is formed at the cross section of channels. Image extracted from reference.¹²⁵

1.8 SERS of lipids

SERS as a structural method is useful for interrogating lipid bilayers and as it is a label free technique that allows for direct and sensitive detection of structures such as proteins and lipid bilayers. It has the advantage over Fourier-transform infrared spectroscopy (FTIR) of low sensitivity to water so well suitable to aqueous biological samples study. Efforts aimed at increasing enhancement, reproducibility and biocompatibility of SERS substrates employed to detect liposomes, exosomes and cells have been made in the last decade.

Meuse et al. were the first to report the use of SERS for the analysis of lipids.¹²⁶ Using an electrochemically roughened silver rod functionalised with an alkanethiol SAM as SERS substrate, they show the formation of a well ordered, non-interdigitated monolayer of phospholipids on the thiols, with the hydrophilic head of the lipid orientated away from the metal surface. This solid supported lipid system categorised as hybrid bilayer membranes, due to the lipid monolayer at the thiols layer, has been frequently used since for studying the structure and function of cell membranes.

Coupling metal nanoparticle to such system allows for dramatical field enhancement necessary to investigate dynamics of lipid membranes, such as drug molecules intercalating into the bilayer. Using this field enhancement, Levin et al. observed the insertion of ibuprofen molecules into hybrid lipid bilayer formed at gold nanoshells surface.¹²⁷ More recently, Driver et al. synthesized small gold citrate capped nanoparticles over which were prepared hybrid bilayer membrane. Those substrates demonstrated good SERS properties and were used to study lipid oxidation over time.

Taylor et al. used what they called a “nanoparticle-on-mirror” geometry to strongly enhance the local optical field and reduce the volume probed to a few nm³, as illustrates Figure 16.¹²⁸ With such platforms, they managed to collect long time sequences of individual lipids flexing within the membrane, with gauche/trans conformational change of the alkane tail.

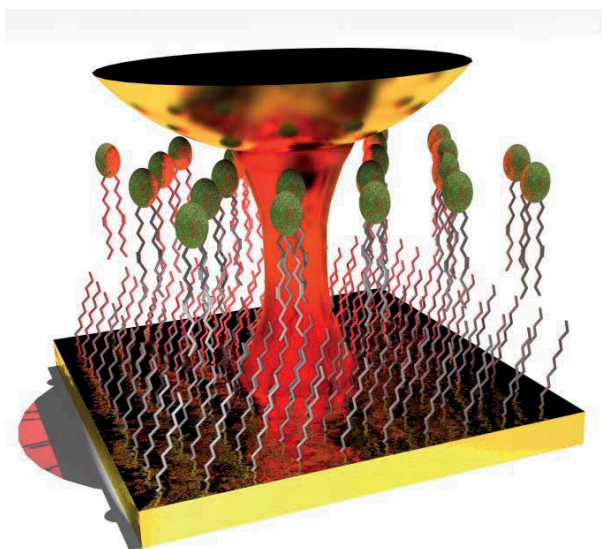


Figure 16: Schematic of a “nanoparticle-on-mirror” geometry. Gold nanoparticle placed extremely close to a gold mirror on which a hybrid bilayer membrane has been formed. Figure reproduced from reference.¹²⁸

On a larger scale, Tip-enhanced Raman Spectroscopy (TERS) was used on mixed lipid monolayer to study phase separated lipid domains. Opilik et al. used the gap between an Atomic Force Microscopy (AFM) silver tip and a template-stripped gold substrate to strongly enhance Raman signal of the studied lipids.¹²⁹ This configuration allowed them to image macroscopic behaviour such as lateral distribution of a binary mixture of phospholipids.

SERS also allowed to study lipid phase transition using hybrid lipid membranes on gold nanoparticles¹³⁰ or adsorbing directly lipid bilayer at gold nanorods surfaces as did Matthews et al.¹³¹ More recently, this group used such SERS active nanostructures to probe the structure of the lipid membrane at their surface but also the position and orientation of tryptophan intercalated in the lipid membrane.¹³²

Calculating electromagnetic field at the nanorods by Finite Element Method (FEM) numerical simulations and molecular polarizability of the lipids and tryptophan by Time Dependent Density Functional Theory (TDDFT), combined to SERS and Raman spectra allow them to conclude structural information in lipid system.

To study membrane-protein interactions, SERS has been coupled to electrochemistry techniques. Milo et al. used AC Voltammetry and EIS in combination with Surface Enhanced Resonance Raman Spectroscopy (SERRS) measurement to study the interaction between the human enzyme cytochrome P450 2D6 and a Hybrid bilayer membrane at a roughened silver electrode.¹³³ More recently, Karabali et al. report the first Electrochemical Surface Enhanced Raman Spectroscopy (EC-SERS) investigation of protein aggregate-biomembrane interaction.¹³⁴ They monitor the interaction between insulin amyloid aggregates implicated in Alzheimer's disease at various stage of aggregation and a supported lipid bilayer at silver nanoparticles screen printed electrodes. However, hybrid bilayer membranes and supported lipid bilayer formed directly at metal surfaces present restricted lateral diffusion due to interaction with the substrate as explained earlier in section 1.6.3.

Kühler et al. used the properties of borosilicate glass to limit this issue for a simple lipid membrane. They reported a plasmonic gold nanoantenna array for SERS of lipid molecules embedded in a bilayer membrane as illustrated in Figure 17.¹³⁵ Gold nanotriangles were fabricated by colloidal lithography using PS spheres onto borosilicate glass substrate and evaporating gold at their interstitial spaces. A 1,2-dioleoyl-sn-glycero-3-phosphocholine (DOPC) bilayer presenting 1 % fraction of Rhodamine lipids was then span at the substrate surface. The thin water layer trapped between the lipids and the solid substrate effectively lubricates the lipids and allow for the fluidity of the membrane.¹³⁶ The probe molecules that are mobile within the membrane could then enter the hot spot created at the nanotriangles gap and be detected by SERS without adsorption to the substrate.

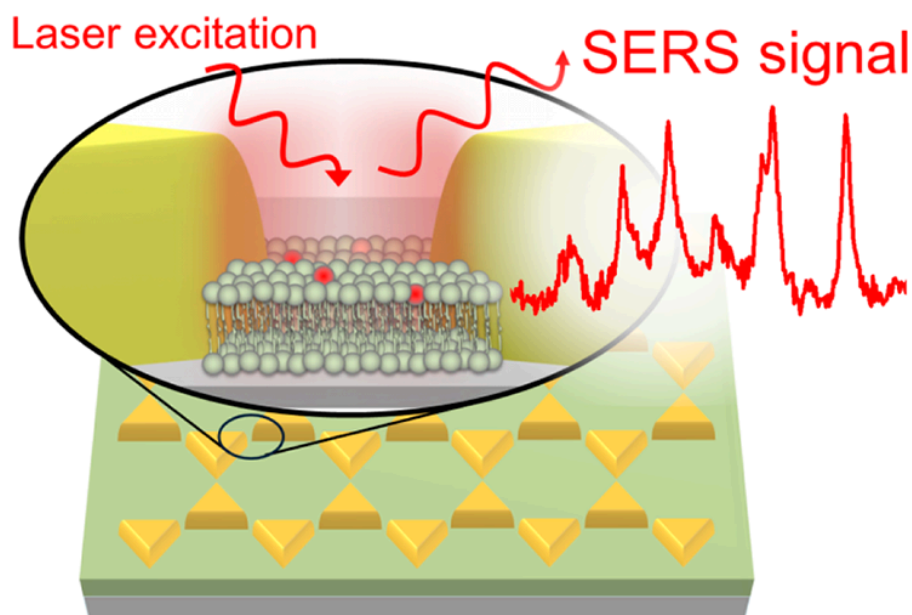


Figure 17 : Combination of plasmonically coupled nanotriangles with a fluid lipid membrane on a solid support. Laser illumination near the LSP resonance gives rise to a strong field enhancement between the tips of adjacent triangles, which can be employed for SERS measurements. Figure reproduced from reference.¹³⁵

More recently, Bruzas et al. reported a silica sol-gel method for LSPR characterization of fluid SLBs over silica-coated gold nanodisks.¹³⁷ Lately, the group managed to adapt this method to a silver film-over-nanospheres (AgFON) for characterisation of fluid SLBs using SERS.¹³⁸ 300 nm diameter silica beads were dispersed at a glass coverslip surface, coated with 200 nm of silver by electron beam physical vapor deposition and finally silica sol-gel spin-coated before deposition of 100 nm lipid vesicles at its surface. Presence of the lipid bilayer at the silica-coated AgFON's surface was verified by AFM measurement and its fluidity using fluorescence recovery after photobleaching (FRAP). Lipids mobility was further assessed using fully protonated and deuterated lipids and monitoring lipids exchange kinetics by SERS. SERS measurement of fluid lipid bilayers on the silica-protected metal nanostructures were found to be reproducible and showed enhancement factor of 8×10^4 .

1.9 SERS in microfluidic devices

SERS has the advantage over other analytical methods to give information both on the concentration but also on the molecular structure of the sample through fingerprint data. With good enhancement, high sensitivity offers this technique potential for use in bioanalytical applications in the field of life science, where, due to

sample rarity or high cost, low volumes are required. In such instances SERS can be combined with microfluidics. This section gives a brief overview of recent developments and advancements in combining SERS into microfluidic devices.

1.9.1 Metal colloids-based microfluidics-SERS platform

Due to their commercial availability, colloidal solutions of metallic nanoparticles are accessible SERS active substrates to use in microfluidic devices. Using this type of device provides an efficient monitoring platform while improving the SERS technology. Indeed, continuous flow could dissipate heat and remove molecules photodamaged by the use of high-power laser. In the last decade, efforts were put on trying to enhance the SERS signal intensity, for example by trapping nanoparticles and analyte at the detection area or forming on-demand nanoparticles aggregates. Several mechanical ways are reported in the literature to create on-demand aggregation of SERS active particles and analytes at the detection area.

Zhou et al. reported a microfluidics-SERS platform for the detection of bovine serum albumin (BSA).¹³⁹ The device consisted of a T-shaped channel and two modified PDMS pneumatic valves. By fabricating nanopost arrays at the bottom of the fluidic channel, the special valve could close partially allowing fluid going through and blocking completely the used gold nanoparticles, forming thus an aggregate in front of the valve and creating SERS-active sites for SERS measurements. When releasing the valve, nanoparticle aggregates could be flushed and renewed for multiple detection.

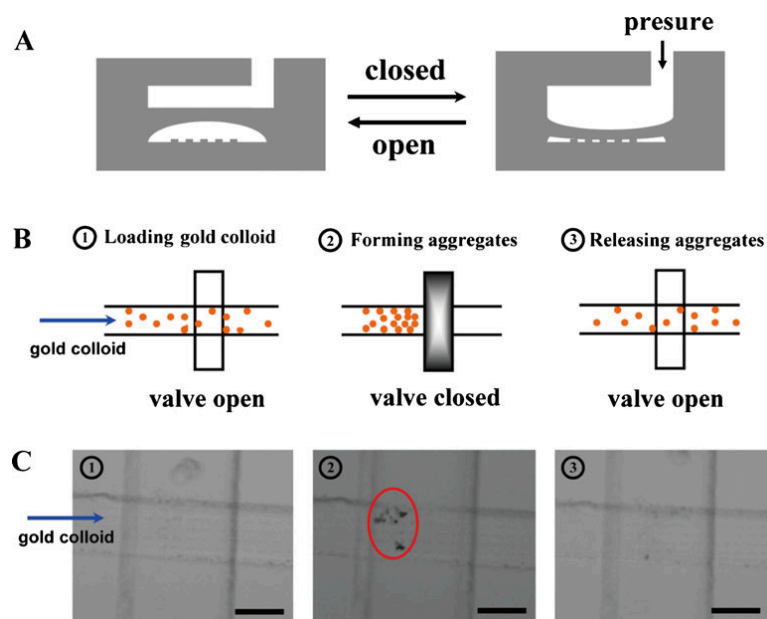


Figure 18: Trapping and releasing 250 nm gold nanoparticles by closing/opening microvalve. (A) Schematic image showing the closed/open states of the modified microvalve; (B) schematics showing the trapping and releasing process of gold nanoparticles. (C) Pictures that correspond to the steps of (B). The circled numbers show the order of the pictures, and each picture corresponds to the schematics in (B) with the same number. The scale bars are 100 μm . Figure reproduced from reference.¹³⁹

Another example is a system developed by Gao et al. for the detection of the anthrax biomarker poly- γ -D-glutamic acid (PGA) in solution using a SERS-based solenoid microfluidic sensor.¹⁴⁰ The system, illustrated in Figure 19, is based on the SERS measurement of PGA after competitive immuno-assay in a dual channel microfluidic device containing a sensing and a control channel, and trapping the immunocomplexes by yoke-type solenoids embedded in the channel. Competitive reaction occurs only in the sensing channel, where antigen-conjugated gold nanoparticles used as “SERS nano-tags” compete with the free antigen to bind at the sites on the anti-body-conjugated magnetic beads used at supporting substrates. Decrease in the SERS intensity of the immunocomplexes is observed as the concentration of PGA in serum increases. The control channel helps here to improve the reliability of the device, where PGA-free serum is injected, acting thus as an internal standard for the analysis. Here the authors combined the advantages of antibody-antigen binding reactions to immobilize conjugated gold nanoparticle at conjugated magnetic beads, and the advantage of magnetic separation allowing to concentrate the

SERS active particles at the detection area, increasing the sensitivity of the measurement by creating an on-demand particles aggregation.

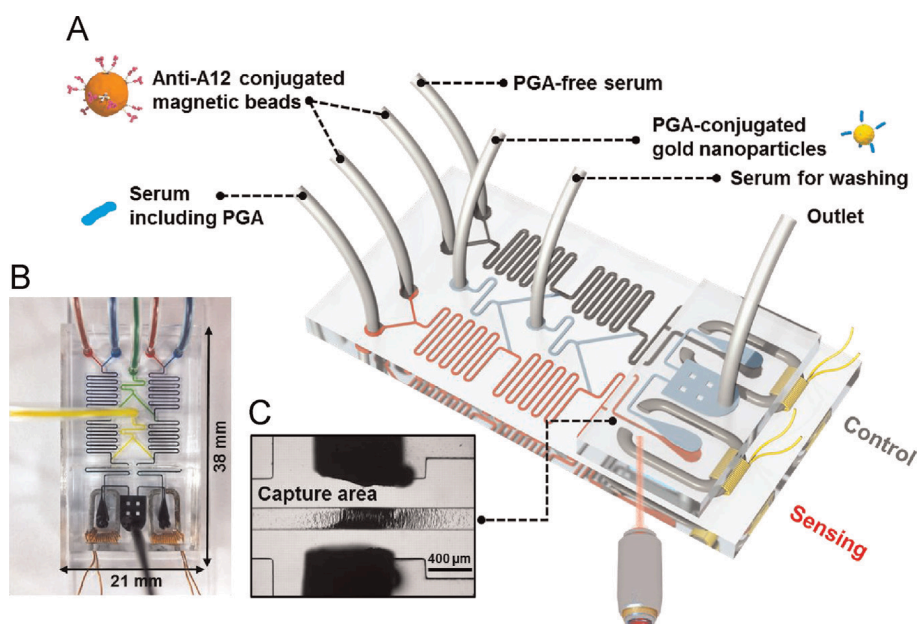


Figure 19 : Schematic illustration of the solenoid-embedded dual channel microfluidic sensor for SERS-based competitive immunoassay. The sensor is composed of two parallel channels: one for PGA sensing (light gray) and the other for control (dark gray). (B) Optical images of the solenoid chip filled with four different colors of inks. (C) Photograph of the capture area for magnetic immunocomplexes. Figure reproduced from reference.¹⁴⁰

1.9.2 Nanostructured solid substrate microfluidics-SERS platform

1.9.2.1 In-situ fabrication

A convenient way to achieve in-situ fabrication of nanostructured solid substrate is to immobilize metal nanoparticles at the channel surface. For example, Parisi et al. reported a method for the fabrication of silver nanoparticles within a PDMS microfluidic channel at in-situ electrodeposited Cu nanowalls or pre-patterned by photolithography Cu surfaces.^{141,142} Silver nanoparticles were formed at the Cu surfaces by galvanic replacement of copper by silver ion at room temperature, leading to in-channel SERS active substrates.

In-situ 3D complex nanostructures fabrication on a wide range of materials can also be achieved using femtosecond laser direct writing. Xu et al. reported the in-situ fabrication of silver SERS substrates through photoreduction of silver salt solution at a glass microchannel surface.¹⁴³ Using laser direct writing allowed flexibility in the pattern design of the SERS active substrate regarding its size, shape, and location inside

the microfluidic channel, as illustrated in Figure 20. Later on, using similar method, the same group reported the fabrication of silver microflowers composed of upright nanoplates with nanoparticles on their surface that showed high catalytic activity and SERS enhancement, and allows for monitoring the catalytic reduction of 4-nitrophenol to 4-aminophenol by SERS detection.¹⁴⁴

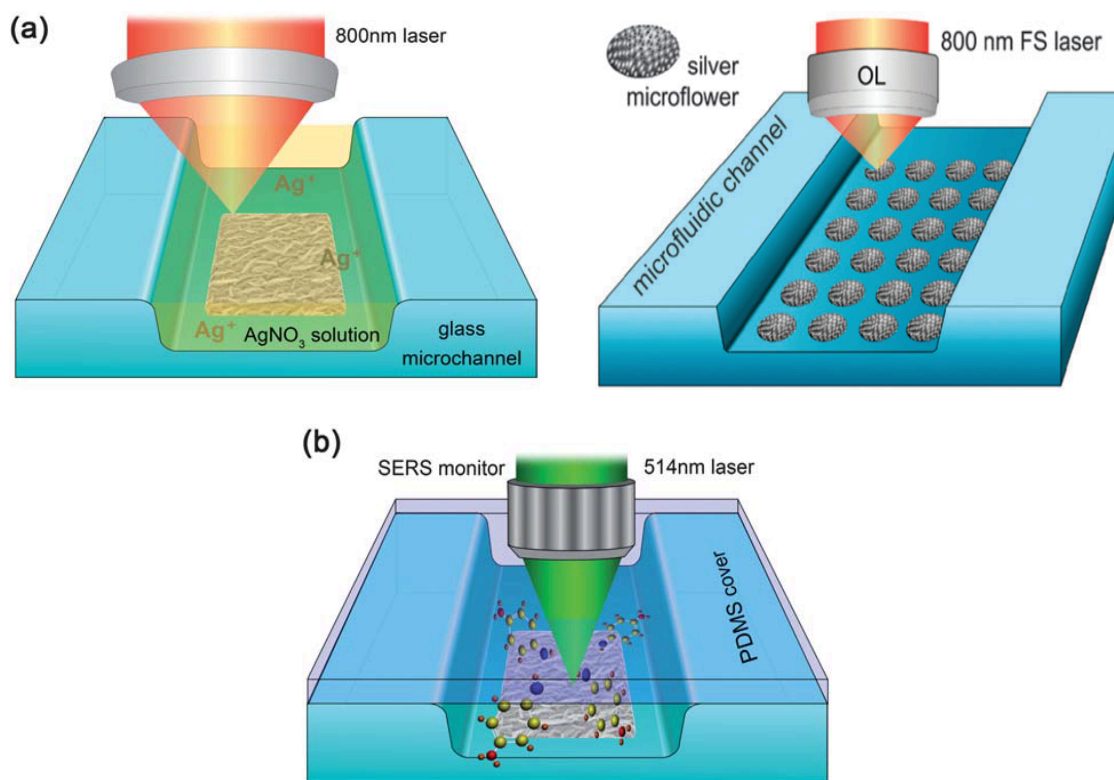


Figure 20: Sketch of femtosecond laser fabrication of the silver SERS substrate inside a microfluidic channel showing the flexibility of the fabrication technique in term of size and shape of the SERS active structure (a), and the application of this SERS monitor for target molecule detection at visible light (514.5 nm) excitation (b). Figure adapted from references.^{143,144}

1.9.2.2 Integrated substrates

An alternative way to fabricate nanostructured solid substrate microfluidics-SERS devices is to implement a pre-fabricated SERS substrate such as presented in sections 1.5.2 to 1.5.3.1 into the microfluidic device. A pre-patterned microfluidic channel can be placed over the SERS platform and bond to close the device. Several examples of such adaptation for ex-situ fabricated SERS structures has been reported in the literature. For example, Vlasko-Vlasov et al. fabricated eight concentric nanoslits on a flat silver substrate using FIB.¹⁴⁵ The SERS substrate was then covered with an 80 μm thick glass slide perforated on two location and which presented an etched elliptic

central part forming a flow channel, creating thus a microscopic plasmon lens. Xu et al. fabricated gratings substrates with tunable periods on a negative tone photoresist, subsequently coated with a 50 nm thick silver layer rendering the gratings SERS active.¹⁴⁶ A PDMS channel prepared by soft lithography was used to cover the SERS substrate and the system was sealed by thermally curing the assembly in a vacuum oven, forming then the microfluidics-SERS device. More recently, Oh and Jeong presented an optofluidic SERS chip, which enabled detection of small molecules with low Raman activity such as dopamine at micromolar level.¹⁴⁷ They used oxygen plasma to roughen a thin silver film evaporated at a PDMS channel surface, thus forming nanotips and nanodots with rich SERS activity. The plasma treatment of both the PDMS substrate and a glass substrate allowed for a permanent bonding between the two materials, leading to a leakage free sealed microfluidic device.

An interesting combination of the two types of microfluidics-SERS platform presented above has been developed by Kamińska et al. for immunoassay application, managing the detection of Hepatitis B virus antigen in human blood plasma.¹⁴⁸ In this work, Au nanoflowers were functionalized first with fuchsin used as a Raman reporter. Hepatitis monoclonal antibody (anti-HBsAg) was then immobilised on the fuchsin using 1-Ethyl-3-(3-dimethylaminopropyl)carbodiimide/ N-hydroxysuccinimide (EDC/NHS) coupling, to form the Raman reporter-labeled immune-Au nanoflowers. In parallel, Au-Ag coated nanostructured GaN substrate was fabricated and functionalised with anti-HBsAg, then surface-blocked with BSA. The capturing substrate was then implemented inside a polycarbonate (PC) microfluidic chip fabricated using Computer numerical-controlled (CNC) milling. Hepatitis B virus surface (HBsAg) antigen in human blood plasma and Raman reporter-labeled immuno-Au-nanoflowers were sequentially injected into the device for the formation of sandwich immunocomplex, which were detected using SERS by measuring the signal of fuchsin. The use of the Au-Ag coated GaN substrate as the immune solid platform increased the sensitivity and performance of the SERS based immunoassay by exhibiting strong surface enhancement factors and offering large active surface for immune reactions. This combination of metal colloids and nanostructured solid substrate into the microfluidic device allowed to decrease considerably the detection limit compared to the similar immunoassay carried out on an inactive SERS surface. The sequential steps of the presented method are illustrated in Figure 21.

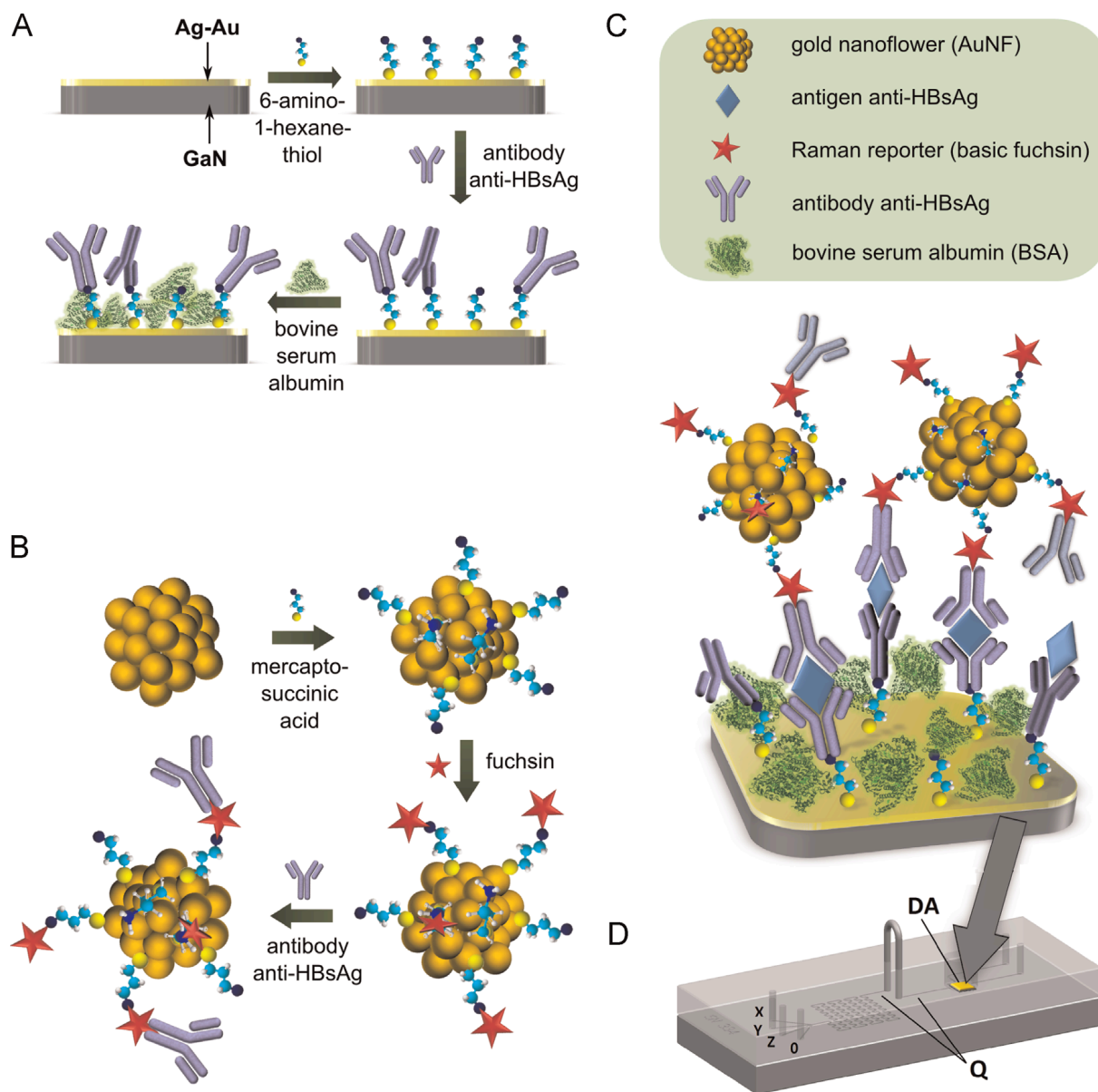


Figure 21 : Sequential steps for the formation of the SERS-based immunoassay. (A) The capturing substrate preparation, (B) the Raman reporter-labeled immuno-Au nanoflowers synthesis, and (C) SERS detection of the sandwich interactions, (D) schematic illustration showing the integration of a microfluidic device with the SERS-active substrate based on Au-Ag coated GaN surface. DA, detection area chamber with GaN/Au-Ag SERS substrate. Figure reproduced from reference.¹⁴⁸

More recently, the group used a similar method with a modified device allowing parallel and simultaneous multiplexed quantification of three interleukins, i.e. IL-6, IL-8, and IL-18, in blood plasma sample using SERS technique.¹⁴⁹ To do so, Au nanoparticles were synthesized and functionalised with three different Raman reporter molecules and associated specific antibodies, which serve as extrinsic label

for each type of interleukin. Using multivariate statistical analysis (Principal Components Analysis), segregation of the three types of studied immunocomplexes encoded by the three types of Raman reporter within mixture was rendered possible. The method presented lead to improvement of the detection limit of the three analytes in comparison to standard ELISA methods and demonstrates again its potential for sensing immune markers in clinical studies.

1.10 Conclusions

The focus of this thesis is on the development of a micro and nano cavity SERS-platforms that are suitable for integration into a microfluidic device. The intended use of the arrays is for lipid membrane study as part of a broader project of our group. A good SERS substrate for biophysical or analytical applications should allow for high sensitivity and reproducibility of the measured signal.

The literature survey reveals first that the intensity and location of the electric field at the metallic nanostructures surface is intimately influenced by the size, shape and intervening space between nanostructures but also by the wavelength of the excitation and its polarization. Reproducibility issues can arise in substrate design and quality but can also be inherent to the SERS technique itself, therefore these influencing parameters need to be taken into consideration during platform development.

This review focuses on different SERS substrates and associated fabrication method available in the literature going from metal NPs in suspension, NPs immobilised at solid substrates, and finally nanolithography- or template-based substrates with a more particular attention to nanovoids platforms in which we are interested. This gives a good overview of the large portfolio of solutions available for SERS substrates that can be used individually or can be combined.

With the intention to use the SERS-microfluidic platform for lipid membrane study, a review of the current state of the art in artificial cell membrane models is given with their advantages and drawbacks, how some groups attempted to implement it into microfluidic devices, and how SERS was applied to their study. It is understood that the cell membrane is a fluidic and fragile structure which needs consideration of specific parameters such as material and structure of the supporting substrate and device.

Finally, recent developments and advancements in SERS-microfluidic platforms are presented showing three trends into the way to combine SERS to microfluidic devices, being the use of metallic colloidal solution as SERS substrate directly inside the device, the fabrication in-situ of nanostructured solid substrates or the implementation of a prefabricated SERS substrate into the microfluidic device.

Micro and nano cavity array are the most suitable substrate in the context of the present project. Indeed, an array will give the advantage to carry multiple SERS acquisitions on the same substrate. However, its fabrication process not being based

on direct nanolithography techniques such as EBL or FIB could lead to some reproducibility issues within or between batches of samples, which needs to be addressed.

In the following chapters I present the development of a micro and nano cavity microfluidic platform designed for lipid membranes study. In chapter 2, I firstly focus on the fabrication of the microfluidic body of the device and the reproducible fabrication via hot-embossing of an optically transparent micro cavity array for potential FCS application to implement into the device. Chapter 3 shows the optimisation of a low-cost method for the preparation of gold micro and nanocavity arrays leading to a more controlled fabrication process and a better homogeneity within and between arrays. FDTD study of the electric field at these plasmonic arrays under different angles of incident light is presented and is verified experimentally for 510 nm diameter cavity array. In chapter 4, the plasmonic properties of the previously optimised arrays are enhanced via nano sub-structuring based on plasma etching. Finally, chapter 5 presents the tailoring of the arrays developed in chapter 3 and 4 into a microfluidic device designed for lipid membrane study.

1.11 References

1. Raman, C. V. & Krishnan, K. S. A New Type of Secondary Radiation. *Nature* **121**, 501–502 (1928).
2. Smith, E. & Dent, G. *Modern Raman spectroscopy: a practical approach*. (J. Wiley, 2005).
3. Ferraro, J. R., Nakamoto, K. & Brown, C. W. *Introductory Raman spectroscopy*. (Academic Press, 2003).
4. Pilot *et al.* A Review on Surface-Enhanced Raman Scattering. *Biosensors* **9**, 57 (2019).
5. Krajczewski, J., Kołataj, K. & Kudelski, A. Plasmonic nanoparticles in chemical analysis. *RSC Advances* **7**, 17559–17576 (2017).
6. Hao, E. & Schatz, G. C. Electromagnetic fields around silver nanoparticles and dimers. *The Journal of Chemical Physics* **120**, 357–366 (2004).
7. Hao, E., Schatz, G. C. & Hupp, J. T. Synthesis and Optical Properties of Anisotropic Metal Nanoparticles. *Journal of Fluorescence* **14**, 331–341 (2004).
8. Petryayeva, E. & Krull, U. J. Localized surface plasmon resonance: Nanostructures, bioassays and biosensing—A review. *Analytica Chimica Acta* **706**, 8–24 (2011).
9. Kneipp, K. *et al.* Single Molecule Detection Using Surface-Enhanced Raman Scattering (SERS). *Physical Review Letters* **78**, 1667–1670 (1997).
10. Kleinman, S. L. *et al.* Single-Molecule Surface-Enhanced Raman Spectroscopy of Crystal Violet Isotopologues: Theory and Experiment. *Journal of the American Chemical Society* **133**, 4115–4122 (2011).
11. Zhan, P. *et al.* DNA Origami Directed Assembly of Gold Bowtie Nanoantennas for Single-Molecule Surface-Enhanced Raman Scattering. *Angewandte Chemie International Edition* **57**, 2846–2850 (2018).
12. Xiong, M. & Ye, J. Reproducibility in surface-enhanced Raman spectroscopy. *Journal of Shanghai Jiaotong University (Science)* **19**, 681–690 (2014).
13. Pettinger, B. Single-molecule surface- and tip-enhanced raman spectroscopy. *Molecular Physics* **108**, 2039–2059 (2010).
14. Le Ru, E. C. & Etchegoin, P. G. Quantifying SERS enhancements. *MRS Bulletin* **38**, 631–640 (2013).
15. Schlücker, S. *Surface Enhanced Raman Spectroscopy*. (Wiley-VCH Verlag GmbH & Co. KGaA, 2011).
16. Ye, J. *et al.* Plasmonic Nanoclusters: Near Field Properties of the Fano Resonance Interrogated with SERS. *Nano Letters* **12**, 1660–1667 (2012).
17. Ko, H., Singamaneni, S. & Tsukruk, V. V. Nanostructured Surfaces and Assemblies as SERS Media. *Small* **4**, 1576–1599 (2008).
18. Banholzer, M. J., Millstone, J. E., Qin, L. & Mirkin, C. A. Rationally designed nanostructures for surface-enhanced Raman spectroscopy. *Chemical Society Reviews* **37**, 885 (2008).
19. Lin, X.-M., Cui, Y., Xu, Y.-H., Ren, B. & Tian, Z.-Q. Surface-enhanced Raman spectroscopy: substrate-related issues. *Analytical and Bioanalytical Chemistry* **394**, 1729–1745 (2009).
20. Lim, D.-K. *et al.* Highly uniform and reproducible surface-enhanced Raman scattering from DNA-tailorable nanoparticles with 1-nm interior gap. *Nature Nanotechnology* **6**, 452–460 (2011).
21. Lee, Y.-J. *et al.* Ultrasoft, Highly Spherical Monocrystalline Gold Particles for Precision Plasmonics. *ACS Nano* **7**, 11064–11070 (2013).
22. Brown, K. R., Walter, D. G. & Natan, M. J. Seeding of Colloidal Au Nanoparticle Solutions. 2. Improved Control of Particle Size and Shape. *Chemistry of Materials* **12**, 306–313 (2000).

23. Xia, Y., Xiong, Y., Lim, B. & Skrabalak, S. E. Shape-Controlled Synthesis of Metal Nanocrystals: Simple Chemistry Meets Complex Physics? *Angewandte Chemie International Edition* **48**, 60–103 (2009).
24. Cialla, D. *et al.* Surface-enhanced Raman spectroscopy (SERS): progress and trends. *Analytical and Bioanalytical Chemistry* **403**, 27–54 (2012).
25. Motl, N. E., Smith, A. F., DeSantis, C. J. & Skrabalak, S. E. Engineering plasmonic metal colloids through composition and structural design. *Chem. Soc. Rev.* **43**, 3823–3834 (2014).
26. McLellan, J. M., Li, Z.-Y., Siekkinen, A. R. & Xia, Y. The SERS Activity of a Supported Ag Nanocube Strongly Depends on Its Orientation Relative to Laser Polarization. *Nano Letters* **7**, 1013–1017 (2007).
27. Fang, J., Liu, S. & Li, Z. Polyhedral silver mesocages for single particle surface-enhanced Raman scattering-based biosensor. *Biomaterials* **32**, 4877–4884 (2011).
28. Brown, R. J. C. & Milton, M. J. T. Nanostructures and nanostructured substrates for surface—enhanced Raman scattering (SERS). *Journal of Raman Spectroscopy* **39**, 1313–1326 (2008).
29. Gopinath, A., Boriskina, S. V., Reinhard, B. M. & Dal Negro, L. Deterministic aperiodic arrays of metal nanoparticles for surface-enhanced Raman scattering (SERS). *Optics Express* **17**, 3741 (2009).
30. Micic, M., Klymyshyn, N., Suh, Y. D. & Lu, H. P. Finite Element Method Simulation of the Field Distribution for AFM Tip-Enhanced Surface-Enhanced Raman Scanning Microscopy. *The Journal of Physical Chemistry B* **107**, 1574–1584 (2003).
31. Kuang, D. *et al.* Modeling the specular spectral reflectance of partially ordered alumina nanopores on an aluminum substrate. *Optics Express* **23**, 4506 (2015).
32. Rajeswari, R. & Jothilakshmi, R. Modeling and Simulation of Plasmonic Nanoparticles Using Finite-Difference Time-Domain Method: A Review. *Materials Science Forum* **781**, 33–44 (2014).
33. Hao, E. & Schatz, G. C. Electromagnetic fields around silver nanoparticles and dimers. *The Journal of Chemical Physics* **120**, 357–366 (2004).
34. Halvorson, R. A. & Vikesland, P. J. Surface-Enhanced Raman Spectroscopy (SERS) for Environmental Analyses. *Environmental Science & Technology* **44**, 7749–7755 (2010).
35. Chen, T. *et al.* Hotspot-Induced Transformation of Surface-Enhanced Raman Scattering Fingerprints. *ACS Nano* **4**, 3087–3094 (2010).
36. Sriram, S. *et al.* Influence of Electric Field on SERS: Frequency Effects, Intensity Changes, and Susceptible Bonds. *Journal of the American Chemical Society* **134**, 4646–4653 (2012).
37. Etchegoin, P. G., Lacharmoise, P. D. & Le Ru, E. C. Influence of Photostability on Single-Molecule Surface Enhanced Raman Scattering Enhancement Factors. *Analytical Chemistry* **81**, 682–688 (2009).
38. Fleischmann, M., Hendra, P. J. & McQUILLAN, A. J. RAMAN SPECTRA OF PYRIDZNE ADSORBED AT A SILVER ELECTRODE. *CHEMICAL PHYSICS LETTERS* **26**, 4.
39. Nedderson, J., Chumanov, G. & Cotton, T. M. Laser Ablation of Metals: A New Method for Preparing SERS Active Colloids. *Applied Spectroscopy* **47**, 1959–1964 (1993).
40. Baladi, A. & Sarraf Mamoory, R. Investigation of different liquid media and ablation times on pulsed laser ablation synthesis of aluminum nanoparticles. *Applied Surface Science* **256**, 7559–7564 (2010).

41. Herrera, G., Padilla, A. & Hernandez-Rivera, S. Surface Enhanced Raman Scattering (SERS) Studies of Gold and Silver Nanoparticles Prepared by Laser Ablation. *Nanomaterials* **3**, 158–172 (2013).
42. Vinod, M. & Gopchandran, K. G. Au, Ag and Au:Ag colloidal nanoparticles synthesized by pulsed laser ablation as SERS substrates. *Progress in Natural Science: Materials International* **24**, 569–578 (2014).
43. Israelsen, N. D., Hanson, C. & Vargis, E. Nanoparticle Properties and Synthesis Effects on Surface-Enhanced Raman Scattering Enhancement Factor: An Introduction. *The Scientific World Journal* **2015**, 1–12 (2015).
44. Turkevich, J., Stevenson, P. C. & Hillier, J. A study of the nucleation and growth processes in the synthesis of colloidal gold. *Discussions of the Faraday Society* **11**, 55 (1951).
45. Lee, P. C. & Meisel, D. Adsorption and surface-enhanced Raman of dyes on silver and gold sols. *The Journal of Physical Chemistry* **86**, 3391–3395 (1982).
46. Dong, X. *et al.* Shape Control of Silver Nanoparticles by Stepwise Citrate Reduction. *The Journal of Physical Chemistry C* **113**, 6573–6576 (2009).
47. Wan, Y. *et al.* Quasi-spherical silver nanoparticles: Aqueous synthesis and size control by the seed-mediated Lee–Meisel method. *Journal of Colloid and Interface Science* **394**, 263–268 (2013).
48. Vitol, E. A., Friedman, G. & Gogotsi, Y. Surface-Enhanced Raman Spectroscopy-Active Substrates: Adapting the Shape of Plasmonic Nanoparticles for Different Biological Applications. *Journal of Nanoscience and Nanotechnology* **14**, 3046–3051 (2014).
49. You, H., Yang, S., Ding, B. & Yang, H. Synthesis of colloidal metal and metal alloy nanoparticles for electrochemical energy applications. *Chem. Soc. Rev.* **42**, 2880–2904 (2013).
50. Tian, F., Bonnier, F., Casey, A., Shanahan, A. E. & Byrne, H. J. Surface enhanced Raman scattering with gold nanoparticles: effect of particle shape. *Anal. Methods* **6**, 9116–9123 (2014).
51. Orendorff, C. J., Gearheart, L., Jana, N. R. & Murphy, C. J. Aspect ratio dependence on surface enhanced Raman scattering using silver and gold nanorod substrates. *Phys. Chem. Chem. Phys.* **8**, 165–170 (2006).
52. Okitsu, K., Sharyo, K. & Nishimura, R. One-Pot Synthesis of Gold Nanorods by Ultrasonic Irradiation: The Effect of pH on the Shape of the Gold Nanorods and Nanoparticles. *Langmuir* **25**, 7786–7790 (2009).
53. Wiley, B., Sun, Y., Mayers, B. & Xia, Y. Shape-Controlled Synthesis of Metal Nanostructures: The Case of Silver. *Chemistry - A European Journal* **11**, 454–463 (2005).
54. Pulit, J. & Banach, M. Does appearance matter? Impact of particle shape on nanosilver characteristics. **6**.
55. Porta, A. L. *et al.* Multifunctional self-assembled composite colloids and their application to SERS detection. *Nanoscale* **7**, 10377–10381 (2015).
56. Jimenez de Aberasturi, D. *et al.* Surface Enhanced Raman Scattering Encoded Gold Nanostars for Multiplexed Cell Discrimination. *Chem. Mater.* **28**, 6779–6790 (2016).
57. Jena, B. K. & Raj, C. R. Seedless, Surfactantless Room Temperature Synthesis of Single Crystalline Fluorescent Gold Nanoflowers with Pronounced SERS and Electrocatalytic Activity. *Chemistry of Materials* **20**, 3546–3548 (2008).
58. Wang, W. & Cui, H. Chitosan-Luminol Reduced Gold Nanoflowers: From One-Pot Synthesis to Morphology-Dependent SPR and Chemiluminescence Sensing. *The Journal of Physical Chemistry C* **112**, 10759–10766 (2008).

59. Dimitrov, A. T., Jordanov, S. H., Popov, K. I., Pavlovic, M. G. & Radmilovic, V. Electrodeposition of Ag from nitrate solutions: Part I. Effect of phosphate ions on morphology. *Journal of Applied Electrochemistry* **28**, 791–796 (1998).
60. Fu, L., Tamanna, T., Hu, W.-J. & Yu, A. Chemical preparation and applications of silver dendrites. *Chemical Papers* **68**, (2014).
61. Ji, J. *et al.* Electrodeposition of Au/Ag bimetallic dendrites assisted by Faradaic AC-electroosmosis flow. *AIP Advances* **4**, 031329 (2014).
62. College of Sciences, Agricultural University of Hebei, Baoding 071001, P.R. China & Li, C. Electrochemical Fabrication of Silver Dendrites as an Excellent Platform for Surface Enhanced Raman Scattering Application. *International Journal of Electrochemical Science* 3252–3262 (2017) doi:10.20964/2017.04.44.
63. Alharbi, O., Xu, Y. & Goodacre, R. Simultaneous multiplexed quantification of nicotine and its metabolites using surface enhanced Raman scattering. *The Analyst* **139**, 4820–4827 (2014).
64. Alharbi, O., Xu, Y. & Goodacre, R. Detection and quantification of the opioid tramadol in urine using surface enhanced Raman scattering. *The Analyst* **140**, 5965–5970 (2015).
65. Mabbott, S., Alharbi, O., Groves, K. & Goodacre, R. Application of surface enhanced Raman scattering to the solution based detection of a popular legal high, 5,6-methylenedioxy-2-aminoindane (MDAI). *The Analyst* **140**, 4399–4406 (2015).
66. Walsh, R. J. & Chumanov, G. Silver Coated Porous Alumina as a New Substrate for Surface-Enhanced Raman Scattering. *Applied Spectroscopy* **55**, 1695–1700 (2001).
67. He, S., Chua, J., Tan, E. K. M. & Kah, J. C. Y. Optimizing the SERS enhancement of a facile gold nanostar immobilized paper-based SERS substrate. *RSC Advances* **7**, 16264–16272 (2017).
68. Chen, J. *et al.* Flexible and Adhesive Surface Enhance Raman Scattering Active Tape for Rapid Detection of Pesticide Residues in Fruits and Vegetables. *Analytical Chemistry* **88**, 2149–2155 (2016).
69. McCann, R. *et al.* Pulsed laser deposition of plasmonic nanostructured gold on flexible transparent polymers at atmospheric pressure. *Journal of Physics D: Applied Physics* **50**, 245303 (2017).
70. Hughes, C. *et al.* Modelling and optimisation of single-step laser-based gold nanostructure deposition with tunable optical properties. *Optics & Laser Technology* **108**, 295–305 (2018).
71. Bibikova, O. *et al.* Towards enhanced optical sensor performance: SEIRA and SERS with plasmonic nanostars. *Analyst* **142**, 951–958 (2017).
72. Kaminska, A., Inya-Agha, O., Forster, R. J. & Keyes, T. E. Chemically bound gold nanoparticle arrays on silicon: assembly, properties and SERS study of protein interactions. *Phys. Chem. Chem. Phys.* **10**, 4172–4180 (2008).
73. Péron, O., Rinnert, E., Lehaitre, M., Crassous, P. & Compère, C. Detection of polycyclic aromatic hydrocarbon (PAH) compounds in artificial sea-water using surface-enhanced Raman scattering (SERS). *Talanta* **79**, 199–204 (2009).
74. Chirumamilla, M. *et al.* 3D Nanostar Dimers with a Sub-10-nm Gap for Single-/Few-Molecule Surface-Enhanced Raman Scattering. *Advanced Materials* **26**, 2353–2358 (2014).
75. Gopalakrishnan, A. *et al.* Bimetallic 3D Nanostar Dimers in Ring Cavities: Recyclable and Robust Surface-Enhanced Raman Scattering Substrates for Signal Detection from Few Molecules. *ACS Nano* **8**, 7986–7994 (2014).

76. Wang, C. G. *et al.* Orientation-dependent nanostructure arrays based on anisotropic silicon wet-etching for repeatable surface-enhanced Raman scattering. **9**.
77. Basit, H., Gaul, V., Maher, S., Forster, R. J. & Keyes, T. E. Aqueous-filled polymer microcavity arrays: versatile & stable lipid bilayer platforms offering high lateral mobility to incorporated membrane proteins. *Analyst* **140**, 3012–3018 (2015).
78. Maher, S., Basit, H., Forster, R. J. & Keyes, T. E. Micron dimensioned cavity array supported lipid bilayers for the electrochemical investigation of ionophore activity. *Bioelectrochemistry* **112**, 16–23 (2016).
79. Berselli, G. B., Sarangi, N. K., Ramadurai, S., Murphy, P. V. & Keyes, T. E. Microcavity-Supported Lipid Membranes: Versatile Platforms for Building Asymmetric Lipid Bilayers and for Protein Recognition. *ACS Applied Bio Materials* **2**, 3404–3417 (2019).
80. Bartlett, P. N., Baumberg, J. J., Birkin, P. R., Ghanem, M. A. & Netti, M. C. Highly Ordered Macroporous Gold and Platinum Films Formed by Electrochemical Deposition through Templates Assembled from Submicron Diameter Monodisperse Polystyrene Spheres. *Chemistry of Materials* **14**, 2199–2208 (2002).
81. Baca, A. J. *et al.* Molded plasmonic crystals for detecting and spatially imaging surface bound species by surface-enhanced Raman scattering. *Applied Physics Letters* **94**, 243109 (2009).
82. Abu Hatab, N. A., Oran, J. M. & Sepaniak, M. J. Surface-Enhanced Raman Spectroscopy Substrates Created *via* Electron Beam Lithography and Nanotransfer Printing. *ACS Nano* **2**, 377–385 (2008).
83. Yue, W. *et al.* Electron-beam lithography of gold nanostructures for surface-enhanced Raman scattering. *Journal of Micromechanics and Microengineering* **22**, 125007 (2012).
84. Brolo, A. G., Gordon, R., Leathem, B. & Kavanagh, K. L. Surface Plasmon Sensor Based on the Enhanced Light Transmission through Arrays of Nanoholes in Gold Films. *Langmuir* **20**, 4813–4815 (2004).
85. Brolo, A. G., Arctander, E., Gordon, R., Leathem, B. & Kavanagh, K. L. Nanohole-Enhanced Raman Scattering. *Nano Letters* **4**, 2015–2018 (2004).
86. Yue, W., Yang, Y., Wang, Z., Chen, L. & Wong, K. C. Surface-Enhanced Raman Scattering on Gold Nanotrenches and Nanoholes. *Journal of Nanoscience and Nanotechnology* **12**, 3018–3025 (2012).
87. Wu, T. & Lin, Y.-W. Surface-enhanced Raman scattering active gold nanoparticle/nanohole arrays fabricated through electron beam lithography. *Applied Surface Science* **435**, 1143–1149 (2018).
88. Stewart, M. E. *et al.* Nanostructured Plasmonic Sensors. *Chemical Reviews* **108**, 494–521 (2008).
89. Ding, T., Sigle, D. O., Herrmann, L. O., Wolverson, D. & Baumberg, J. J. Nanoimprint Lithography of Al Nanovoids for Deep-UV SERS. *ACS Applied Materials & Interfaces* **6**, 17358–17363 (2014).
90. Mosier-Boss, P. A. Review of SERS Substrates for Chemical Sensing. *Nanomaterials (Basel)* **7**, (2017).
91. Botti, S., Cantarini, L., Almaviva, S., Puiu, A. & Rufoloni, A. Assessment of SERS activity and enhancement factors for highly sensitive gold coated substrates probed with explosive molecules. *Chemical Physics Letters* **592**, 277–281 (2014).
92. Kahraman, M., Daggumati, P., Kurtulus, O., Seker, E. & Wachsmann-Hogiu, S. Fabrication and Characterization of Flexible and Tunable Plasmonic Nanostructures. *Scientific Reports* **3**, (2013).

93. Mallon, C. T., Forster, R. J. & Keyes, T. E. Fabrication of gold sphere to cuboid nanoarrays using PDMS templates. *Chem. Commun.* **47**, 7605–7607 (2011).
94. Mallon, C. T., Kho, K. W., Gartite, H., Forster, R. J. & Keyes, T. E. Fabrication and Optical Properties of Periodic Ag Nano-Pore and Nano-Particle Arrays with Controlled Shape and Size over Macroscopic Length Scales. *Advanced Engineering Materials* **20**, 1700532 (2018).
95. Bartlett, P. N., Birkin, P. R. & Ghanem, M. A. Electrochemical deposition of macroporous platinum, palladium and cobalt films using polystyrene latex sphere templates. *Chemical Communications* 1671–1672 (2000) doi:10.1039/b004398m.
96. Xu, L. *et al.* Electrodeposited nickel and gold nanoscale metal meshes with potentially interesting photonic properties. *Chemical Communications* 997–998 (2000) doi:10.1039/b000404i.
97. Mahajan, S. *et al.* Tuning plasmons on nano-structured substrates for NIR-SERS. *Phys. Chem. Chem. Phys.* **9**, 104–109 (2007).
98. Kelf, T. A., Sugawara, Y., Baumberg, J. J., Abdelsalam, M. & Bartlett, P. N. Plasmonic Band Gaps and Trapped Plasmons on Nanostructured Metal Surfaces. *Physical Review Letters* **95**, (2005).
99. Mueller, P., Rudin, D. O., Tien, H. T. & Wescott, W. C. METHODS FOR THE FORMATION OF SINGLE BIMOLECULAR LIPID MEMBRANES IN AQUEOUS SOLUTION. *J. Phys. Chem.* **67**, 534–535 (1963).
100. Castellana, E. T. & Cremer, P. S. Solid supported lipid bilayers: From biophysical studies to sensor design. *Surface Science Reports* **61**, 429–444 (2006).
101. Zhu, Z.-W. *et al.* Electrochemical Impedance Spectroscopy and Atomic Force Microscopic Studies of Electrical and Mechanical Properties of Nano-Black Lipid Membranes and Size Dependence. *Langmuir* **28**, 14739–14746 (2012).
102. Czogalla, A., Grzybek, M., Jones, W. & Coskun, Ü. Validity and applicability of membrane model systems for studying interactions of peripheral membrane proteins with lipids. *Biochimica et Biophysica Acta (BBA) - Molecular and Cell Biology of Lipids* **1841**, 1049–1059 (2014).
103. Hope, M. J., Bally, M. B., Webb, G. & Cullis, P. R. Production of large unilamellar vesicles by a rapid extrusion procedure. Characterization of size distribution, trapped volume and ability to maintain a membrane potential. *Biochimica et Biophysica Acta (BBA)-Biomembranes* **812**, 55–65 (1985).
104. Angelova, M. I. & Dimitrov, D. S. Liposome electroformation. *Faraday Discuss. Chem. Soc.* **81**, 303–311 (1986).
105. Starr, T. E. & Thompson, N. L. Total internal reflection with fluorescence correlation spectroscopy: combined surface reaction and solution diffusion. *Biophys J* **80**, 1575–1584 (2001).
106. Egawa, H. & Furusawa, K. Liposome Adhesion on Mica Surface Studied by Atomic Force Microscopy. *Langmuir* **15**, 1660–1666 (1999).
107. Cremer, P. S. & Boxer, S. G. Formation and Spreading of Lipid Bilayers on Planar Glass Supports. *J. Phys. Chem. B* **103**, 2554–2559 (1999).
108. Kalb, E., Frey, S. & Tamm, L. K. Formation of supported planar bilayers by fusion of vesicles to supported phospholipid monolayers. *Biochimica et Biophysica Acta (BBA) - Biomembranes* **1103**, 307–316 (1992).
109. Nollert, P., Kiefer, H. & Jähnig, F. Lipid vesicle adsorption versus formation of planar bilayers on solid surfaces. *Biophys J* **69**, 1447–1455 (1995).
110. Jass, J., Tjärnhage, T. & Puu, G. From liposomes to supported, planar bilayer structures on hydrophilic and hydrophobic surfaces: an atomic force microscopy study. *Biophys J* **79**, 3153–3163 (2000).

111. Elender, G., Kühner, M. & Sackmann, E. Functionalisation of Si/SiO₂ and glass surfaces with ultrathin dextran films and deposition of lipid bilayers. *Biosens Bioelectron* **11**, 565–577 (1996).
112. Hillebrandt, H., Wiegand, G., Tanaka, M. & Sackmann, E. High Electric Resistance Polymer/Lipid Composite Films on Indium–Tin–Oxide Electrodes. *Langmuir* **15**, 8451–8459 (1999).
113. Baumgart, T. & Offenhäuser, A. Polysaccharide-Supported Planar Bilayer Lipid Model Membranes. *Langmuir* **19**, 1730–1737 (2003).
114. Shen, H.-H., Lithgow, T. & Martin, L. Reconstitution of Membrane Proteins into Model Membranes: Seeking Better Ways to Retain Protein Activities. *International Journal of Molecular Sciences* **14**, 1589–1607 (2013).
115. Lang, H., Duschl, C. & Vogel, H. A new class of thiolipids for the attachment of lipid bilayers on gold surfaces. *Langmuir* **10**, 197–210 (1994).
116. Bunjes, N. *et al.* Thiopeptide-Supported Lipid Layers on Solid Substrates. *Langmuir* **13**, 6188–6194 (1997).
117. Jose, B., Mallon, C. T., Forster, R. J., Blackledge, C. & Keyes, T. E. Lipid bilayer assembly at a gold nanocavity array. *Chemical Communications* **47**, 12530 (2011).
118. Ramadurai, S. *et al.* Microcavity-Supported Lipid Bilayers; Evaluation of Drug–Lipid Membrane Interactions by Electrochemical Impedance and Fluorescence Correlation Spectroscopy. *Langmuir* **35**, 8095–8109 (2019).
119. Zagnoni, M. Miniaturised technologies for the development of artificial lipid bilayer systems. *Lab on a Chip* **12**, 1026–1039 (2012).
120. Ide, T. Simultaneous Optical and Electrical Recording of Single Molecule Bonding to Single Channel Proteins. *Chemphyschem : a European journal of chemical physics and physical chemistry, Chemphyschem : a European journal of chemical physics and physical chemistry.* **11**, 3408–3411 (2010).
121. Ide, T. & Ichikawa, T. A novel method for artificial lipid-bilayer formation. *Biosensors and Bioelectronics* **21**, 672–677 (2005).
122. Dorvel, B. R. *et al.* Formation of Tethered Bilayer Lipid Membranes on Gold Surfaces: QCM-Z and AFM Study. *Langmuir* **23**, 7344–7355 (2007).
123. Suzuki, H., Tabata, K., Kato-Yamada, Y., Noji, H. & Takeuchi, S. Planar lipid bilayer reconstitution with a micro-fluidic system. *Lab Chip* **4**, 502–505 (2004).
124. Malmstadt, N., Nash, M. A., Purnell, R. F. & Schmidt, J. J. Automated Formation of Lipid-Bilayer Membranes in a Microfluidic Device. *Nano Lett.* **6**, 1961–1965 (2006).
125. Funakoshi, K., Suzuki, H. & Takeuchi, S. Lipid Bilayer Formation by Contacting Monolayers in a Microfluidic Device for Membrane Protein Analysis. *Anal. Chem.* **78**, 8169–8174 (2006).
126. Meuse, C. W., Niaura, G., Lewis, M. L. & Plant, A. L. Assessing the Molecular Structure of Alkanethiol Monolayers in Hybrid Bilayer Membranes with Vibrational Spectroscopies. *Langmuir* **14**, 1604–1611 (1998).
127. Levin, C. S. *et al.* Interactions of Ibuprofen with Hybrid Lipid Bilayers Probed by Complementary Surface-Enhanced Vibrational Spectroscopies. *J. Phys. Chem. B* **112**, 14168–14175 (2008).
128. Taylor, R. W. *et al.* Watching individual molecules flex within lipid membranes using SERS. *Sci Rep* **4**, (2014).
129. Opilik, L., Bauer, T., Schmid, T., Stadler, J. & Zenobi, R. Nanoscale chemical imaging of segregated lipid domains using tip-enhanced Raman spectroscopy. *Physical Chemistry Chemical Physics* **13**, 9978 (2011).
130. Suga, K. *et al.* Membrane Surface-Enhanced Raman Spectroscopy for Sensitive Detection of Molecular Behavior of Lipid Assemblies. *Analytical Chemistry* **87**, 4772–4780 (2015).

131. Matthews, J. R., Payne, C. M. & Hafner, J. H. Analysis of Phospholipid Bilayers on Gold Nanorods by Plasmon Resonance Sensing and Surface-Enhanced Raman Scattering. *Langmuir* **31**, 9893–9900 (2015).
132. Matthews, J. R., Shirazinejad, C. R., Isakson, G. A., Demers, S. M. E. & Hafner, J. H. Structural Analysis by Enhanced Raman Scattering. *Nano Letters* **17**, 2172–2177 (2017).
133. Millo, D. *et al.* Characterization of hybrid bilayer membranes on silver electrodes as biocompatible SERS substrates to study membrane–protein interactions. *Colloids and Surfaces B: Biointerfaces* **81**, 212–216 (2010).
134. Karaballi, R. A., Merchant, S., Power, S. R. & Brosseau, C. L. Electrochemical surface-enhanced Raman spectroscopy (EC-SERS) study of the interaction between protein aggregates and biomimetic membranes. *Phys. Chem. Chem. Phys.* **20**, 4513–4526 (2018).
135. Kühler, P., Weber, M. & Lohmüller, T. Plasmonic Nanoantenna Arrays for Surface-Enhanced Raman Spectroscopy of Lipid Molecules Embedded in a Bilayer Membrane. *ACS Appl. Mater. Interfaces* **6**, 8947–8952 (2014).
136. Castellana, E. T. & Cremer, P. S. Solid supported lipid bilayers: From biophysical studies to sensor design. *Surface Science Reports* **61**, 429–444 (2006).
137. Bruzas, I., Unser, S., Yazdi, S., Ringe, E. & Sagle, L. Ultrasensitive Plasmonic Platform for Label-Free Detection of Membrane-Associated Species. *Anal. Chem.* **88**, 7968–7974 (2016).
138. Bruzas, I. *et al.* Surface-Enhanced Raman Spectroscopy of Fluid-Supported Lipid Bilayers. *ACS Appl. Mater. Interfaces* **11**, 33442–33451 (2019).
139. Zhou, J., Ren, K., Zhao, Y., Dai, W. & Wu, H. Convenient formation of nanoparticle aggregates on microfluidic chips for highly sensitive SERS detection of biomolecules. *Analytical and Bioanalytical Chemistry* **402**, 1601–1609 (2012).
140. Gao, R. *et al.* Fast and sensitive detection of an anthrax biomarker using SERS-based solenoid microfluidic sensor. *Biosensors and Bioelectronics* **72**, 230–236 (2015).
141. Parisi, J., Su, L. & Lei, Y. In situ synthesis of silver nanoparticle decorated vertical nanowalls in a microfluidic device for ultrasensitive in-channel SERS sensing. *Lab on a Chip* **13**, 1501 (2013).
142. Parisi, J., Dong, Q. & Lei, Y. In situ microfluidic fabrication of SERS nanostructures for highly sensitive fingerprint microfluidic-SERS sensing. *RSC Advances* **5**, 14081–14089 (2015).
143. Xu, B.-B. *et al.* Localized flexible integration of high-efficiency surface enhanced Raman scattering (SERS) monitors into microfluidic channels. *Lab Chip* **11**, 3347–3351 (2011).
144. Xu, B.-B. *et al.* On-chip fabrication of silver microflower arrays as a catalytic microreactor for allowing in situ SERS monitoring. *Chem. Commun.* **48**, 1680–1682 (2012).
145. Vlasko-Vlasov, V. *et al.* Liquid cell with plasmon lenses for surface enhanced Raman spectroscopy. *Applied Physics Letters* **96**, 203103 (2010).
146. Xu, B.-B. *et al.* A SERS-active microfluidic device with tunable surface plasmon resonances. *ELECTROPHORESIS* **32**, 3378–3384 (2011).
147. Oh, Y.-J. & Jeong, K.-H. Optofluidic SERS chip with plasmonic nanoprobe self-aligned along microfluidic channels. *Lab on a Chip* **14**, 865 (2014).
148. Kamińska, A. *et al.* Detection of Hepatitis B virus antigen from human blood: SERS immunoassay in a microfluidic system. *Biosensors and Bioelectronics* **66**, 461–467 (2015).

149. Kamińska, A. *et al.* SERS-based Immunoassay in a Microfluidic System for the Multiplexed Recognition of Interleukins from Blood Plasma: Towards Picogram Detection. *Scientific Reports* **7**, 10656 (2017).

2 Chapter 2: Fabrication of a FLIM/FCS optically transparent microfluidic device for micropore arrays

2.1 Introduction

Microfluidics which deals with the control and manipulation of volumes at the microscale has emerged as a crucial component of analytical chemistry over the past 20 years. As it offers the opportunity to reproducibly work at microliter volumes, the simplest, most widely applied microfluidic format is the moulding of micron (radii) dimensioned-channels moulded in polymer, applied onto to a flat surface such as glass. Thus, various techniques have been developed in the last two decades for the fabrication of polymer based microfluidic devices. Most widely used are photolithography^{1,2} and moulding methods, such as injection moulding³⁻⁵, hot embossing^{6,7} or soft-lithography^{8,9}, but also machining methods such as micromilling¹⁰⁻¹², laser micromachining^{6,13,14}, xurography¹⁵, or more recently 3D printing.^{16,17} The choice of the technique to be used is mainly driven by the characteristics of the polymer to be processed but also by the size and shape of the wanted features.

The overall objective of this project is to design and build a microfluidic device that encapsulates an ordered micro to nano -pore array. The underlying rationale was that such pore arrays can be exploited for preparation of microcavity supported lipid bilayers. The device should thus be suitable for different analytical modalities such as FCS, EIS and Raman spectroscopy, and reagent can be introduced to the array via flow channels.

Micro or nano pore array patterning is achievable with high reproducibility of fabrication and high flexibility in term of size and design of the array, using methods such as electron-beam lithography or photolithography.^{18,19} Indeed, depending on the mode of photolithography used, the resolution of the structures created can go from few microns (contact and proximity printing) to few tens of nanometres (projection printing).²⁰ Also, photoresists are lately increasingly used as an integral part of the microfluidic devices for their physical and chemical properties, rather than as a simple sacrificial layer. However, such techniques are expensive and laborious with low throughput, and from a research laboratory perspective, the accessibility to complex equipment, the costs and the time spent for the fabrication of the device can also be parameters to take in consideration.

Soft lithography or embossing are more accessible techniques with also high reproducibility capabilities in terms of fabrication. Replica molding allows through only one processing step for the reproduction with high throughput of shape, structure

and other information of a unique master, which is often built by photolithography.²¹ However, the biggest strength of those methods is that cloning process is possible through creating a master or mold with other fabrication process, that are considerably less complicated and low cost compared to photolithography.

Lately, in an effort to improve substrates reproducibility, attempts to develop cavity array by moulding 3 μm height cylindrical pillars, obtained by photolithography, onto PDMS were performed in Prof. Keyes' group.²² Results showed that size and shape of the cavities may play a critical role in reliably spanning a lipid membrane across the pore aperture. Data indicated that, likely due to pore depth and sharp curvature of the water meniscus at such substrates due to poor aqueous filling of the wells, bilayers were not stable. Thus, it was concluded that the spherical shape, where the pore depth was comparable to the sphere radius, was best in ensuring bilayer assembly. Therefore, it was decided to translate the cavity suspended lipid bilayer model with spherical shape voids developed by our group into a microfluidic platform using hot embossing as fabrication method of the cavity arrays. The advantage of using micro imprinting rather than colloidal lithography to generate these voids is the much more facile and scalable fabrication, which produces stamps that can be reused many times and thus insure reproducibility between substrates from batch to batch. The resulting embossed rigid polymer substrate could then be implemented into a pre-fabricated microfluidic device, as it is a common practice in the field, such as illustrated in the previous chapter with nanostructured solid substrates microfluidics-SERS platform.

In this first working chapter, the first focus is on the fabrication of the main body of the microfluidic device. For this purpose, it is essential to keep in mind the overall objective of the project and to choose the design, materials, fabrication and assembly methods accordingly. The second focus is put onto the fabrication of a Fluorescence-lifetime imaging microscopy (FLIM)/FCS compatible microcavity array that could be integrated to the microfluidic device while keeping the structural integrity of the suspended lipid membrane at its surface. We report here two effective and economical ways of fabricating micron dimension cavities on PMMA substrates that combines the advantages of microsphere lithography, soft lithography and hot-embossing methods.

2.2 Experimental

2.2.1 Microfluidic device manufacturing and operational principle

As one of the key objectives in creating the array was to make it amenable to lipid membrane formation described later in section 2.2.3, the microfluidic device had to be designed in two main parts so that the lipid bilayer can be prepared at the section carrying the pore array. This part can then be easily assembled with the second section that contains the inlet and outlet just before proceeding to EIS or FCS measurement. The function of the first section of the device is to supply reagents to the second part of the microfluidic device, which contains the lipid membrane cavity array substrate where the study of drug-lipid membrane interactions is carried out.

Figure 22 describes the detailed structure of the sealed microfluidic device and the liquid journey from the inlet to the outlet.

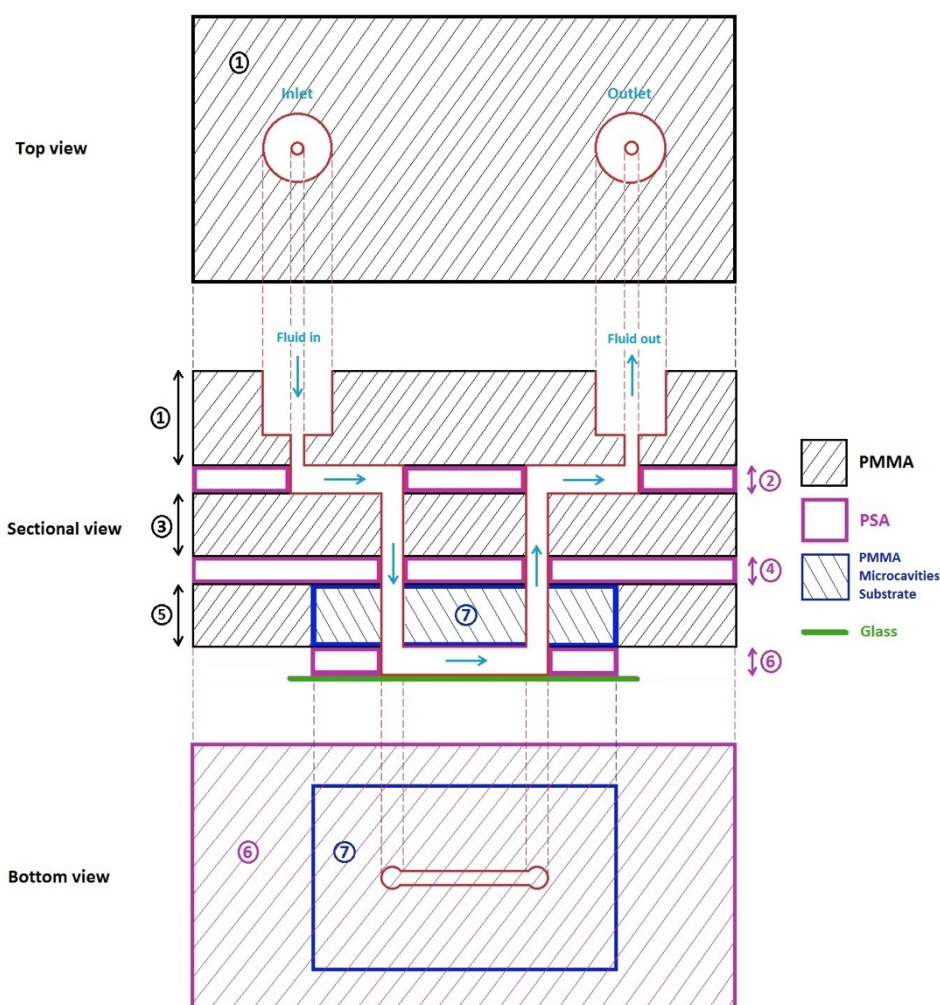


Figure 22 : Schematic of the microfluidic device detailed structure for drug-lipid membrane interactions study.

The different layers constituting the device were first drawn with AutoCad software as shown in Figure 23 and saved as a “.dxf” file for transfer to the CO₂ laser and cutting plotter software. Each layer presents at least two 1mm diameter holes in their corners, ensuring a perfect alignment during the assembly.

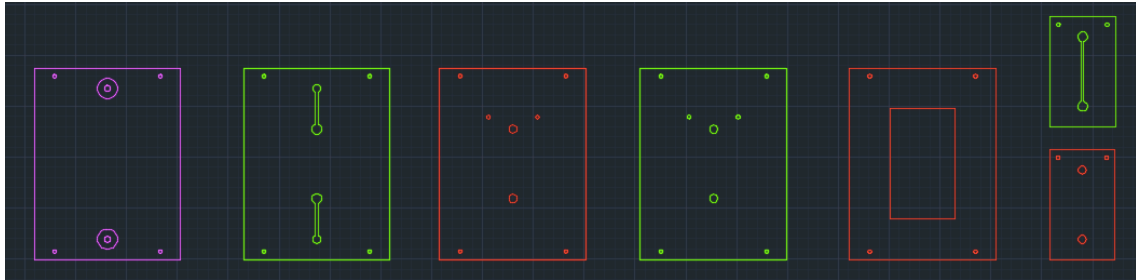


Figure 23 : Picture showing the AutoCad file used to process the different layers of the microfluidic device (purple : 6 mm PMMA ; red : 2 mm PMMA ; green : double-sided PSA).

Layers of PMMA were processed from 2mm thick sheets from Radionics. The design built in AutoCad file was transferred to CorelDRAW X5 and the different PMMA parts were processed with the CO₂ laser Zing 16 Model 10000 from Epilog Laser. Appropriate parameters were set up for the CO₂ laser to avoid the “lip” phenomenon described in further section 2.3.1, reducing thereby the risk of leakage when flowing liquid into the microfluidic device. Table 3 presents the suitable parameters to use according to the thickness of the PMMA.

Table 3 : Suitable parameters used to prevent the « lip » phenomenon when processing PMMA with the CO₂ laser.

PMMA thickness (mm)	Vector speed (%)	Vector Power (%)
1.5	24	20
2	18	32
6	16	88

Layers of double-sided Pressure-sensitive adhesive (PSA) (AR Part # - MH-92712-6) from Adhesives Research were processed by xurography. The AutoCad file was opened with Robo Master Pro software to process the different PSA layers with the cutting plotter Craft Robo Pro from Graphtec.

Once the different PMMA and PSA layers were processed, the assembly of the device was performed. On one side, layers 1 to 5 were successively assembled to each other after removing their protective layers, ensuring the material is kept clean until the assembling step, and using steel pins for alignment. On the other side, following the same procedure, layers 6 and 7 were assembled to each other to form the second part of the microfluidic device, measuring 16mm x 27mm. The small dimension of this part was critical and could not be increased, as it had to fit into the Langmuir-Blodgett trough for lipid-bilayer assembly. To benefit from the full potential of the PSA, the two parts of the microfluidic device were rolled using a laminator, allowing the formation of a strong bond between the different PMMA layers, which is essential for a good sealing. Finally, the two main parts of the microfluidic device were assembled, but pressure was applied only manually for this step, in order to be the closest possible to the final conditions of use of the assembled device. Then, a glass microscope coverslip was stuck onto the bottom channel to fully seal the device.

The microfluidic device was then connected to a pump and a leak test was performed with a red food dye (cf. section 2.3.1).

2.2.2 Fabrication of a PMMA substrate for Cavity Supported Lipid Bilayers

2.2.2.1 Method A: Hot embossing cavities using a silicone-based master

The method used herein was adapted from Steigert et al.²³ In their work on the rapid prototyping of microfluidic chips in Cyclic Olefin Copolymer (COC), the group used the elastomeric material Elastosil® RT607 (Wacker) to build an embossing master aiming at replicating channels in a COC substrate. This method has been adapted here for the replication of a micron dimensioned cavity array onto PMMA substrates.

2.2.2.1.1 Fabrication of a Gold microcavity array negative mould

A negative mould for the gold microcavity array was prepared using a gold-silicon wafer from AMS biotechnology as a substrate (Product code AU.1000.SL1). This silicon substrate coated with a 100nm layer of gold on top of a 5nm layer of titanium acting as an adhesion layer was cut into 1cm by 2cm pieces and washed carefully with acetone, ethanol and water before drying under nitrogen. Pieces of duct tape presenting a free area of 1cm by 0.5cm were then cut and stuck on the gold-silicon

wafer sample as illustrated in Figure 24, leaving two bands of gold exposed to the air. The top band allows connection with the potentiostat, while the centred band allows a better control of the PS spheres solution deposition and gold electrodeposition.

A 0.1 % PS microspheres solution with an average of $2.88 \pm 0.28 \mu\text{m}$ diameter was prepared by diluting a 13.8 % stock solution from Bang Laboratories (catalogue code PS05N) in deionised water. 75 μL of this solution was carefully drop-casted onto the deposition area of the gold-silicon wafer and sample was left to dry overnight at room temperature.

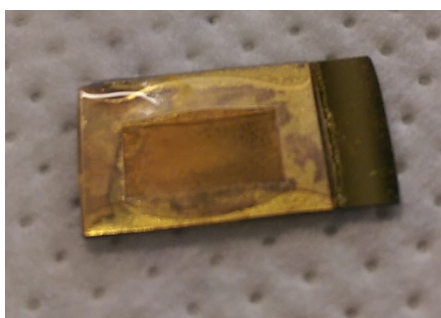


Figure 24 : 1 cm x 2 cm gold-silicon wafer sample after gold electrodeposition. A piece of duct-tape presenting a free area of 1 cm x 0.5 cm was stuck before polystyrene beads dropcasting allowing a better control of the spheres' deposition and gold growth.

Gold electrodeposition was then performed through the PS microspheres template using a potentiostat CH Instrument model 660 electrochemical workstation and a gold salt solution from Technic Inc. USA. The solution degassed by purging for 30 minutes with nitrogen. In the electrodeposition, the gold-silicon wafer is the working electrode, with an Ag/AgCl reference electrode and a platinum wire the counter electrode. Gold was then electrodeposited at an applied potential of -0.95 V until a cumulated charge of 0.85 C was reached. These conditions were determined through iterating the charge across a range of depositions solutions and correspond to gold growth to the equator of the first layer of microspheres, trapping them into the substrate.

The duct tape was then peeled off and the sample rinsed with deionised water to wash any gold salt solution remaining. Finally, the gold substrate was sonicated in Tetrahydrofuran (THF) for 30 minutes to dissolve the PS microsphere template yielding the gold microcavities negative mould that was used to cast the silicone based embossing master. Figure 25 illustrates the all process of gold microcavities fabrication

from the PS beads deposition, through the gold electroplating, ending with the template spheres removal.

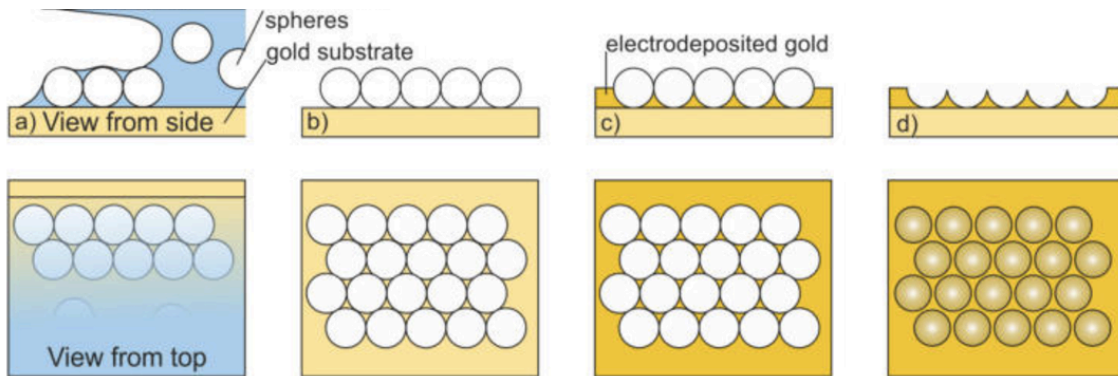


Figure 25: Schematic of the process of gold microcavities fabrication from the PS beads deposition (a and b), through the gold electroplating (c), ending with the template spheres removal (d). Image adapted from reference.²⁴

2.2.2.1.2 Silicone based embossing master casting

To overcome the problem of master level and thickness heterogeneity described in further section 2.3.2.1, an aluminium mould lent by Prof. Jens Ducrée's group was modified to cast the embossing master. A 6 mm thick PMMA disc was designed to fit into the mould and cut in a way that it allowed to insert a 40 mm by 60 mm rectangle in it, as shown in Figure 26 a).

It was important that the positives structures in the mould corresponding to the cavities in the cast structure were the first to be in contact with the PMMA during the embossing process. Therefore, a small stand holding the gold microcavities negative mould was designed to cast the silicone, avoiding any other cured material lower than the level of the features to emboss. Figure 26 b) shows the PMMA stand that was used with a central window leaving accessible only the area of interest to the silicone mixture. The rest of the cured material constituting the base of the embossing master will then be at a different level than the embossing features and does not interfere the embossing process. This stand was placed into the aluminium mould before silicone casting.

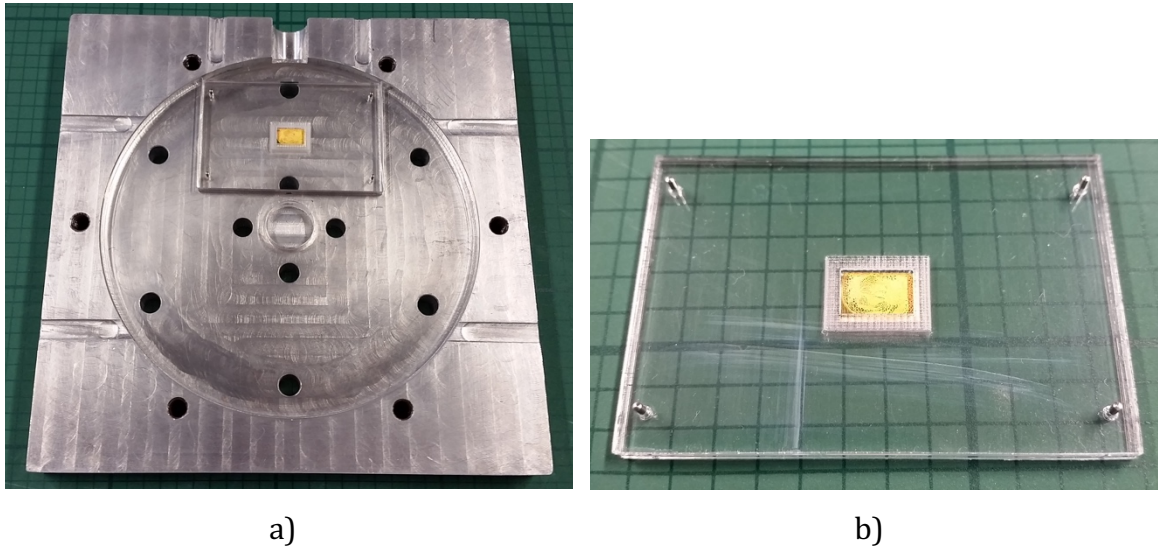


Figure 26 : a) Picture of the aluminium mould adapted to be able to cast the silicone based embossing master; b) PMMA stand holding the gold microcavities substrates onto which the silicone has been cast.

Elastosil® RT607 was thoroughly mixed in a ratio 21:1 by weight (elastomer base : curing agent) according to the hardness optimisation results presented later on in section 2.3.2.1.1. After degassing the silicone mixture for 5 minutes into a vacuum desiccator, a thin layer was poured onto the cavities area in order to cover it. The mould and the rest of the mixture were degassed further for a period of 25 minutes. The silicone mixture being viscous, this step was realised to enhance the cavities feeling by facilitating the air trapped into the gold structures to escape. The thinner the layer of silicone, the easier it is for the air to travel across it. After degassing, the aluminium mould was filled to the top before being closed and put to stand vertically to finish the filling process up to the top of the mould aperture as illustrated in Figure 27.



Figure 27 : Illustration of the aluminium mould filled to the top with Elastosil® RT607 before curing.

The aluminium mould was left in the vacuum desiccator for 30 more minutes to remove remaining air bubbles potentially formed when pouring the silicone and closing the mould. The system was then placed into a preheated oven at 40 °C for an overnight curing. Once the silicone had cured, the embossing master could be unmoulded by peeling it off carefully from the gold cavities/PMMA substrate. The excess of cured material present at the edges was removed gently using a scalpel yielding to a silicone based embossing master devoid from interfering material, as shown in Figure 28.

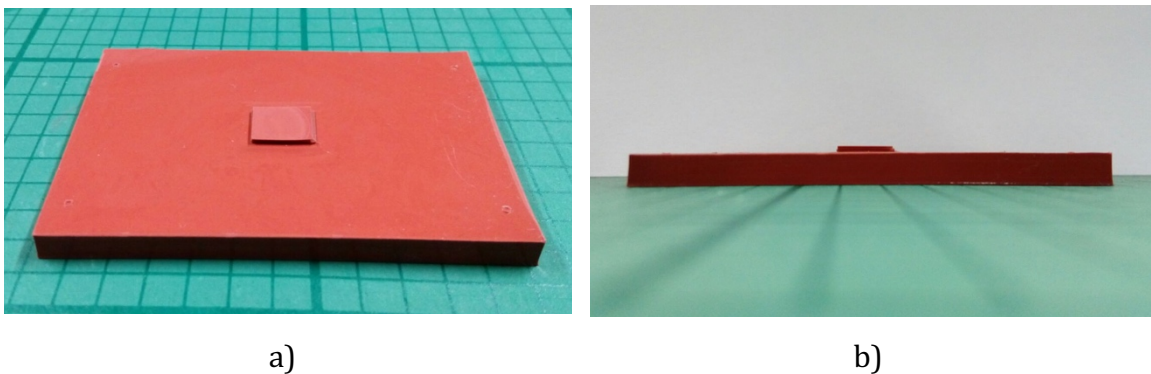


Figure 28 : a) Top view of the silicone based embossing master with the embossing area of interest in the centre; b) Side view of the silicone based embossing master highlighting the difference of level between the embossing area of interest and the base of the master.

2.2.2.1.3 Hot embossing microcavities on a PMMA substrate

The previously described silicone based embossing master was used to reproduce cavities onto PMMA substrates as illustrated in Figure 29. For this purpose, the embossing system HEX 02 from Jenoptik Mikrotechnik was used.

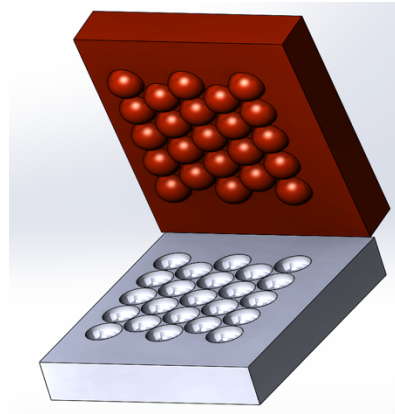


Figure 29: Schematic of a silicone based master (top) embossing microcavities in a PMMA substrate (bottom).

PMMA sheets of a 2mm thickness were cut with the CO₂ laser in rectangular sample of 60 mm by 40 mm. The ready to emboss PMMA was placed on a glass plate avoiding it to be in direct contact with embosser metal hot plate. The silicone based embossing master was centred on top of the PMMA with the positive structures to emboss facing the polymer substrate. A last glass plate was placed on top of the master to protect its backside, yielding to a (glass/PMMA/master/glass) set up ready for embossing. Once the “master/substrate” set up assembled it was placed into the embossing chamber for hot embossing.

The macro presented in Table 4 was then used performing automatically each instruction one after the other until the end of the program, enabling access to the chamber to take out the embossed sample.

Table 4 : Macro used for the hot embossing of microcavities with a silicone-based master into a PMMA substrate, and description of each query.

Macro lines	Description of the action
<i>Open File Measure()</i>	Opens a file select window
<i>Initialize ForceControl(true/false=0)</i>	Basic system unit (force unit) is initialised
<i>Show Chart Window>Show/Hide=01/0)</i>	Displays force, position and temperature graphs
<i>Show Chart Window>Show/Hide=11/0)</i>	Displays force, position and temperature graphs
<i>Heating(Top=190.0°C,Bottom=160.0°C)</i>	Preheat hot plates to values higher than desired for faster embossing cycle
<i>Close Chamber()</i>	Closes the vacuum chamber
<i>Evacuate Chamber()</i>	Evacuates the chamber until a pressure of 5 mbar has been reached
<i>Touch Force(Force=50N)</i>	Embossing master and polymer substrates move towards each other until they touch to a force of 50 N, ensuring a good heat transfer
<i>Temperature >=(Temperature=130.0deg,Channel=12)</i>	Waits until the embossing master and the substrate reach a temperature above 130 °C
<i>Heating(Top=200.0°C,Bottom=145.0°C)</i>	Heat hot plates to the desired values
<i>Temperature >=(Temperature=152.0deg,Channel=12)</i>	Waits until the embossing master and the substrate reach a temperature above 152 °C
<i>Heating(Top=155.0°C,Bottom=145.0°C)</i>	Heat hot plates to temperature used for embossing step
<i>Temperature >=(Temperature=154.0deg,Channel=12)</i>	Waits until the embossing master and the substrate reach a temperature above 154 °C
<i>Wait Time(Time=900s)</i>	Wait 900 s during embossing time
<i>Cooling(Top=20.0deg,Bottom=20.0deg)</i>	Cools down embosser plates to temperatures below the ones required for the master and PMMA substrate to be unmoulded
<i>Temperature <=(Temperature=40.0deg,Channel=12)</i>	Waits until the embossing master and the substrate reach a temperature below 40 °C
<i>Wait Time(Time=300s)</i>	Waits 300 s to allow master and PMMA substrate to cool down
<i>Open Chamber()</i>	Opens and vents the chamber
<i>Unlock door()</i>	Unlock the door to be able to access the embossed sample
<i>Close File Measure()</i>	Stops data recording

The flexibility of the silicone embossing master facilitated the unmoulding process, as it could be peeled-off easily from the embossed PMMA substrate without damaging it. After embossing, the area of interest was isolated by cutting out the

outs skirt part and drilling 1 mm diameter holes for inlet and outlet, yielding to a flat PMMA sample presenting cavities ready to use as a lipid bilayer support.

2.2.2.2 Method B: Hot embossing cavities using an Si beads/Au-Si wafer based master

Due to deformation of the positive features on the silicone-based master during the hot embossing process (cf. sections 2.3.2.1.3 to 2.3.2.1.5), a different route was considered to build a harder embossing master with the same shape and dimensions of the positive features. This alternative method consists in using silica beads assembled onto an Au-Si wafer. Contrary to method A described previously, microspheres trapped into the gold substrate were not dissolved, the aim being to use them as positive microstructures to emboss cavities in PMMA substrates, as illustrates Figure 30.

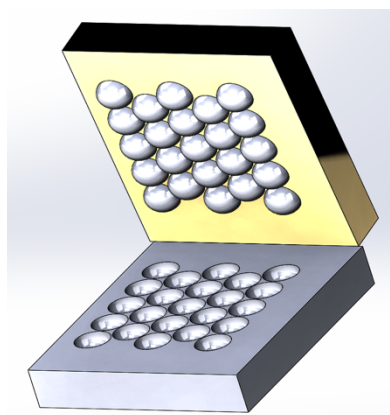


Figure 30 : Schematic of a silica microspheres/Gold-silicon wafer based master (top) embossing microcavities in a PMMA substrate (bottom).

2.2.2.2.1 Fabrication of a Gold-Silica based embossing master

To fabricate the gold-silica based embossing master, a very similar technique to the one described in previously for the fabrication of the gold microcavities negative mould was performed. Indeed, the major difference here was the nature of the microspheres used.

A 2 cm x 1 cm piece of gold-silicon wafer was treated the same way as described in section 2.2.2.1.1. to allow deposition of microsphere and electrochemical gold growth. Non-functionalized silica microspheres with an average diameter of 3.17 μm were ordered from Bangs Laboratories (catalog code SS05N). The surface chemical

modification of those beads is described later in section 2.2.2.2.2. In order to achieve approximately the same coverage density of cavities on the embossed substrate as for the method A, 75 μL of a 0.1 % (w/w) solution of thiolated silica microspheres was deposited onto the gold-silicon sample, in the 0.5 cm x 1 cm tape-free area. The sample was left in a water-saturated atmosphere for 2 hours before drying overnight at room temperature, to slow down evaporation of solvent and allow a maximum of sulphur-gold bonds to form, anchoring silica microspheres to the gold surface.

Gold was electroplated at an applied potential of -0.95 V as described in section 2.2.2.1.1, until a cumulated charge of 0.85 C was reached. This charge allowed a gold growth to the equator of the first layer of microspheres, trapping them into the substrate. The new embossing master was then rinsed with deionized (DI) water followed by Isopropyl alcohol (IPA) to remove any gold solution left from the electroplating step, but also to try to detach multilayers of silica microsphere that could interfere during the embossing process.

2.2.2.2.2 Thiolation of Si beads

To bond the silicate to the substrate, one approach based on R. Rostamian et al. work was followed.²⁵

The 9.9% (wt.) silica microsphere solution was vortexed for 30 seconds and sonicated for 10 minutes to ensure a good dispersion of the beads. A volume of 100 μL of the solution was transferred to a 2 mL Eppendorf tube and spheres were washed three times with 1 mL of ethanol followed by centrifugation during 5 minutes at 8000 rpm, followed by three toluene washes under the same conditions. Spheres were transferred to a 10 mL round bottom flask with 5 mL of toluene as the reaction solvent, 2.5 μL of n-Butylamine as a catalyst and 88 μL of MPTMS. The mixture was then refluxed for 2 h 30 min. After allowing the solution to cool down, spheres were transferred to a 14 mL Eppendorf tube and round bottom flask was washed with two times 2 mL of toluene that were added to the Eppendorf tube. Spheres were then washed three times by centrifugation during 5 minutes at 8000 rpm with 1 mL of toluene. Finally, after removing the maximum of supernatant, spheres were allowed to dry at 130 °C during 2 h 30 min.

The dry thiol-modified silica microspheres were then characterised by SEM, FTIR-ATR and Raman Spectroscopy and results are shown in section 2.3.3.1.1. After

characterisation, the spheres were resuspended in water to allow deposition onto Au-Si wafer as described previously.

2.2.2.2.3 Hot embossing microcavities on a PMMA substrate

Microcavities were hot embossed in PMMA substrates using the new gold-silica based embossing master. The system used was the same as described for method A, with the exception that the silicone based embossing master was substituted for the gold-silica based one. As the embossing master changed in size, thickness and material nature, a new macro was developed to yield to a good quality imprint of microcavities in the PMMA substrate. Embossing parameters allowing the best result to date are given in the macro in Figure 31. Results obtained with these parameters are presented in further section 2.3.3.1.2.

```
Open File Measure()  
Initialize ForceControl(true/false=0)  
Show Chart Window(Show/Hide=01/0)  
Show Chart Window(Show/Hide=11/0)  
Heating(Top=155.0°C,Bottom=115.0°C)  
Close Chamber()  
Evacuate Chamber()  
Touch Force(Force=50N)  
Temperature >=(Temperature=90.0deg,Channel=12)  
Heating(Top=113.0°C,Bottom=102.0°C)  
Temperature >=(Temperature=95.0deg,Channel=12)  
Wait Time(Time=1200s)  
Force – Force controlled(Force=150N, Velocity=0.10000mm/min)  
Wait Time(Time=300s)  
Cooling(Top=30.0deg,Bottom=30.0deg)  
Temperature <=(Temperature=40.0deg,Channel=12)  
Temper(Top=60.0deg,Bottom=60.0deg)  
Open Chamber()  
Unlock door()  
Close File Measure()
```

Figure 31 : Macro used to hot emboss micro cavities in a PMMA substrate with a gold-silica based embossing master.

2.2.3 Lipid bilayer formation

The method used in this chapter to build a lipid bilayer over a buffer filled microcavity substrate followed the procedure reported by Basit et al.²⁶ The surface of the embossed PMMA microcavity substrate was first chemically modified to allow the formation of a lipid monolayer at its surface using the Langmuir-Blodgett method. The polymer substrate was then assembled to the rest of the microfluidic device to form the lipid upper leaflet by introduction of SUVs fusing with the lipid monolayer to form a bilayer, which was then characterised by FCS.

2.2.3.1 Plasma cleaning

PMMA is relatively hydrophobic with a contact angle of 68-83 degrees.^{6,27-29} For this reason, the polymer surface was modified to render it more hydrophilic to promote a spanning of the lipid bilayer.

Planar PMMA or substrates following embossing were thoroughly rinsed with deionised water and dried under nitrogen, before being placed in a Harrick PDC-002 plasma cleaner (Harrick Plasma Inc.). Air plasma cleaning was performed during 5 minutes at 1000 mTorr using high power setting (29.6 W applied to the radio frequency (RF) coil).³⁰ Immediately after surface modification, the hydrophilic substrate was sonicated for 30 minutes in Phosphate-buffered saline (PBS) to allow filling of the cavities before spanning of a lipid monolayer by Langmuir-Blodgett technique.

2.2.3.2 Preparation of Small Unilamellar Vesicles

SUVs were prepared by extrusion of MLVs through a PC membrane with a porosity of 100 nm.

Firstly, 20 μ L of a 50 mg/mL solution of DOPC in chloroform was pipetted into a glass vial along with a fluorescent labelled lipid at a ratio of 1:5000 (moles:moles). Two 1,2-dioleoyl-sn-glycero-3-phosphoethanolamine (DOPE) labelled probes (DOPE-Naphta-Bodipy or DOPE-Atto655) were used to enable fluorescence measurement at the layers. The lipid mixture was dried under nitrogen stream then left in a vacuum chamber for minimum 30 minutes to ensure full solvent evaporation. The lipid film was then resuspended in 1 mL of 0.01 M PBS buffer at pH 7.4 and vortexed to ensure the dry lipid detached from the glass vial and dispersed homogeneously into the solution. The resulting vesicles containing solution was then extruded to obtain SUVs by passing

the MLVs solution 11 times through a polycarbonate membrane of a 100 nm porosity using the Avanti mini extruder (Avanti polar lipids, Inc.) as described in Figure 32. The two supplementary filter supports from either side of the membrane reduce the flow rate and prevent the membrane to tear under pressure when flushing the solution from one syringe to another. After extrusion, the 1 mL of recovered SUV solution was diluted with 3 mL of 0.01 M PBS buffer pH 7.4, yielding to a final concentration 0.25 mg/mL DOPC containing solution.

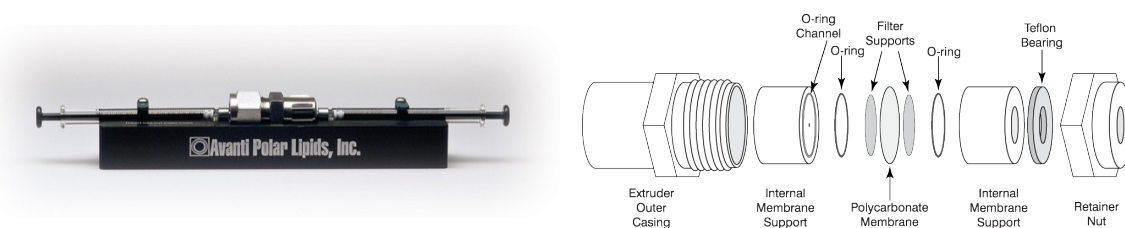


Figure 32 : Picture of the Avanti Mini Extruder (left) at schematic of its assembly (right) used for the preparation of SUVs by extrusion of MLVs.

2.2.3.3 Formation of monolayer by Langmuir-Blodgett technique

Formation of the lower leaflet of the lipid bilayer was performed by the Langmuir-Blodgett method using a NIMA model 102M Langmuir-Blodgett trough. The trough was cleaned thoroughly with ethanol prior use to prevent cross contamination with unwanted lipid or chemical from previous experiments. After cleaning, the equipment was filled with deionised water and barriers were compressed to check the cleaning efficiency.

100 μ L of a 50 mg/mL solution of DOPC in chloroform was mixed into a glass vial with a fluorescent labelled lipid at a ratio of 1:5000 (moles:moles). The lipid mixture was carefully suspended on the trough at the water-air interface between the two barriers and the organic solvent was allowed to evaporate for 15 to 30 minutes. In a first time, compression of the suspended lipids was performed in several compression cycles at a rate of 50 cm^2/min until a constant surface pressure between 38 and 42 mN/m was obtained to ensure a proper lateral packing of the lipids at the water-air interface. Rate of compression was then changed to 30 cm^2/min and lipids were compressed and maintained at a constant surface pressure of 32 mN/m . The buffer filled microcavity PMMA substrate was dipped under the water surface at a relatively high speed of 66 mm/min preventing transfer of a lipid layer and surface pressure was allowed to stabilise for 20 seconds. The substrate was then withdrawn

at a low speed of 5 mm/min so as to transfer a consistent lipid monolayer onto its surface.

2.2.3.4 Microfluidic device assembling

Once the lipid monolayer was formed on the PMMA substrate, the protective film covering the PSA channel was removed and a microscope glass coverslip was stuck to it to seal the chip. In this particular case, pressure was applied only manually and carefully on the chip to prevent the glass coverslip from breaking. The PMMA micro-cavity substrate was then adhered to the fluidic supplying part as explained previously. The vesicles solution was injected into the microfluidic device and left in contact with the microcavity substrate for at least 10 minutes, thus allowing disruption of the vesicles onto the monolayer and yielding to the lipid bilayer formation. 1 mL of PBS was then flushed into the device to remove any unwanted extra vesicles. The sample was then ready for FCS characterisation.

2.2.4 Material and instrumentation

2.2.4.1 Device manufacturing

The microfluidic device presented in this chapter comprised mainly PMMA and PSA. The materials have been respectively processed using laser machining and xurography.

2.2.4.1.1 CO₂ laser

Laser machining involves removing layers of material from a substrate by laser irradiation. Depending on the application and the material processed, different types of laser are used, ranging from ultraviolet (UV) to infrared (IR) lasers.⁶ CO₂ lasers are IR lasers commonly used to process PMMA for the fabrication of microfluidic devices. PMMA has a low heat conductance and heat capacity, absorbs in the IR region and presents a good thermal decomposition into volatile by-products, rendering it highly compatible with this machining technique.^{14,31} By driving a focused laser beam of high energy density across the surface of the polymer, the desired features are milled out by heating, melting and evaporating material from the substrate.

Figure 33 illustrates the classic configuration of a direct-write laser machining system similar to the CO₂ laser Epilog Zing 16 from Epilog Laser used in this work to process PMMA layers of the microfluidic device. PMMA sheets of different thickness,

such as 1.5 mm (Code 824-480), 2mm (Code 824-632) and 6 mm (Code 825-253) were purchased from Radionics Ltd.

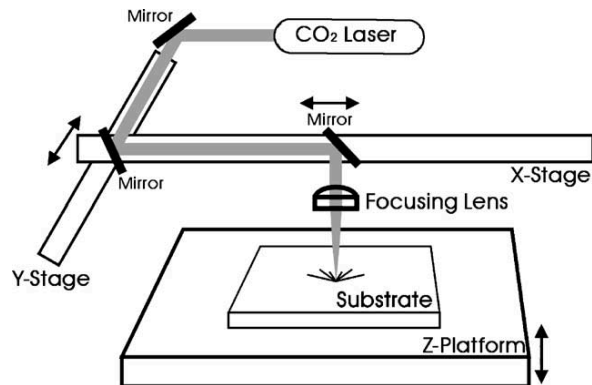


Figure 33 : Configuration of a direct-write laser machining system with an X-Y stage. Image extracted from reference.³¹

2.2.4.1.2 Cutting plotter

Xurography consists in cutting 2D structures in a polymer film ranging from 25 μm to 1 mm thickness with the use of a cutting plotter.³²

In this work, inlets, outlets and channels were cut by xurography into double-sided Pressure Sensitive Adhesive (PSA) sheets. Processed parts were used to bind the different PMMA layers and allow a good sealing of the microfluidic device. PSA layers of the microfluidic device described in this report have been processed using a cutting plotter Craft Robo Pro from Graphtec. Double-sided PSA rolls (reference AR Part # - MH-92712-6) were purchased from Adhesives Research.

2.2.4.2 Cavities substrate manufacturing and characterisation

2.2.4.2.1 Plasma cleaner

By applying a RF oscillating electric field through magnetic induction at a low pressure, plasma can be generated.³⁰ The partially ionised gas containing ions, electrons and neutral atom and molecules can react with the exposed surface. Depending on the nature of the gas used different interactions can occur, modifying the chemical and physical properties of the surface exposed.³³ The principle is usually as follows: the sample is introduced in the vacuum chamber and the atmospheric air is extracted using a vacuum pump. When the pressure is low enough, the chosen gas is injected inside the chamber and applying an electric field forms plasma. The surface exposed is bombarded and energy is transferred from the gas to the material surface.

This reliable, low cost, and low temperature technique is used for different applications such as surface ablation, chemical etching, surface activation, coating or cross-linking.

In this study, air plasma treatment was used to enhance the wettability of PMMA substrates to promote a uniform spanning of a lipid bilayer at its surface. Indeed, the formation of hydroxyl and carboxyl group increases the surface energy of the PMMA and renders it hydrophilic. The plasma cleaner used during this work to treat PMMA surfaces was a Harrick PDC-002 plasma cleaner from Harrick Plasma Inc. Treatment were performed during 5 minutes with air chosen as the plasma gas, at a vacuum of 1000 mTorr and a power applied to the RF coil of 29.6 W.

2.2.4.2.2 Contact angle analyser

A number of techniques are available to evaluate contact angle and wetting properties such as Wilhelmy balance method, capillary rise at a vertical plate, capillary tube, etc., but the most common is direct measurement by "telescope-goniometer".³⁴ The setup used in this last method has been improved since its invention in 1946 by Bigelow et al. but the technique remains the same and consists of depositing a liquid drop, typically water, on a solid surface and viewing the drop with a magnifying lens. The drop will then reach an equilibrium driven by the forces arising from the three interfacial tensions, as solid-liquid, solid-vapour and liquid-vapour. Taking an image of the drop allows one to measure the contact angle formed by the solid-liquid interface and the liquid-vapor interface as illustrated in Figure 34. The hydrophilic or hydrophobic character of the solid substrate is determined by the magnitude of the contact angle, usually in the range of 10° to 80° for a hydrophilic material and above 80° for hydrophobic substrates.

During this study, static contact angle measurements were performed at room temperature using a FTA 200 Dynamic Contact Angle Analyser from First Ten Angstroms, Inc.

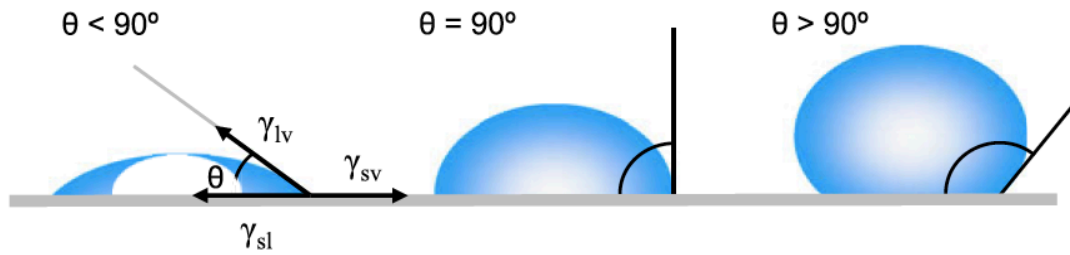


Figure 34 : Illustration of contact angles formed by sessile liquid drops on a smooth homogeneous solid surface. Image extracted from reference.³⁴

2.2.4.2.3 Silicone master

One of the strategies presented in this chapter was to build a silicone-based master to replicate microcavities into PMMA substrates by hot embossing process. Silicone rubbers are usually one-part or two-parts polymers of different chain lengths constituted by a siloxane backbone onto which organic groups are bound. These organic groups can be methyl, as for the PDMS, or a mixture between methyl and vinyl, phenyl or other groups.

The material used in this work to manufacture the silicone based embossing master was Elastosil® RT607 A/B from Wacker Silicones.

2.2.4.2.4 Hot embosser

Hot embossing was used in this chapter to build micro cavity array in PMMA substrates. This technique involves the inverted replication of a master template onto a thermoplastic polymer using pressure and heat. By heating the thermoplastic to near its glass transition temperature (T_g), the polymer softens and can be reshaped according to the features present on the master. A variety of thermoplastics can be hot embossed⁴, such as PMMA, PS, polyvinylchloride (PVC), polyethyleneterephthalate glycol (PETG), PC, or COC.

As illustrated in Figure 35, the system used for this technique consists generally of two parallel temperature controlled plates mounted in a vacuum chamber.⁶ The master template, also called the embossing tool, and the flat sheet of polymer to be embossed are assembled in between the two plates. A hydraulic system controlling one of the plates allows one to apply the required force during the embossing process by bringing the two plates in contact.

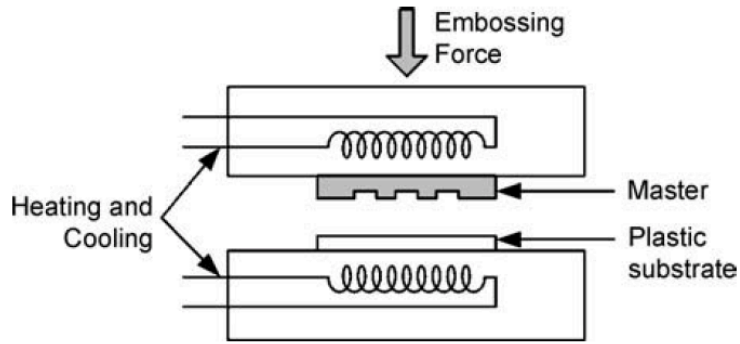


Figure 35 : Schematic diagram of a hot embossing system. Image reproduced from reference.⁶

The temperature and pressure profile used during a conventional hot embossing process are illustrated in Figure 36. At the very beginning of the cycle, the thermoplastic substrate to be embossed and the master template are put in contact and placed into evacuated embossing chamber. The vacuum promotes removal of air bubbles trapped into microstructures. The temperature of the system is then increased progressively from room temperature to a temperature just above the T_g of the polymer (heating stage, phase 1) and maintained at this temperature (constant temperature stage, phase 2). Once the desired embossing temperature has stabilised, pressure between the master and the substrate is applied (A2) and held (C2), allowing the softened polymer to fill the cavities of the master template. The system is then progressively cooled down (cooling stage, phase 3 and 4), bringing the temperature from above (phase 3) to below the T_g (phase 4), whilst maintaining constant pressure (C3). This step is really important as it allows the softened polymer to go back to its rigid state whilst maintaining contact with the master. De-embossing is then possible by releasing the pressure and allowing the sample to cool down to room temperature before separating the master from the embossed polymer substrate presenting the desired microstructures.

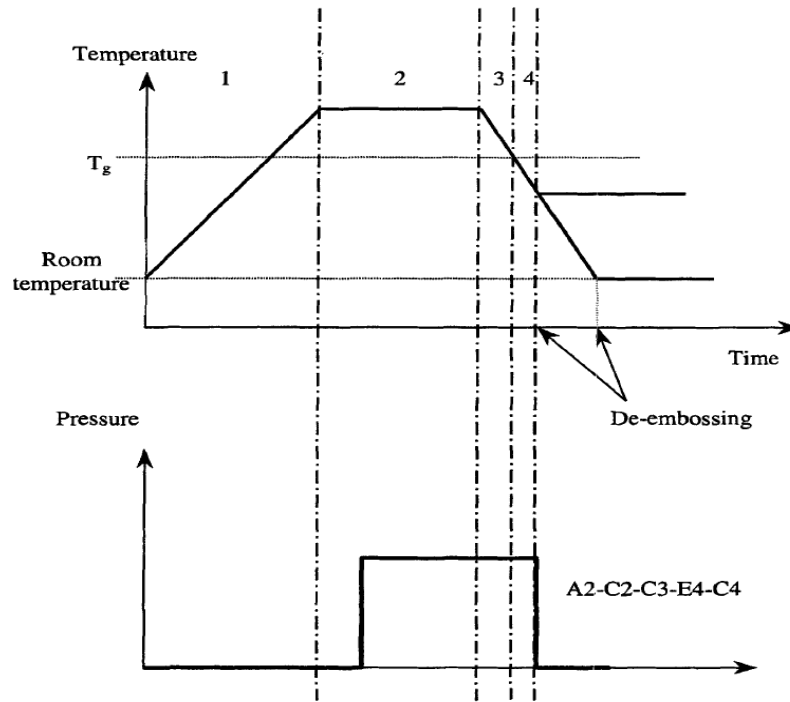


Figure 36: Schematic of a temperature (top) and pressure (bottom) profile during a classic embossing cycle. Image reproduced from reference.⁷

Usually made of metal or silicon, the embossing master template can actually be made of any material as long as it will resist the temperature and pressure conditions used during the embossing process. Shamsi et al. developed an embossing master made by standard lithography with SU-8 microstructures on a glass support.³⁵ The master allowed the replication of microchannels with a depth of 50 μm and a width of 15 μm . PDMS has also been used as an embossing tool for rapid prototyping of plastic microfluidic devices³⁶. A first template, usually built by classic lithography, is used to cast the PDMS mould, which will act later as an embossing master. However, the compressibility of the PDMS can affect the embossing process as the master tends to deform under heat and pressure. More recently describing prototyping of microfluidic chips in COC, Steigert et al. overcame this drawback by simply using a different reference of elastomer.²³ They used Elastosil® RT607 from Wacker which still presents a low viscosity allowing filling of channels cavity but has a higher hardness than the commonly used Sylgard 184 (Dow Corning).

In the presented work, hot embossing of PMMA substrates was performed on the embossing system HEX 02 from Jenoptik Mikrotechnik.

2.2.4.2.5 Shore A Durometer

Hardness of the silicone used in the fabrication of the embossing master was evaluated using a Shore A Durometer. As hardness value is a function of the elastic behaviour of the material, different preparation conditions could be compared (i.e. curing temperature, ratio elastomer base vs. curing agent) to ensure an embossing master the hardest possible, preventing thus deformation during the embossing process. The technique measures the reaction force of the material on an indenter when pressed into a material, through a calibrated spring.³⁷ A comparison of different shore hardness scales is given in Figure 37, going from extra soft rubbers to extra hard plastics.

For this study, the Shore A Durometer was provided by Mr. Christopher Crouch from the department of Mechanical and Manufacturing Engineering, Dublin City University.



Figure 37 : Illustration of different polymeric materials placed on 3 shore hardness scales. Image extracted from reference.³⁸

2.2.4.2.6 Compressive strength analyser

To complete shore A Hardness measurements and evaluate the stiffness of the silicone used in the fabrication of the embossing master, compressive strength measurements were performed. A uniaxial stress was applied to cured Elastosil® RT607 samples prepared under different conditions and stress vs. strain curves were plotted. Those measurements were carried out with a Zwick/Roell Materials Testing Machine model Z5.0TN and the Zwick TestXpert simulation software V11.02. Flat grips bigger than the studied sample have been mounted on the machine to obtain the more

homogeneous pressure on the whole sample surface, as illustrated in Figure 38. The main parameters have been set up as follow:

- Pre-load force: 1 N
- Test speed 2.5 mm/min
- Force shutdown threshold: 80 %
- Upper force limit: 4500 N

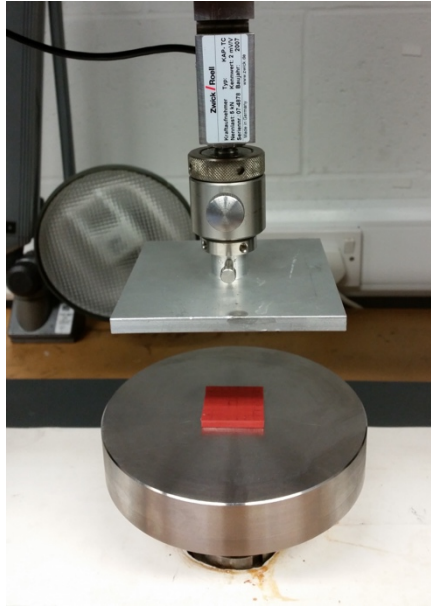


Figure 38 : Illustration of a sample of Elastosil® RT607 placed between two flat grips of the equipment before performing a compressive strength measurement.

2.2.4.3 Scanning Electron Microscopy

SEM involves focusing a beam of high energy electrons onto a sample under high vacuum, which generates different signal at the surface of the solid sample and can be converted in high-resolution images. Those signals, such as Secondary Electrons (SE) and Back Scattered Electrons (BSE), result from the interaction of atoms at or near the surface of the sample with the electron beam and contains various analytical information of the material properties, such as its surface topography or chemical composition. Figure 39 illustrates the different processes resulting from an incident electron bombardment onto a sample and their related information.

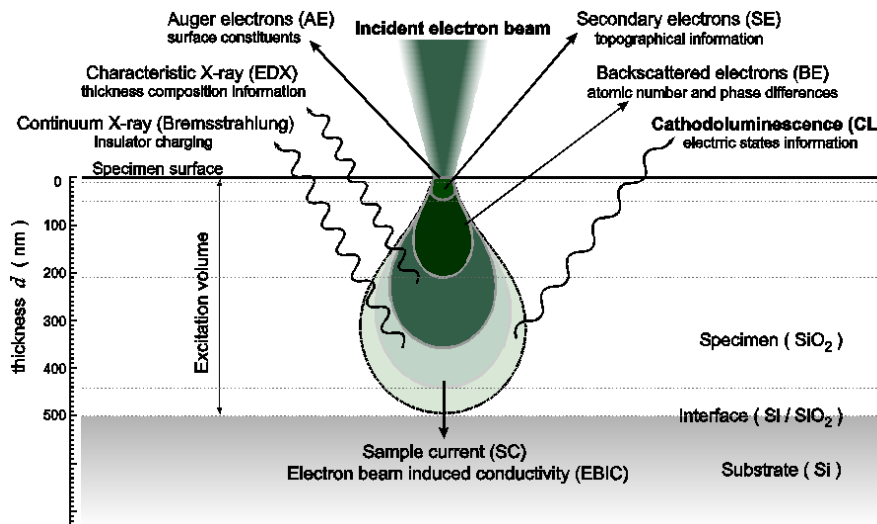


Figure 39: Schematic representation of processes resulting from electron bombardment and related information. Image reproduced from reference.³⁹

However, to prevent accumulation of electrostatic charge at the surface when scanning the sample with the electron beam, and thus possible distortion of the image, samples should be electrically conductive. Therefore, non-conductive samples are usually sputter coated with a thin layer of conducting material, such as gold, chromium or carbon. Samples are then mounted on a special SEM stub with electrically conducting pads or paste (e.g. carbon tape) to ensure a conduction path to ground.⁴⁰

In this chapter, characterization of the embossed PMMA microcavity substrates and the different tools involved in their fabrication, such as gold microcavity moulds, silicone or Si beads/Au-Si wafer based embossing masters, were performed by SEM imaging. PMMA and silicone based sample were sputter coated with a thin layer of gold prior to SEM imaging. All images were collected using a Hitachi S3400n SEM, Tungsten system instrument.

2.2.4.4 Atomic Force Microscopy

Allowing a resolution up to 1000 times than optical diffraction limit, AFM is a high-resolution type of scanning probe microscopy technique used for imaging, measuring or manipulating matter at a nanoscale range and can be used as a biosensor.⁶ This technique involves scanning the sample surface with the use of a sharp tip mounted at the end of a microscale cantilever, which deflects under interactions between the tip and the sample surface. This deflection is usually detected through a laser beam reflected at the back of the cantilever into a photo-diodes array as

illustrated in Figure 40. AFM can be operated under three regions mode such as contact mode, non-contact mode and tapping mode.

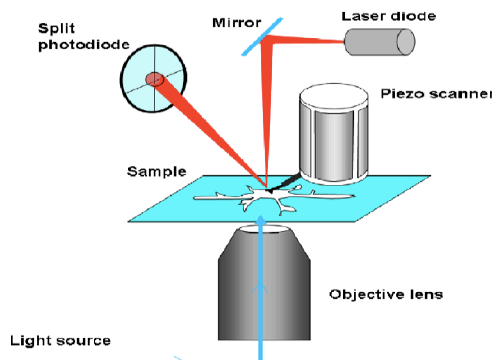


Figure 40: Schematic of AFM operation coupled with an inverted vertical microscope. Image reproduced from reference.⁴¹

In tapping mode, the cantilever is oscillated at or near its natural resonant frequency and brought close to the sample until it barely touches its surface by intermittence. This mode prevents friction and adhesion phenomenon that can occur in contact mode.⁴² The amplitude of the cantilever tip vibrations varies according to the topography of the sample surface and is collected by the optical system. Different information collected is then used to create a 3D image of the surface with an atomic scale resolution, which is an advantage over SEM restricted to 2D.

The AFM measurements presented in this chapter were performed using a Veeco Bioscope II Multimode Atomic Force Microscope with a Nanoscope III controller. Samples were imaged in tapping mode in air using a MikroMasch Ultrasharp noncontact 15 series tip.

2.2.4.5 Lipid bilayer characterisation by Fluorescence Correlation Spectroscopy

FCS is a technique based on monitoring the fluctuation of the emission intensity of a fluorophore. As illustrated in Figure 41, FCS involves excitation of fluorescent molecules by a collimated laser beam focused into a confocal volume within the sample.⁴³ By entering or exiting the confocal volume, fluorophores induce a fluctuation in the emitted light intensity, which is collected by the objective and separated from the excitation light by a dichroic mirror and an emission filter. Light not originating from the confocal volume is then stopped by a pinhole and photons passing through it can reach the detector. The relative change in emitted light intensity is dependant of the number of fluorescent molecules in the confocal volume. Indeed, the less molecules,

the bigger the fluctuation in intensity is when one is entering or leaving the confocal volume, which is the reason why FCS is considered as a single molecule detection technique.

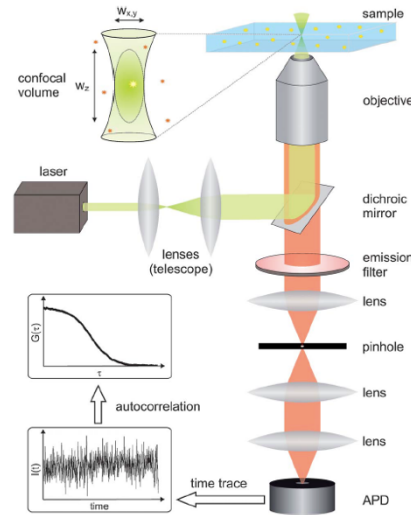


Figure 41 : Schematic of a typical FCS setup. Image reproduced from reference.⁴³

Autocorrelation function measures the self-similarity of the fluorescence signal with time. Monitoring the fluctuation of fluorescence intensity over a period of time (time trace) allow to build a correlation curve $G(t)$ according to the equation below:

Equation 4 : Autocorrelation function based on fluctuation of fluorescence intensity over time. with $\delta F(t) = \langle F \rangle - F(t)$ and $\delta F(t + \tau) = \langle F \rangle - F(t + \tau)$, where $\langle F \rangle$ is the average intensity, $F(t)$ the fluorescence intensity a time t , and $F(t + \tau)$ the fluorescence intensity after a delay time.

$$G(t) = \frac{\langle \delta F(t) \delta F(t + \tau) \rangle}{\langle F \rangle^2}$$

Parameters such as the diffusion coefficient or the concentration can be calculated by fitting data of the experiment to the autocorrelation function.⁴⁴ Due to the spatial restriction of the system, data obtained for a planar lipid bilayer will be fitted to a 2D system according to the following equation, rather than a 3D one more adapted for molecules freely diffusing in solution.

Equation 5 : Autocorrelation function fitted to a 2D system.

$$G(\tau) = 1 + \frac{1}{N} \frac{1}{1 + (\tau/\tau_D)^\alpha}$$

Here, N represents the average number of fluorescent particles in the confocal volume, α the anomalous exponent and τ_D the diffusion time. N and τ_D can be extracted from the experimental data and once the radius (ω) of the observed confocal volume is known, the diffusion coefficient D can be calculated according to the equation below.

Equation 6 : Einstein's equation for the calculation of the diffusion coefficient of the fluorescent probe.

$$D = \frac{\omega^2}{4\tau_D}$$

Regarding data presented in this chapter, Fluorescence correlation spectroscopy measurements were performed by Dr. Siva Ramadurai using a Pico Quant Micro Time 200 microscope.

2.3 Results and discussions

2.3.1 Microfluidic device testing

Compared to the current method used in the group to do FCS measurements of MSLBs on PDMS cavities²⁶, the microfluidic fabrication method presented in this chapter may allow a better reproducibility of the cavities chamber's dimensions, particularly its height within a sample and from batch to batch, which can be critical to be able to focus on the lipid for the measurement. Indeed, the water immersion objective used on the FCS system allows a working distance of only few hundred micrometres.

The method currently used in the group to build the microfluidic chamber consists of curing PDMS over a piece of mica, which has been glued to a microscope glass slide. However, if this mica substrate is too thick, it is not possible to focus on the PDMS surface, therefore layers have to be peeled off before first use until a correct height is reached. Unfortunately, this parameter is only verified at a late stage, during the FLIM measurement of the sample. Also, layers of mica are peeled off heterogeneously from the microscope glass slide from batch to batch, as they are sticking to the PDMS during the curing process, modifying the height of the chamber and mostly creating an unlevelled surface.

Regarding the new microfluidic fabrication method proposed here, the constant thickness of the double-sided PSA used to create the fluidic chamber could overcome variability of the PDMS chamber due to different issues such as the amount of glue used to stick the mica sheets, to seal the PDMS chamber on the glass slide, or from the mica thickness that can vary from batch to batch for reasons explained previously.

The critical part in the fabrication of the different parts used to build up the device was the parameters of the CO₂ laser. Adjustment of the cutting velocity (vector speed) and the laser power (vector power) depending on the thickness of the PMMA was essential to ensure a good quality of the cut. As the HAZ (Heat Affected Zone) increases with the laser power and decreases with the cutting velocity⁴⁵, a compromise had to be found to allow the laser to cut through the whole PMMA thickness without creating unwanted shape at the edge of the cut. Indeed, over-heating the thermoplastic during the cutting process induces a "lip phenomenon" due to a burr instead of getting a sharp 90 degrees cut as illustrated in Figure 42. This small defect leads to leakage issues, as the PMMA cannot bind properly to any other flat rigid surface at this specific area.

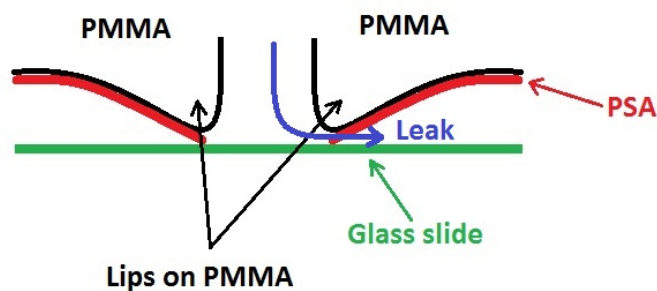


Figure 42 : Schematic of the “lip phenomenon” leading to a leakage issue of the microfluidic device at the edge of the cut.

Once the CO₂ laser processing parameters were optimised, the different parts were assembled as described previously and a leaking test was performed. Figure 43 shows the red food dye travelling without any leakage from the inlet of the “supplying” part of the microfluidic device, to the chip where the MSLB will be and where measurements will take place. This shows the successful assembling and connection between the two parts of the microfluidic device.

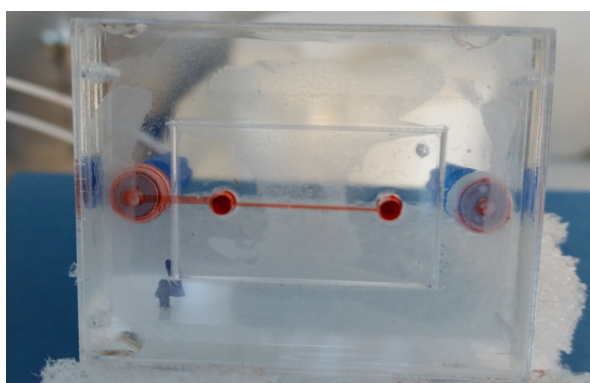


Figure 43 : Picture of the assembled microfluidic device leakage test performed with a red food dye.

For the sake of simplicity during the device development, the cavities substrate has been designed with only one channel. However, multiple inlets and outlets associated to channels could be easily implemented as shown in Figure 44, making the device a multi-channel microfluidic device to allow the study of different drugs and/or concentrations at the same time. On one hand, this would considerably decrease the time of sample preparation, and on the other hand could improve the variability of results, as the lipid bilayer tested in the different channels would be formed on a unique sample. Due to the versatility of the lipid bilayer formation method used in this project,

this device could also allow the study of various asymmetric lipid membrane compositions on the same sample, by having a common first lipid monolayer formed by Langmuir-Blodgett technique, but different vesicles injected in the independent channels, thus forming lipid bilayers of diverse nature.

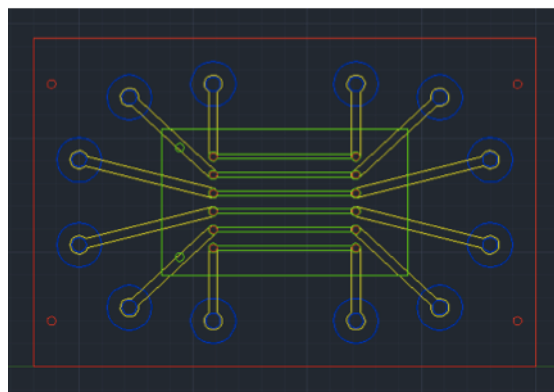


Figure 44: CAD design showing the superposition of different layers composing a multi-channel device (6 independent channels) built on the same configuration as the single channel one.

2.3.2 Fabrication of a PMMA substrate for Supported Lipid Bilayers

Several considerations motivated the choice of PMMA as a substrate for cavity supported lipid bilayers. PMMA is commonly used in microfluidics device due to its biocompatibility and its good optical properties, but also it can easily be processed. This transparent material presents very low auto-fluorescence, which is a critical parameter for our FCS application. The major drawback of this material lies in its natural hydrophobicity with a static contact angle of 68° to 83° , which would not allow a uniform spanning of the lipid bilayer at its surface.^{6,27-29} However, its top surface can be easily rendered hydrophilic by chemical modification. Finally, as the first part of the microfluidic device is PMMA based, the same assembling technique involving PSA intermediate layers could be used as described previously to assemble the two main parts of the device.

Regarding the fabrication of the micro cavity array aimed at supporting the lipid membrane, the choice of the fabrication method used was mainly driven by the constraints in size and shapes of the desired microstructures. Indeed, lately published by our group, lipid bilayer can be formed over a buffer filled gold⁴⁶ or PDMS²⁶ micro cavity array, with appropriate prior chemical treatment to render the top surface hydrophilic. In both case, cavities were up to $3\mu\text{m}$ diameter and had a spherical shape.

Trials done to replicate bilayer formation at cylindrical shaped cavities in PDMS did not lead to supported lipid bilayers and this was attributed to incomplete filling of the cavities, suggesting that the hemispherical shape of the cavities has its importance.²²

As the challenge in the fabrication of this micro cavity array is not in the aspect ratio but more in the respect of the size and shape of the cavities, replication by hot embossing could, in principle, answer our needs.

2.3.2.1 Method A: Hot embossing cavities using a silicone-based master

The easiest way to cast silicone to achieve replication of features is by pouring the material over a mould presenting the structures to cast at the bottom, that is fully open at the top. However, this approach can lead to nonuniformity in level and thickness issues that can disrupt the embossing process. Indeed, the homogeneity of the embossed structures depends strongly on the quality of the embossing master. Achieving a good embossing master using this technique demands the mould to be placed into a perfectly levelled curing chamber. This is particularly difficult to assure, as ovens are not made for this purpose and because the structures are only 1.5 μm high spread across a few millimetres. An uneven master would exert a greater pressure on the PMMA substrate at its thickest region, due to the parallelism of the embossing system hot plates. This difference in pressure leads to inhomogeneity of the microfeatures across the whole embossed area.

To avoid this issue, the strategy adopted was to hold the substrate to be replicated vertically inside a closed mould instead of horizontally. The level of the silicone based embossing master was then given by the parallelism of the mould inside faces rather than by the level of the mould support or the oven during the curing process.

2.3.2.1.1 Hardness optimisation of the silicone based embossing master

Elastosil® RT 607 was chosen over the commonly used PDMS Sylgard 184 as it presents a higher hardness while keeping a low viscosity allowing filling and moulding of cavities. This pourable, addition-curing RTV-2 silicone rubber is widely used as an encapsulant for electric circuits, as it is flame retardant and has a good heat resistance. RTV-2 refers to a Room Temperature Vulcanization silicone composed of two parts that need to be mixed together to form a homogeneous compound. The fact that this silicone can cure at room temperature makes it easy to use and does not require any special equipment to be processed. As opposed to condensation-curing compounds,

addition-curing silicones are composed of two parts, one containing a polymer and a platinum catalyst (part A), the other containing a polymer and a crosslinker (part B). When put in contact, the curing process starts to form the final elastomer, as illustrated in Figure 45. The hydrogenosilane containing crosslinker will bind the end of the polymer chains by hydrosilylation of vinyl groups.

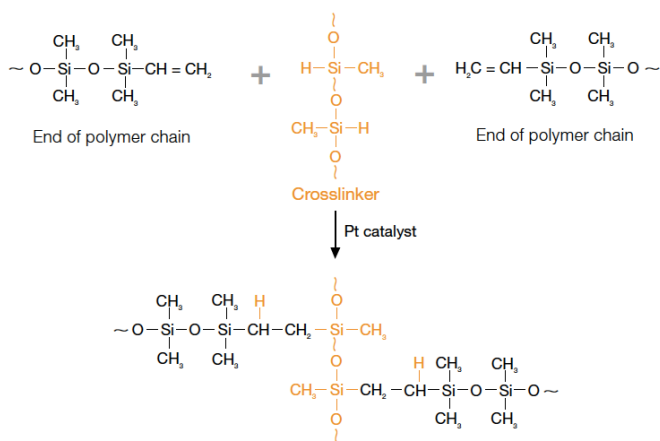


Figure 45 : Schematic of the chemistry involved during curing of addition curing RTV-2 silicone rubber. Reproduction from Wacker Silicones – Elastosil® - Bonding, Sealing, Potting/Encapsulation and coating with RTV silicone rubber compounds.⁴⁷

The first embossing trials done on PMMA were performed with a silicone embossing master prepared in a 9:1 (w/w) ratio of (silicone elastomer base : curing agent) according to the supplier recommendations⁴⁸ and also as reported by J. Steigert et al. in the prototyping of microfluidic chips in COC.²³ However, despite optimisation of the embossing parameters, this silicone-based master did not allow a correct replication of the cavities, as presented later on in section 2.3.2.1.4. Therefore, various curing parameters of Elastosil® RT 607 were studied in order to obtain:

- the hardest cured embossing master possible, to achieve heat and pressure resistance, to enable the substrate to be reused for several hot embossing cycles;
- a viscosity of the mix before curing low enough to fill up the cavities and yield a well resolve moulding.

Key parameters that can influence the hardness of the cured material are:

- the ratio of silicone elastomer base vs. curing agent used to prepare the mix;
- the temperature used during the curing process.

For this study, a 6 mm thick PMMA disc was designed to fit in the aluminium mould, to cast 3 samples of silicone simultaneously as shown in Figure 46. Dimensions of each squared cured sample after demoulding was approximately 35 mm x 35 mm x 4.2 mm. To evaluate the hardness of the obtained material, hardness shore A and compressive strength measurements were examined.

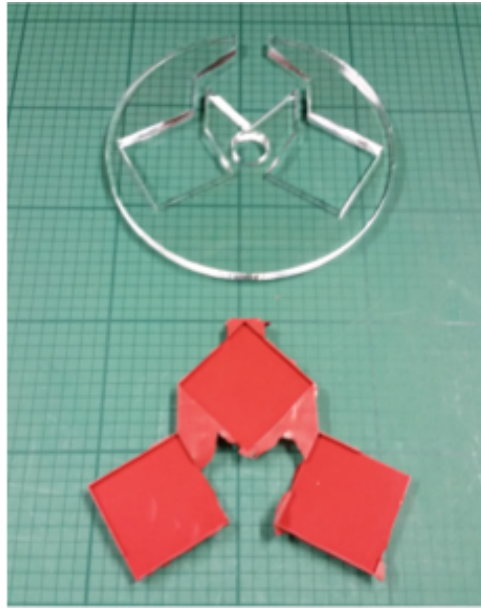


Figure 46 : PMMA disc mould used to build silicone samples for hardness optimisation study.

2.3.2.1.1.1 Study of the curing temperature

Seven different curing temperatures were evaluated for Elastosil® RT 607 samples. In each case sample were prepared according to the supplier recommendations by mixing the silicone elastomer base and the curing agent at a ratio of 9:1 in weight. To ensure complete curing, samples cured at temperatures below 70 °C were left in the oven overnight and samples cured above 70 °C were cured for 30 minutes before cooling down to room temperature and demoulding.

Hardness shore A measurements

High hardness of the embossing master is desirable for our application to prevent the deformation of the silicone-based master during the embossing process under temperature and pressure constraints, ensuring accurate replication of the desired features.

In order to measure polymer hardness, a grid was drawn on each sample allowing a maximum of 36 measurements of hardness shore A with a durometer, as illustrated in Figure 47 and Figure 48. Measurements were separated by 5 mm from each other, ensuring a representative study of each sample. For each series of measurements, outliers were excluded using the statistical Grubbs' test at a 0.05 significance level on a minimum population of 31 measurements per sample. Excluded data, i.e. outliers below the average value are thought to arise from the presence of air bubbles under the measurement point. These make the material more compressible, and thus appearing softer. To study reproducibility of the manufacturing process, a second batch of 3 samples per curing temperature was prepared under the same conditions and the hardness compared across each batch.



Figure 47 : Durometer used for hardness shore A measurements.

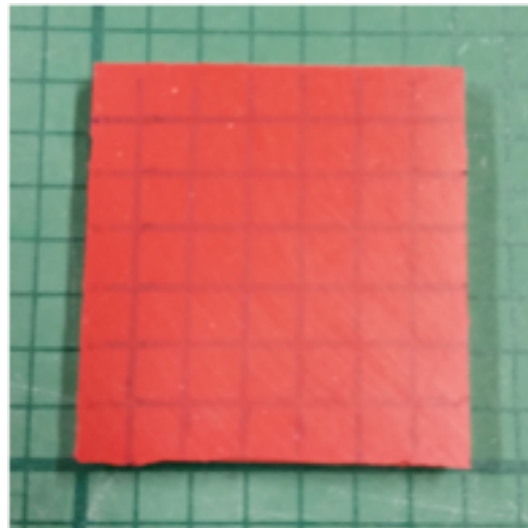


Figure 48 : Elastosil® RT607 sample for hardness shore A measurements.

Figure 49 gives a representation of the reproducibility of the hardness shore A depending on the curing temperature. Detailed results obtained for the first and second batch of samples can be seen in Appendix A.

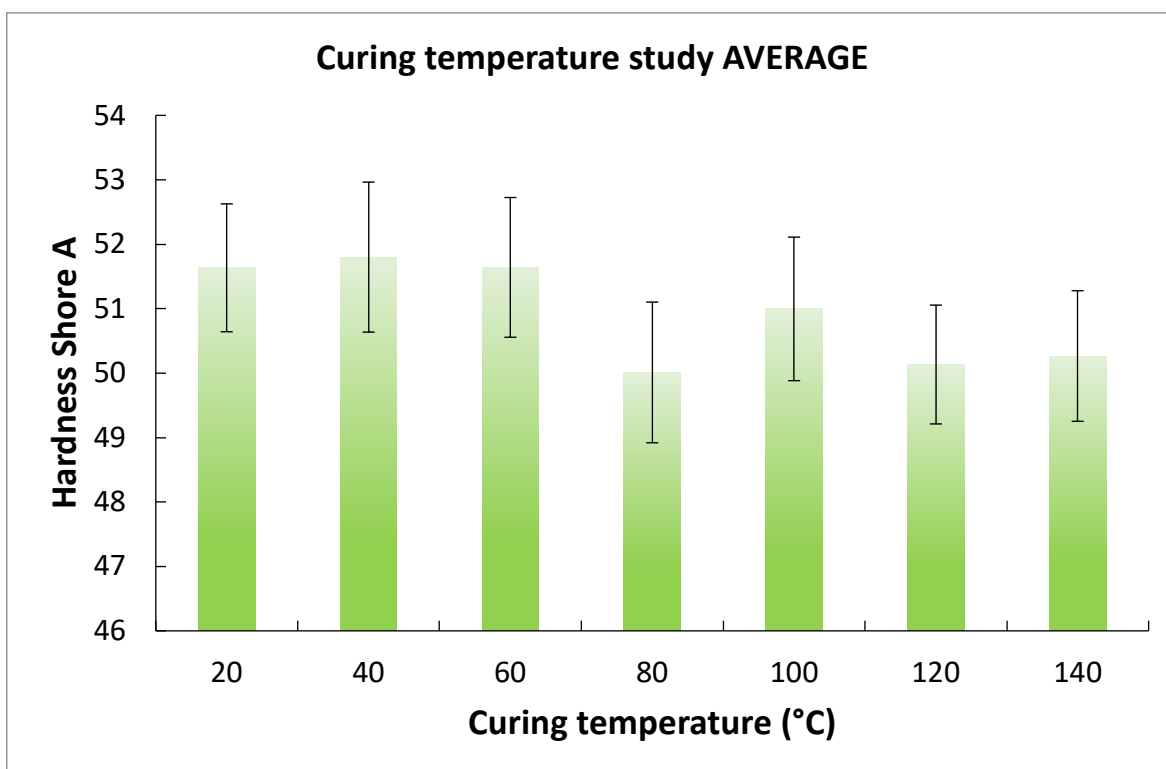


Figure 49 : Results of Hardness shore A measurements completed on two batches of Elastosil® RT607 samples fabricated under reproducibility conditions (3 samples per batch per temperature tested with a minimum of 31 measurements per sample after statistical treatment). Samples have been prepared in a 9 :1 ratio (elastomer : curing agent) and cured at different temperature.

Results obtained show that within experimental error, the curing temperature has little impact on polymer hardness. This result conflicts with what D. Johnston et al. reported in their experimental study on the variation of the mechanical properties of Sylgard 184 (Dow Corning).⁴⁹ Indeed, they reported that, like various other elastomers, PDMS mechanical properties vary with curing temperature. The most commonly used elastomer used in microfluidic applications presented a Hardness Shore A varying from 44 to 54 over a range of curing temperature tested going from 25 °C to 200 °C. As it varies from 50.0 to 51.8 over the different temperature tested, Hardness Shore A of Elastosil® RT607 seems independent of the curing temperature.

Compressive strength measurements

With the same samples used for hardness shore A measurements, we also studied compressive strength. As explained previously, compressive strength reflects the material's stiffness by applying a compressive stress to the substrate and measuring its deformation. In this study, the results of measurements helped us to understand what the influence of the curing temperature is on the stiffness of the material. Similar measurements are shown in following section to understand the influence of the ratio (elastomer : curing agent) during the embossing master preparation. Figure 50 shows the average stress versus strain measured on a batch of 3 samples for each curing temperature tested.

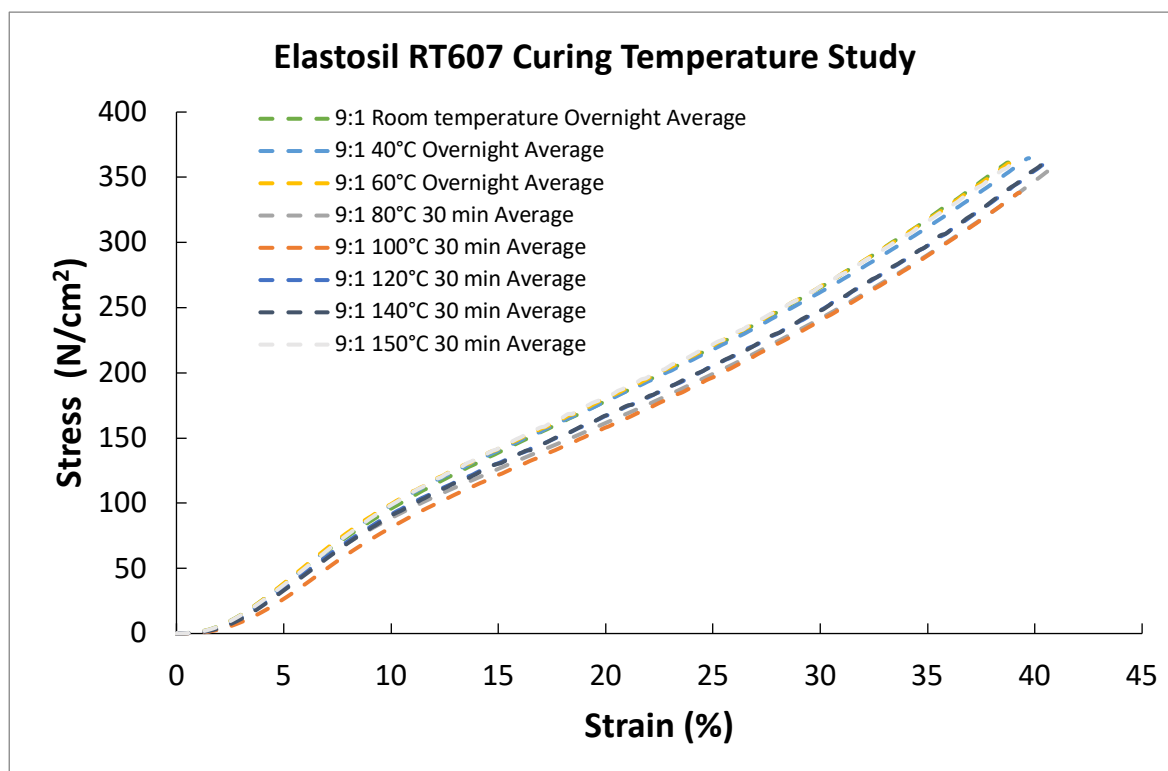


Figure 50 : Compressive strength measurements done on Elastosil® RT607 samples. Samples have been prepared in a 9 :1 ratio (elastomer : curing agent) and cured at different temperature.

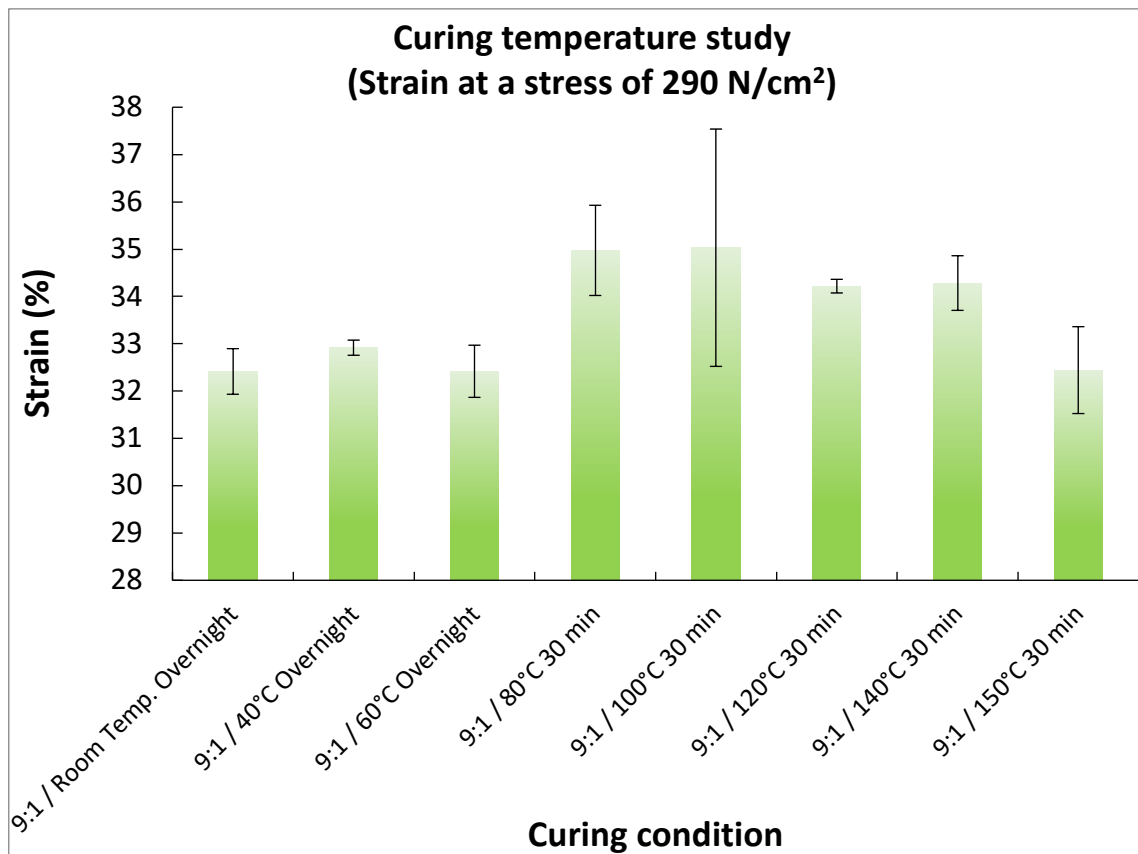


Figure 51: Strain values at a stress of 290 N/cm² obtained during compressive strength measurements done on Elastosil® RT607 samples. Samples have been prepared in a 9:1 ratio (elastomer : curing agent) and cured at different temperature.

For an embossing pressure of 290 N/cm² suggested in the internal Standard Operating Procedure⁵⁰ as a parameter for process optimisation, strain of the different sample tested varied from 32.4 % to 35.0 % as illustrated in Figure 51, which represents a small variation between preparation conditions. These results show that within experimental error the curing temperature does not affect the hardness of the cured Elastosil® RT607. The variability observed could be associated mainly with reproducibility of sample preparation or to the measurement itself.

Combined therefore, the data obtained for the hardness shore A and compressive strength studies indicate that the curing temperature has little impact on the material strength or hardness. It was thus decided to cure Elastosil® RT607 at the relatively low temperature of 40 °C overnight when fabricating the silicone-based master for hot embossing purpose. Such a temperature was selected in order to reduce the risk of shrinkage of micro-features during the curing process.

2.3.2.1.1.2 Study of the impact of the ratio silicone elastomer base vs. curing agent on Elastosil® RT607

To evaluate the impact of mixing conditions on the polymer hardness and strength, 11 different ratios in weight of (silicone elastomer base : curing agent) for Elastosil® RT607 were tested. Samples were prepared in batches of three using the set-up described in section 2.3.2.1.1. All samples were cured at 80 °C for 30 minutes before cooling down at room temperature and demoulding. Curing conditions of 40 °C overnight highlighted in the previous section were not chosen for this experiment as the two studies were conducted simultaneously and conclusions were drawn only later on. Nevertheless, results obtained for this study can be extrapolated to these curing conditions as it was shown that curing temperature does not impact the hardness and strength of cured Elastosil® RT607.

Hardness shore A measurements

The same measurement protocol and statistical analysis described for previous hardness shore A measurements was applied to the (elastomer base : curing agent ratio). Two batches of 3 samples per mixing ratio were examined. Figure 52 gives a representation of the reproducibility of the hardness shore A depending on the mixing ratio between the elastomer base silicone and the curing agent. Detailed results obtained for the first and second batch of samples can be seen in Appendix B.

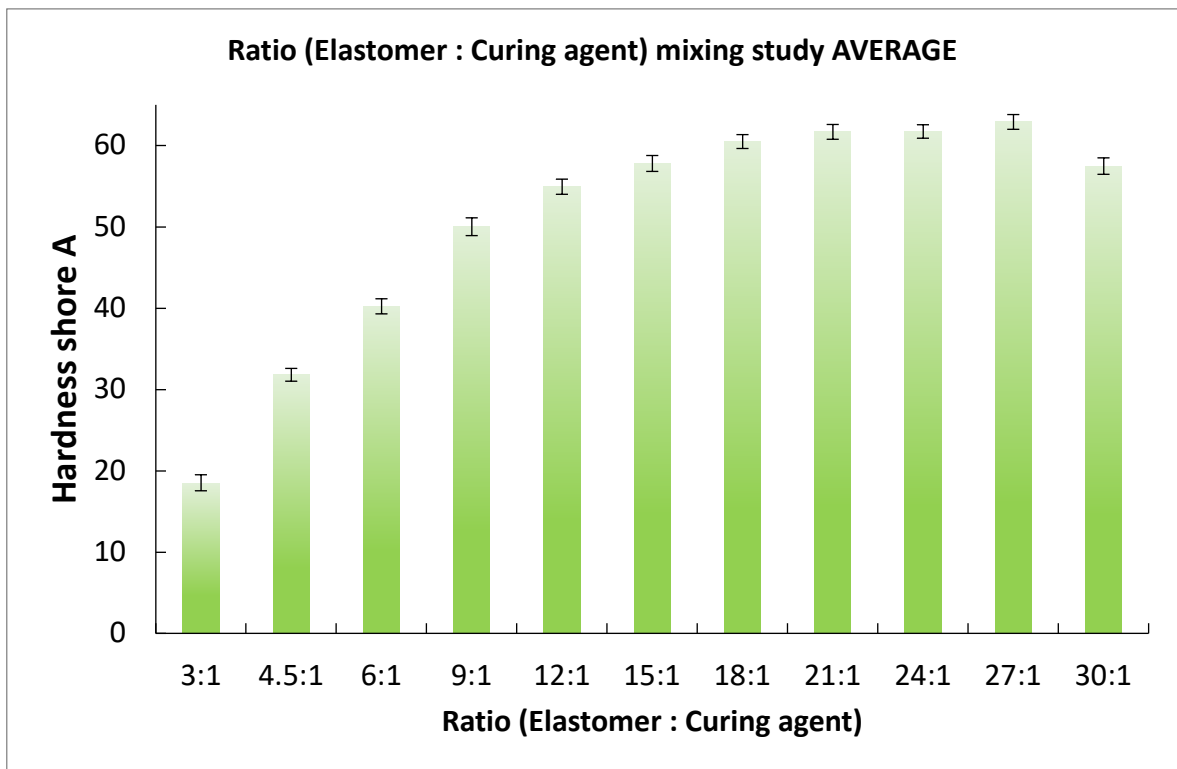


Figure 52 : Results of Hardness shore A measurements done on two batches of Elastosil® RT607 samples fabricated under reproducibility conditions. Samples have been prepared in different ratio (elastomer : curing agent).

Results obtained for this study show the importance of the mixing ratio (silicone elastomer base : curing agent) on the hardness of the cured material. Indeed, the average hardness shore A obtained with a durometer varies from a minimum of 18.5 for the cured material prepared at a 3:1 ratio mix, increasing and reaching a plateau at a 21:1 ratio with a hardness of 61.7. After reaching a maximum of 62.9 for a 27:1 ratio mix, the hardness of the cured material tends to decrease again as the ratio of silicone elastomer to curing agent is increased further.

This relatively large dependence of the hardness of the cured material on the mixing ratio could considerably influence the quality of the hot embossing process, as a softer embossing master would tend to deform due to the applied pressure and prevent the transfer and retention of the desired microstructures to the substrate. Conversely, a harder material would be less subject to distortion during embossing and would increase the chance of obtaining accurate replicas.

The small standard deviation in measured hardness from sample to sample for a same ratio mix indicates a well-controlled fabrication process. In case of the embossing master being damaged after several hot embossing cycles, a new one could be manufactured again using the original gold micro cavities negative mould and

insuring the reproducibility in time from batch to batch of the microstructures in the PMMA substrate.

Figure B1 in Appendix B shows also the results obtained for a sample of “clear PDMS” mixed in a ratio of 9:1 in weight (silicone elastomer base : curing agent) cured for 30 minutes at 80 °C. This “clear PDMS” is a sample of Sylgard® 184, silicone elastomer used broadly in the fabrication of microfluidic devices. A hardness shore A of 40.2 was obtained for this material, which is consistent with the supplier data⁵¹, which quoted a hardness of 43 for a cured sample prepared in a 10:1 ratio mix. This value justifies again the preferred choice of Elastosil® RT 607 to Sylgard® 184 as a base material for the fabrication of the embossing master, as it is harder.

Another reference for silicone from the same supplier with a higher hardness shore A was also tested. Elastosil® RT675 is a pourable, addition curing RTV-2 silicone rubber used for encapsulation of electronic compounds, and once cured following the supplier mixing recommendations, has a hardness shore A of 80 ⁵², versus 55 for Elastosil® RT 607. However, the limitation of this material was its higher viscosity of 50 000 mPa.s compared to 12 000 mPa.s for the Elastosil® RT 607. This high viscosity prevented correct moulding of the cavities as the silicone would not fill the cavities properly, resulting flat positive structures when demoulding as illustrated in Figure 53, with an aspect ratio too low to ensure a good embossing.

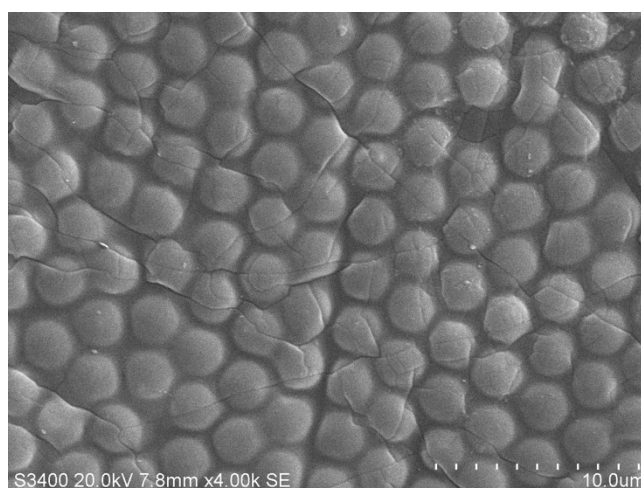


Figure 53 : Illustration of a silicone-based elastomer casted onto a gold microcavity array showing flat positive structures due to high viscosity before curing, which prevented correct moulding of the cavities.

Compressive strength measurements

The samples described above examined by hardness shore A measurements were then evaluated for compressive strength. Figure 54 shows results obtained for one batch of samples analysed on two different days. Samples prepared with a ratio (elastomer : curing agent) between 3:1 and 15:1 were analysed the same day and samples with a ratio 18:1 to 30:1 a different day.

Sample prepared with a ratio (elastomer : curing agent) 9:1 were analysed each day to check validity of the results.

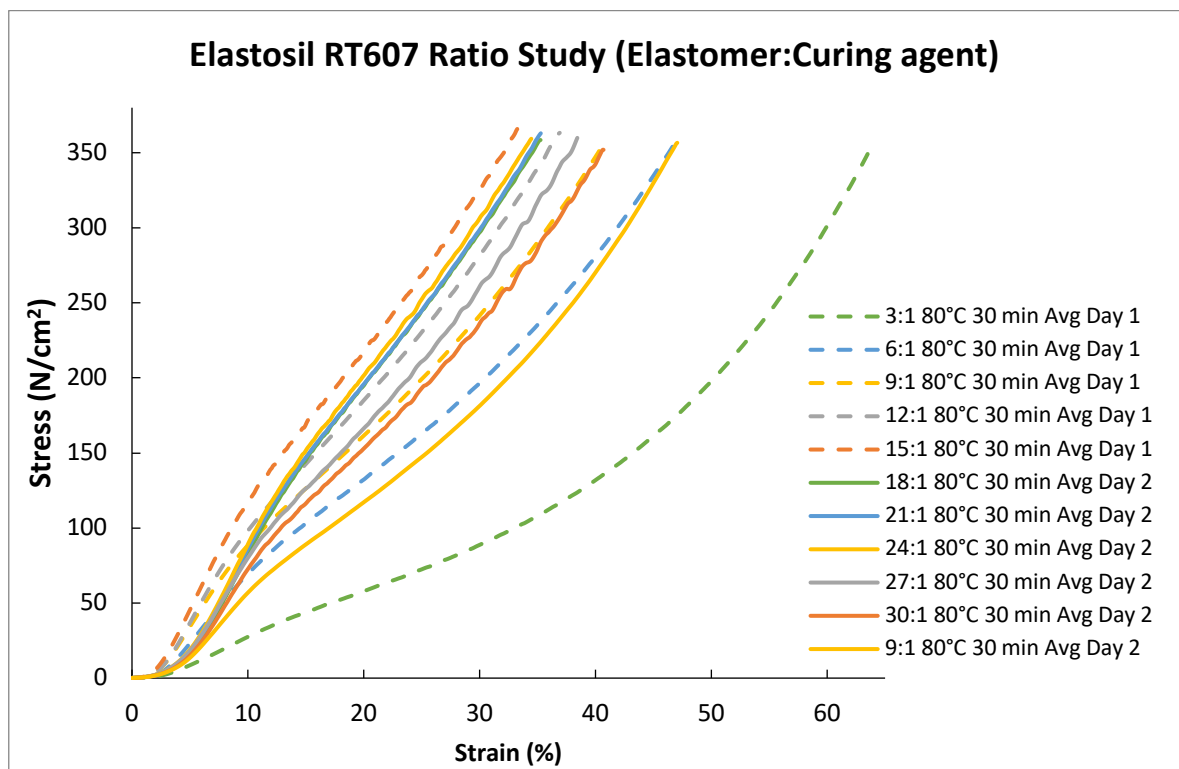


Figure 54 : Compressive strength measurements done on Elastosil® RT607 samples. Samples were prepared in different ratio (elastomer : curing agent).

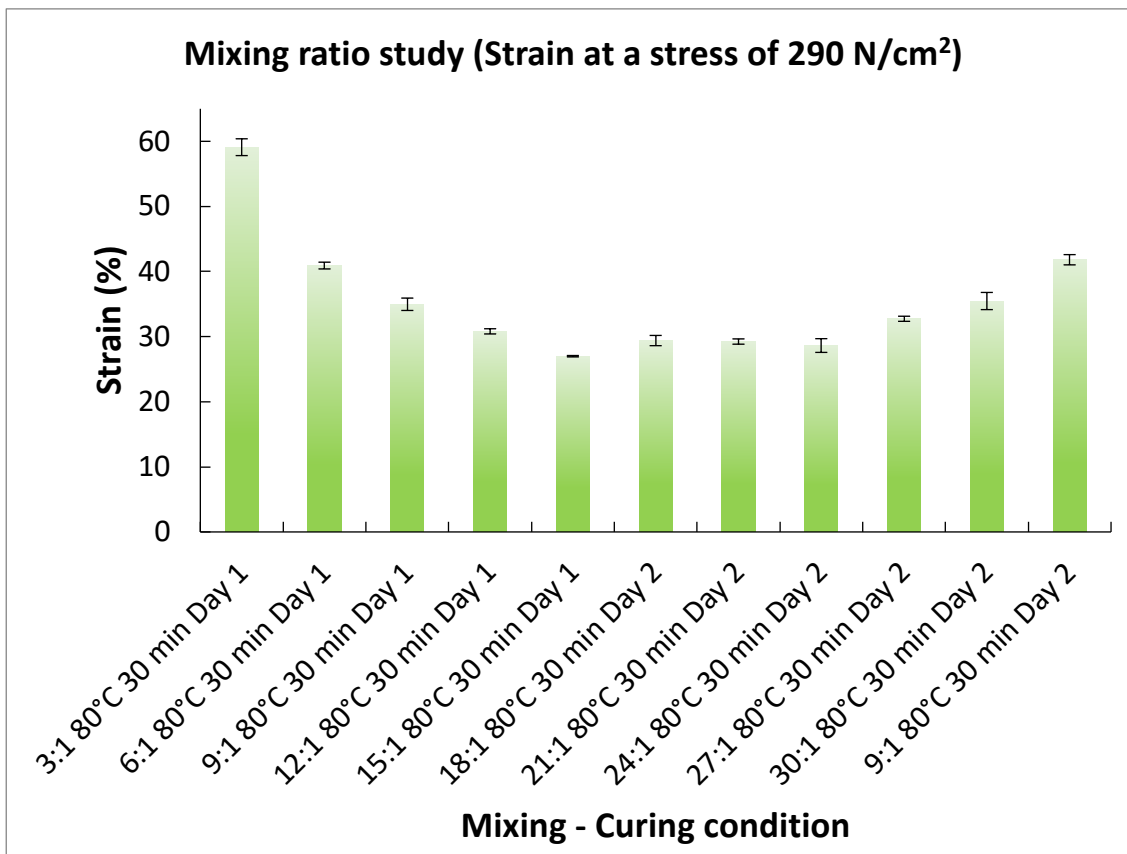


Figure 55: Strain values at a stress of 290 N/cm² obtained during compressive strength measurements done on Elastosil® RT607 samples over 2 days of measurements. Samples were prepared in different ratio (elastomer : curing agent).

From Figure 54 can clearly be seen that the difference between results obtained on sample 9:1 across the two days is likely due to systematic error. On day 1 the curve representing sample 9:1 presents a strain lower than the one corresponding to sample 6:1, meaning the sample is deforming less under a given pressure, thus is harder. However, the curve obtained for the same sample 9:1 obtained on day 2 presents a strain higher than the one corresponding to sample 6:1, contradicting the first conclusion. This is also illustrated in Figure 55, where strain values obtained for an applied stress of 290 N/cm² corresponding to the suggested embossing pressure have been isolated. Further measurements will prove that this shift in result was due to the equipment despite setting it with the identical parameters. Despite this shift in strain for a given mixing ratio/curing temperature between different days of analysis, this tool remains adequate to study a trend between process conditions of the Elastosil® RT607. Indeed, the relative change between samples prepared under different conditions is more of concern to the present work than the absolute value itself. To eliminate bias in the data obtained that could lead to a wrong interpretation due to the

equipment and not the sample nature itself, it has been decided to analyse samples from the same batch the same day.

Also, previous measurements show that the preload force needed before the grip was levelled was between 3 and 4 Newton, probably due to the small size of sample compare to the grip itself. Therefore, main parameters have been set up as follow:

- Pre-load force: 6 N
- Test speed 2.5 mm/min
- Force shutdown threshold: 80 %
- Upper force limit: 4500 N

As all samples have been made using the same mould, their respective height varied between 4.3 mm to 4.4 mm from one to another, ascertained by calipers before each measurement and sample height was set to an average of 4.35 mm for the compressive strength measurement. Data obtained for the two batches of samples are presented in Appendix C.

As the two series of samples have been analysed on different days, a bias can be noticed for sample prepared under the same conditions between batch 1 and batch 2. However, the trends within a single batch remains the same, showing that strain decreases as the ratio (elastomer : curing agent) increases, until a plateau is reached at a ratio of 18:1, where samples are the hardest. Strain starts again to increase as the ratio becomes higher than 27:1, rending the prepared sample softer. Average results of these two sets of measurements are presented in Figure 56 and a zoom of data obtained for an applied stress of 290 N/cm² is presented in Figure 57.

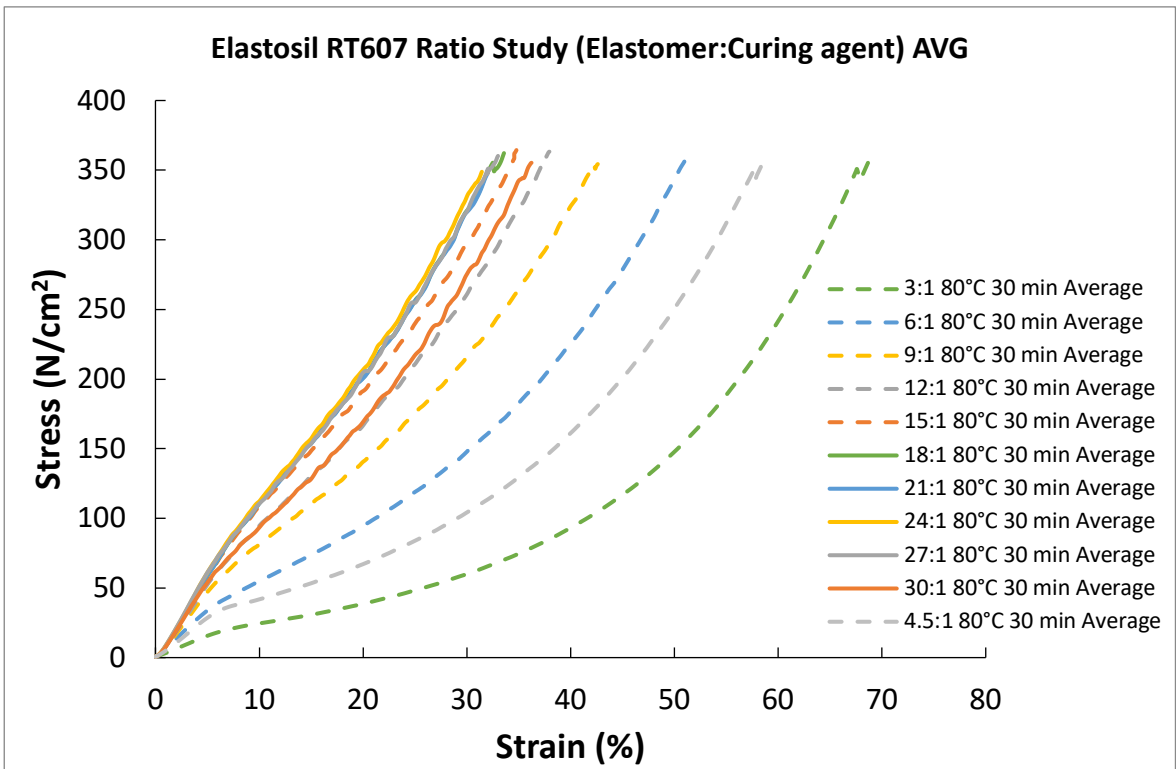


Figure 56: Compressive strength measurements done on two batches of Elastosil® RT607 samples fabricated under reproducibility conditions. Samples were prepared in different ratio (elastomer : curing agent) and analysed at different days.

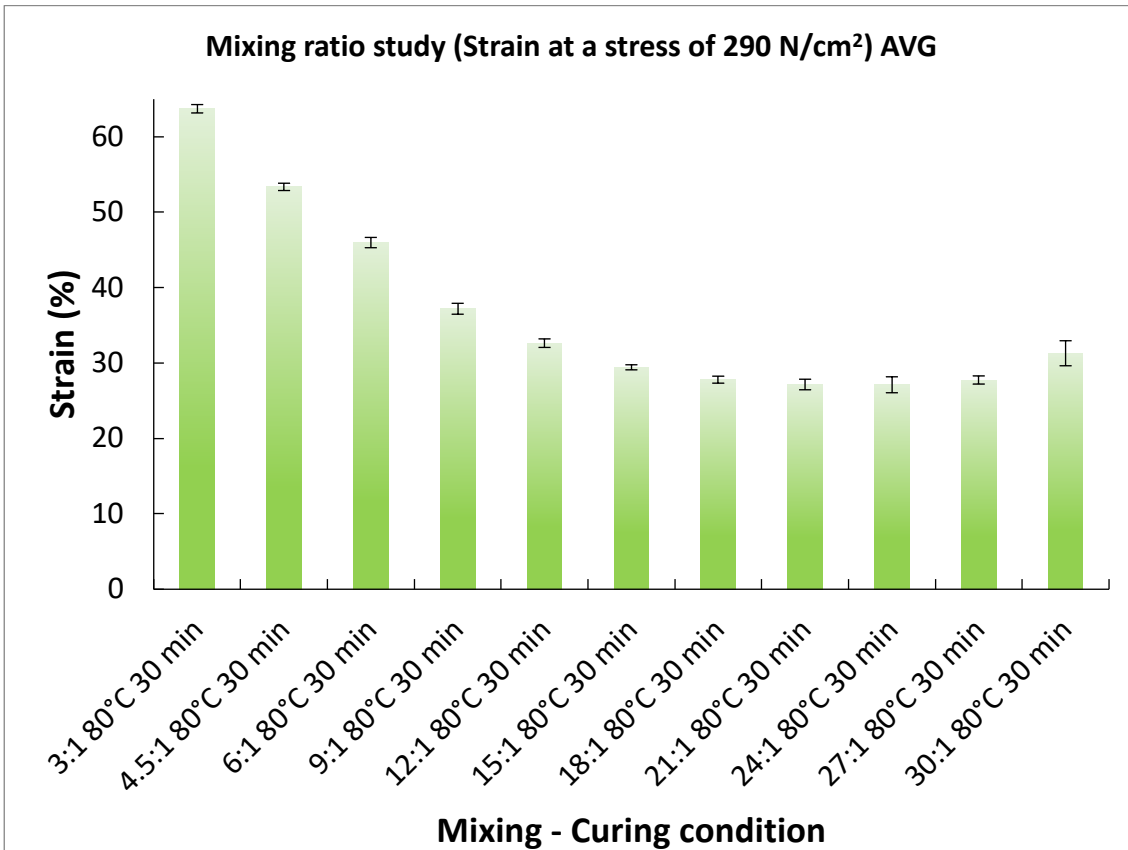


Figure 57: Average strain values at a stress of 290 N/cm² obtained during compressive strength measurements done on Elastosil® RT607 samples over 2 batches of 3 samples. Samples were prepared in different ratio (elastomer : curing agent).

Understanding the impact of curing temperature and ratio (elastomer : curing agent) on hardness and compressive strength on the polymer enabled us to define the parameters to yield hardest material possible for the embossing master. We define these as a curing temperature of 40 °C overnight and a ratio (elastomer : curing agent) of 21:1. Results obtained with hardness shore A or compressive strength measurement technique are consistent and allow us to conclude that the hardness of the cured Elastosil® RT607 is, as expected, strongly influenced by the ratio (elastomer : curing agent), but is not significantly affected by the curing temperature.

Table 5 presents the evolution of the strain for a given sample of Elastosil® RT607 prepared under different conditions along the hardness optimisation study. Combining results obtained on the curing temperature and mixing ratio studies, hardness of cured Elastosil® 607 has been increased by 32 % based on the strain values measured for an applied pressure of 290 N/cm², which is the pressure suggested for a good replication during the hot embossing process. The study also showed the resistance of the improved material, which did not break under pressure, which is a crucial characteristic for an embossing master.

Table 5 : Strain values of Elastosil® RT607 sample under an applied stress of 290 N/cm² showing the improvement of the material hardness along the study by changing parameters during the preparation.

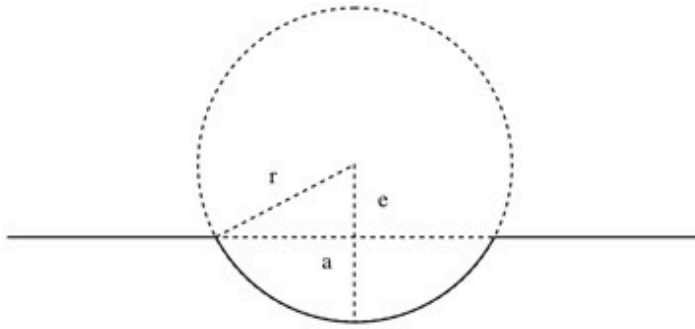
Curing conditions	Ratio (Elastomer : Curing agent)	Strain for an applied stress of 290 N/cm ²
30 mins at 80 °C	9:1	37.2 %
30 mins at 80 °C	21:1	27.2 %
Overnight at 40 °C	21:1	25.3 %

These new fabrication parameters provide a compromise between hardness and brittleness of the cured material, while maintaining low viscosity before curing insuring reliable formation of the desired positive microstructures. This should ensure reproducibility of the embossed cavities from batch to batch. However, the fact that the cured Elastosil® RT607 presents a strain of 25.3 % at the applied pressure of 290 N/cm² recommended in the internal standard operating procedure (SOP) suggests that the positive microstructures will still deform under pressure during the hot embossing

process, leading to cavities wider and shallower than the desired one. An alternative to this could be the use of a lower applied pressure during the hot embossing process to reduce the deformation of the embossing master, or to change strategy in the manufacturing of the embossing master as the use of Elastosil® RT607 shows its limitations.

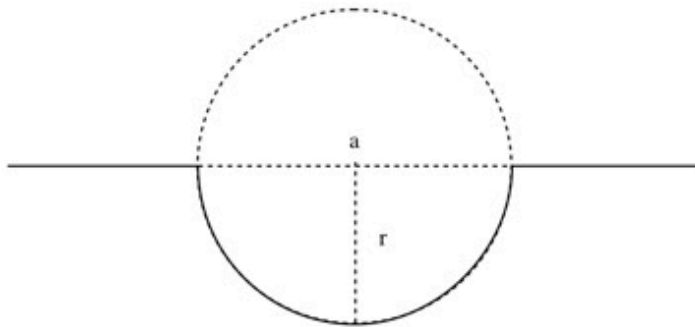
2.3.2.1.2 Importance and characterisation of gold microcavities dimensions

The gold microcavities prepared by electrodeposition were assessed by SEM to confirm their dimensions and verify that gold was grown to a depth of the hemisphere. SEM gives a good indication of the dimensions of the substrate during development stage but is not precise enough to accurately characterise the depth of the cavities. Indeed, variations in apparent aperture size from SEM can correspond to relatively large variations in depth, since aperture dimensions smaller than the templating sphere diameter may be due to gold growth either above or below the sphere equator. Figure 58, Equation 7, Equation 8, and Equation 9 illustrate the three scenarios possible around the equator and the relation between aperture and cavity height in the case of a perfect sphere.



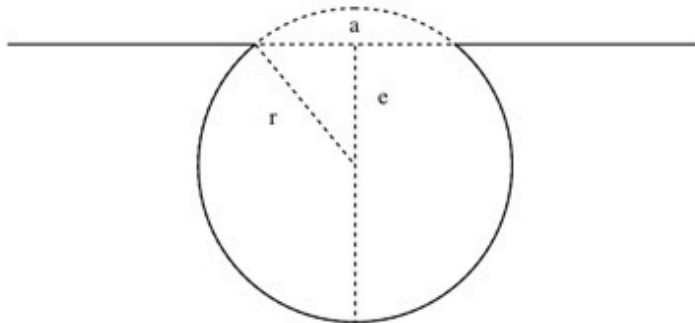
Equation 7 : Theoretical height of a cavity grown above the equator of the sphere.

$$h = r - \sqrt{r^2 - \left(\frac{a}{2}\right)^2}$$



Equation 8 : Theoretical height of a cavity grown at the equator of the sphere.

$$h = r = \frac{a}{2}$$



Equation 9 : Theoretical height of a cavity grown below the equator of the sphere.

$$h = r + \sqrt{r^2 - \left(\frac{a}{2}\right)^2}$$

Figure 58 : Schematic representing the 3 scenarios possible during gold electrodeposition around microspheres.

Equation 7, Equation 8, and Equation 9 give respectively the theoretical height of a cavity grown below, at and above the equator of the sphere.

« h » represents the theoretical height of the cavity;

« a » represents the diameter of the cavity aperture;

« r » represents the radius of the sphere used;

« e » represents the undergrown height for a cavity grown below the equator, or the overgrown height for a cavity grown above the equator.

Using 2.88 μm diameter spheres to build the substrate, the expected height of cavities should be 1.44 μm if gold electrodeposition is done to the sphere equator. Importantly, a cavity with a diameter of 2.82 μm measured with SEM, representing only 2 % variation in aperture size, will have a theoretical height of 1.15 μm if gold was

undergrown, corresponding to 20 % variation in depth compared to the expected depth, which is significant. Therefore, the 2D characterisation of the cavities by SEM should be completed by a 3D characterisation by AFM at the end of the development process to be sure of reaching the desired characteristics of the cavities and to ensure the successful formation of a lipid bilayer over a deep enough well.

Figure 59 shows a SEM top view image of the gold microcavities negative mould. Aperture diameter of the cavities appears to be around 2.80-2.90 μm , which matches with the average diameter of the polystyrene beads used of 2.88 μm . This difference between cavities could be attributed to the polydispersity of the solution.

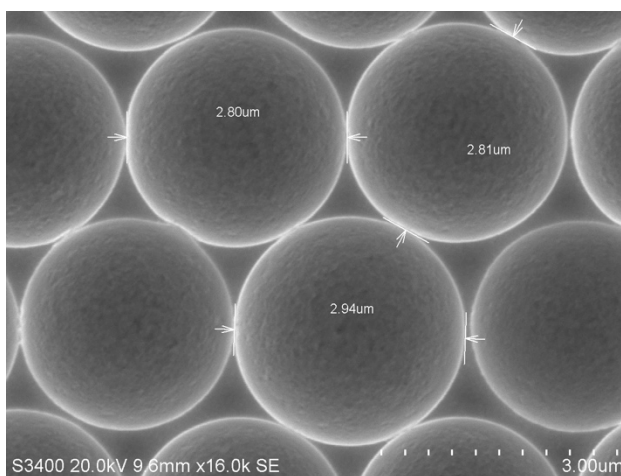


Figure 59 : SEM image of gold microcavities negative mould prepared with 2.88 μm diameter polystyrene spheres as a template. Gold solution was electrodeposited over a gold-silicon wafer at potential of -0.95 V until a charge of 0.8 C was reached.

Figure 60 shows 3D (a) and 2D (b and c) AFM images of the same substrate taken to characterize the aperture diameter and the height of the cavities. Aperture diameters of three adjacent cavities were measured (Figure 60 b) and were found to match with the SEM data. Although, Figure 60 c) shows that the corresponding heights of those cavities varies between 645 nm and 660 nm, where they should theoretically vary between 1427 nm and 1496 nm if cavities were grown until the equator of the polystyrene spheres. This 55 % deficit would be carried through the whole manufacturing process, resulting in shallow PMMA cavities despite hardness improvements achieved on the silicone based embossing master and the hot embossing parameters used. Therefore, characterisation of the gold microcavities negative mould is a critical parameter that needs to be checked in the early stage of the PMMA substrate fabrication process.

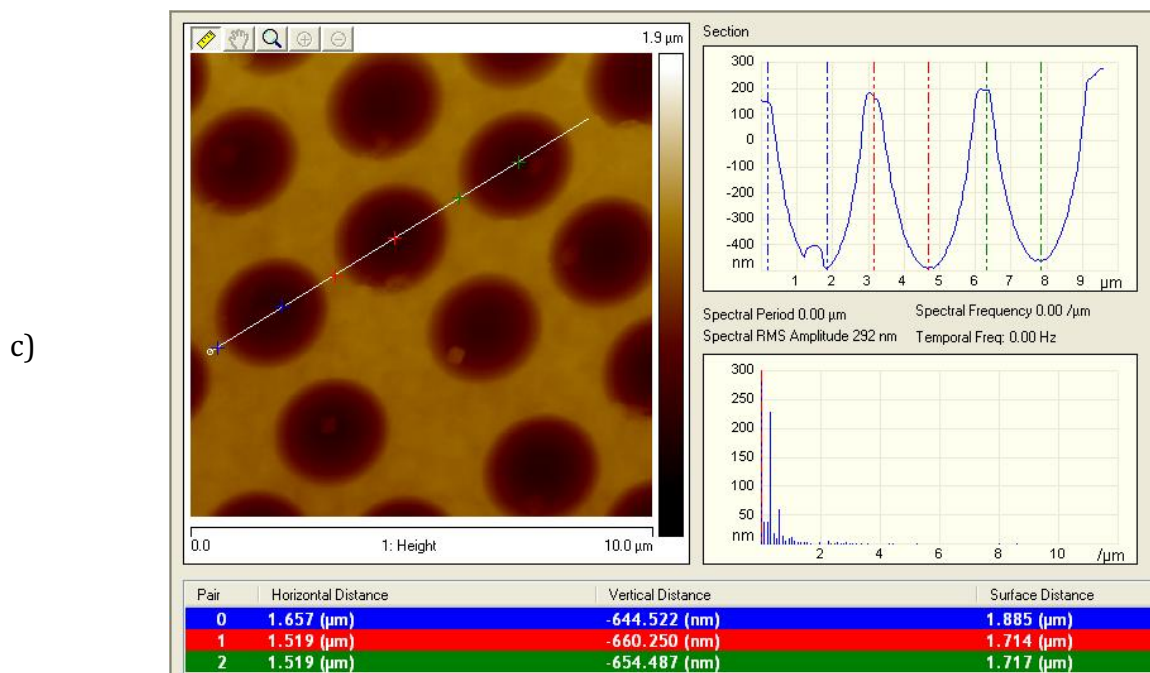
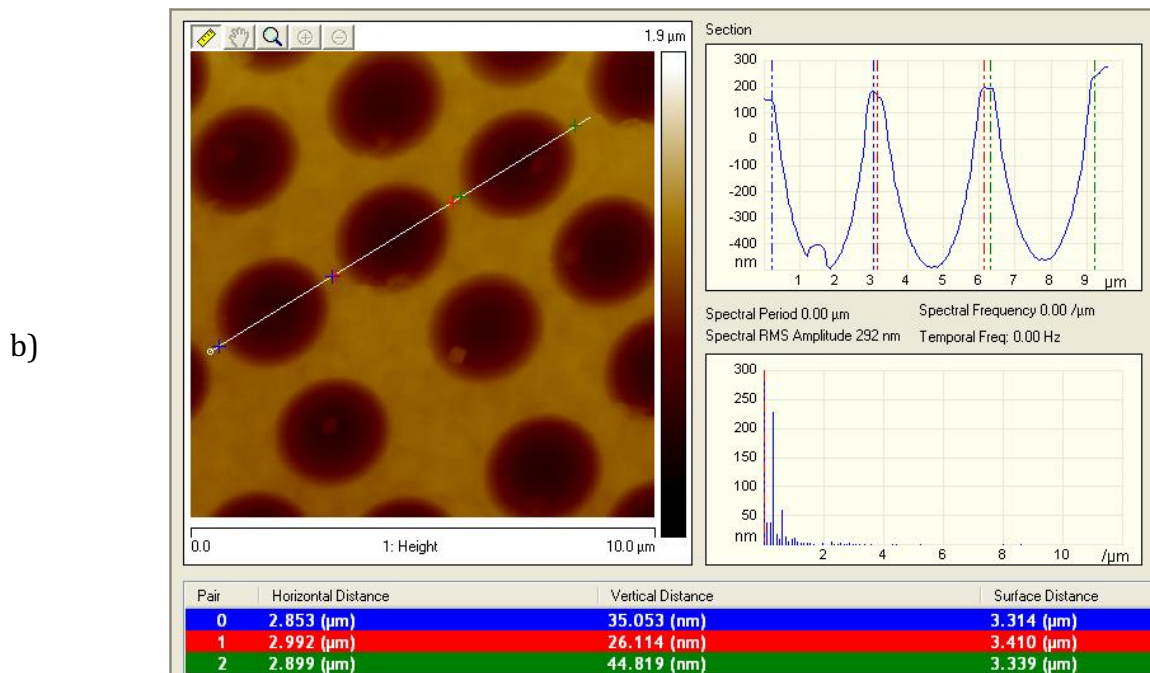
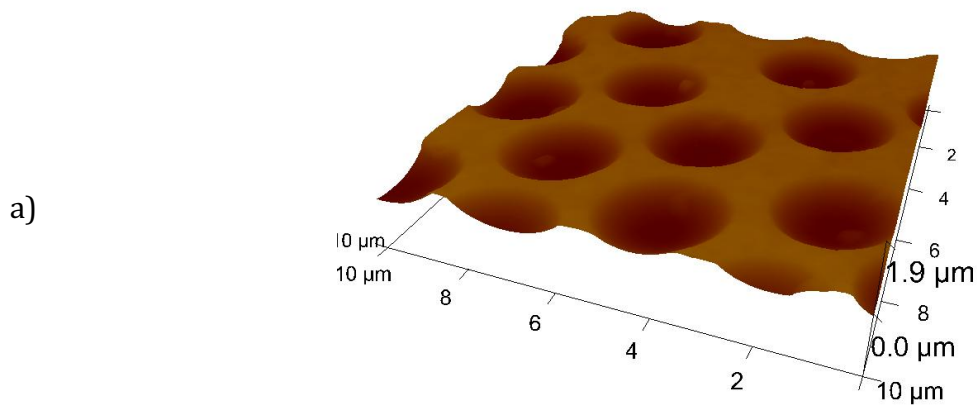


Figure 60 : 3D (a) and 2D (b and c) AFM images of a gold microcavities negative mould. Sample was imaged in tapping mode in air using a MikroMasch Ultrasharp noncontact 15 series tip.

After slightly adjusting the charge reached during the gold electrodeposition to 0.85 C, AFM measurements were then carried out on several samples until one with acceptable characteristics was identified, shown in Figure 61. The aperture diameter of 2.90 μm corresponds well to the average diameter of the polystyrene beads used of 2.88 μm and the height is now measured to be 1357 nm, which corresponds to only 6 % difference compared to the expected height if gold was grown perfectly to equator of the sphere template. This variation is acceptable as it should not affect the embossing process and would generate the desired positive structures for the silicone based embossing master.

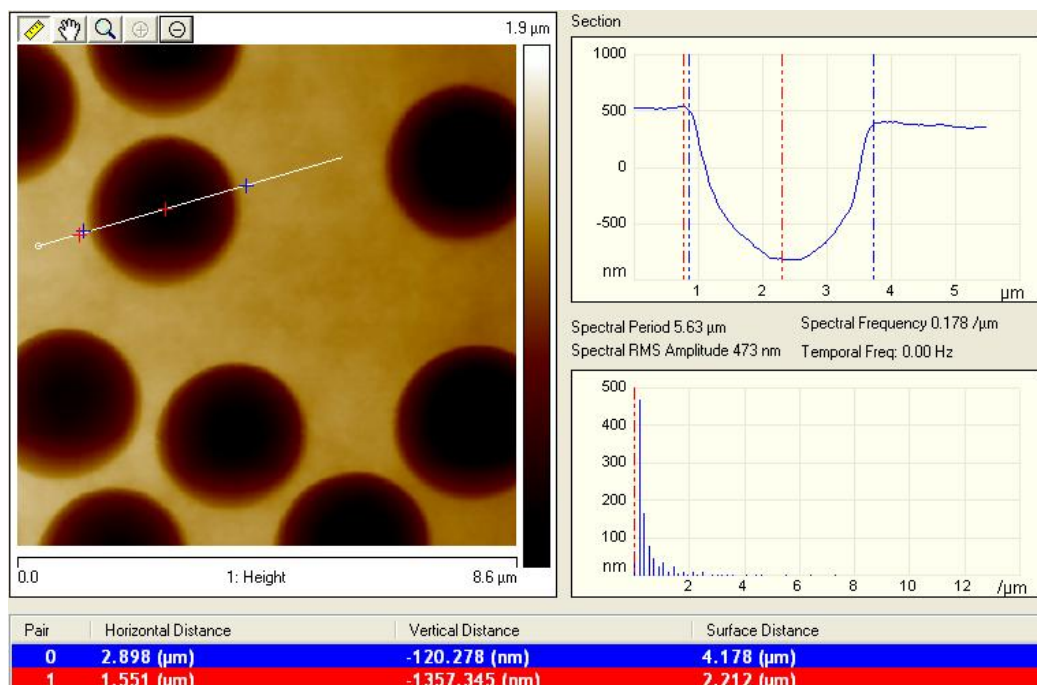


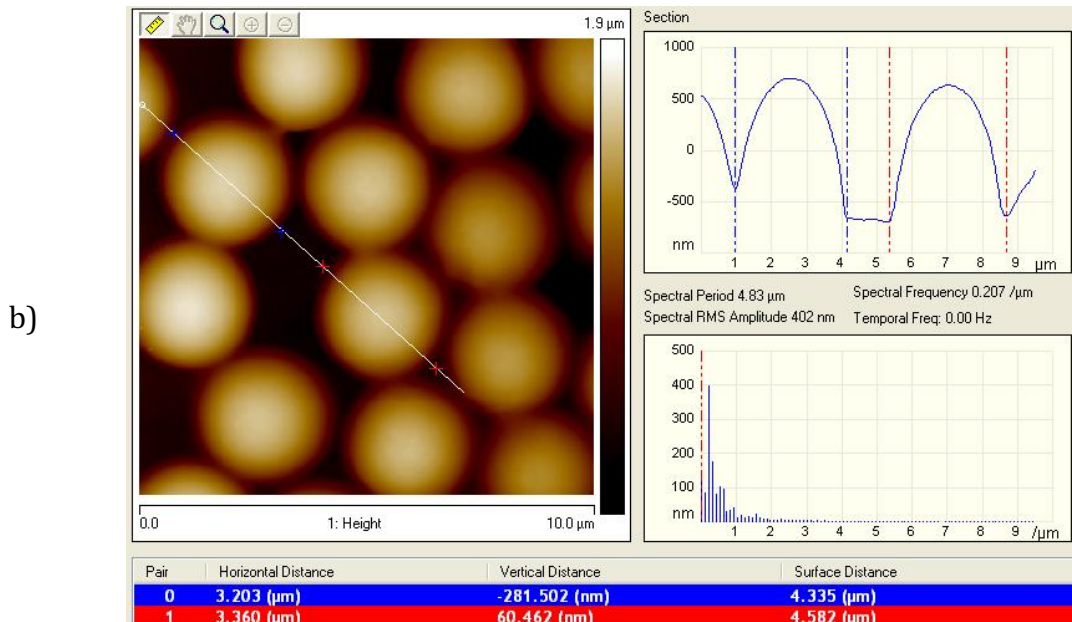
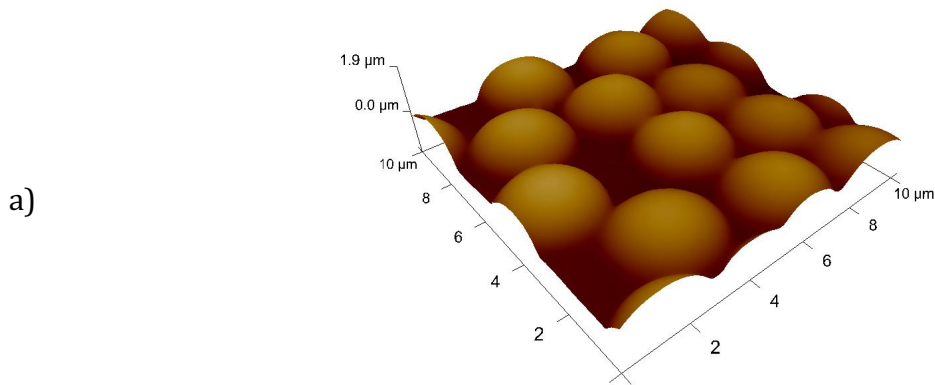
Figure 61 : 2D AFM image of an optimised gold microcavities negative mould (give details of AFM). Sample was imaged in tapping mode in air using a MikroMasch Ultrasharp noncontact 15 series tip.

2.3.2.1.3 Characterisation of positive features of the embossing master

To ensure that the filling of the entire cavities' volume by the uncured polymer was successful and that the demoulding process did not impact the shape of final structures, e.g. leading to fractured structures, the silicon embossing master was characterised.

Figure 62 shows 3D (a) and 2D (b and c) AFM images of the silicone based embossing substrate cast in the gold negative substrate characterised in Figure 61,

From AFM the diameter of positive structures presented in Figure 62 b) (3.20 μm and 3.36 μm) is larger than the aperture size of cavities on template substrate. The features height, Figure 62 c), is of the same order of magnitude as the cavities' templates. This difference in diameter is attributed to deformation of the master under the heat and pressure applied during the embossing process, showing that after just a few cycles it does not revert to its original shape. Such deformation is well known in mechanical testing where the cross section of cylindrical specimens is varying, and samples are "barrelling" during axial compression.^{53,54} Regarding the height of the structure, if compared to the theoretical value with correct gold growth to the equator of the 2.88 μm diameter spheres, the difference represents only 5 % to 8 % loss, which is acceptable. This loss could also be related to the deformation of the positive structure during the embossing cycle.



c)

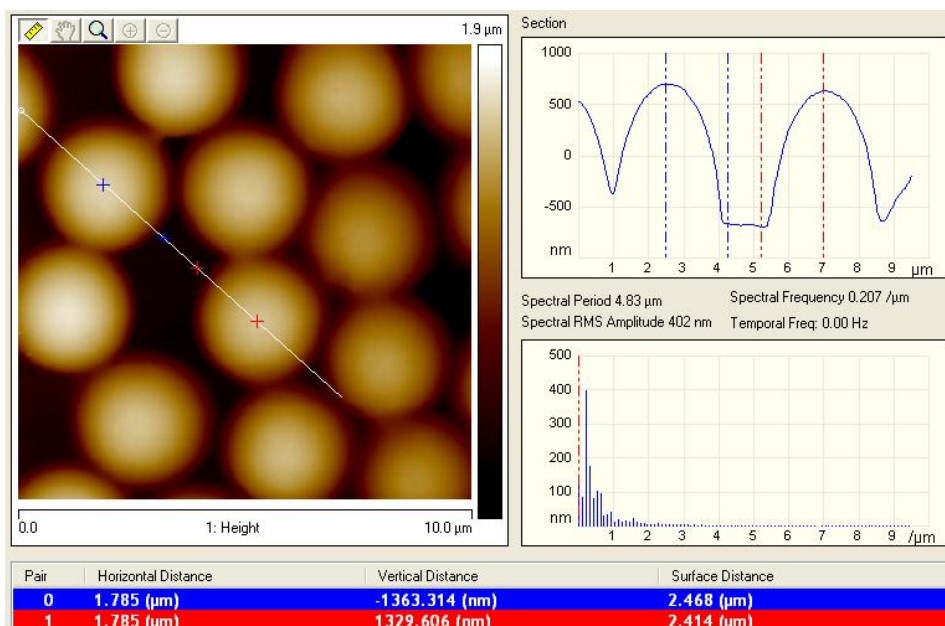


Figure 62 : 3D (a) and 2D (b and c) AFM images of the silicone based embossing substrate. Sample was imaged in tapping mode in air using a MikroMasch Ultrasharp noncontact 15 series tip.

2.3.2.1.4 Optimisation of hot embossing parameters

In order to optimise hot embossing of the substrates, parameters recommended in the internal SOP were initially applied.⁵⁰ However, those were not suitable as they are intended for hot embossing of PMMA discs using a SU-8 based embossing master with reservoirs and channels, with widths ranging from a few hundred micrometres to millimetres and heights ranging from 35 to few hundreds micrometres.^{23,55} The size of microstructures to be embossed in our case were much smaller, thus optimisation was required for our application.

First, the embossing temperature applied during the embossing cycle was optimised. This parameter depends on the T_g of the used PMMA. The SOP⁵⁰ suggested working at an embossing temperature between 15 to 40 °C above the T_g of the polymer. A compromise needed to be found to facilitate the filling of the embossing master microstructures in order to reduce the viscosity of the PMMA, without impacting negatively on its chemical and physical properties.

T_g of PMMA can vary widely from 85 °C to 165 °C depending on its composition, the fabrication process, and inclusion of co-polymers and co-monomers other than MMA.⁵⁶ Several techniques exist to measure this parameter, such as Differential Scanning Calorimetry (DSC), Thermal Mechanic Analysis (TMA) and Dynamic Mechanical Analysis (DMA). However, it has been reported that results could vary up to 20 °C or more depending the technique and conditions used.^{57,58} Therefore, as the

PMMA supplier was not able to give this information, several trials were carried out to estimate the best embossing temperature to be used for an embossing pressure fixed at 290 N/cm² and an embossing time of around 300 s (as recommended in the SOP).

Figure 63 shows images of the silicone based embossing master before hardness optimisation cured in a ratio 9:1 (elastomer : curing agent) at 80 °C during 30 minutes, and the PMMA substrates, embossed at the different temperatures. Corresponding images taken with a white light microscope at a 50 times magnification are presented in Figure 64.

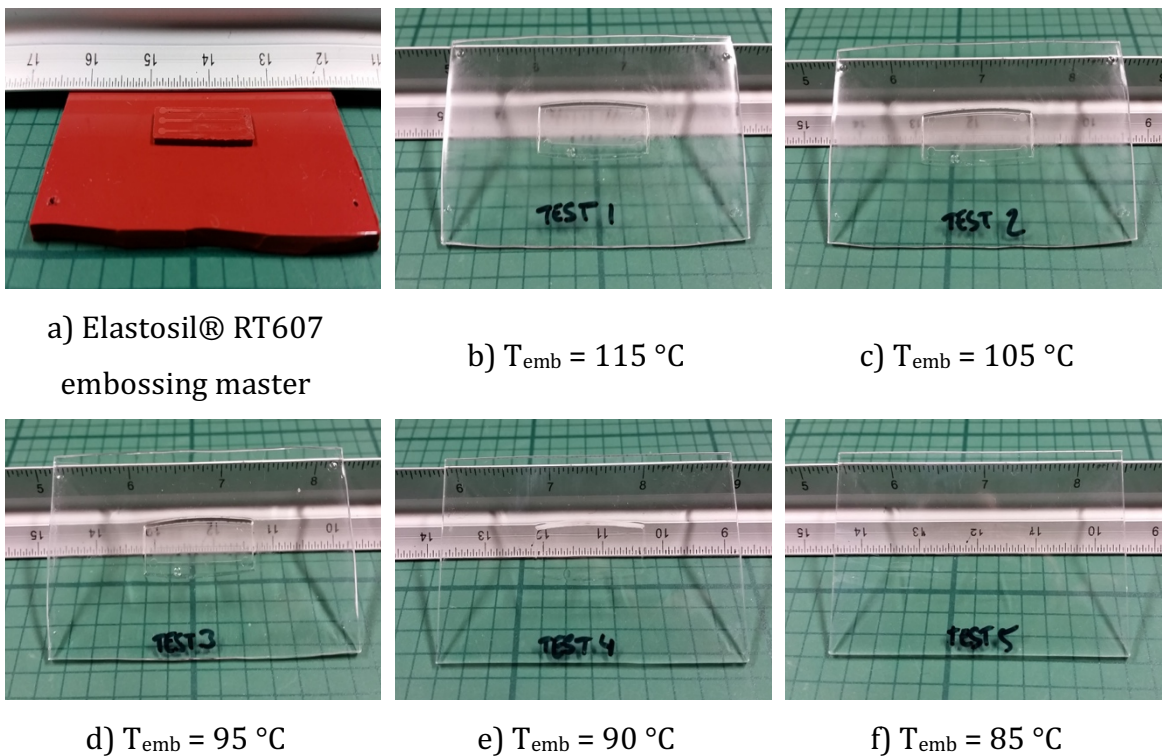


Figure 63 : Pictures of a) the silicone based embossing master cured in a ratio 9:1 (elastomer : curing agent) at 80 °C during 30 minutes, and the corresponding PMMA substrates embossed at b) 115 °C, c) 105 °C, d) 95 °C, e) 90 °C, f) 85 °C.

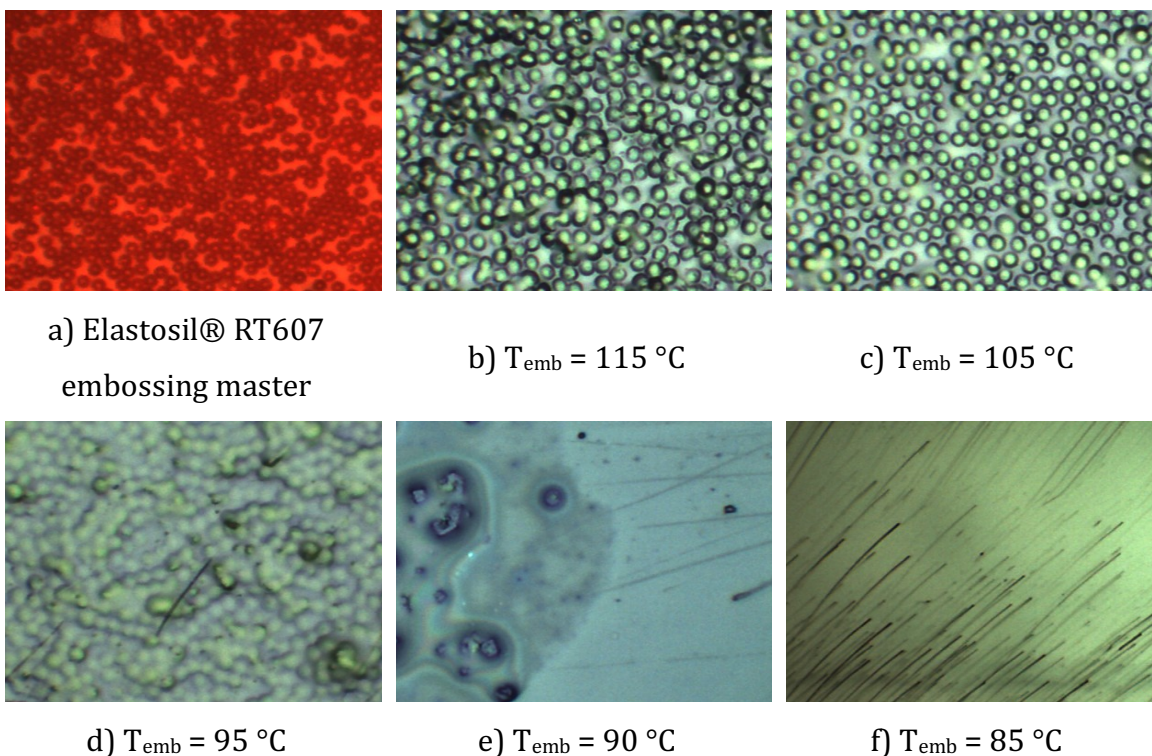


Figure 64 : White light microscope images at a $\times 50$ magnification of a) the silicone based embossing master cured in a ratio 9:1 (elastomer : curing agent) at $80 \text{ }^{\circ}\text{C}$ during 30 minutes, and the corresponding PMMA substrates embossed at b) $115 \text{ }^{\circ}\text{C}$, c) $105 \text{ }^{\circ}\text{C}$, d) $95 \text{ }^{\circ}\text{C}$, e) $90 \text{ }^{\circ}\text{C}$, f) $85 \text{ }^{\circ}\text{C}$.

Under these conditions, a temperature below $90 \text{ }^{\circ}\text{C}$ did not lead to a discernible imprint of the polymer, suggesting that the T_g of PMMA was not yet reached. At a temperature of $95 \text{ }^{\circ}\text{C}$, cavities were just barely imprinted at the polymer surface, meaning that the replication process had started but was not sufficient to fully imprint the structures. $105\text{-}115 \text{ }^{\circ}\text{C}$ yielded the best results as shape of cavities were clearly defined. However, embossing between $105 \text{ }^{\circ}\text{C}$ and $115 \text{ }^{\circ}\text{C}$ with a silicone based embossing master built according to the supplier recommendations was not reproducible as the master was found to deform under pressure. Therefore, optimisation of Elastosil® RT607 hardness was then carried out as described in section 2.3.2.1.1.

Further embossing trials were performed with the new embossing master built at a ratio 21:1 (elastomer : curing agent) and cured overnight at $40 \text{ }^{\circ}\text{C}$. Despite temperature optimisation during the embossing process, PMMA cavities obtained with the optimised silicone-based master were still wider and shallower than expected, indicating deformation of the microstructures under high pressure.

A different approach was then applied and best results were obtained with the macro presented in section 2.2.2.2.3. The strategy adopted was firstly to reduce the pressure used during the embossing process to a minimum, to limit the deformation of the silicone microstructures. Indeed, despite optimisation of the hardness of Elastosil® RT607, compressive strength measurements showed that the strain of the material under a stress of 290 N/cm² was still 25.3 %.

Touch force was then reduced to the minimum of 50 N controlled by the software, which considerably reduced the strain of the silicone-based master according to compressive strength data shown previously. This parameter was essential to ensure good contact and correct heating distribution across the upper hot plate, embossing master, PMMA substrate and lower hot plate. However, the minimum of 100 N embossing pressure allowed by the software during the embossing cycle could not be maintained accurately and was generating macros error from batch to batch. Therefore, it was decided to remove the pressure parameter from the macro and to allow the applied pressure to then consist of the touch force and the weight of the upper glass plate and the embossing master itself.

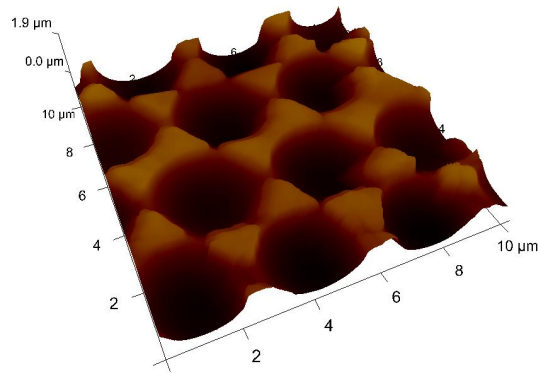
Secondly, temperature used during the embossing process was increased to reduce the viscosity of the PMMA substrate and to facilitate filling of the silicone-based master.

Thirdly, to increase the chance of good replication of the microstructures, the holding time was increased to 900 s, giving more time for the viscous PMMA to flow between empty spaces in the absence of controlled applied pressure.

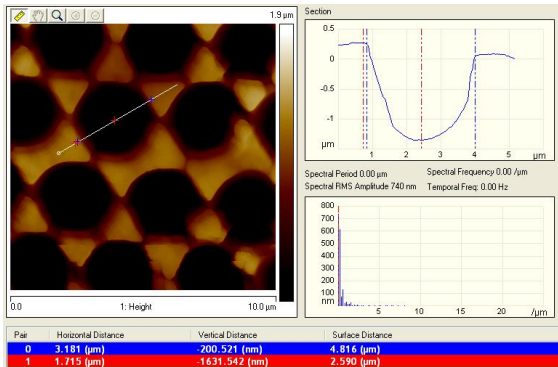
Finally, the wait time at the end of the cooling step and before de-embossing was increased to 300 s to ensure that the temperature of the PMMA was below its *T_g* to improve replication, as the silicone based embossing master tended to hold the heat. The temperatures shown on the screen are estimates as master and substrates do not have any temperature sensor.

2.3.2.1.5 Characterisation of the PMMA embossed cavities

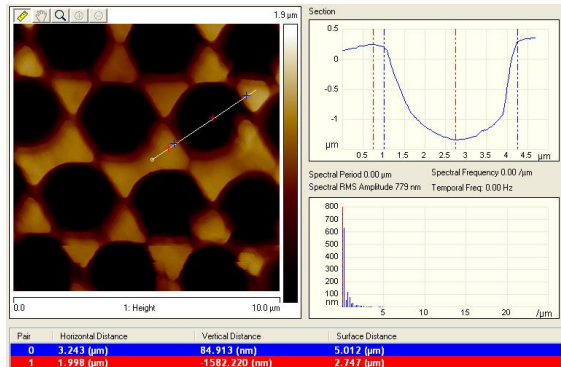
Figure 65 shows 3D (a) and 2D (b, c, d and e) AFM images of the PMMA substrate embossed with a silicone based embossing master using the embossed parameters described above.



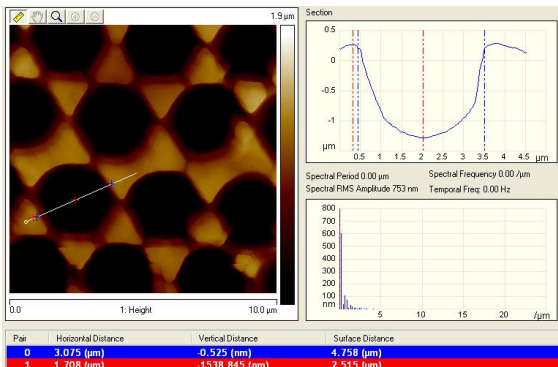
a)



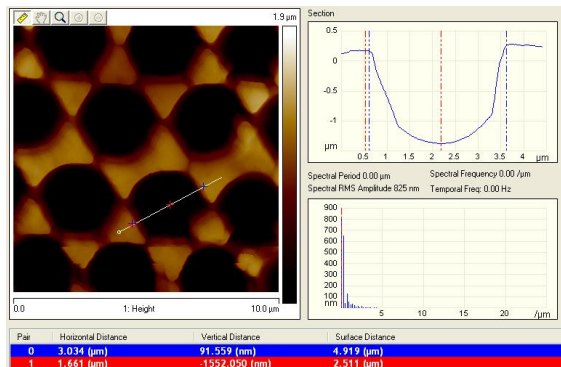
b)



c)



d)



e)

Figure 65 : 3D (a) and 2D (b, c, d and e) AFM images of a PMMA substrate after hot embossing optimisation. Sample was imaged in tapping mode in air using a MikroMasch Ultrasharp noncontact 15 series tip.

The 3.13 μm average diameter of structures presented in Figure 65 is larger than the 2.88 μm average diameter of the polystyrene spheres used to build the original negative mould, confirming the phenomenon described in section 2.3.2.1.3, which corresponds to the positive structures of the silicone based embossing master possibly deforming under heat and pressure. Indeed, despite data obtained during the compressive strength study, which indicated that deformation of an Elastosil® RT607 sample should be negligible due to the low force applied during the embossing process,

microstructures deformed. This can be explained as compressive strength measurement is a good tool to measure the deformation of the material at a large scale and allow its hardness improvement but is not sensitive enough to predict micro deformation phenomena happening at the surface of the sample.

The 1576 nm average height of the cavities measured for this sample is slightly above the theoretical value of 1440 nm for gold growth to the equator of spheres used. This difference is likely due to slightly overgrowth of the gold mould, as suggested by the presence of small valleys in between adjacent cavities, which is a characteristic of overgrowth as illustrated in Figure 66.

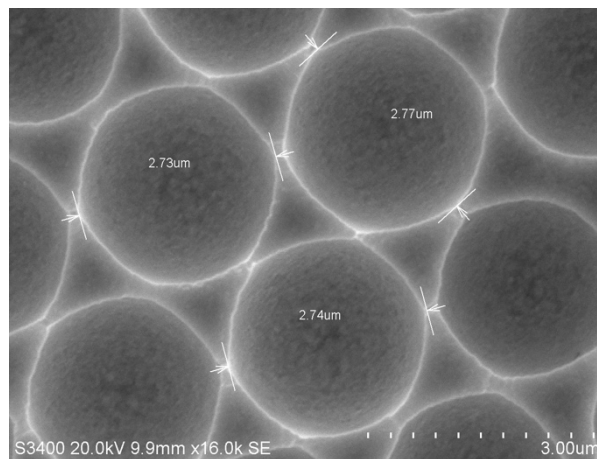


Figure 66 : SEM image of a gold negative mould presenting cavities slightly overgrown.

After hardness optimisation of the silicone based embossing master and adjustments of the embossing parameters, cavities with an average aspect ratio of 0.50 were successfully, and reproducibly embossed in a PMMA substrate. Overall, the aspect ratio of the template was maintained and matches with the theoretical target of 0.50 corresponding of a perfect hemisphere.

We can conclude therefore, that under these optimized conditions, hot embossing is an effective means of preparing the cavity arrays in PMMA.

Although the method works well, the embossing master may be prone to deformation after extended cycles of heat and pressure, thus limiting the lifetime of a single embossing master. Therefore, in parallel, a second route was also investigated toward embossing master fabrication, which should avoid deformation issues due to the “softness” of the material used in the master.

2.3.3 Method B: Hot embossing cavities using an Si beads/Au-Si wafer based master

Hot embossing trials were performed using an alternative embossing master. This master comprised silica microspheres assembled onto gold on silicon wafer. The new master was initially built using non-functionalized silica beads as described in section 2.2.2.2.1, and a SEM close image of it can be seen in Figure 67.

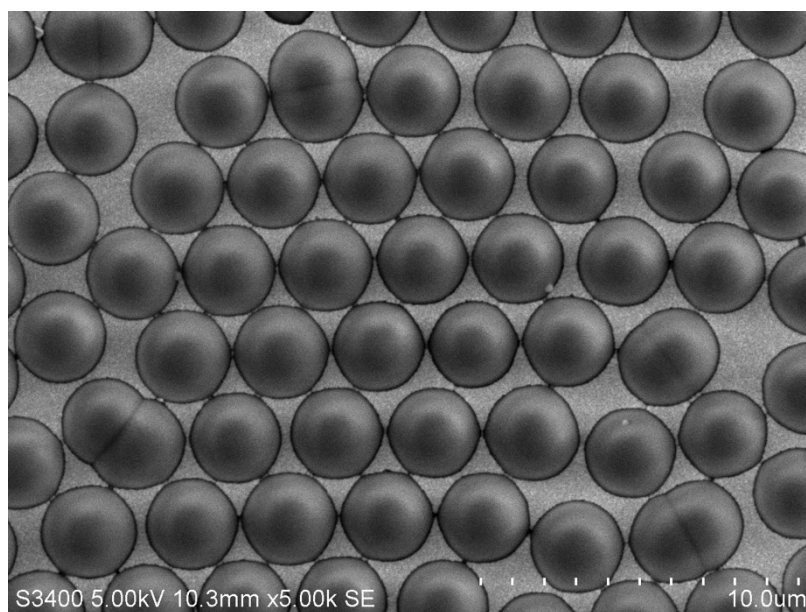


Figure 67: SEM image of a (silica microspheres/gold-silicon wafer) based embossing master. Non-functionalised silica microspheres with an average diameter of $3.17\ \mu\text{m}$ were deposited onto a gold-silicon wafer and gold was electrodeposited at a potential of -0.95V (vs. Ag/AgCl) until a total charge of 0.85 C was reached.

With the use of the new master (method B), the embossing parameters had to be reoptimized. The gold-silicon wafer master has greater thermal conductivity than the Elastosil® RT607 based master^{47,59}, thus the temperature of the upper hot plate of the embossing chamber was reduced. Also, the thickness of the new master B was approximately 0.6 mm , compared to the silicone master A which had a thickness of 5.1 mm to 5.2 mm . This difference in thickness also influences also the temperature needed for embossing. Wherein on the one hand, heat transfer is facilitated by the thickness of the master, but on the other hand, the upper hot plate of the embossing system is then closer to the PMMA top surface to be embossed than previously and contributes also to the viscosity of the substrate. Finally, as the gold-silicon wafer is a harder material than Elastosil® RT607, it is more brittle and tends to snap easily under pressure if not in contact with a truly flat surface. This characteristic is also important

for the de-moulding step at the end of the hot embossing process as the gold-silicon wafer can tend to break if partially embedded in the PMMA substrate.

First embossing trials were completed to optimise temperature and pressure. Figure 68 shows SEM images of a PMMA substrate embossed using parameters suggested in the internal SOP⁵⁰, for embossing small structures with a SU-8 embossing master. Under these conditions, the silica microspheres originally present on the embossing master transferred to the PMMA substrate and stayed embedded in it. This remained a problem over the range of embossing temperature and pressure applied.

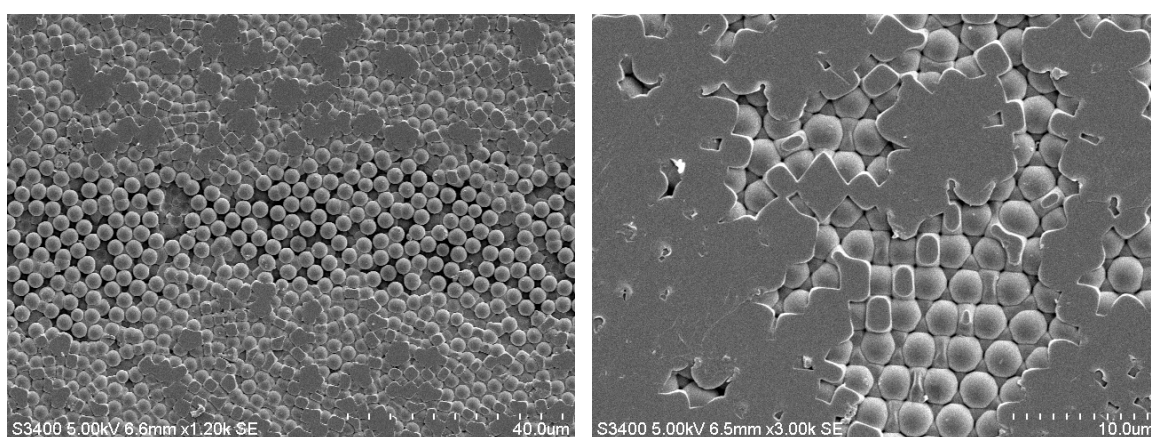


Figure 68 : SEM image of silica microspheres embedded in a PMMA substrate after hot embossing with a master build with non-functionalised silica micro spheres.

Using an embossing master that lost the majority of its silica microspheres from the first embossing cycle would probably lead to the replication of positive microstructures as the embossing master would be left with cavities. Therefore, it was decided to chemically modify the silica micro spheres surfaces with a thiolated compound to promote their bonding to the gold surface of the embossing master and limit their loss during the embossing process.

2.3.3.1.1 Thiolation of the silica spheres to improve adhesion to the gold embossing master

First embossing trials using unfunctionalized silica microsphere arrays as the embossing master, led to the spheres being transferred from the master to the PMMA substrate during the hot embossing process. This indicates that their adhesion to the gold substrate was not strong enough. Therefore, chemical surface modification of the silica spheres to form a chemical bond between the master surface and the spheres was

deemed necessary. Two methods adapted from literature and using MPTMS were explored to thiolate the surface of the silica microspheres^{25,60} as illustrated in Figure 69.

Surface modification of the silica microspheres was first performed using a method adapted from *Goss et al.* work.⁶⁰ This method consisted of a reflux of the silica spheres in an isopropanolic solution of MPTMS, allowing a good dispersion of the microspheres in solution, preventing the formation of clusters. However, characterisation of the functionalization process did not give any conclusive results, therefore the method chosen for future work was one based on R. Rostamian et al. work²⁵ and for which results are shown below.

In this procedure, firstly, the stoichiometry of the reaction was considered. In his study of various amorphous silica substrates such as silica, silica gels and porous glass, L.T. Zhuralev reported in 1986 that the silanol number α_{OH} , or surface density of -OH groups, could be considered as a constant of 5.0 OH groups per nm^2 and was independent of the origin and structural characteristic of the fully hydroxylated silica-based substrate.⁶¹ Knowing the number of microspheres per volume of stock solution and the average diameter of the spheres, the amount of reagent was calculated and adapted to the procedure.

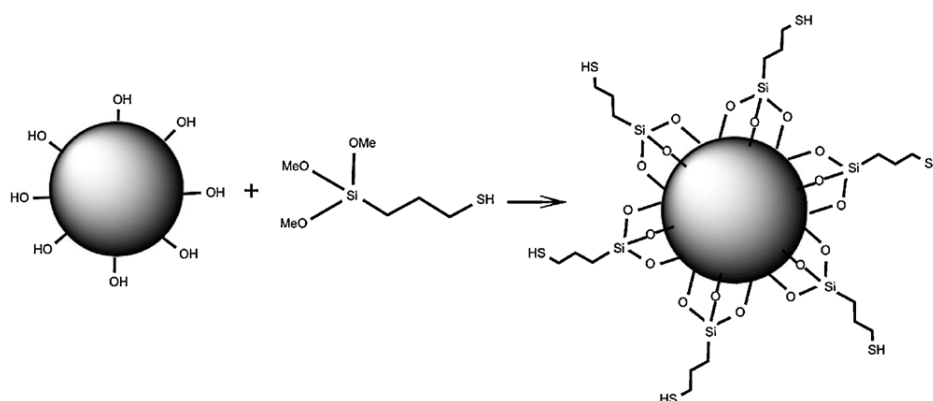


Figure 69 : Illustration of the thiolation process of a silica sphere using MPTMS. Due to its three methacrylate site, one MPTMS can bind to three Hydroxyl groups. Image reproduced from reference.²⁵

ATR-FTIR analysis was carried out to verify the surface modification of the spheres as shown in Figure 70. Strong bands associated with Si-O and Si-O-Si stretching vibrations can be observed respectively at 796 cm^{-1} and 1043 cm^{-1} , which suggests the

condensation of silicon alkyloxy.⁶² The weak peak at 2981 cm^{-1} , characteristic of C-H bonds stretching vibrations, indicates the adsorption of organics groups on the spheres.

The S-H mode is very weak in the infrared⁶³ and was thus not visible here. However, this mode is typically strong in Raman and as shown in Figure 71 was evident at 2505 cm^{-1} , clearly indicating thiolation had occurred. The feature at 2328 cm^{-1} is attributed to atmospheric nitrogen⁶⁴.

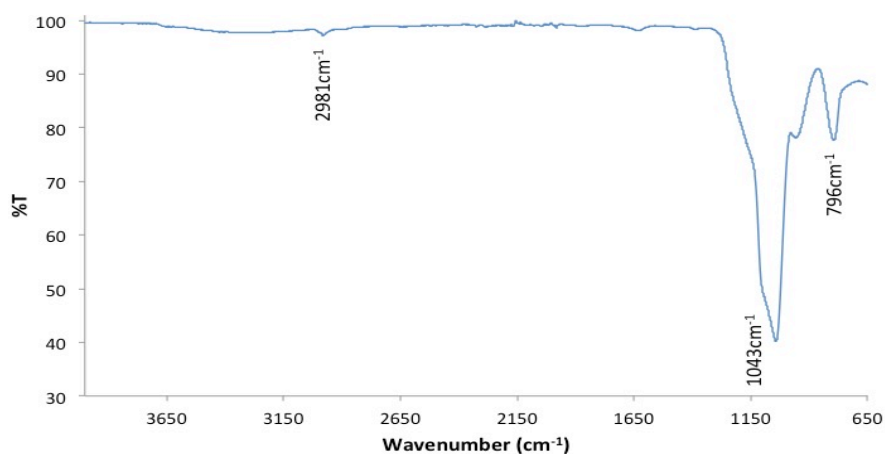


Figure 70 : ATR-FTIR spectrum of silica micro spheres after surface modification with MTPMS.

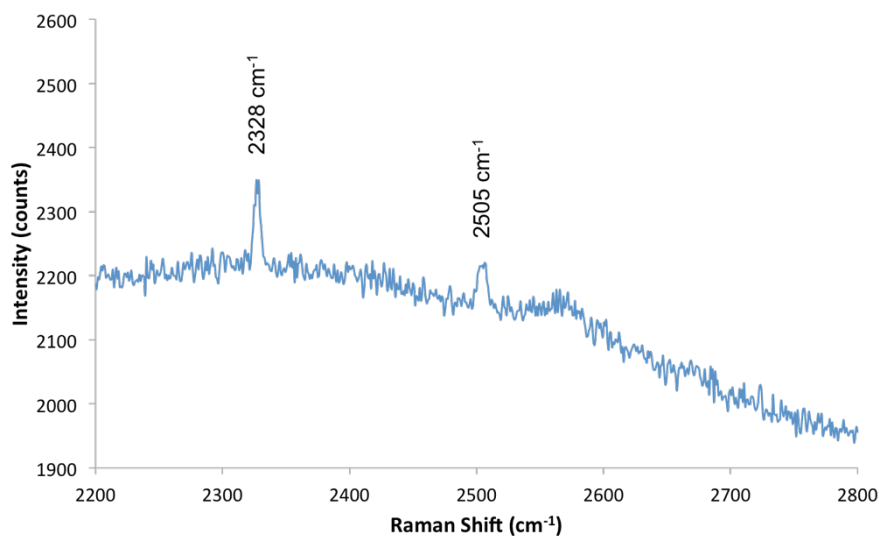


Figure 71 : Raman spectrum of silica microspheres after surface modification with MTPMS. The excitation wavelength was 633 nm.

SEM imaging further confirms that surface chemical modification of the silica spheres was successful. Indeed, despite the different washing steps after the reflux of the spheres with MPTMS, structures could be noted on its surface as shown in Figure 72. Those agglomerates could be related to MPTMS polymers rather than well-ordered monolayers as described by M. Hu et al in their study on the effect of MPTMS concentration on the structure and morphology of MPTMS layers on SiO_2 .⁶⁵

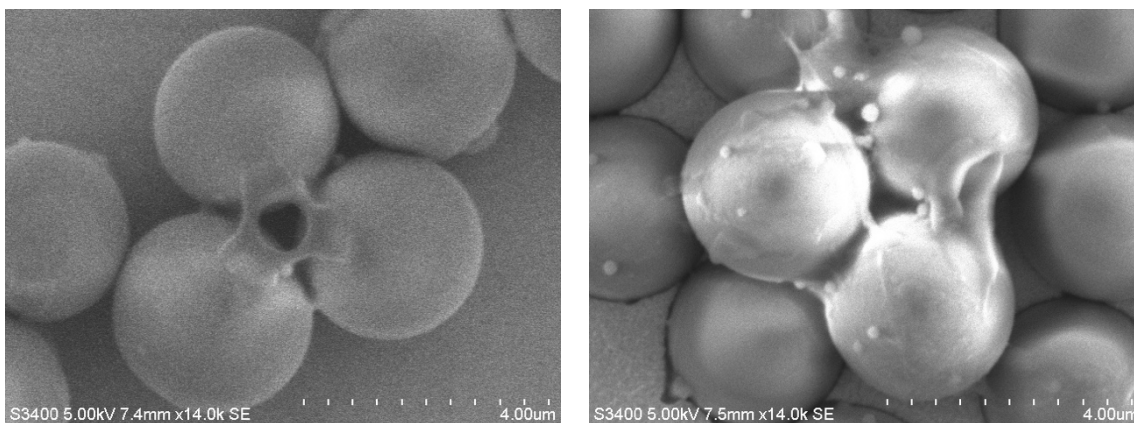


Figure 72 : SEM images of functionalised silica microspheres presenting MPTMS polymer at its surface.

It was suggested that competitive reactions might occur during the surface modification process as illustrated in Figure 73, leading to randomly distributed thiol head groups at the SiO_2 surface in the case of the self-polymerization of hydrolysed MPTMS molecules. This polymerisation of the MPTMS cleaved at the surface of the silica spheres could explain the relatively low intensity of the Raman signal as the density of thiol group is less than the one expected for a well-ordered monolayer of MPTMS. The signal in Raman seems relatively weak suggesting that thiolation is not extensive but is nonetheless sufficient for our purpose.

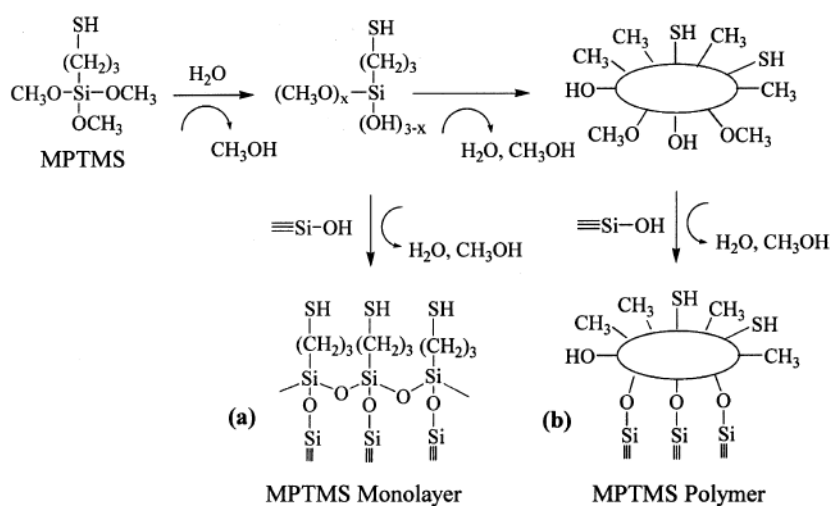


Figure 73 : Competitive reaction in the formation of self-assembled MPTMS layers on the SiO₂ surface : (a) surface dehydration on the SiO₂; (b) self-polymerization in the solvent. Image extracted from reference.⁶⁵

The surface modification could be then further improved by adjusting some critical parameters as the concentration of MTPMS and water in the reaction media in order to obtain a more homogeneous repartition of thiol head groups at the surface of the spheres mainly due to a monolayer rather than polymer agglomerates. However here the aim was to create sufficient thiol functional groups at the surface of the silica microsphere to promote their adhesion to the gold substrate and prevent their transfer to the PMMA during the embossing process. Another pathway to improve adhesion of the silica microspheres to the gold substrate would be to use a longer chain thiolated compound as suggested by Kaminska et al., who found that such modification lead to arrays more uniform and physically stable for extended periods than with MPTMS.⁶⁶ This could probably extend the lifetime of the embossing master, if this method was to be used for mass production of PMMA substrates.

2.3.3.1.2 Hot embossing with thiolated silica microspheres/Au-Si wafer based embossing master

Preliminary SEM data indicated that the approach of thiolating the silica spheres improved the moulding. The positive structures imprinted well onto PMMA and a dramatic reduction in the transfer of silica beads to the PMMA was noted. Figure 74 shows representative SEM images of cavities embossed on a PMMA substrate using the most advanced parameters up to date for this embossing master. As described, the chemical surface modification of the silica microspheres reduces the loss of spheres

from the gold surface onto the embossed PMMA compared to trials performed with non-chemically functionalised beads. The consistency in the dimensions of the resulting pores is also excellent across the substrate.

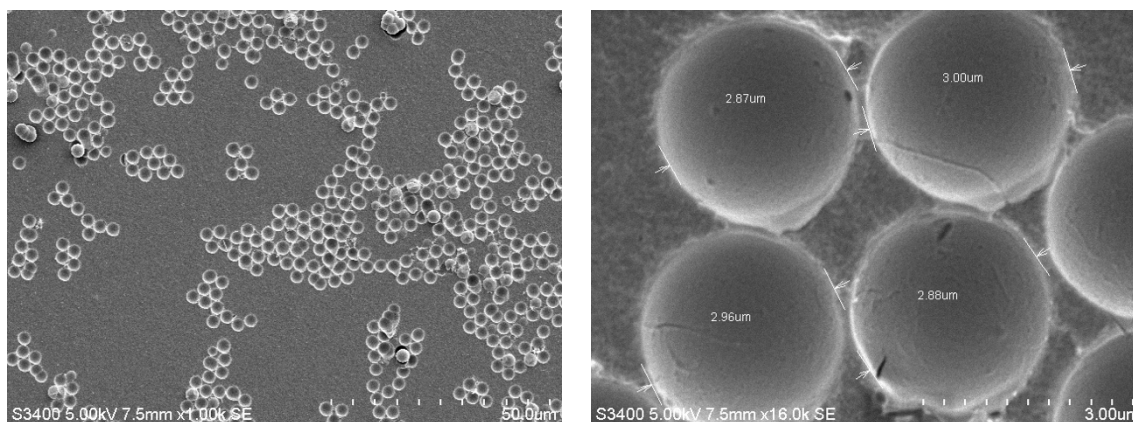


Figure 74 : SEM images of cavities imprinted on a PMMA substrate after hot embossing with a master build with thiolated silica micro spheres. (left: magnification 1000x; right: magnification 16000x)

2.3.3.2 Supported Lipid Bilayer formation and characterisation

2.3.3.2.1 Diffusion study of Supported Lipid Bilayers on planar PMMA for material compatibility check

The ultimate aim of this work was to prepare reproducible arrays of micropores in PMMA for application in microcavity supported lipid bilayer cell membrane models. Therefore, to complete this study we explored the capacity of the PMMA to support a lipid bilayer.

Previous work on PDMS has shown that hydrophilicity of the substrate is crucial for lipid bilayer fabrication and stability at the polymer surface²⁶. Several techniques have been reported for modifying the hydrophilic-hydrophobic properties of polymers, such as excimer laser ablation⁶⁷, UV/Ozone graft polymerization⁶⁸⁻⁷⁰, chemical reduction with LAH (Lithium Aluminium Hydride)¹³, chemical etching⁷¹ with KI:I₂, vapour phase deposition of organic films⁷², or simply plasma treatment.^{27,73-76} This last technique currently used in the group on PDMS to increase its hydrophylicity was chosen to modify the PMMA surface as it is a fast and clean method. Figure 75 illustrates the surface modification of PMMA under the effect of plasma, converting ester functional groups to carboxylic acid groups rendering the material more hydrophylic.

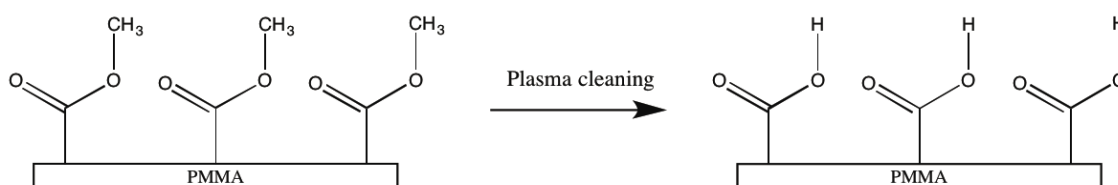


Figure 75: Surface modification of PMMA under plasma to indicate conversion of the ester function to a carboxylic acid.

Before forming a phospholipid bilayer at the surface of the PMMA substrate, the surface wettability of the material was assessed by contact angle measurement before and after air plasma treatment. Figure 76 shows the water contact angle of planar PMMA decreases from (a) 85° prior to air plasma treatment to (b) 40° after air plasma treatment. Results are consistent with literature values for the same polymer^{27,29} and indicate that the surface becomes strongly hydrophilic after plasma treatment suggesting the surface should support a uniform lipid bilayer.

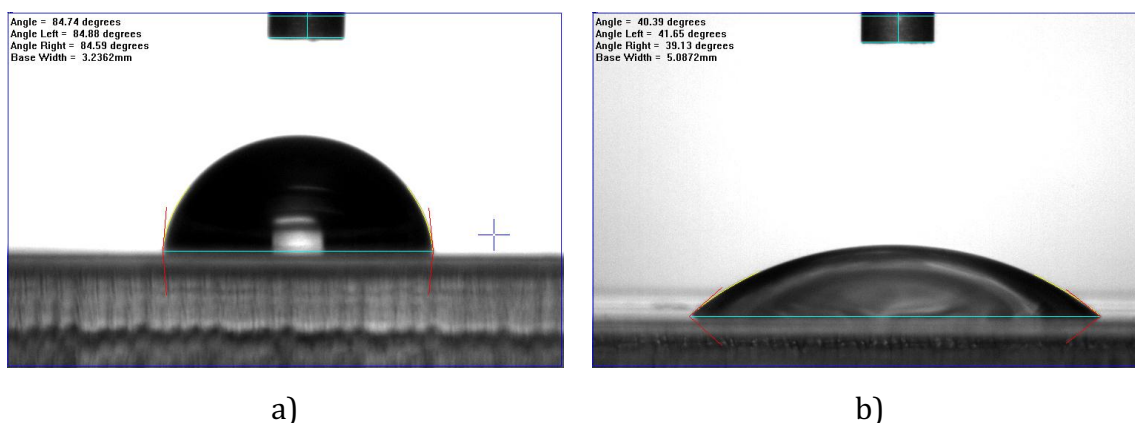


Figure 76: Water contact angle of PMMA substrate before (a) and after plasma treatment (b).

Before starting the development of the cavities array formation on PMMA substrate, a preliminary analysis has been done to confirm the compatibility of this material with FCS study. As FCS is a single molecule method, low fluorescence background from the material is critically important in ensuring the fluorescence signal from the probe molecules can be measured. To date, our group has used PDMS for such studies, as it has a low background fluorescence and scattering.

FLIM/FCS measurements were performed at a room temperature of 20 °C on a flat PMMA sample. The diffusion coefficient measurements of the DOPE-Naphta-Bodipy lipid probe in the DOPC lipid bilayer formed on the PMMA surface were carried out by Dr. Siva Ramadurai.

From the FLIM image presented in Figure 77 a), we can see some micro structures (fibres or scratches) that might be artefacts from the PMMA. The lipid probe appears to aggregate around these structures reflected in bright emission compared to flat surfaces in between. The immobility of these molecules is reflected as bleaching in the time trace in Figure 77 b). Again, this is consistent with binding / aggregation at these points. In contrast, as shows the time trace in Figure 77 c), the number of counts recorded on planar regions of the surface is constant during the measurement and probes are diffusing, indicating a supported lipid bilayer has formed.

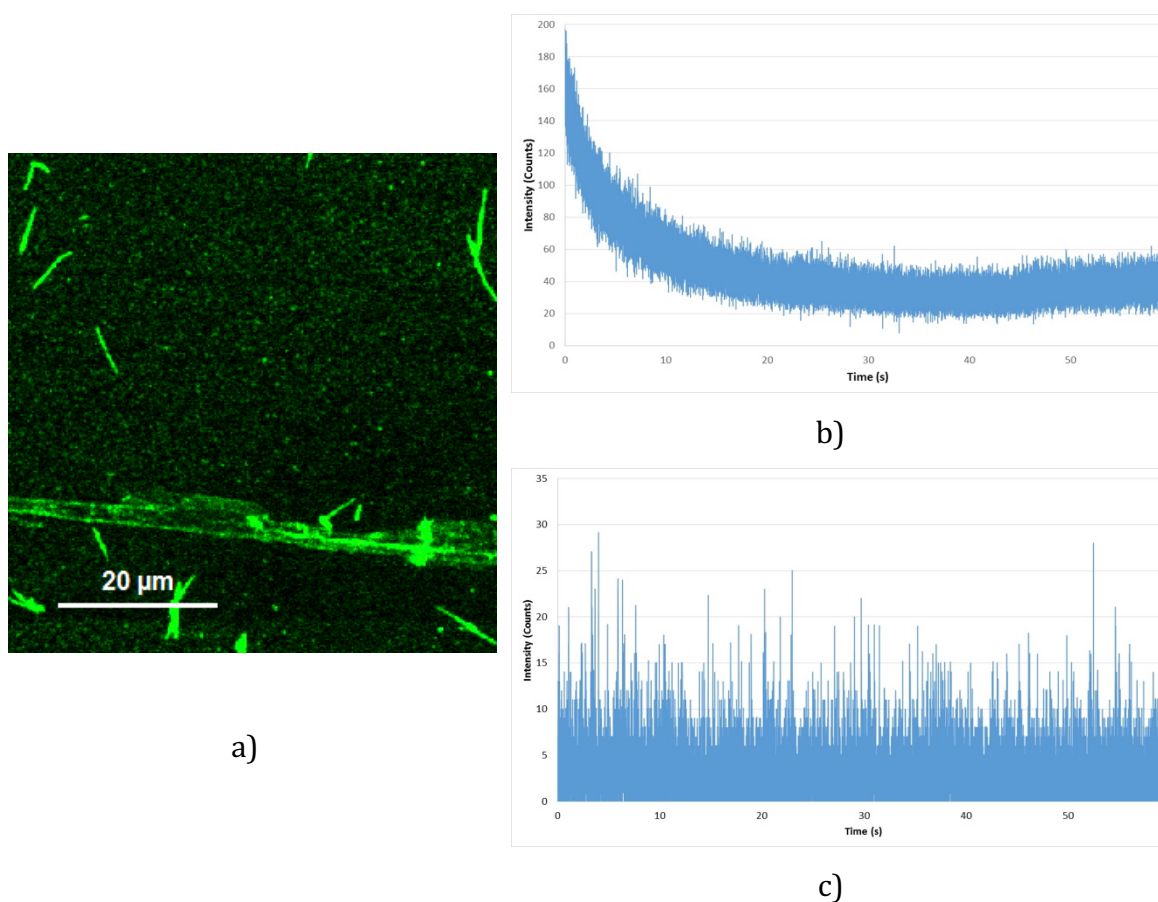


Figure 77 : a) FLIM image of DOPC bilayer on air plasma treated PMMA and corresponding time trace on b) fibres structures and c) flat surface. Courtesy of Dr. Siva Ramadurai.

Figure 78 shows a representative FCS curve of lipid diffusion on flat PMMA surface. The experimental data fits to a 2D diffusional model, from where the diffusion time of the molecule was calculated. The average diffusion coefficient for the DOPE-Naphta-Bodipy within a DOPC bilayer suspended on a planar plasma treated PMMA surface was calculated as $D_{d0} = 4.74 \pm 1.5 \mu\text{m}^2 \text{s}^{-1}$. The standard deviation was calculated from eight measurements done at different sites across the substrate. This

diffusion coefficient is comparable to literature values obtained for the same lipid bilayer composition on other planar hydrophilic substrates.⁷⁷⁻⁷⁹ To our knowledge, no report of diffusion values of lipid bilayer on flat PMMA surface has been done to date in the literature.

Overall, this preliminary measurement indicates that PMMA, once plasma treated, is a suitable substrate for FCS and that this substrate can support a fluidic supported lipid bilayer.

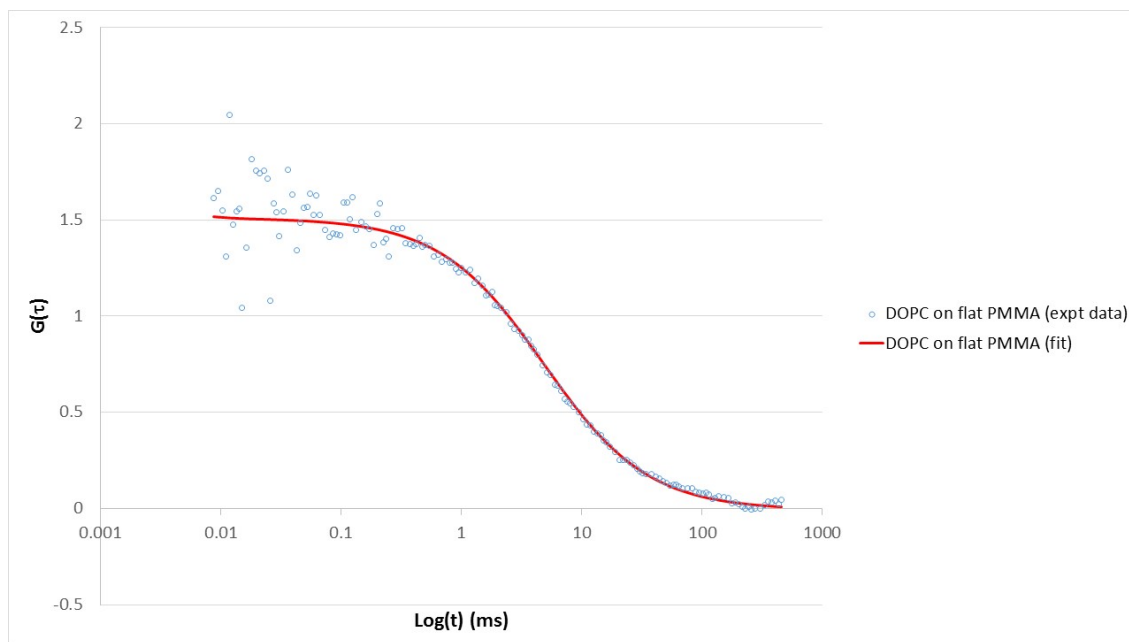


Figure 78 : Representative FCS curve of the lipid marker in DOPC membrane found on flat PMMA surface. Courtesy of Dr. Siva Ramadurai. FCS autocorrelation function for DOPC, labelled with DOPE-Naphta-Bodipy, fitted to 2D diffusion model. Fluorescent fluctuations at a single point on the PMMA flat surface were recorded. The excitation laser wavelength was at 532 nm and fluorescence was collected with a 560 long pass filter.

To examine the stability of the DOPC bilayer at PMMA over time, the inlet and outlet tubes of the sample were clamped as illustrated in Figure 79 to isolate the sample chamber, i.e. to prevent drying out of the liquid environment around the lipid bilayer. The platform was stored at +4 °C for 10 days and a second series of FCS measurements was performed.

D_{d10} after this time was obtained as $3.98 \pm 0.5 \mu\text{m}^2 \text{s}^{-1}$, which within experimental error is unchanged compared with the first measurements. The error on the initial value was relatively large, likely due to the heterogeneity of the surface. The decrease in the D value may be due to the partial recovery of hydrophobicity of the PMMA substrate over time as demonstrated by A. Vesel and M. Mozetic in their study

on the ageing of PMMA treated with oxygen plasma.²⁹ The small change in D indicates the bilayer is stable and that the PMMA is a viable substrate for lipid bilayer study. The stability of the bilayer over a 10 days period is a real advantage regarding measurements, particularly during kinetics studies. Also, from a commercial perspective, the microfluidic device could be prepared, sealed and shipped to the customer who will have to use it within this stable period post fabrication.



Figure 79 : Picture of the simplified microfluidic platform used for FCS measurement of a DOPC lipid bilayer spanned at a plasma treated flat PMMA surface.

2.3.3.2.2 Diffusion study of Supported Lipid Bilayers on PMMA cavities

Using the optimised embossed PMMA cavity substrates, FCS measurements of lipid bilayer were performed after their assembly over buffer filled cavities to check the correct spanning of the bilayer. Samples were surface modified and prepared as described in section 2.2.3. However, despite improvements done on the replication quality of the cavities to promote a shape deep enough to retain the buffer, which is critical in supporting the lipid bilayer, no spanning of lipid could be observed, as was observed for PDMS substrates²⁶, over the cavities neither on surrounding flat surfaces as illustrated in Figure 80.

This suggests that the hot embossing process modified the nature of the PMMA, as good results comparable to literature values were achieved during the preliminary tests on flat PMMA, described in the previous section.

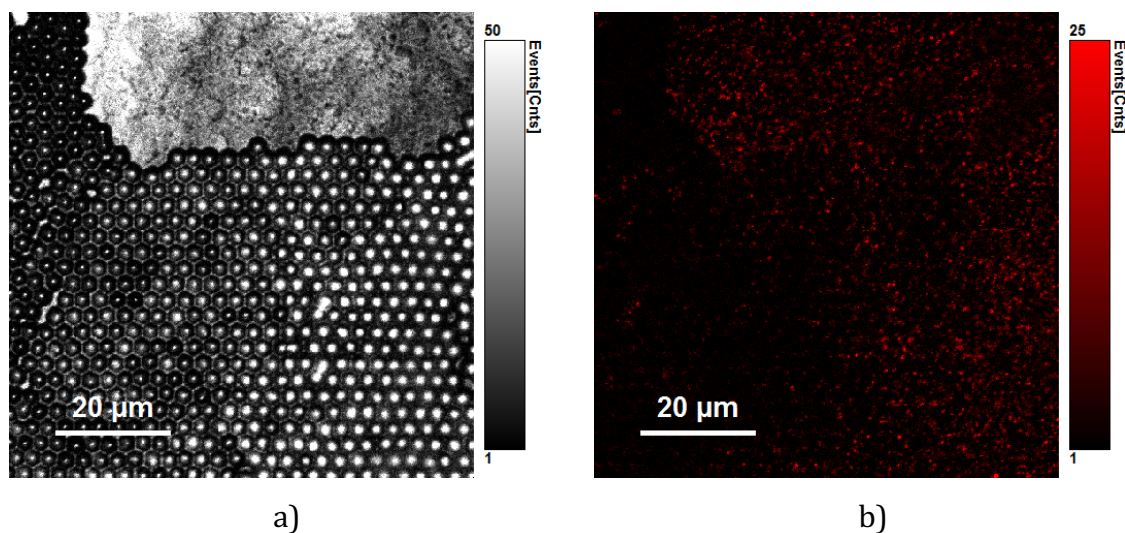
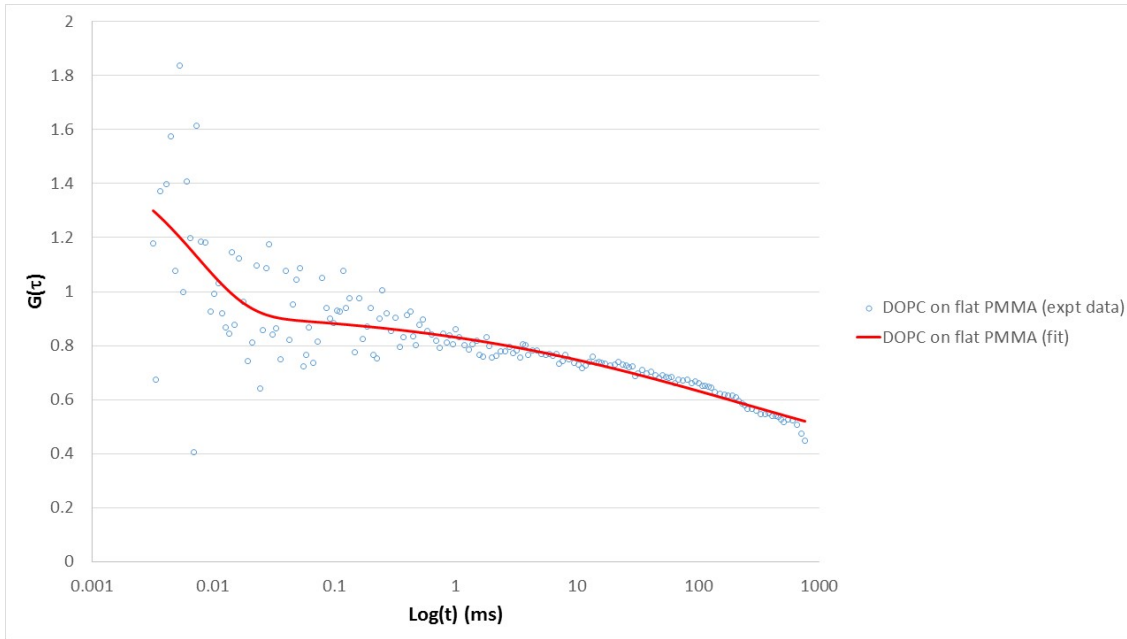


Figure 80 : Reflectance a) and fluorescence lifetime image b) of DOPC/DOPE-Atto 655 bilayer over cavities hot embossed PMMA plasma treated. Excitation wavelength was 640 nm, and fluorescence was collected using a 635 long pass filter. Courtesy of Dr. Siva Ramadurai.

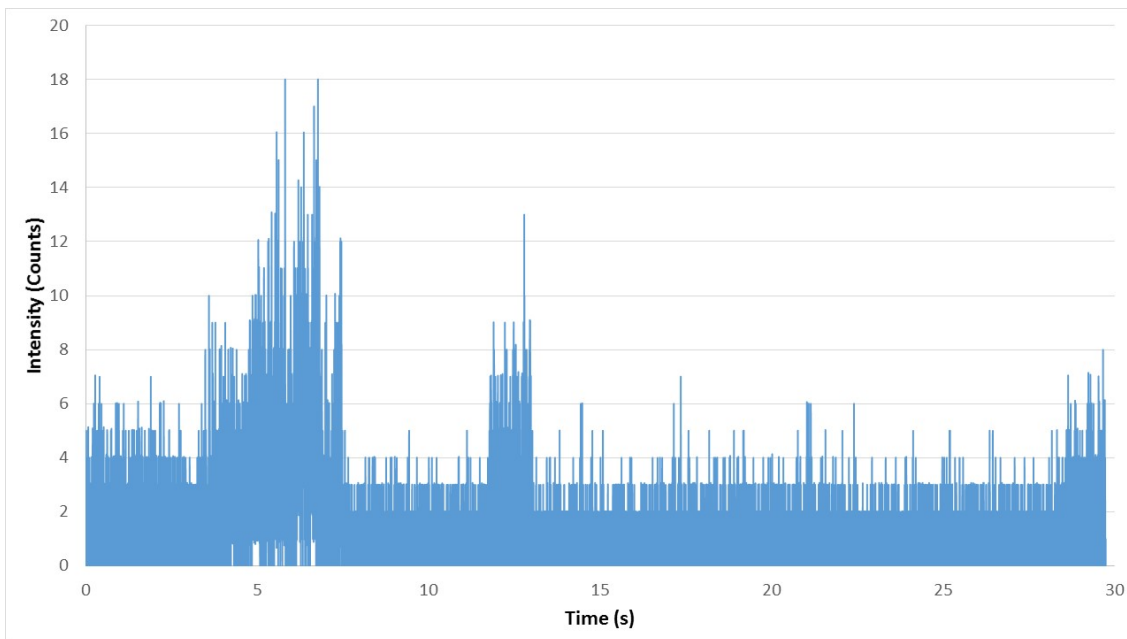
FCS measurements were then reiterated on plasma treated flat PMMA surfaces in similar conditions to those described in section 2.3.3.2.1. for preliminary tests. Different PMMA references from different suppliers were sourced allowing the choice of the more adapted for the lipid study in the case of successful results.

Unfortunately, none of the different PMMA references selected allow similar results to the ones achieved during the preliminary tests. Only a few FCS curves presenting a high signal to noise ratio could be obtained for lipid bilayer on PMMA, and once fitted to a 2D diffusional model showed very low diffusion values. For example, Figure 81 a) shows a representative FCS curve of lipid diffusion on flat PMMA surface giving this time a diffusion coefficient $D = 0.14 \mu\text{m}^2 \text{s}^{-1}$, which can be compared to a FCS curve of lipid diffusion obtained on the coverslip side of the same sample shown in Figure 82 a), which showed a diffusion coefficient of $D = 3.68 \mu\text{m}^2 \text{s}^{-1}$. This comparison was done to confirm a bilayer formed on glass under the deposition conditions used here.

The study of the corresponding time traces shown in Figure 81 b) and Figure 82 b) gives also some insights into the low diffusion coefficient obtained. The time trace corresponding to the measurement on the PMMA surface shows fewer counts than those from the glass coverslip. This suggests a low quantity of lipids present at the PMMA surface. Also, lipids are not homogeneously distributed on the PMMA surface, and appear to move in clusters, reflected on the time trace by an increase of intensity for few seconds followed by the signal coming back to the base line.



a)



b)

Figure 81 : Representative FCS curve a) of the lipid marker in DOPC membrane found on flat PMMA surface giving a diffusion coefficient $D = 0.14 \mu\text{m}^2\text{s}^{-1}$, and its corresponding time trace. Courtesy of Dr. Siva Ramadurai.

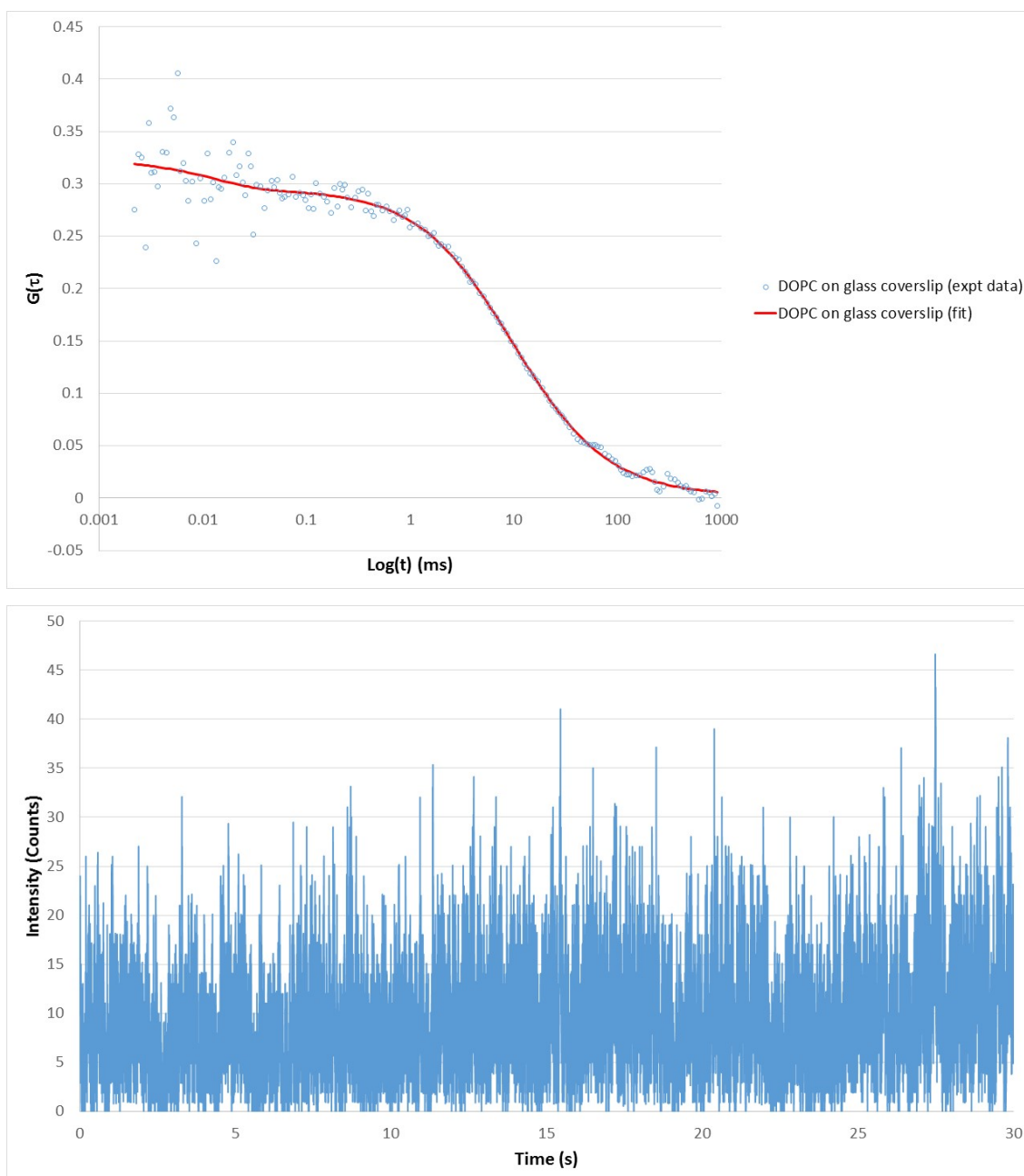


Figure 82 : Representative FCS curve a) of the lipid marker in DOPC membrane found on coverslip surface of the cell, giving a diffusion coefficient $D = 3.68 \mu\text{m}^2\text{s}^{-1}$, and its corresponding time trace. Courtesy of Dr. Siva Ramadurai.

These final results indicate that the lipid bilayer is not spread homogeneously across the substrate, probably due to nanoscale roughness of the substrate itself. However, this is likely due to the polymer grain size and not necessarily because of the embossing process. Results presented in this section 2.3.3.2. indicate that lipid bilayer can be supported on PMMA, under very discrete conditions. The success in forming a homogeneous lipid bilayer depends on a balance between nanoroughness of the surface induced by the plasma treatment and hydrophilicity. It will take further work to define conditions for preparing low roughness hydrophilic PMMA substrates.

2.4 Conclusions

The aim of this work was to develop a low-cost microfluidic device incorporating reproducible micropore arrays. Ultimately device should be capable of supporting a lipid bilayer suitable for the study of drug-lipid membrane interactions using analytical techniques such as FCS, SERS or EIS. With focus on a substrate suitable for FCS in this first working chapter, optically transparent PMMA was explored herein.

Due to constraints around lipid bilayer formation, the device was designed in two main parts, the first one supplying reagents to the second one, where the artificially formed lipid membrane is supported.

The choice of the material/method for the fabrication of the microfluidic device leant towards a combination of PMMA and PSA layers respectively, processed by CO₂ laser machining and xurography. The assembling and leak testing of the microfluidic device confirmed the suitable choice as a sealed device could be obtained. Moreover, the straight forward fabrication process will allow facile conversion of the single channel microfluidic device developed into a multichannel device giving more configuration possibilities for drug-lipid membrane study.

Development of the second part of the device was then performed to manufacture a substrate aiming at supporting the lipid bilayer for FCS study. This work lead to the development of two new effective and reproducible means of embossing micron dimension cavities on PMMA.

The first method was adapted from Steigert et al. and involved embossing with a silicone-based master to allow the replication of distinctive features of one to two orders of magnitude smaller than the type of structures embossed in their work (e.g. cavities with a diameter of 3.1 μm and height of 1.6 μm vs. channels ranging from 35 μm to few hundreds micrometers in height and hundreds micrometers to few millimetres wide). This was made possible through hardness improvement of the silicone based embossing master prepared in a 21:1 ratio (elastomer : curing agent) cured overnight at 40 °C. Those conditions reduce deformation of the material used for the embossing master (32 %), at a suggested embossing pressure of 290 N/cm², compared to a master built according to the manufacturer suggestions. However, the deformation of the microstructures of the embossing template under heat and

pressure after few embossing cycles led to the development of another master fabrication method.

The second approach aimed at building a more rigid embossing master made of silica microspheres embedded in a gold substrate that would resist heat and pressure. Surface modification of the beads using MPTMS was required to improve their adhesion to the gold-silicon wafer through thiolated groups and avoid their transfer to the PMMA substrate during the embossing process. It was noted in this work that the quality of the final replica depends on the embossing parameters used but also dramatically on the quality of the embossing master, thus requiring its accurate characterisation before embossing.

Surface modification of PMMA substrate was necessary to allow formation of a lipid bilayer. Its natural hydrophobicity of 85° was reduced to 40° after air plasma treatment confirming hydrophilicity of the modified surface suitable to support a uniform lipid bilayer was achieved.

FCS measurements done on surface modified flat PMMA substrates indicated at first the suitability of the material for our device due to its low auto-fluorescence and the demonstrated lipid bilayer formation. Indeed, diffusion coefficient obtained for DOPC on flat PMMA surface was comparable to literature values obtained for the same lipid on other planar hydrophilic surfaces, and was shown relatively stable within experimental error over a 10 days period when stored at +4 °C.

However, preliminary FCS data on the optimised micro cavity embossed PMMA substrate suggests that the lipid bilayer does not form over the substrate despite surface modification by air plasma treatment. This suggests that a balance needs to be reached between hydrophilicity and nanoroughness of the substrate that perturbs the lipid bilayer formation.

In response, future work should focus on two different aspects of the microfluidic device development.

On one side, focus could be directed towards surface chemistry and hydrophilicity improvement of the PMMA substrate to promote water filling of the embossed cavities and to allow formation of a homogeneous cavity supported lipid bilayer, while maintaining the smoothness of the material surface. An alternative route to air plasma treatment to render the PMMA surface hydrophilic could be to implement a cushion

polymer allowing thus to form a polymer cushioned supported bilayer. There are drawbacks of this membrane model in terms of interactions between the bilayer and the polymer cushion but in our case, the polymer cushion thickness is minimal in comparison to the cavity volume, such that the cavity should remain sufficiently filled with buffer to support a suspended lipid bilayer and decoupling it from the substrate and/or the polymer cushion.

On the other side, development has to be done on the microfluidic device to integrate a microcavity array substrate allowing EIS and SERS measurements. Lately, our group published work involving the fabrication of a micron-dimensioned cavity array supported lipid bilayers for the electrochemical investigation of ionophore activity.⁴⁶ Integrating such a platform in our microfluidic device could lead to a multi-modal detection device which is a primary aim of this project. However, the group report a large variability in EIS results from sample to sample, which has been linked to method used to build the substrates that is difficult to consistently reproduce.²²

Therefore, it was decided to focus on this second aspect of the microfluidic device development in the following working chapter.

2.5 References

1. Pimpin, A. & Srituravanich, W. Review on Micro- and Nanolithography Techniques and their Applications. *Eng. J.* **16**, 37–56 (2012).
2. *Microfluidic techniques: reviews and protocols*. (Humana Press, 2006).
3. McCormick, R. M., Nelson, R. J., Alonso-Amigo, M. G., Benvegnu, D. J. & Hooper, H. H. Microchannel Electrophoretic Separations of DNA in Injection-Molded Plastic Substrates. *Anal. Chem.* **69**, 2626–2630 (1997).
4. Fiorini, G. S. & Chiu, D. T. Disposable microfluidic devices: fabrication, function, and application. *BioTechniques* **38**, 429–446 (2005).
5. Becker, H. & Gärtner, C. Polymer microfabrication methods for microfluidic analytical applications. *Electrophoresis* **21**, 12–26 (2000).
6. Dongqing, L. *Encyclopedia of Microfluidics and Nanofluidics*. (Springer, 2008).
7. Juang, Y.-J., Lee, L. J. & Koelling, K. W. Hot embossing in microfabrication. Part I: Experimental. *Polym. Eng. Sci.* **42**, 539–550 (2002).
8. Xia, Y. & Whitesides, G. M. Soft Lithography. *Angew. Chem. Int. Ed.* **37**, 550–575 (1998).
9. Anderson, J. R. *et al.* Fabrication of Topologically Complex Three-Dimensional Microfluidic Systems in PDMS by Rapid Prototyping. *Anal. Chem.* **72**, 3158–3164 (2000).
10. Guckenberger, D. J., de Groot, T. E., Wan, A. M. D., Beebe, D. J. & Young, E. W. K. Micromilling: A method for ultra-rapid prototyping of plastic microfluidic devices. *Lab. Chip* **15**, 2364–2378 (2015).
11. Friedrich, C. R. & Vasile, M. J. Development of the micromilling process for high-aspect-ratio microstructures. *J. Microelectromechanical Syst.* **5**, 33–38 (1996).
12. Wilson, M. E. *et al.* Fabrication of circular microfluidic channels by combining mechanical micromilling and soft lithography. *Lab. Chip* **11**, 1550–1555 (2011).
13. Cheng, J.-Y., Wei, C.-W., Hsu, K.-H. & Young, T.-H. Direct-write laser micromachining and universal surface modification of PMMA for device development. *Sens. Actuators B Chem.* **99**, 186–196 (2004).
14. Yuan, D. & Das, S. Experimental and theoretical analysis of direct-write laser micromachining of polymethyl methacrylate by CO₂ laser ablation. *J. Appl. Phys.* **101**, 024901 (2007).
15. Lab on a Chip Technology: Fabrication and microfluidics - Google Livres. https://books.google.ie/books?id=Bovn3JO_YLwC&printsec=frontcover&dq=lab-on-a-chip+technology+book&hl=fr&sa=X&ved=0ahUKEwj08evDjcbLAhXClQ8KHQK6BvQQ6AEIJDA#v=onepage&q=lab-on-a-chip%20technology%20book&f=false
16. Bhattacharjee, N., Urrios, A., Kang, S. & Folch, A. The upcoming 3D-printing revolution in microfluidics. *Lab. Chip* **16**, 1720–1742 (2016).
17. Waheed, S. *et al.* 3D printed microfluidic devices: enablers and barriers. *Lab. Chip* **16**, 1993–2013 (2016).
18. Abu Hatab, N. A., Oran, J. M. & Sepaniak, M. J. Surface-Enhanced Raman Spectroscopy Substrates Created *via* Electron Beam Lithography and Nanotransfer Printing. *ACS Nano* **2**, 377–385 (2008).
19. Yue, W. *et al.* Electron-beam lithography of gold nanostructures for surface-enhanced Raman scattering. *J. Micromechanics Microengineering* **22**, 125007 (2012).
20. Gates, B. D. *et al.* New Approaches to Nanofabrication: Molding, Printing, and Other Techniques. *Chem. Rev.* **105**, 1171–1196 (2005).
21. Kang, S.-W. Application of Soft Lithography for Nano Functional Devices. in *Lithography* (ed. Wang, M.) (InTech, 2010). doi:10.5772/8186.

22. Maher, S. Microcavity PDMS and gold substrates for supported lipid bilayers. (Dublin City University, 2016).
23. Steigert, J. *et al.* Rapid prototyping of microfluidic chips in COC. *J. Micromechanics Microengineering* **17**, 333–341 (2007).
24. Lloyd, B. P., Bartlett, P. N. & Wood, R. J. K. Wetting of Surfaces Made of Hydrophobic Cavities. *Langmuir* **31**, 9325–9330 (2015).
25. Rostamian, R., Najafi, M. & Rafati, A. A. Synthesis and characterization of thiol-functionalized silica nano hollow sphere as a novel adsorbent for removal of poisonous heavy metal ions from water: Kinetics, isotherms and error analysis. *Chem. Eng. J.* **171**, 1004–1011 (2011).
26. Basit, H., Gaul, V., Maher, S., Forster, R. J. & Keyes, T. E. Aqueous-filled polymer microcavity arrays: versatile & stable lipid bilayer platforms offering high lateral mobility to incorporated membrane proteins. *Analyst* **140**, 3012–3018 (2015).
27. Rymuszka, D., Terpiłowski, K., Hołysz, L. & Chibowski, E. Changes in surface properties of polymethylmethacrylate (PMMA) treated with air plasma. *Ann. UMCS Chem.* **70**, (2015).
28. Ma, Y., Cao, X., Feng, X., Ma, Y. & Zou, H. Fabrication of super-hydrophobic film from PMMA with intrinsic water contact angle below 90°. *Polymer* **48**, 7455–7460 (2007).
29. Vesel, A. & Mozetic, M. Surface modification and ageing of PMMA polymer by oxygen plasma treatment. *Vacuum* **86**, 634–637 (2012).
30. *User's manual for the expanded plasma cleaner PDC-002 (230V) (and optional plasmaflo)*. (Harrick Plasma).
31. Cheng, J.-Y., Wei, C.-W., Hsu, K.-H. & Young, T.-H. Direct-write laser micromachining and universal surface modification of PMMA for device development. *Sens. Actuators B Chem.* **99**, 186–196 (2004).
32. Bartholomeusz, D. A., Boutte, R. W. & Andrade, J. D. Xurography: rapid prototyping of microstructures using a cutting plotter. *J. Microelectromechanical Syst.* **14**, 1364–1374 (2005).
33. *Atmospheric plasma treaters for High-Speed web applications*. (Sigma Technologies, Inc., 2006).
34. Yuan, Y. & Lee, T. R. Contact Angle and Wetting Properties. in *Surface Science Techniques* (eds. Bracco, G. & Holst, B.) vol. 51 3–34 (Springer Berlin Heidelberg, 2013).
35. Shamsi, A. *et al.* Low cost method for hot embossing of microstructures on PMMA by SU-8 masters. *Microsyst. Technol.* **20**, 1925–1931 (2014).
36. Narasimhan, J. & Papautsky, I. Polymer embossing tools for rapid prototyping of plastic microfluidic devices. *J. Micromechanics Microengineering* **14**, 96 (2004).
37. Qi, H. J., Joyce, K. & Boyce, M. C. Durometer Hardness and the Stress-Strain Behavior of Elastomeric Materials. *Rubber Chem. Technol.* **76**, 419–435 (2003).
38. A guide to shore durometers | Albright Silicone Technologies. *Albright Technologies / Silicone Molding, Medical Silicone Prototyping, Injection Molding & More* <https://albrightsilicone.com/a-guide-to-shore-durometers/> (2015).
39. Salh, R. Defect Related Luminescence in Silicon Dioxide Network: A Review. (2011) doi:10.5772/22607.
40. Vernon-Parry, K. D. Scanning electron microscopy: an introduction. *III-Vs Rev.* **13**, 40–44 (2000).
41. Alessandrini, A. & Facci, P. AFM: a versatile tool in biophysics. *Meas. Sci. Technol.* **16**, R65 (2005).

42. Jalili, N. & Laxminarayana, K. A review of atomic force microscopy imaging systems: application to molecular metrology and biological sciences. *Mechatronics* **14**, 907–945 (2004).
43. Wöll, D. Fluorescence correlation spectroscopy in polymer science. *RSC Adv* **4**, 2447–2465 (2014).
44. García-Sáez, A. J. & Schwille, P. Single molecule techniques for the study of membrane proteins. *Appl. Microbiol. Biotechnol.* **76**, 257–266 (2007).
45. Davim, J. P., Oliveira, C., Barricas, N. & Conceição, M. Evaluation of cutting quality of PMMA using CO₂ lasers. *Int. J. Adv. Manuf. Technol.* **35**, 875–879 (2006).
46. Maher, S., Basit, H., Forster, R. J. & Keyes, T. E. Micron dimensioned cavity array supported lipid bilayers for the electrochemical investigation of ionophore activity. *Bioelectrochemistry* **112**, 16–23 (2016).
47. Wacker Silicones. Wacker Silicones - Elastosil - Bonding, Sealing, Potting/Encapsulation and coating with RTV silicone rubber compounds. https://www.wacker.com/cms/media/publications/downloads/6019_EN.pdf.
48. Elastosil® RT 607 A/B Technical Data Sheet. Elastosil® RT 607 A/B Technical Data Sheet. (2014).
49. Johnston, I. D., McCluskey, D. K., Tan, C. K. L. & Tracey, M. C. Mechanical characterization of bulk Sylgard 184 for microfluidics and microengineering. *J. Micromechanics Microengineering* **24**, 035017 (2014).
50. SOP - PMMA Embossing v1.0. SOP - PMMA Embossing v1.0. (2011).
51. Dow Corning. Sylgard® 184 silicone elastomer, Product informations. (2014).
52. Elastosil® RT 675 A/B Technical Data Sheet. Elastosil® RT 675 A/B Technical Data Sheet. (2014).
53. Papirno, R. Axial compression testing. in *ASM Handbook: Mechanical Testing Ed. 9th* vol. 8 55–58 (ASM International).
54. Banerjee, J. K. Barreling of Solid Cylinders Under Axial Compression. *J. Eng. Mater. Technol.* **107**, 138–144 (1985).
55. Kirby, D. *et al.* Centrifugo-magnetophoretic particle separation. *Microfluid. Nanofluidics* **13**, 899–908.
56. Ashby, M. F. *Materials selection in mechanical design*. (Butterworth-Heinemann, 2005).
57. Thermal Analysis Application No. HB 30 - A comparison of the glass transition measured by DSC, TMA and DMA. *Mettler Toledo TA Application Handbook Thermosets* vol. 1.
58. A Closer Look: Techniques for Obtaining Glass Transition Temperature of Polymeric Materials. <http://www.intertek.com/blog/2013-04-15-glass-transition-temperature/>.
59. Amsbio. *Gold coated substrates - Data sheet AU.1000.ALSI*.
60. Goss, C. A., Charych, D. H. & Majda, M. Application of (3-mercaptopropyl) trimethoxysilane as a molecular adhesive in the fabrication of vapor-deposited gold electrodes on glass substrates. *Anal. Chem.* **63**, 85–88 (1991).
61. Zhuravlev, L. T. Concentration of hydroxyl groups on the surface of amorphous silicas. *Langmuir* **3**, 316–318 (1987).
62. Brinker, C. J. Hydrolysis and condensation of silicates: effects on structure. *J. Non-Cryst. Solids* **100**, 31–50 (1988).
63. Socrates, G. Infrared and Raman Characteristic Group Frequencies - Tables and charts. in *Infrared and Raman Characteristic Group Frequencies - Tables and charts* (Wiley).
64. Tuschel, D. Headspace Raman Spectroscopy. *Spectroscopy* **29**, 14–21 (2014).

65. Hu, M., Noda, S., Okubo, T., Yamaguchi, Y. & Komiyama, H. Structure and morphology of self-assembled 3-mercaptopropyltrimethoxysilane layers on silicon oxide. *Appl. Surf. Sci.* **181**, 307–316 (2001).
66. Kaminska, A., Inya-Agha, O., Forster, R. J. & Keyes, T. E. Chemically bound gold nanoparticle arrays on silicon: assembly, properties and SERS study of protein interactions. *Phys. Chem. Chem. Phys.* **10**, 4172–4180 (2008).
67. Qi, H., Chen, T., Yao, L. & Zuo, T. Hydrophilicity modification of poly(methyl methacrylate) by excimer laser ablation and irradiation. *Microfluid. Nanofluidics* **5**, 139–143 (2008).
68. Shah, J. J. *et al.* Surface modification of poly(methyl methacrylate) for improved adsorption of wall coating polymers for microchip electrophoresis. *ELECTROPHORESIS* **27**, 3788–3796 (2006).
69. Zangmeister, R. A. & Tarlov, M. J. UV Graft Polymerization of Polyacrylamide Hydrogel Plugs in Microfluidic Channels. *Langmuir* **19**, 6901–6904 (2003).
70. Takashi Ishigaki, Nobuyuki Sugii, Ryuta Tsuchiya, Shin'ichiro Kimura & Yusuke Morita. *Ultralow-power LSI Technology with Silicon on Thin Buried Oxide (SOTB) CMOSFET*. (INTECH Open Access Publisher, 2010).
71. Shamsi, A., Delaram, S., Esfandiari, M. & Hajghassem, H. Fabrication, sealing and hydrophilic modification of microchannels by hot embossing on PMMA substrate. *RECENT Adv. Biomed. Chem. Eng. Mater. Sci.* 138 (2014).
72. Hiratsuka, A., Muguruma, H., Lee, K.-H. & Karube, I. Organic plasma process for simple and substrate-independent surface modification of polymeric BioMEMS devices. *Biosens. Bioelectron.* **19**, 1667–1672 (2004).
73. Borcia, C., Borcia, G. & Dumitrascu, N. Surface treatment of polymers by plasma and UV radiation. *Romanian J. Phys.* **56**, 224–232 (2011).
74. Tan, S. H., Nguyen, N.-T., Chua, Y. C. & Kang, T. G. Oxygen plasma treatment for reducing hydrophobicity of a sealed polydimethylsiloxane microchannel. *Biomicrofluidics* **4**, (2010).
75. *21st Annual Conference of Doctoral Students, WDS'12 'Week of Doctoral Students 2012', May 29, 2012 to June 1, 2012:: dedicated to 60th anniversary of Faculty of Mathematics and Physics, Charles University in Prague, Czech Republic; [proceedings of contributed papers]. Pt. 2: Physics of plasmas and ionized media.* (Matfyzpress, 2012).
76. Vlachopoulou, M. E. *et al.* Plasma etching technology for fabrication and surface modification of plastic microfluidic devices. *Pure Appl. Chem.* **86**, (2010).
77. Benda, A. *et al.* How To Determine Diffusion Coefficients in Planar Phospholipid Systems by Confocal Fluorescence Correlation Spectroscopy. *Langmuir* **19**, 4120–4126 (2003).
78. Tabarin, T., Martin, A., Forster, R. J. & Keyes, T. E. Poly-ethylene glycol induced super-diffusivity in lipid bilayer membranes. *Soft Matter* **8**, 8743–8751 (2012).
79. Štefl, M., Kułakowska, A. & Hof, M. Simultaneous Characterization of Lateral Lipid and Prothrombin Diffusion Coefficients by Z-Scan Fluorescence Correlation Spectroscopy. *Biophys. J.* **97**, L1–L3 (2009).

3 Chapter 3: Optimized fabrication of uniform gold cavity arrays of controlled dimension over extended (cm²) surfaces and angle dependent SERS

3.1 Introduction

Cavity arrays fabricated at different substrates surface through nanosphere lithography techniques have been fairly widely reported in the last two decades by several groups.¹⁻⁴ Using silica or PS spheres assembled at glass or metallic surfaces, porous substrates can be obtained after performing metal deposition (e.g. through vapour or electrodeposition) and then removal of the template spheres.

The key to achieving uniform arrangement of the cavities within the array lies in the quality of the sphere's assembly at the substrate interface. Strong capillary interactions, taking place near the meniscus of the evaporating liquid they are dispersed in, facilitates the assembly by bringing the spheres together as described by Denkov et al.⁵ However, it seems that over a 1 μm threshold value for sphere diameter, other forces acting on the spheres that are assembling at a solid substrate are involved, as suggested by Tull et al.⁶, that can perturbate the convective flux between particles leading to less uniform arrangement compared to packing obtained with nanospheres. However, it may be possible to compensate for such forces using a well-controlled assembly process.

From a lipid membrane study perspective, although pore-suspended lipid membranes can show good stability for pores below 1 μm diameter, such a nanostructural dimension limits the diffusional area over which lipid or reconstituted protein can migrate, and thus can strongly affect the measurable signal obtained in electrochemical investigation. Furthermore, for optical investigation, if one wants to only confine measurement to free standing bilayer, pore sizes of 1 μm diameter or greater are required because of the diffraction limit and limitations in confining interrogation to single smaller pores.⁷ Therefore, there is a strong need to develop reproducible and controlled fabrication methods suitable for uniform arrays of cavities sizes with dimensions greater than 1 μm diameter.

Uniform arrangement of the cavity will also lead to better, more reliable and reproducible plasmonic properties of the array, particularly in terms of reproducibility of the signal. To date, Bartlett and co-workers are probably the group that has studied, most extensively, the properties of such gold cavity arrays. In their work on plasmons in nanoscale voids, they characterize the plasmon energies and field of localized modes in void structures and show the influence of incident light on a size cavity with different cavity depths due to variation of the gold film thickness.⁸ They suggest that void

plasmon can couple with rim dipoles depending on the geometry of the void, and intensity and location of hot spots in cavity can be tuned through change in the cavity truncation and orientation compared to the incident light. All of their calculations have focussed on single cavity rather than a multiplex of highly ordered cavities, which reflects the reality of the array.

We were interested in studying a fixed geometry (height) of cavity, to study the effect of different cavity diameter on the distribution and intensity of the electric field at the void under different angles of light excitation, but on arrayed cavities. This knowledge could help us to understand how the LSPR at the void can be tuned depending on the orientation of the array and determine which parameters to be used for a better response of the SERS enhancement depending the location of the field.

In this chapter, a markedly improved method for generating gold pore array substrates across cm^2 dimensioned areas with reproducible electroactive surface area of the gold micro cavity arrays is reported. These substrates are suitable for lipid bilayer models' studies through optimisation of the fabrication process. This was achieved by first focussing on increasing the uniformity of the array on large area through improving the arrangement of the micro dimensioned PS spheres at the gold surface achieved by gravity-assisted convective assembly that leads to centimetre sized uniform hexagonally packed monolayer of PS spheres on gold substrates. An electrodeposition method was then established that reliably produces equator level deposition, independent of substrate and spheres dimensions. This was achieved by careful characterisation of the I-t curve for gold electrodeposition around the spheres, ensuring reproducible cavity size and shape from batch to batch and limiting the interstitial space between wells by growing gold exactly up to the equator.

Once the fabrication of the substrates was improved and reliably established, the SERS properties of the resulting arrays were examined, supported by FDTD simulations to evaluate the distribution and amplitude of the electromagnetic field at the cavities under different incident angles of illumination. A new experimental set up was built to verify experimentally the theoretical predictions regarding the possibility to tune the SERS signal of molecules assembled at the cavity surface by simply changing the illumination angle of the array and potentially monitor a lipid membrane suspended at the voids surface.

3.2 Experimental

3.2.1 Easy and robust fabrication of large uniform well-ordered gold nano and micro cavity arrays for SERS applications

3.2.1.1 Large uniform assembly of a hexagonally close packed monolayer of polystyrene spheres onto a gold-silicon wafer

A 1.5 cm by 0.8 cm Au-Si sample was cut, cleaned with acetone, water and ethanol, dried, then air plasma treated for 5 minutes before being placed on a deposition stage fabricated for this purpose. 20 μL of a 1 % (solid wt. in solution) PS spheres solution was drop-cast on the Au-Si substrate. A cleaned glass slide was placed over the sample forming a 2° angle with the substrate base. The deposition stage was left to dry overnight in the presence of silica-gel at a temperature of 4°C , with a tilted front angle of 2° and side angle of 1° . Once the water had fully evaporated, the Au-Si substrate shows an iridescent deposit indicative of a close packed monolayer of dry PS spheres. Figure 83 illustrates the different steps leading to the hexagonal close packed monolayer assembly onto the Au-Si substrate.

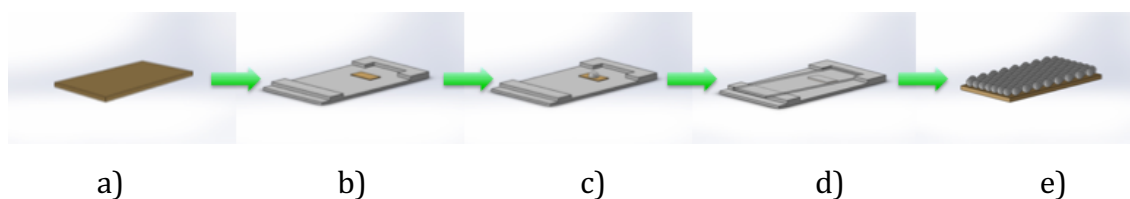


Figure 83 : Schematic of the fabrication method of a PS spheres hexagonally close packed monolayer onto an Au-Si wafer by convective assembly. a) Clean 0.8 x 1.5 cm Au-Si substrate, b) Substrate stuck onto deposition stage, c) 20 μL of a 1 % (solid wt. in solution) PS spheres drop cast onto Au-Si substrate, d) Glass slide placed over sample forming a 2° angle with the substrate, e) Monolayer assembled at the Au-Si surface in a hexagonally close packed arrangement.

3.2.1.2 Fabrication of hemisphere gold cavities by controlled electrodeposition up to the equator

Once the PS spheres monolayer has been assembled at the Au-Si surface, gold electrodeposition through the spheres template was performed. The method used and described in chapter 2 has been improved to gain in precision and reproducibility in the fabrication process from one sample to another and details of this work is shown in further section. The electrochemical cell consists in the Au-Si wafer being the working electrode, an Ag/AgCl reference electrode and a platinum wire as counter electrode, linked to a potentiostat CH Instrument model 900 electrochemical station.

Electroplating gold solution Elevate gold 7990 RTU (8.2 g/L) was purchased from Technic Inc. USA. As slight variations might occur from batch to batch, best electrodeposition potential needs to be defined and was found here to be -600 mV. The solution degassed by purging for 30 minutes with nitrogen. The I-t curve was monitored, and gold electroplating was stopped when current reached the minimum corresponding to the equator level of the spheres monolayer as illustrated in Figure 84. Sample were finally rinsed with deionised water avoiding salt to crystallise at the gold surface and were dried under nitrogen stream.

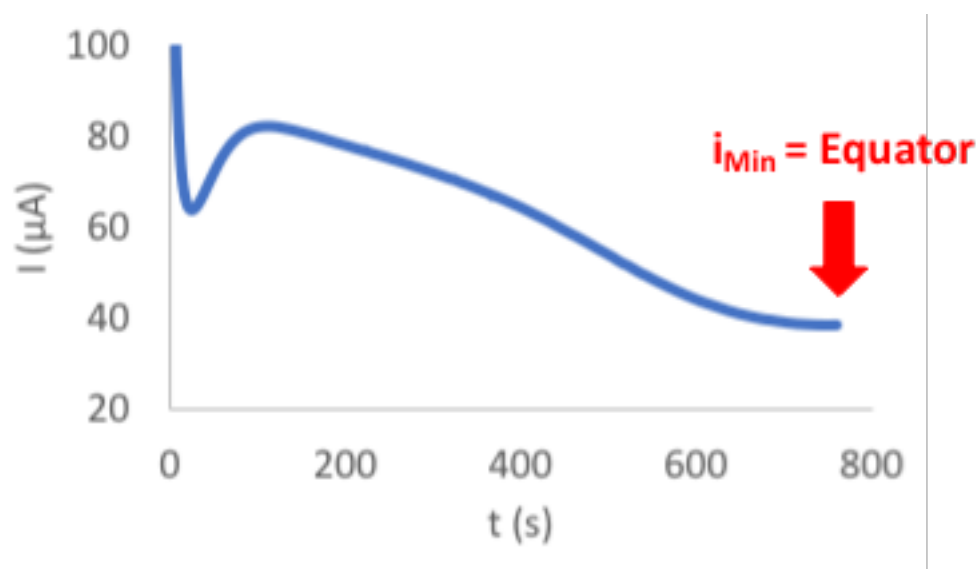


Figure 84 : Representative I-t curve obtained during the electrodeposition of gold around the hexagonal close packed PS spheres monolayer assembled onto an Au/Si substrate, up to a depth of the equator of the spheres. ($E = -0.6 \text{ V vs. Ag/AgCl}$).

3.2.1.3 Assessment of the fabrication method reproducibility by electrochemically active area determination

Electrochemically active area determination was performed by running cyclic voltammetry of different gold cavity arrays in 0.1 M H_2SO_4 between -0.35 V and 1.5 V, using a CHI 660A Potentiostat with a standard three electrodes system. The tested gold cavity array acted as working electrode, an Ag/AgCl electrode as reference and a platinum wire as counter electrode.

3.2.1.4 Characterisation of optimised gold micro and nano cavity arrays.

Characterisation of gold cavity arrays made with template spheres of indicative diameter of 3 μm and 2 μm were achieved using Hitachi S3400 Variable Pressure SEM. Arrays made with smaller template spheres of indicative diameter of 1 μm and 510 nm

were characterised using both the SEM and a Hitachi S5500 cold Field Emission in lens Scanning Electron Microscope (FESEM) as a higher resolution was needed for accurate measurements.

3.2.2 FDTD simulations

To understand the location and amplitude of the electric field at the gold cavity array, FDTD simulations were carried out using Lumerical FDTD solutions software. Models were established by Dr. Kiang Wei Kho. Optical constant for Au was obtained from Johnson & Christy.⁹ As the array contains large contrast between feature sizes (e.g. inter-cavity gap-size is more than 30 times smaller than cavity diameter), conformal variant 2 was used as the mesh refinement method to ensure simulation accuracy. Simulations were performed with a resolution of 5.15 nm, 9.9 nm, 18.4 nm and 29.9 nm respectively for cavity diameter of 510 nm, 1 μm , 2 μm and 3 μm . For field calculations, illumination laser bandwidth was set at 0.02nm. The central wavelengths used in the simulations are 473nm, 532nm, 633nm and 785nm. All simulations were terminated at an auto shutoff threshold of 10^{-5} . To simulate an infinitely large periodic structure, Bloch boundary condition was used.

3.2.3 Selective modification of the array for angle dependence study of SERS signal from molecules adsorbed at the gold surface.

With the aim to check experimentally and hopefully match FDTD simulations regarding the location of the hotspot at the cavity array, selective functionalisation of cavities was performed with two different surface-active agents.

Hexagonal close packed monolayer assemblies of 510 nm and 1 μm diameter PS spheres were fabricated for the study. After electrodepositing gold around the spheres up to the equator as described in the previous section, arrays were selectively modified using a method modified from that reported by Mallon et al.^{10,11}

Two sets of selectively modified cavities were prepared per cavity size.

The first set were prepared by dipping substrates with spheres still present at the array in a 10 mM ethanolic solution of 4-Aminothiophenol (4-ATP) for 72 hours. Structure of 4-ATP is illustrated in Figure 85. This allowed 4-ATP molecules to be adsorbed at the interstitial space available in between spheres, at the top surface of the gold array only, via chemisorption of the thiol terminus at gold. Substrates were then rinsed with copious amounts of ethanol to make sure excess of 4-ATP molecules that

could be physisorbed were removed. PS spheres were then dissolved by sonicating the substrates in THF for 1 minute and sample were left to soak for another 30 minutes. Finally, the samples were thoroughly rinsed with ethanol followed by deionised water and sonicated in deionised water for measurement.

The second set of samples were functionalised in the same manner with a 10 mM ethanolic solution of 1-octanethiol, which structure is illustrated in Figure 86. The long 72 hours treatment allowed time for the 1-octanethiol adsorbed molecules to reorient and ensures complete backfills of any remaining gaps or discontinuities in the film leading to a tightly packed crystalline assembly of alkane thiol at the gold top surface.¹²⁻¹⁵ PS spheres were removed, and the substrates thoroughly rinsed with ethanol. The interiors of cavities were subsequently functionalised by dipping the substrates in a 10 mM ethanolic solution of 4-ATP for 3 hours. This short exposure time prevented 4-ATP molecules from adsorbing at the top edges of cavities, as these potential binding sites were already occupied by 1-octanethiol molecules. Samples were finally thoroughly rinsed with ethanol followed by deionised water and sonicated in deionised water for measurement, resulting in samples selectively modified with 1-octanethiol at the top surface and 4-ATP inside cavities.

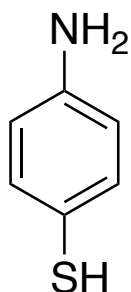


Figure 85 : Chemical structure of 4-Aminothiophenol.

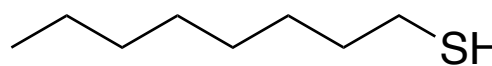


Figure 86 :Chemical structure of 1-octanethiol.

3.2.4 Angle dependence set up and measurements

For the following SERS measurements presented in this thesis, a Horiba Labram HR instrument was used with a 5x (0.13 N.A. (Numerical Aperture)) long distance magnification objective from Motic, or a 50x (0.55 N.A.) long distance magnification objective from Leica. In this chapter, 633 nm and 785 nm laser presenting respectively a full power at the sample of 5.0 mW and 60.2 mW were used as excitation wavelength.

The first step was to control the polarisation of the light for the lasers to be used in the experiment with a polariser placed on top of an Si sample as illustrated in Figure 88 a). Raman signal was collected between 475 and 575 cm^{-1} for both laser at full power, in air, for 10 s, 3 accumulations, with a 500 μm pin hole, while rotating the polariser over a range of 180° with a 10° step. Each measurement was done in 3 repetitions.

After this, the setup was modified and orientated under the Raman spectrometer objective in a way that the axis of inclination of the studied sample was perpendicular to the electric field. The “in-house” manufactured stage illustrated in Figure 88 b) consisted in a rotary stage mounted on top of a post fixed on a breadboard, in a way that the rotation axis was perpendicular to the laser light. Two supplementary posts were fixed parallel to the axis of rotation, acting as a stage to hold the sample to be studied. The scale of the rotary stage allowed a precise angular adjustment every degree over a 180° window. The sample was placed in the reusable microfluidic device illustrated in Figure 87 which was taped onto the stage of the angle dependence setup to ensure stability while tilting the stage.

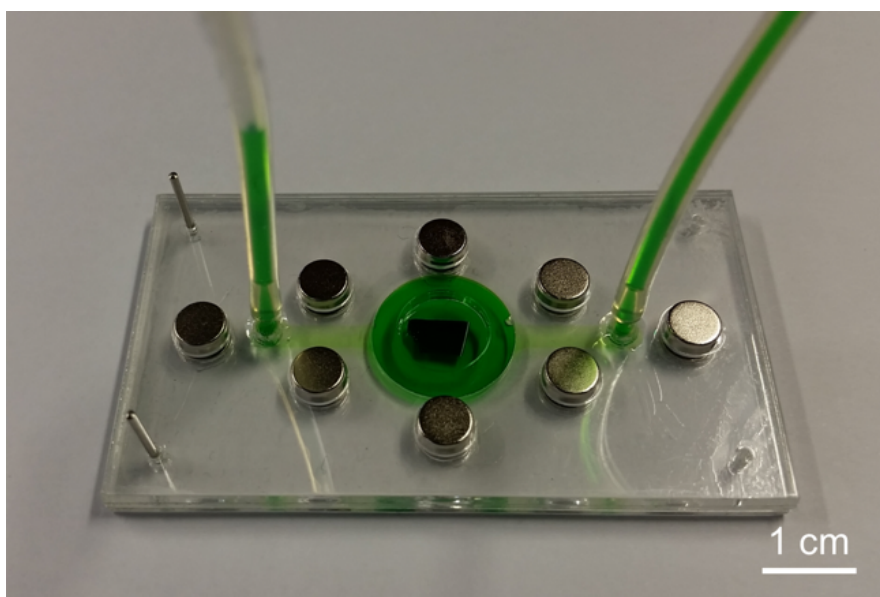


Figure 87 : Reusable PMMA based microfluidic device designed for Raman measurement in liquid. The green liquid is a food dye used to test the sealing efficiency of the system.

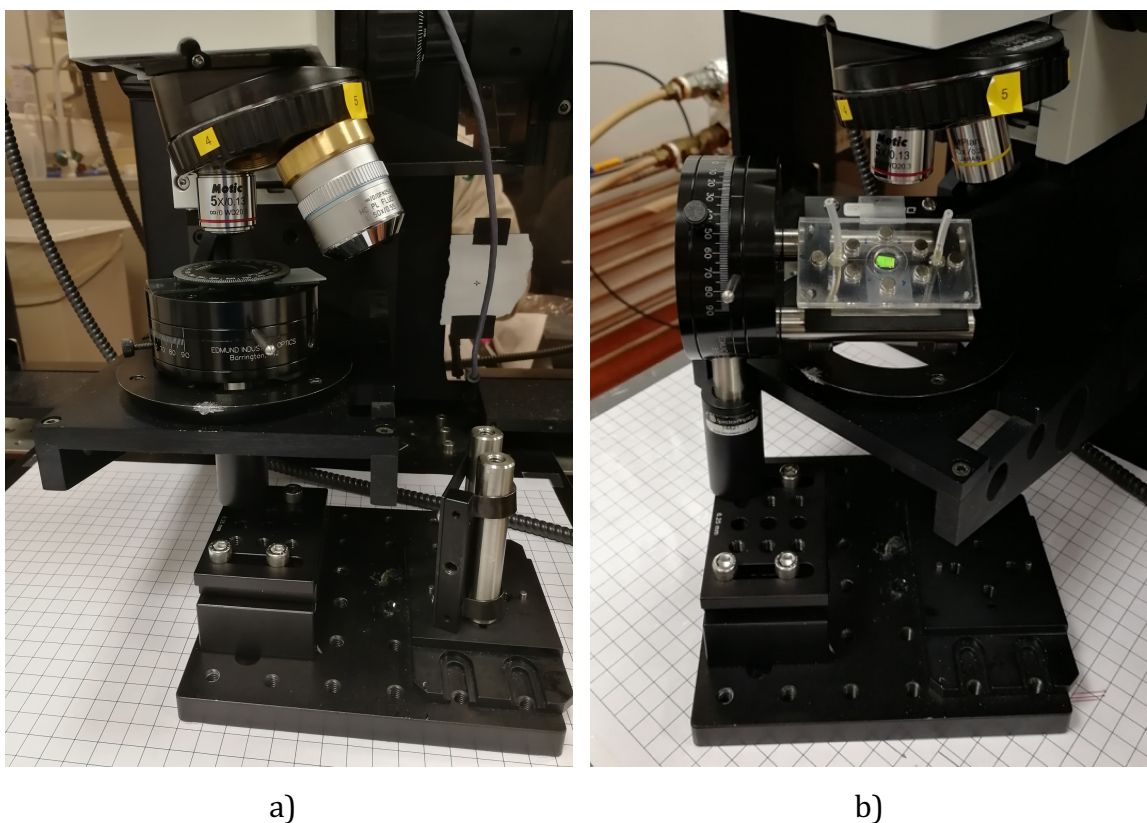


Figure 88 : a) Setup used for the determination of the polarisation angle of lasers used on the Raman spectrometer. B) Converted setup used for angle dependence study allowing to tilt the sample in line with the polarisation of the electric field.

Intensity of 4-ATP SERS signal was recorded while changing the angle of the incident light illuminating the sample. SERS measurements were acquired for a minimum of 6 points across the tested sample per angle, in water, using full power of the 633 nm laser for arrays with 510 nm diameter cavities and the 785 nm laser for arrays with 1 μm diameter cavities. The confocal pin hole was opened to 500 μm to avoid any confocality and collect the maximum signal. Data were acquired every 10° over a 60° window, between 300 and 2200 cm^{-1} for 3 accumulations of 30 s each. For these measurements, a x5 low numerical aperture objective (0.13 N.A.) was used to ensure the field to behave like a plane wave across the focus spot and be as closest as possible to the FDTD simulations shown in further section. SERS signal recorded was normalised to the signal measured for the Si peak on the day of analysis during the calibration of the equipment.

3.2.5 Angle Dependent Raman Measurements of a DOPC lipid bilayer suspended at a gold nano cavity array

Given the results obtained for the angle dependence study on the 510 nm diameter cavity arrays, it has been decided to suspend a DOPC lipid bilayer, which structure is illustrated in Figure 89, on such substrates using Langmuir-Blodgett followed by vesicles disruption¹⁶, and check the Raman response over different angles.

Substrates were prepared according to the method described previously in section 3.2.1 using PS spheres with an indicative diameter of 510 nm. Samples were then left overnight in an 10 mM ethanolic solution of 6-mercapto-1-hexanol, which structure is illustrated in Figure 90, to functionalise their top surface and render it hydrophilic for a good spanning of the lipid bilayer^{7,17}. PS spheres were removed by dissolving them in THF for 3 minutes and sonicating the samples for 1 minute. Samples were thoroughly rinsed with ethanol, then water and sonicated in PBS for 15 minutes.

DOPC SUVs were prepared as described in Chapter 2. The formation of the DOPC monolayer onto liquid filled cavities was optimised by Guilherme B. Berselli in our group, leading to a robust and reliable method for a highly organised monolayer of lipids at the air-water interface, avoiding lipid collapse into three-dimensional structures and guaranteeing a single layer to be transferred onto the substrate by Langmuir-Blodgett technique. 50 μ L of a 1 mg/mL DOPC solution in chloroform was added dropwise gently over 2-3 minutes on the subphase of the Langmuir-Blodgett trough and allowed solvent to evaporate for 15 minutes. Multiple compression-expansion cycles were then performed before reaching the collapse surface pressure and monolayer was then transferred at a highly condensed surface pressure of 32 mN/m by vertical withdrawal of the submerged cavity substrate at a speed of 5 mm/min.

Sample was then left in contact with previously prepared SUVs for one hour, allowing disruption of the vesicles onto the monolayer to yield a lipid bilayer suspended across the aqueous filled pores. After rinsing this with PBS, it was assembled onto a microscope glass coverslip similarly to the way described in Chapter 2.

SERS measurements were then acquired varying the angle of the incident light, using a 50x (0.55 N.A.) objective and a 633 nm laser line with a power of 1 mW measured at the sample.

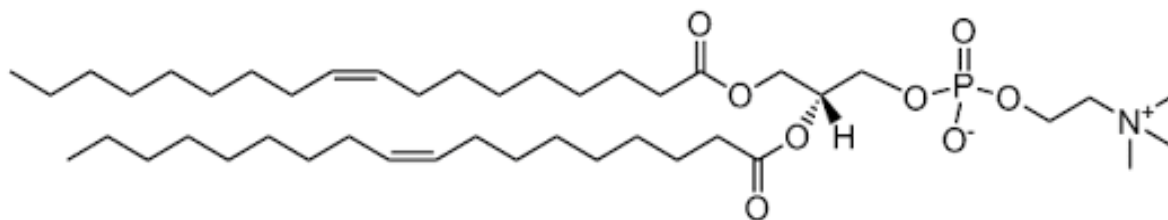


Figure 89 : Chemical structure of 18:1 (Δ 9-Cis) lipid (DOPC).

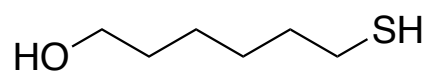


Figure 90 : Chemical structure of 6-mercapto-1-hexanol.

3.3 Results and discussion

3.3.1 Optimisation of the gold micro and nano cavity arrays fabrication

A primary aim of this chapter was to optimise a low-cost method for preparing spherical pore array in the most reproducible way possible. This can be achieved through a better assembly of the template sphere and a more controlled gold electrodeposition. All trials presented below were performed initially with 3 μm diameter PS spheres with the aim to build substrates matching the dimensions of cavities used by Keyes' group on PDMS for FLIM/FCS applications.^{7,16} Different techniques to arrange monodisperse PS spheres at the gold surface were iterated to obtain a well organised assembly and results are presented and discuss below.

3.3.1.1 *Optimisation of the PS spheres arrangement at the gold surface*

3.3.1.1.1 Simple drop casting

Gold cavity arrays for protein and lipid bilayers studies have been previously used in Keyes' group ^{10,7,18}, however the fabrication technique did not allow to obtain a uniform close packed array for micro dimensioned cavities over a full centimetre squared size area. Small spheres below 1 μm can be brought together by capillary forces, but same forces bring large spheres over 1 μm to be immobilized at the substrate surface.⁶

Figure 91 a) shows a photographic image of a 3 μm diameter gold cavity array obtained by simple dropcasting of a PS spheres solution onto an Au-Si electrode, left to dry overnight before gold electrodeposition around the spheres, as described in chapter 2.

Although such substrates gave promising results in the past, they can present defects in pore packing that can reduce reproducibility and stability, particularly for electrochemical measurements and for applications that require sampling across multiple spots on the substrate, like SERS. Also, fabrication reproducibility depended deeply on user skill. Indeed, the electrode shown here and used for electrochemical measurements presents large flat areas surrounding the cavity array due to the way the drop dried. Uniformity over extended areas is in particular important for application in MSLB fabrication, as lipid bilayer at these regions will interact with the substrate and contribute to the overall electrochemical signal, giving a representation of a supported lipid membrane rather than suspended as initially intended. Therefore,

the importance of achieving well-ordered large dimensions areas – mm² to cm² – to fit the conventional electrodes sizes and smaller electrodes used in microfluidics, giving concurrently the capacity to examine across several spots on a surface in Raman to build statistics.

An important limitation in previous methods is that multilayers of PS spheres can form during the drying process and can be noticed, dispersed at the centre of the array but most particularly at its outer rim, due to a well-known “coffee-ring effect”.¹⁹ Such multilayers impact strongly the rest of the arrangement across the substrate, particularly the arrangement of the underlying stratum situated directly at the gold electrode surface and being the layer of interest in our case.

Figure 91 b), c), d) and e) shows representative regions observed at a gold cavity arrays obtained by simple drop casting method. Interstitial flat areas between cavities increase depending on the arrangement of the spheres being hexagonally packed (b and c), squared packed (b and c), randomly dispersed (d) or aggregated (e), leaving larger flat areas as spheres from the first layer move to upper levels. Figure 91 b) illustrates the different layout of the spheres as the number of layers increases, going from a hexagonal arrangement for the first layer (bottom yellow), to a squared arrangement for the second layer (middle light brown), and go back to a hexagonal arrangement for the third layer (top dark brown). In contrast to report by Prevo and Velev²⁰ who described this phenomenon, we noticed that even the first layer arrangement can be squarely packed as shows the resulting cavities grown up to the equator of the first layers of spheres and presented in Figure 91 c).

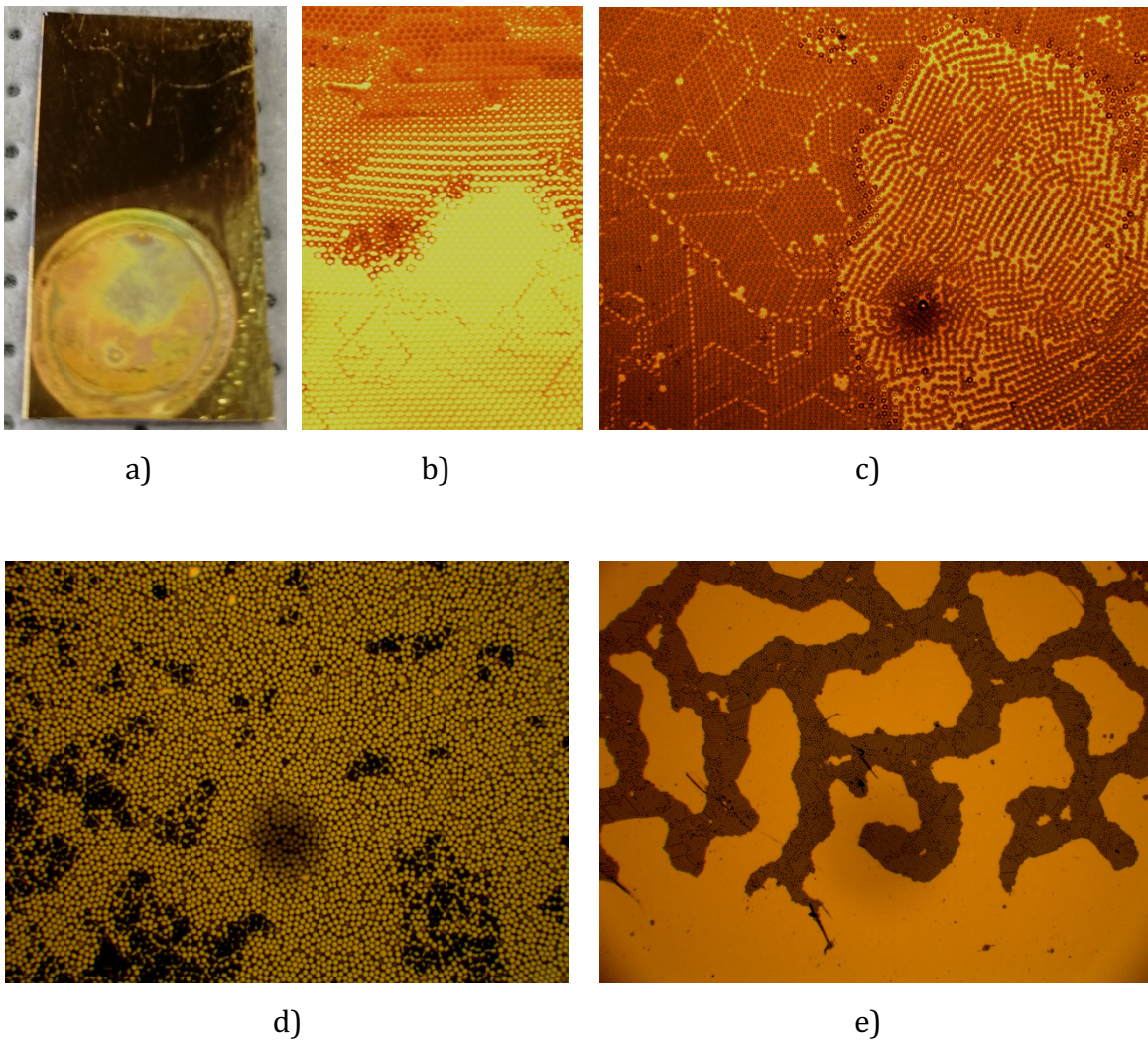


Figure 91 : a) Picture of a 3 μm diameter gold cavity array obtained by simple dropcasting of a PS spheres solution onto an Au-Si electrode, left to dry overnight before gold electrodeposition around the spheres. b), c), d) and e) White light image of different regions observed at a gold cavity arrays obtained by simple drop casting method.

Also, depending on the number of strata, multilayers can reduce the accessibility of the gold electroplating solution to the gold electrode surface as depicted in Figure 92, leading to non-uniform cavities across the substrate. This phenomenon is even more pronounced for smaller radii template spheres as the size of the triangular interstitial space between beads packed hexagonally decreases with the size of the sphere.

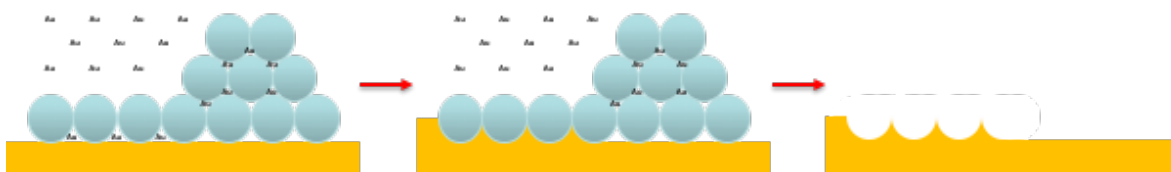


Figure 92 : Illustration of spheres multilayers blocking the accessibility of gold electroplating solution to the gold electrode surface during the electrodeposition process and leading to non-uniform cavities or flat areas.

Those irregularities can occur even across a single substrate, creating variability in surface coverage, leading to variation in electrode area from substrate to substrate that will affect electrochemical signal where the materials are used as electrodes. Therefore, it is necessary to improve the method used to fabricate substrates by reproducibly improving the cavity packing and preventing formation of multilayers at the gold surface.

3.3.1.1.2 Vertical dry out in oven

The first approach attempted to improve the assembly of PS spheres at the gold surface was a simple vertical dry out of a 1 % aqueous solution of 2.88 μm diameter PS spheres onto a 5 mm by 20 mm Au-Si substrate. A PMMA based chamber was fabricated for this purpose as shown in Figure 93, aimed at reducing the volume of solution (400 μL maximum) used to coat a single sample. The sample in its chamber was placed in an oven at 40 $^{\circ}\text{C}$ until full evaporation of the solution. Concentration and volume of solution used were calculated to have about 30 times excess of beads in solution to ensure full coverage of the dipped area.

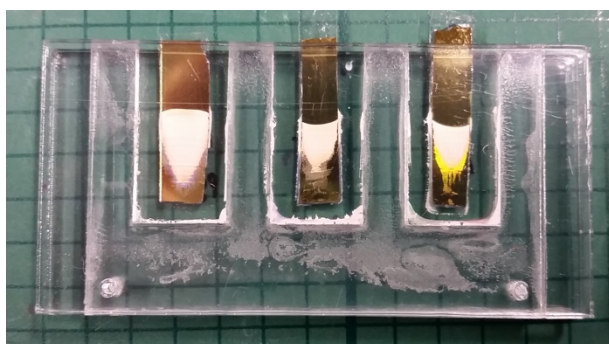


Figure 93 : PMMA based chamber fabricated for vertical dry out of PS spheres onto 1 cm^2 Au-Si wafer.

The solution took more than 24 hours to fully evaporate and the beads adhered to the top part of the dipped area only, in a multilayer assembly. This result suggests first that evaporation of the solution might be too slow promoting the formation of multilayers at the gold surface. Despite the large excess of beads in solution, full coverage of the sample was not achieved due to spheres forming multilayers, but also due to beads settling during the long drying process, evident from the large white aggregates present at the bottom of the chamber. More trials could have been done to study the impact of the evaporation rate on the assembly by increasing the drying temperature, but it was decided to control the level of the air-liquid interface with a different technique to achieve better control.

3.3.1.1.3 Inverted dip-coating

Work has been reported by other groups to create large-area assembly of spheres by simple dip coating method^{21,22} or by Langmuir-Blodgett method.^{23,24} One advantage of the Langmuir-Blodgett method is that it compensates for the loss of spheres deposited at the substrate surface by keeping the surface pressure constant and guaranteeing a close packed monolayer of spheres transferred to the substrate. However, this technique wastefully consumes large quantities of material as the trough size is usually huge compared to the substrates to be coated. The simple dip-coating method was not attempted as the equipment available in our group would not allow a slow enough withdrawal of the substrate from the PS spheres solution, leading surely to a disperse assembly at its surface. To face this issue, it was decided to withdraw the spheres solution rather than the substrate to be coated. A new set up was then devised and fabricated to compensate for the low evaporation rate of the PS sphere solution encountered previously.

A disposable plastic spectrophotometer cuvette was modified by gluing barbed tubed fitting at its bottom and plugging it to a syringe. The device was then plugged to a syringe pump allowing to control accurately overtime the extraction of liquid from the cuvette at a constant rate. Figure 94 a) illustrates the full setup.

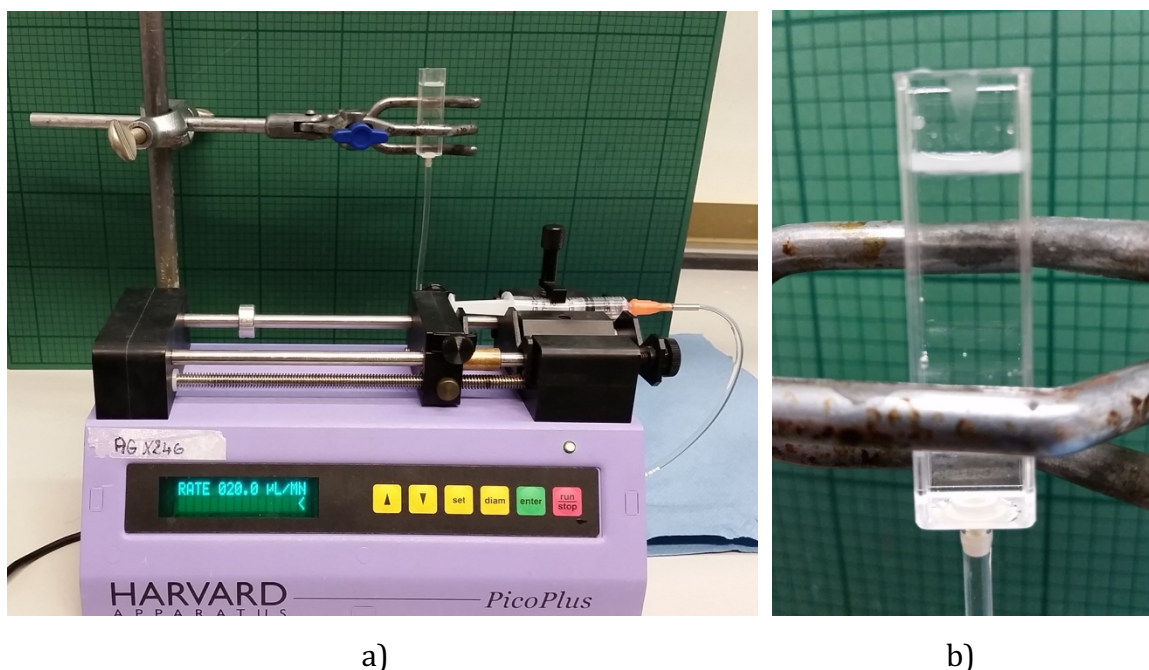


Figure 94 : a) Set up used for the inverted dip coating method. b) Spectrophotometer plastic cuvette modified with a barbed tube fitting at its bottom and filled up with a concentrated solution of 2.88 μm diameter PS sphere solution at the perfluorohexane surface.

First trials were attempted by sticking similar substrates to those used for the vertical dry out to the inside wall of the cuvette, which was filled with a 1 % aqueous solution of 2.88 μm diameter PS spheres. The sphere solution was then extracted at different rates over the range 10 to 100 $\mu\text{L}/\text{min}$, but PS beads assembled in a close packed monolayer only on the first millimetre of the substrate and the rest of the surface remained free of spheres.

Formation rate of the monolayer at the vertical surface was then estimated according a method reported by Dimitrov and Nagayama²⁵ as $v_c = 0.2417 \mu\text{m}/\text{s}$ for the 2.88 μm diameter spheres. To form a close packed monolayer of spheres at the gold surface, the extraction rate of the solvent should match this value. Given the dimensions of the cuvette, extraction of the solution should be carried out at 1.45 $\mu\text{L}/\text{min}$, meaning the deposition will take 11.5 hours to cover 1 cm of substrate length. The sample was thus left overnight at this rate of solvent extraction, but results were inconclusive.

Controlling the concentration of spheres close to the air-water interface is important as the interfacial particles are the one constrained by capillary forces and involved in the formation of the monolayer.^{26,27} Settling velocity of the spheres V_s estimated to $2.54 \times 10^{-7} \text{ m}/\text{s}$ from Stokes' law in Equation 10 remains an order of magnitude lower than the extraction rate of the solvent. Therefore, this parameter

should not be limiting and should guarantee sufficient spheres stay close to the air-water interface. Nonetheless, a trial using a large excess of beads at the air-solvent interface was attempted by increasing the buoyancy. With a density of 1.6910 g/cm³ at 20 °C, a low viscosity and because it will not damage physically PS, perfluorohexane was found to be the best candidate and was used to support a small volume of concentrated PS sphere solution as illustrated in Figure 94 b). This attempt was not successful, likely due to the hydrophobicity of the solvent influencing the capillary forces involved at the gold surface.

Equation 10 : Stokes' law used for the calculation of the settling velocity V_s of PS spheres in water. ρ_p is the particle density of 1050 kg/m³, ρ_f is the fluid density of 1000 kg/m³, μ is the fluid dynamic viscosity at 25 °C of 8.9×10^{-4} Pa.s, g is the acceleration due to gravity of 9.8 m/s², and r is the radius of the particle.

$$V_s = \frac{2(\rho_p - \rho_f)gr^2}{9\mu}$$

3.3.1.1.4 Approaches to overcome the “coffee ring” effect for horizontal drop casting

Several methods were attempted to overcome the “coffee ring” effect to improve uniformity of PS monolayer deposition.

Firstly, a method adapted from Majumder et al.²⁸ work using Marangoni flow was performed. Here, a similar method as the one described previously for simple drop casting was performed but with a different drying process. After dropcasting the dilute PS sphere solution onto the Au-Si substrate, sample was left to dry in an ethanol vapor atmosphere inside a Petri dish. The surface tension gradient created generates a recirculating flow of the particles inside the drop and allow them to spread at the surface while the drop is drying. Although this technique yielded a more uniform monolayer of PS spheres at the gold surface with less large free areas and avoided the “coffee-stain” ring, the packing arrangement was very disordered.

Trying to increase the surface tension at the air-liquid surface of the PS solution for a better arrangement of the spheres was also attempted using different solutions of sucrose. While drying, sucrose left a visible thin film on top the spheres as illustrated in Figure 95. The viscosity of this film might be the reason for the low-quality arrangement of the spheres as it might slow down the packing motion.

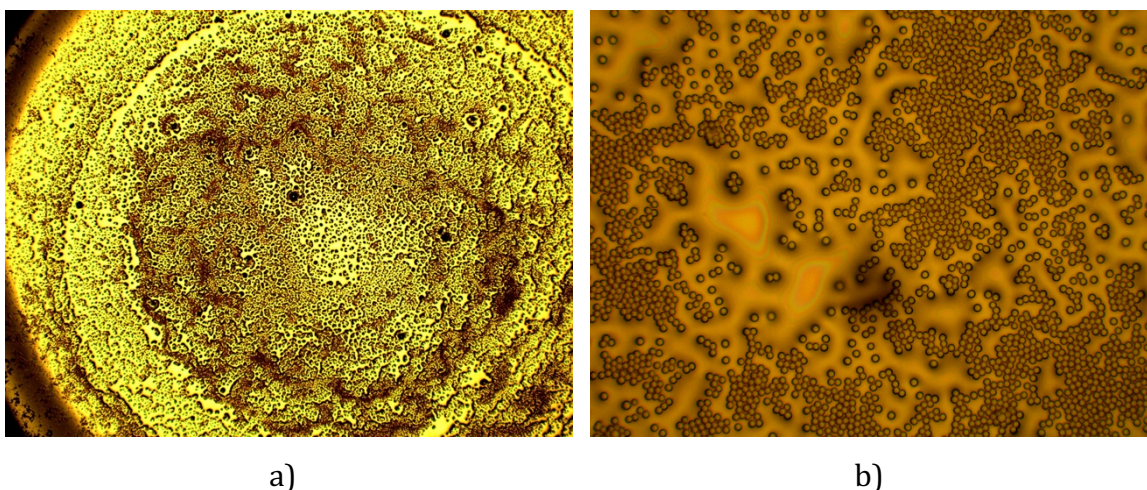


Figure 95: White light images of a 10 % sucrose solution with 0.2 % PS spheres of 2.88 μm diameter captured with a 5x (a) and a 50x (b) objective.

Finally, a method adapted from Denkov et al.⁵ work was attempted. In their study, they observe that ordering is mainly driven by the attractive capillary forces due to the meniscus formed between two adjacent particles and the convective transport of particles towards the ordered region. To increase convective transport, they tuned the shape of the drying droplet meniscus using a Teflon ring cut slant wise, to form a concave air-water surface. Trying to mimic the hydrophobicity and the “cut angle” of the cell-based shown in their paper, a nitrile O-ring was simply placed on top of an Au-Si sample and spheres solution was dropped in its centre. First attempts with the simplified cell gave promising results as illustrated in Figure 96, showing the drop dried from the centre towards the edge of the O-ring. From Figure 96 a), we can see that dark regions in the centre, corresponding to multilayers, are progressively fading towards the outskirts and give way to lighter regions corresponding to monolayers organised in hexagonal close packed pattern, as shown in Figure 96 b). To limit multilayer formation during drying the volume and concentration of the drop was reduced. However, multilayers still formed in a concentric pattern alternated with free areas, bare from PS spheres. Full coverage of the electrode with hexagonally close packed cavities was not achieved.

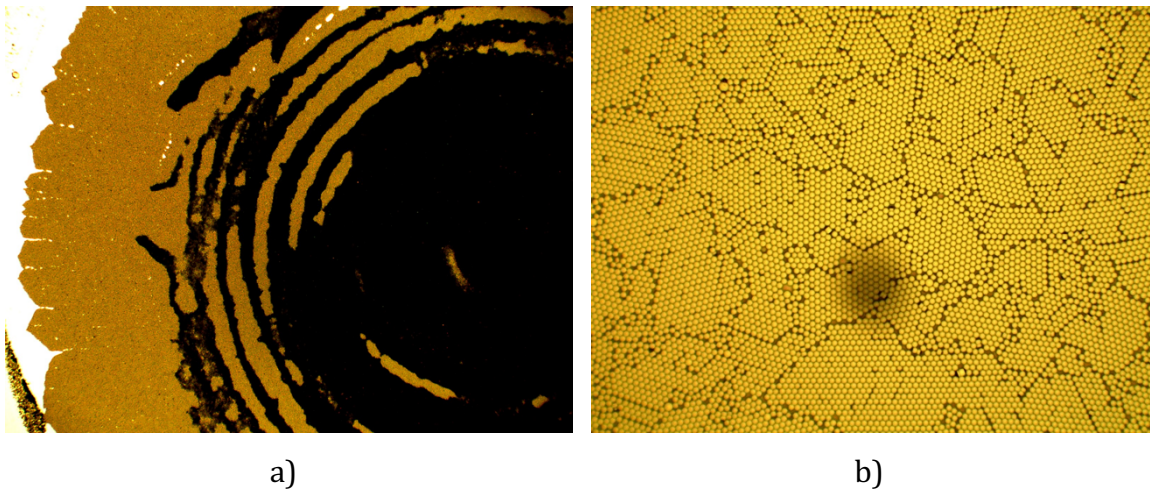


Figure 96 : White light images of 15 μL of a 2.88 μm diameter PS spheres solution at 0.2 % dried on a gold substrate into an O-ring cell, captured with a 5x (a) and a 50x (b) objective.

3.3.1.1.5 Convective assembly on tilted stage

The convective assembly of the spheres at the gold surface was then examined. The method presented here is adapted from Sun et al. and Ye et al. work.^{29,30} In their research, they study the assembly of a large uniform two-dimensional colloidal crystals using capillary forces between two glass slides. Using a wedge-shaped cell helps to keep the liquid layer relatively thin while keeping a straight contact line of colloidal suspension, which is critical in ensuring the spheres' assembly as a monolayer. Indeed, we can summarize our previous attempts by stating that curved contact lines always resulted in the formation of multilayers, convex ones giving multilayers at the outer rim (e.g. simple drop casting) and concave ones at the centre of the array (e.g. O-ring method).

Also, another improvement compared to the previously methods tested by concentric drying is that less gaps tend to form in between particles during the arrangement due to the shape of the drying front of the suspension, leading in theory to a more uniform single domain orientated hexagonally packed array, as illustrated in Figure 97.²⁹

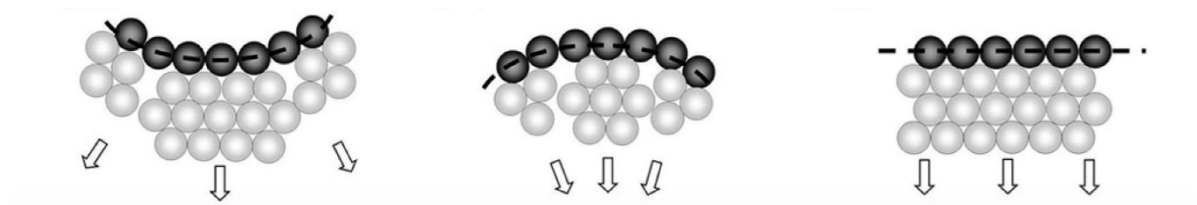


Figure 97 : Schematic of the assembling process in a concentric way towards the outside of the array (left), in a concentric way towards the inside of the array (middle), and linearly from one side to the other of the array (right). Dashed line depicts the drying front of the suspensions and the arrows indicates its receding direction. Figure adapted from Sun et al.²⁹

Finally, tilting the sample during drying helps the particles to concentrate closer to the drying front as spheres are moving mainly due to gravity forces rather than to the convective water influx for conventional convective assembly, as illustrated by Ye et al.³⁰

Based on the size of Au-Si sample to be used, the number of spheres per mL of PS stock solution given by the supplier, and the size of the smallest unit cell for a hexagonal close packed arrangement of spheres given in Equation 11, preliminary calculations were done to make sure number of particles to be assembled at the gold surface was in slight excess that required to form a full monolayer while limiting the risk to form multilayers. Theoretical full coverage of a 0.8 x 1.5 cm Au-Si sample was calculated to require 20 μL of a 1.09 % of the 2.88 μm diameter PS spheres solution, for over 16.7 million of spheres assembled at the gold surface.

Equation 11 : Equation for the calculation of the area of the smallest unit cell in a hexagonal close packed arrangement using spheres of diameter d .

$$A_{\text{unit cell 1 sphere}} = \frac{d^2\sqrt{3}}{2}$$

First attempts were not conclusive as beads did not adhere well to the gold surface, tending to assemble at the outskirts as multilayers. This was attributed to the different substrates used here compared to the original method, as the hydrophilicity of the surface plays a key role on the capillary forces involved in the arrangement. To evaluate hydrophilicity, Figure 98 illustrates contact angle measurements performed at the gold surface. Au-Si substrates cleaned with acetone and ethanol before use present an average contact angle of 81.4°. Air plasma treating substrates for 5 minutes improved the hydrophilicity of the gold, reflected in a decreased contact angle to 39.3° attributed to surface contamination removal and gold oxide film formation.

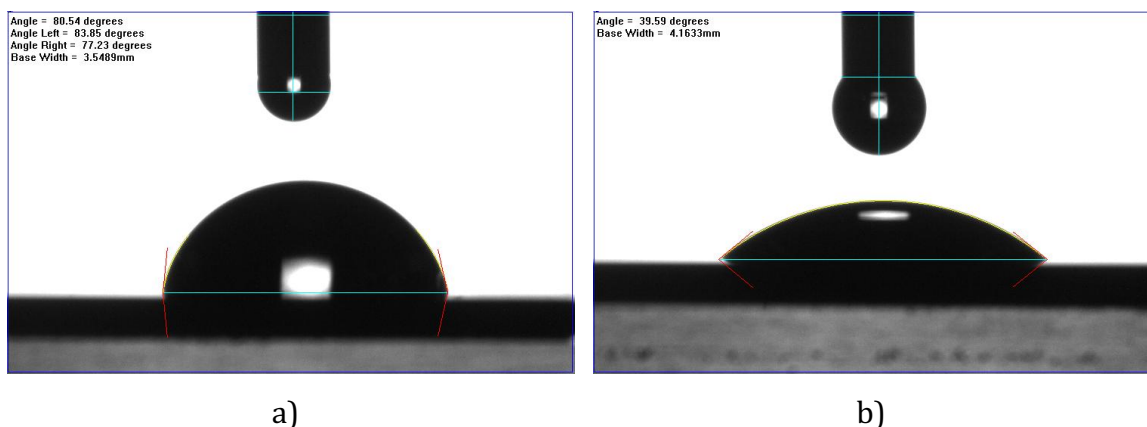


Figure 98 : Representative contact angle measurement of a drop of water onto a gold substrate cleaned with acetone and ethanol (a) and air plasma treated for 5 minutes (b).

Experimentally, hydrophobicity recovery could be noticed by observing the shape of the drop of solution at the gold surface. Although gold oxide is stable, plasma treated gold might not lead to full Au_2O_3 surface and leave room to hydrophobicity recovery due to carbon contamination.^{31,32} To limit the hydrophobicity recovery of the gold substrates impacting the assembly, PS spheres solution was drop casted shortly after plasma treatment. This treatment improved sphere adhesion as a monolayer, however success rate of well-formed arrays was around 15 to 25 % of good substrates.

Thus, the method was then iteratively adapted to improve the success rate of monolayer formation.

Firstly, orientation of the Au-Si substrate on the stage was changed to ensure the liquid film to dry was the thinnest possible.

Secondly, we tried to control the drying atmospheric conditions to ensure they were closely matched from batch to batch. To do this, the stage was placed into a box with silica gel to limit the air movement and try keep the humidity to a low level. The box was then placed into a fridge, to slow down drying to give time to particles to get close to each other and fill up the gaps.

Thirdly, the concentrations and volume of PS solution drop casted were varied systematically. In this regard, 20 μL seemed to be the best volume, allowing complete wetting of the substrate without overflow. An excess of 10 % over the theoretical concentration to be used gave very satisfactory results.

Finally, after implementation of the three modifications just described, by eye we noticed that disperse white patches characteristic of multilayers were forming

among the nicely packed iridescent monolayers. Microscopic imaging lead to the conclusion that blank regions were initiated by presence of spheres of anomalously large diameter as shown clearly in Figure 99, and could vary from tiny to very large area. This phenomenon has been described by Denkov et al.⁵ and is due to the water layer being thicker in the vicinity of the large particles. The smaller particles aggregate in the conical space below the air-water surface formed around the large particle, forming progressive multilayers. Thus, the monodispersity of the PS spheres applied is crucial to the success of the method.

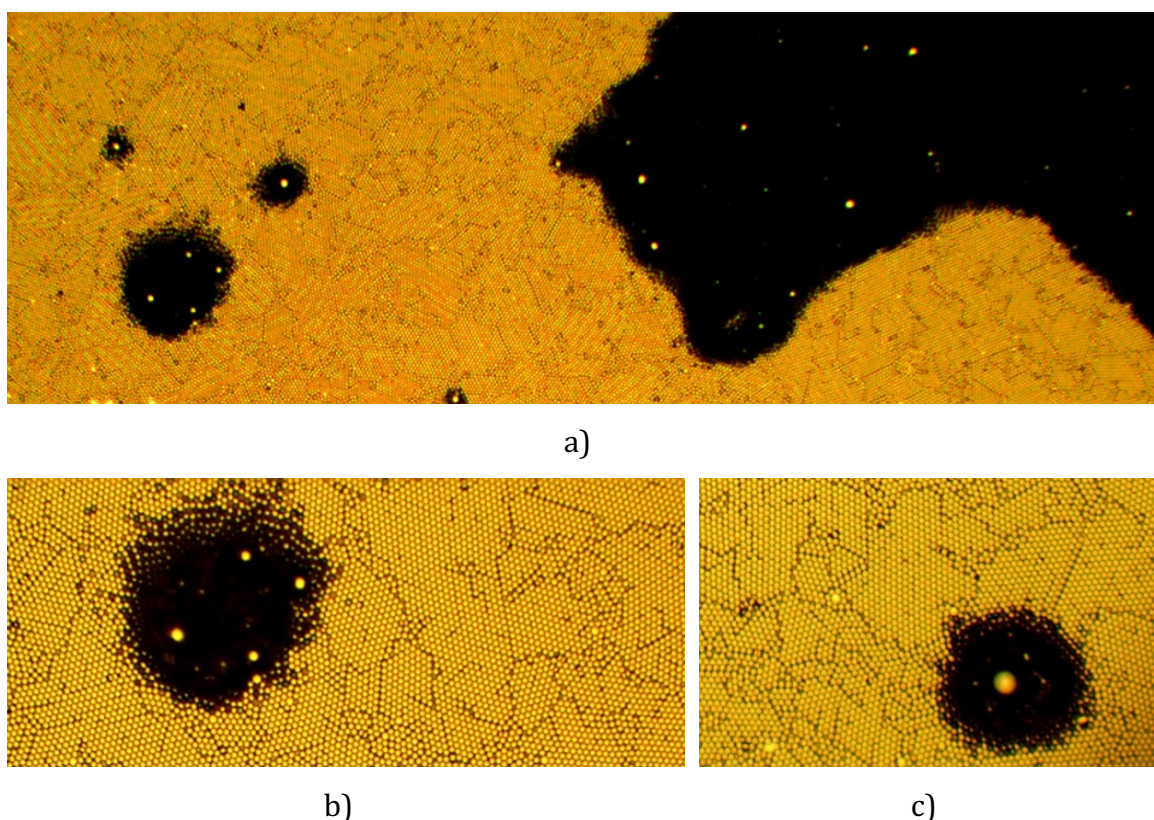


Figure 99 : White light images of a 2.88 μm diameter PS spheres monolayer (bright regions) at the gold surface with multilayers (dark regions) forming around spheres of a bigger diameter captured with a 10x objective (a) and 20x objective (b and c).

The 2.88 μm diameter PS sphere solution originally used, given by the manufacturer Bangs Laboratories, Inc with a polydispersity of 10 %, was replaced by a 3.0 μm diameter one from Polysciences, Inc presenting a polydispersity of only 2 %.

With these final modifications, in combination with the above method, the success rate of the method was dramatically improved, bringing it over 85% of well-formed substrates for every batch of fabrication as illustrated in Figure 100 and Figure

101, which show an iridescent region on centimeter squared areas characteristic of the uniform hexagonally packed monolayer assembly of the spheres. To maintain this high success rate, care should particularly be taken in the cleanliness of the equipment used, the well positioning of the substrate on the stage and the size of the substrate to be covered. Indeed, if solution overflows the Au-Si sample, other capillary forces would be involved, perturbing the assembly of the PS spheres into a hexagonal close packed monolayer. This high success rate will allow for higher throughput in the fabrication of uniform gold cavity array, reducing variabilities coming from operators.



Figure 100 : White light image captured with a 20x objective of a 3 μm diameter PS spheres monolayer assembled at the gold surface following the most optimized version of the method described previously.



Figure 101 : Picture of three 1.2 cm² gold-silicon samples on which was assembled a 3 μm diameter PS spheres monolayer following the most optimized version of the method described previously. Samples are presenting an iridescent surface characteristic of well-organized hexagonally packed assembly of the spheres.

3.3.1.1.6 Extrapolation to 2 μm, 1 μm, 510 nm diameter PS spheres

The previously described method was then extended to a range of PS spheres of 2 μm, 1 μm and 510 nm diameter from Polysciences, in all cases ensuring a low polydispersity of the spheres in solution. All of the parameters defined above for excellent packing were kept constant except the concentration of the PS sphere solution used. Given the supplier data, the minimum concentrations to be used for 20 μL solution were calculated respectively to be 0.76 %, 0.38 % and 0.18 % (solid wt.). The best results were obtained for concentration of 1 % for 2 μm and 1 μm diameter spheres and 1.4 % for 510 nm diameter spheres solution. Those concentrations are in large excess compared to the theoretical values, particularly for the two smaller radii particles.

This may be due to the slower particle settling velocity for smaller particle sizes which cause smaller diameter spheres immersed in the solution to take longer to reach the gold surface where they assemble. Particles partially immersed at the gold surface are constrained by capillary forces between particles, which are many orders of magnitude greater than the flotation capillary forces of fully immersed particles⁵. They assemble due to interparticle interaction but are depleted quickly by lack of supply of new particles, leading to formation of disperse free areas. Increasing the concentration of the solution compensates by increasing the population of beads at the solid interface. Increasing the angle of the platform for a better gravity-assisted assembly or slowing down the drying process by allowing a sedimentation period prior to initiate the drying and/or increasing the moisture of the atmosphere in the box could be improvement pathways but were not tested.

Small changes to particle concentration in excess does not perturbate the monolayer assembly significantly. Indeed, particles still fully immersed and sedimenting on top the monolayer due to combined gravity and convective water influx are rolling on top of the monolayer assembly as the solution is drying. The drying front pushes progressively those particles towards the back of the well-ordered monolayer, filling the gaps at the substrate surface before being organised into the monolayer by lateral capillarity forces, as described by Ye et al.³⁰ Particles in excess will then find themselves agglomerated at the very back of the substrates once the solution fully dried. Despite not using concentrations close to the theoretical values, the success rate of this method for 2 μm and 1 μm diameter was found to be similar to that obtained for 3 μm diameter spheres solution. The success rate for 510 nm diameter PS spheres was relatively lower as multilayers formed on some samples so further adjustment of the method might be wanted if it is applied to larger-scale production of SERS substrates.

Characterisation of cavity arrays obtained with those sizes of PS spheres are discussed below.

3.3.1.2 Model study for a reproducible growth of gold cavities at and above the equator

A potential challenge in using the pore arrays as electrodes is the variation in electroactive area that can arise from variable packing and this can affect for example, EIS measurements on bilayers. Naturally, the arrangement of the spheres at the gold surface determines the interstitial space between cavities and can be better controlled using the technique described above. Other influencing parameters of the electroactive area are the size and shape of the grown cavities. Indeed, cavities grown below, at, or above the equator will lead to different electroactive areas from one electrode to another.

The electrochemical growth method used by the group is based on the cumulative charge passed during the electrodeposition^{10,11}, following Faraday's law of electrolysis in Equation 12, where n is the number of moles of deposited species, Q the cumulative charge passed through the cell, z the number of electrons involved in the redox equation and F the Faraday's constant.

electrodeposition to another. Figure 103 shows a representative I-t curve obtained during gold electrodeposition around 3 μm diameter PS spheres, for which gold was purposely over grown.

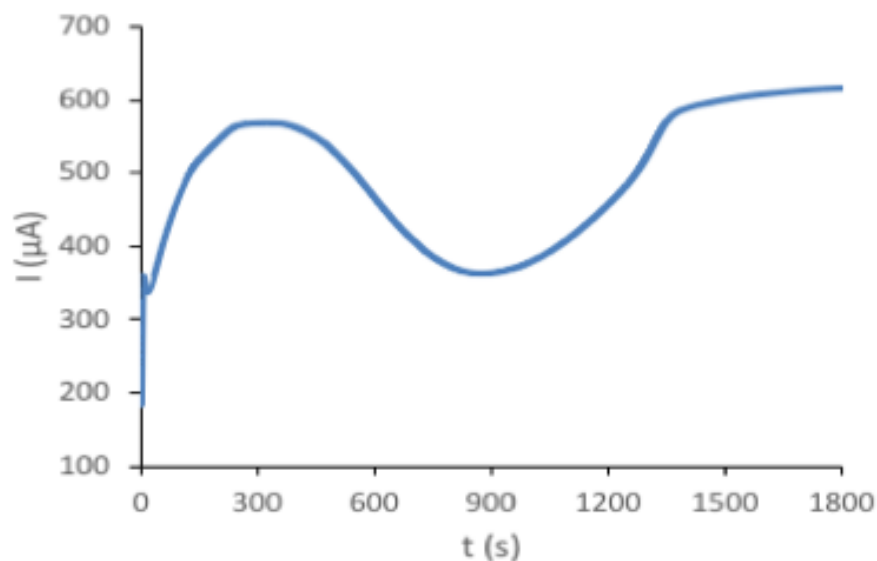


Figure 103 : Representative I-t curve obtained during gold electrodeposition around a 3 μm diameter PS spheres array until beads are fully covered by gold ($E=-0.6\text{ V vs. Ag/AgCl}$).

This I-t curve can be divided into four different regions to explain the gold electrodeposition around the PS spheres.

The first phase, between 0 s and 325 s, can be attributed to combined phenomena comprising gold nucleation, diffusion layer establishment and gold deposition around nuclei until reaching an equilibrium. This first phase of the I-t curve presents a first stage for which the behaviour might vary from one sample to another but is of relatively short duration (less than 20 s here) compared to the second stage which is marked by an increase in current up to 325 s.

During the second phase, between 325 s and 875 s, current decreases and this can be attributed to the gold electrodeposition around the sphere until reaching the equator. Indeed, the interstitial space between spheres is narrowing progressively as the gold layer thickness increases, which is why current decreases with each stratus formed over time. Here, it is important to have low polydispersity of the PS spheres to obtain such a pattern of the I-t curve. Indeed, beads with a large variation in diameter would be expected to perturbate the shape and interpretation of the curve.

Once the equator of the first layer of spheres is reached, the third phase initiates with a progressive increase in current from 875 s to 1800 s corresponding to gold electroplating above the equator of the spheres and beyond.

Finally, the fourth and last phase of the I-t curve plateaus above 1800 s and current stays ideally constant over time as no more spheres are remaining because they are embedded within the film and gold is growing at a now planar interface in a uniform manner.

Although the absolute values of time, current and cumulative charge vary from one sample to another, the I-t curve shape and constituent phases described above remains the same regardless of the size of the spheres and the size of uncovered areas. This allows for identification of the same point in the deposition, reliably every time. Where there are substantial flat areas at the electrode surface, the I-t curve will tend to flatten the pattern described, making more difficult the distinction of the critical points of the electroplating process. However, the excellent reproducibility of the sphere assembly described herein avoids such a situation.

SEM characterisation of several samples with different PS sphere diameters shown in section 3.3.3 confirmed that stopping the electrodeposition at the beginning of phase III accurately replicated deposition as far as the equator of the spheres. This technique highly reproducible and by filling only to the equator of the spheres minimises the interstitial space between cavities in a simple and reproducible manner from one sample to another.

Based on the previously described I-t curve, electroplating of several samples with 3 μm diameter PS sphere assembly was achieved by stopping the electrodeposition at different level of growth above the equator, while taking note of the cumulative charge at the beginning of phase II (Q_b), at the equator (Q_e), and at the end of the hypothetical wanted gold height (Q_w). Despite reducing interstitial flat areas by using the improved assembly method, cumulative charge at the equator varied between 293 mC and 495 mC across the different samples used in the study, which would have surely led to different cavity sizes as previously illustrated, if decided to grow gold to the equator based on the same cumulative charge reached across all samples.

In parallel, characterisation of the built substrates was performed by SEM, measuring the aperture of cavities once the spheres have been fully dissolved and

determining the hypothetical height of the created well equivalent to the gold film thickness³³, based on calculation for perfectly round spheres as shown previously in chapter 2. Figure 104 shows the progressive closing of the cavity aperture along the study.

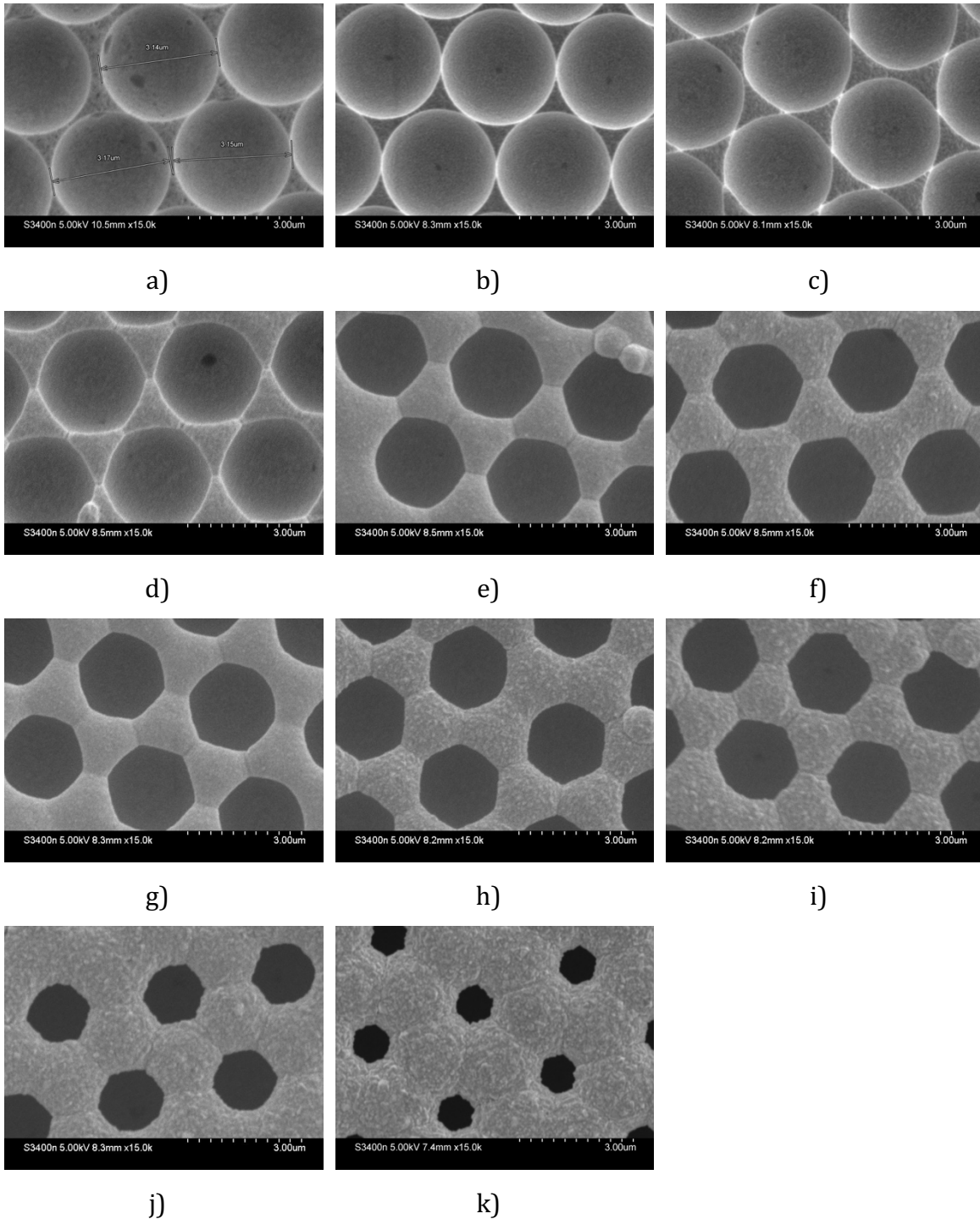


Figure 104 : SEM images of a gold cavity array made with 3 μm diameter PS spheres along different stages of the gold electrodeposition. The relative height of the cavity " h_{rel} " was calculated compared to the theoretical height of the well based on the size of the aperture and considering perfectly round spheres. a) $h_{rel} = 0.500$; b) $h_{rel} = 0.611$; c) $h_{rel} = 0.689$; d) $h_{rel} = 0.754$; e) $h_{rel} = 0.840$; f) $h_{rel} = 0.857$; g) $h_{rel} = 0.864$; h) $h_{rel} = 0.896$; i) $h_{rel} = 0.920$; j) $h_{rel} = 0.935$; k) $h_{rel} = 0.979$.

Assuming a perfect packing of the spheres as a monolayer in a hexagonal close packed assembly, and 100 % coulometric efficiency during the electroplating, the volume of gold formed above the equator in between spheres should be directly proportional to the cumulative charge. To simplify, volume of the gold (V_{gold}) formed in the smallest unit cell of the hexagonal arrangement as illustrated in Figure 105, for one cavity grown above the equator can be expressed as Equation 13, where $V_{unit\ cell}$ is the volume of the smallest unit cell at the cavity's height, V_{sphere} the volume of the template sphere, and $V_{sph.\ cap}$ the volume of the spherical cap missing that would otherwise complete the sphere³⁴, described respectively in Equation 14, Equation 15 and Equation 16.

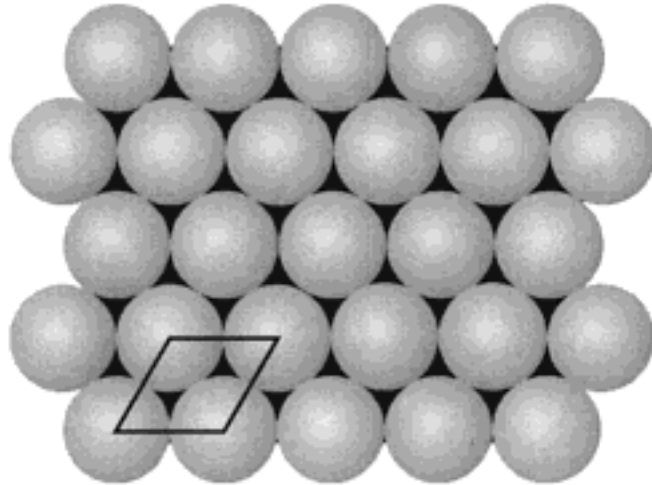


Figure 105 : Schematic of the smallest unit cell (diamond) in the hexagonal close packed arrangement of the polystyrene spheres monolayer at the gold surface. Image reproduced from reference.³⁵

Equation 13 : Equation for the volume of gold for cavities grown above the equator.

$$V_{gold} = (V_{unit\ cell} - V_{sphere}) + V_{sph\ cap}$$

Equation 14 : Equation for the volume of the smallest unit cell comprising one single pore for a hexagonal close packed assembly.

$$V_{unit\ cell} = \frac{d^2\sqrt{3}}{2} \times h_{cavity}$$

Equation 15 : Equation for the volume of a sphere.

$$V_{sphere} = \frac{4}{3} \pi \left(\frac{d}{2}\right)^3$$

Equation 16 : Equation for the volume of the spherical cap missing to complete the sphere.

$$V_{sph.cap} = \frac{\pi h_{sph.cap}^2}{3} \left(3 \frac{d}{2} - h_{sph.cap}\right)$$

Equation 17 : Equation for the height of the spherical cap missing to complete the sphere.

$$h_{sph.cap} = d - h_{cavity}$$

Using data from the SEM characterisation, the relative overgrown volume of gold after passing the equator ($\%OG_{gold}$) calculated according to Equation 18 can be compared to the relative charge needed in the overgrowth phase III ($\%OG_Q$) calculated according to Equation 19 and results are presented in Figure 106.

Equation 18 : Equation for the relative volume of gold grown after passing the cavity's equator.

$$\%OG_{gold} = \frac{V_{gold} - V_{gold\ equator}}{V_{gold\ equator}} \times 100$$

Equation 19 : Equation for the relative charge needed in phase III during the electrodeposition.

$$\%OG_Q = \frac{Q_w - Q_e}{Q_e} \times 100$$

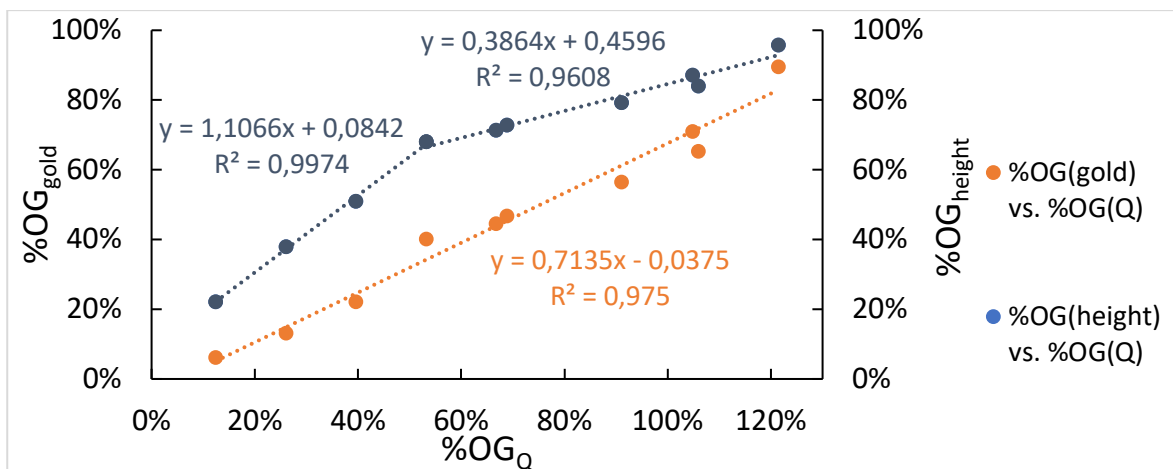


Figure 106 : Representation of the relative volume of gold and relative overgrown cavity's height after passing the equator as a function of the relative charge needed during the overgrowth phase III.

The relative charge varies linearly with the relative volume of gold as expected. However, it seems that charge increases faster than volume of gold does. Indeed, it can easily be seen for the last three data points that relative charge is above 100 %, meaning the sphere should be fully covered with gold, which is not the case according to SEM characterisation.

It is tempting to speculate that defects in particles' assembly leading to the presence of flat areas could be the reason of such results. However, the corresponding charges should be constant along the gold deposition process, not affecting the slope of the curve. The most plausible reason therefore, is that gold grows anisotropically and tends to be electrodeposited faster upwards than laterally. This is firstly confirmed by SEM images in Figure 104 which show cavities' rim and interstitial thinner wall being lower than centre of triangles separating three adjacent cavities. At those particular points, gold is lacking underlying conductive material, slowing down its growth along the electrodeposition process. This is also confirmed by results presented in Figure 106, where relative height overgrowth ($\%OG_{height}$) is compared to the relative charge needed in phase III. Data can be categorised in two linear portions for which slope changes drastically past 50 % of relative height overgrowth. This goes in line with the geometry of the template structure, as for a given height after this critical point the sphere gets further and further from the closest gold particle grown laterally.

The establish model could then help to predict the charge needed for a wanted cavity's height when gold is grown over the equator, knowing the drawback of the characteristic dome shape at the interstitial triangle separating cavities. However, this model will vary with size of the template spheres and would need full characterisation to be applied to other cavity arrays.

3.3.2 Assessment of the new fabrication method by comparison to the standard one.

In order to assess the reproducibility of the more controlled assembly and electrodeposition methods established in the preceding sections, a comparison of electroactive areas variability was performed on samples fabricated with 3 μm diameter PS spheres following the previously established method.

Scanlon et al.³⁶ showed that measuring the charge required to strip a gold oxide layer is the most accurate method to determine the total electrochemically active area of nanoporous gold electrodes. Therefore, cyclic voltammetry was performed to determine the electroactive area (A_{real}) of the array exposed to the sulfuric acid solution. A_{real} was calculated according to Equation 20, using the integrated area under the gold oxide reduction peak (A_p) centred around 0.8 V, and applying a correction factor of $390 \mu\text{C}\cdot\text{cm}^{-2}$ suggested for polycrystalline gold.³⁷

Equation 20 : Equation for the calculation of the electrochemically addressable electrode surface area of different gold cavity arrays.

$$A_{real} = \frac{A_p}{390\mu\text{C}\cdot\text{cm}^{-2}}$$

Three types of electrode were then measured. Each type comprised five independent electrodes. The first type consisted of electrodes used in the group for EIS measurements presenting large flat areas around the cavity array due to the drying of the PS spheres solution. For the second type, a 3 mm diameter mask was centred on top of the array of the electrodes used in the first experiment, in order to hide surrounding flat areas from the electrolyte. Finally, the third type consisted of electrodes built following the optimized assembly and gold deposition methods described here, on which a 3 mm diameter mask was centred on top of the array, allowing comparison with the results obtained for the second type of electrodes. Figure 107 shows the variability in electroactive area obtained for the three types of electrodes.

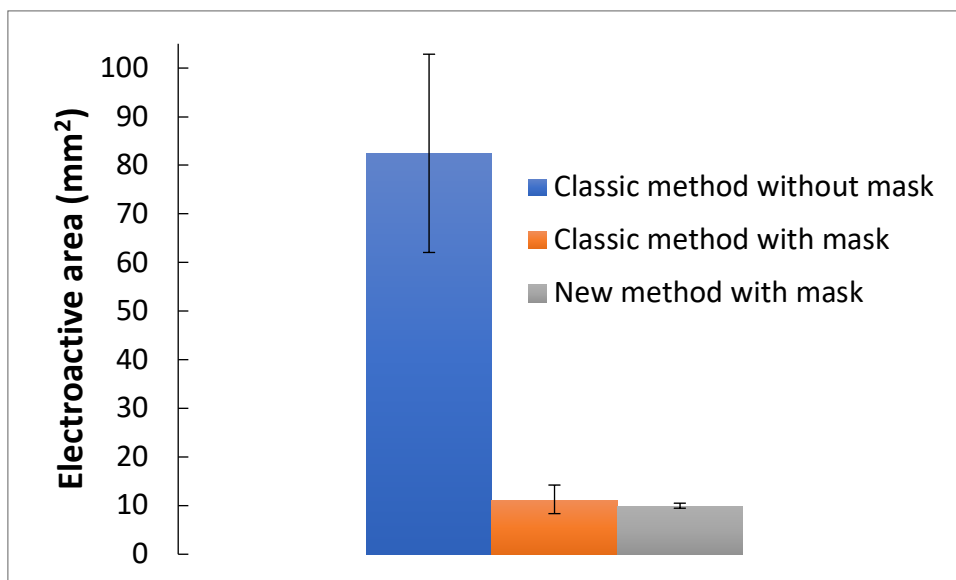


Figure 107: Electroactive area measurement by cyclic voltammetry in H_2SO_4 0.1 M of gold electrodes with $3 \mu m$ diameter cavity arrays fabricated following different methods ($-0.35V < E < 1.5V$ vs. Ag/AgCl). Each set is constituted of 5 independent electrodes.

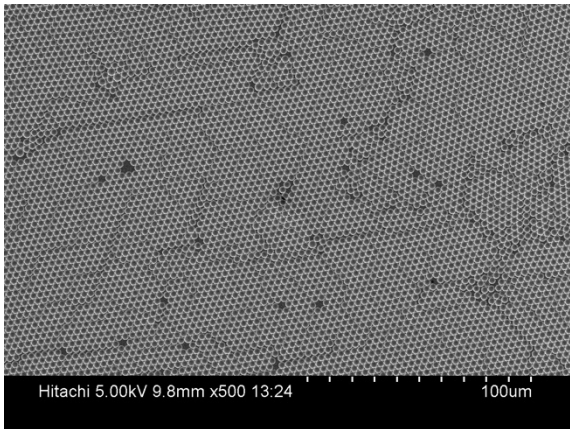
As expected when the geometrical surface in contact with the electrolyte is not controlled by masking, the first type of electrodes presents a large electroactive area of 82 mm^2 compared to the other two types which are very similar within experimental error and found respectively to be 11.3 mm^2 and 9.99 mm^2 . Although, controlling the geometrical surface of the electrode did not impact the variability of the results as the first type of electrodes presents a coefficient of variation (CV) of 25 %, comparable to the one of the second type being of 26 %.

However, using the fabrication method improved here, for the cavity array electrodeposition, combining a densely packed arrangement of cavities and limiting interstitial spaces between wells with an accurate and reproducible electrodeposition technique, reduced the CV of the electroactive area down to 5.2% for the third type of electrodes, which represents a considerable improvement in variability between samples over current methods.

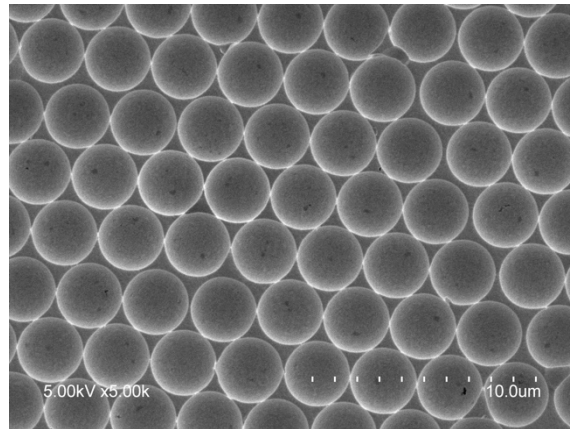
3.3.3 Characterisation of optimised gold micro and nano cavity arrays

Representative SEM images of gold cavity arrays fabricated following the previously described method and grown up to the equator of the sphere monolayer are displayed in Figure 108. For each size of cavity, one image depicts a low magnification view representative of the centimetre size fabricated array proving the uniform hexagonal close packed arrangement of cavities on a large area, and another image

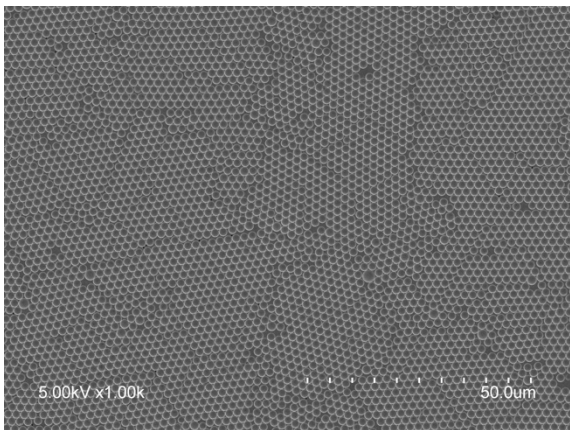
gives a higher magnification view allowing accurate characterisation of cavities' diameter.



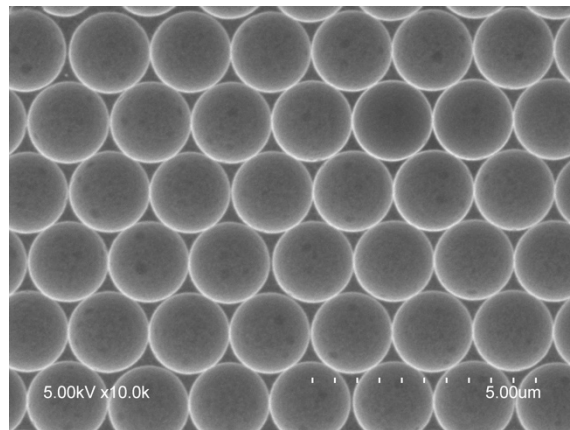
a)



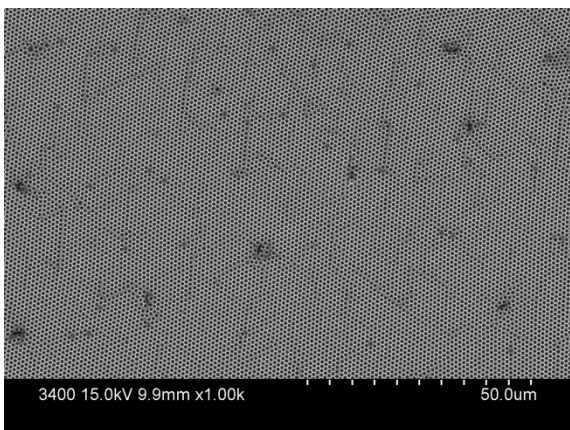
b)



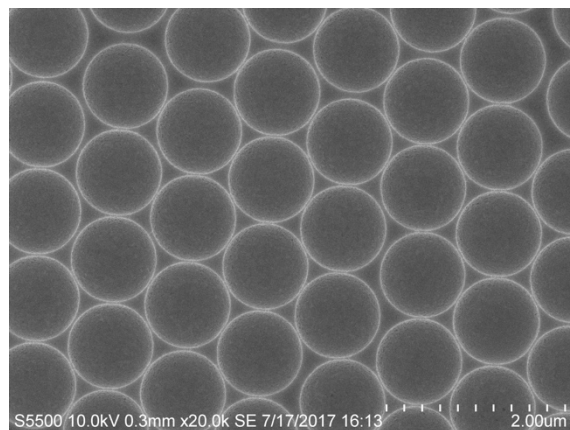
c)



d)



e)



f)

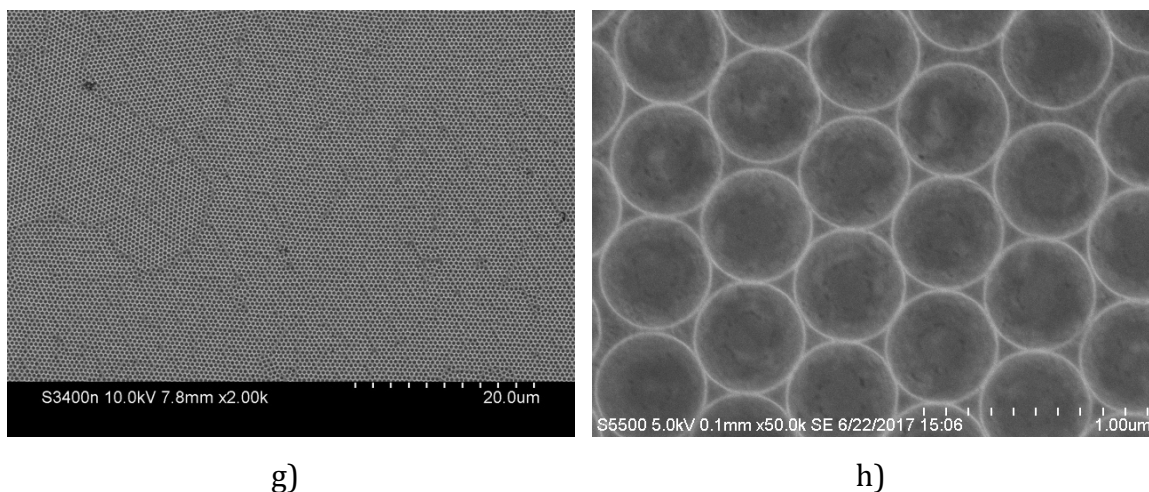


Figure 108 : Representative images of gold micro and nano cavity arrays grown until the equator of the spheres' monolayer for different sizes of PS spheres templates. (a) x500 and (b) x5k SEM images corresponding to 3 μm diameter PS spheres. (c) x1k and (d) x10k SEM images corresponding to 2 μm diameter PS spheres. (e) x1k SEM image and (f) x20k FESEM image corresponding to 1 μm diameter PS spheres. (g) x2k SEM image and (h) x50k FESEM image corresponding to 510 nm diameter PS spheres.

Measurement of cavities diameter was performed using Image J software and were respectively found to be $2.969 \pm 0.019 \mu\text{m}$, $1.837 \pm 0.009 \mu\text{m}$, $0.971 \pm 0.007 \mu\text{m}$ and $0.511 \pm 0.005 \mu\text{m}$ for 3 μm , 2 μm , 1 μm and 510 nm indicative diameter of the templated spheres.

3.3.4 Angle dependence of SERS signal at gold cavity arrays

3.3.4.1 FDTD simulations

Based on SEM characterisation of the different sizes of cavity arrays prepared above, FDTD models were established by Dr. Kiang Wei Kho using Lumerical® software to understand the magnitude and location of the electric field at the array as a function of excitation angle.

Simulations were carried out under 473 nm, 532 nm, 633 nm, 785 nm and 1064 nm excitation light with different incident angles, from 0° (normal incidence) up to 60° with an increment of 10°. The electric fields were examined with two different approaches for each cavity size.

The first approach examines the plasmonic fields for each wavelength without normalizing the field amplitude. This is so that regions of the most intense electric fields can be easily visualized, as illustrated in Figure 109, Figure 111, Figure 113, and Figure 115, which corresponds to the FDTD simulations for 510 nm, 1 μm, 2 μm and 3 μm diameter cavity arrays respectively.

In the second approach, the same set of simulation results was replotted, but with the electric field strength normalized to the highest amplitude attainable for each excitation wavelength. This allows for the identification of an optimal incident angle at which the highest electric field is obtained and to understand the variation of its intensity as a function of the incident angle. Figure 110, Figure 112, Figure 114 and Figure 116, show the FDTD simulations results for 510 nm, 1 μm, 2 μm and 3 μm diameter cavity arrays respectively, normalised with this second approach.

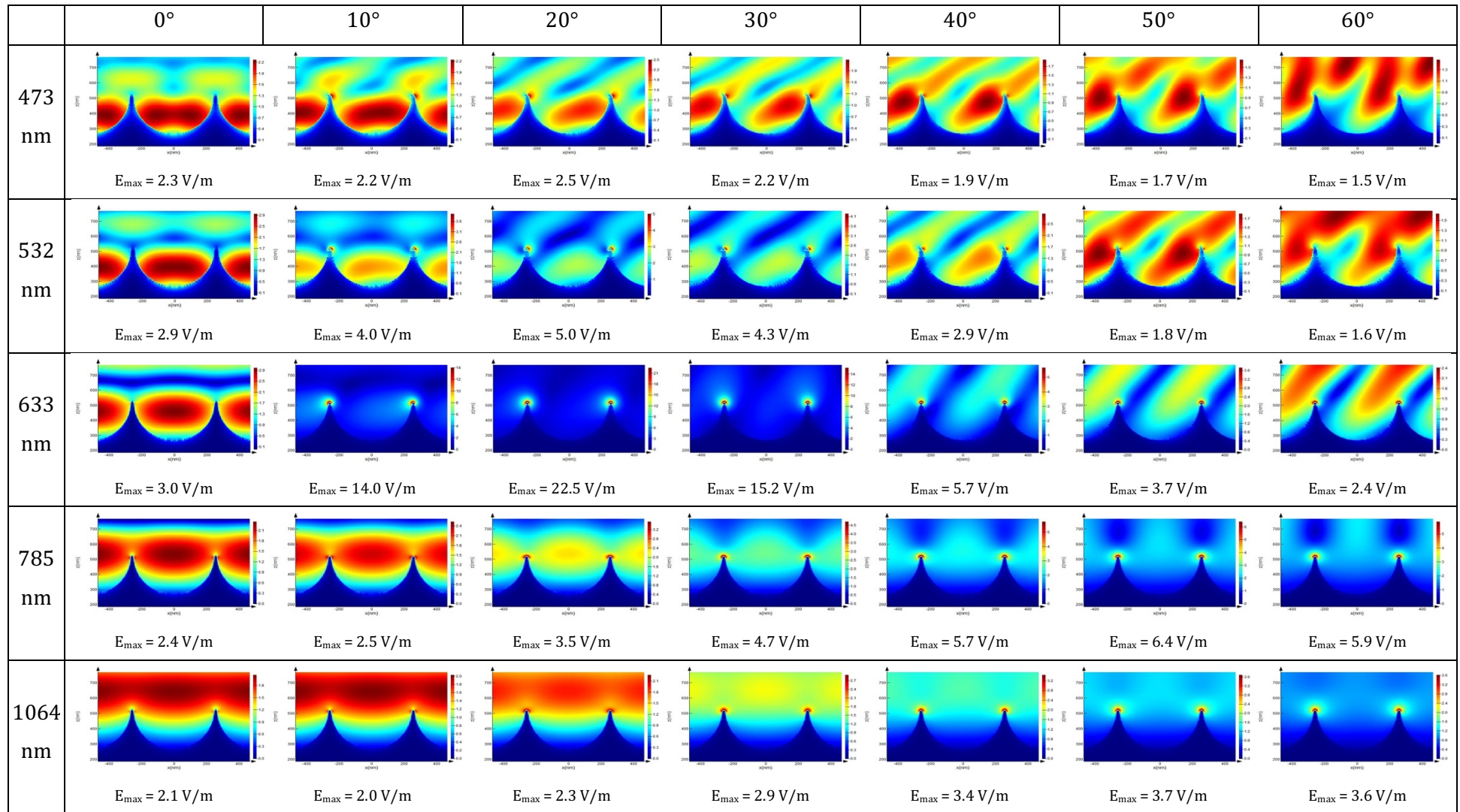


Figure 109: FDTD simulations for a 510 nm diameter gold cavity arrays illuminated under different excitation lights while varying the incident angle of illumination.

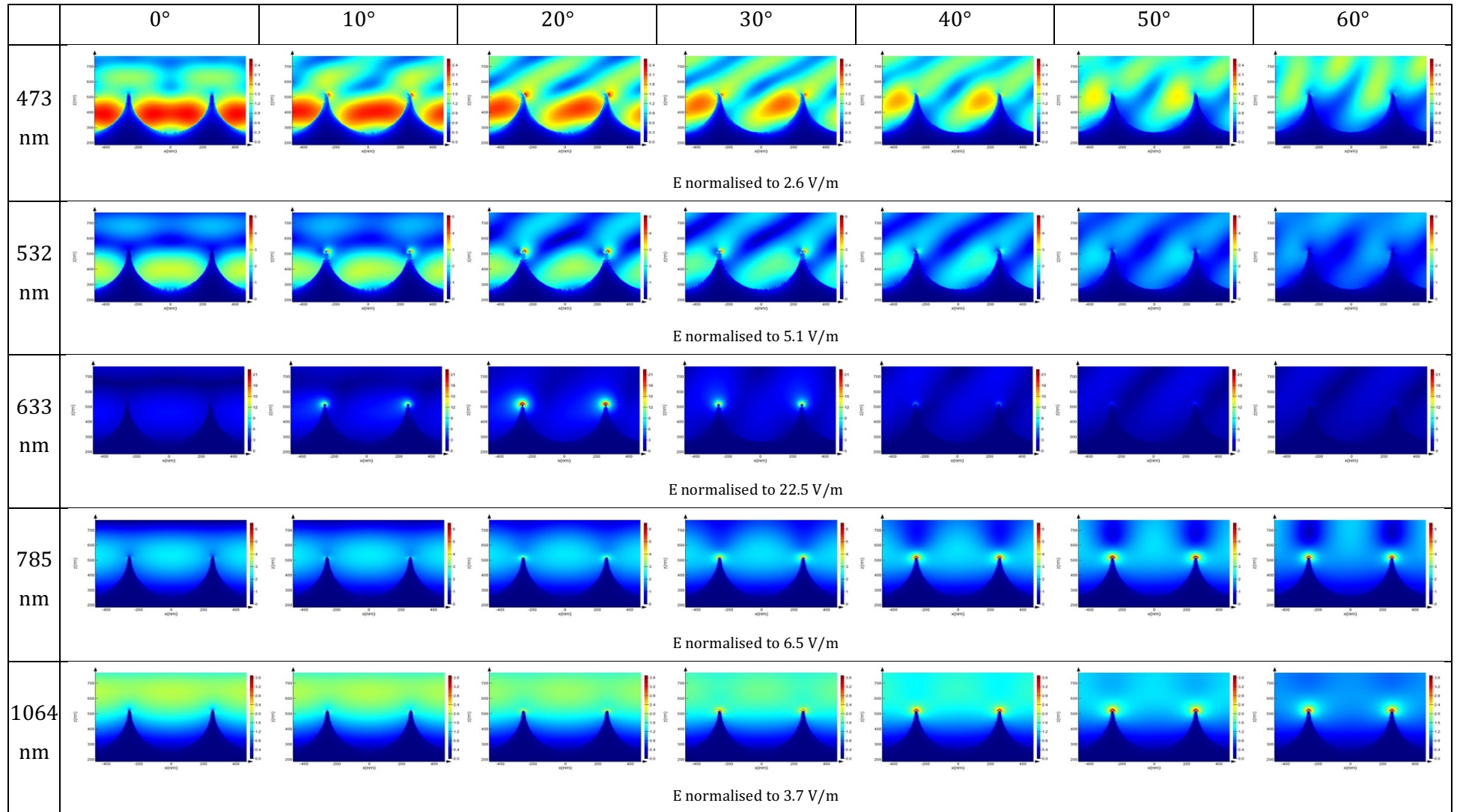


Figure 110: FDTD simulations for a 510 nm diameter gold cavity arrays illuminated under different excitation lights while varying the incident angle of illumination. Results are normalized to the highest value of the electric field for a fixed excitation wavelength.

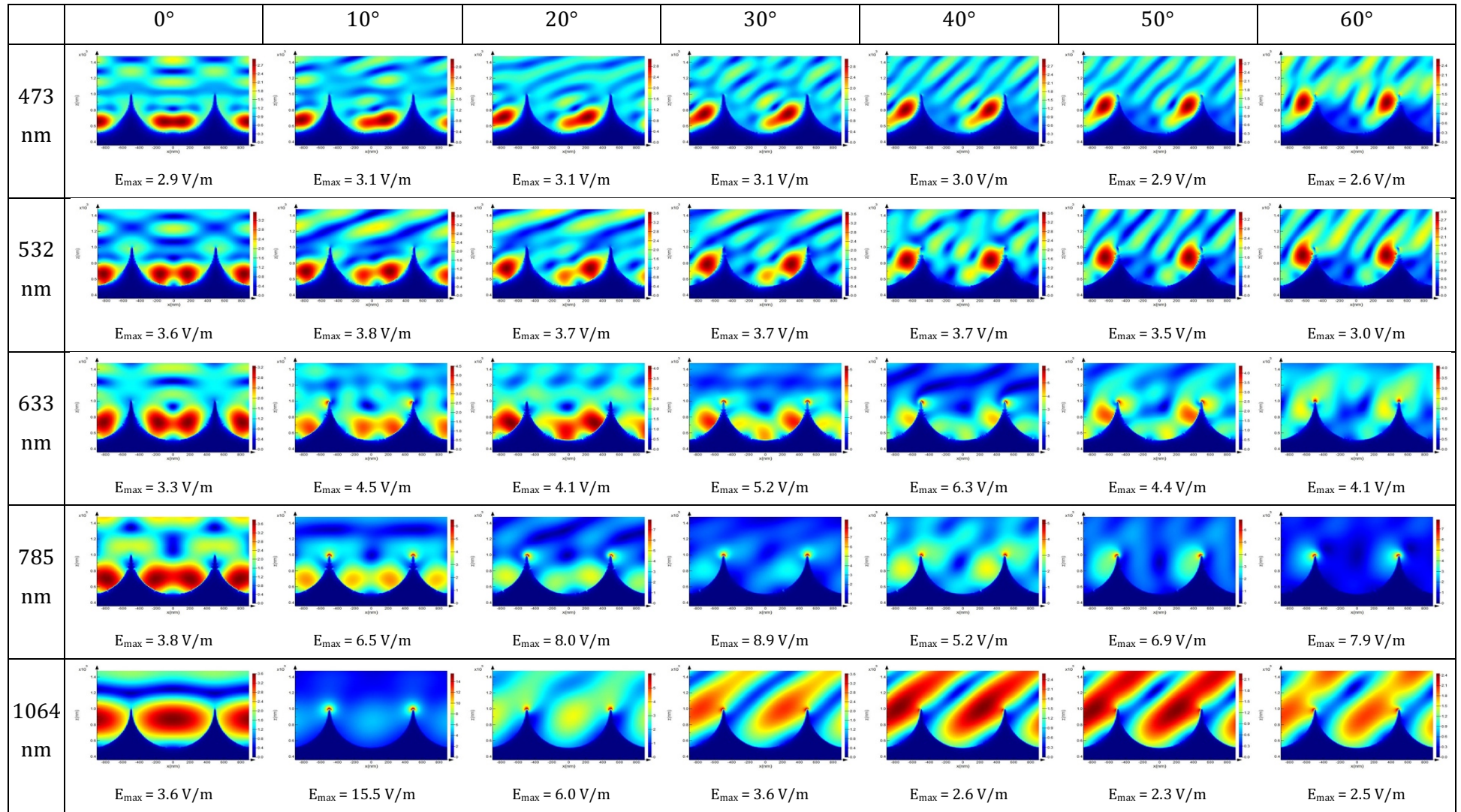


Figure 111 : FDTD simulations for a $1 \mu\text{m}$ diameter gold cavity arrays illuminated under different excitation lights while varying the incident angle of illumination.

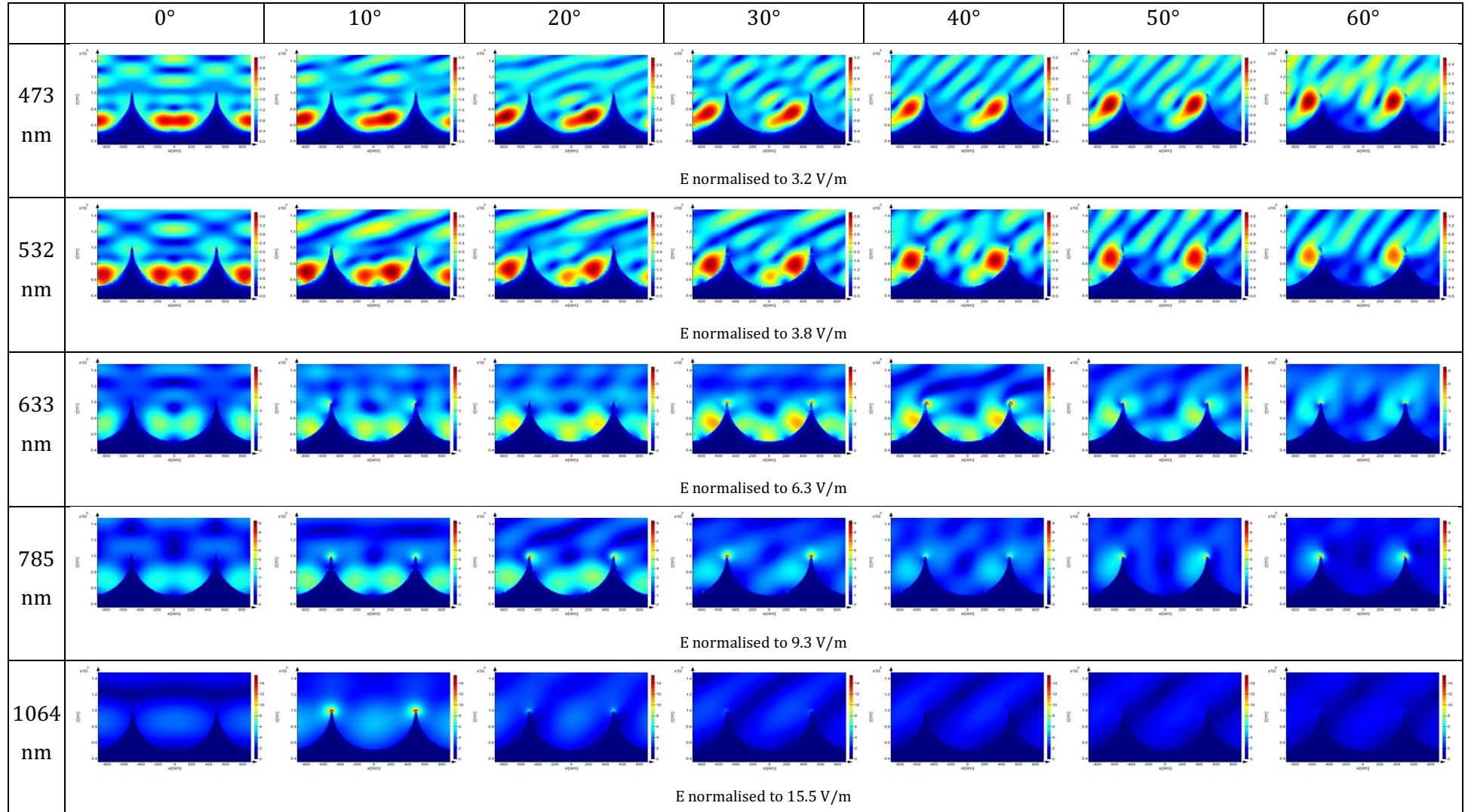


Figure 112 : FDTD simulations for a 1 μm diameter gold cavity arrays illuminated under different excitation lights while varying the incident angle of illumination. Results are normalized to the highest value of the electric field for a fixed excitation wavelength.

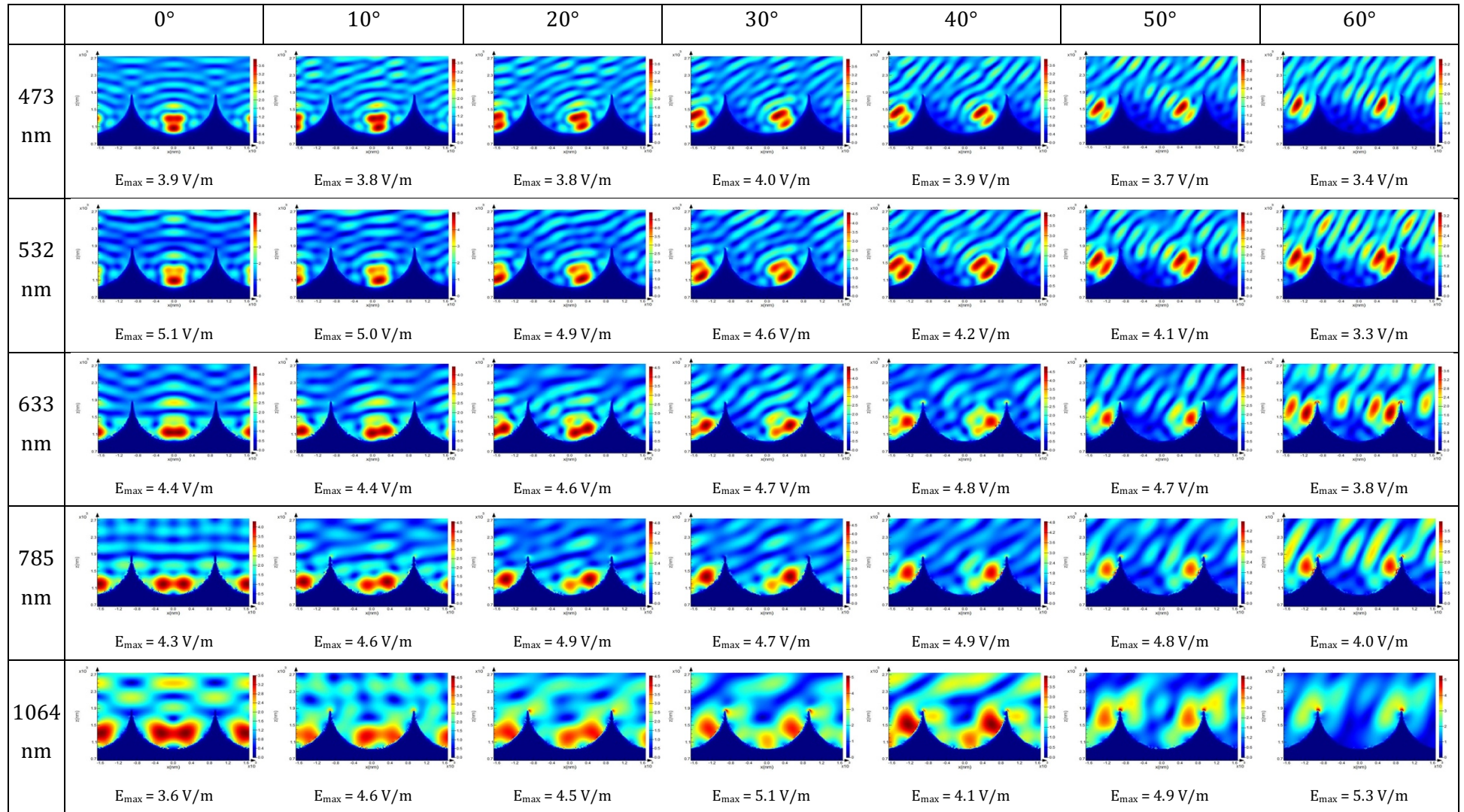


Figure 113 : FDTD simulations for a 2 μm diameter gold cavity arrays illuminated under different excitation lights while varying the incident angle of illumination.

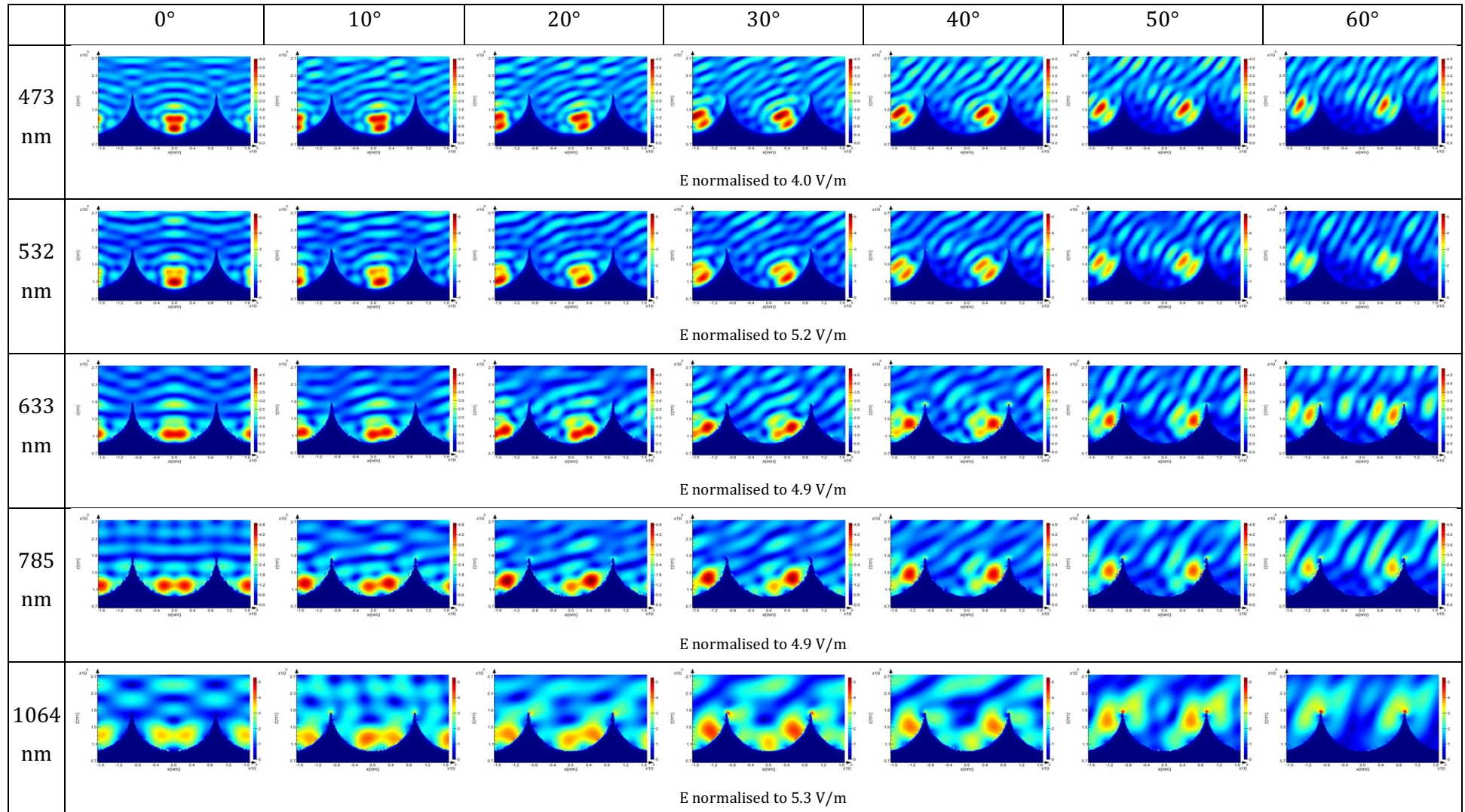


Figure 114 : FDTD simulations for a 2 μm diameter gold cavity arrays illuminated under different excitation lights while varying the incident angle of illumination. Results are normalized to the highest value of the electric field for a fixed excitation wavelength.

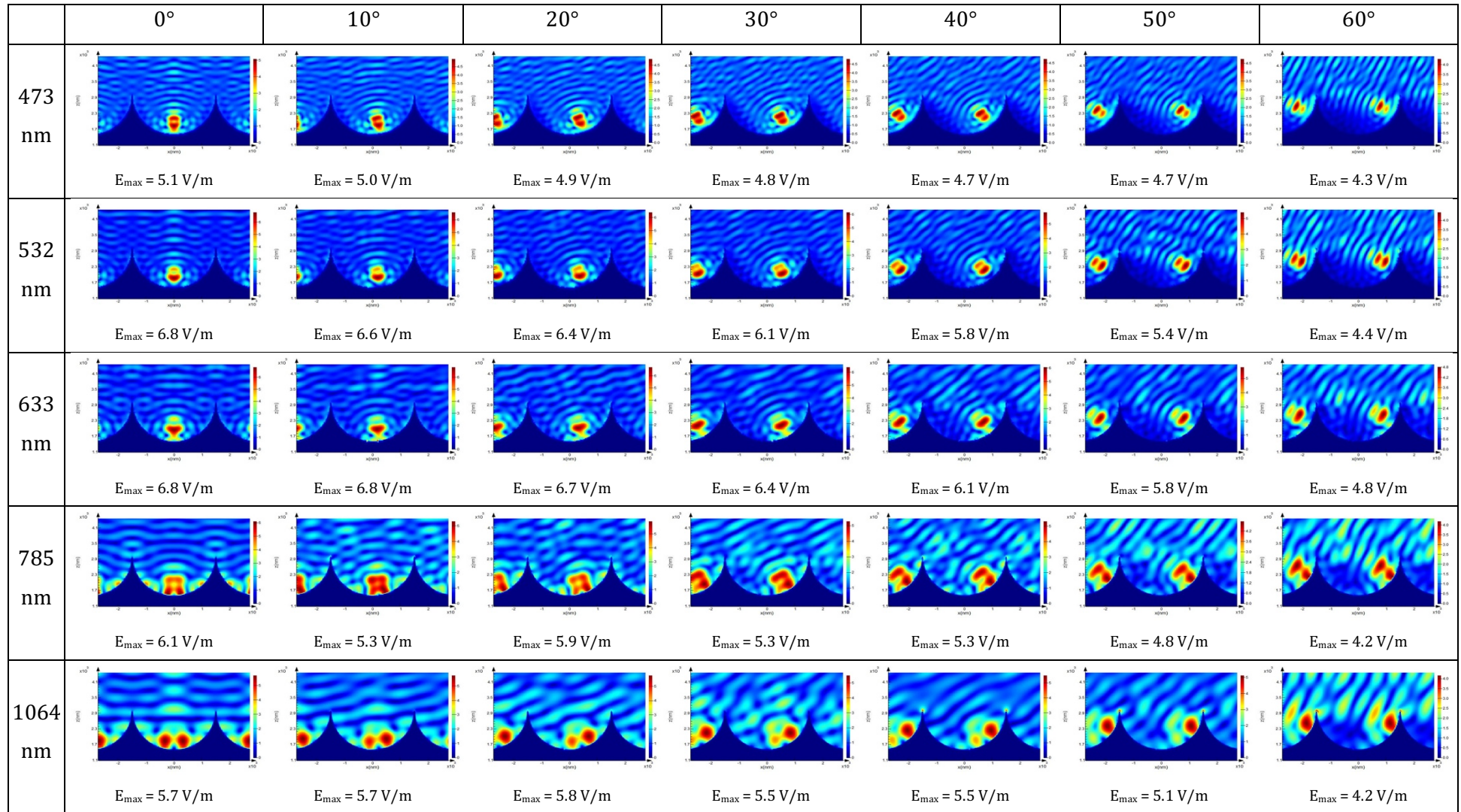


Figure 115 : FDTD simulations for a 3 μm diameter gold cavity arrays illuminated under different excitation lights while varying the incident angle of illumination.

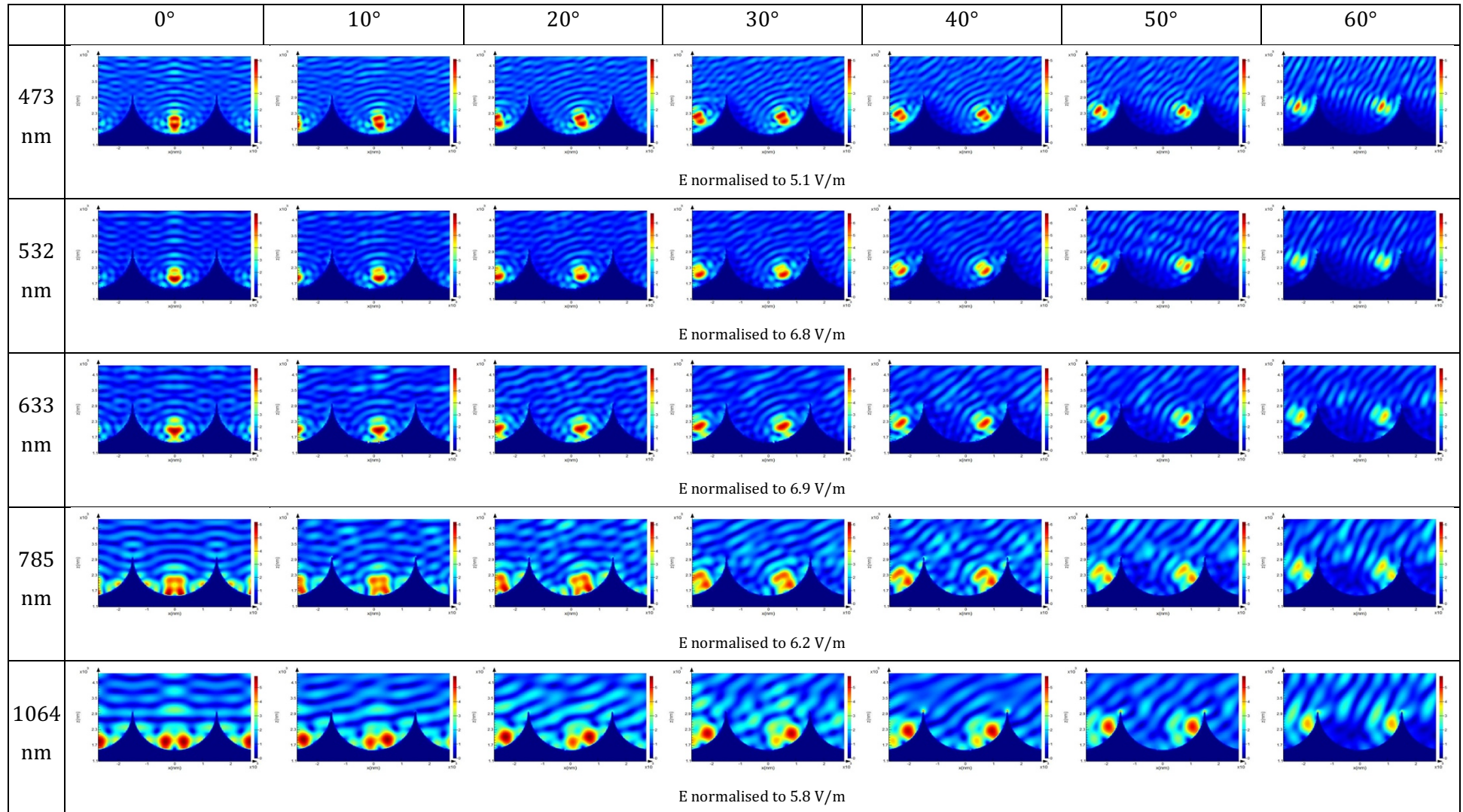


Figure 116 : FDTD simulations for a 3 μm diameter gold cavity arrays illuminated under different excitation lights while varying the incident angle of illumination. Results are normalized to the highest value of the electric field for a fixed excitation wavelength.

For the unnormalized electric field intensities (i.e. Figure 109, Figure 111, Figure 113, and Figure 115), it can be seen that, for each excitation wavelength, the position of the plasmonic hotspots generally shifts progressively from the bottom of the cavity towards its mouth along the side wall of the well, as the angle of the incident light increases.

In the case of smaller cavities (e.g. 510 nm and 1 μm diameter), the plasmonic hot-spots appears to arise at the bottom of the well toward the rim, as the excitation wavelength increases from blue to the red (see Figure 109 and Figure 111). This phenomenon can be interpreted in two ways. As the excitation wavelength increases and exceeds the dimension of the cavities, the plasmonic fields expand and become impossible to contain within the void region, resulting in the hot-spot exiting the cavity at longer wavelengths. Alternatively, one can also explain the observation in terms of Bragg-coupling between the free-space propagating fields and the 2nd order surface propagating plasmon mode (^0D in Cole et al. work).⁸ As described in Cole et al. and Kelf et al. work, the plasmonic lobes can be considered a 'reminiscent' of a 2D Surface Plasmon Polariton (SPP) standing-wave.^{8,38}

These lobes grow weaker when the Bragg condition is no longer satisfied at longer wavelengths; hence, the disappearance of intense hot-spots within the void at low excitation energy. For bigger cavity sizes, on the other hand, such a phenomenon is absent (see Figure 113 and Figure 115). The plasmonic hot-spots in this case remain well encapsulated and confined to the cavity surface regardless of the excitation wavelengths, since the void is large enough to contain the fields. It is important to note that the number and size of plasmonic field lobes varies depending on the simulation conditions (wavelength, cavity size and incident angle) and alongside the intensity of their electric field will influence the magnitude of the SERS signal of molecules present at the hotspots.

From the second analytical approach, the optimal incident excitation angles, for our purposes, where the most intense electric fields occurred at the bottom and at the top of the well for a given wavelength, becomes discernible using this approach.

For instance, the most intense hotspots were simulated for 510 nm and 1 μm diameter cavity arrays, with electric field reaching respectively 22.5 m/V for a 633 nm incident light at an angle of 20° and 15.5 m/V for a 1064 nm incident light at an angle of 10°.

2 μm and 3 μm diameter cavities give similar peak intensities among the different excitation wavelengths tested, varying respectively between 4.0 m/V and 5.3 m/V for 2 μm and between 5.1 V/m and 6.9 V/m for 3 μm depending on the excitation wavelength. Moreover, electric fields for these cavity sizes are predominantly concentrated inside the well and rarely at its mouth regardless of the incident angles. It is observed that whenever hot-spots do occur at the mouth of the cavities, the amplitude of the field within the cavity remains unaffected. As such, the overall SERS signal intensities are always dictated by the size and number of lobes on the cavity array.

Overall, for application in monitoring the arrival of a molecule into the cavity well, e.g. from across a bilayer, it seems that 1 μm and 510 nm diameter cavity arrays are the best candidates for our study as they can give a high intensity electric field localised at the mouth of the cavity for laser lines available on our Raman system. Since FDTD simulations used here give only 2D information of the amplitude and localisation of the electric field at the cavity array, it was decided to get supplementary 2D simulations for 1 μm diameter cavity arrays illuminated with a 785 nm laser and for 510 nm diameter cavity arrays illuminated with a 633 nm laser. This gives us more insight on the 3D geometry of the plasmonic fields within the cavities.

As cavities are arranged in a hexagonal close packed manner, simulations can be summarized with a 30° angle around the z axis. As illustrated in Figure 117, fields in the Ω_1 - Ω_2 - and γ -planes were calculated with the Ω_1 -plane being the slice where the interstitial space between cavity is minimum, Ω_2 -plane where the interstitial space between cavity is maximum, and the γ -plane being the xy-section at the array top surface. For γ -plane, the beam axis was aligned with either Ω_1 - ($\phi = 0^\circ$) or Ω_2 -planes ($\phi = 30^\circ$). Intensity of the electric field was then normalised to the maximum amplitude found among the different simulations for the different angles of incident light. Results obtained are shown respectively in Figure 118 and Figure 119 for 510 nm and 1 μm diameter cavity arrays.

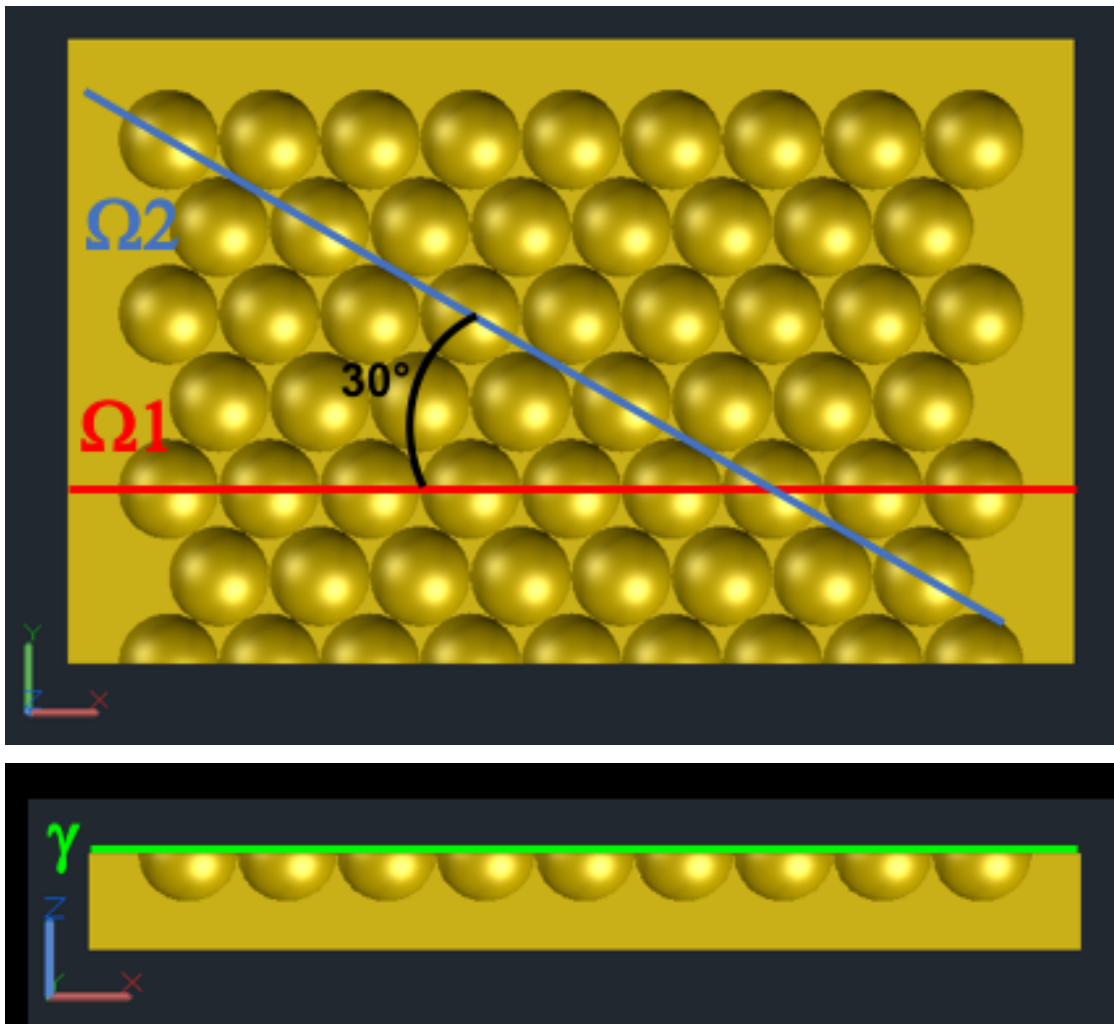


Figure 117 : Schematic of the different planes used for FDTD simulations, with the $\Omega 1$ -plane (red) being the slice where the interstitial space between cavity is minimum, $\Omega 2$ -plane (blue) where the interstitial space between cavity is maximum, and the γ -plane (green) being the xy -section at the array top surface.

Further simulations confirm that high intensity electric field is created near the rim of cavities, particularly at the region of smallest interstitial space between two adjacent wells. However, we do not attribute these fields as arising from a rim dipole mode⁸, but instead attribute it to plasmonic focusing akin to a lightning rod effect due to the high metal surface curvature at these positions.

For 510 nm diameter cavity arrays, intensity of the created hotspot at the rim of the cavities increases progressively with the angle of the incident light to reach a maximum of 22.5 V/m at 20° angle and decreases afterwards. The high intensity reached is of such amplitude that the electric field inside the cavity seems by comparison very weak.

The 1 μm diameter cavity arrays give an electric field of a lower intensity compared to the 510 nm arrays, with a maximum of 12.2 V/m reached for a 30° angle of the incident light. For higher incident angle, intensity fluctuates but remains quite intense at the rim of the wells. However, for those substrates, the amplitude of the electric field intensity difference between top and inside cavity is less pronounced, with the presence of two quite broad and moderately intense lobes situated at the bottom of the well, particularly from 0° to 20° inclination. Those hotspots may contribute to the overall signal during the experiment, reducing specificity regarding the localisation of the studied molecule.

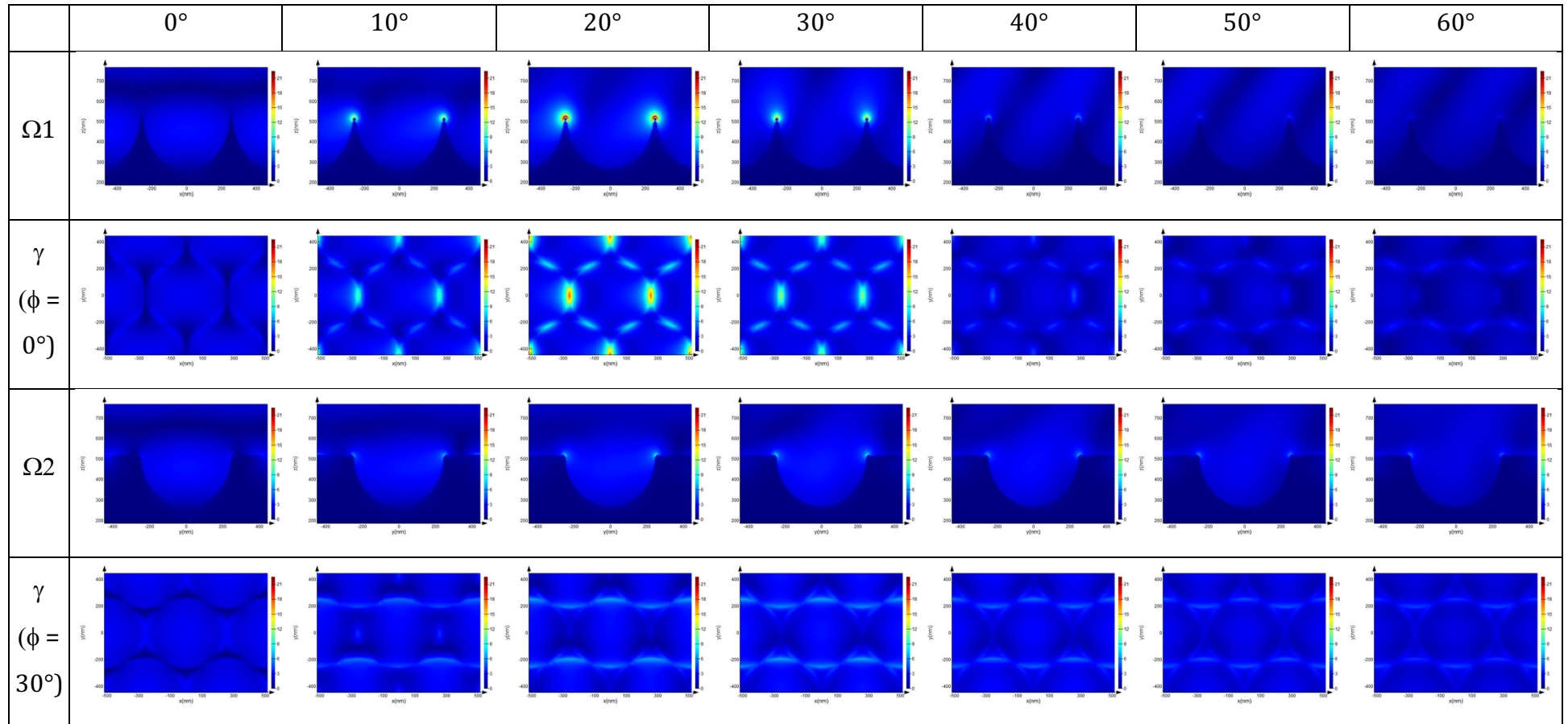


Figure 118 : FDTD simulated field in the $\Omega 1$, $\Omega 2$ and γ -planes for a 510 nm diameter gold cavity arrays illuminated with a 633 nm excitation wavelength. For the γ -plane, fields were calculated for $\phi = 0^\circ$ and 30° . Results were normalized to the highest value of the electric field (22.5) found among the different simulations.

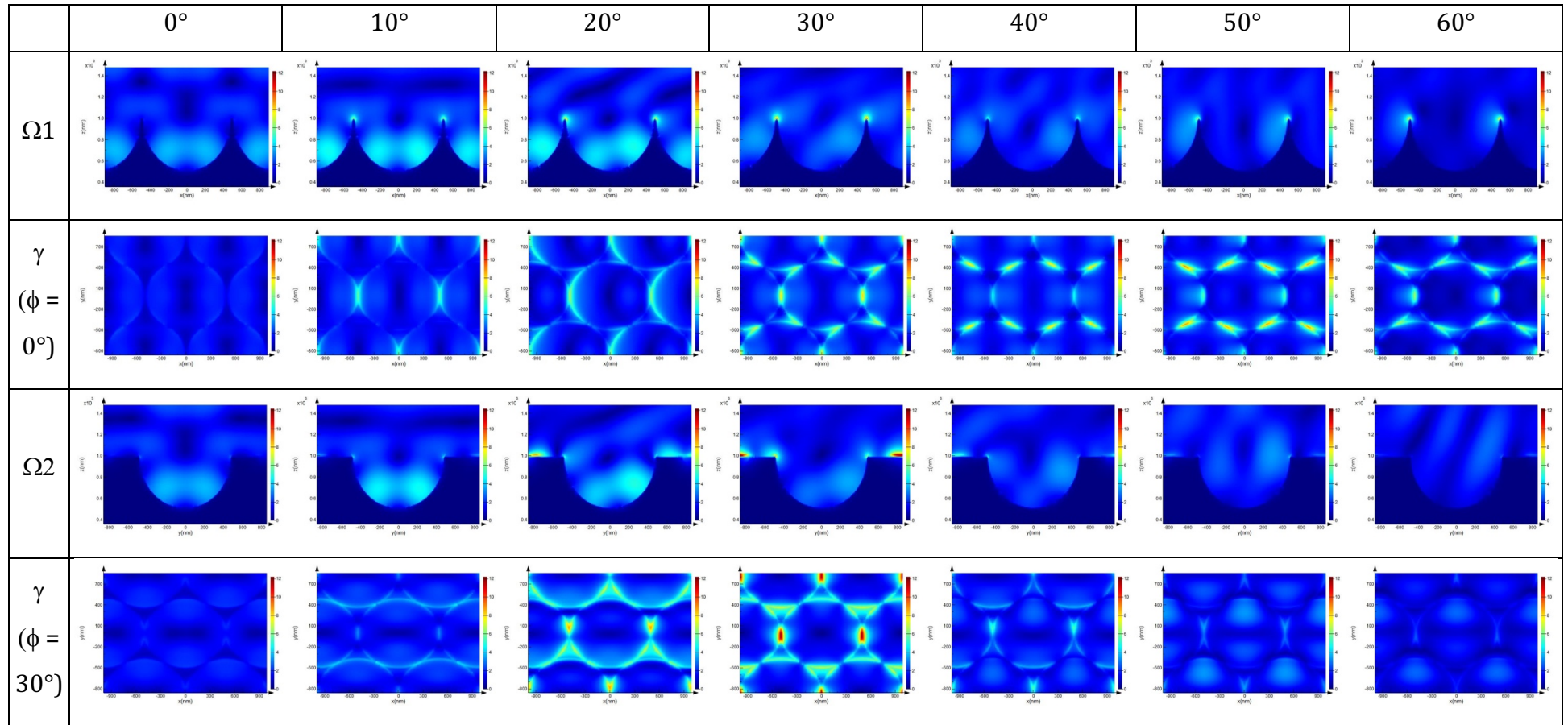


Figure 119 : FDTD simulated field in the $\Omega 1$, $\Omega 2$ and γ -planes for a $1 \mu\text{m}$ diameter gold cavity arrays illuminated with a 785 nm excitation wavelength. For the γ -plane, fields were calculated for $\phi = 0^\circ$ and 30° . Results were normalized to the highest value of the electric field (12.2) found among the different simulations.

3.3.4.2 Polarisation angle of laser on Raman spectrometer

To best match experimentally the conditions of the FDTD simulations, the polarisation of the laser to be used in the experiment was established. Indeed, the substrates need to be inclined with their axis of inclination perpendicular to the electric field, for the measurements to be the most closely aligned to the FDTD simulations described in the previous section. Intensity of the Si line varied when rotating the polarizer. To facilitate interpretation of the results, intensity of the signal measured was background corrected and normalized to 1. Results obtained for the 633 nm and 785 nm lines are respectively shown in Figure 120 and Figure 121.

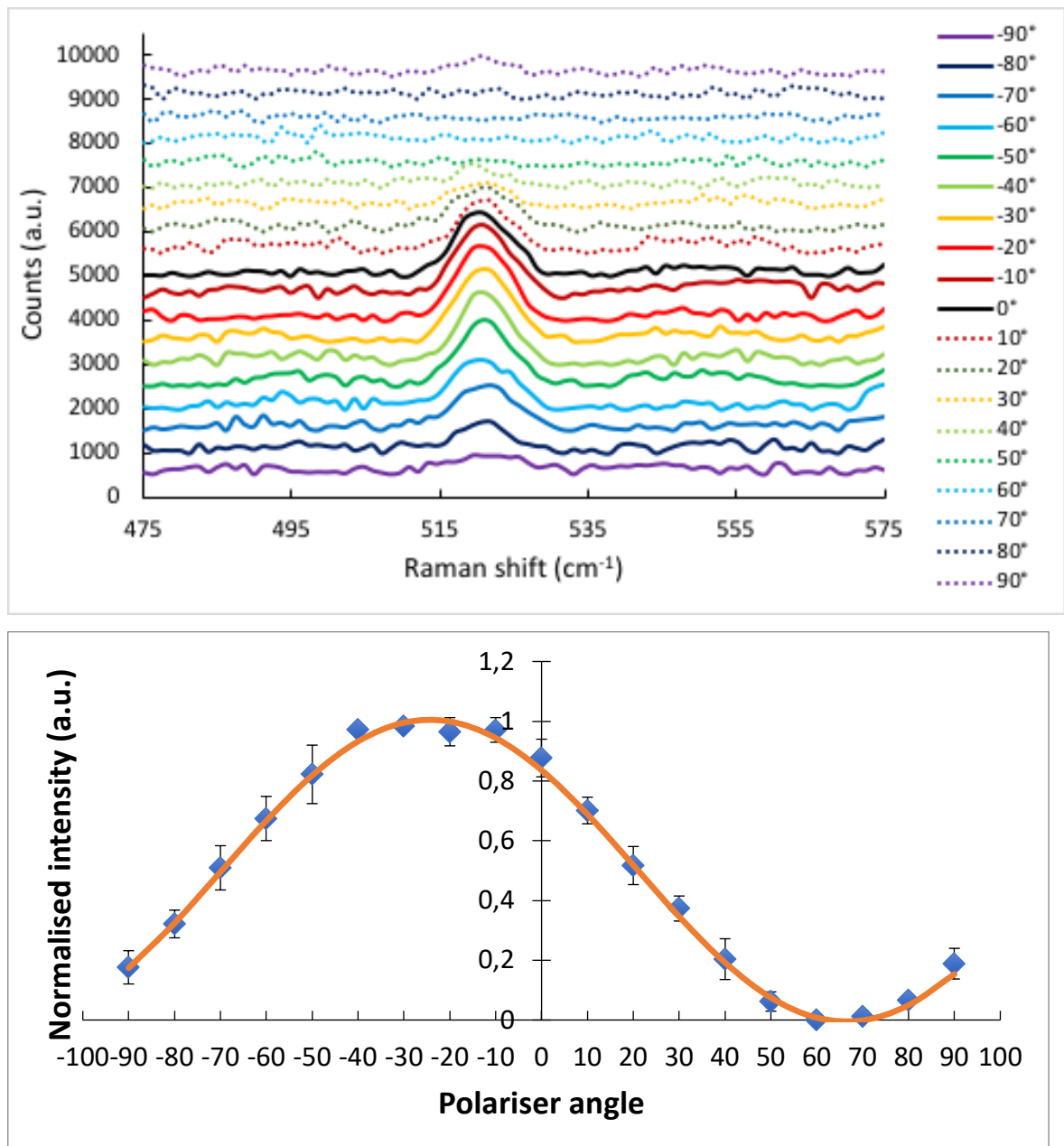


Figure 120 : Polarisation angle measurements of the 633 nm laser available on the Raman spectrometer. (Top) Representative Raman spectra of the Si sample; (Bottom) Intensity of the Si line measured, background corrected and normalized to 1 ($n=3$).

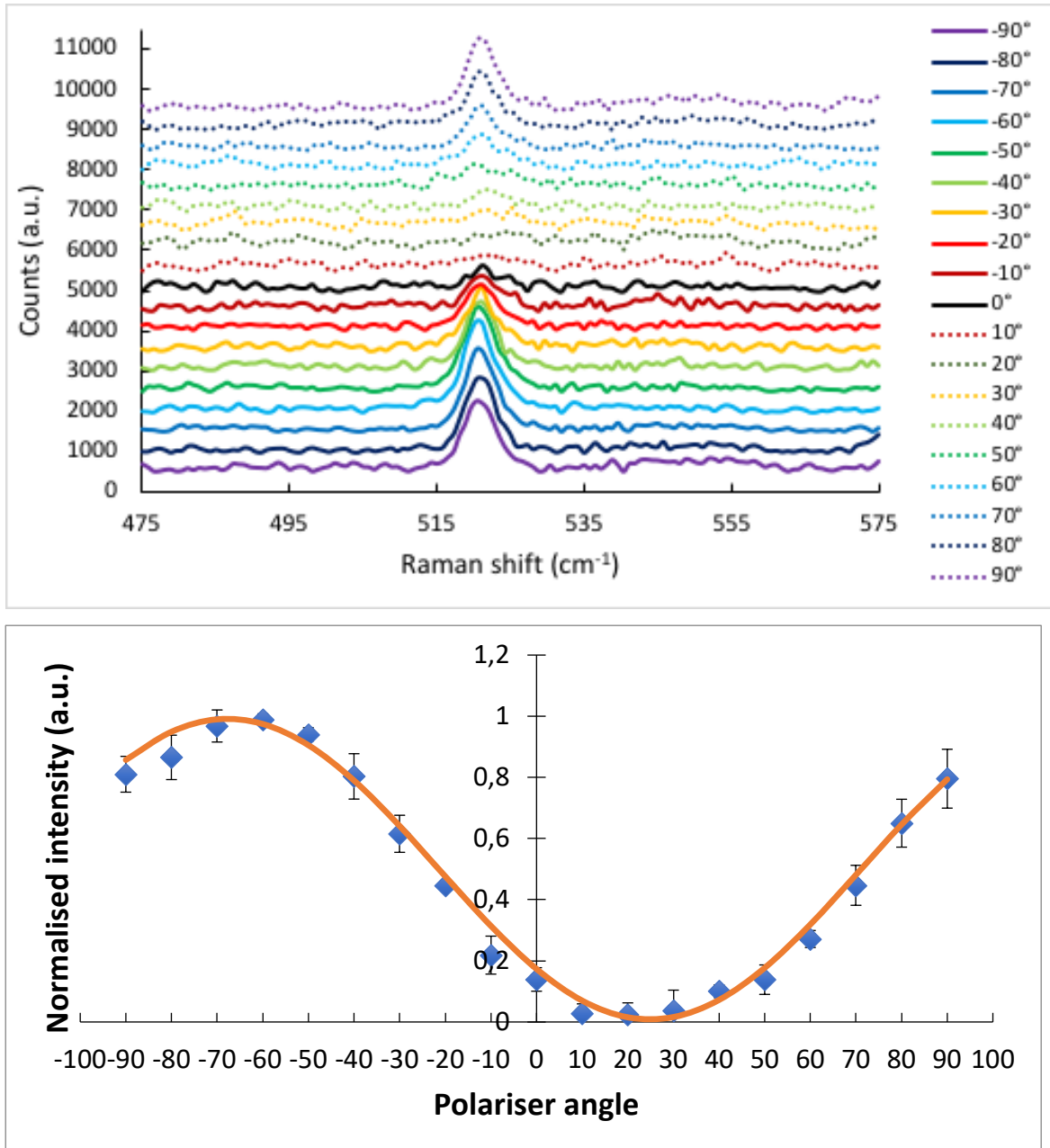


Figure 121 : Polarisation angle measurements of the 785 nm laser available on the Raman spectrometer. (Top) Representative Raman spectra of the Si sample; (Bottom) Intensity of the Si line measured, background corrected and normalized to 1 ($n=3$).

Using Microsoft Excel® solver, data were fitted to a sine wave model following Equation 21, where I is the normalised intensity of the Si peak signal, A the amplitude of the sine wave, ω the frequency, P the polariser angle and ϕ the phase and can be modeled as:

✓ $I = 0.491 \sin(0.0339P_{633 \text{ nm}} + 3.869) + 0.5$ for the 633 nm line,

✓ $I = 0.505 \sin(0.0346P_{785 \text{ nm}} + 2.413) + 0.5$ for the 785 nm line.

The maximum intensity is reached when $\omega t + \phi = \frac{\pi}{2}$, therefore using Equation 22, parameters of each model allow to determine the polarisation angle to be aligned with during angle dependence study and were found to be $P_{633\text{ nm}} = -24^\circ$ and $P_{785\text{ nm}} = -68^\circ$.

Equation 21 : Sine wave equation for light polarization angle measurements fitting.

$$I = A \sin(\omega P + \phi) + 0.5$$

Equation 22 : Equation for the determination of the polarization angle of the laser used for angle dependence study.

$$P = \frac{\frac{\pi}{2} - \phi}{\omega}$$

Following those measurements, marks were put on the grid under the Raman spectrometer objective and the “in-house” manufactured stage built to check the polarisation angle of the laser lines was converted in a stage used for angle dependence study as illustrated in Figure 88 and was positioned accordingly depending which laser line was to be used.

3.3.4.3 Angle dependence study of SERS signal from molecules adsorbed on selectively modified gold cavity arrays

While varying the incident light angle, achieved by tilting the sample, trials to determine enhancement and to identify the location of the hotspot of the electric field at the cavity array were performed using two Raman active compounds for selective functionalisation of the top area and cavity interior in a similar manner as described in section 3.2.3.

A number of surface active pairs of molecules were explored, including deuterated and non-deuterated pyridine, but also 4,4'-Bipyridine (4,4'-BPY) and Diphenyl disulphide (DPDS) which respective structures are shown in Figure 122 and Figure 123, and finally 4-ATP. Particular attention was taken to limit the risk of displacement of the first monolayer formed by the second one due to the difference in bond dissociation energy between Au-S and Au-N, as suggested by Stolbert et al.^{39,40} Best intensities were obtained with the couple DPDS / 4-ATP. However, sufficient

resolution of peak intensities was not achieved and SERS intensity of one compound was partially covering the signal of the second one while changing the angle of the incident light, which did not allow to conduct a robust data analysis. Deconvolution of the two signals could have been attempted but would probably add uncertainty to the measurements, therefore an easier methodology was adopted based on the signal of a unique SERS active compound.

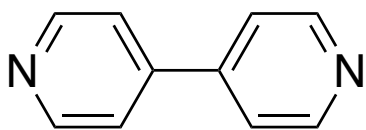


Figure 122 : Structure of 4,4'-Bipyridine (4,4'-bpy).

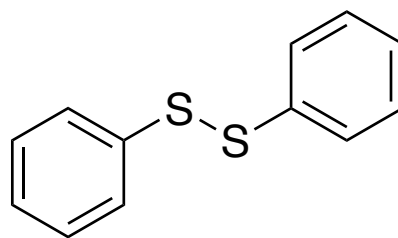


Figure 123 : Structure of Diphenyl disulfide (DPDS).

4-ATP provided the best SERS signal, in terms of intensity and signal to noise, among the surface-active compounds tested when inside and outside cavities. Given the issues encountered with the association of DPDS and 4-ATP, it was finally decided for this study to associate 4-ATP with a chemical of a low Raman cross section. 1-octanethiol was chosen as this compound was not giving any SERS signal in the chosen measurement conditions.

Samples were then selectively modified as described previously in section 3.2.3 and the normalised intensity of the C-S stretching mode at 1080 cm^{-1} ($\nu_{\text{C-S}}$, 7a (a1))⁴¹⁻⁴³ was recorded. Results obtained for 1 μm and 510 nm diameter cavity arrays are shown respectively in Figure 124 and Figure 125. The challenge here was to find acquisition parameters that balanced sufficient SERS intensity while keeping the background as low as possible, avoiding saturating the detector as background intensity varied with the inclination of the sample.

From these two figures it can be seen that both substrates show excitation angle sensitive SERS intensities, whereby the SERS signal of molecules present at the metal surface varies with the angle of the incident light. This correlates well with measurements completed by Ferdele et al. on a smaller window going from 0° to 25°

incident angle, during their study on strong coupling in porphyrin J-aggregate excitons and plasmons in nano-void arrays fabricated with 820 nm diameter spheres.⁴⁴

In our study, the range of angles studied was extended to a 60° window of stage inclination, corresponding to an angle of the incident light of 40.6°. For an easier interpretation of the results, stage inclination angles were converted using Equation 23 to the real incident light angle due to the measurement being done in water and not in air. In this equation, 1 is the refractive index of air, 1.33 the refractive index of water, and angles were expressed in radians. Past the angle of 40.6° of the incident light, focus of the laser spot on the array without the microfluidic device touching the side of the objective was not possible.

Equation 23 : Equation for the conversion of stage inclination angle to real incident light angle for measurement done in water.

$$1.33 \times \sin(\text{Incident light angle}) = 1 \times \sin(\text{Stage inclination angle})$$

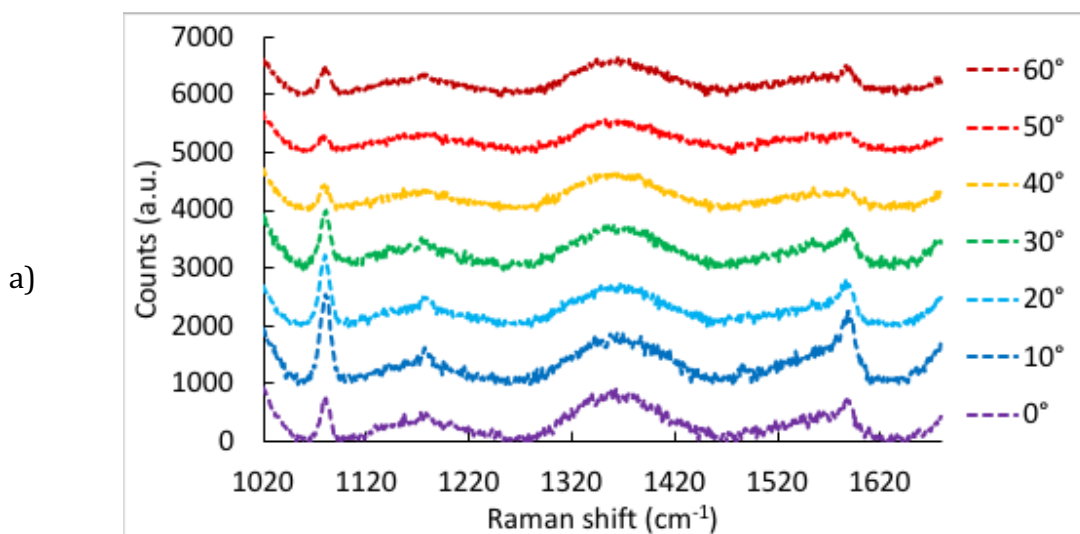
From Figure 124 we can see that 4-ATP signal from molecules assembled at the cavity walls increases progressively to reach a maximum close to 15°. Signal decreases then to up to 35° where signal starts to rise slightly again. This correlates perfectly with FDTD simulations shown in Figure 112 and Figure 119 where the area inside of the cavity is seen brightening up following exactly the same pattern. Regarding molecules situated at the top edge of the cavities, the SERS signal obtained shows a sharp rise to reach a maximum around 10°, that then progressively decreases up to 35° and increase again afterwards. FDTD simulations show that a maximum should be reached around 30° rather than 10°. Also, for this angle of the incident light, intensity of the field for molecules at the top should be at least two times stronger than molecules inside cavities. However, SERS signal obtained for molecules at the top of the cavities is in general lower or of the same amplitude compared to signal for molecules inside cavities.

The origin of differences between theory and experiment may arise firstly because of approximations and limitation in the FDTD simulation. This may occur particularly where hotspots generated by sharp nanoscale features, such as the rim of cavities. However, particular attention was taken while creating the model to round the top edge of the interstitial wall between two adjacent cavities based on FESEM characterisation. However, nanoroughness present at the cavity walls, as can be seen

in figures presented in section 3.3.3 for the characterisation of the arrays, could generate some hotspots that are not considered in the FDTD simulation.

Alternatively, the selective modification may not be completely selective, perhaps some molecules might have diffused around the PS beads or continue to diffuse after SAM formation and partially coat the inside of the cavities.⁴⁵ According to simulation, the field is anticipated to be stronger at the top surface. However, compared to the top surface, the number of molecules inside the cavity might compensate for the lower field intensity, giving most of the SERS signal collected. Indeed, assuming each 4-ATP molecule has a footprint of about 0.2 nm^2 on the gold surface^{46,47}, 7.85×10^6 molecules should cover the side wall of a single $1 \mu\text{m}$ diameter gold cavity grown up to the equator. Compared to the corresponding interstitial space in the smallest unit cell of the hexagonal arrangement, this represents an excess of nearly twenty times as the number of molecules at this location should be around 4×10^5 .

The amplitude of the field between the two types of molecules is not large enough to distinguish the two locations due to the quality of the selective modification.



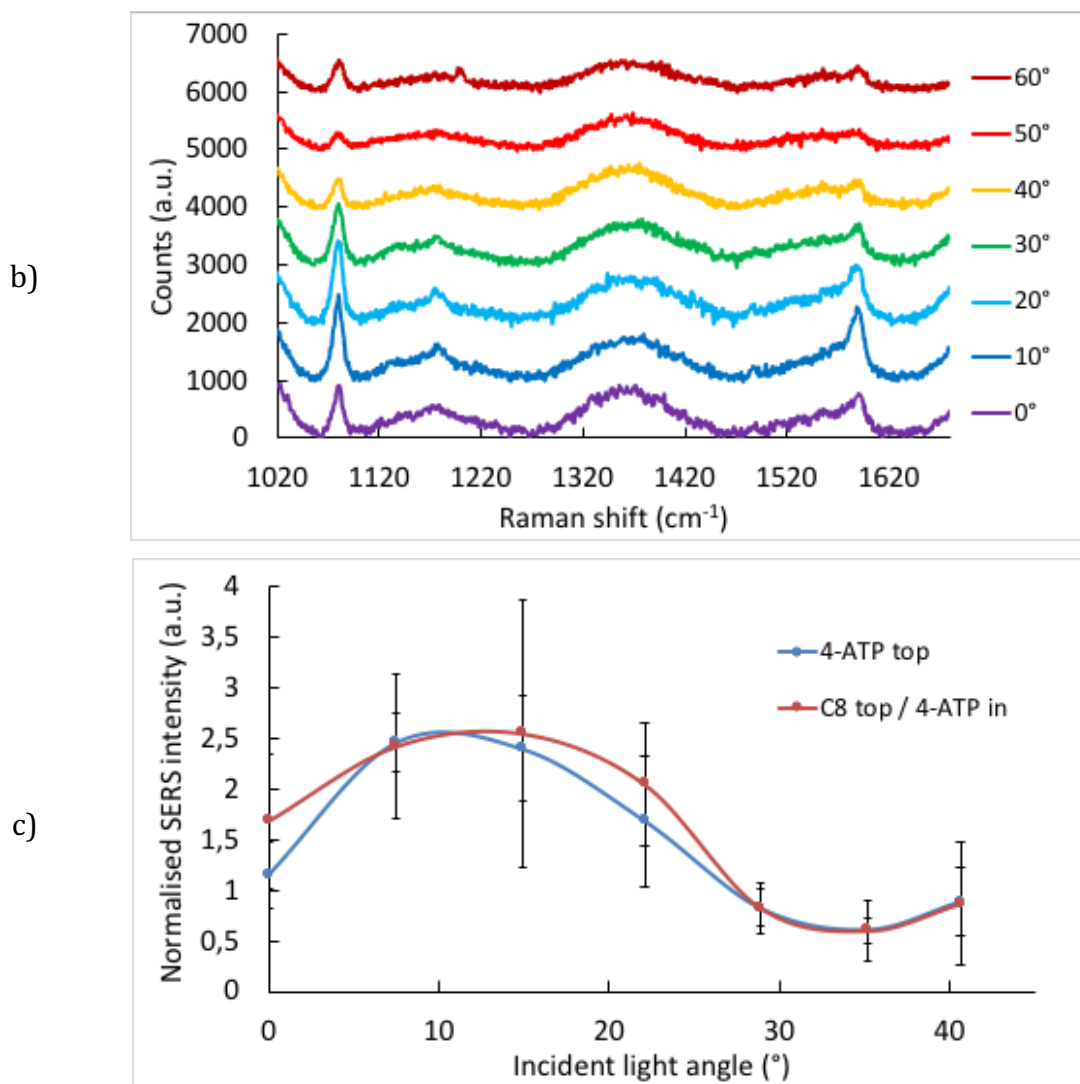
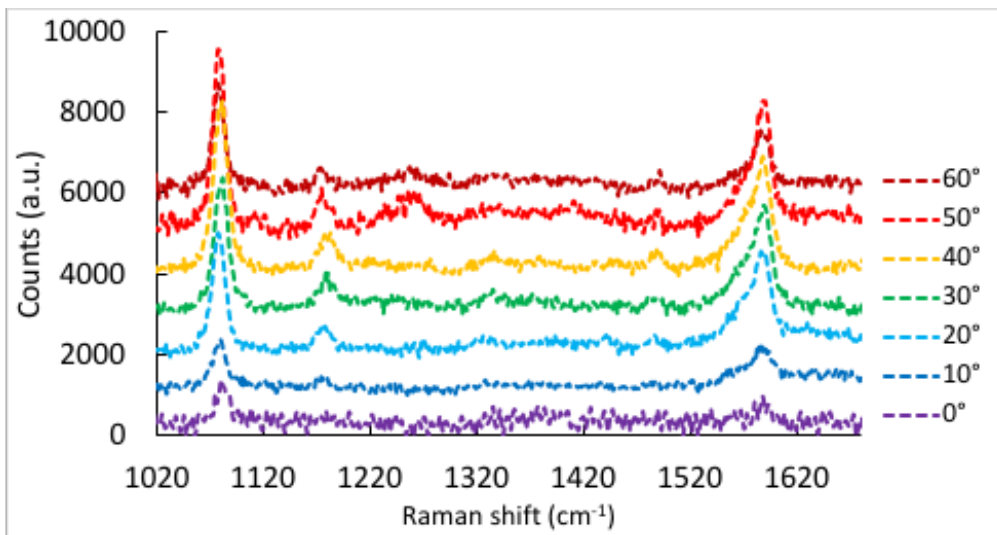


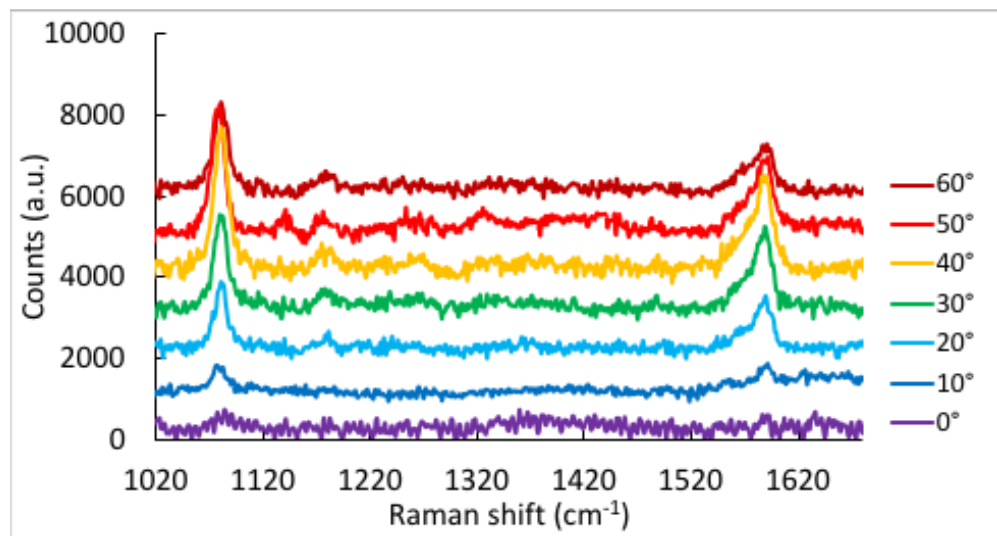
Figure 124 : SERS angle dependence measurements of selectively modified 1 μm diameter gold cavity arrays with 4-ATP and 1-octanethiol. Representative Raman spectra of samples selectively modified with only 4-ATP at its top surface (a) and samples with 1-octanethiol on top and 4-ATP inside cavity (b). Intensity of the SERS signal was normalized to signal obtained for an Si standard on the day of analysis (c).

From Figure 125 we can see that both samples follow the same pattern with the intensity of the SERS signal increasing progressively to reach a maximum when the incident light is at 30°. In this window, intensity of signals acquired for molecules at the top of the cavity is stronger than for molecules inside cavities. After this point, signals decrease progressively and are of similar amplitude. According to FDTD simulations shown in Figure 118, maximum SERS intensity for molecules at the top edges of cavities should be reached when samples are illuminated at 20° inclination angle. This shift between experimental data and theory could be again here due to molecules present inside cavity and contributing to the overall SERS intensity.

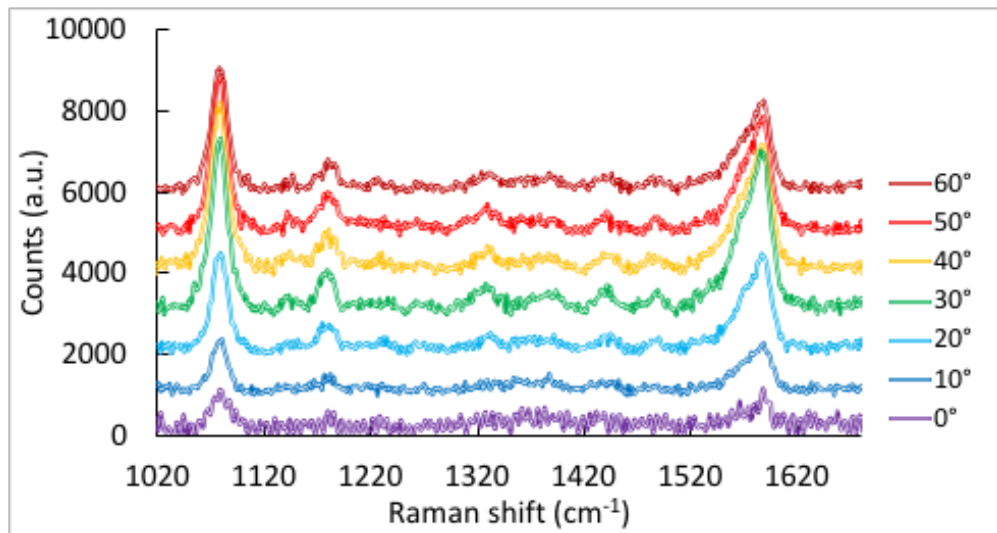
a)



b)



c)



d)

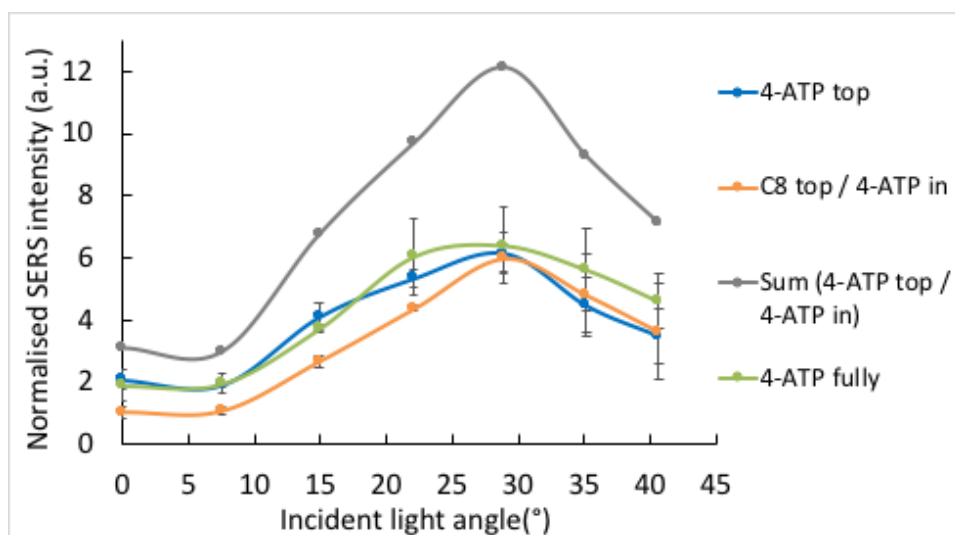


Figure 125 : SERS angle dependence measurements of selectively modified 510 nm diameter gold cavity arrays with 4-ATP and 1-octanethiol. Representative Raman spectra of samples selectively modified with only 4-ATP at its top surface (a), samples with 1-octanethiol on top and 4-ATP inside cavity (b), and samples fully functionalised with 4-ATP (c). Intensity of the SERS signal was normalized to signal obtained for an Si standard on the day of analysis (d).

For 510 nm diameter gold cavity arrays, the amplitude difference of electric field at the top edge and inside cavities is large, making it more difficult to estimate the contribution from molecules on the inside wall of the cavities on the FDTD simulations. To compensate for this lack of specificity during the selective surface modification, it was decided to acquire an additional control to help in understanding the field distribution.

Indeed, as top surface modification with 4-ATP may let some molecules coat the inside of the cavities, samples were dipped again in 10 mM ethanolic solution of 4-ATP after PS removal for an extra 72 hours, to ensure samples were fully covered with the selected compound. Results obtained are shown in Figure 125 and confirm the selective modification is not fully efficient as intensity of SERS signal measured for this fully coated sample is much lower than the sum of intensities recorded for the two oppositely modified samples. Signal coming from molecules at the top edges of cavities can be estimated by subtracting signal given by samples with molecules inside the cavity from signal given by the newly coated sample.

As SERS intensity is known to be proportional to the squared electromagnetic field⁴⁸⁻⁵⁰, results were plotted as a function of the angle of the incident light and compared to the square of the field intensity at the top edge of cavities, estimated from FDTD simulation previously shown.

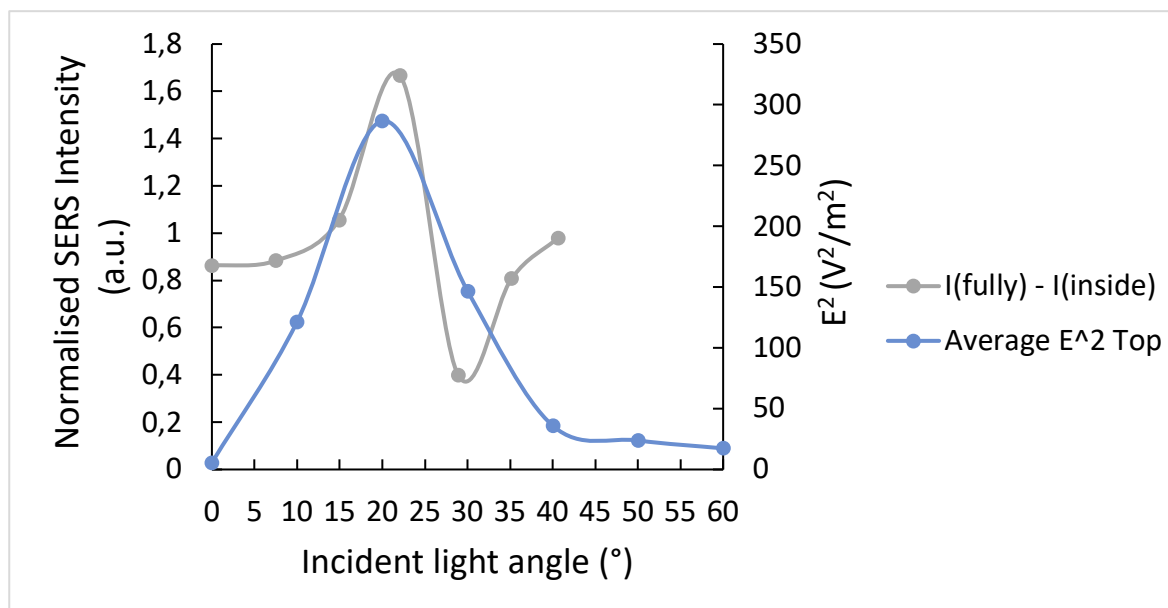


Figure 126 : Comparison of FDTD estimated electromagnetic field and measured SERS intensity of 4-ATP molecules at the top edges of a 510 nm diameter cavity array.

Interestingly, from this figure we can see that the two curves exhibit similar patterns until 30° with their maximum matching perfectly around 21°. This experiment shows excellent correspondence with FDTD simulations suggesting they provide a meaningful estimate of angle dependence of the plasmonic field excitation, confirming that this technique is a very powerful tool to predict field distribution and location, as long as the structures are well characterised, and model does not deviate too much from the manufactured SERS substrates.

3.3.4.4 Angle dependence study of a DOPC lipid bilayer suspended at a gold nano cavity array

Excitation angle dependence of selectively modified gold cavity arrays showed that 510 nm diameter cavity arrays were the best candidates to be integrated in the final microfluidic device for study of lipid membranes interactions. Indeed, those substrates show angle dependence and the precise localisation of the hotspot could be used for an accurate monitoring of a drug arriving at and crossing the lipid membrane.

We therefore carried out Raman spectroscopy as a function of angle on a DOPC lipid bilayer suspended across 510 nm diameter cavity arrays. First attempts were performed using the 5x (0.13 N.A.) objective to ensure in similar conditions to the

previous angle dependence study of selectively modified cavity arrays. However, under these measurement conditions, DOPC lipids, which have weak Raman cross sections, did not show sufficient SERS signal constraining us to use the 50x (0.55 N.A.) with a lower window of stage inclination due to its shorter working distance. The larger numerical aperture of the objective meant greater angle of light collected increasing the SERS signal. However, signal measured in these experimental conditions could not be directly compared to FDTD simulations previously shown, as the field would not behave like a plane wave across the focus spot when using this objective, meaning probably that for one chosen stage inclination angle, the SERS intensity would correspond to an average of FDTD simulations surrounding this incident angle.

In their work on the assignment of the C-H stretching vibrational frequencies in the Raman spectra of lipids⁵¹, Faiman and Larsson demonstrated that the peak at 2850 cm^{-1} arises mainly from the methylene symmetric stretching modes. This peak was chosen for this study as it could be easily distinguished from background. Results displayed in Figure 127 show the average intensity measured for this mode per stage angle inclination.

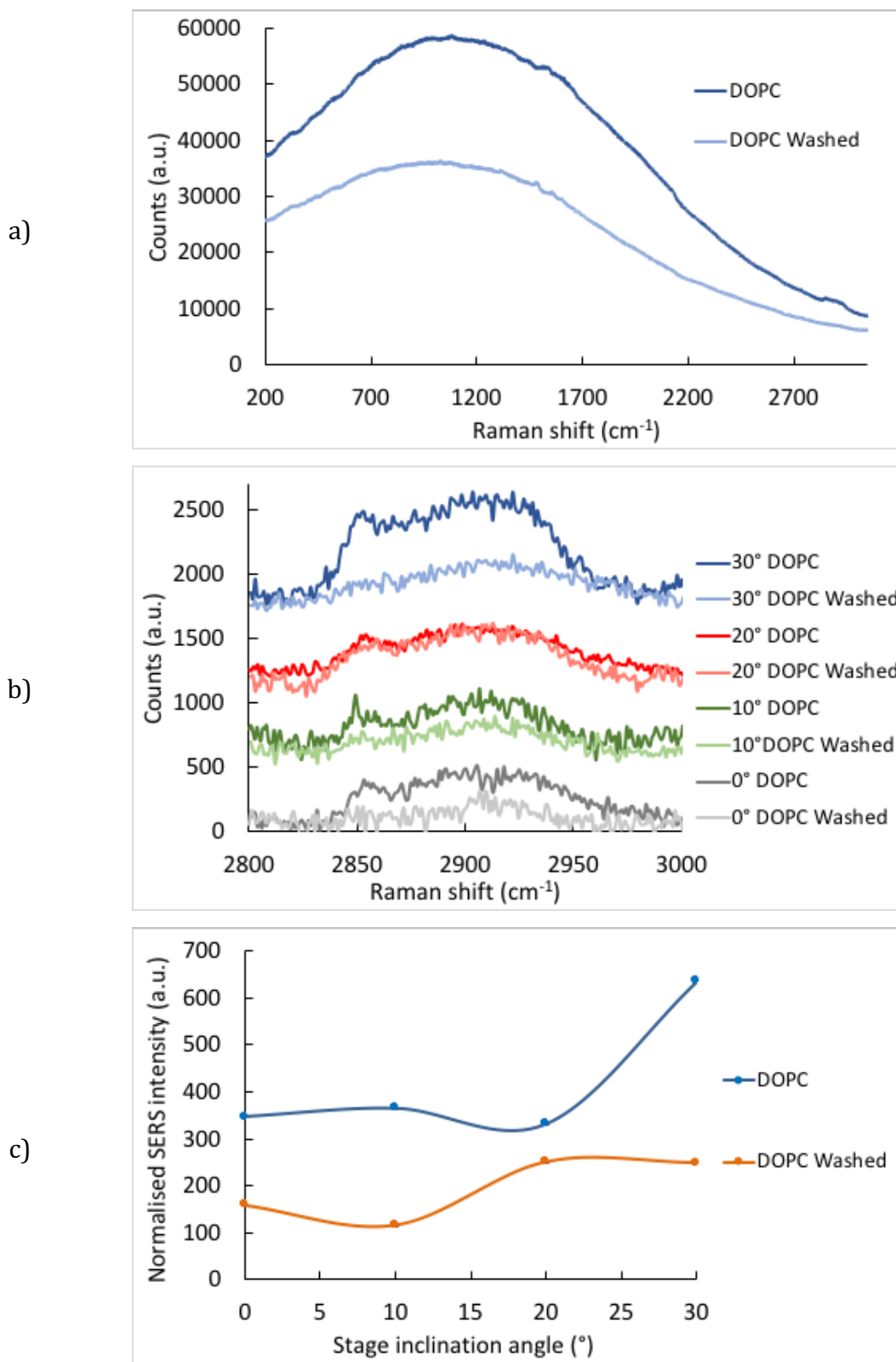


Figure 127 : SERS angle dependence measurements of a DOPC lipid bilayer suspended at a 510 nm diameter gold cavity array. Sample was illuminated with a 633 nm laser with a power of 350 μ W at the sample. (a) Representative Raman spectra of sample with a DOPC lipid bilayer suspended at the cavity array with a stage inclination of 30° before (dark blue) and after washing DOPC (light blue). (b) Representative Raman spectra of the same sample over the different stage inclination angle studied before (dark colour) and after washing DOPC (light colour) (Zoom on the mode of interest 2850 cm^{-1}). (c) Normalised intensity of the 2850 cm^{-1} mode was recorded for the substrate with suspended DOPC bilayer (blue) and after DOPC removal with chloroform (orange).

From there it can be seen that the signal attributed to the lipid is constant from 0° to 20° and increases when the stage is tilted at 30° , which would correspond to an incident light angle of 22° if a 5x objective was used. This increase matches with results shown in previous section where the highest intensity of the SERS signal for a compound at the gold cavity top edge was obtained for an incident light at 21° angle.

Washing the array on which the DOPC bilayer was spanned by dipping it for few seconds in chloroform resulted in a notable decrease of the mode at 2850 cm^{-1} , confirming the initial presence of DOPC lipid at the array. The remaining signal, which is much weaker can be attributed to the covalently bond 6-mercaptohexanol SAM present at the top edges of the cavity and that was not washed away by the chloroform.

Although results cannot be strictly compared to FDTD simulations previously shown, the same trend is observed, which suggests this technique may be suited to monitor the arrival and/or crossing of a drug at the lipid membrane by simply tilting the stage to target the hotspot at the bottom or at the top edge of the cavity.

3.4 Conclusions

A key objective of this chapter was to dramatically improve the fabrication and reproducibility of the previously developed gold cavity array over existing methods. The challenge here was to obtain a large well-ordered layout of micrometre cavities being comparable in sizes with the ones used on PDMS substrates for FLIM/FCS application, allowing then to correlate results obtained for lipid bilayers under similar conditions with different analysis techniques, and at the same time increase the aqueous environment available for the suspended membrane on the electrode ensuring a better representability of natural cell membranes.

Initially focussing on micrometre sized PS spheres template assembly, different techniques were tested to obtain a close packed array of cavities. Best results were obtained for over-micron spheres assembly were by gravity-assisted convective assembly that leads to centimetre sized uniform hexagonally packed monolayer of PS spheres on gold substrates. The success of the assembly lied in respecting few conditions that appeared to be critical. A clean and hydrophilic substrate helped the PS solution to spread at its surface, promoting a uniform assembly of the spheres and limiting defects. Using a colloidal solution calculated in slight excess to fully cover the substrate and with a low polydispersity of 2 % were other parameters that limited defects while preventing formation of multilayers. Finally, controlling the drying process revealed to be essential. This was done by orientating the sample in a 2° angle wedge-shaped cell in a way to ensure the drying film was as thin as possible along the drying process duration. Placing the sample to be dried overnight in the fridge with a tilted front angle of 2° and side angle of 1°, allowed for slowing down the drying process and gave time to spheres to concentrate at the drying front by gravity. Once fully dried, the iridescent centimetre sized deposit at the whole gold surface could attest the formation of a close packed monolayer of dry PS spheres.

An optimised gold electrodeposition method was then developed. By characterising the I-t curve for deposition around the spheres, rather than applying a constant cumulative charge across the different fabricated arrays that might present variations in size and sphere coverage, electrodeposition was stopped when current reached a minimum during gold growth at a potential of -600 mV vs. Ag/AgCl, this rendered possible thanks to the specific shape of the I-t curve obtained with

homogeneous close packed monolayer of dry PS spheres at the gold surface. Study of gold electrodeposition around 3 μm diameter PS spheres demonstrated outstanding and reproducible sphere array packing over extended areas and established a method for predicting of the growth for cavities grown post equator through monitoring of the relative cumulated charge.

Finally, combined improvement on the assembly, electrodeposition and geometrical control of the array allowed comparison of the electroactive areas for electrodes obtained following the previous and the newly developed fabrication method. Results show a considerable improvement in the reproducibility of surface area from electrode to electrode, bringing its variability from 26 % originally down to 5.2 %.

This new fabrication technique presents a high success rate and minimise volume and concentration of PS spheres solution needed to obtain a uniform and well-ordered centimetre size full coverage of gold substrates compared to other techniques. Fabrication and characterisation of four different diameters of gold nano and microcavity arrays shows the versatility and robustness of the fabrication method, which only requires little control when changing the nature of the gold solution, such as the determining the potential needed for gold deposition.

Having generated highly ordered reproducible arrays, we were then able to study the angle dependence of the spectroscopic enhancement for different sizes of gold cavity arrays, knowing that any variation of angle is not due to variations in packing. Characterisation of arrays with cavities of 510 nm, 1 μm , 2 μm and 3 μm lead to FDTD simulation to understand the intensity and the repartition of the electric field at the array when illuminated under a range of wavelength going from 473 nm to 1064 nm at different incident angles going from 0° to 60°.

Angle dependence study showed that the hot spot at the top edge of the cavity could be tuned by a simple inclination of the sample, allowing potentially to enhance SERS signal of molecules situated at the lipid bilayer. Indeed, FDTD simulations show that the position and intensity of the plasmonic hotspots generally shifts progressively from the bottom of the cavity towards its mouth along the side wall of the well, as the angle of the incident light increases.

Arrays with 510 nm diameter cavities show to have the best selectivity in field intensity between the bottom and the top of the cavity when tilted at 20° compared to normal incidence, which was confirmed by experimental data. Formation of a DOPC lipid bilayer suspended at such arrays was achieved and confirmed by SERS measurements matching FDTD simulation.

Despite high electric field intensity observed at the mouth of the cavity through this technique, amplitude of the field at the bottom of the cavity remains of lower amplitude. Therefore, targeting the enhancement at the bottom of the cavity by nanostructuring constitutes the base of the following chapter of this thesis.

3.5 References

1. Wijnhoven, J. E. G. J. *et al.* Electrochemical Assembly of Ordered Macropores in Gold. *Advanced Materials* **12**, 888–890 (2000).
2. Lei, Z. *et al.* Fabrication of well-ordered macroporous active carbon with a microporous framework. *Journal of Materials Chemistry* **11**, 1975–1977 (2001).
3. Lacharaise, P. D. *et al.* Imaging optical near fields at metallic nanoscale voids. *Physical Review B* **78**, (2008).
4. Bartlett, P. N., Birkin, P. R. & Ghanem, M. A. Electrochemical deposition of macroporous platinum, palladium and cobalt films using polystyrene latex sphere templates. *Chemical Communications* 1671–1672 (2000) doi:10.1039/b004398m.
5. Denkov, N. *et al.* Mechanism of formation of two-dimensional crystals from latex particles on substrates. *Langmuir* **8**, 3183–3190 (1992).
6. Tull, E. J., Bartlett, P. N. & Ryan, K. R. Controlled Assembly of Micrometer-Sized Spheres: Theory and Application. *Langmuir* **23**, 7859–7873 (2007).
7. Maher, S., Basit, H., Forster, R. J. & Keyes, T. E. Micron dimensioned cavity array supported lipid bilayers for the electrochemical investigation of ionophore activity. *Bioelectrochemistry* **112**, 16–23 (2016).
8. Cole, R. M. *et al.* Understanding Plasmons in Nanoscale Voids. *Nano Lett.* **7**, 2094–2100 (2007).
9. Johnson, P. B. & Christy, R. W. Optical Constants of the Noble Metals. *Physical Review B* **6**, 4370–4379 (1972).
10. Mallon, C. T., Jose, B., Forster, R. J. & Keyes, T. E. Protein nanopatterning and release from gold nano-cavity arrays. *Chem. Commun.* **46**, 106–108 (2010).
11. Jose, B., Mallon, C. T., Forster, R. J. & Keyes, T. E. Regio-selective decoration of nanocavity metal arrays: contributions from localized and delocalized plasmons to surface enhanced Raman spectroscopy. *Physical Chemistry Chemical Physics* **13**, 14705 (2011).
12. *Biomolecular films: design, function, and applications.* (Marcel Dekker, 2003).
13. Colorado, R. & Lee, T. R. Thiol-based Self-assembled Monolayers: Formation and Organization. in *Encyclopedia of Materials: Science and Technology* 9332–9344 (Elsevier, 2001). doi:10.1016/B0-08-043152-6/01682-X.
14. Schwartz, D. K. MECHANISMS AND KINETICS OF SELF ASSEMBLED MONOLAYER FORMATION. *Annual Review of Physical Chemistry* **52**, 107–137 (2001).
15. Love, J. C., Estroff, L. A., Kriebel, J. K., Nuzzo, R. G. & Whitesides, G. M. Self-Assembled Monolayers of Thiolates on Metals as a Form of Nanotechnology. *Chemical Reviews* **105**, 1103–1170 (2005).
16. Basit, H., Gaul, V., Maher, S., Forster, R. J. & Keyes, T. E. Aqueous-filled polymer microcavity arrays: versatile & stable lipid bilayer platforms offering high lateral mobility to incorporated membrane proteins. *Analyst* **140**, 3012–3018 (2015).
17. Frese, D., Steltenkamp, S., Schmitz, S. & Steinem, C. In situ generation of electrochemical gradients across pore-spanning membranes. *RSC Adv.* **3**, 15752–15761 (2013).
18. Jose, B., Mallon, C. T., Forster, R. J., Blackledge, C. & Keyes, T. E. Lipid bilayer assembly at a gold nanocavity array. *Chemical Communications* **47**, 12530 (2011).
19. Deegan, R. D. *et al.* Capillary flow as the cause of ring stains from dried liquid drops. *Nature* **389**, 827–829 (1997).
20. Prevo, B. G. & Velez, O. D. Controlled, Rapid Deposition of Structured Coatings from Micro- and Nanoparticle Suspensions. *Langmuir* **20**, 2099–2107 (2004).
21. Wang, Y. *et al.* Large-Area Self Assembled Monolayers of Silica Microspheres Formed by Dip Coating. 13.

22. García Núñez, C., Navaraj, W. T., Liu, F., Shakthivel, D. & Dahiya, R. Large-Area Self-Assembly of Silica Microspheres/Nanospheres by Temperature-Assisted Dip-Coating. *ACS Applied Materials & Interfaces* **10**, 3058–3068 (2018).
23. Ruan, W. *et al.* Facile Fabrication of Large Area Polystyrene Colloidal Crystal Monolayer via Surfactant-free Langmuir-Blodgett Technique. *Chemical Research in Chinese Universities* **23**, 712–714 (2007).
24. Bardosova, M., Pemble, M. E., Povey, I. M. & Tredgold, R. H. The Langmuir-Blodgett Approach to Making Colloidal Photonic Crystals from Silica Spheres. *Advanced Materials* **22**, 3104–3124 (2010).
25. Dimitrov, A. S. & Nagayama, K. Continuous Convective Assembling of Fine Particles into Two-Dimensional Arrays on Solid Surfaces. *Langmuir* **12**, 1303–1311 (1996).
26. Kralchevsky, P. A. & Denkov, N. D. Capillary forces and structuring in layers of colloid particles. *Current Opinion in Colloid & Interface Science* **6**, 383–401 (2001).
27. Danov, K. D., Pouligny, B. & Kralchevsky, P. A. Capillary Forces between Colloidal Particles Confined in a Liquid Film: The Finite-Meniscus Problem. *Langmuir* **17**, 6599–6609 (2001).
28. Majumder, M. *et al.* Overcoming the “Coffee-Stain” Effect by Compositional Marangoni-Flow-Assisted Drop-Drying. *J. Phys. Chem. B* **116**, 6536–6542 (2012).
29. Sun, J. *et al.* Fabrication of Centimeter-Sized Single-Domain Two-Dimensional Colloidal Crystals in a Wedge-Shaped Cell under Capillary Forces. *Langmuir* **26**, 7859–7864 (2010).
30. Ye, R., Ye, Y.-H., Zhou, Z. & Xu, H. Gravity-Assisted Convective Assembly of Centimeter-Sized Uniform Two-Dimensional Colloidal Crystals. *Langmuir* **29**, 1796–1801 (2013).
31. Smith, T. The hydrophilic nature of a clean gold surface. *Journal of Colloid and Interface Science* **75**, 51–55 (1980).
32. Yamamoto, M. *et al.* Comparison of Argon and Oxygen Plasma Treatments for Ambient Room-Temperature Wafer-Scale Au–Au Bonding Using Ultrathin Au Films. *Micromachines* **10**, 119 (2019).
33. Bartlett, P. N., Baumberg, J. J., Coyle, S. & Abdelsalam, M. E. Optical properties of nanostructured metal films. *Faraday Discuss.* **125**, 117–132 (2004).
34. Handbook of Mathematics for Engineers and Scientists. 1543.
35. Haynes, C. L. & Van Duyne, R. P. Nanosphere Lithography: A Versatile Nanofabrication Tool for Studies of Size-Dependent Nanoparticle Optics. *The Journal of Physical Chemistry B* **105**, 5599–5611 (2001).
36. Scanlon, M. D. *et al.* Characterization of Nanoporous Gold Electrodes for Bioelectrochemical Applications. *Langmuir* **28**, 2251–2261 (2012).
37. Trasatti, S. Real surface area measurements in electrochemistry. *Pure & Appl. Chem.* **63**, 711–734 (1991).
38. Kelf, T. A. *et al.* Localized and delocalized plasmons in metallic nanovoids. *Physical Review B* **74**, 245415–1 to 245415–12 (2006).
39. Stolberg, L. Adsorption of pyridine at the Au(110)-solution interface. *J. Electroanal. Chem* **296**, 171–189 (1990).
40. Stolberg, L. Adsorption of pyridine at the Au(111)-solution interface. *J. Electroanal. Chem* **307**, 241–262 (1991).
41. Wilson, E. B. The Normal Modes and Frequencies of Vibration of the Regular Plane Hexagon Model of the Benzene Molecule. *Physical Review* **45**, 706–714 (1934).
42. Gardner, A. M. & Wright, T. G. Consistent assignment of the vibrations of monosubstituted benzenes. *The Journal of Chemical Physics* **135**, 114305 (2011).

43. Osawa, M., Matsuda, N., Yoshii, K. & Uchida, I. Charge transfer resonance Raman process in surface-enhanced Raman scattering from p-aminothiophenol adsorbed on silver: Herzberg-Teller contribution. *The Journal of Physical Chemistry* **98**, 12702–12707 (1994).
44. Ferdele, S., Jose, B., Foster, R., Keyes, T. E. & Rice, J. H. Strong coupling in porphyrin J-aggregate excitons and plasmons in nano-void arrays. *Optical Materials* **72**, 680–684 (2017).
45. Sheehan, P. E. & Whitman, L. J. Thiol Diffusion and the Role of Humidity in “Dip Pen Nanolithography”. *Physical Review Letters* **88**, (2002).
46. Zhang, W. *et al.* Tuning Interior Nanogaps of Double-shelled Au/Ag Nanoboxes for Surface-Enhanced Raman Scattering. *Scientific Reports* **5**, (2015).
47. Kim, J.-H. *et al.* A well-ordered flower-like gold nanostructure for integrated sensors via surface-enhanced Raman scattering. *Nanotechnology* **20**, 235302 (2009).
48. Le Ru, E. C. & Etchegoin, P. G. *Principles of surface-enhanced Raman spectroscopy: and related plasmonic effects*. (Elsevier, 2009).
49. Schlücker, S. *Surface Enhanced Raman Spectroscopy*. (Wiley-VCH Verlag GmbH & Co. KGaA, 2011).
50. Gillibert, R. *et al.* Directional surface enhanced Raman scattering on gold nano-gratings. *Nanotechnology* **27**, 115202 (2016).
51. Faiman, R. & Larsson, K. Assignment of the C–H stretching vibrational frequencies in the Raman spectra of lipids. *Journal of Raman Spectroscopy* **4**, 387–394 (1976).

4 Chapter 4: Fabrication of nano sub-structures towards enhancement of in-cavity signal

4.1 Introduction

Having demonstrated a highly reproducible method for nano and micro cavity array fabrication over cm^2 area, the focus in this chapter is on achieving reliable means of nano sub-structuring the arrays. The purpose is twofold, (a) focus the electric field at the bottom of the well, (b) to augment the electric field at this position. Beyond this thesis, the final target of these materials is to use them as lipid membranes supports where molecular arrival across the membrane can be monitored through SERS or MEF when the molecule reaches the hot spot.

The rationale for this approach is based on theoretical reports that SERS and fluorescence can be enhanced by the use of NPs in a metal cavity through strong coupling between the NP and their image inside the metallic void. Huang et al. performed such a theoretical study regarding the field enhancement increase when placing a single Au NP inside a single Au nanovoid.¹ Calculations suggest that tuning the particle-void separation affects the electromagnetic hot spot created at the junction of the void and NP. The NP further focuses the optical fields and concentrates light near the surface of the nano-voids.

Speed et al. studied experimentally the effect of Ag NPs in sphere segment voids.² Au nanocavity arrays were made through 600 nm diameter template spheres and gold electrodeposition to a film height of $0.75d$. Arrays were then functionalized with 4-mercaptoaniline and 4-mercaptobenzoic acid as SERS probes. Finally, the arrays were soaked in aqueous suspensions of polydisperse citrate stabilized 18 nm diameter Ag NPs for 2 hours before rinsing and acquiring SERS spectra. They reported a large increase in the SERS signal (x83 factor) compared to arrays without NP. However, by reducing the size of the laser spot during measurement, they noticed that variability of the signal was dramatically increasing, going from 13 % for a sampled area of 19 voids to 68 % for a single void, proving that the number of nanoparticles per void and/or their position in the voids plays an important part in the magnitude of the enhancement.

Figure 128 illustrates the potential outcomes when flushing a colloidal solution of nanoparticles over a cavity array, a wide variety of distribution of particles can result which explains the variability noted by Speed et al. The key drawback of this approach is that this technique does not provide any control on the presence or not of NP in voids, neither control of their number and location when in-cavity.

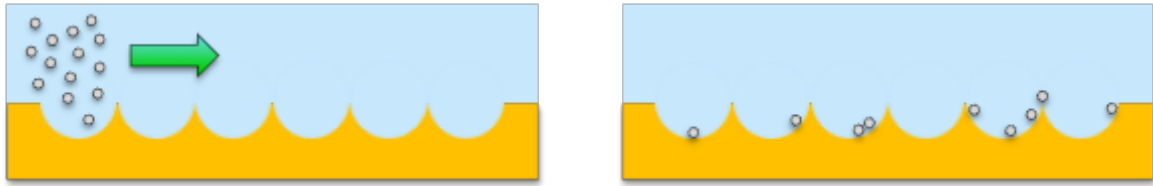


Figure 128 : Illustration of possible scenarii whilst flushing a colloidal solution of nanoparticles over a cavity array, which shows that number and/or position of nanoparticle per void can differ among the array.

Later, Lordan et al. studied the effect on plasmonic properties of dispersed Ag NPs and Ag NPs aggregates at Au nanovoid arrays.³ Their arrays were built similarly to ones described by Speed et al. but were presenting a different truncation of $0.25d$ this time. $[\text{Ru}(\text{bpy})_2(\text{Qbpy})]^{2+}$ was adsorbed at the cavity array surface and used as a SERRS and MEF probe. Here again, they observed field enhancement that they described as a combination of fields generated from single/few nanoparticles within the void, a filled void, NPs on the surface between cavities and empty unfilled cavities, with best enhancement obtained with deposited Ag NPs aggregates. However, again the control over the distribution of particles was not high.

Li et al. fabricated a highly ordered Ag-particle-in-Au-bowl structure array based on nanosphere lithography and Atomic Layer Deposition (ALD).⁴ They used a Al_2O_3 layer deposited via ALD onto the Au nanobowl to act both as a protective and a dielectric layer separating the Ag particle from the Au bowl with a distance of 5-15 nm. Annealing a silver layer at the bowl surface at $300\text{ }^\circ\text{C}$ for 1h allowed for resolidification into individual Ag nanoparticles with the biggest one centered at the bottom of the well. Neglecting the contribution coming from the small particles at the side walls, they found that SERS enhancement was strongly depending on the Ag particle size and gap separation with the nanobowl.

More recently, Malinovskis et al. reported an accessible alternative for the fabrication of plasmonic Au nanoparticle arrays deposited on nanoporous anodic alumina templates.⁵ However, the quality of the pore filling is limited by the size of the nanoparticles used, and the dimensions of ordered region is limited by the anodization time during the fabrication process if not extended above 10h. The developed structures are potential substrates for SERS-based sensors but do not present a significant EF over nonporous anodic alumina templates without nanoparticles.

In this chapter, two novel approaches to selectively build in-cavity nanoparticles (icNPs) are described. Our particular focus was on trying to establish a novel, low cost method that produced reproducible positioning and size of particles within the pore. The first method exploits the presence of nano air bubbles arising from incomplete filling of the pore. The second, a top down approach, based on oxygen plasma etching to reduce the size of PS spheres at the array, taking advantage of their original presence in every single cavity due to the nature of the fabrication process. Once coated with gold, the resulting nano structures present plasmonic properties and are improved based on their capability to enhance the SERS signal of molecules adsorbed at their surface. Four sizes of nano sub-structured cavity are developed, ranging from 510 nm to 3 μm diameter and are physically characterised by FESEM to understand the suitability of the substrates for further studies. Diffuse reflectance measurements and FDTD simulations help to correlate SERS activity and to get a better understanding of the distribution and intensity of the electric field at the NP surface. Finally, SERS and MEF characterisation of the different developed substrates are performed to assess the enhancement potential of the optimised array and the robustness of the fabrication method.

4.2 Experimental

4.2.1 Fabrication of nano substructures within gold cavity (Au-cav) array using a top-down approach

Gold micro and nanocavity arrays were fabricated using sphere lithography following the method described in chapter 3. PS spheres with diameters of 510nm, 1 μ m, 2 μ m and 3 μ m were used to obtain different size of cavity / sub structures. The method developed here takes advantage of the core principle of the array fabrication method, which is the presence of a single PS sphere forming each well. Once gold has been electrodeposited up to the equator of the spheres, the sphere templates remain captive inside each well, ensuring the presence of a single particle centred in the cavity. These trapped PS beads were then physically modified by a plasma etching method adapted from the literature.^{6,7} The RIE Plasmalab 80 Plus from Oxford Instruments was used to this purpose.

A range of settings were investigated to identify the optimal etching conditions including RF power, O₂ flow ratio, chamber pressure and etching time. It was found that optimal settings depended on the size of the PS bead, which presumably arises because bigger spheres have more material to be etched than smaller ones. Optimum parameters were chosen based on the best SERS signal for each cavity/nano structure size and results from this study is shown in section 4.3.2.3. Table 6 summarises the etching conditions to be used to obtain the optimum nano structure for each cavity size.

Table 6: Optimised etching parameters used for the different sizes of PS spheres during the fabrication of nanostructures in cavities.

PS sphere size	RF Power (W)	O ₂ flow ratio (sccm)	Chamber pressure (mTorr)	Etching time (min)
500 nm	50	25	50	11
1 μ m	100			8
2 μ m				30
3 μ m				50

Following dry etching, substrates were sputter coated with gold for 30 s using a current of 30 mA to render the etched polymeric nano substructures SERS active. Figure 129 shows the overall steps involved in nano substructure fabrication following

the initial steps of obtaining a close packed array of PS spheres and electrodepositing gold around them as described in chapter 3.

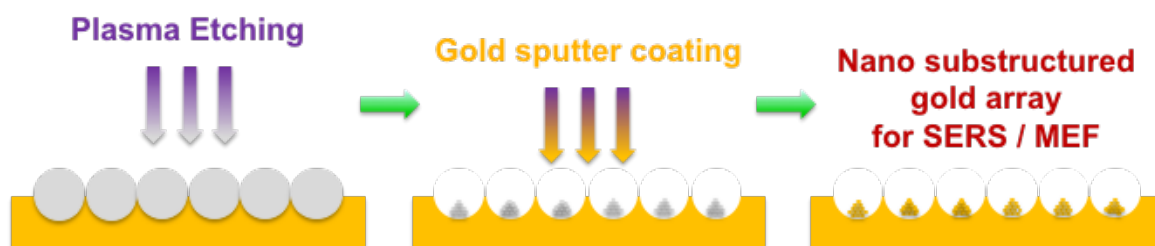


Figure 129 : Schematic of the fabrication method of gold nano structures within an Au-cav array.

4.2.2 Sputtered gold thickness study

4.2.2.1 Gold sputter coating

Nano sub-structured arrays were sputter coated with gold to render them SERS and MEF active using a sputter coater Cressington Model 108 mounted with a gold target. Gold was sputtered for 30s at a set current of 30 mA.

4.2.2.2 Profilometry

To estimate and relate SERS activity to the thickness of the coated gold layer on the NPs, thickness was measured by profilometry, using a DektakXT® stylus profiler from Brücker. To do this, a microscope glass coverslip, was used as a mask to a flat gold sample while sputtering gold. Sputtering time varied from 30 to 240 seconds for a set current of 30 mA. A step was then formed onto the sample, the masked surface being lower than one exposed to the coater.

4.2.3 Diffuse reflectance

Diffuse reflectance measurements were carried out in air using a Jasco V-670 Spectrophotometer with a 60 mm diameter integrating sphere Jasco ISN-723. Spectra were acquired between 200 and 1200 nm using Spectra Manager software. Aiming at focusing the light at the close packed cavity array and limiting exposure of surrounding flat gold areas, a black mask (black paper) with a 4 mm diameter window was applied onto the measured samples.

4.2.4 SEM and FESEM characterisation

SEM images were collected using a Hitachi S3400n SEM, Tungsten system instrument. FESEM images were captured using a Hitachi S5500 cold Field Emission in lens Scanning Electron Microscope (FESEM) ensuring high resolution images of the nano sub-structures. Working distance, accelerating voltage and magnification used in Secondary Electron mode are reported on the images.

4.2.5 FDTD simulations

To understand the location and amplitude of the electric field at the nano sub-structured array, FDTD simulations were performed by Dr. Kiang Wei Kho using Lumerical software. A program was written to generate an assembly of pill shape structures, reducing their number for each successive layer until reaching the desired height of nanostructure. To emulate as closely as possible the structures from FESEM characterisation, randomness in the aggregation was introduced in the simulation code to render each NP unique. Only the shell of the nano pills was simulated as gold, with a varying thickness of the film up to 36 nm. For this study, only arrays with 1 μm diameter cavities were simulated. Optical constant for Au was obtained from Johnson & Christy.⁸ As the array contains large contrast between feature sizes (e.g. inter-cavity gap-size is more than 30 times smaller than cavity diameter), conformal variant 2 was used as the mesh refinement method to ensure simulation accuracy. Simulations were performed with a resolution of 8 nm. For field calculations, illumination laser bandwidth was set at 0.02nm. The central wavelengths used in the simulations are 473nm, 532nm, 633nm and 785nm. All simulations were terminated at an auto shutoff threshold of 10^{-5} . To simulate an infinitely large periodic structure, Bloch boundary condition was used.

4.2.6 SERS and MEF measurements

SERS and fluorescence spectroscopy measurements were carried out on a Horiba Labram HR instrument was used with a 50x (0.55 N.A.) long distance magnification objective from Leica. The different laser sources used as excitation wavelength were 473 nm, 532 nm, 633 nm and 785 nm presenting respectively a full power at the sample of 5.03 mW, 1.02 mW, 6.00 mW and 60.2 mW. Neutral density filters were applied to reduce the intensity of the laser and the corresponding power at the sample is given with the acquisition conditions in the presented figures.

To evaluate SERS properties of the fabricated arrays, samples were dipped overnight in a 10 mM ethanolic solution of 4,4'-BPY and SERS spectra were acquired. To ensure physisorbed molecules do not contribute to the SERS signal, samples were rinsed with a large volume of ethanol and dried under nitrogen stream before Raman analysis.

For fluorescence measurements, only 473 nm excitation wavelength was used as the luminophore [Ru(bpy)₃]Cl₂ was chosen as a probe to assess the MEF properties of the arrays. SERS and fluorescence signals recorded were normalised to the Raman signal measured for the Si peak on the day of analysis during the calibration of the equipment.

4.3 Results and discussion

The aim of this chapter is to simultaneously focus and enhance the electric field at the bottom of the cavity. It is understood that this can be achieved by nano structuring. However, one of the challenges here is to nano modify a structure already at a micro or nano scale. Also, another challenge is to precisely localise the nano sub-structuring in-cavity without altering the cavity top surface aimed at supporting lipid membranes. So, two novel approaches are described here, one based on the presence of an air bubble in cavity due to incomplete filling and the other one on plasma etching.

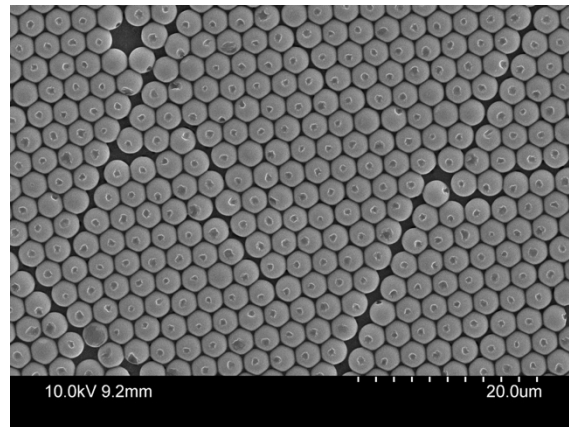
4.3.1 Air bubble as a method for nano particles formation

Previous reports from Keyes' group described that in Au-cavs, particularly for 1 μm diameter cavity or below, sonication is required to completely fill the wells. In the absence of sonication, fluorescence imaging indicated that the bottom of the well remained unfilled, which was attributed to the presence of air bubble within the cavity that forms from incomplete filling with aqueous solutions.⁹ This phenomenon can originate from different sources. Stability theories for nanobubbles at solid-liquid interfaces have been reviewed by Sun et al.¹⁰. The fact that the solution has not been degassed can lead to the presence of nanobubbles in solution. The nature of the substrate can also play a major role into the presence of bubbles at its interface. Indeed, a very smooth and hydrophilic substrate is less prone to sustain small gas bubbles than a more hydrophobic surface presenting some roughness where nanobubbles seem quite stable.¹¹

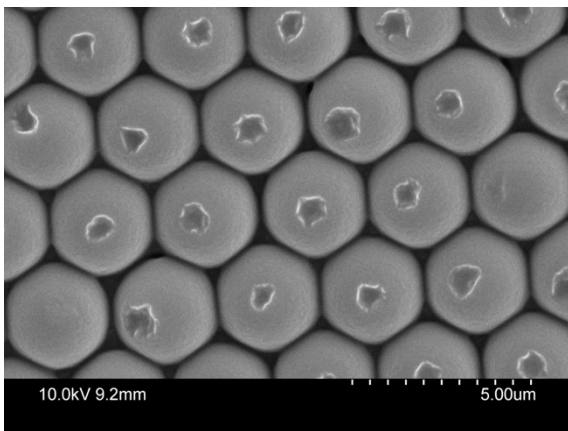
To see if we could, firstly confirm and then exploit such bubbles on filing of the array we carried out trials to assess the presence, size, shape and position of air nanobubbles within the cavity array by creating a positive mold with PDMS.

Firstly, 3 μm and 1 μm diameter cavity arrays were fabricated following the method described in chapter 3. After dissolving the PS spheres, the substrates were dipped overnight in a 10 mM ethanolic solution of perfluorodecanethiol to render their surface hydrophobic and facilitate demoulding. Indeed, without this surface modification, the PDMS cast can stick to the gold surface and nanostructures moulded risk shredding during the demoulding step. Substrates were rinsed thoroughly with ethanol and dried under nitrogen stream. Then, to create the cast, PDMS Sylgard 184 (Dow Corning) was mixed in a ratio 10:1 by weight (elastomer base : curing agent) according to the manufacturer recommendations.¹² After degassing the silicon mixture

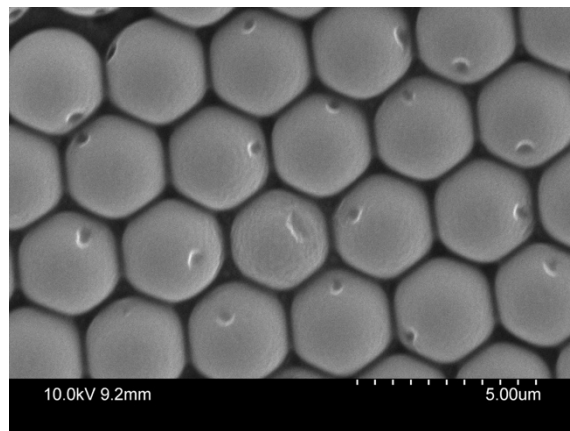
for 5 minutes into a vacuum desiccator, a thin layer was poured onto the cavities area in order to cover it. Samples were degassed further for a period of 25 minutes. As the silicone mixture is viscous, this step was carried out to enhance the cavities filling by facilitating the air trapped into the gold structures to escape. The thinner the layer of silicone, the easier it is for the air to diffuse across it. Samples were cured for 20 minutes in an oven at 150 °C. Figure 130 and Figure 131 show respectively top view images of the PDMS casts for 3 μm and 1 μm sizes cavities.



a)



b)



c)

Figure 130 : Top view SEM image of a 3 μm diameter cavities PDMS cast at magnification x2k (a) and x8k (b and c) at different locations on the same substrate.

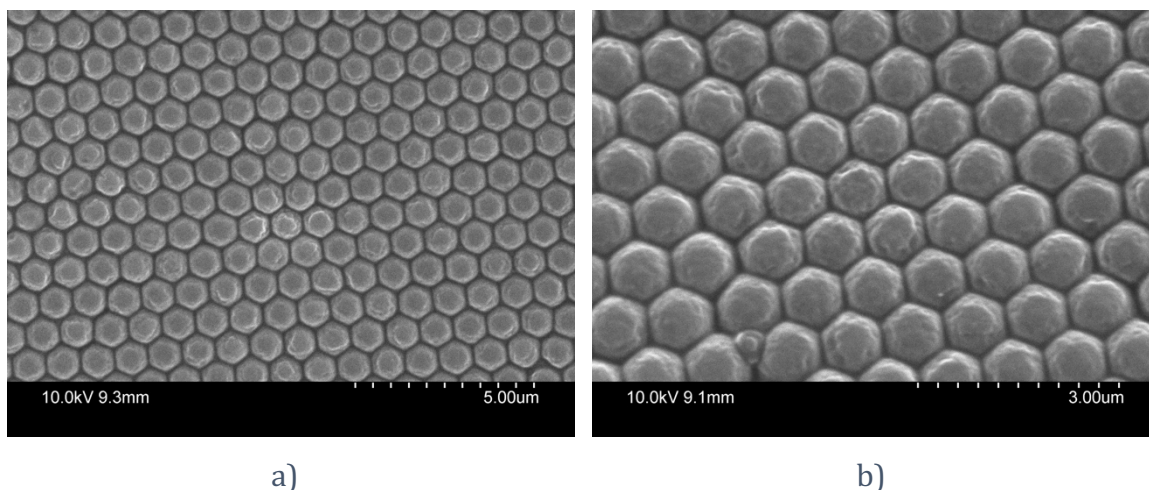


Figure 131 : Top view SEM image of a 1 μm diameter cavities PDMS cast at magnification x8k (a) and tilted from 18° angle at x15k (b).

From Figure 130 a) it can be seen that 3 μm diameter cavity arrays present in most instances gas bubbles in the wells. However, depending on the area imaged of the same substrate, size of the bubble varies considerably (Figure 130 b) and c)). Also, it can be noticed that location of the bubble varies somewhat cavity to cavity, most arise close to the centre of the bottom of the well, but some also occur on the side wall.

The 1 μm diameter cavity arrays casts did not present distinctive bubbles inside their wells despite a good imprint of the microstructures with the PDMS, as shown in Figure 131. However, the imprint does show some roughness which may indicate an air void that is flattened but covers the bottom of the well. This is very consistent with the behaviour observed by Jose et al. on filling this size cavity array with aqueous fluorophore.⁹

Moulds of 510 nm and 372 nm diameter cavities were attempted but were not successful as the nano bumps did not imprint reproducibly well due to the viscosity of the PDMS.

Experimental trials to electrochemically grow gold nanoparticles were carried out by Dr. Sean Maher in Keyes' group to demonstrate that the bubbles can be used to generate nanofeatures. 1-Dodecanethiol solution was prepared in an ethanol/water mixture to promote the formation of gas bubble in cavity. Indeed, as ethanol has a surface tension lower than water, an ethanolic solution of alkane thiol would likely fill up the cavity without forming any bubble. However, use of a fully aqueous solution of alkane thiol was not possible due to poor solubility. The top surface of samples was first functionalised with 1-dodecanethiol by incubating arrays in a 10 mM ethanolic

solution of 1-dodecanethiol while PS spheres were still present. This step was necessary to block the electrochemical activity at the cavities' interstitial space and avoid nanoparticles growing between wells. After PS sphere dissolution, samples were functionalised for two hours with the ethanol/water mixture of 1-dodecanethiol, then rinsed with ethanol and dried under nitrogen stream. Nanoparticles were electrochemically grown in a manner similar to the method described in chapter 3 to grow cavity, using a shorter electrodeposition time of few seconds.

Figure 132 shows an SEM image of nanostructures grown for 60 seconds within 3 μm diameter cavities. The presence of multiple nanoparticles within each cavity suggests that particles nucleated from nanoscale defects in the alkane thiol assembly during their lateral packing rather than from the presence of a single bubble as shown previously in Figure 130. The larger particles are of fairly uniform size, but the distribution looks bimodal with small structures also present. The difference in size of structures within the same cavity can be explained by an agglomeration of adjacent particles during the electrodeposition. This phenomenon of defects in the formation of the SAM is well reported in the literature¹³⁻¹⁶ and was exploited in Keyes/Forster's group for DNA detection using nanoparticles.¹⁷

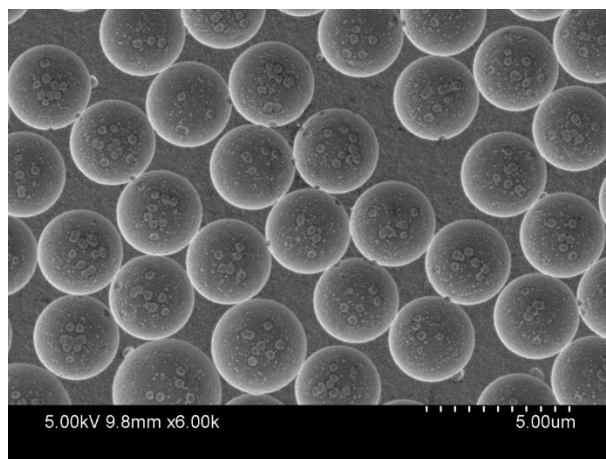


Figure 132 : SEM image of gold nanoparticles electrochemically grown for 60 s in 3 μm diameter cavities. Courtesy of Dr. Sean Maher.

Given the poor control over size and distribution of the particles formed using this approach, this method was abandoned in favour of the novel approach described in section 4.2.1 involving plasma etching.

4.3.2 Cavity sub-nanostructure development using plasma etching

This novel method takes advantage of the presence of uniform polystyrene sphere during the fabrication process of Au-cav arrays developed in chapter 3 and unlike in previous method where they are removed, they are left in situ, and modified to obtain the SERS/MEF active structures, thus reducing the number of steps involved in the fabrication process. Using a technique such as plasma etching involves equipment where handling sample by the operator is reduced, leading to less operator skill dependent steps, hence reducing variability between substrates when prepared by different operators. Also, human errors are reduced as physical parameters such as RF power, O₂ flow ratio, chamber pressure and etching time are accurately controlled by the equipment.

One of the main parameters that was considered from the conception of the structures was the size of the final particles. As the end aim of the nano sub-structured arrays was to be able to support a lipid bilayer suspended over buffer filled cavities for the study of drug/lipid interactions. The PS sphere presents in each cavity had to be shrunk to an extent that the maximum height of the resulting etched particles was below the level of the top of the cavities. This was essential to ensure that any protrusion emerging from the cavity would not disrupt the suspended lipid bilayer. Having considered this, the next characteristic of the array was to enhance the best possible SERS signal as this technique was to be used for the lipid bilayer study.

4.3.2.1 Control on SAM formation kinetic

Intensity of SERS signal depends of the SERS structures characteristics, but primarily of the chosen SERS probe and its surface coverage at the array. To avoid disparity in SERS measurement from sample to sample due to differences in density of the SERS probe, 4,4'-BPY SAM formation kinetics was first studied to ensure that equilibrium coverage had been achieved at all substrates prior to measurement.

Two 1 μm diameter cavity arrays with NPs were prepared independently as described in section 4.2.1. Before surface functionalisation, SERS spectrum of each sample was acquired to verify the absence of signal around 1293 cm^{-1} . This frequency corresponds to the well isolated mode due to the 4,4'-BPY SAM in the SERS study. Samples were then dipped in a 10 mM ethanolic solution of 4,4'-BPY and SERS spectra were acquired periodically during 24 hours reaction time.

Figure 133 presents Raman spectra of PS and 4,4'-BPY crystals and Figure 134 representative SERS spectra of a 1 μ m diameter cavity array with NPs before and after functionalisation with 4,4'-BPY for 23 hours.

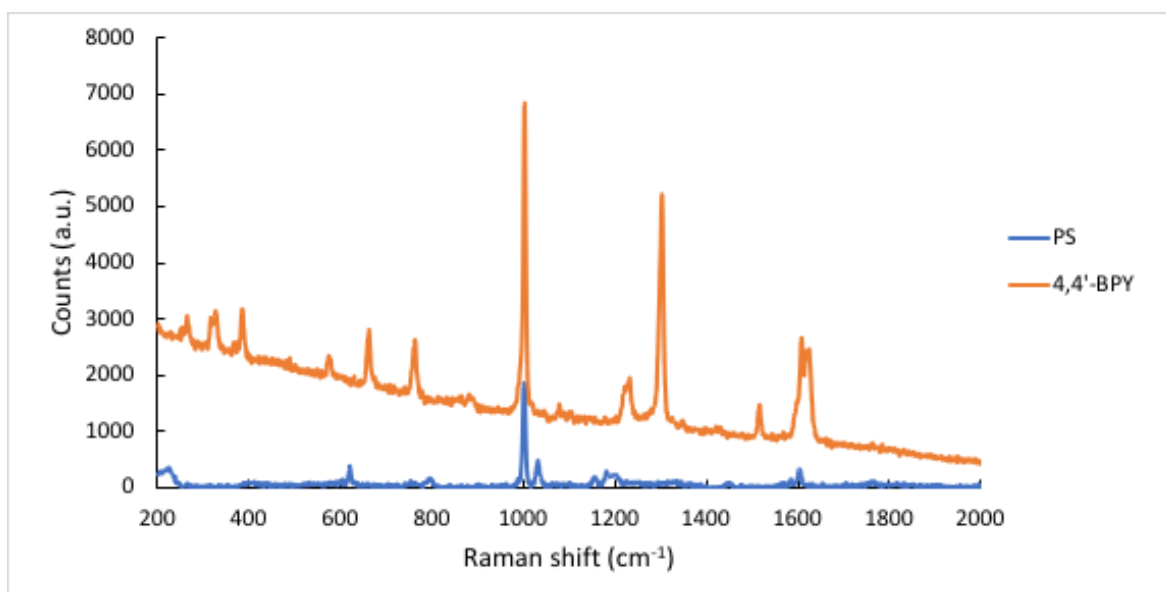


Figure 133 : Representative Raman spectra of PS pellets and 4,4'-BPY crystals under $\lambda_{exc} = 785$ nm.

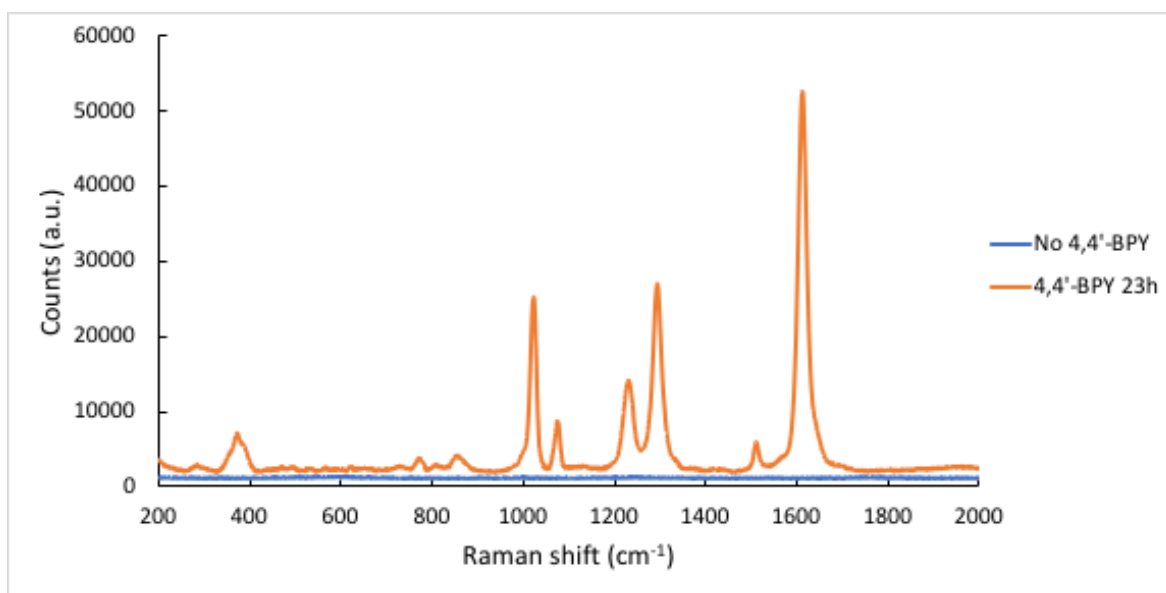


Figure 134 : Representative Raman spectra of 1 μ m diameter cavity array with NPs before and after functionalisation with 4,4'-BPY for 23 hours. ($\lambda_{exc} = 785$ nm, 10 acc. 2 s., pin hole 900 μ m, laser power at sample 429 μ W)

The spectra of the 4,4'-BPY corresponded to that previously reported and the ν_{8a} mode at 1610 cm^{-1} attributed to ring C-C stretching (A_1 ring mode) was the most

enhanced as reported previously by S.-W. Joo.^{18,19} However it was decided to use the ν_3 mode at 1293 cm^{-1} assigned to inter-ring stretching (B_2 ring mode) as the reference mode to measure enhancement.²⁰⁻²² This mode is the third most relatively enhanced band of 4,4'-BPY in Au SERS compared to the ordinary Raman spectrum of the compound in the solid state¹⁹, and its SERS signal is among the three strongest on the spectrum shown in Figure 134. It was selected here because it is well isolated in the spectrum and is not superimposed on PS vibrations that could render the signal more complicated to analyse.²³⁻²⁵ Figure 135 presents representative Raman spectra illustrating the evolution of the SERS intensity for a 4,4'-BPY SAM at a $1\text{ }\mu\text{m}$ diameter cavity array with NP as a function of incubation time.

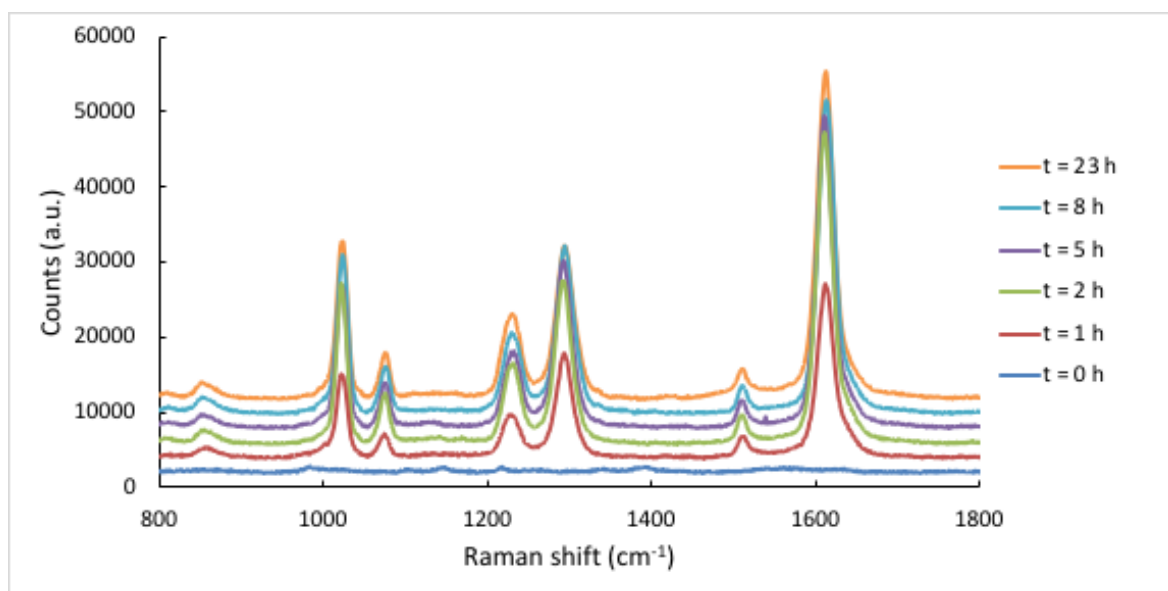


Figure 135: Representative Raman spectra of a 4,4'-BPY SAM formation on a $1\text{ }\mu\text{m}$ diameter cavity array with NPs. A 10 mM ethanolic solution of 4,4'-BPY was used to functionalise the samples. ($\lambda_{exc} = 785\text{ nm}$, $10\text{ acc. } 2\text{ s}$, pin hole $900\text{ }\mu\text{m}$, laser power at sample $429\text{ }\mu\text{W}$)

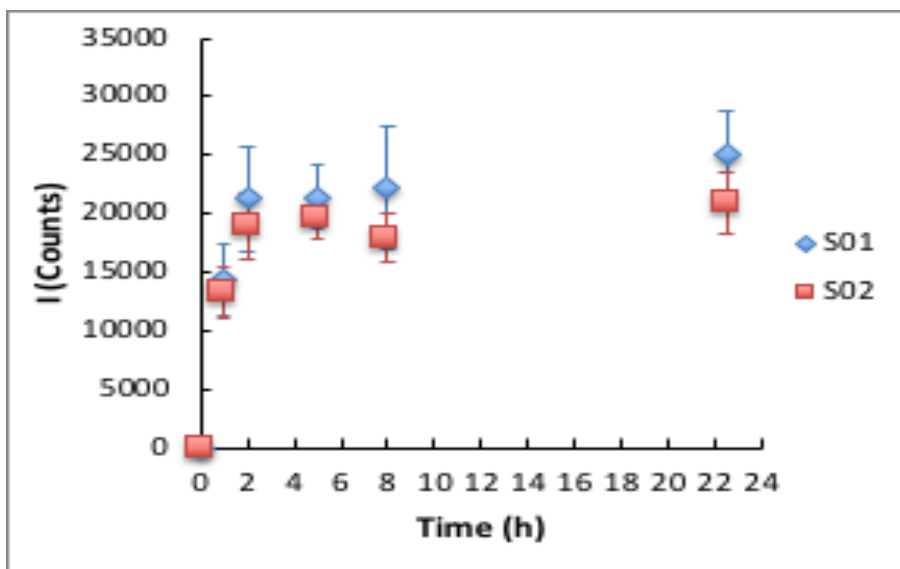


Figure 136 : Kinetic study of a 4,4'-BPY SAM formation on a 1 μm diameter cavity array with NPs. A 10 mM ethanolic solution of 4,4'-BPY was used to functionalise the samples. Intensity reported correspond to B₂ ring mode at 1293 cm^{-1} (ν_3). ($\lambda_{\text{exc}} = 785 \text{ nm}$, 10 acc. 2 s., pin hole 900 μm , laser power at sample 429 μW , $n = 8$)

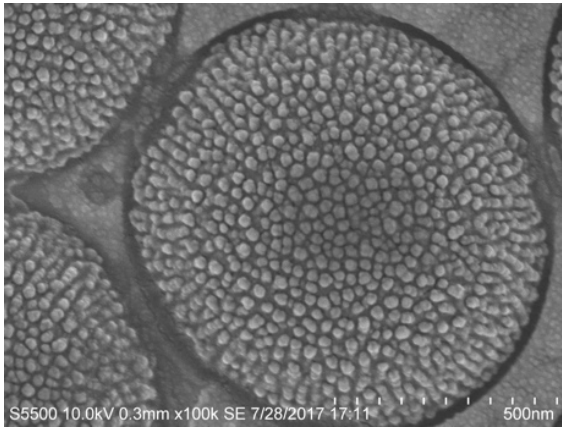
Kinetic data showing the intensity evolution of B₂ ring mode at 1293 cm^{-1} (ν_3) versus time, are shown in Figure 136 and are highly reproducible across the two samples explored, as reflected in the error bars shown in the plot. It can be seen that more than 80 % of the SERS intensity is attained after only 2 hours incubation, beyond which over the proceeding 23 hours the intensity barely changes. This observation is in line with what is widely described in the literature regarding kinetic studies of SAM from solution, although it is much more widely studied for thiols than pyridines.^{26,27} We can speculate that similar phenomenon is happening with 4,4'-BPY as reported for thiol, where it is reported to stand vertically on gold.²⁸ In the first minutes when the substrate is in contact with the solution, molecules adsorbed randomly at the metal surface. They then reorganise based on lateral packing and bond to the surface, leaving progressively room for new molecules to stack in the same manner.

This control confirms for subsequent study that an overnight functionalisation of the substrate is more than sufficient to ensure saturation SAM coverage of the surface, thus ensuring variation in SERS signal between samples cannot be attributed to an incompletely formed SAM but to other phenomena, such as disparities in the arrays due to the fabrication process for example.

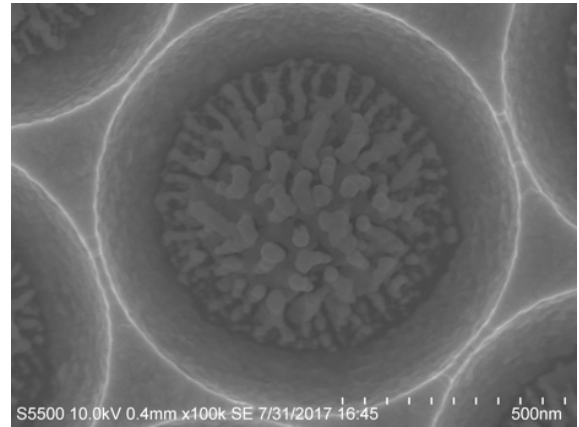
4.3.2.2 Influence of etching parameters on nano structures' shape

During the development of the sub-nanostructure fabrication method, initial focus was on 1 μm diameter cavity arrays using similar parameters to those reported by Yang *et al.* for their 870 nm diameter PS spheres on planar surfaces.⁷

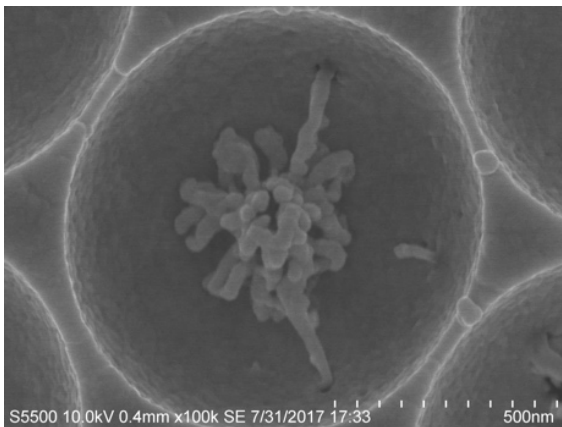
Four parameters of the etching process were iterated to determine which most influenced the size and the shape of the NPs: RF power, etching gas nature, etching gas flow ratio, and etching time. Figure 137 shows representative FESEM images reflecting how the plasma exposure time influences the shape of the polymer. PS spheres in cavity array were etched at constant RF Power of 100 W, chamber pressure of 50 mTorr and oxygen flow rate of 25 sccm, etching time was increased from 1 to 10 minutes.



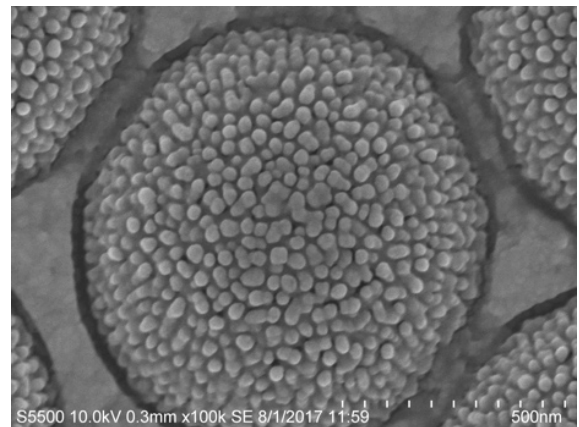
a)



b)



c)



d)

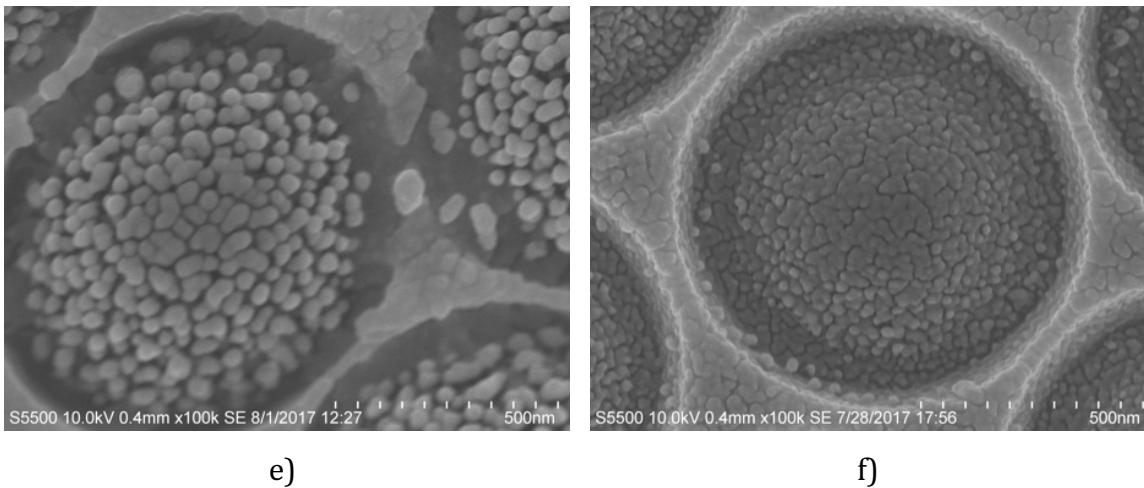


Figure 137 : Representative FESEM images of 1 μm diameter PS sphere in cavity etched under different conditions. a) RF Power = 100 W, P = 50 mTorr, O_2 = 25 sccm; t = 1 min; b) RF Power = 100 W, P = 50 mTorr, O_2 = 25 sccm; t = 5 min; c) RF Power = 100 W, P = 50 mTorr, O_2 = 25 sccm; t = 10 min; d) RF Power = 100 W, P = 50 mTorr, O_2 = 50 sccm; t = 1 min; e) RF Power = 200 W, P = 50 mTorr, O_2 = 25 sccm; t = 1 min; f) RF Power = 100 W, P = 50 mTorr, Ar = 50 sccm; t = 10 min.

The first parameter to be studied was the etching time. For this, RF Power, O_2 flow ratio and chamber pressure were kept constant to respectively 100 W, 25 sccm and 50 mTorr. The influence of the etching time on the shape of the resulting PS sphere can be seen with Figure 137 a), b) and c). As time increases, the PS sphere decreases in size and roughens, leading to an agglomerate of PS stripes for extended exposure to plasma. As described by Li et al. the plasma flow contains ions, electrons, excited neutrals, radicals, and UV radiation, which are highly reactive and lead to the chain scission of the PS molecules, generating low-molecular-weight fragments.²⁹ It seems that for short exposure time, the small size of the fragments allows for a uniformly roughened sphere. As the etching time increases, the morphology of the PS spheres becomes more and more random and might lead to reproducibility issues from cavity to cavity.

The second parameter tested was the gas flow ratio. This time only the flow ratio of oxygen was increased from 25 and 50 sccm for a constant RF power of 100 W, chamber pressure of 50 mTorr and etching time of 1 min, and results are illustrated in Figure 137 a) and d). From these SEM images it seems that the size of the PS sphere does not vary much under these two conditions. PS etched at lower gas flow ratio appears to be visually slightly rougher as it presents more imperfections at its surface. However, the size of the sphere remains of the same order and it can be then concluded that varying the gas ratio has little influence on the structure of the resulting etched polymer.

The third parameter investigated was the influence of the RF power. O₂ flow ratio, chamber pressure and etching time were respectively kept constant to 25 sccm, 50 mTorr and 1 min, and RF power was increased from 100 W to 200 W. Results illustrated in Figure 137 a) and e) shows that the etching of the particle happens faster at high RF power. The resulting particle decreased in size and bigger fragments of polymer were etched away.

Finally, the nature of the etching gas was explored by changing from oxygen to argon. Results are illustrated in Figure 137 c) and f), where RF Power and etching time were kept respectively constant to 100 W and 10 min. Although in this case the flow ratio was set to 25 sccm for O₂ and 50 sccm for Ar, this should have little cross-influence on the result as previously concluded regarding the effect of the gas flow ratio on the etching process. Etching done under Ar shows a much smoother and slower etching of the PS compared to etching done under O₂, as the bead decreased slightly in size for the relatively long plasma exposure. Despite presenting some imperfection at its surface, the polymer looks like having melted partially in the well.

From these results it can be concluded that the parameters found to have the most influence on PS etch rate are the RF power, the etching time and the gas used.

As O₂ gave promising results compared to Ar, and due to limits in diversity of gas available only this gas was explored during the optimisation of the etching process as only PS needed to be etched on the array. The final steps of the development were based on the SERS performance of the array as described later in section 4.3.2.3, keeping in mind that the final particle should not exceed the cavity's height for lipid bilayer stability purpose.

After reaching the optimised etching conditions for the 1 µm diameter cavity arrays, we moved to the 510 nm diameter particles. As the spheres are small, less material is removed, therefore, similar conditions were used but shorter etching time was applied. Figure 138 shows the fast diminution in size of the 510 nm diameter PS bead after 2, 4, and 6 minutes exposure to oxygen plasma.

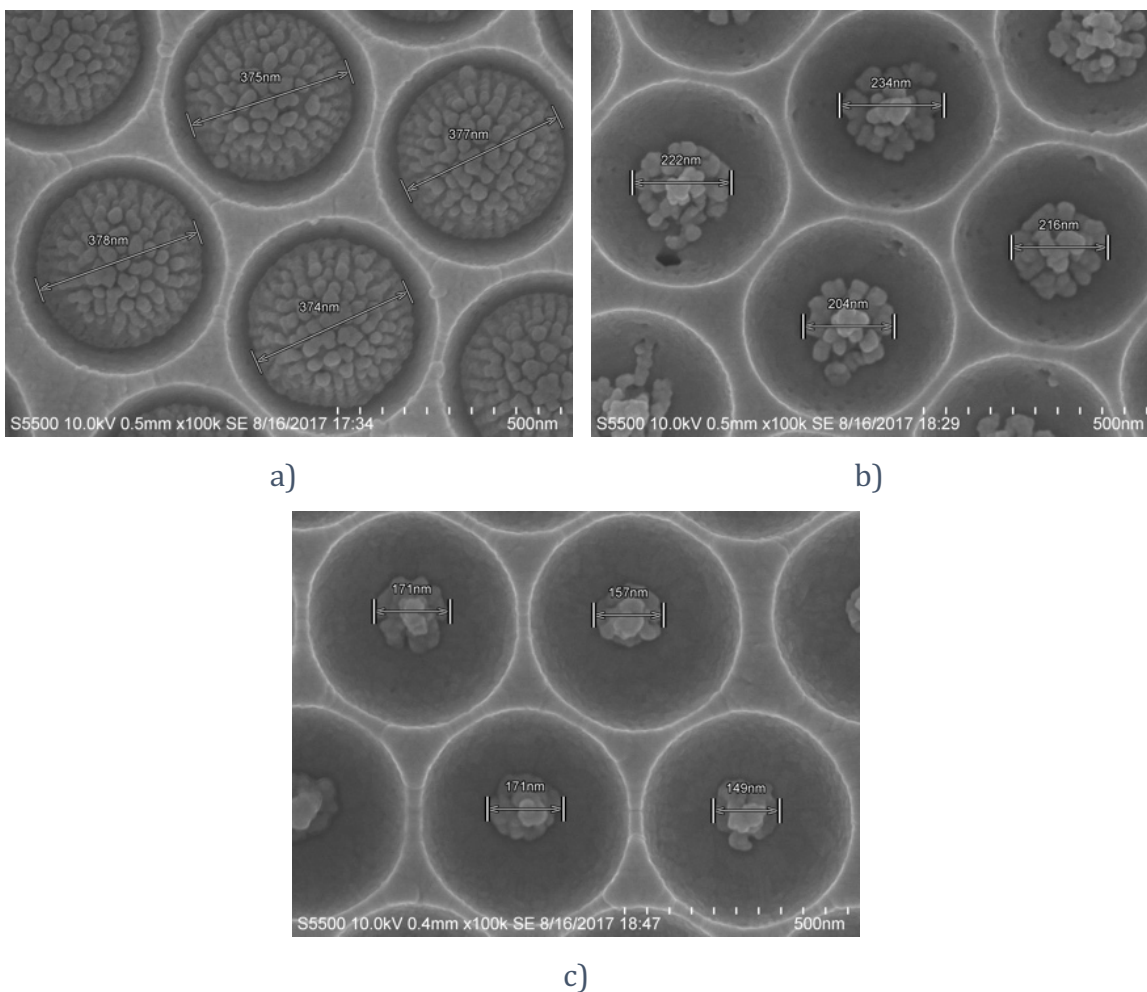


Figure 138 : FESEM images of 510 nm diameter PS spheres in cavity etched for 2 min (a), 4 min (b), and 6 min (c) with a RF power of 100 W.

The results show the PS sphere is drastically diminished within 6 minutes. Despite the etching time being controlled by the equipment, timing changes of just a few seconds can greatly influence the variability of the substrate and therefore the reproducibility of the SERS performance of the arrays. To limit this risk, it was decided to apply a gentler etching process by using a reduced RF power of 50 W for all subsequent optimization studies regarding this size of particles. The results are presented in Figure 139, where it can be seen that the size of the PS decreases as the etching time increases. Number of imperfections at their surface tend to remain of constant size among the different etching time tested, therefore appear to be fewer for smaller resulting particles. However, etched particles are of similar sizes among a single substrate. SERS performance was again used to gauge optimal etching conditions and are discussed in the sections below.

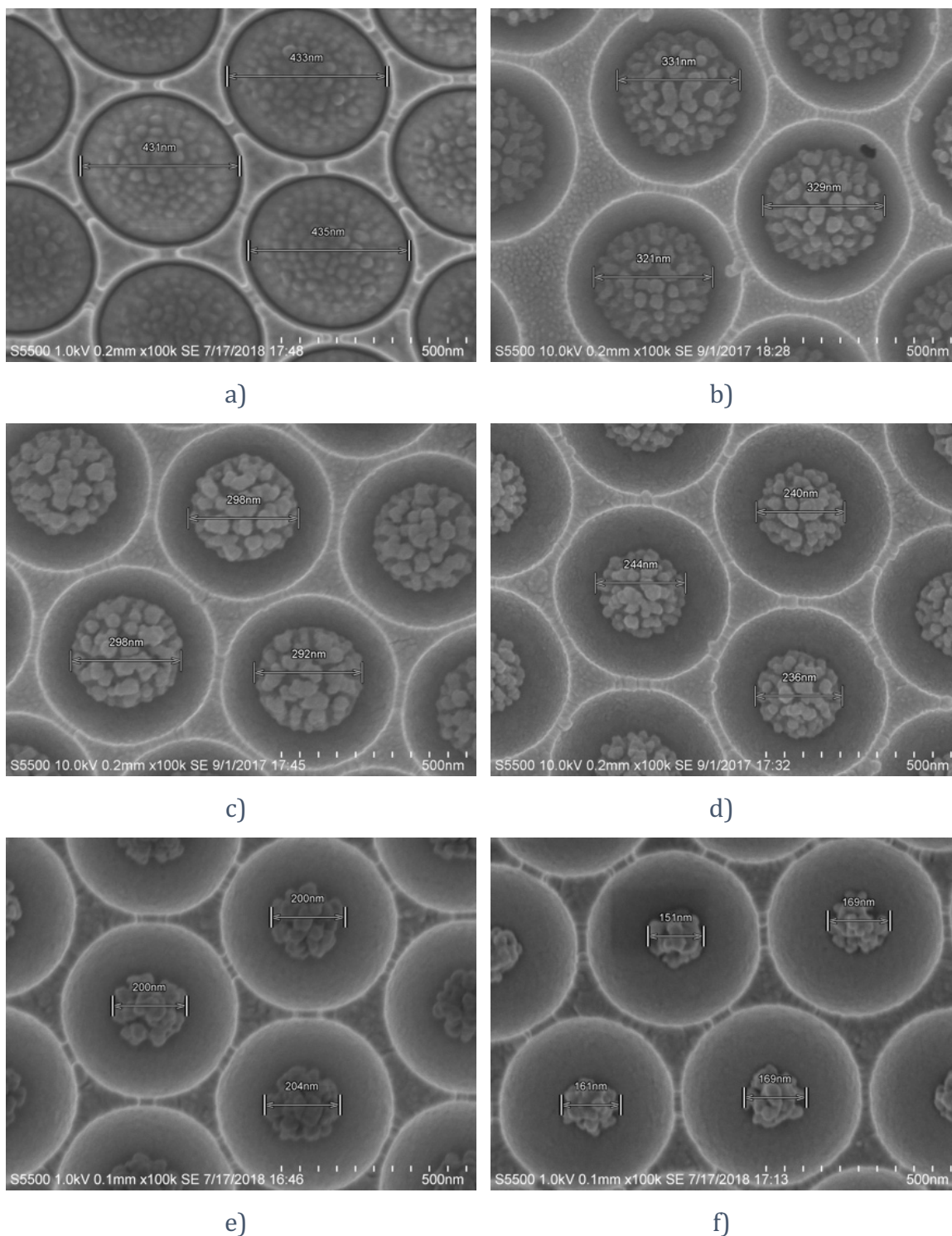


Figure 139 : FESEM images of 510 nm diameter PS spheres in cavity etched for 4 min (a), 7 min (b), 8 min (c), 9 min (d), 11 min (e) and 14 min (f) with a RF power of 50 W.

Finally, development of 3 μm and 2 μm diameter cavity arrays was achieved to complete the range of sizes of NPs and study their SERS and MEF properties. Applying a RF power of 50 W to etch the 3 μm diameter PS spheres led to long etching times for a low size-reduction efficiency, e.g. over 80 minutes plasma exposure stripping PS strings from the original sphere reducing its volume by only a third as shown in Figure

140 a). Conversely, using 200 W to speed up the process seemed to melt the PS sphere rather than strip it, leading after 15 minutes to a flattened “water lily” shaped particle as shown in Figure 140 b), c) and d). The outside of the sphere melted smoothly making the harder core of the particle bloom like a flower of about 1.5 μm diameter on top of a water lily leaf measuring approximately 2.3 μm diameter. To compromise between etching time and morphology of the resulting structure, a RF power of 100 W was applied to etch both 3 μm and 2 μm diameter PS spheres and form best performing SERS substrates.

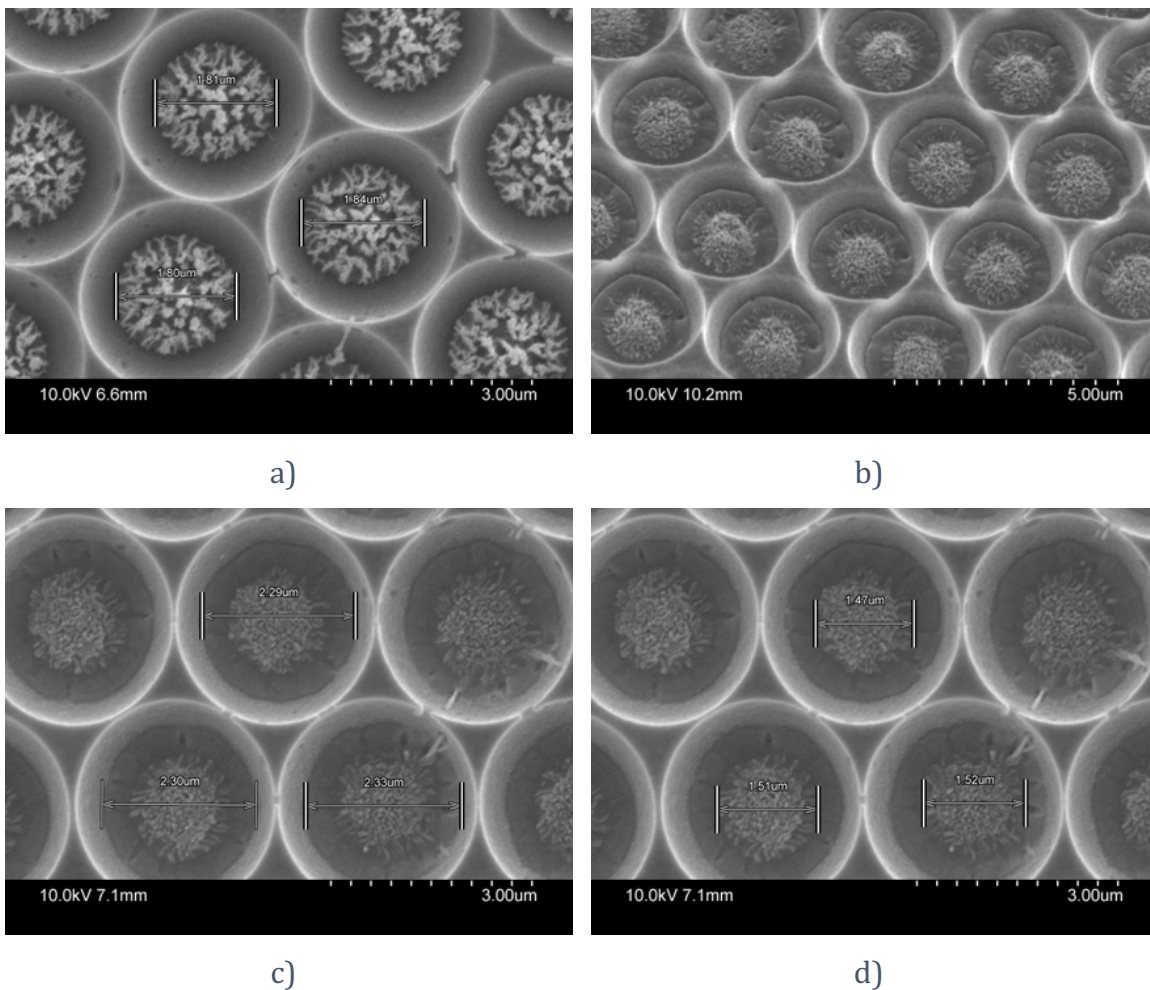


Figure 140 : SEM images of 3 μm diameter PS spheres in cavity etched for 80 min with a RF power of 50W (a) and 15 min with a RF power of 200 W (b, c and d).

Gold arrays of different cavity sizes with optimised nano-substructures were finally physically characterized by FESEM as SEM was not giving a good enough resolution for a precise characterisation of structures below 1 μm and results are shown in section 4.3.3.1.

4.3.2.3 Optimisation of nanostructures based on SERS signal

Having concluded that plasma exposure time was the key parameter to control in progressively and reproducibly reducing the size of the created nanostructure in cavity, the resulting influence on the SERS activity of the etched array was examined.

For each size of cavity, RF power, oxygen flow ratio and chamber pressure were fixed, and etching time was increased progressively. Based on the physical characterisation by SEM and FESEM presented previously, it was decided to fix the oxygen flow ratio to 25 sccm and the chamber pressure to 50 mTorr. Arrays made of 500 nm diameter PS spheres were exposed to plasma with a RF power of 50 W while arrays with 1 μm , 2 μm and 3 μm diameter cavities were treated with a RF power of 100 W due to their larger volume to be etched. Samples were then coated with gold as described in section 4.2.1 and functionalised overnight with a SAM of 4,4' BPY used as a SERS probe.

Figure 141 to Figure 144 present results obtained for the different cavity sizes studied. Each sample analysed was etched under four different conditions. Indeed, once gold was electrochemically grown around the PS sphere, each sample was split into four sub-samples, to reduce the variability coming from array preparation. Despite precautions taken to limit this variability, intensity of SERS signal can still vary between samples. Therefore, to limit further introducing a bias in the interpretation of the results, some etching conditions were repeated to overlap results from two different samples and ensure a better analysis of the trend.

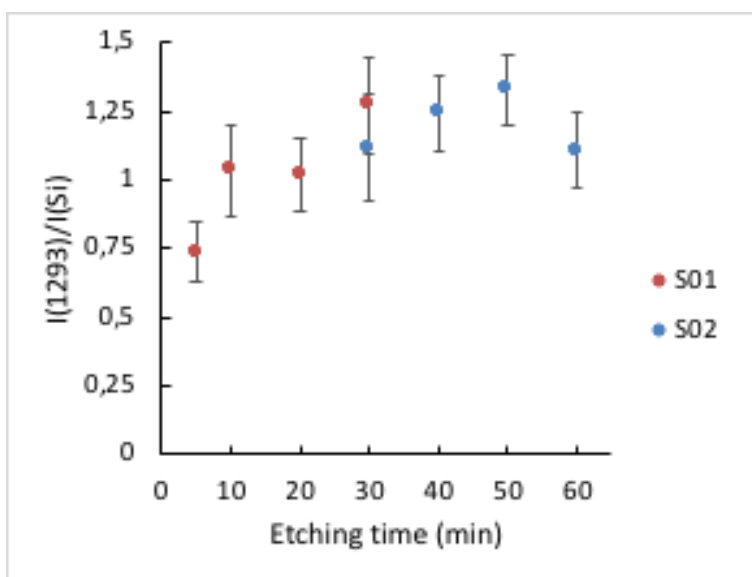


Figure 141 : Nanoparticles development in 3 μm diameter cavities (RF power 100 W). Intensity reported correspond to B_2 ring mode at 1293 cm^{-1} (ν_3) and was normalised to the Raman signal of Si standard measured on the day of analysis during the calibration of the equipment. ($\lambda_{\text{exc}} = 785\text{ nm}$, 10 acc. 2 s., pin hole $500\text{ }\mu\text{m}$, laser power at sample $429\text{ }\mu\text{W}$, $n = 8$)

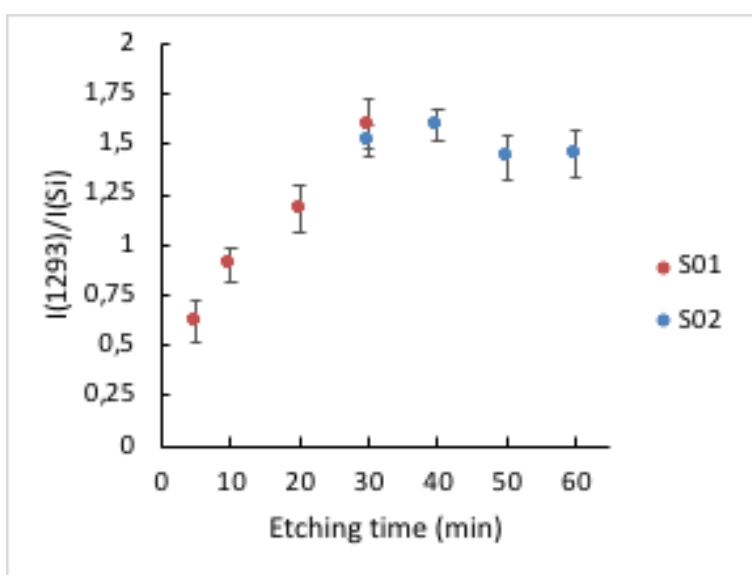


Figure 142 : Nanoparticles development in 2 μm diameter cavities (RF power 100 W). Intensity reported correspond to B_2 ring mode at 1293 cm^{-1} (ν_3) and was normalised to the Raman signal of Si standard measured on the day of analysis during the calibration of the equipment. ($\lambda_{\text{exc}} = 785\text{ nm}$, 10 acc. 2 s., pin hole $500\text{ }\mu\text{m}$, laser power at sample $429\text{ }\mu\text{W}$, $n = 8$)

From Figure 141, Figure 142, and Figure 143 it can be seen that SERS activity of the arrays progressively increases with etching time until SERS response plateaus or indeed, in the case of 1 μm spheres decreases with longer plasma exposure times. The peak of SERS intensity is identified and defines the optimal conditions of fabrication of the nano sub-structured arrays and is respectively reached at 50 min, 30 min and 8

min for 3 μm , 2 μm and 1 μm diameter cavity arrays. Paradoxically, despite sphere reducing along the etching process and potentially decreasing the number of hotspots at its surface, the PS bits taken away make the structure rougher and rougher, leading to sharper nanogaps with higher field enhancement potential resulting in the SERS signal increase. Once the structure reaches its maximum efficiency, it seems that no more hot spots are created, and the signal starts to decrease along with the structure size.

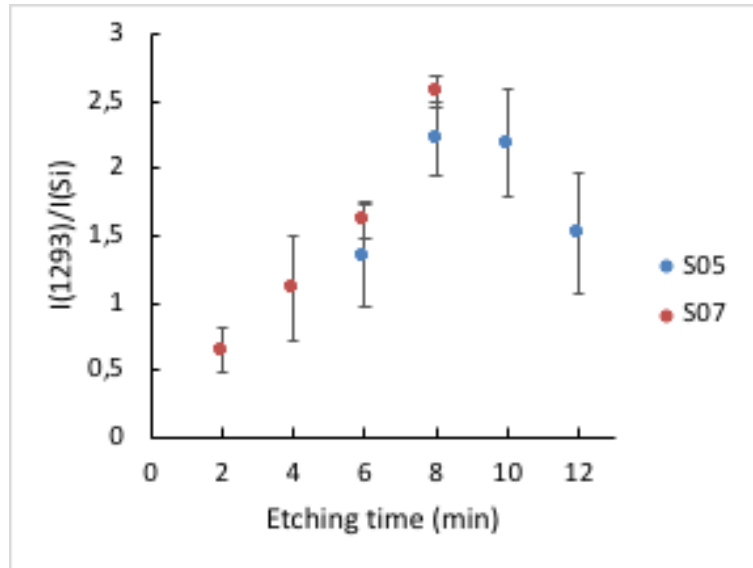


Figure 143 : Nanoparticles development in 1 μm diameter cavities (RF power 100 W). Intensity reported correspond to B_2 ring mode at 1293 cm^{-1} (ν_3) and was normalised to the Raman signal of Si standard measured on the day of analysis during the calibration of the equipment. ($\lambda_{exc} = 785\text{ nm}$, 10 acc. 2 s., pin hole 500 μm , laser power at sample 429 μW , $n = 8$)

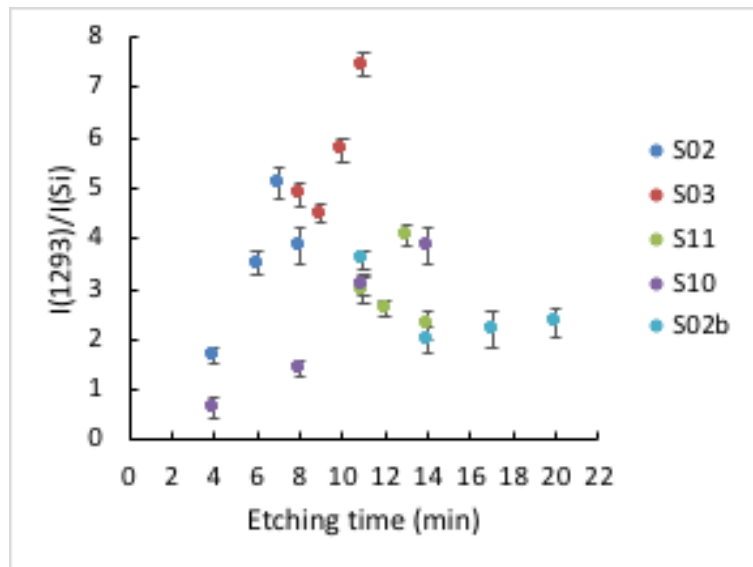


Figure 144 : Nanoparticles development in 510 nm diameter cavities (RF power 50 W). Intensity reported correspond to B_2 ring mode at 1293 cm^{-1} (ν_3) and was normalised to the Raman signal of Si standard measured on the day of analysis during the calibration of the equipment. ($\lambda_{exc} = 785\text{ nm}$, 10 acc. 2 s., pin hole 500 μm , laser power at sample 429 μW , $n = 8$)

For 510 nm diameter cavities, more repeats were needed to extrapolate a trend, as shown in Figure 13 there is good degree of variability from etch to etch. The origin of this is variation is not clear and might come from the quality of the sputter target that varies over time, but by extending the number of samples over which optimization was investigated it was possible to define the optimum conditions giving the best SERS activity. Figure 144 shows that 510 nm diameter cavity arrays have similar behaviour to bigger cavity arrays. S02 and S03 gave consistent results with what has been described previously, producing increasing SERS signal as the arrays is more exposed to the plasma. However, sample S02b showed an intensity of SERS signal twice lower than sample S03 prepared in the same conditions with an etching time of 11 minutes. Beyond this time, SERS activity seems to stabilise until 20 minutes. To be confident the results were not sample dependent, two extra samples were analysed, to cross check the different etching time previously tested. S10 and S11 gave lower intensity than S02 and S03 but the trend was respected, namely an increase of the SERS activity until 11 minutes. After this point, results tend to stabilise, but variability increases as intensity is fluctuating. 11 minutes was therefore selected for etching time for this size of PS spheres, which is a good compromise between high SERS activity and good reproducibility of the fabrication method.

4.3.2.4 Gold coating thickness optimisation

Following nano/microparticle plasma etching, gold must be sputtered over the etched arrays to create the final SERS substrates. Therefore, we also investigated the impact of sputtering conditions on the SERS activity of the final arrays, by varying the sputter time and studying the created film thickness.

Figure 145 shows a characteristic step profile obtained after 60 seconds of gold sputter coating onto the flat gold sample with a current of 30 mA. Selected in red is the area that was used as reference corresponding to the gold under the glass coverslip. In green correspond the area on which the gold was sputtered and formed the step. The average difference in height between those two selected ranges correspond to the thickness of the sputtered gold layer.

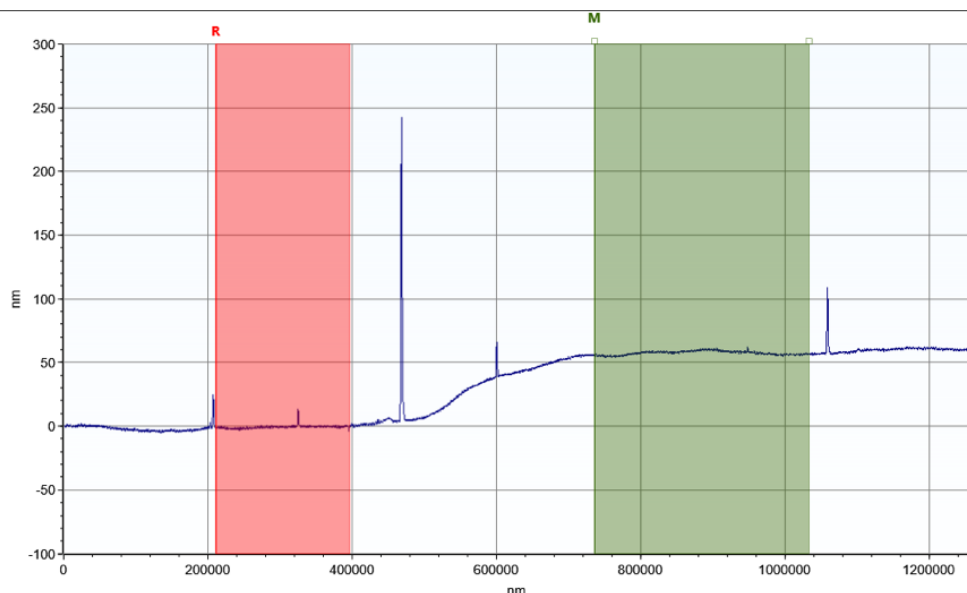


Figure 145 : Step profile obtained from the profilometer for a gold sputtering cycle of 60 s onto a flat gold sample at 30 mA. (Red: area used as reference corresponding to the gold under the glass coverslip; Green: area on which the gold was sputtered and formed the step)

Samples were exposed for different times and a calibration curve was plotted, as shown in Figure 146. As expected, for a constant vacuum and current, the film thickness varies linearly with the sputtering time.³⁰

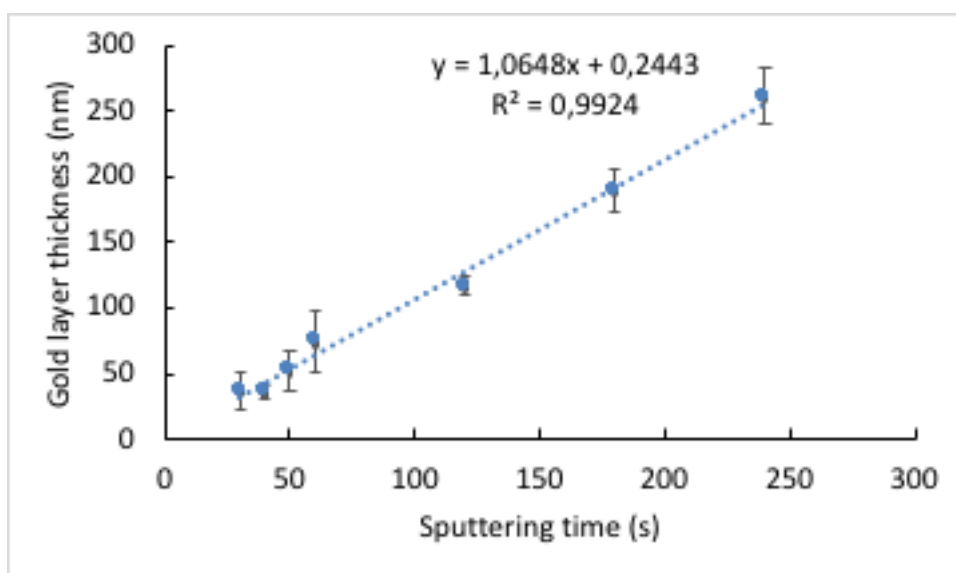


Figure 146 : Gold layer thickness obtained for different sputtering times (n=5).

Regarding the SERS study, each set of measurements comprised a sample with 1 μm diameter PS spheres within cavities etched and each substrate was split in four before gold coating to limit the contributions from inter-sample variation. Such an

approach allows us to isolate variation in SERS signal mostly to the influence of the gold layer thickness. Figure 147 shows SERS signal obtained for 1 μm cavity arrays with NPs fabricated as described in section 4.2.1 and exposed to different gold sputtering times. Samples were functionalized over night with 10 mM ethanolic solution of 4,4'-BPY for the study.

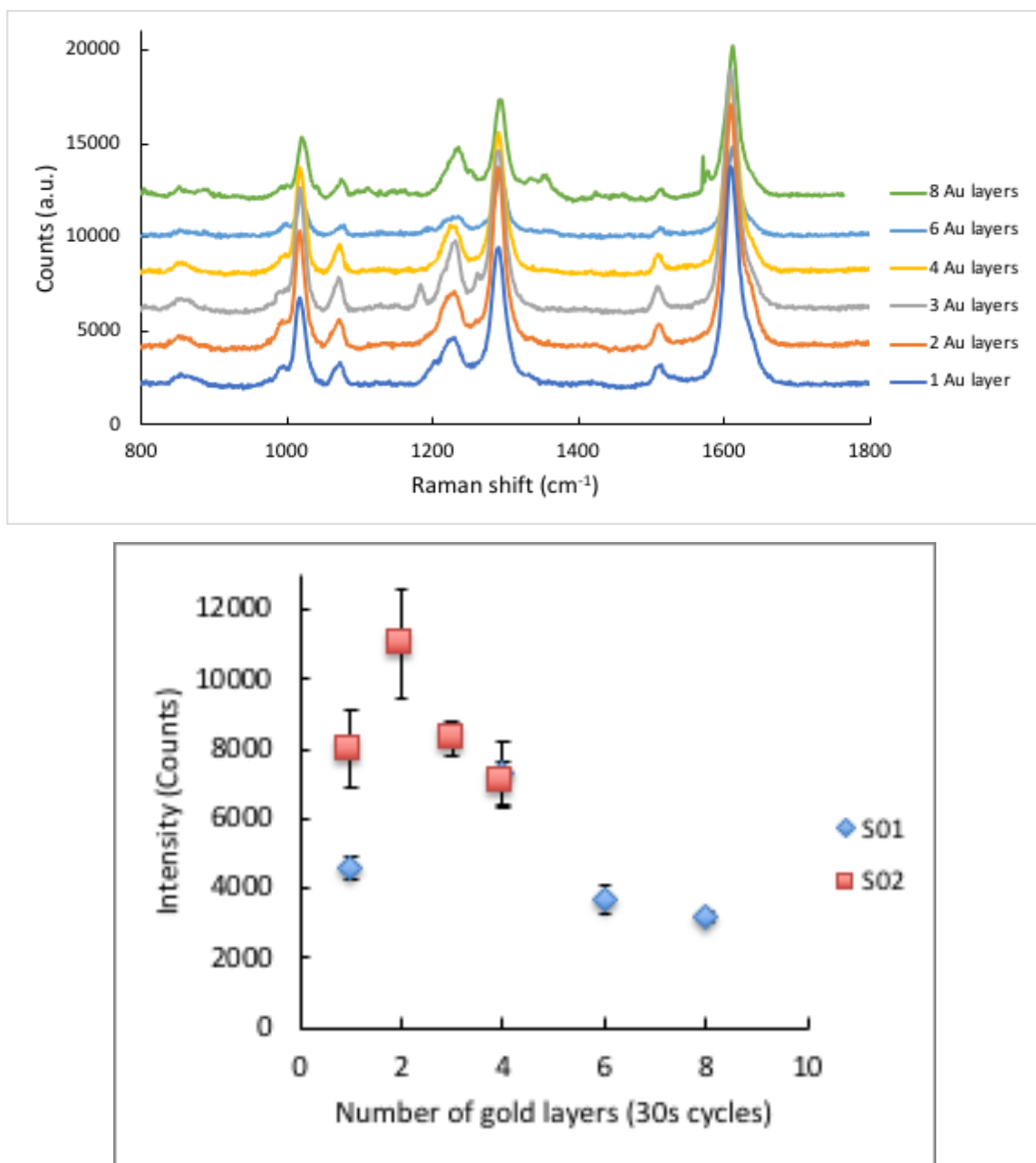


Figure 147 : SERS measurement of 1 μm diameter cavity array with optimized NP size sputtered with several gold layers. A 10 mM ethanolic solution of 4,4'-BPY was used to functionalise the samples. (Top) Representative Raman spectra; (Bottom) Intensity reported correspond to B_2 ring mode at 1293 cm^{-1} (ν_3). ($\lambda_{exc} = 785 \text{ nm}$, 10 acc. 2 s., pin hole $900 \mu\text{m}$, laser power at sample $429 \mu\text{W}$, $n = 8$)

It is likely that most of the SERS signal is coming from the hot spots created by the nano gaps present on the etched NP as seen from FESEM. The gaps appear to be only few nanometres wide and are relatively shallow. Presumably, the sputtered gold layer will conform to the NPs shape perfectly at low coverage but will then start to fill the gaps, smoothening out the nanostructure at higher coverage. This would be expected to reduce SERS performance with extended sputtering. And, indeed, a decrease in SERS signal intensity was observed after more than 60 seconds sputter, where the gold layer is estimated from Figure 146 to be 75 nm thick. Similar effect was reported by Xia et al., where arrays of gold coated etched PS spheres presenting nano gaps at adjacent beads gave better SERS enhancement than arrays without interstitial coupling gap due to gold coating.³¹

This might suggest samples coated for 30 seconds would give the best SERS intensity, as this is the thinnest layer tested. However, as Figure 147 shows, this was not the case. The lower intensity is likely attributed to the quality of the gold layer at thin coverage rather than its thickness, as gold was coated over a polymer without intermediate adhesion layer and may be etched partially during the functionalization of the sample by the 4,4'-BPY ethanolic solution. However, this is difficult to verify and a coating time between 30 and 60 seconds seem to be the best compromise for the last step in the fabrication process of the NP array.

Another explanation could be that the SERS active nano gaps became progressively narrower and sharper as the gold layer was building up, generating stronger electromagnetic fields as described by Nam et al. and Huang et al. with their nano crevices between particles.^{32,33} Overall, however, SERS signal increased until 60 seconds of sputtering, where nano gaps blunted, then decreased, similar to behaviour described by Wei et al. when their nanostructures coalesced as they were closing progressively the gap between it.³⁴

4.3.3 Characterisation

4.3.3.1 FESEM

The optimised arrays with icNPs prepared as described in section 4.2.1 were characterised using FESEM. Figure 148 to Figure 151 show representative FESEM images for NPs in 3 μm , 2 μm , 1 μm and 510 nm diameter cavities.

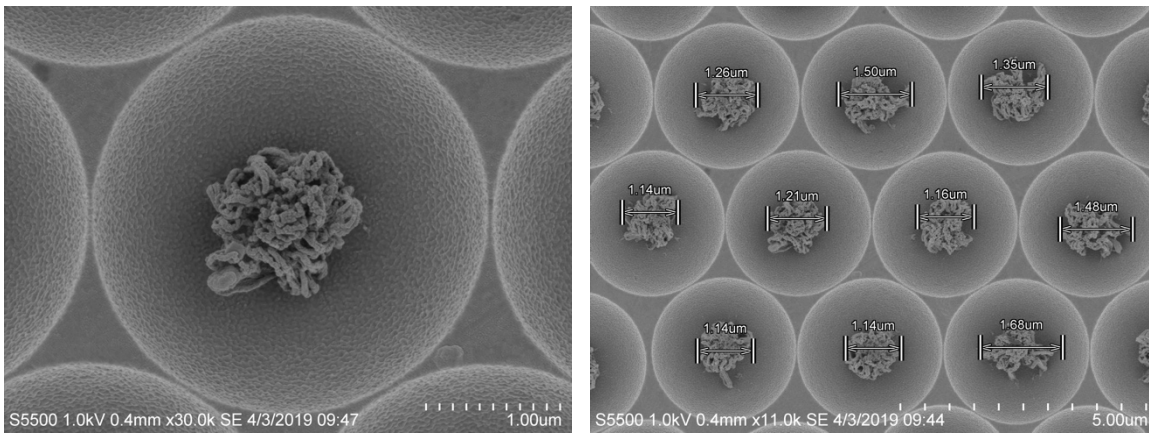


Figure 148 : Representative FESEM images of 3 μm diameter PS spheres in cavity etched for 50 min with a RF power of 100 W.

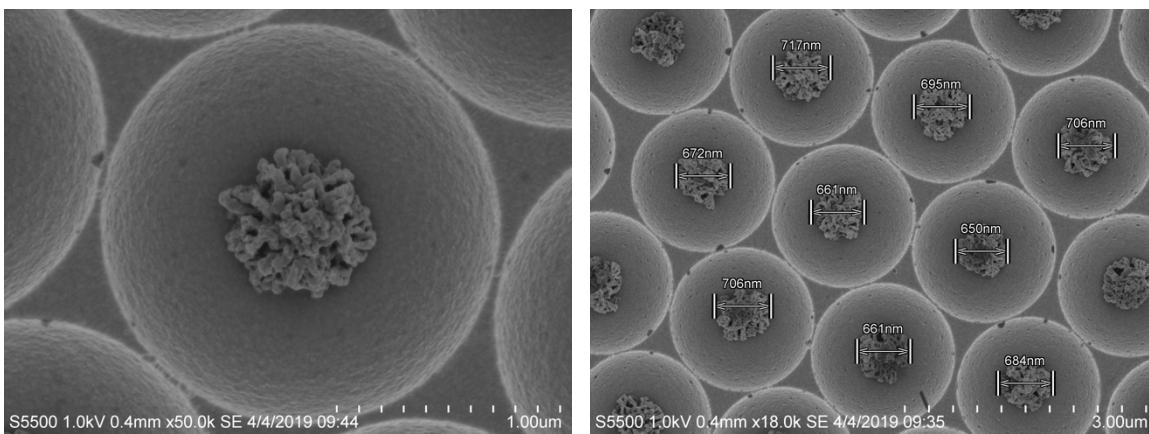


Figure 149 : Representative FESEM images of 2 μm diameter PS spheres in cavity etched for 30 min with a RF power of 100 W.

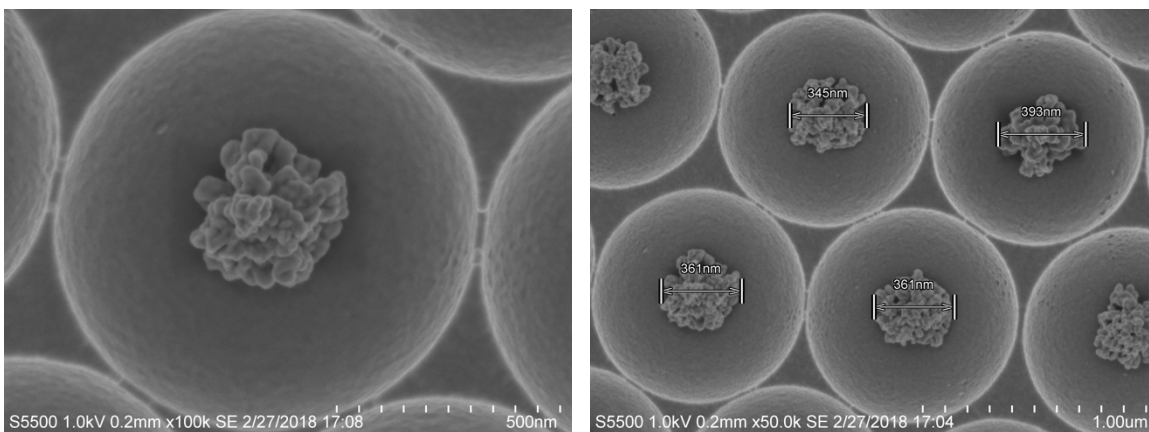


Figure 150 : Representative FESEM images of 1 μm diameter PS spheres in cavity etched for 8 min with a RF power of 100 W.

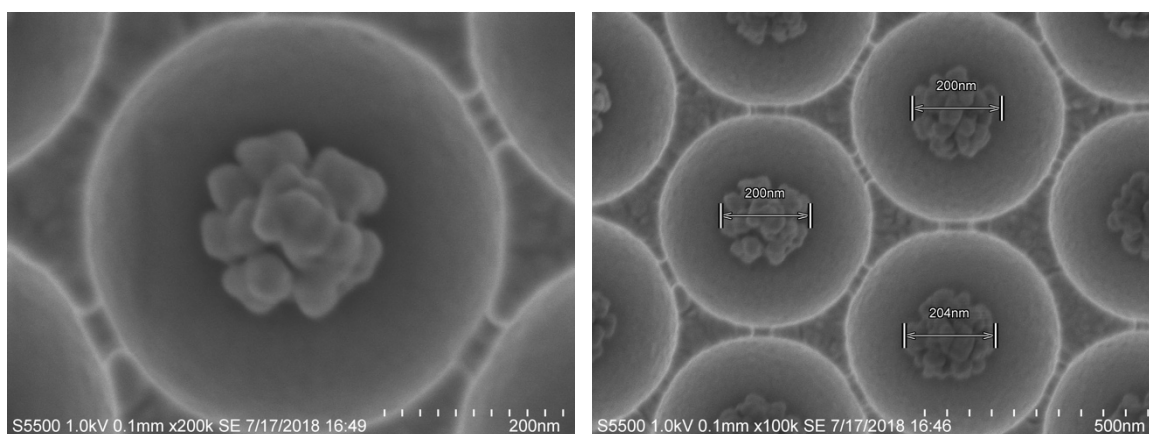


Figure 151 : Representative FESEM images of 510 nm diameter PS spheres in cavity etched for 11 min with a RF power of 50 W.

From these figures can be seen that for each size of cavity array, icNPs are morphologically and dimensionally similar from one cavity to another and at different locations of the same array. Dimensions might vary slightly from one batch to another but remain of the same order of magnitude with variation of only few tens of nanometres. Regarding the morphology of the NPs, large PS spheres of 3 μm and 2 μm diameter seems to etch in a different way than smaller spheres of 1 μm and 510 nm diameter. Indeed, PS fragments induced by the plasma etching tend to be of long filaments shape for large spheres compared to small spheres that etch in small “pills” as illustrated in Figure 152.

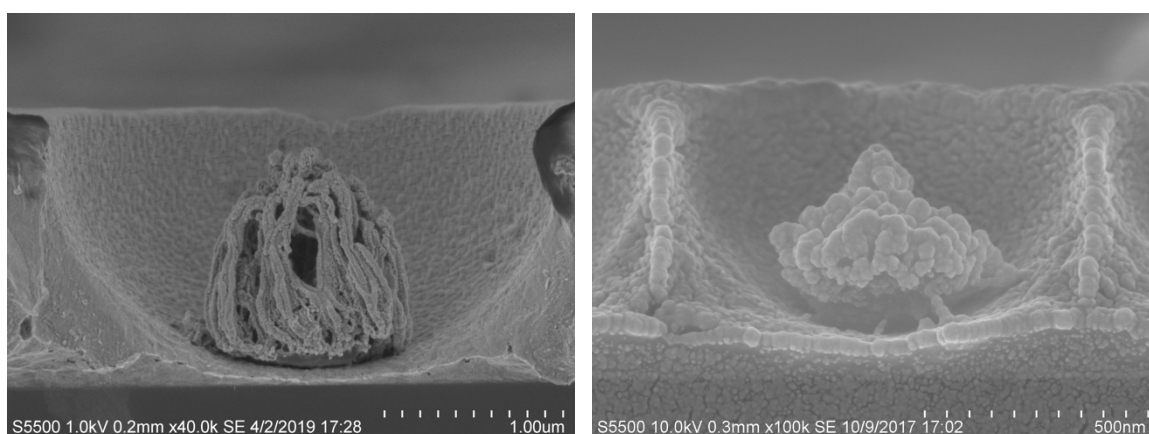


Figure 152 : Side view FESEM images of a 3 μm diameter PS spheres in cavity etched for 50 min with a RF power of 100 W (left) and a 1 μm diameter PS spheres in cavity etched for 8 min with a RF power of 100 W.

Plasma etching of PS spheres within cavities proved a surprisingly reproducible method of nano-modifying the arrays, with nanostructures of very similar shape and

size produced both within a single substrate but also between batches of arrays. This technique has the advantage to leave a nano substructure at the bottom of every single cavity that presents multiple nano-defects with a potential plasmonic activity once coated with a metal. Also, as shown, this fabrication method applies equally to different sizes of PS spheres upon simply adjusting some parameters influencing the etching rate. However, morphology of the obtained nanostructure depends on the etching parameters and also on the material itself as big beads can etch in a different manner than small ones. Hence, number and quality of the hotspots created will vary from one size to another, which is described later in this chapter using different techniques.

However, certain conditions need to be respected if those substrates are aiming to support a lipid bilayer suspended on top of the liquid filled cavities. Indeed, obtaining a monolayer of PS spheres before growing cavities seems to be a key element in the good preparation of the substrates. As explained previously in chapter 3, creating monolayers rather than multi layers of PS spheres at the gold surface helps to a homogeneous hexagonally close packed assembly rather than squarely packed patterns. But more than that, as plasma is damaging the polymer from top to down, any superficial PS spheres would prevent the one in cavity to be etched correctly. Although this might lead to beautiful artistical patterns as presented in Figure 153 with potential plasmonic activity, they will surely though affect the stability of the lipid bilayer if ever it has managed to form.

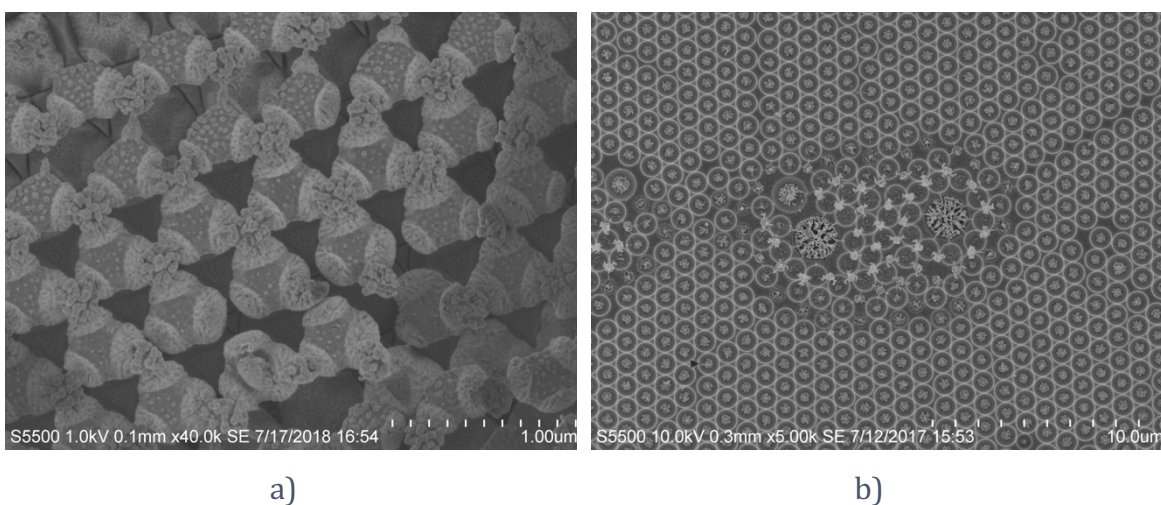


Figure 153 : FESEM images of defects created by etching multilayers assembly of PS spheres at the superficial interstitial space of 500 nm diameter (a) and 1 μm diameter cavity arrays.

4.3.3.2 Diffuse reflectance characterisation

The optimised arrays were characterised by studying their optical properties using diffuse reflectance spectroscopy to obtain insight into their plasmonic resonance.

Starting with 1 μm diameter cavity arrays, diffuse reflectance following every step of the nano structures fabrication was acquired to understand the influence of the fabrication process on the optical properties of the arrays. Background spectra were collected using Spectralon[®] as a standard. Also, bare cavity arrays were compared to the nanoparticle modified arrays and subjected to the same conditions of etching and sputtering process. This enabled gain of direct insights in the impact of the nano structures on the optical properties of the array. Figure 154 and Figure 155 show respectively the diffuse reflectance spectra following the fabrication steps for the array without and with icNPs.

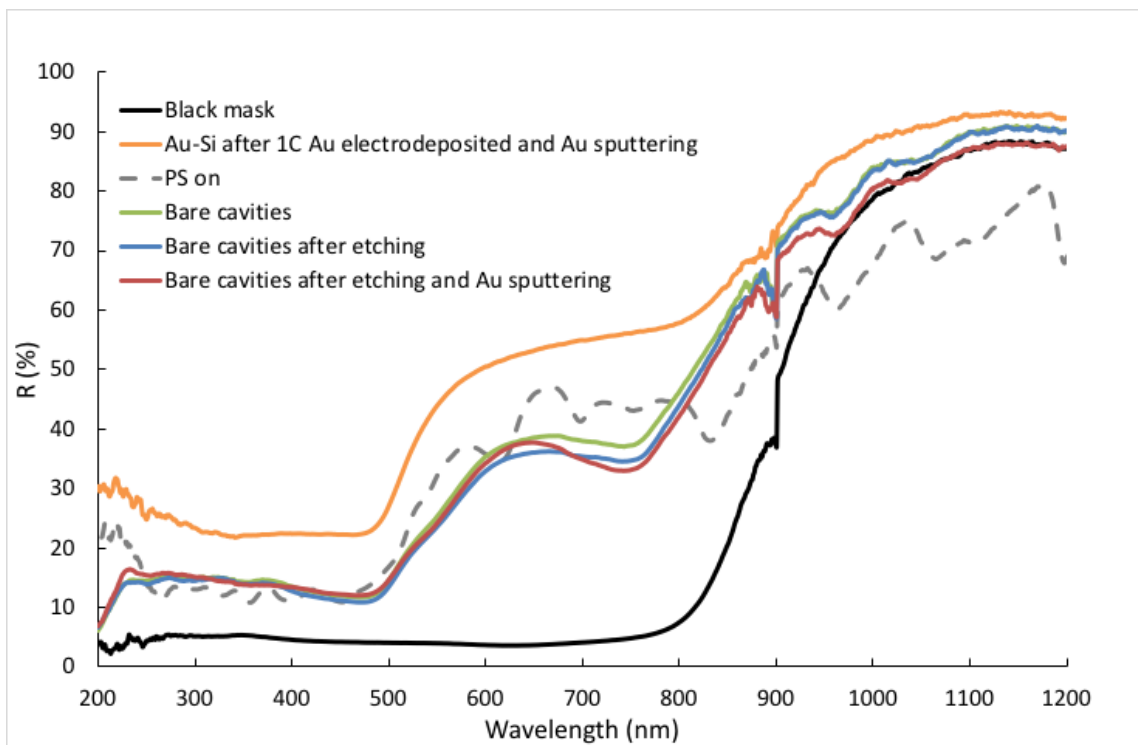


Figure 154 : Diffuse reflectance spectra of the different fabrication steps of a dry bare 1 μm diameter cavity array treated under same etching and coating conditions alongside the icNP array.

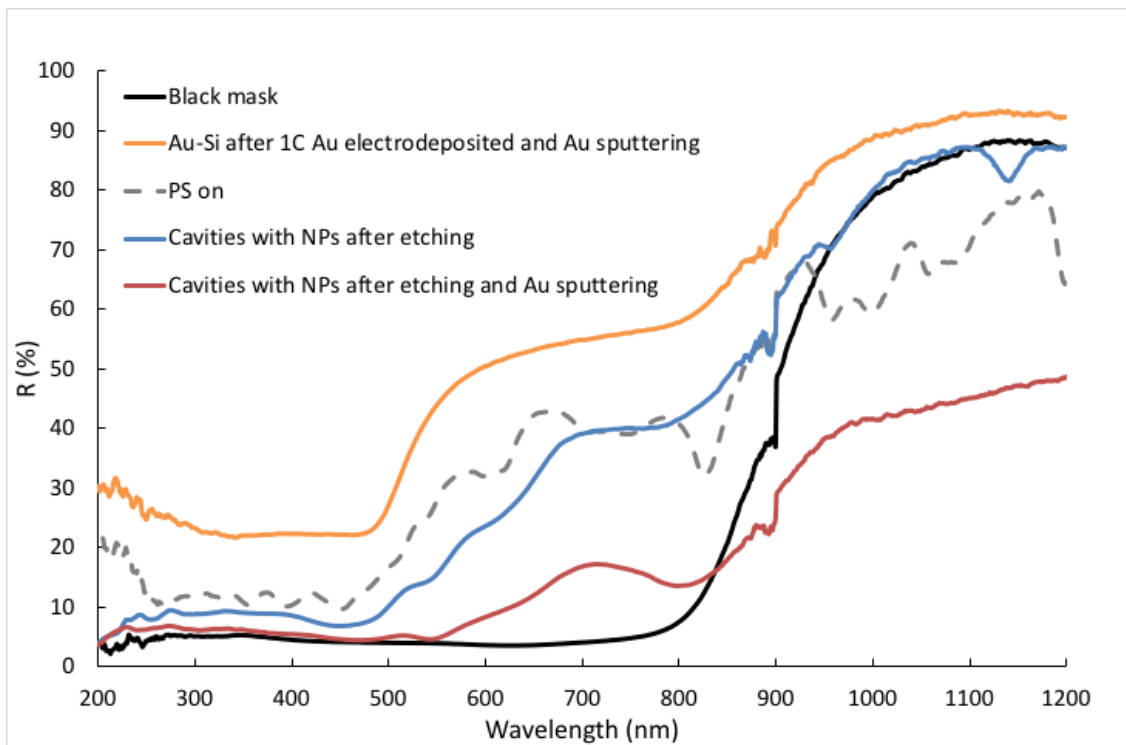


Figure 155 : Diffuse reflectance spectra of the different fabrication steps of a dry 1 μm diameter cavity array with NPs.

It can be seen that the black mask contributes to the reflectance spectra, particularly at wavelengths above 800 nm, where its reflectance increases strongly from 5 % to reach values above 85 %. This is probably due to the illuminated area of the integrating spheres being wider than the measured cavity array. Despite this not being an issue as here we are more interested in shifts of reflectance dips in term of wavelength rather than their absolute values. However, aiming at increasing the sensitivity and specificity for further measurements, base line correction was done by using the Spectralon® standard behind the black mask. Results obtained in these conditions for 510 nm, 2 μm and 3 μm diameter cavity array with and without NPs are presented respectively in Figure 156 to Figure 158.

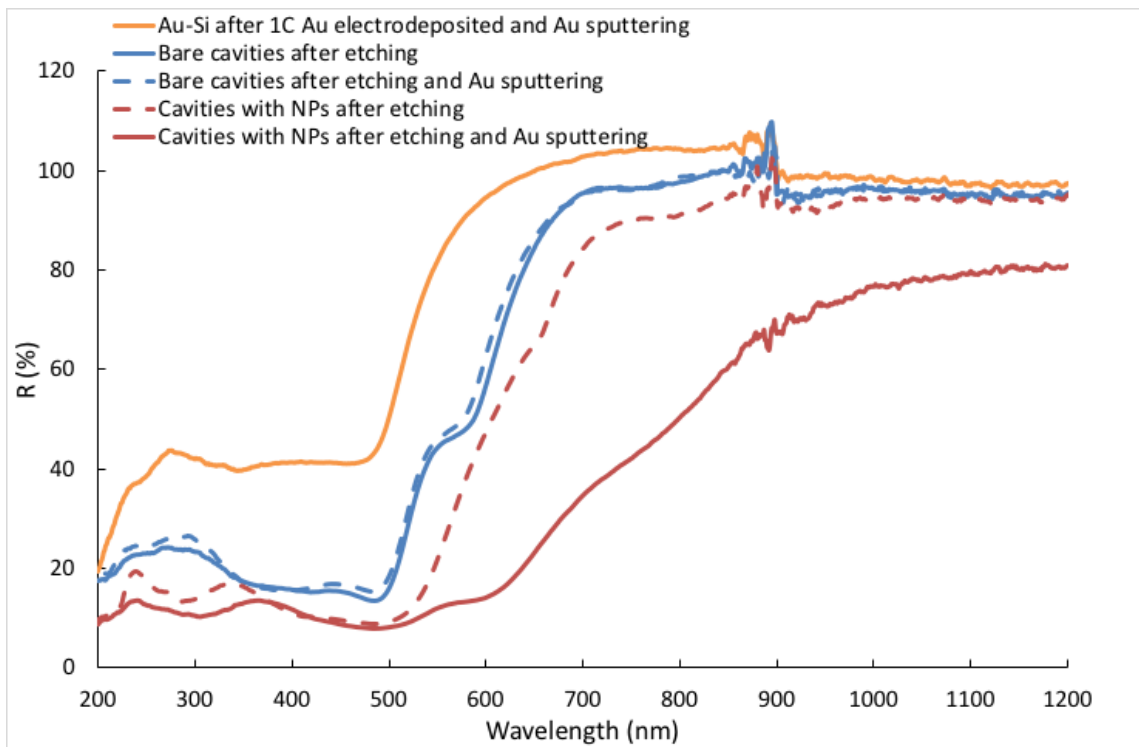


Figure 156 : Diffuse reflectance spectra of a dry 500 nm diameter cavity array with and without NPs.

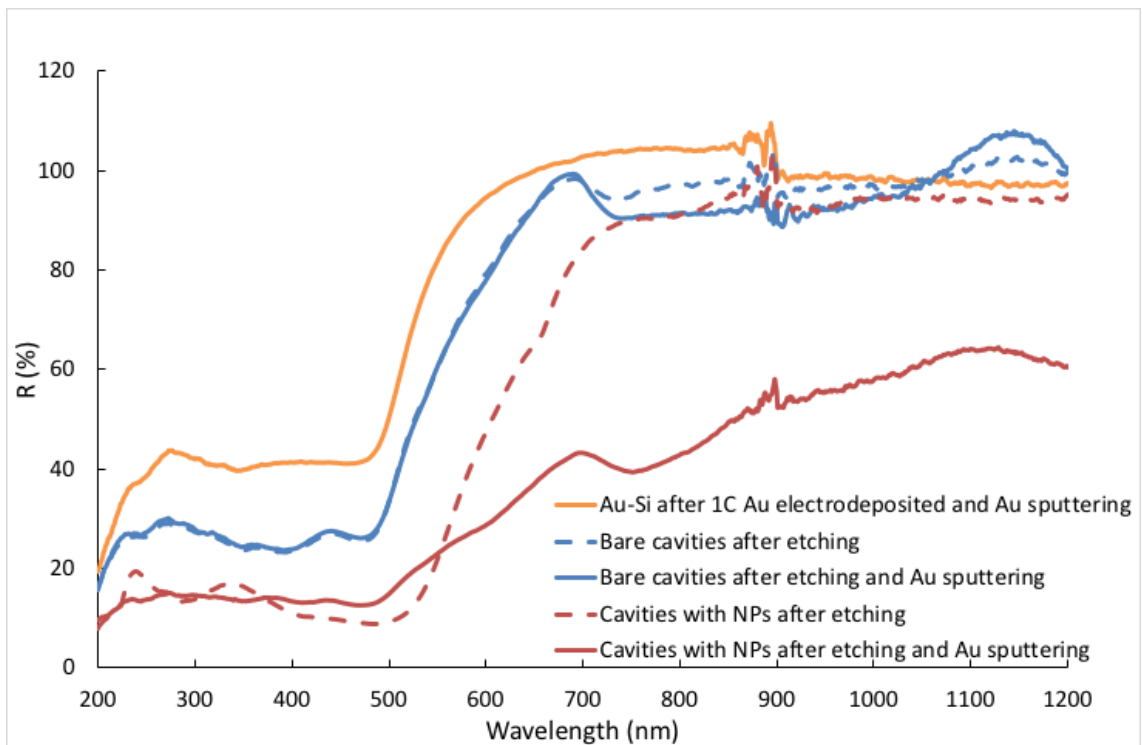


Figure 157 : Diffuse reflectance spectra of a dry 2 μm diameter cavity array with and without NPs.

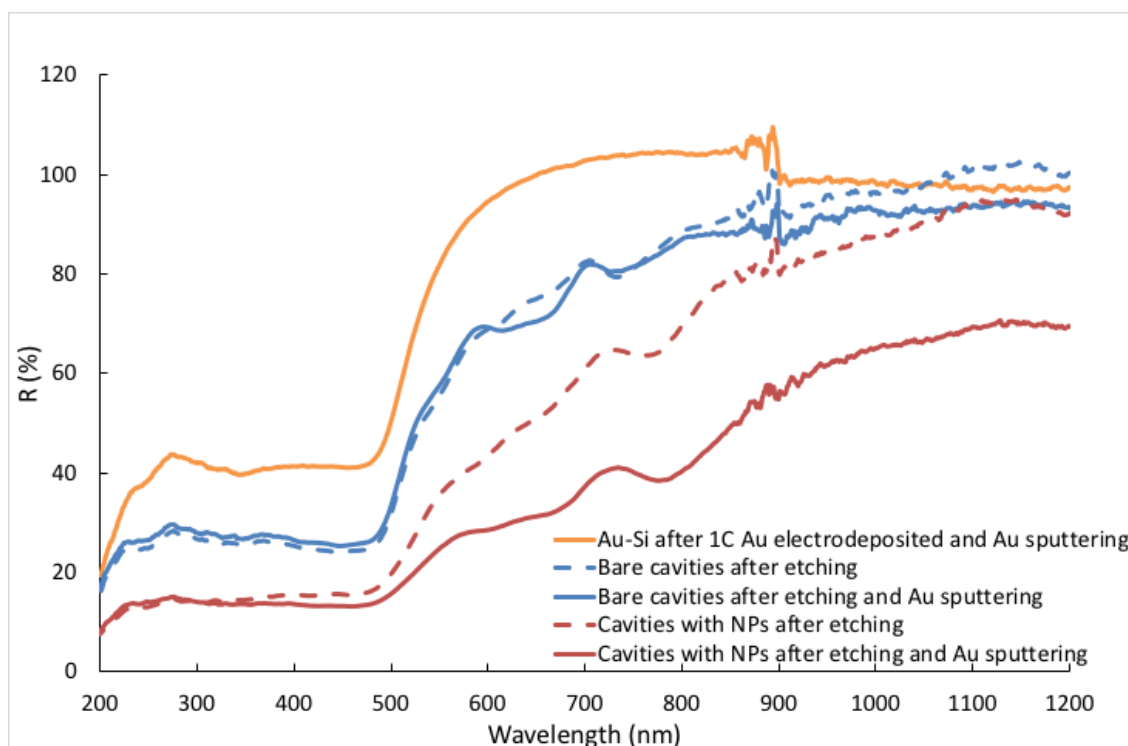


Figure 158 : Diffuse reflectance spectra of a dry 3 μm diameter cavity array with and without NPs.

The yellow line indicates the reference spectrum, which is the reflectance spectrum of gold electrodeposited onto a smooth Au-Si wafer. In all instances, reflectance decreases dramatically for pore arrays compared to planar gold and decreases significantly further, across the visible to NIR optical window, for the nano-structured substrates. This is expected as progressive nano-structuring is anticipated to increase absorbance due to localised surface plasmon modes.³⁵ There is also a systematic shift to the red of the maximum absorbance for a given cavity size on introduction of nanostructuring but the change across the nanostructured arrays as a function of underlying cavity size does not appear to be systematic, i.e. the Surface Plasmon Resonance (SPR) does not systematically shift to the red from large to small cavity with nanostructure. Specifically, 510 nm diameter cavities, the lowest energy resonance shifts from 570 nm to 600 nm, for 1 μm diameter cavities, it shifts from 745 nm to 800 nm, for 2 μm diameter cavities, it shifts from 740 nm to 750 nm, and finally for 3 μm diameter cavities, it shifts from 735 nm to 780 nm.

In addition, within the different sizes of nano-structured substrates, one must consider the surface morphology of the icNP, i.e. shape and roughness, which differs significantly for different particle sizes, as discussed above (cf. Figure 152).

Remembering that the diffuse reflectance spectra contains contribution from both localised and propagating plasmon, the shift is influenced by three factors. The first, the surface morphology, can be viewed as series of inter-coupled plasmonic nanoparticles (see Figure 159 b)).³⁶ In general, this implies that the shift should increase with the increasing nano roughness. The second is the 3D geometry of the icNP, i.e. diameter and height of the structure influences the number of hot spots at the structure surface. Finally, the red shift can also be attributed to the electromagnetic coupling between the icNPs and the 2nd order surface propagating plasmon mode (⁰D in Cole et al.),^{1,37}

4.3.3.3 FDTD simulations

As explained in chapter 3, FDTD simulation is a powerful tool that can help to understand the evolution and location of the electric field at the array. To understand more deeply the impact of the NP on the optical properties of the array, FDTD was performed by Dr. Kiang Wei Kho for arrays with 1 μm diameter cavities. To approximate the nanostructure, based on what we understand of its structure from FESEM characterisation, we used a superposition of elongated nano beads that form a pyramidal shape as a representation of the etched PS spheres.

FDTD simulations for 1 μm diameter cavity array with NPs, illuminating the sample with a normal incidence and 785 nm light, are presented in Figure 159 and compared with the simulation under the same conditions for a bare cavity sample. This figure allows comparison of the location and intensity of the electric field at the array. For the bare cavity two lobes corresponding to hotspots at the bottom of the well are seen. The amplitude of the electric field at this location is only about 50 % higher than the one at the mouth of the cavity. By comparison for the same diameter cavities with NPs, the amplitude of the electric field at the NPs is about 700% higher than at the mouth of the cavity. In comparison with the electric field at the bottom of bare cavities, this represents approximately a 4-fold increase. From the perspective of isolating enhancement to below the suspended bilayer and maximising signal amplitude, this suggests that the nano-substructures offer significant advantage over the bare cavity.

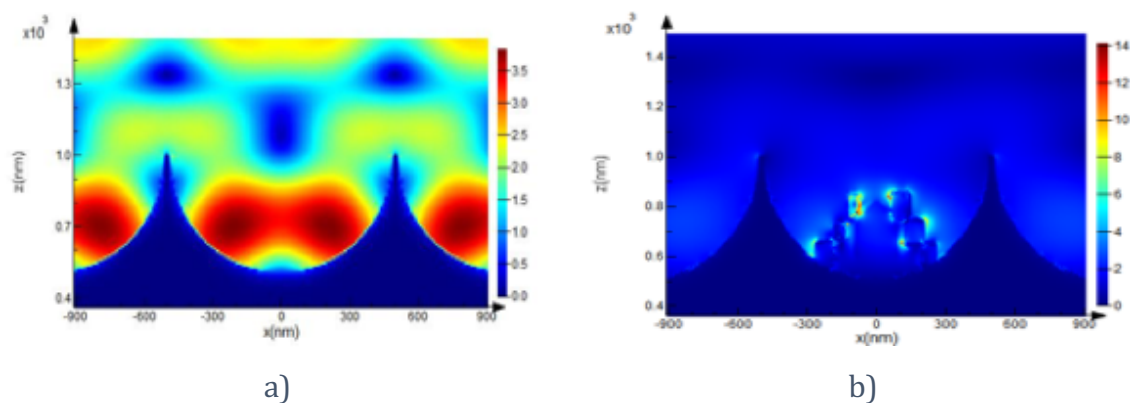


Figure 159: FDTD simulation of a 1 μm diameter cavity array without (a) and with (b) nanostructures under a 785 nm excitation laser at a normal incidence. Here, the field amplitude (right y axis) was not normalized and indicates the most intense value achieved at the nanostructure.

FDTD simulations were carried out under excitation corresponding to the three other lasers available in our laboratory (473 nm, 532 nm and 633 nm) and corresponding SERS experimental data were acquired. To measure SERS, the arrays were modified with a 4,4'-BPY self-assembled monolayer by overnight incubation with a 10 mM ethanolic solution. Figure 160 shows FDTD simulation obtained for 473 nm, 532 nm, 633 nm and 785 nm excitation and the corresponding SERS spectra after normalisation to the signal obtain for a silicon sample during calibration. Simulations are displayed here with the same scale of electric field to enable interpretation of variation of intensity with wavelength of light. As excitation shifts to the red, FDTD simulations show increasing intensity of the electric field at the NP surface. Experimental data correlate with these predictions as the intensity of the SERS signal increases with red excitation, with best SERS performance under 785 nm excitation laser. This also correlates with diffuse reflectance results shown in previous section, where the plasmon absorbance maxima was found to be around 800 nm for such arrays.

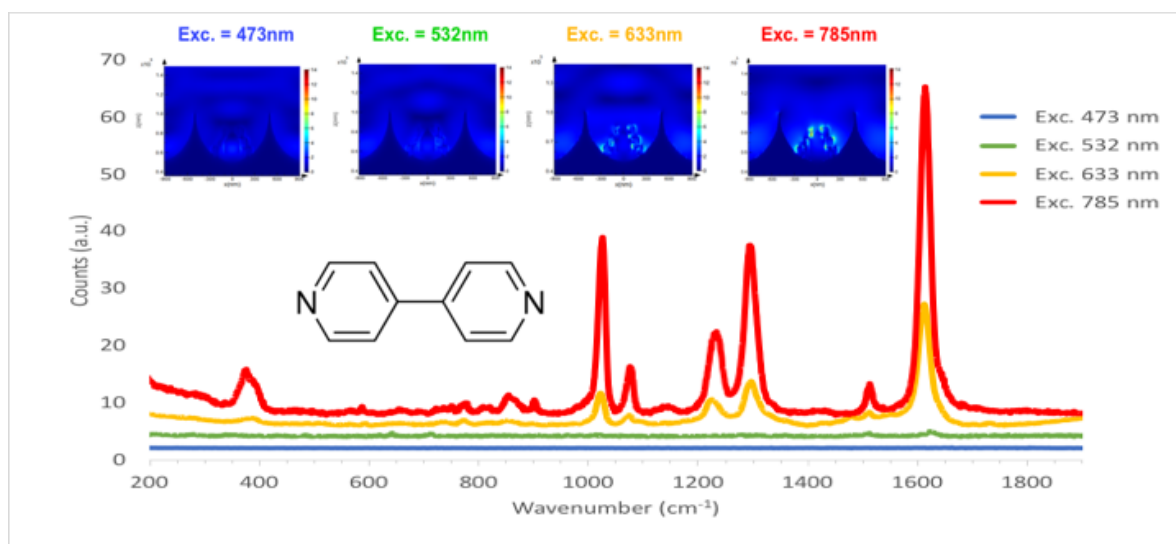


Figure 160 : FDTD simulations of a 1 μm diameter cavity array with nanostructures under 473 nm, 532 nm, 633 nm and 785 nm excitation laser and their corresponding normalized SERS spectra of a 4,4' BPY SAM functionalized at their surface.

Although FDTD simulations need to be interpreted carefully, particularly 2D simulations which are not ideally representative of 3D structures, they remain a powerful tool to understand intensity and repartition of the field at the array. Also, they can aid in predicting the number of hotspots at the surface of the NP contributing to the SERS signal is a challenge due to factors such as non-3D simulations, variability of structures between cavities and the approximate nature of the shape used in the simulation. Differences at a nanoscale can obviously have a dramatic influence on the intensity of hotspots.

Despite these limitations, the presented simulations match well to experimental data, suggesting they reflect accurately the developed substrates. FDTD simulations for other sizes of cavity / NPs are not yet studied as the shape of the nanostructure differs, as shown during the FESEM characterisation, and would need more details to adjust the morphology closer to the reality.

4.3.3.4 Influence of medium on SERS signal: air vs. water measurements

SERS measurement of surface modified 1 μm cavity arrays with and without NPs were first acquired on dry samples. To make sure variation in signal between bare cavity and NPs arrays was only coming from the presence of the nano structures, samples were split in half and comparison of signal was done among two sub-samples from the same array. Both types of array were giving good SERS signal, but their relative enhancement varied drastically from one batch to another, showing

sometimes better SERS intensity from bare arrays compared to ones with NPs, thus questioning the reproducibility of the fabrication process.

Measurement of identical sample were carried out in water and air to understand if medium played a role. A reusable microfluidic device presented in chapter 3 was then designed, to host samples for SERS / MEF measurements in liquid to maximise reproducibility of experimental conditions.

Initially to ensure liquid filling, arrays were sonicated in water for three minutes, however, even under such relatively short sonication, damage was cause to the NPs causing detachment of NPs from several cavities, as shown in Figure 161.

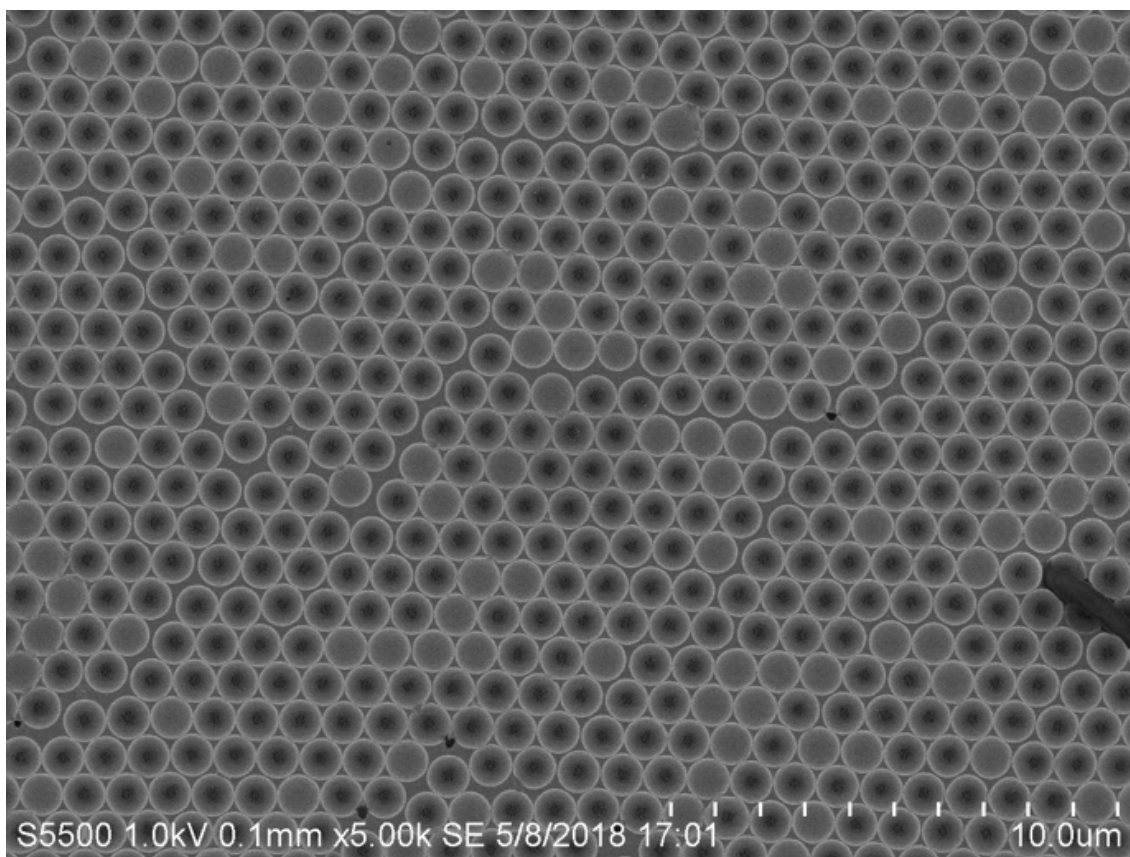


Figure 161 : SEM image of 1 μm diameter cavity arrays with nano substructures damaged by sonication in water.

A gentler method was adopted to ensure the physical integrity of the samples, whereby arrays were first dipped in ethanol. As ethanol has a lower surface tension than water, cavities were pre-wet allowing water to penetrate easily in cavities because of its high solubility in ethanol. Arrays were then rinsed with a copious amount of deionised water to make sure no ethanol remained in cavities. Figure 162 presents

results obtained for samples functionalised with 4,4'-BPY and for which SERS signal was acquired in air (a) and in water (b) for comparison.

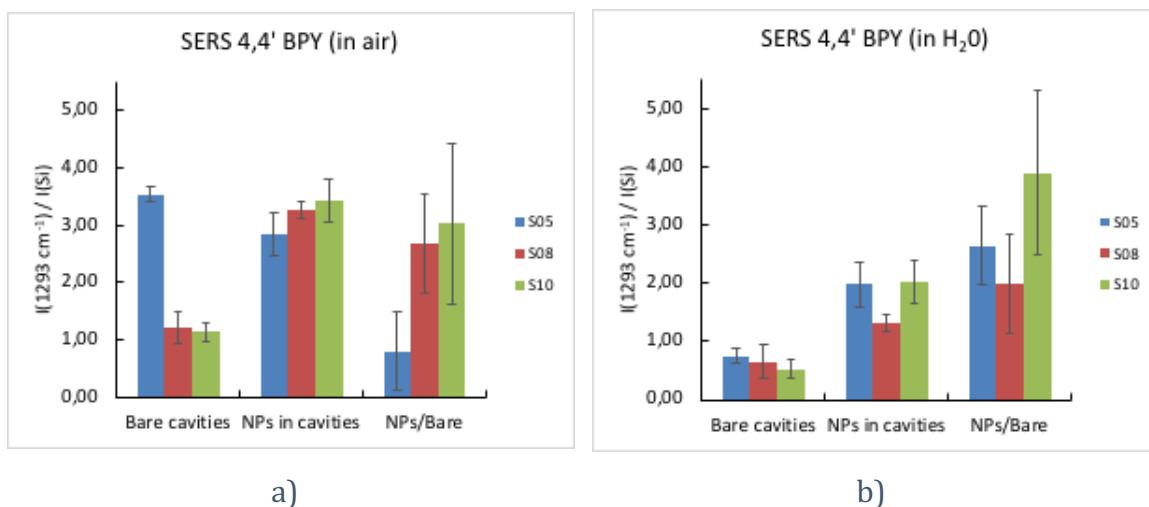


Figure 162 : SERS measurement of a 4,4' BPY SAM formed onto 1µm diameter cavity arrays with and without NPs in air (a) vs. in water (b). in reproducibility conditions. A 10 mM ethanolic solution of 4,4'-BPY was used to functionalise the samples. Intensity reported correspond to B₂ ring mode at 1293 cm⁻¹ (ν₃). (λ_{exc} = 785 nm, 10 acc. 2 s., pin hole 900 µm, laser power at sample 94 µW)

Interestingly, SERS signal in air proved generally to be more intense than in water for both bare cavities and cavities with nanoparticles. However, variability across bare samples was lower for measurements done in water than on dry samples, giving a more stable SERS signal between the different batches fabricated. Despite the intense and reproducible signal obtained with nanoparticles present, SERS measurement at dry samples does not allow one to conclude if the enhancement is coming from the nanoparticles or from the cavity itself as some samples do not show relative enhancement between the two types of arrays (cf. S05 sample). Though, once measurement is acquired in water, relative enhancement fluctuates between factors of two and four where signal from bare cavities is always significantly lower than signal from array with NPs. Those results suggest that water helped to cool down samples and to obtain more reproducible results from batch to batch.

This observation agrees with a study by Zeng et al.³⁸, who concluded through simulations that very high temperatures can be created at hotspots of aggregated NPs and confirm by experiment that heating effect must be minimised to maintain a stable SERS signal. Doing measurement with particles in contact with water, sitting on a conductive substrate gave the lowest increase in temperature. A rise in temperature can be an advantage for some applications such as photothermal therapy, where metal

nanoparticles have been successfully used to selectively kill cells as the metal converts rapidly the absorbed photon energy from the laser into heat. Gregory V. Hartland reviews in his paper³⁹ events that occur following absorption of photons when using metal nanoparticles, discussing the different photophysical process that can induce heating. In our work, heat is a disadvantage as it may alter physically the NP by changing its morphology due to the heat-induced annealing of the particles and the underlying PS.

Thus, all subsequent SERS or MEF measurements were acquired in water using the above described microfluidic device. Also, as the end application of the device is aqueous, it is most important to understand the behaviour of the nano sub-structured arrays in water.

4.3.3.5 Optimised cavity / nano particle sizes for SERS measurements

The performance and signal reproducibility of arrays made through the optimised route defined above, were then evaluated. SERS performance from NPs modified cavity arrays was compared to bare cavity arrays fabricated under identical conditions.

This was achieved by preparing a large array of the cavities of the desired size as described in section 4.2.1. Each sample was then split in half, with one half used as bare cavity array once the PS spheres were washed out, and the second half subjected to plasma etching of the spheres for NPs modification. To ensure as much analogy as possible between each array, each of the split arrays were etched and sputtered with gold at the same time, following the optimised parameters for the corresponding cavity size. Samples were then left to functionalise overnight to form a SAM of 4,4'-BPY for SERS characterisation.

This methodology was repeated for a minimum of three pairs of bare / NPs in cavity arrays obtained from completely independent fabrication batches. Each result presented below is an average of minimum height SERS spectra acquired across the whole area of the tested sample, which guarantee representative results of the capability of each substrate regarding SERS performance. Figure 163 to Figure 166 show results obtained respectively for 3 μm , 2 μm , 1 μm and 510 nm diameter cavity arrays with and without NPs.

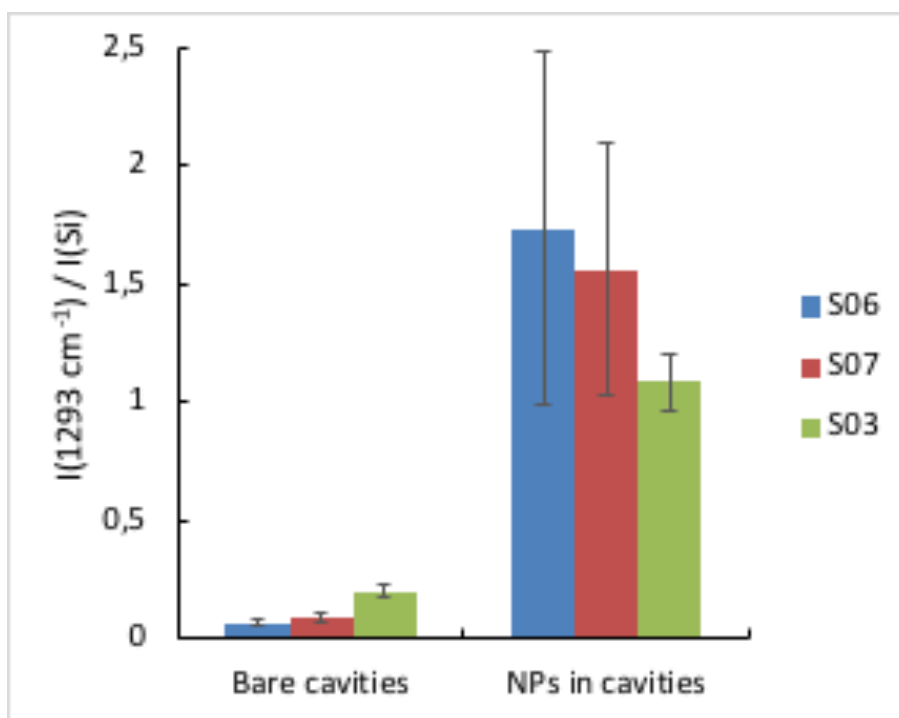
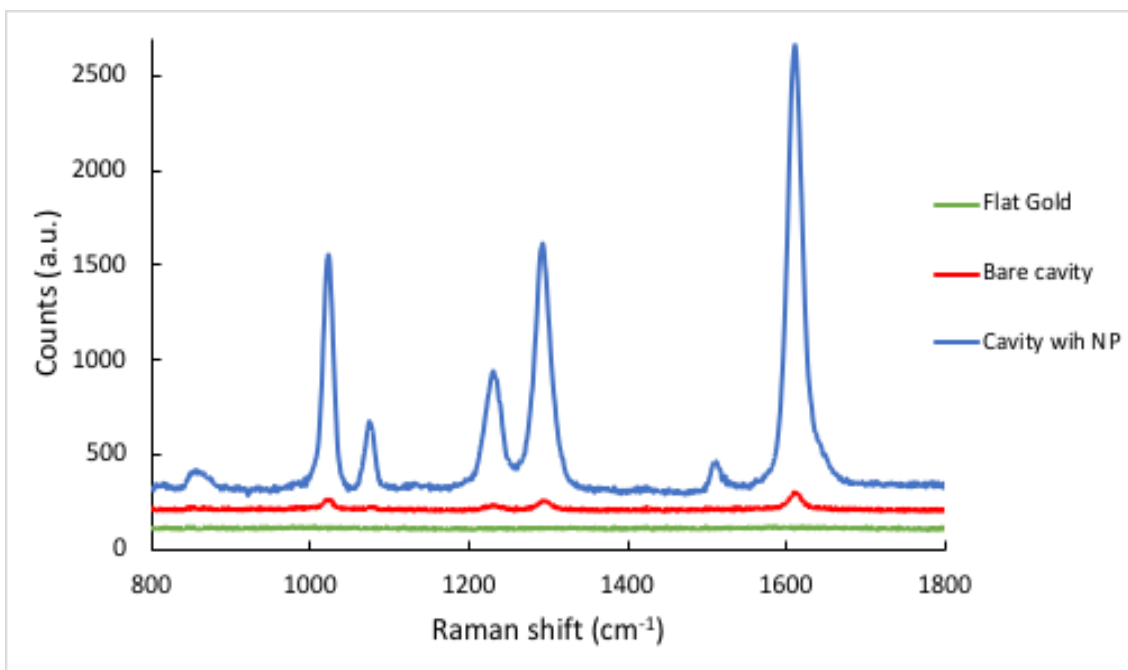


Figure 163 : SERS measurement of a 4,4' BPY SAM formed onto 3 μm diameter cavity arrays with and without NPs fabricated in reproducibility conditions. A 10 mM ethanolic solution of 4,4'-BPY was used to functionalise the samples. (Top) Representative Raman spectra; (Bottom) Intensity reported correspond to B₂ ring mode at 1293 cm^{-1} (ν_3). ($\lambda_{\text{exc}} = 785 \text{ nm}$, 10 acc. 2 s., pin hole 500 μm , laser power at sample 429 μW)

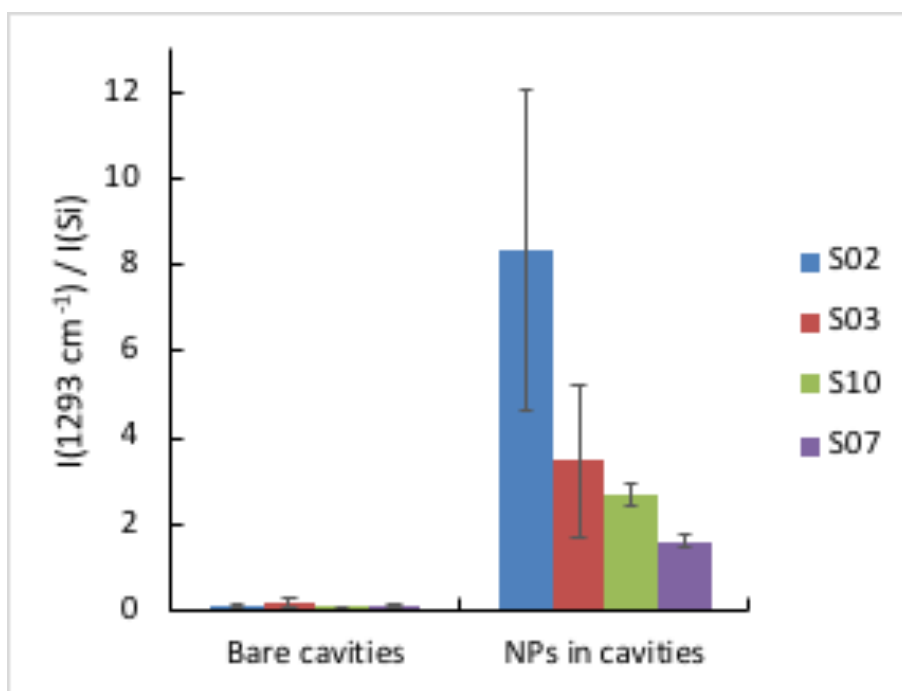
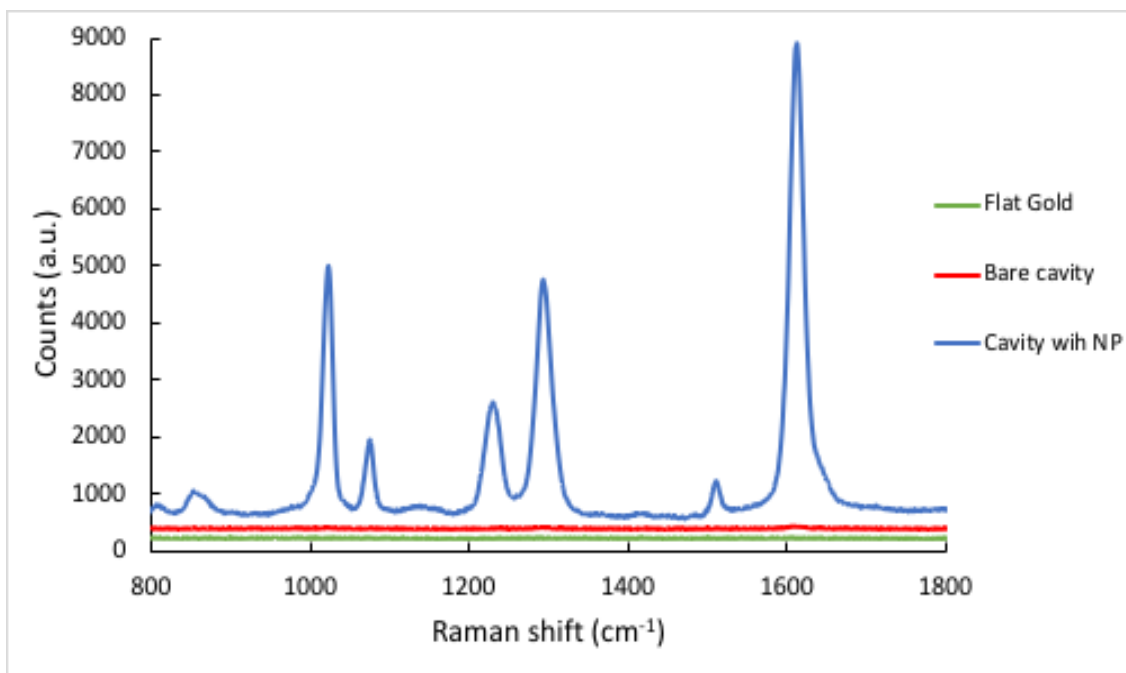


Figure 164 : SERS measurement of a 4,4' BPY SAM formed onto 2 μm diameter cavity arrays with and without NPs fabricated in reproducibility conditions. A 10 mM ethanolic solution of 4,4'-BPY was used to functionalise the samples. (Top) Representative Raman spectra; (Bottom) Intensity reported correspond to B_2 ring mode at 1293 cm^{-1} (ν_3). ($\lambda_{\text{exc}} = 785 \text{ nm}$, 10 acc. 2 s., pin hole $500 \mu\text{m}$, laser power at sample $429 \mu\text{W}$)

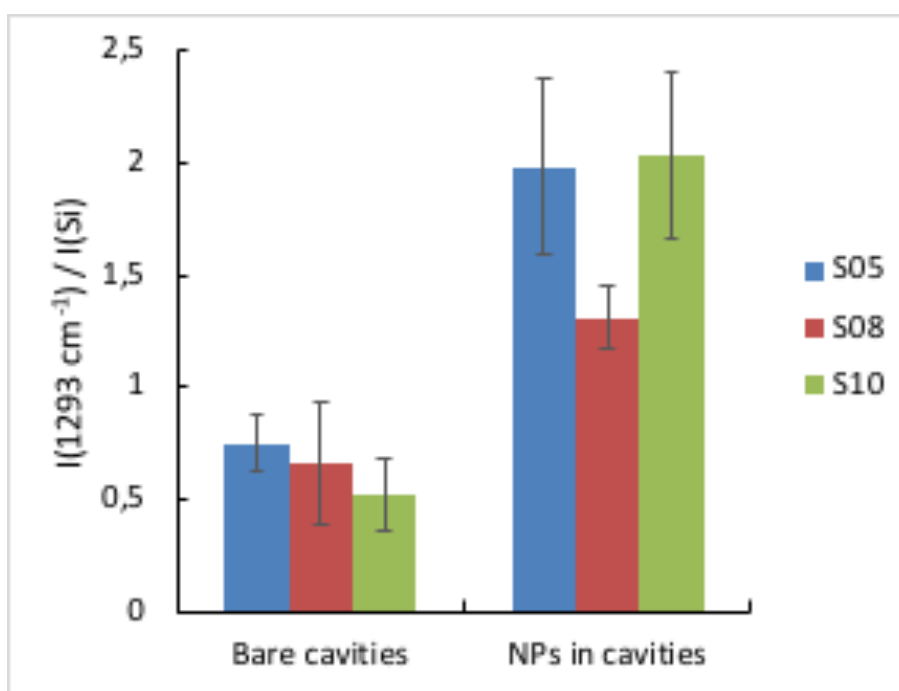
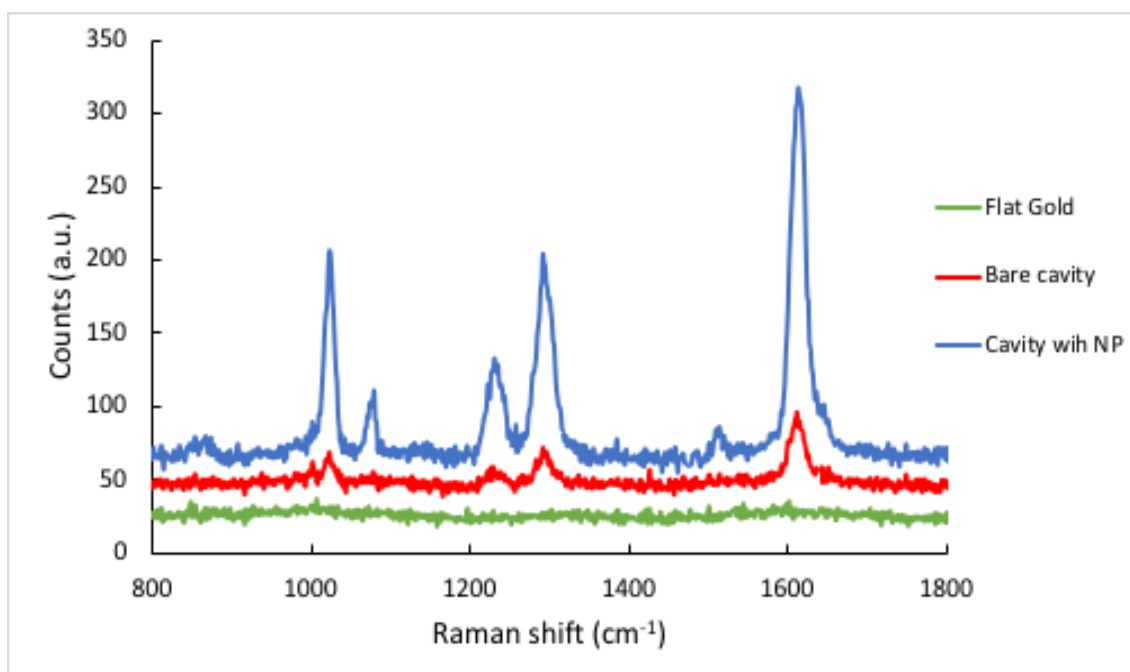


Figure 165 : SERS measurement of a 4,4' BPY SAM formed onto 1 μm diameter cavity arrays with and without NPs fabricated in reproducibility conditions. A 10 mM ethanolic solution of 4,4'-BPY was used to functionalise the samples. (Top) Representative Raman spectra; (Bottom) Intensity reported correspond to B_2 ring mode at 1293 cm^{-1} (ν_3). ($\lambda_{\text{exc}} = 785 \text{ nm}$, 10 acc. 2 s., pin hole 500 μm , laser power at sample 94 μW)

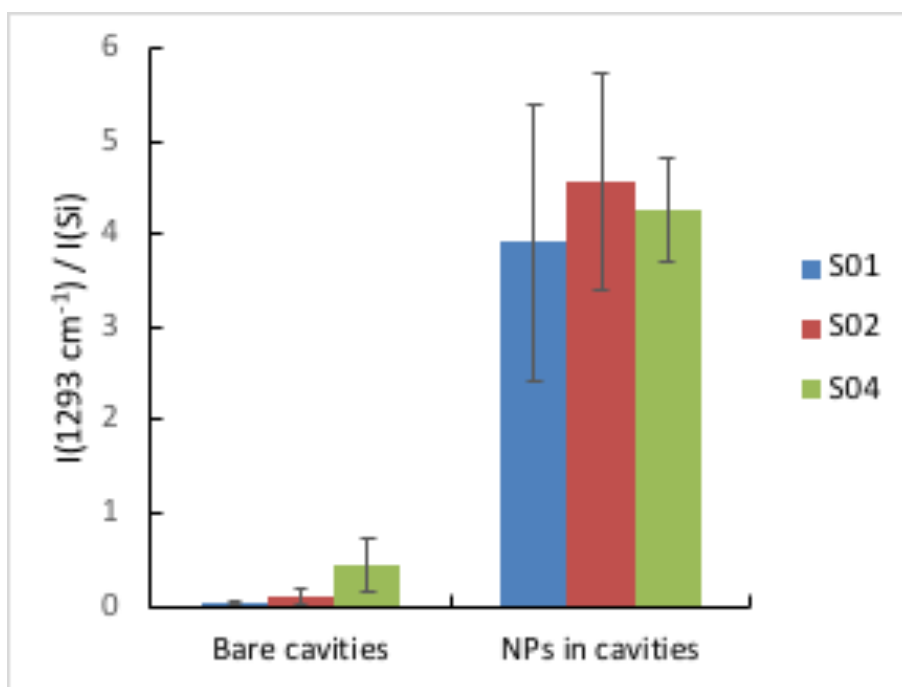
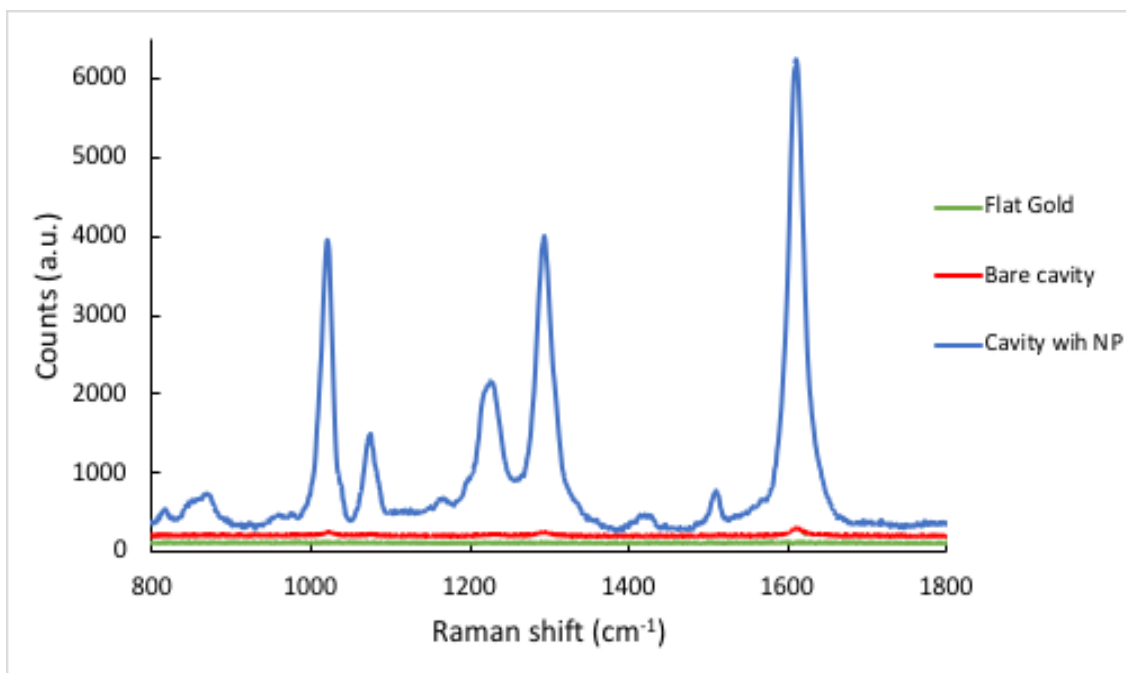


Figure 166 : SERS measurement of a 4,4' BPY SAM formed onto 510 nm diameter cavity arrays with and without NPs fabricated in reproducibility conditions. A 10 mM ethanolic solution of 4,4'-BPY was used to functionalise the samples. (Top) Representative Raman spectra; (Bottom) Intensity reported correspond to B₂ ring mode at 1293 cm⁻¹ (ν₃). (λ_{exc} = 785 nm, 10 acc. 2 s., pin hole 500 μm, laser power at sample 429 μW)

Regardless of cavity size, the presence of NPs inside the wells always leads to a better enhancement of the SERS signal than for bare cavity arrays. 3 μm diameter cavities with NPs gave on average the lowest intensity of SERS signal among the four types of nano sub-structured arrays. 510 nm and 2 μm diameter cavities with NPs gave on average the highest intensity of SERS compared with their bare cavity array

analogues. However, intra- and inter-sample variability differs widely among the different types of substrates tested, reflected in the error bars shown.

Table 7 to Table 10 summarize and allow to compare the intra- and inter-sample variability for bare and cavities with NPs of the different developed sizes.

Intra-sample measurements show a reasonable variability, which is acceptable regarding the nature of the fabrication process involved here. Indeed, the developed method is not expensive or laborious as EBL, FIB or photolithography but can still guarantee a good control over the arrangement of the SERS active structures. Variability across different sites of a single substrate range between 16 % and 30 % on average, except for 510 nm diameter bare cavities for which the intra-sample CV could be as high as 59%. The higher variability is likely due to the greater difficulty in controlling the fabrication process for small cavities close packed arrays. Indeed, uniform large array areas are more difficult to obtain with PS spheres below 1 μm diameter as described in chapter 3. The arrangement of the spheres on the gold surfaces may differ from one sample to another, impacting the surface plasmon resonance of the array. Furthermore, gold electrodeposition around the spheres is also likely to play a key role in reproducibility of the array. As the layer of gold is thinner for smaller diameter arrays, controlling the height of the cavity over the whole area of the substrate is more challenging. One way to improve this would be to use a lower potential during the electrodeposition which will decrease the rate of gold growth and might help obtain a more homogeneous substrate.

Regarding inter-sample variability, it seems that the presence of NPs stabilises SERS performance for arrays of 3 μm and 510 nm diameter cavities as the inter-sample CV improves respectively from 60 % to 23 % for 3 μm and from 111 % to 8 % for 510 nm diameter cavities. This last result shows that despite the difficulty to control the early stage of the fabrication process for nanocavities, i.e. the shape and arrangement over the whole array, the fabrication of the nanostructures within cavities is reproducible and give consistent results over the three samples tested, as the enhancement comes mainly from the nano sub-structure. The dramatic reduction in variability also strongly indicates that primary enhancement from the nano-sub-structured substrates is coming from the particles in the cavity interior for these substrates. However, interestingly, the relatively low variability of 1 μm diameter bare

cavity arrays of 18 % is not improved by the presence of NPs which shows CV inter-sample of 23%. Finally, despite good enhancement of SERS signal, the NP modified 2 μm diameter cavity arrays gives very variable results, for both bare and NPs substrates with inter-sample CVs of 46% and 74% respectively.

Table 7 : SERS measurement of a 4,4' BPY SAM formed onto 3 μm diameter cavity arrays with and without NPs fabricated in reproducibility conditions with their associated CV.

3 μm diam.	Bare cavities		NPs in cavities	
	$I_{\text{SERS}} / I_{\text{Si}}$	CV (%)	$I_{\text{SERS}} / I_{\text{Si}}$	CV (%)
S06	0.07	21 %	1.74	43 %
S07	0.09	18 %	1.57	34 %
S03	0.20	12 %	1.09	11 %
Intra-sample		17 %		29 %
Inter-sample	0.12	60 %	1.46	23 %

Table 8 : SERS measurement of a 4,4' BPY SAM formed onto 2 μm diameter cavity arrays with and without NPs fabricated in reproducibility conditions with their associated CV.

2 μm diam.	Bare cavities		NPs in cavities	
	$I_{\text{SERS}} / I_{\text{Si}}$	CV (%)	$I_{\text{SERS}} / I_{\text{Si}}$	CV (%)
S02	0.09	13 %	8.33	45 %
S03	0.17	47 %	3.47	51 %
S10	0.05	41 %	2.70	10 %
S07	0.11	14 %	1.60	9 %
Intra-sample		28 %		28 %
Inter-sample	0.11	46 %	4.02	74 %

Table 9 : SERS measurement of a 4,4' BPY SAM formed onto 1 μm diameter cavity arrays with and without NPs fabricated in reproducibility conditions with their associated CV.

1 μm diam.	Bare cavities		NPs in cavities	
	$I_{\text{SERS}} / I_{\text{Si}}$	CV (%)	$I_{\text{SERS}} / I_{\text{Si}}$	CV (%)
S05	0.75	17 %	1.98	20 %
S08	0.66	42 %	1.31	11 %
S10	0.52	31 %	2.03	18 %
Intra-sample		30 %		16 %
Inter-sample	0.64	18 %	1.78	23 %

Table 10 : SERS measurement of a 4,4' BPY SAM formed onto 510 nm diameter cavity arrays with and without NPs fabricated in reproducibility conditions with their associated CV.

500 nm diam.	Bare cavities		NPs in cavities	
	$I_{\text{SERS}} / I_{\text{Si}}$	CV (%)	$I_{\text{SERS}} / I_{\text{Si}}$	CV (%)
S01	0.04	36 %	3.92	38 %
S02	0.11	79 %	4.56	26 %
S04	0.46	62 %	4.25	13 %
Intra-sample		59 %		26 %
Inter-sample	0.20	111 %	4.25	8 %

Based on the relative Raman intensity of the ν_3 inter-ring stretching (B_2 ring) mode at 1293 cm^{-1} , SERS enhancement factors (EF_{SERS}) could be estimated for the different cavity dimensions with and without icNPs using Equation 24, where I_{RS} and N_{RS} are respectively the Raman signal intensity and the corresponding number of molecules for 4,4'-BPY in its solid form, and I_{SERS} and N_{SERS} the SERS signal intensity and the corresponding number of molecules at the SERS substrate's surface.

Equation 24

$$EF_{SERS} = \frac{I_{SERS}}{I_{RS}} \times \frac{N_{RS}}{N_{SERS}}$$

Equation 25

$$N_{RS} = \frac{V_{exc} \times \rho_{4,4'-BPY} \times \mathcal{N}_A}{MW_{4,4'-BPY}}$$

Equation 26

$$N_{SERS} = N_{Unit\ cell} \times \frac{A_{Laser\ spot}}{A_{Unit\ cell}}$$

N_{RS} was estimated following Equation 25, where:

- the optical excitation volume $V_{exc} = \pi \times r^2 \times h$

with the laser spot radius $r = 0.61 \times \frac{\lambda_{exc}}{N.A.}$

and the depth of focus $h = 2 \times \frac{\lambda_{exc}}{N.A.^2}$

(Excitation wavelength $\lambda_{exc} = 785\text{ nm}$, Numerical aperture $N.A. = 785\text{ nm}$)

- the density of 4,4'-BPY $\rho_{4,4'-BPY} = 1.232$ at room temperature. Value calculated based on unit cell and atoms in molecule from crystallography data base.⁴⁰
- the Avogadro number $\mathcal{N}_A = 6.022140857 \times 10^{23}\text{ mol}^{-1}$
- the molecular weight of 4,4'-BPY $MW_{4,4'-BPY} = 156.19\text{ g.mol}^{-1}$

To estimate N_{SERS} , the surface area available for functionalisation of 1 unit cell for cavities without and with icNPs was first approximated. Considering a hexagonal close packed arrangement of hemispherical Au-cavs on the SERS substrates, the surface of a unit cell was calculated using the nominal diameter of the PS spheres used to fabricate the arrays. In this type of arrangement, a unit cell consists of 1 cavity and 2 interstitial triangles. For cavities with NPs, correlating morphology characterised by FESEM to SERS performance as a function the NPs optimisation through variation of the etching time, it can be estimated that best SERS enhancement is obtained when the ratio η (NPs diameter / cavity diameter) is around 0.4, corresponding to a NP's height of circa two-third of the cavity's height. Based on those dimensions, NPs were assimilated to 3D-shapes formed by a cone mounted onto a spherical cap at the base fitting perfectly to the bottom of the cavity (i.e. shape of an inverted one scoop ice-cream cone). The corresponding surface area of a unit cell could then be estimated.

Number of molecules in 1 unit cell ($N_{unit\ cell}$) was then estimated assuming:

- 4,4'-BPY molecules were adsorbed as a monolayer, as samples were rinsed with a large volume of ethanol after overnight functionalisation to ensure physisorbed molecules do not contribute to the SERS signal;
- 100% adsorption efficiency leading to full coverage of the available surface area;
- Surface area of a single 4,4'-BPY molecule was estimated to be 0.4 nm^2 .²¹

Finally, N_{SERS} was estimated following Equation 26, where:

- the laser spot size $A_{Laser\ spot} = \pi \times r^2$
- the planimetric area of 1 unit cell $A_{Unit\ cell} = d_{cav}^2 \times \frac{\sqrt{3}}{2}$, with d_{cav} the diameter of 1 cavity.

Results are presented in Table 11.

Table 11 : EF_{SERS} obtained for different size of Au-cavs with and without icNPs using 4,4'-BPY SAM as SERS probe.

Cavity diameter	EF_{SERS} Au-Cavs	EF_{SERS} Au-icNPs
3 μm	1.3×10^3	1.6×10^4
2 μm	1.2×10^3	4.4×10^4
1 μm	7.1×10^3	1.9×10^4
510 nm	2.2×10^3	4.6×10^4

Overall, the results presented highlight the advantages of incorporating nano-substructuring at the close packed cavity array in enhancing SERS signal and in improving reproducibility compared to cavities without NPs. The relative EF_{SERS} of Au-icNPs as compared to Au-cavs ranges from x3 (1 μm diameter cavities) to x37 (2 μm diameter cavities), which is greater than ones obtained with alternative method of pore filling with plasmonic structures.^{2,3,5} In addition, they reliably ensure, unlike other approaches to nano-substructuring cavity arrays, that the particle and the hotspot are reliably positioned at the bottom of the well. Finally, the approach discussed can improve the variability of the SERS intensity measured from spot-to-spot and from substrate-to-substrate.

4.3.3.6 *Impact of nanoparticle modified cavities on luminescence*

We used the luminophore $[\text{Ru}(\text{bpy})_3]\text{Cl}_2$ as a probe to assess the MEF properties of the arrays. This probe was selected as it has a relatively low quantum yield, which is required for a MEF probe, it also has a large Stokes shift, reducing the prospect of self-quenching and its emission maxima at 620 nm should coincide reasonably well with the gold plasmon. Furthermore, as $[\text{Ru}(\text{bpy})_3]\text{Cl}_2$ was used to probe cavities MEF in this way in a previous report, it is a useful reference⁹. This study will help understanding by how much can a signal be amplified when reaching the bottom of the cavity.

4.3.3.6.1 Concentration dependence study on NPs in 1 μm cavities using $[\text{Ru}(\text{bpy})_3]\text{Cl}_2$ probe

A challenge was to find a compromise between laser power and concentration of the probe in solution as it was found that emission intensity decreased over relatively short irradiation times. Although $[\text{Ru}(\text{bpy})_3]\text{Cl}_2$ generally exhibits good photostability^{41,42} and indeed in a control, the signal obtained in free solution of this complex with the same laser power did not cause photodecomposition, the photochemistry of $[\text{Ru}(\text{bpy})_3]\text{Cl}_2$ is temperature dependent so may be promoted by temperature at the hotspots. In addition, some change to NP properties, arising from the local heat generated at the NP surface, may modify the geometry of the nanostructures and thus the hotspots, although such an affect would be expected also to change Raman intensities over time and this was not observed, so hot-spot promoted photodecomposition is likely to be a primarily cause. To reduce this affect after different trials, reducing the power at the sample to 57 μW was found to be best compromise, allowing maximum signal intensity with best temporal stability.

The effect of concentration of the dye on the MEF signal was then evaluated. Solutions of $[\text{Ru}(\text{bpy})_3]\text{Cl}_2$ were prepared in water, ranging from 500 pM to 50 μM . Full emission spectra were acquired as described in section 4.2.6. Results show that with those acquisition parameters, emission from the probe can be detected from 50 nm and above. Absolute intensity increases with the concentration for the bulk solution as expected and remains stable over time allowing acquisition of full spectra. However, at high concentrations, signal obtained with NPs in cavities was of similar intensity to free solution. Therefore, to understand the influence of the different type of substrates on the probe luminescence, results were plotted relative to the signal obtained for free

solution and are presented in Figure 167. From this figure it can clearly be seen that concentration of the probe influences dramatically the relative enhancement given by the nanostructures in cavities for concentrations above 500 nM.

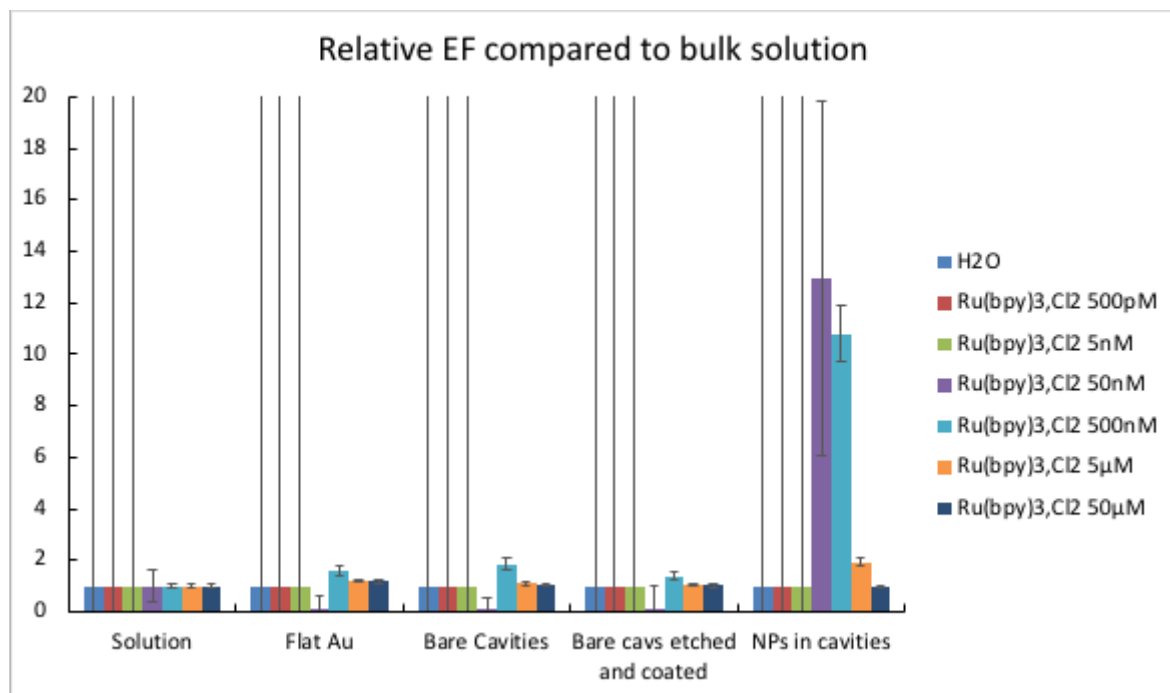


Figure 167: Emission measurement of different concentrations of $[Ru(bpy)_3]Cl_2$ aqueous solutions ranging from 500 pM to 50 μM , over different gold substrates. Results were plotted as the relative enhancement factors compared to the signal obtained for the bulk solution used. Area under the curve integrated between 475 nm and 875 nm. ($\lambda_{exc} = 473$ nm, 3 acc. 0.5 s., pin hole 500 μm , laser power at sample 57 μW)

Primary inner filter effect is reported to be happening for larger concentration of dye where the excitation beam is attenuated by the sample so only the surface facing the beam is emitting, but not for such low concentration. Secondary inner filter effect is most likely not happening giving the large Stoke shift of the used probe. Due to the low overlapping of the absorption and emission spectra of $[Ru(bpy)_3]Cl_2$, molecules in solution will not self-quench and thus will not affect the overall emission. Also, the fluorometer system used here is not a conventional one with a right-angle geometry but is closer to the characteristics of a front-face geometry setup as described by Eisinger and Flores.⁴³ Excitation light is focused to the front face of the sample and the emission is collected from the same region, therefore inner filter effects should be reduced.⁴⁴

To avoid variability due to small changes in concentration, the study was conducted using the same sample by increasing the concentration incrementally at a

single substrate. Results from this method and one using the same sample cleaned after the study and reanalysed with a new 500nM $[\text{Ru}(\text{bpy})_3]\text{Cl}_2$ solution demonstrated sample adsorption was not contributing to the effect.

Combined results suggest that above a specific concentration, the luminescence contribution from molecules in free solution in the focal volume exceeds one from the low number of molecules in the vicinity of NPs hotspots.

Figure 168 shows representative emission spectra obtained from bulk solution and at the arrays with NPs with varying concentration of the probe. The emission maximum of the luminescence spectra from cavities with NPs blue shifts when concentration of dye increases to match progressively the maximum emission obtained for bulk solution. This observation conforms to theory that at some stage the contribution of luminescence from molecules at the NPs hotspots is minimal compare to the luminescence given by molecules in the bulk solution.

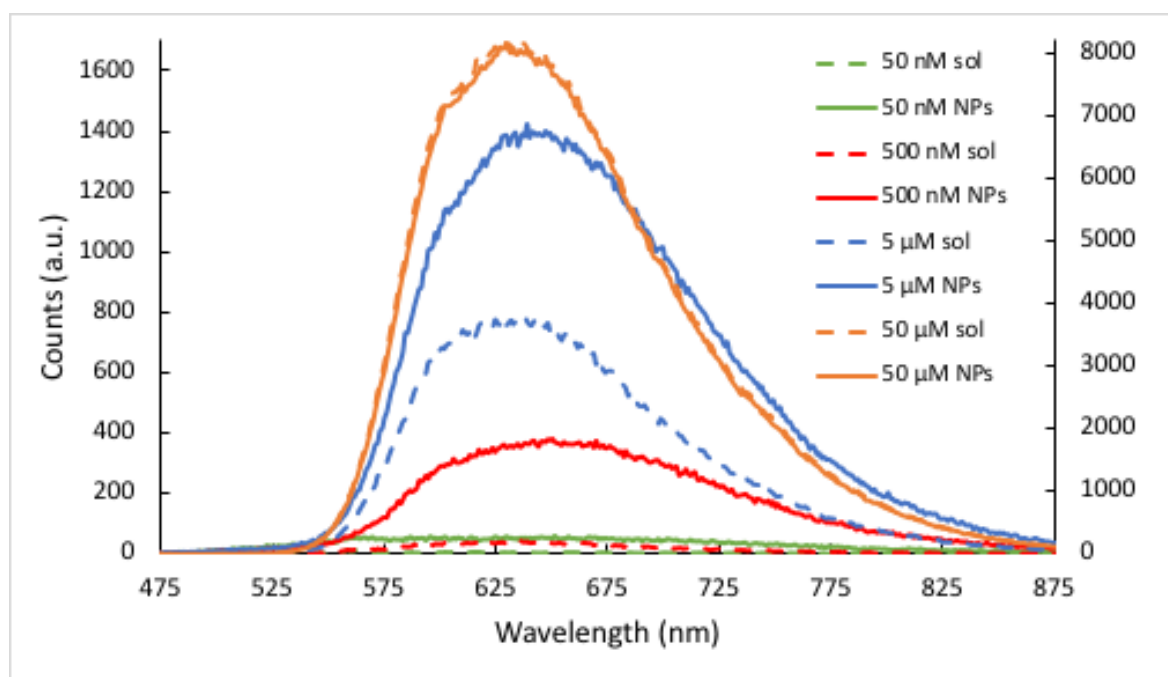


Figure 168 : Representative emission spectra of different concentrations of $[\text{Ru}(\text{bpy})_3]\text{Cl}_2$ aqueous solutions ranging from 50 nM to 50 μM , as bulk solution (sol) and over a 1 μm cavity array with NPs. For clarity purpose, spectra obtained for measurements with 50 μM solution are plotted according to the secondary axis on the right. Area under the curve integrated between 475 nm and 875 nm. ($\lambda_{\text{exc}} = 473 \text{ nm}$, 3 acc. 0.5 s., pin hole 500 μm , laser power at sample 57 μW)

Given the results of this study, it was decided that 500 nM $[\text{Ru}(\text{bpy})_3]\text{Cl}_2$ in water was the most appropriate concentration to work with, as it was giving consistently high

relative enhancement factor, which was dramatically decreasing for higher concentrations.

4.3.3.6.2 MEF characterisation of different sizes of cavity / NPs

The concentration of $[\text{Ru}(\text{bpy})_3]\text{Cl}_2$ was kept constant to 500 nM in water, allowing a comparison of the relative enhancement factors obtained with different sizes of cavities / nanostructures.

Figure 169 to Figure 172 show results obtained respectively for 3 μm , 2 μm , 1 μm and 510 nm diameter cavity arrays with and without NPs. As for the SERS study in section 4.3.3.5, each result presented below is an average of minimum eight emission spectra acquired across the whole area of the tested sample. Also, all results have been corrected from their respective luminescence background in deionised water.

For each cavity dimension, a common trend can be described with the dye emission compared to bulk solution increasing with substrates' structure complexity, going from low enhancement with flat Au surfaces, progressively increasing with cavities without NPs and dramatically enhanced when presence of icNPs.

As the concentration is the same across all substrates and the probe is not surface active, suggestion that SERS and MEF enhancement come from the difference in surface area between substrates can be rejected. Indeed, luminescence from molecules bonded or very close to the metal surface should be quenched, and number of molecules in the focal volume would actually be less for measurements on substrates versus measurement in bulk solution, as a part of the substrate will physically occupy part of the sampled volume instead of probe molecules in the measured volume. Luminescence signal originates from molecules in solution which have been enhanced or from the substrate itself. To eliminate background (bkg) from bulk, controls of the different substrates measured in water were subtracted from the overall luminescence signals allowing for a clear interpretation of the enhancement coming solely from the molecules in solution exposed to hotspots at the micro / nanostructures.

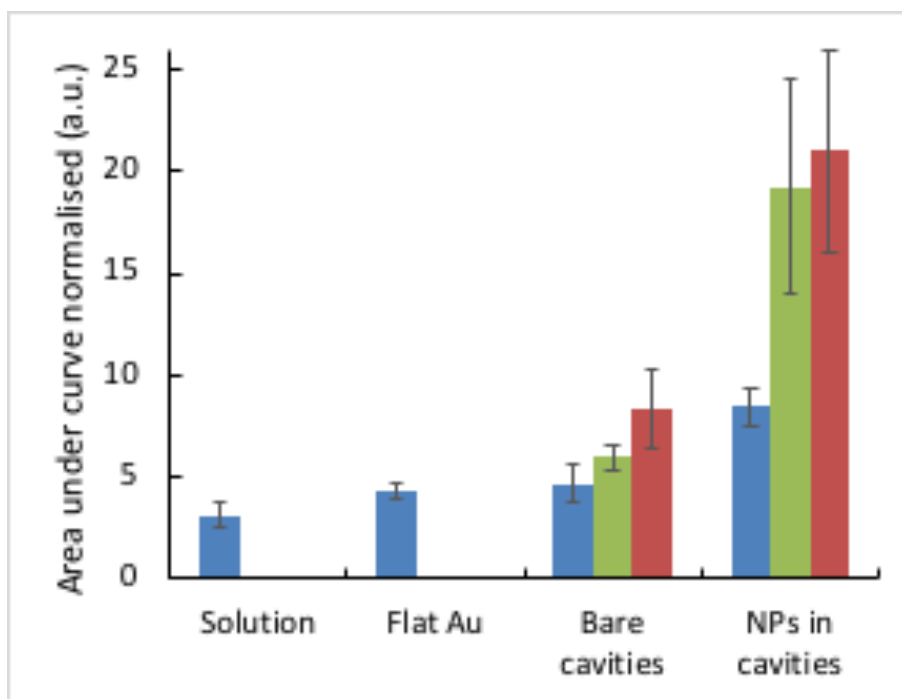
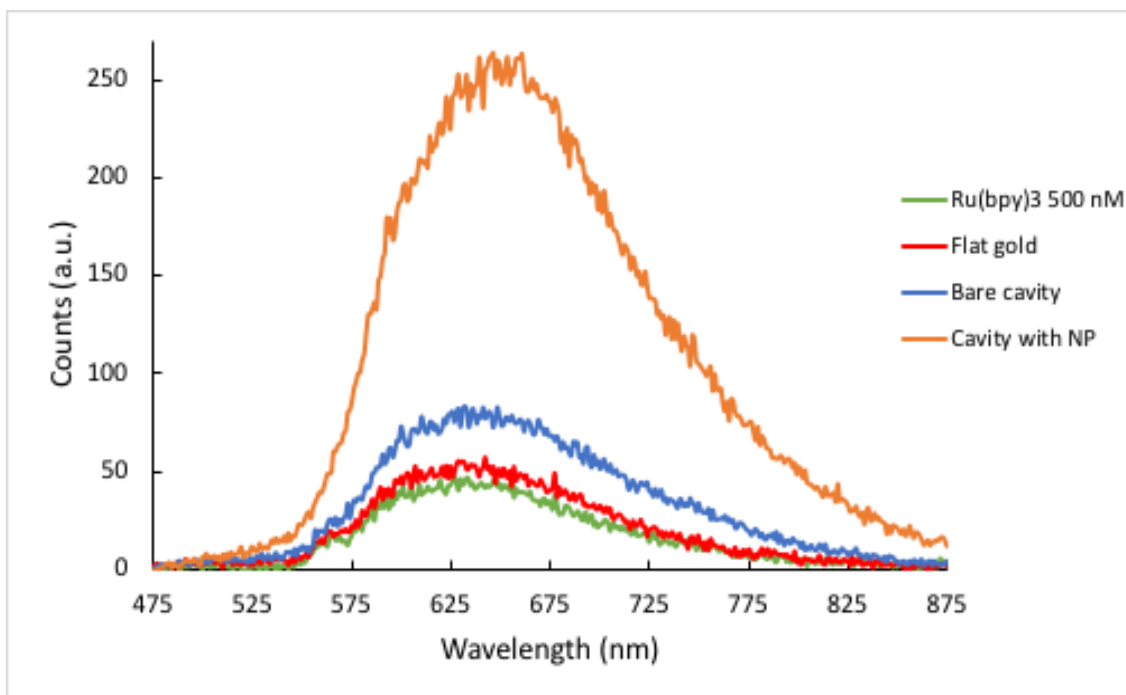


Figure 169 : Emission measurement of a 500 nM $[Ru(bpy)_3]Cl_2$ solution, over flat gold and within 3 μm diameter cavity arrays with and without NPs fabricated in reproducibility conditions. (Top) Representative emission spectra; (Bottom) Area under the curve between 475 nm and 875 nm. ($\lambda_{exc} = 473$ nm, 3 acc. 0.5 s., pin hole 500 μm , laser power at sample 57 μW)

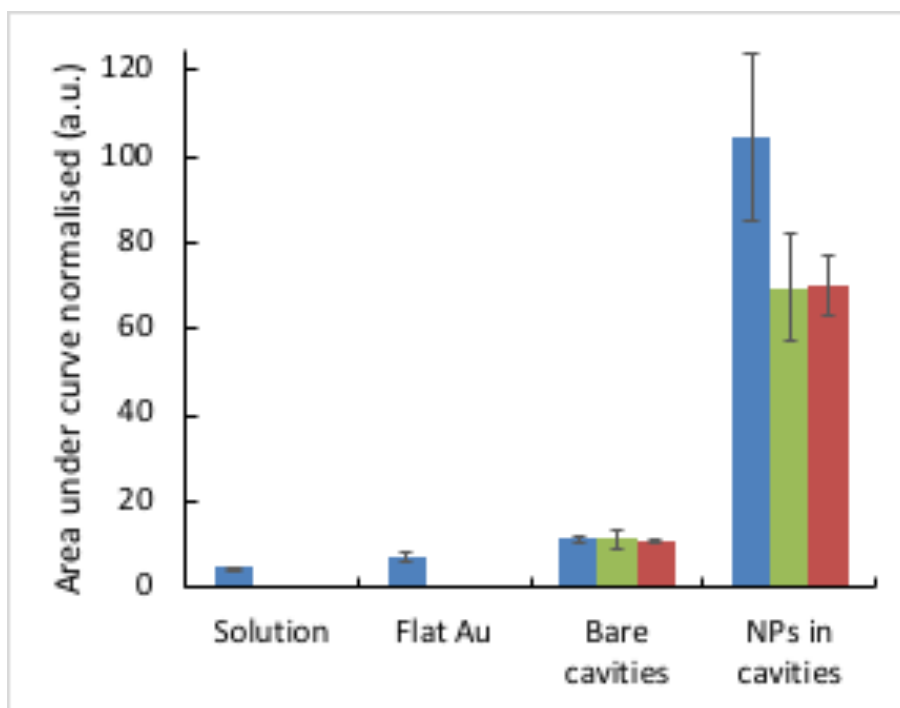
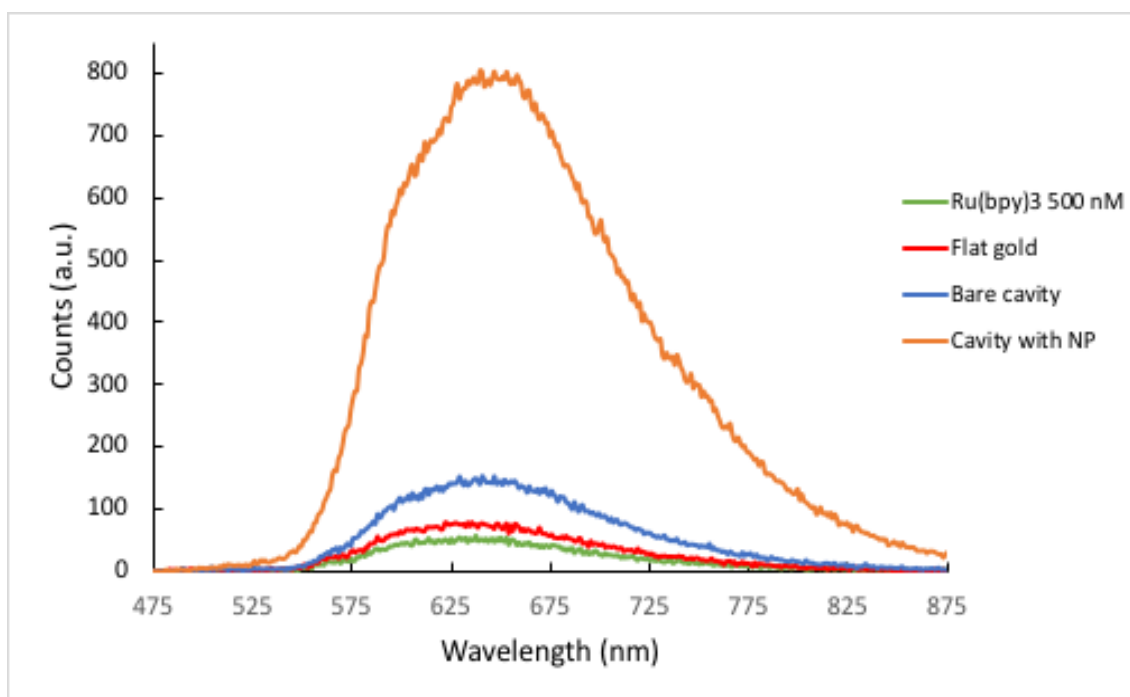


Figure 170 : Emission measurement of a 500 nM $[Ru(bpy)_3]Cl_2$ solution, over flat gold and within 2 μm diameter cavity arrays with and without NPs fabricated in reproducibility conditions. (Top) Representative emission spectra; (Bottom) Area under the curve between 475 nm and 875 nm. ($\lambda_{exc} = 473$ nm, 3 acc. 0.5 s, pin hole 500 μm , laser power at sample 57 μW)

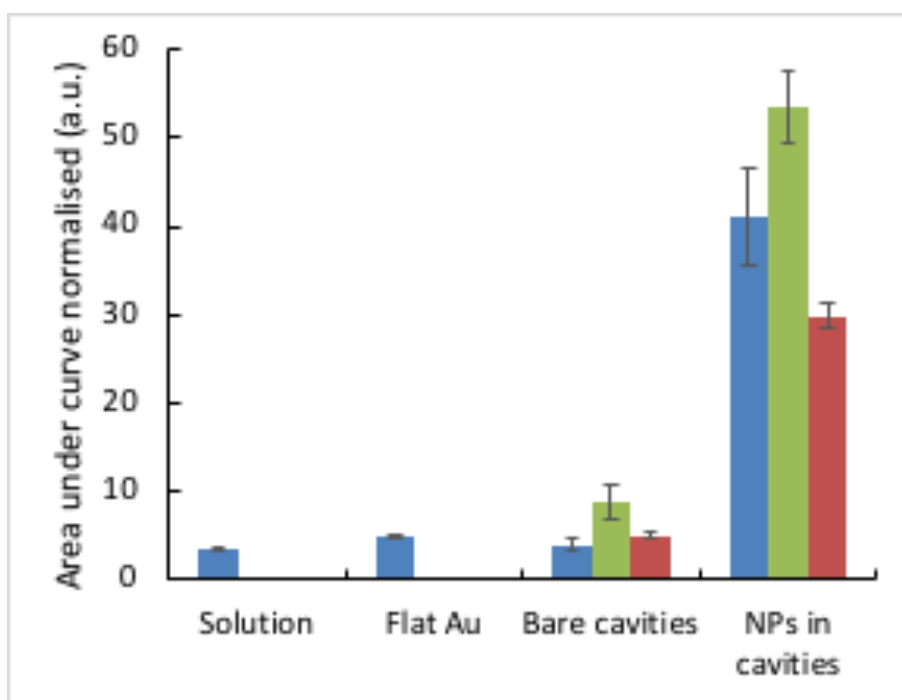
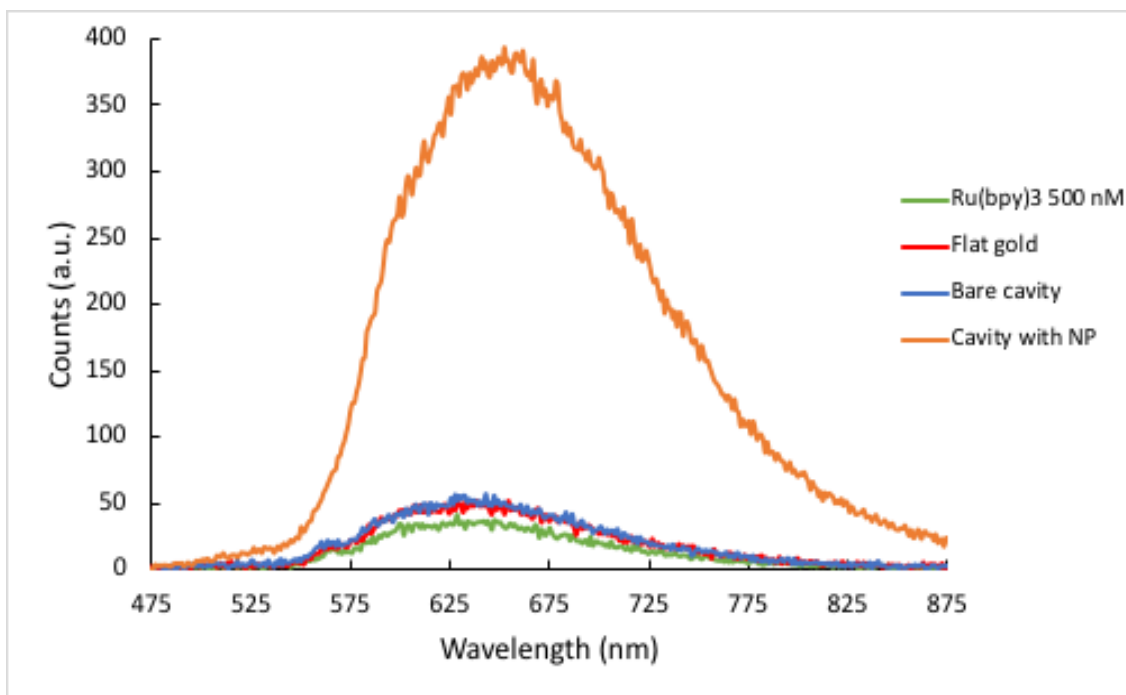


Figure 171 : Emission measurement of a 500 nM $[Ru(bpy)_3]Cl_2$ solution, over flat gold and within 1 μm diameter cavity arrays with and without NPs fabricated in reproducibility conditions. (Top) Representative emission spectra; (Bottom) Area under the curve between 475 nm and 875 nm. ($\lambda_{exc} = 473$ nm, 3 acc. 0.5 s., pin hole 500 μm , laser power at sample 57 μW)

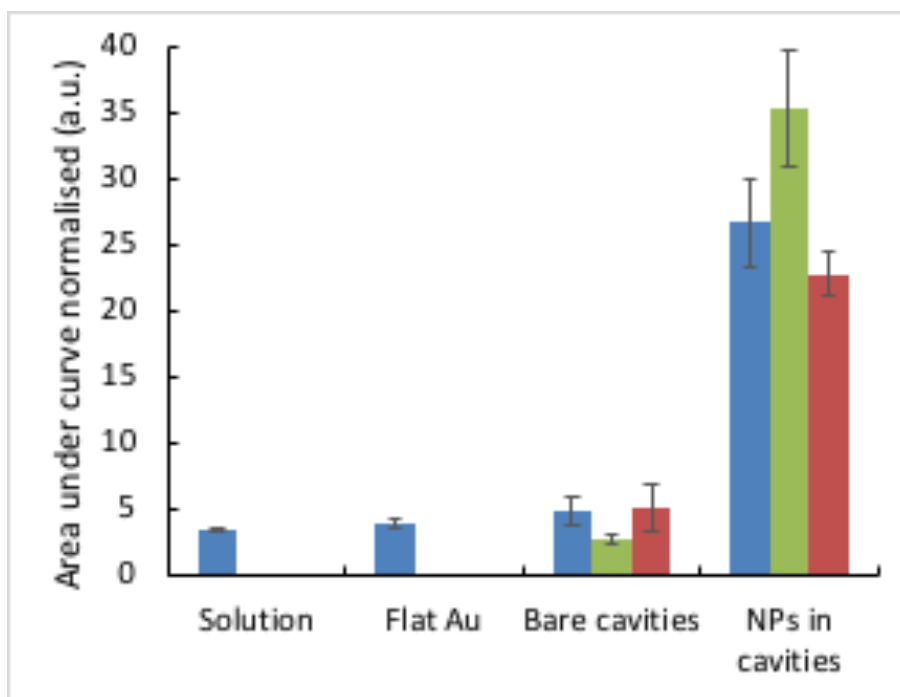
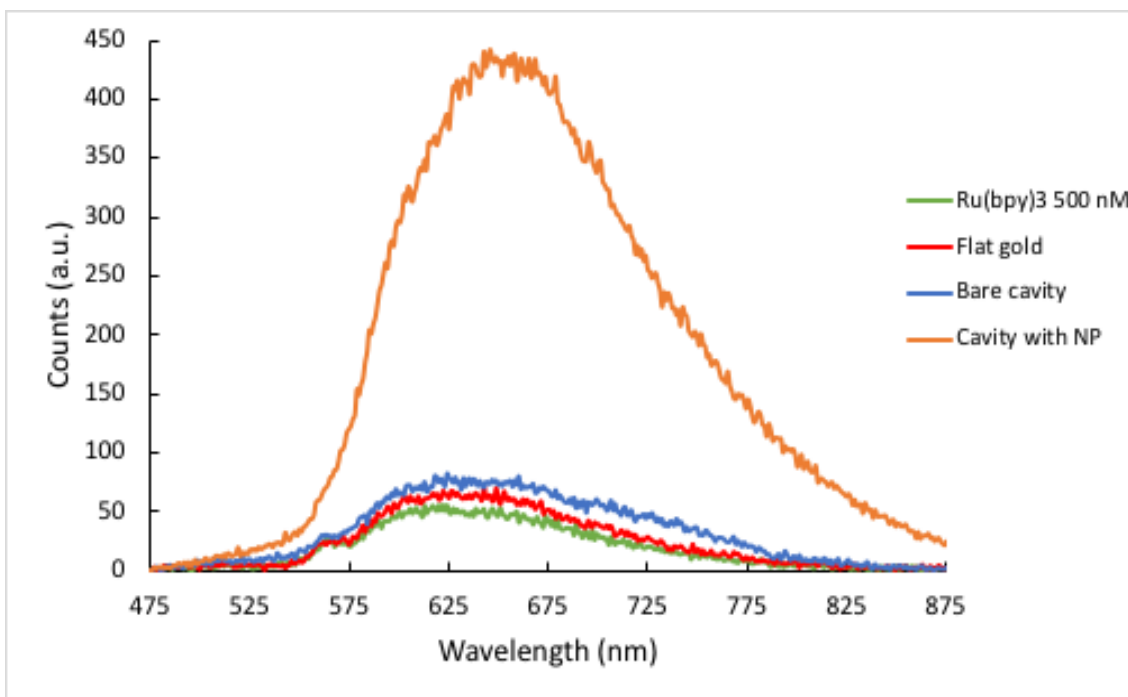


Figure 172 : Emission measurement of a 500 nM $[Ru(bpy)_3]Cl_2$ solution, over flat gold and within 510 nm diameter cavity arrays with and without NPs fabricated in reproducibility conditions. (Top) Representative emission spectra; (Bottom) Area under the curve between 475 nm and 875. nm ($\lambda_{exc} = 473$ nm, 3 acc. 0.5 s., pin hole 500 μm , laser power at sample 57 μW)

Among the different sizes tested, 2 μm diameter cavities gave the best enhancement both without and with NPs. Indeed, emission signal corrected from the respective back ground was enhanced up to x2.4 factor for a sample with bare cavities and up to x22.7 factor for a sample with NPs, compared to bulk $[\text{Ru}(\text{bpy})_3]\text{Cl}_2$. Conversely, 3 μm diameter cavities were the least enhancing with emission enhanced up to x6.7 factor for a sample with NPs the more performant, compared to bulk $[\text{Ru}(\text{bpy})_3]\text{Cl}_2$. Those results are in line with what was found above from our SERS study, where samples with NPs giving respectively the highest and the lowest SERS performance were made on 2 μm and 3 μm diameter cavity substrates.

Table 12 to Table 15 summarize the different averaged results obtained on bare and nano sub-structured substrates for the different sizes of cavities developed and optimised previously and display their respective CV to compare their intra- and inter-sample variability.

Table 12 : Emission measurement of a 500 nM $[\text{Ru}(\text{bpy})_3]\text{Cl}_2$ solution, over flat gold and within 3 μm diameter cavity arrays with and without NPs fabricated in reproducibility conditions with their associated CV.

3 μm diam.	Bare cavities		NPs in cavities	
	Area (a.u.) _{bkg corr.}	CV (%)	Area (a.u.) _{bkg corr.}	CV (%)
S03	4.66	20 %	8.42	11 %
S06	5.96	11 %	19.25	27 %
S07	8.38	23 %	21.00	23 %
Intra- sample		18 %		20 %
Inter- sample	6.33	30 %	16.22	42 %

Table 13 : Emission measurement of a 500 nM [Ru(bpy)₃]Cl₂ solution, over flat gold and within 2 μm diameter cavity arrays with and without NPs fabricated in reproducibility conditions with their associated CV.

2 μm diam.	Bare cavities		NPs in cavities	
	Area (a.u.) _{bkg corr.}	CV (%)	Area (a.u.) _{bkg corr.}	CV (%)
S01	11.22	6 %	104.63	19 %
S03	11.24	19 %	69.46	18 %
S10	10.65	4 %	70.02	10 %
Intra- sample		10 %		16 %
Inter- sample	11.04	3 %	81.37	25 %

Table 14 : Emission measurement of a 500 nM [Ru(bpy)₃]Cl₂ solution, over flat gold and within 1 μm diameter cavity arrays with and without NPs fabricated in reproducibility conditions with their associated CV.

1 μm diam.	Bare cavities		NPs in cavities	
	Area (a.u.) _{bkg corr.}	CV (%)	Area (a.u.) _{bkg corr.}	CV (%)
S02	3.90	18 %	41.03	13 %
S11	8.64	22 %	53.58	8 %
S12	4.92	8 %	29.81	5 %
Intra- sample		16 %		9 %
Inter- sample	5.82	43 %	41.47	29 %

Table 15 : Emission measurement of a 500 nM [Ru(bpy)₃]Cl₂ solution, over flat gold and within 500 nm diameter cavity arrays with and without NPs fabricated in reproducibility conditions with their associated CV.

500 nm diam.	Bare cavities		NPs in cavities	
	Area (a.u.) _{bkg corr.}	CV (%)	Area (a.u.) _{bkg corr.}	CV (%)
S01	4.88	21 %	26.77	13 %
S02	2.76	12 %	35.50	12 %
S05	5.12	36 %	22.81	7 %
Intra-sample		23 %		11 %
Inter-sample	4.25	30 %	28.36	23 %

EF_{MEF} at the different gold substrates studied, was estimated by comparison to luminescence (L) obtained for the probe in bulk solution, using Equation 27 and are given in Table 16.

Equation 27

$$EF_{MEF} = \frac{L_{Au \text{ sample in probe}} - L_{Au \text{ sample in water}}}{L_{probe \text{ bulk solution}} - L_{water}}$$

Table 16 : EF_{MEF} obtained for flat gold and different size of Au cavity with and without icNPs using 500 nM aqueous solution of [Ru(bpy)₃]Cl₂ as luminescent probe.

Cavity diameter	EF_{MEF} Flat Au	EF_{MEF} Au-Cavs	EF_{MEF} Au-icNPs
3 μm	1.4	2.0	5.2
2 μm	1.5	2.4	17.9
1 μm	1.4	1.7	12.4
510 nm	1.1	1.2	8.1

Depending on the diameter of the wells, bare cavity arrays can give on average 1.2 to 2.4 times stronger emission signal compared with bulk solution. 2 μm diameter cavities substrates gave the best results in terms of both intensity and low variability of results, with a CV of 10 % intra-sample and 3 % inter-sample over the three samples tested. Those results are really good given the large area tested across each substrate

and the fact that the fabrication technique is not based on techniques such as EBL, FIB or photolithography.

The considerable improvement here in terms of enhancement of the luminescence signal is originating from the presence of NPs at the bottom of the wells, phenomenon that was not reported in previous work when comparing luminescence between cavities with and without NP.³ Indeed, signal can range on average from 5x up to 18x factor for NPs modified cavities compared to bulk solution depending on the size of cavity / nanostructure. Our results have not been normalised to the number of molecules in the focal volume, therefore even higher EF_{MEF} could be expected, as, as described above, a part of the substrate is occupying part of the interrogation volume.

Given the extra steps of the fabrication process, we could think that the presence of the NPs will implement some variability in the results as these nanostructures are randomly formed and could be different across a same substrate and moreover among different batches of fabrication. However, intra- at inter-sample CVs improved for substrates with small cavities sizes presenting NPs, i.e. 510 nm and 1 μm diameter cavities, and were found to be similar to ones reported in the literature for plasmon-enhanced fluorescence substrates.⁴⁵

Variability in the results obtained for 2 μm diameter cavities substrates with NPs did not improve as the variability for bare cavities was already exceptionally low, but it corresponded to variability obtained for smaller cavities sizes with NPs, with a CV of 16 % intra-sample and 25 % inter-sample, which remains acceptable given the fabrication method employed not based on photolithography, EBL or FIB and the large area sampled during MEF measurements.

4.4 Conclusions

The SERS properties of the gold cavity array presented in chapter 3 were improved by building nano sub-structuring into the arrays at the bottom of the well to increase and concurrently localise intensity of the electric field at this location. Two routes to reproducibly nano sub-structuring the pore arrays were initially investigated.

Firstly, fabrication of nanostructures following a bottom-up approach was attempted, based on the presence of air bubble in cavity due to partial filling with aqueous solution, as previously reported by our group. Given the poor control over the presence and location in each well, but also the size and distribution of the particles formed using this approach, this method was abandoned in favour of a top-down fabrication method involving plasma etching.

This new method used the work developed in chapter 3 and took advantage of the templating sphere left in place after electrodeposition. The PS sphere was then etched to create a NP in-cavity before depositing a second layer of gold to render the array SERS active.

To optimise SERS response, study of etching parameters on the morphology of PS spheres trapped at the array post gold electrodeposition were carried out and, consistent with literature reports, it was found that most influence on the etching rate are the RF power, the nature of the gas used and the etching time. Choosing oxygen as etching gas, RF power and etching time were adapted to nanostructure cavity arrays made of spheres with 3 μm , 2 μm , 1 μm and 510 nm diameter. Here, optimisation was based on SERS signal intensity obtained for a 4,4' BPY SAM adsorbed at the gold coated nano sub-structured array.

FESEM characterisation of the optimised substrates allowed us to ensure that morphology of the nanostructure would be compatible with the intended use of the array to monitor lipid membrane suspended at the cavity array. Indeed, PS needed to be reduced to a size where no part would protrude above the cavity aperture as such protrusion could disrupt the bilayer formed at the cavity aperture.

FDTD simulation for an optimised NP within a 1 μm diameter cavity allowed for a clear visualisation of high intensity field at the NP nano gaps, showing the successful

approach to target the enhancement at the bottom of the cavity with increase of the field intensity compared to bare cavity of same dimensions studied in chapter 3.

Diffuse reflectance measurements of the different optimised nano sub-structured arrays were compared to their bare equivalent showed systematically a maximum absorbance related to presence of LSPR shifting to the red. This peak more centred around 785 nm for arrays with NPs than for bare cavities may lead to a better enhancement of SERS signal at this excitation wavelength.

Those results correlated well with SERS characterisation of the different substrates, which showed enhancement of SERS signal for molecules adsorbed at the metal surface of nano sub-structured arrays by one to two order of magnitude greater than their bare cavity equivalent, with highest SERS intensity obtained for 2 μm and 510 nm diameter nano sub-structured array. Also, nano structuring allowed in some cases to improve the variability of the signal measured from spot-to-spot and from substrate-to-substrate.

MEF characterisation of the different arrays was also performed using 500 nM aqueous solution of $[\text{Ru}(\text{bpy})_3]\text{Cl}_2$ as luminescent probe. Consistent with SERS results, nano-sub-structured arrays always allowed for a better enhancement of the probe emission compared to bare arrays typically by one order of magnitude, with 2 μm diameter cavity arrays giving the best results. Despite introducing a randomly formed structure that are not perfectly identical in each well, results variability obtained among a single substrate or between different batches with same cavity dimensions surprisingly improved for small diameter cavity arrays, with CV around 10 % similar to what has been reported in the literature for lithographically produced substrates

In summary, plasma etching of PS spheres within cavities proved a surprisingly reproducible method of nano modifying the arrays, with nanostructures of very similar shape and size produced both within a single substrate but also between batches of arrays. This technique has the advantage to leave a nano sub-structure at the bottom of every single cavity that presents multiple nano-defects with a plasmonic activity once coated with gold. Despite number and quality of the hotspots created varying from one size of array to another, SERS and MEF results obtained give good confidence into the efficiency and robustness of the fabrication method, which exhibit high uniformity and reproducibility across a wide area prepared with a low-cost method.

4.5 References

1. Huang, F. M. *et al.* Dressing Plasmons in Particle-in-Cavity Architectures. *Nano Lett.* **11**, 1221–1226 (2011).
2. Speed, J. D. *et al.* SERS from molecules bridging the gap of particle-in-cavity structures. *Chem. Commun.* **47**, 6335–6337 (2011).
3. Lordan, F. *et al.* The Effect of Ag Nanoparticles on Surface-Enhanced Luminescence from Au Nanovoid Arrays. *Plasmonics* **8**, 1567–1575 (2013).
4. Li, X., Zhang, Y., Shen, Z. X. & Fan, H. J. Highly Ordered Arrays of Particle-in-Bowl Plasmonic Nanostructures for Surface-Enhanced Raman Scattering. *Small* **8**, 2548–2554 (2012).
5. Malinovskis, U. *et al.* High-Density Plasmonic Nanoparticle Arrays Deposited on Nanoporous Anodic Alumina Templates for Optical Sensor Applications. *Nanomaterials (Basel)* **9**, 531–1 to 531–10 (2019).
6. Plettl, A. *et al.* Non-Close-Packed Crystals from Self-Assembled Polystyrene Spheres by Isotropic Plasma Etching: Adding Flexibility to Colloid Lithography. *Adv. Funct. Mater.* **19**, 3279–3284 (2009).
7. Yang, Z.-H. *et al.* Interfacial adhesion and superhydrophobicity modulated with polymeric nanopillars using integrated nanolithography. *J. Micromech. Microeng.* **22**, 125026 (2012).
8. Johnson, P. B. & Christy, R. W. Optical Constants of the Noble Metals. *Physical Review B* **6**, 4370–4379 (1972).
9. Jose, B. *et al.* Emission enhancement within gold spherical nanocavity arrays. *Phys. Chem. Chem. Phys.* **11**, 10923–10933 (2009).
10. Sun, Y., Xie, G., Peng, Y., Xia, W. & Sha, J. Stability theories of nanobubbles at solid–liquid interface: A review. *Colloids and Surfaces A: Physicochemical and Engineering Aspects* **495**, 176–186 (2016).
11. Borkent, B. M., Dammer, S. M., Schönherr, H., Vancso, G. J. & Lohse, D. Superstability of Surface Nanobubbles. *Physical Review Letters* **98**, (2007).
12. Dow Corning. Sylgard® 184 silicone elastomer, Product informations. (2014).
13. Finklea, H. O., Avery, S., Lynch, M. & Furtch, T. Blocking oriented monolayers of alkyl mercaptans on gold electrodes. *Langmuir* **3**, 409–413 (1987).
14. Ulman, A. Formation and Structure of Self-Assembled Monolayers. *Chemical Reviews* **96**, 1533–1554 (1996).
15. Schwartz, D. K. MECHANISMS AND KINETICS OF SELF ASSEMBLED MONOLAYER FORMATION. *Annual Review of Physical Chemistry* **52**, 107–137 (2001).
16. Love, J. C., Estroff, L. A., Kriebel, J. K., Nuzzo, R. G. & Whitesides, G. M. Self-Assembled Monolayers of Thiolates on Metals as a Form of Nanotechnology. *Chemical Reviews* **105**, 1103–1170 (2005).
17. Spain, E., Brennan, E., McArdle, H., Keyes, T. E. & Forster, R. J. High Sensitivity DNA Detection Based on Regioselectively Decorated Electrocatalytic Nanoparticles. *Analytical Chemistry* **84**, 6471–6476 (2012).
18. Joo, S. Adsorption of Bipyridine Compounds on Gold Nanoparticle Surfaces Investigated by UV-Vis Absorbance Spectroscopy and Surface Enhanced Raman Scattering. *Spectroscopy Letters* **39**, 85–96 (2006).
19. Joo, S.-W. Surface-enhanced Raman scattering of 4,4'-bipyridine on gold nanoparticle surfaces. *Vibrational Spectroscopy* **34**, 269–272 (2004).
20. Topaçlı, A. & Akyüz, S. 4,4'-Bipyridyl: vibrational assignments and force field. *Spectrochimica Acta Part A: Molecular and Biomolecular Spectroscopy* **51**, 633–641 (1995).

21. Suzuki, M., Niidome, Y. & Yamada, S. Adsorption characteristics of 4,4'-bipyridine molecules on gold nanosphere films studied by surface-enhanced Raman scattering. *Thin Solid Films* **496**, 740–747 (2006).
22. Zhuang, Z. *et al.* Surface-enhanced Raman scattering of 4,4'-bipyridine on silver by density functional theory calculations. *Vibrational Spectroscopy* **49**, 118–123 (2009).
23. Hong, P. P., Boerio, F. J., Clarson, S. J. & Smith, S. D. An investigation of the interdiffusion of polystyrene and deuterated polystyrene using surface-enhanced Raman scattering. *Macromolecules* **24**, 4770–4776 (1991).
24. Venkatachalam, R. S., Boerio, F. J., Carnevale, M. R. & Roth, P. G. Degradation of Polystyrene on Silver Substrates during Surface-Enhanced Raman Scattering. *Applied Spectroscopy* **42**, 1207–1213 (1988).
25. Anema, J. R., Brolo, A. G., Felten, A. & Bittencourt, C. Surface-enhanced Raman scattering from polystyrene on gold clusters. *Journal of Raman Spectroscopy* **41**, 745–751 (2010).
26. *Biomolecular films: design, function, and applications.* (Marcel Dekker, 2003).
27. Bain, C. D. *et al.* Formation of monolayer films by the spontaneous assembly of organic thiols from solution onto gold. *Journal of the American Chemical Society* **111**, 321–335 (1989).
28. Cunha, F. *et al.* Potential-Induced Phase Transitions in 2,2'-Bipyridine and 4,4'-Bipyridine Monolayers on Au(111) Studied by *in Situ* Scanning Tunneling Microscopy and Atomic Force Microscopy. *Langmuir* **12**, 6410–6418 (1996).
29. Li, N. *et al.* Fabrication of a resist pattern based on plasma-polystyrene interactions. *RSC Adv.* **6**, 14948–14951 (2016).
30. Quorum Technologies. Sputter Coating Technical Brief. (01/02).
31. Xia, L. *et al.* Surface enhanced Raman scattering substrate with metallic nanogap array fabricated by etching the assembled polystyrene spheres array. *Optics Express* **21**, 11349 (2013).
32. Nam, J.-M., Oh, J.-W., Lee, H. & Suh, Y. D. Plasmonic Nanogap-Enhanced Raman Scattering with Nanoparticles. *Accounts of Chemical Research* **49**, 2746–2755 (2016).
33. Huang, Y., Chen, Y., Wang, L.-L. & Ringe, E. Small morphology variations effects on plasmonic nanoparticle dimer hotspots. *J. Mater. Chem. C* **6**, 9607–9614 (2018).
34. Wei, S., Zheng, M., Xiang, Q., Hu, H. & Duan, H. Optimization of the particle density to maximize the SERS enhancement factor of periodic plasmonic nanostructure array. *Optics Express* **24**, 20613 (2016).
35. Bergström, D., Powell, J. & Kaplan, A. F. H. The absorption of light by rough metal surfaces—A three-dimensional ray-tracing analysis. *Journal of Applied Physics* **103**, 103515 (2008).
36. Ghosh, S. K. & Pal, T. Interparticle Coupling Effect on the Surface Plasmon Resonance of Gold Nanoparticles: From Theory to Applications. *Chem. Rev.* **107**, 4797–4862 (2007).
37. Cole, R. M. *et al.* Understanding Plasmons in Nanoscale Voids. *Nano Lett.* **7**, 2094–2100 (2007).
38. Zeng, Z.-C., Wang, H., Johns, P., Hartland, G. V. & Schultz, Z. D. Photothermal Microscopy of Coupled Nanostructures and the Impact of Nanoscale Heating in Surface-Enhanced Raman Spectroscopy. *The Journal of Physical Chemistry C* **121**, 11623–11631 (2017).
39. Hartland, G. V. Optical Studies of Dynamics in Noble Metal Nanostructures. *Chemical Reviews* **111**, 3858–3887 (2011).

40. Candana, M. M., Eroğlu, S., Özbeya, S., Kendi, E. & Kantarci, Z. Structure and Conformation of 4,4'-Bipyridine. *Spectroscopy Letters* **32**, 35–45 (1999).
41. Sciuto, E. L. *et al.* Photo-physical characterization of fluorophore Ru(bpy)₃²⁺ for optical biosensing applications. *Sensing and Bio-Sensing Research* **6**, 67–71 (2015).
42. Müller, P. & Brettel, K. [Ru(bpy)₃]²⁺ as a reference in transient absorption spectroscopy: differential absorption coefficients for formation of the long-lived 3MLCT excited state. *Photochemical & Photobiological Sciences* **11**, 632 (2012).
43. Eisinger, J. & Flores, J. Front-face fluorometry of liquid samples. *Analytical Biochemistry* **94**, 15–21 (1979).
44. Lakowicz, J. R. & Masters, B. R. Principles of Fluorescence Spectroscopy, Third Edition. *Journal of Biomedical Optics* **13**, 029901 (2008).
45. Sun, J. *et al.* Uniform and reproducible plasmon-enhanced fluorescence substrate based on PMMA-coated, large-area Au@Ag nanorod arrays. *Nano Research* **11**, 953–965 (2018).

5 Chapter 5: Towards a microfluidic platform based on gold micropore arrays lipid membrane supports

5.1 Introduction

The aim of this last working chapter is to check if substrates developed in previous chapters can be easily transposed into a microfluidic device while keeping in mind its final aim, to help the study of artificial lipid membranes. Therefore, the device should be compatible with the formation of stable lipid membranes and, if possible, with several analytical techniques.

Attempts to transfer identical or substrates with similar material are presented and preliminary electrochemical tests are achieved.

A new microfluidic device was developed taking into consideration the lipid membrane formation and the analytical techniques to be used, going from the design of the device, through the choice of material, the fabrication of the electrodes and the transfer of the cavity array with and without nano sub-structuring.

5.2 Experimental

5.2.1 Electrochemical measurements

5.2.1.1 EIS trials on Au-Si electrodes for microfluidic device

EIS measurements were performed using a standard 3-electrode set up linked to a Potentiostat CH Instrument model 760E electrochemical workstation. The counter electrode and the reference electrodes were respectively a platinum wire and an Ag/AgCl saturated in 1 M KCl. Impedance measurements were acquired on a frequency range of 100 000 Hz to 0.01 Hz with an alternating current (AC) modulation of 0.01 V at a potential bias of 0 V (vs. Ag/AgCl). All measurements were run in PBS buffer at pH 7.4.

5.2.1.2 Electrochemical compatibility of new gold electrodes on PET

Cyclic voltammetry presented in this work were performed using a standard 3-electrode set up linked a Potentiostat CH Instrument model 900 electrochemical workstation. The counter electrode and the reference electrodes were respectively a platinum wire and an Ag/AgCl saturated in 1 M KCl. The gold electrode sputtered on PET substrate acted as working electrode.

Gold electrodes were cleaned by cycling voltammetry between 0 V and 1.6 V at a scan rate of 0.1 V/s in H₂SO₄ 0.1 M.

The gold working electrode performance was characterised by performing cyclic voltammetry in the presence of a 1 mM K₃[Fe(CN)₆]/K₄[Fe(CN)₆] (1:1 mol/mol) mixture used as a redox probe dissolved in PBS buffer containing additional 1 M KCl as the supporting electrolyte. Potential was cycled between -0.2 V and 0.6 V vs. Ag/AgCl at a scan rate of 50 mV/s.

5.2.1.3 Contact angle measurement

Contact angle measurements for the study of silicon and gold wettability were performed at room temperature using a FTA 200 Dynamic Contact Angle Analyser from First Ten Angstroms, Inc as described in chapter 2.

5.2.2 SEM characterisation

SEM images presented in this chapter were collected using a Hitachi S3000 and a Hitachi S3400n SEM, Tungsten system instrument. Working distance, accelerating

voltage and magnification used in Secondary Electron mode are reported on the images.

5.2.3 Choice of material for electrode substrate

PMMA, PS and COP were cut using the CO₂ laser Epilog Zing 16 as described in chapter 2. PMMA was purchased from Radionics Ltd, PS substrates were obtained by cutting Petri dishes lids, and a sample disc of COP (Zeonor® 1060R) used for this trial was kindly provided by Prof. Jens Ducreé's group.

PET films Melinex 506 from HiFi Industrial Film Ltd were 175 µm thick and were cut by xurography using the cutting plotter Craft Robo Pro from Graphtec described in chapter 2.

Gold electrode were sputtered at different polymers surface using a sputter coater Cressington Model 108 mounted with a gold target.

To ensure substrates were as close as possible to the Au-Si wafer used in previous chapters, gold was sputtered for 100 s with a set current of 30 mA. Based on results obtained in chapter 4, gold layer should be approximately 100 nm thick.

5.3 Results and discussions

5.3.1 Working electrode for microfluidic device

Our aim herein is to integrate the gold substrate developed and presented in the previous chapter, into a microfluidic device, using some of the principles learned in chapter 2, to enable flow of sample/analytic containing solution across the substrate, while allowing for incubation and wash through. Ultimately the device should be suitable for dual spectroscopic and electrochemical interrogation. The dimensions of the array need to be reduced while still ensuring that reliable electrical contact can be made to a potentiostat for electrochemical applications. Decreasing the area over which the lipid membrane is to be suspended could also improve the variability of results by limiting the chance that a defect will be present at the membrane.

Using a mask to delimit the working electrode area proved previously to improve considerably the electroactive surface reproducibility between samples, as shown in chapter 3. Preliminary EIS measurements were thus performed using a flat 1.5 x 0.8 cm Au-Si electrode onto which a PSA mask was applied to control the electrode surface in contact with the solution. Masks with a circular open window of different diameters were explored by running EIS measurement in similar conditions as for the study of lipid bilayer membranes¹, and results are presented in Figure 173.

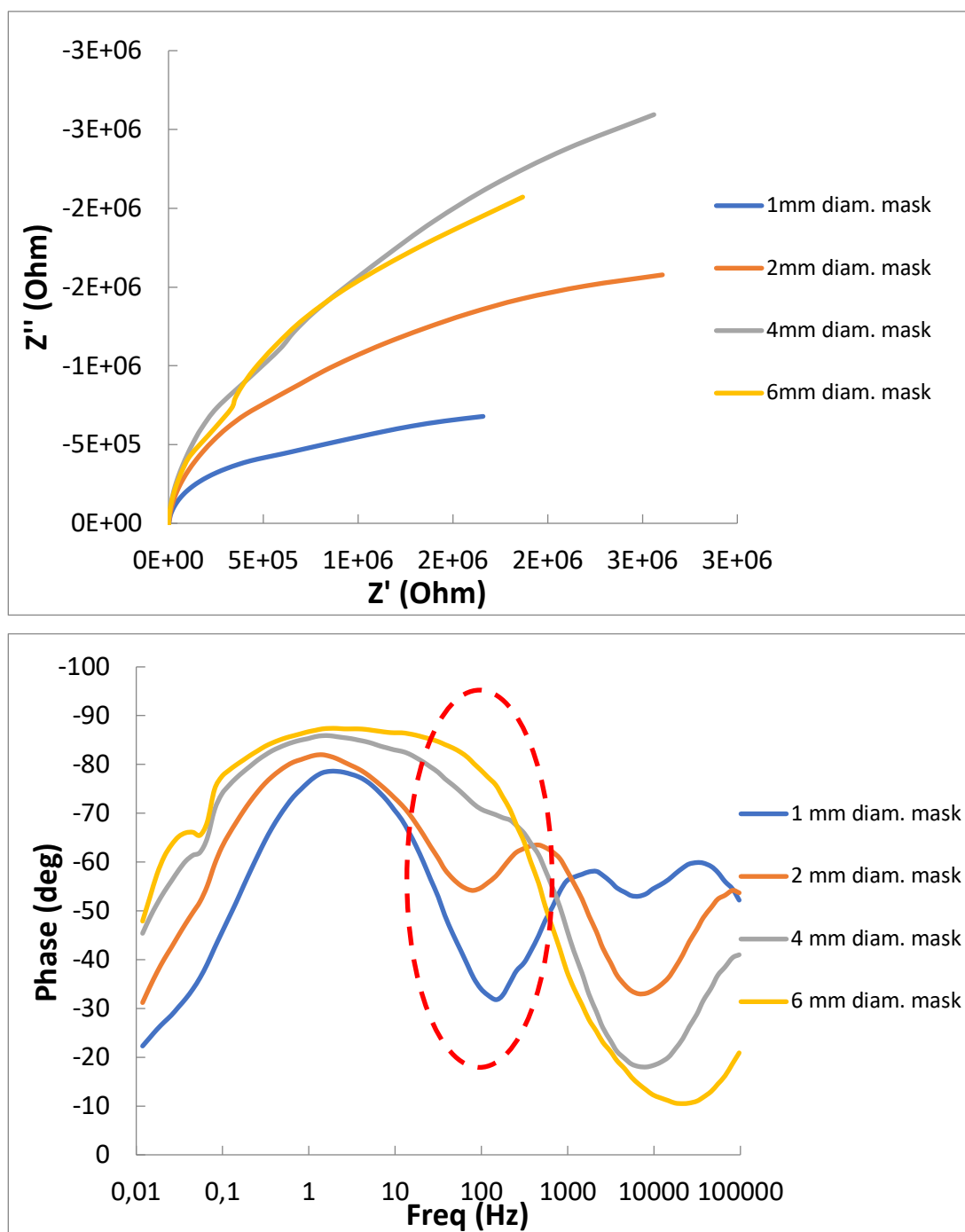


Figure 173 : Nyquist plot (top) and Bode plot (bottom) obtained from EIS measurement of flat Au-Si wafer electrode. Masked with PSA of different circular apertures. Measurements were carried out using a standard 3-electrode set-up at a potential bias of 0 V (vs. Ag/AgCl) in PBS buffer at pH 7.4, using AC amplitude of 0.01 V with a frequency range of 100 000 Hz to 0.01 Hz.

The Bode plot shown in Figure 173 shows an artefact around 100 Hz, which tends to disappear as the circular window of the mask increases. This feature is likely to be related to capacitance originating from contact of the adhesive film at the conductive masked surface of the electrode, which increases as the size of the electrode in contact with the solution decreases.

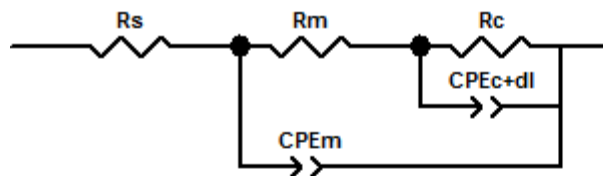


Figure 174 : Equivalent circuit model used to fit EIS data obtained for microcavities supported lipid bilayers. R_s is the solution resistance, R_m and CPE_m represent the resistance and constant phase element (CPE) of the membrane and R_c and CPE_c represents the cavity resistance and CPE of the gold substrate.

The EIS characteristics of the electrode are reminiscent of EIS electrodes with an organic coating or paints as shown by the profile of the Bode plot.² Such systems are usually fitted with equivalent circuit models similar to the one developed by Keyes' group for the monitoring of a lipid bilayer by EIS¹ and shown in Figure 174. Therefore, to avoid complicating the EIS circuit for the bilayer and electrode with an additional contribution from the masking PSA we sought alternative substrates with less conductive area.

MicroFabSolutions s.r.l., an external contractor, were asked to build gold electrodes of a specific size onto silicon wafers. Electrodes were built onto an SiO_2 layer, with a square-shaped working area of 2 mm by 2 mm. The only part of the conductive electrode in contact with the PSA channel of the future microfluidic device would be then restricted to the connection wire between the working area and the connection for the potentiostat. Illustration of the said electrode is given later in Figure 175. The gold layer was deposited on Silicon via evaporation technique onto a Chrome adhesion layer and presented a thickness of 401.9 nm. Electrodes were firstly designed as single electrode per substrate to study the feasibility of the experiment and several trials were performed to support a lipid bilayer on those well-defined electrodes.

The first step was to transfer the cavity array fabrication technique presented in chapter 3 to the new substrates, to attempt to achieve full coverage of the future working electrode area with a tightly close packed cavity array. As the thickness of the substrates was of similar dimension to the one previously used, modification of the drop-casting equipment was not necessary. However, the challenge came regarding the nature of the surface on which the PS spheres needed to be assembled. Unlike Au-Si wafer fully covered with gold, the new substrates presented two different interfaces,

i.e. Au and SiO₂, each with different affinity for the PS spheres. First trials on untreated electrodes showed that no PS beads would assemble at the gold surface as illustrated in Figure 175 a).

Contact angle studies were carried out after different surface treatments to understand the hydrophilicity properties of the substrate's surface. Measurements were performed on the silicon parts of the substrates and on Au-Si wafer fully covered with gold to be assimilated to the electrode. Indeed, the gold electrode on the new substrates was too small compared to the drop size, which would have led to inaccurate results and wrong interpretations due to contribution of the surrounding Si. Results are summarized in Table 17.

Table 17: Contact angle measurements on Si and Au surfaces before and after physical and chemical surface treatments. Average and CVs were obtained with a minimum of n = 6 measurement per sample.

Substrate	Si		Au	
	Contact Angle	CV (%)	Contact Angle	CV (%)
No treatment	65.9°	0.8 %	81.4°	2.2 %
Plasma cleaning 5 min	24.9°	2.3 %	39.3°	34.8 %
Hellmanex II 30 min 35 °C	14.0°	6.6 %	74.6°	1.7 %
Hellmanex II 30 min 35 °C + Mercaptoethanol 10 mM overnight in EtOH	37.4°	2.5 %	57.5°	8.4 %
Hellmanex II 30 min 35 °C + Mercaptoethanol 10 mM overnight in H ₂ O	17.5°	6.6 %	69.1°	5.1 %

From this table it can be understood that, with a contact angle of 81.4°, before any surface treatment the gold substrate is not hydrophilic enough to facilitate the deposition of the PS beads, unlike the slightly hydrophilic Si surface with a contact angle of 65.9°. Despite the preliminary acetone wash recommended by the electrode

manufacturer to get rid of the protective film at the surface of the substrate, the values remain slightly higher than values typically reported for gold^{3,4} and silicon oxide^{5,6} substrates, probably due to organic substances still present at the surface.

Physical and chemical surface treatment showed a considerable improvement in the hydrophilicity of the Si surface with best results obtained by cleaning the substrate with a 2 % (v/v) solution of Hellmanex® II at 35 °C for 30 minutes, which reduced the contact angle to 14°. Those substrates were also tested with a combination of the cleaning solution followed by an overnight immersion in a 10 mM Mercaptoethanol aimed at creating a hydrophilic SAM at the gold electrode surface. It can be seen that when the solution of thiols is mixed in ethanol rather than in water, the contact angle of the Si substrate increases to 37.4° as it is recovering some hydrophobicity.

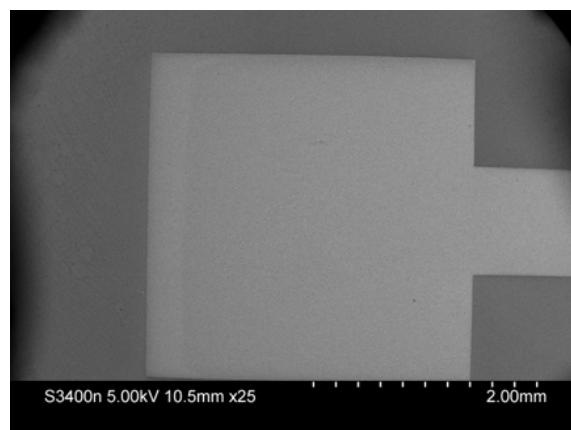
On the other hand, Au hydrophilicity was mostly influenced by the physical treatment using plasma cleaning which brought its surface contact angle to 39.3°. The cleaning solution did not have a considerable impact on the hydrophilicity of the Au surface. Though, as expected, functionalising the Au surface with a hydroxylated thiol reduced contact angle to 69.1° and 57.5° when mixed respectively in water and in ethanol. Surface treatment was more efficient in ethanol than in water, probably due to the better solubility of the compound in this solvent.

Trials to fully cover the gold electrode of the new substrates with a monolayer of closely packed PS spheres were successful both after plasma cleaning and after chemical treatment with the Hellmanex® II solution followed by the functionalisation of the gold surface with mercaptoethanol, as illustrated in Figure 175 b).

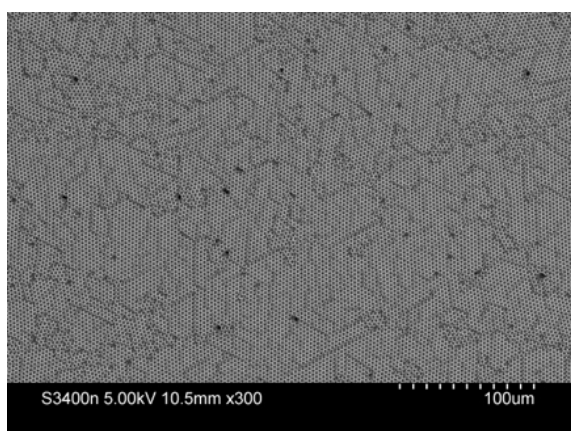


Figure 175 : Deposition of a hexagonal close packed monolayer of 3 μm diameter PS spheres onto 4 mm^2 gold electrode on Si wafer before (a) and after (b) surface optimization.

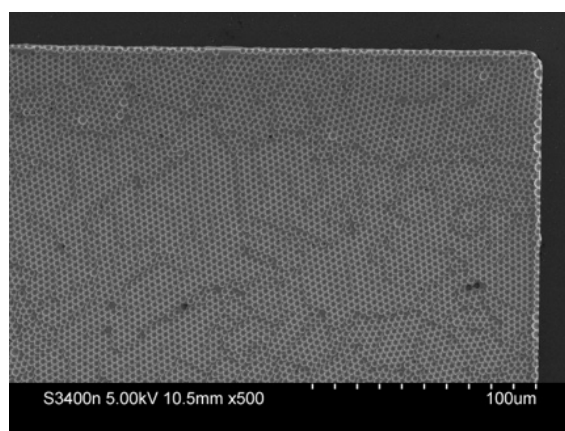
Cavities were then electrochemically grown around the spheres following the method described in chapter 3. Characterisation of the new electrodes by SEM was carried out to make sure surface of the gold electrode was fully covered with closely packed cavities, to ensure minimum planar electrode area. Figure 176 illustrates the full coverage of the gold electrodes once 3 μm diameter PS spheres have been dissolved and reveals excellent close packing with a very low defect density.



a)



b)



c)

Figure 176 : SEM images of a hexagonal close packed 3 μm diameter cavities array covering fully a 4 mm² gold electrode on Si substrate. a) x25 view of the whole electrode, b) x300 view at the centre of the electrode, c) x500 view at one electrode corner.

EIS measurements carried out in similar conditions as described for the masked electrodes above showed the disappearance of the feature around 100 Hz, thus matching more to the typical profile of Bode plot obtained for standard cavity arrays previously used in our group.¹

However, several attempts to suspend a DOPC lipid bilayer on the substrates with large pores of 3 μm diameter showed a low success rate. Indeed, despite selectively modifying the top surface of the array with an alkane thiol to promote hydrophilicity of the surface critical for a good spanning of the lipid bilayer^{1,7}, the membrane would not form homogeneously. This may be due to the very tight close packing of cavities, as more interstitial space between pores may be required with such large apertures to allow better anchor points to support the bilayer. While the electroactive area reproducibility between samples has been improved by the work presented in chapter 3 on the close packed arrangement of cavities, the stability of the lipid bilayer seems to have been affected regarding its formation over large aperture cavities. Researchers might need to consider this parameter in future work and try to space out cavities if wanting to work with suspended lipid bilayers on such large apertures. Unfortunately, obtaining a well-ordered arrangement of spaced 3 μm spheres by convective assembly is a real challenge. Functionalisation of the spheres with long carbon chain molecules could be tried to keep beads away from each other but this might have an influence onto attraction/repulsion forces and perturbate the wanted hexagonal arrangement.

One approach that will be more controllable and that is currently under investigation by Keyes' group is the use of a two-photon polymerisation 3D printer. Preliminary data shown in Figure 177 was attempted based on the data presented in chapter 2. 1 μm diameter positive hemispheres were 3D printed using this technique aiming at using this sample as a template. From this picture can be seen that the technique has a high enough resolution to fabricate distinct 1 μm diameter hemispheres, hence should be suitable for bigger structures sizes and could solve the above-mentioned issue. The separation between structures is not yet optimal to facilitate a good moulding and ensure the minimum interstitial flat surface between cavities necessary to a good lipid bilayer formation, but we believed this parameter can be easily adjusted by modification of the original drawing used for the fabrication. This technique looks really promising regarding the reproducible fabrication of a microcavity array by soft lithography.

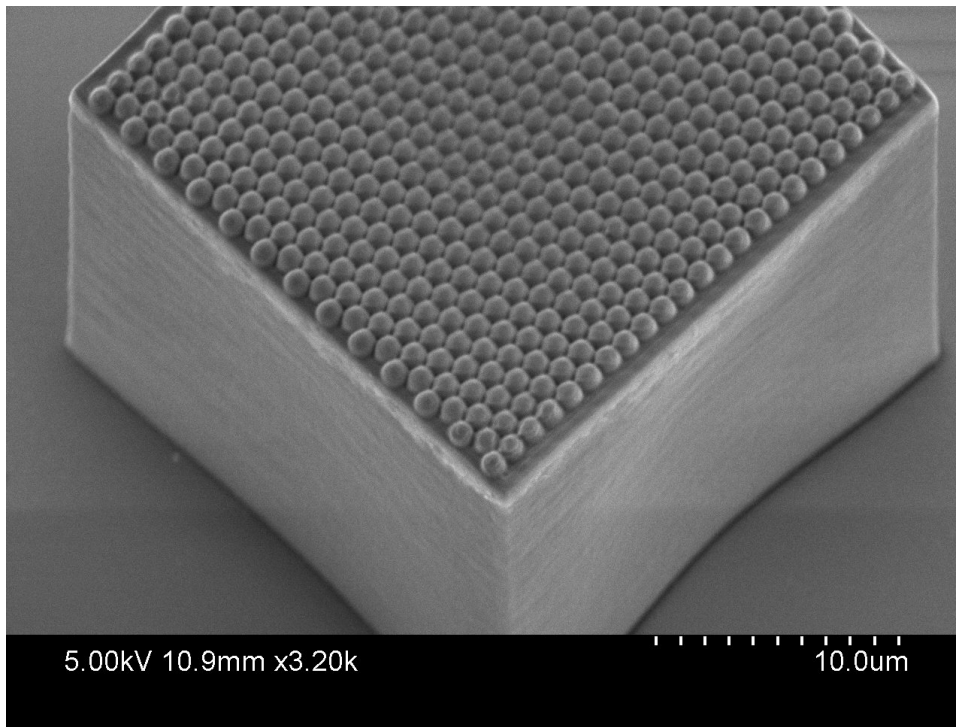


Figure 177 : 20° angle tilted SEM image of a 25 x 25 μm array of 1 μm diameter hemispheres obtained by two-photon polymerization 3D printing technique.

Despite the improvement of the EIS signal shape, substrates made by the external contractor were not suitable for the assembly of the microfluidic device. Indeed, the very smooth SiO_2 surface was not compatible with the PSA based device. To make the different layers of the device stick together, pressure needed to be applied as per the PSA principle. The material constituting the electrode substrate being brittle, only a low pressure could be applied without risking damaging it. This was leading to the channel layer peeling off from the substrate, creating leakages in the microfluidic devices when filled with buffer.

5.3.2 Alternative design of the device

5.3.2.1 Choice of material as electrode substrate

In spite of the excellent packing and electrode performance, the high fail rate of the above electrodes in supporting a bilayer and challenges in assembly of it in the device, meant an alternative means of building bilayer supporting cavity electrodes needed to be explored. The main body of the device presented in chapter 2 was in PMMA and showed good suitability in term of assembling and sealing properties, however it did not integrate electrodes for EIS measurement.

The first step in the development of the new microfluidic device was to find a substrate that could both withstand pressure and adhesion of PSA, unlike the previously used silicon wafer, but also would be suitable as a good base for sputtered gold electrodes.

PMMA, PS and COP were all tested as they are commonly used in microfluidic device fabrication.⁸⁻¹⁰ All substrates presented good characteristics in term of binding to PSA. Gold electrodes were then sputtered at the polymer surfaces and a PSA layer was placed simulating the channel of the future microfluidic device, as shown in Figure 178. A piece of Scotch-tape was placed on the top electrode and peeled off. The bottom electrode was used as a reference for comparison.

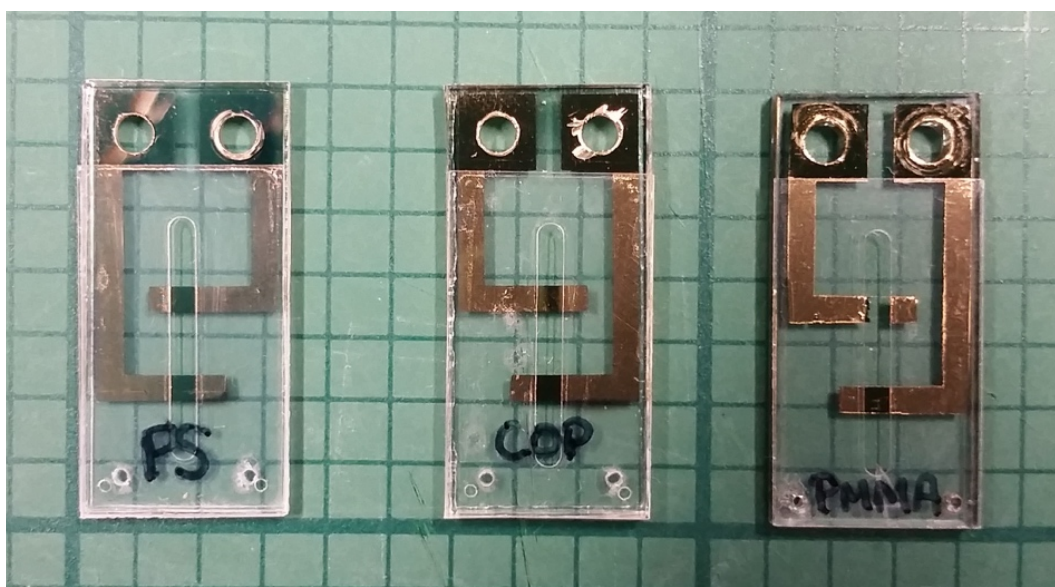


Figure 178 : Peeling test performed on gold electrodes sputtered at PS (left), COP (middle) and PMMA (right) surface.

The adhesion test shows that PS substrate was the best candidate among the three materials as the coated gold layer was most resistant to peeling. Gold on PMMA was fully peeled-off and gold on COP showed damage after the tape was removed. However, choosing PS as substrate for the gold cavity array meant fabricating the cavity array in a different way to the method previously optimised for gold on silicon, as dissolving the PS spheres to form cavities would also damage the underlying substrate. A key step in the fabrication after gold deposition is the dissolution of the PS spheres but the PS substrate would not be sufficiently resistant to organic solvent to withstand this step. Therefore, to facilitate the method transfer of cavity and nano structures fabrication, another polymer substrate was investigated.

In the first instance, the microfluidic device was to be built with only gold electrodes acting as working and reference/auxiliary. However, thinking of upgrading the device in the future to a three electrodes setup similar to the one currently used in a beaker, attention was given to a base substrate compatible for screen printed electrodes. Indeed, screen printing reference electrodes such as Ag/AgCl as thick film has been done by several groups.¹¹⁻¹³ PET (Polyethylene terephthalate) sheets specifically treated for good adhesion of the paste during the screen-printing process were tested. As Kotal et al. showed good adhesion of gold onto argon plasma treated PET¹⁴, gold electrodes were sputtered at the polymer surface.

PET was assessed in an analogous way as described above for the other polymers and showed excellent binding to PSA and good results to the peeling test without delamination of the gold layer. It was then decided to continue the development of the microfluidic device with this polymer as substrate for the gold cavity arrays. To reinforce the adhesion of the gold to the polymer, sputtering a chromium adhesion layer onto the polymer prior to the gold could be considered, as done by other groups.¹⁵⁻¹⁷

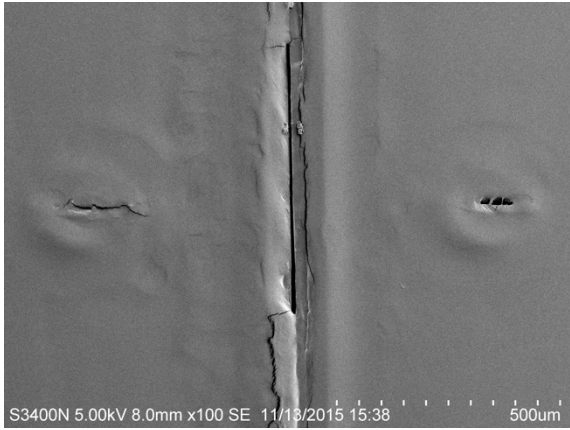
5.3.2.2 Design towards a substrate for lipid membranes study from PET

For practical reasons it was decided in the first instance to develop a two electrodes Au-Au system with the possibility to upgrade it in the future to a more conventional three electrodes system as mentioned previously. For impedance measurements where no faradaic process a two-electrode cell is suitable.

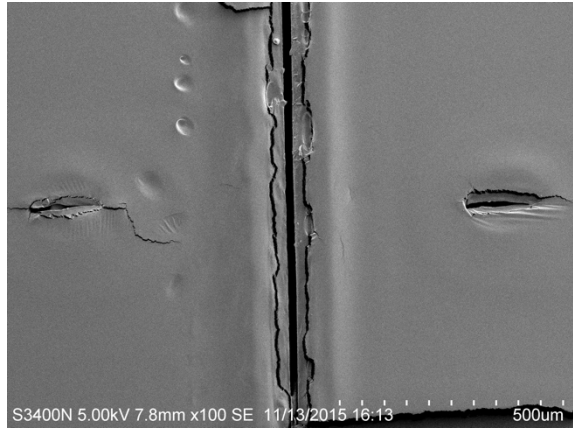
5.3.2.2.1 Electrodes size and shape

The shape of the electrode was controlled by the superimposition of a transfer tape mask used during the gold sputtering step and the width of the channel placed on top of the electrode giving a squared shape to it. The different layers used in the fabrication of the electrodes and the device are illustrated below in Figure 180.

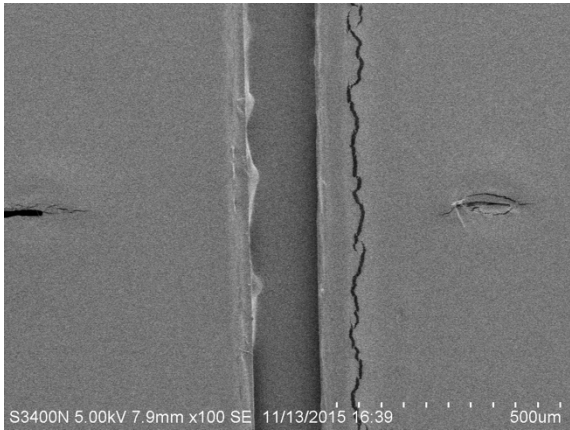
To start with, the working electrode geometrical surface area was designed to be close to the dimensions of standard 2 mm diameter gold disc electrodes. The width of the mask was set to 2 mm for the area where the electrode will be in contact with the electrolyte and restricted to 0.5 mm for the wiring in contact with the PSA layer which acts as the channel. This restriction was applied due to the issues described previously in section 5.3.1, to limit the conductive area under the adhesive. This simple and straight shape of the mask is within the capability of the knife cutter used, which has been tested as shown in Figure 179, and avoid damaging the electrode when peeling it off the mask needed to delimit its shape. 200 μm width seems to be the limit of the knife cutter capability, as below this value the precision of the equipment is not good enough to ensure an open channel on its whole length.



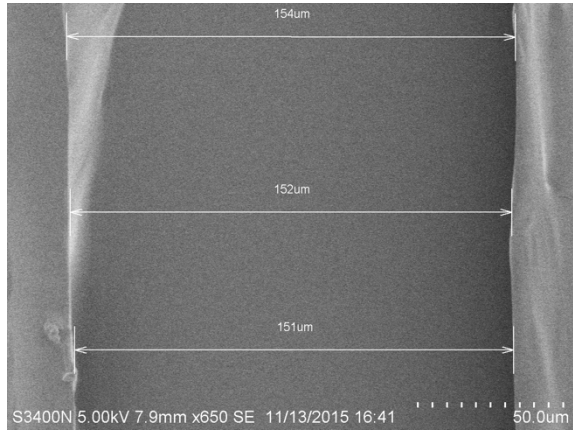
a)



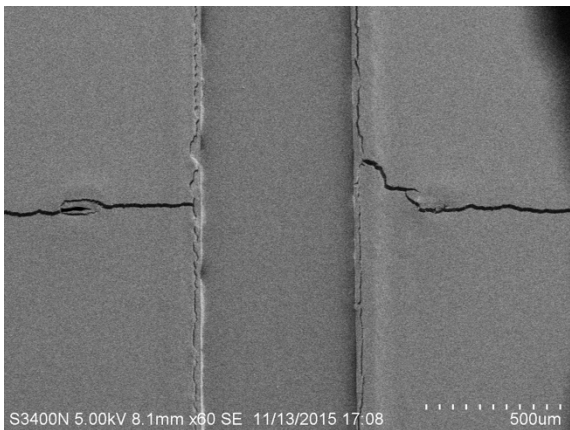
b)



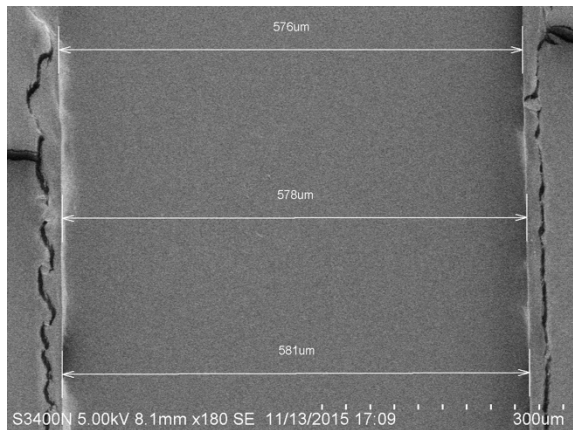
c)



d)



e)



f)

Figure 179 : SEM images of different PSA channel width cut by xurography. a) $w = 100 \mu\text{m}$, b) $w = 150 \mu\text{m}$, c) & d) $w = 200 \mu\text{m}$, e) & f) $w = 500 \mu\text{m}$.

Using the same fabrication principle, reference / auxiliary electrodes was designed to be 9 times the size of the working electrode. In the electrochemical system, the reaction of interest is occurring at the working electrode, the counter electrode closes the circuit and current flows between the two electrodes. To sustain a current flow, the electroactive area of the counter electrode must be larger than the area of the working electrode so that it acts as a source/sink of electrons, providing them at a rate that does not limit the kinetics of the electrochemical process at the working electrode.¹⁸ Large surface area of the auxiliary electrode will lead to high capacitive currents. This way, reactions such as solvent electrolysis and gas production that can interfere with the measurement can be avoided. This is particularly crucial in the small volume of solution used such as in microfluidic devices.¹⁹

5.3.2.2.2 Device design

Figure 180 shows the AutoCad® design of the different layers constituting the microfluidic device and a representation of their assembly. The device was designed with two channels, each integrating one reference / auxiliary electrode in the middle surrounded by two working electrodes distant from 1 cm. This separation allows one to comfortably span a lipid monolayer by Langmuir-Blodgett method onto the working electrodes situated on one side of the middle electrode, without risking coating the reference / auxiliary electrode. By flipping upside down the electrodes' substrate, a lipid monolayer of a different nature can be deposited onto the working electrodes on the other side of the device.

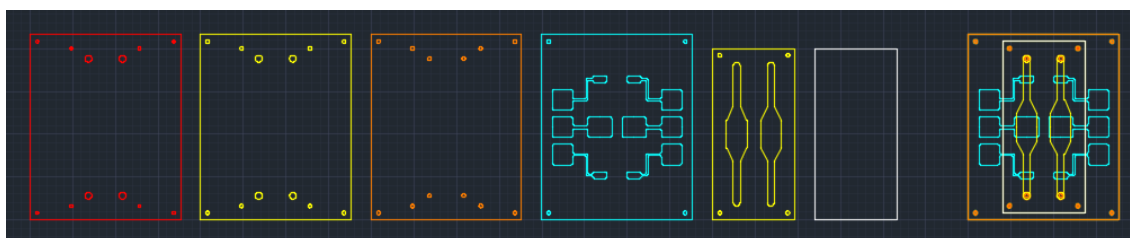


Figure 180 : AutoCad® design of the different layers for the fabrication of the microfluidic device. From left to right: 2 mm thick PMMA (red); 50 μm thick double-sided PSA (yellow); 175 μm thick PET (orange); transfer tape for electrodes sputtering (turquoise); 50 μm thick double-sided PSA channel (yellow); microscope glass coverslip (white); superimposed assembly of the different layers.

This overall configuration allows for a versatile device, Langmuir Blodgett deposition and/or vesicle disruption compatible, and able to support up to four different lipid bilayer compositions:

- two different lower leaflet compositions,
- two different vesicles composition for upper leaflet formation in each channel.

5.3.2.3 Assembly and leakage test

To evaluate the effectiveness of sealing of the device once assembled, and its viability due to the different steps involving liquid during the formation of the lipid membrane and its study, water containing green and red food dyes were used. Figure 181 shows that the method produced well-sealed and independently addressable microfluidic channels. Small air bubbles sometimes formed, probably due to the dye not being degassed before the test. Also, air plasma treating the substrate before lipid bilayer spanning at its surface might increase wettability of the polymer and limit this phenomenon.

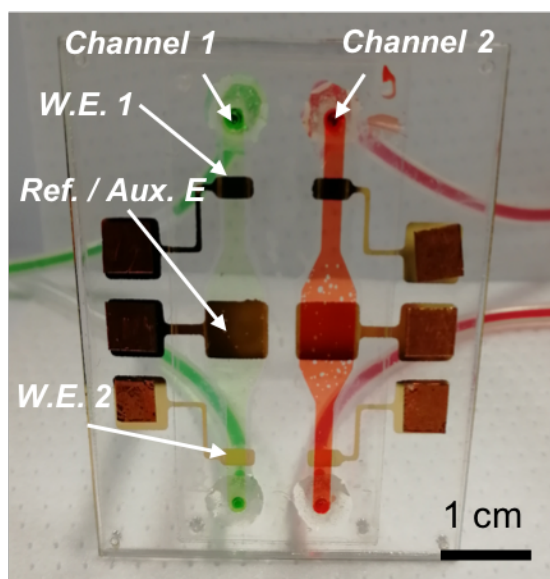


Figure 181 : Picture of the assembled 2 channels microfluidic device leakage test performed with green and red food dyes. (Device dimensions 44 x 54 mm)

5.3.3 Electrochemical compatibility

As the microfluidic device is intended for use with dual spectroscopic and electrochemical methods, preliminary tests were conducted to evaluate the suitability of the device for electrochemistry, in particular the dimensions of the working electrode relatively to the channel.

After fabricating gold electrodes on PET substrates, working electrodes were cycled in 0.1 M H₂SO₄ solution to check the gold surface was clean for further electrochemistry tests. The electrodes were cycled consecutively 3 times between 0 V and 1.6 V, as illustrated in Figure 182, which shows a gold oxide monolayer starting to form at 1.1 V. Scan was reversed at 1.6 V to avoid further bulk gold oxidation and risk to create surface roughness. Reduction of the gold oxide peak can be observed centred at 0.87 V. The voltammogram is very well behaved and matches perfectly the characteristics of gold oxide voltammetry under conventional electrode system indicating the system behaves very well as an electrochemical cell.

However, with extensive cycling in H₂SO₄ the gold electrode started to delaminate from the polymer surface. Therefore, if cleaning is needed in the future, it is advised to limit it to 3 cycles maximum to avoid damaging the electrode surface.

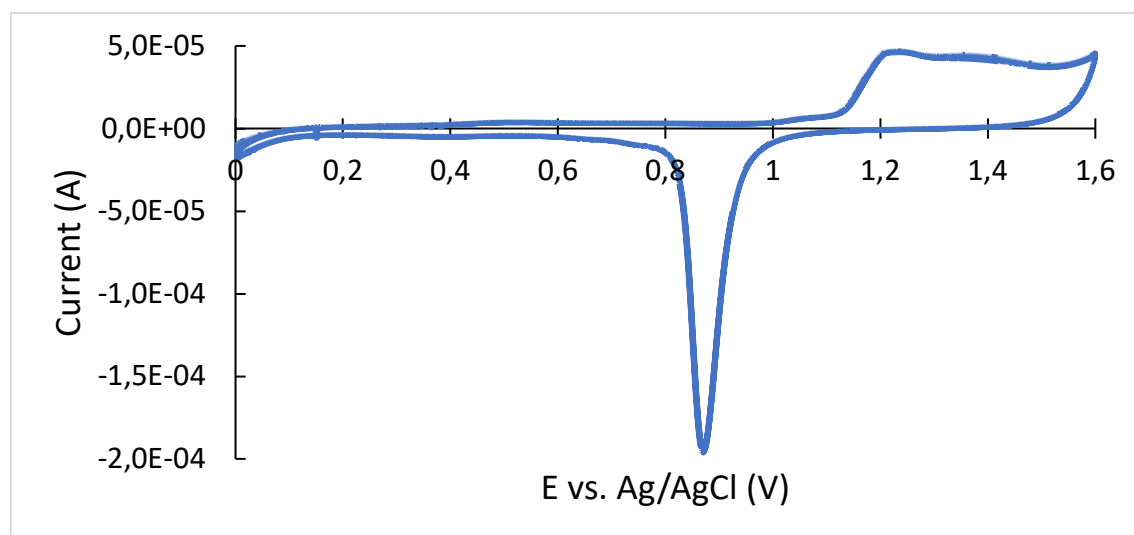


Figure 182 : Cyclic voltammogram of a gold electrode sputtered at PET surface cycled 3 times in 0.1 M H₂SO₄. The counter electrode and the reference electrodes were respectively a platinum wire and an Ag/AgCl saturated in 3 M KCl. Scan rate was 0.1 V/s.

The gold working electrode performance was then characterised by performing cyclic voltammetry using the standard redox couple Fe(CN)₆³⁻ / Fe(CN)₆⁴⁻. Figure 183 shows results obtained in several environmental conditions. Firstly, potential was cycled with the electro active surface uncontrolled, then delimited geometrically to 4 mm² by applying a PSA channel but not controlling the thickness layer of electrolyte above the electrode. Finally, we varied the channel thickness and closed the device with a glass coverslip to understand the effect of the cell geometry on the redox probe.

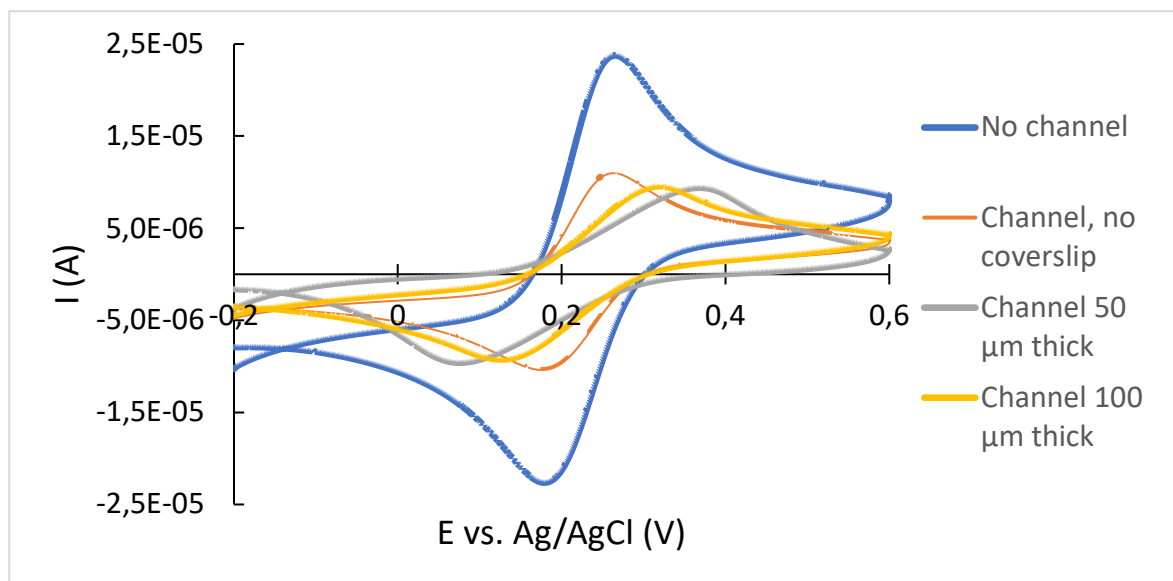


Figure 183 : Cyclic voltammogram of gold working electrode sputtered at PET surface in different environmental conditions. 1 mM $K_3[Fe(CN)_6]/K_4[Fe(CN)_6]$ (1:1 mol/mol) mixture was used as a redox probe dissolved in PBS buffer containing additional 0.1 M KCl as the supporting electrolyte. Scan rate was 0.05 V/s.

From Figure 183 it can be seen that the peak to peak separation (ΔE_p) varies with the thickness of the electrolyte layer above the working electrode.

Without the channel, $\Delta E_p = 88$ mV, which is higher than the theoretical 59 mV for a Nernstian electrochemically reversible one-electron redox response, but, 59 mV is a theoretical ideal Nernstian response and difficult to obtain even in close to ideal, but real electrode systems due to uncompensated resistance and relative orientation of electrodes. $\Delta E_p = 88$ mV indicates the cell is working very well and furthermore the system shows excellent chemical reversibility with peak current ratios (i_{pa}/i_{pc}) close to 1.²⁰ As expected, applying a PSA channel on top of the working electrode to restrict its geometrical surface to 4 mm² does not influence the peak to peak separation, but reduces the peak currents, as less volume of redox species is in contact with the gold electrode. However, as soon as the channel is covered with a glass cover slip, the separation between peaks increases drastically with ΔE_p equal respectively to 293 mV and 194 mV for 50 μ m and 100 μ m thick channel. This peak to peak separation differences can be attributed to uncompensated iR drop due to the influence of the geometry of the electrochemical cell. Ideally the working and reference should be as close as possible, and the auxiliary should not be obscured from the working electrode.²¹

A key issue is that for this experiment, only the sputtered working electrode has been tested vs. a classic Ag/AgCl reference electrode placed in the same vessel used for electrochemical cell. For future work, it would be interesting to check the performance of the working electrode within the microfluidic device, with the potentiostat linked to the central gold reference electrode. This would allow us to check if the reference electrode is not too far from the working one, given the low thickness of the channel. If the system appears still to be not fully reversible, then a compromise will need to be reached by adjusting channels height, distance between electrodes, increasing electrolyte concentration and reducing scan rate. Increasing the channel height will probably have the most influence on the peaks separation but might lead to restrictions of use, particularly if the device needs to be used with immersion objective for which the working distance is short.

In spite of the Ohmic drop, it is clear that we have achieved a functional microfluidic electrochemical cell.

5.3.4 Cavity array and nano structuring

Transferring the previously developed method of hexagonal close packed cavity array at the surface of gold electrodes built onto PET was then achieved in several steps.

The first step was to find a solvent that could dissolve PS spheres without damaging PET. Indeed, acetone or THF that are usually used for this purpose cause immediate damage to both polymers, hence are not suitable. Cyclohexane proved to be the best selective solvent to meet this need.²²

The second step was to achieve a full coverage of a hexagonal close packed assembly of PS spheres at the working electrode surface. To do so, the method developed in chapter 3 was adopted, however instrumentation needed to be modified to fit the dimensions of the substrate to be treated. Figure 184 illustrates the successful uniform assembly of the spheres reflected in the characteristic opal iridescence of the electrode surfaces.

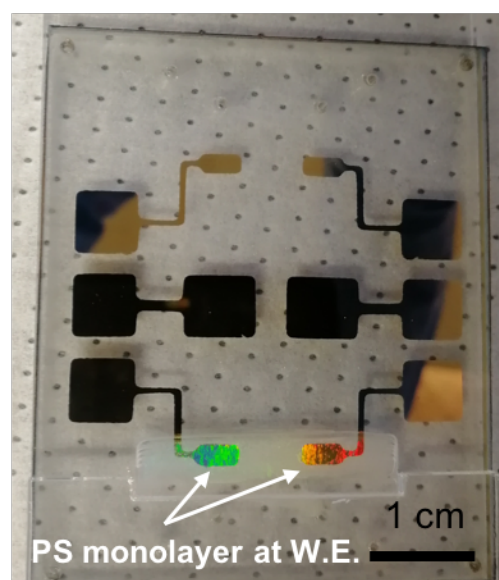


Figure 184 : Picture of a hexagonal close packed 1 μm diameter PS sphere monolayer assembled at gold electrodes surface sputtered onto a PET substrate. (Substrate dimensions 44 x 54 mm)

The third step was to electrodeposit gold around the assembled spheres at working electrodes using the method developed in chapter 3. The *i-t* curve for electrodeposition followed closely that reported in chapter 3 which accurate control of the gold electrodeposition up to the equator of the beads. Besides achieving reliable gold growth, this step proved the mechanical resistance of the sputtered gold electrodes were able to withstand a potential of -600 mV for a minimum of 12 to 15 minutes depending on the electrode, without delaminating the gold from the PET substrate.

Finally, nano sub-structuring was achieved following the method described in chapter 4, while taking care not to damage the underlying PET substrate during the etching process. This was done by applying a mask made of a copper tape stuck onto a piece of PMMA, presenting an aperture over the PS array, preventing most of the PET to be etched at the same time. The uniform packing of 1 μm diameter cavities, each containing nano-substructuring was verified by SEM as shown in Figure 185. Applying the same copper-mask, arrays were sputter coated with gold to render the etched polymeric nano substructures SERS active.

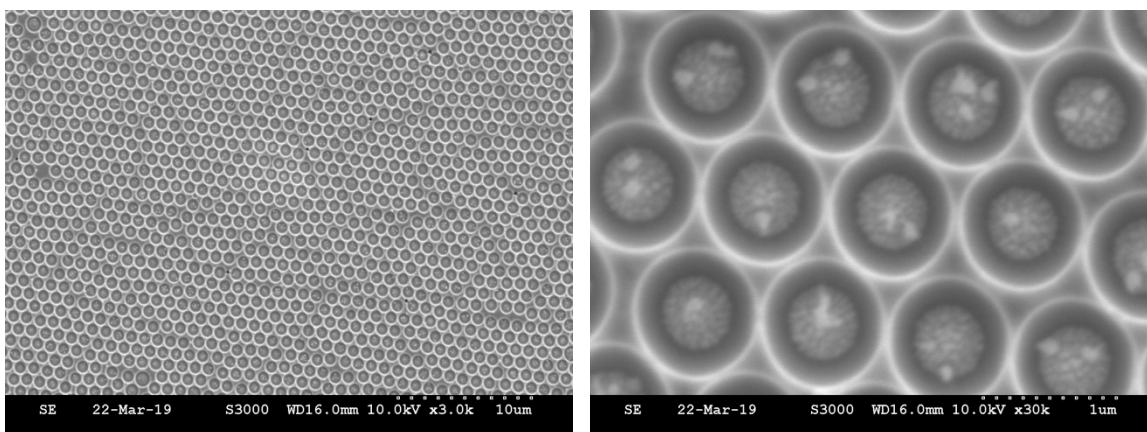


Figure 185 : SEM images of gold electrode sputtered onto PET film presenting 1 μm diameter PS spheres in cavity etched for 8 min. (RF = 100W; O_2 = 25 sccm; P = 50 mTorr)

Further work still needs to be achieved to fully characterise the newly fabricated SERS-microfluidic platform. However, this last result constituting the core of the microfluidic device looks morphologically identical to substrates studied in previous chapters in term of cavity array uniformity and nano-substructuring and gives thus good hope as for its potential to achieve at least similar results in term of signal enhancement and reproducibility.

5.4 Conclusion

The work presented in this chapter demonstrated the successful transfer of the previously developed SERS substrates into an electrochemically addressable microfluidic device.

First attempts to transfer the Au-Si structured array as working electrode in the device, in identical format as described in chapter 3 and 4, suffered from high contribution to the impedance signal due to the large conductive area under the masking PSA acting as the microfluidic device channel. Reducing the underlying conductive area with a new electrode design on Si substrate solved the issue but this option had to be abandoned, mostly due to device assembly problems caused by the very smooth polished SiO₂ surface preventing efficient sealing of the device.

A PET/PMMA-based two-channel microfluidic device was then designed and manufactured, intended to host up to four different lipid membrane compositions, symmetric or asymmetric, spanned by Langmuir-Blodgett / vesicle fusion method. Preliminary tests show the successful fabrication of gold electrodes by simple sputter coating at a PET film surface, which were mechanically and electrically resistant. Working electrodes were able to sustain a potential in a window of -0.6 V to 0.6 V, tested during cyclic voltammetry and gold electrodeposition for cavity formation. Due to the new nature and dimensions of the chosen material acting as electrode substrates, modification of the array fabrication method described in chapter 3 was achieved, leading to a uniform well organised close packed cavity array covering the full electrode surface.

Finally, after taking precautions not to damage the underlying PET substrate surrounding the gold electrode, arrays could be used as desired with nano substructures after etching PS as described in chapter 4, or with bare cavities as described in chapter 3 after dissolving the polymer with cyclohexane instead of THF.

In summary a gold nano-structured electrochemically addressable microfluidic array, in dual channel format was achieved, prepared from PET and PMMA layers assembled with PSA. The format of the array should make it suitable for dual SERS/electrochemical work in its present format.

5.5 References

1. Maher, S., Basit, H., Forster, R. J. & Keyes, T. E. Micron dimensioned cavity array supported lipid bilayers for the electrochemical investigation of ionophore activity. *Bioelectrochemistry* **112**, 16–23 (2016).
2. Gamry Instruments, Inc. EIS of Organic Coatings and Paints - Application note Rev. 2.1.
3. Erb, Robert A. Wettability of gold. *The Journal of Physical Chemistry* **72**, 2412–2417 (1968).
4. Abdelsalam, M. E., Bartlett, P. N., Kelf, T. & Baumberg, J. Wetting of Regularly Structured Gold Surfaces. *Langmuir* **21**, 1753–1757 (2005).
5. Yanazawa, H., Matsuzawa, T. & Hashimoto, N. Evaluation of hydrophobic SiO₂ surfaces prepared by fluorinated organosilane treatments. *Journal of Adhesion Science and Technology* **4**, 145–153 (1990).
6. Thomas, R. R., de Nemours, I. D. & Laboratory, J. Wettability of Polished Silicon Oxide Surfaces. 6.
7. Frese, D., Steltenkamp, S., Schmitz, S. & Steinem, C. In situ generation of electrochemical gradients across pore-spanning membranes. *RSC Adv.* **3**, 15752–15761 (2013).
8. Chen, Y., Zhang, L. & Chen, G. Fabrication, modification, and application of poly(methyl methacrylate) microfluidic chips. *ELECTROPHORESIS* **29**, 1801–1814 (2008).
9. Becker, H. & Locascio, L. E. Polymer microfluidic devices. *Talanta* **56**, 267–287 (2002).
10. Rodrigues, R. O., Lima, R., Gomes, H. T. & Silva, A. M. Polymer microfluidic devices: an overview of fabrication methods. *U. Porto Journal of Engineering* **1**, 67–79 (2015).
11. Simonis, A., Krings, T., Lüth, H., Wang, J. & Schöning, M. A „Hybrid“ Thin-Film pH Sensor with Integrated Thick-Film Reference. *Sensors* **1**, 183–192 (2001).
12. Tymecki, ?ukasz, Zwierkowska, E. & Koncki, R. Screen-printed reference electrodes for potentiometric measurements. *Analytica Chimica Acta* **526**, 3–11 (2004).
13. Prasek, J. *et al.* Optimization of planar three-electrode systems for redox system detection. *Int. J. Electrochem. Sci* **7**, 1785–1801 (2012).
14. Kotál, V. *et al.* Gold Coating of Poly(ethylene terephthalate) Modified by Argon Plasma. *Plasma Processes and Polymers* **4**, 69–76 (2007).
15. Cosofret, V. V. *et al.* Microfabricated Sensor Arrays Sensitive to pH and K⁺ for Ionic Distribution Measurements in the Beating Heart. *Analytical Chemistry* **67**, 1647–1653 (1995).
16. Henry, C. S. & Fritsch, I. Microfabricated Recessed Microdisk Electrodes: Characterization in Static and Convective Solutions. *Analytical Chemistry* **71**, 550–556 (1999).
17. Lindner, E. & Buck, R. P. Microfabricated Potentiometric Electrodes and Their In Vivo Applications. *Analytical Chemistry* **72**, 336 A–345 A (2000).
18. Metrohm Autolab B.V. Basic overview of the working principle of a potentiostat/galvanostat (PGSTAT) – Electrochemical cell setup. *Autolab Application Note EC08* (2011).
19. Electrodes of a potentiostat. *PalmSens Corrosion* <https://www.palmsenscorrosion.com/knowledgebase/electrodes-of-a-potentiostat/>.
20. Bard, A. J. & Faulkner, L. R. *Electrochemical methods: fundamentals and applications*. (Wiley, 2001).

21. Myland, J. C. & Oldham, K. B. Uncompensated Resistance. 1. The Effect of Cell Geometry. *Analytical Chemistry* **72**, 3972–3980 (2000).
22. Bangs Laboratories, Inc. Tech Support Doc 0023 Rev 002 - Common Solvents and Non-solvents of Polystyrene. (2018).

6 Chapter 6: Conclusions and future work

6.1 Conclusions

The objective of this thesis was to two-fold; to understand and optimise gold pore arrays for application as SERS platforms and to design and build microfluidic devices that encapsulates a pore array, one in an optically transparent substrate suitable for FCS and one prepared in metal, suitable for combining SERS with EIS. Long term, the device is intended to support a lipid bilayer for dual impedance/spectroscopic measurements.

As outlined in the introduction chapter, diverse solutions are reported in the literature for the fabrication of SERS substrates suitable for biophysical or analytical applications. From a fundamental and practical point of view, researchers are interested in high SERS signal intensity but in analytical applications high reproducibility of fabrication and ultimately of the SERS response are critical and often the former is compromised at the expense of the latter depending the fabrication method employed. There is also growing interest in applying microfluidics to SERS methods, as combining those two fields leave the door open to platforms that permits study low and reproducible volumes of analyte. For study of lipid bilayers or supported lipid bilayers, SERS is a useful approach given the interfacial nature of such platforms and can allow understanding of the biophysical behaviour of the cell membranes away from the complexity of the cell. Though there are less microfluidic examples of SERS substrates applied to this end.

Chapter 2 focussed on the fabrication of the microfluidic device that incorporated an array of micropores initially in an optically transparent material that should be compatible with fluorescence microscopy and FCS, but also suitable for the constraints related to the formation and stability of artificial lipid membranes. The device was designed in two main parts, the first one supplying reagents to the second one, where the artificially formed lipid membrane is supported. The choice of the material/method for the fabrication of the microfluidic device leant then towards a combination of PMMA and PSA layers respectively, processed by CO₂ laser machining and xurography. In this chapter, particular focus was put towards the fabrication of a micron dimension cavity array onto PMMA substrate for easy implementation into the device. Based on hot embossing, two new effective and reproducible methods are presented. The first

method used a silicone-based master for which hardness was improved through study of (elastomer : curing agent) ratio and curing conditions. Preparing the positive master in a 21:1 ratio and curing it overnight at 40 °C reduced its deformation by 32 % and lead to PMMA embossed cavities with a diameter of 3.1 μm and height of 1.6 μm . The second method used a more rigid embossing master made of silica microspheres embedded in a gold substrate. Thiolation of the silica beads using MPTMS revealed to be a good way to limit their transfer onto the PMMA substrate during the embossing process. Preliminary attempts to assemble a bilayer at the PMMA pores were unsuccessful but should be overcome with additional modifications to hydrophilicity and nanoroughness of the substrate. Nonetheless, a sealed leak-free device incorporating reproducible pore arrays that are capable of post assembly following surface modification was demonstrated.

Chapter 3 then focussed on preparing the pore arrays in a plasmonic metal, here gold, and on optimising a low-cost method for preparing spherical pore arrays of outstanding order over cm area, ultimately for implementation into the microfluidic device for dual electrochemical and SERS applications. The underlying aim was also to increase the aqueous environment available for the suspended membrane on the electrode and thus ensuring a better representability of natural cell membranes. An optimised method for achieving uniform and well-ordered nano and micro cavity arrays with minimal interstitial space between cavities was developed. This was achieved through optimisation of two steps; firstly through improvement of PS spheres assembly at an Au-Si surface, and secondly through optimized control of gold electrodeposition around the arrayed beads. Achieving such extended ordered arrangement of the particles at the gold surface was particularly challenging for spheres over 1 μm diameter, however, controlling the hydrophilicity of the substrate, polydispersity and concentration of the colloidal solution, as well as careful control of the drying process allowed for an iridescent centimetre sized deposit at the whole gold surface, characteristic of the uniform and well-ordered monolayer of spheres. SEM confirmed the excellent, low defect density order achieved and this was reflected in a dramatic reduction in inter-substrate variability of electroactive area from electrodes fabricated through the conventional reported method of 26 % and the new method of 5.2 %. Finally, FDTD simulations and experimental setup were designed to study the angle dependence of incident light on improved arrays of different sizes. This allowed

for a deep understanding of electric field location, intensity and distribution at the cavity's surface under different conditions and revealed 510 nm diameter cavity arrays having the best selectivity in field intensity between the bottom and the top of the cavity when tilted at 20° compared to normal incidence.

Chapter 4 then took the fabrication method a step further, and focused on a new, low-cost method for nano sub-structuring the arrays. The purpose was to both maximise SERS performance but also to ensure that the hot spot was localised at the bottom of the well. A reproducible fabrication method for nano-sub structuring arrays of voids of four different diameters ranging from 510 nm to 3 µm was demonstrated. The new method comprised using the method developed in chapter 3 and leaving the templating sphere in place after electrodeposition, etching the PS sphere before depositing a second layer of gold. Controlling parameters during oxygen plasma etching led to formation of nanostructures of reproducible shape and size produced both within a single substrate, with good reproducibility between batches of arrays. This technique has the advantage to leave a nano sub-structure at the bottom of every single cavity that presents multiple nano-defects with a plasmonic activity once coated with gold. Using 4,4'-BPY SAM and [Ru(bpy)₃]Cl₂ respectively as SERS and MEF probes, arrays were characterised and nano structured 2µm diameter cavity arrays showed the best enhancement potential. Despite the technique not being based on photolithography, EBL or FIB, variability of the results was significantly improved for nano structured arrays compared to their bare equivalent versions, particularly for small size cavities, which give good confidence into the efficiency and robustness of the fabrication method exhibiting high uniformity and reproducibility.

Finally, chapter 5 reported preliminary steps toward the successful transfer of the developed SERS substrates from chapter 3 and 4 into an electrochemically addressable microfluidic device. After several attempts to implement directly Au-Si cavity arrays into the PMMA based device by PSA assembly, the strategy was changed to develop gold cavity electrodes directly at a PET film surface and implement into a tightly sealed microfluidic device. Modifications of the array fabrication method were necessary to adapt to the new nature of substrate without damaging it and thus achieving fabrication of bare and nano sub-structures cavity arrays at the gold electrode surface. Preliminary tests showed the mechanical and electrical resistance of

the device, giving confidence on its suitability for dual SERS/electrochemical work in its present format.

Overall, we have developed a PET/PMMA-based two-channel microfluidic device designed to host up to four different lipid membrane compositions, symmetric or asymmetric, spanned at hemispherical gold cavity array by Langmuir-Blodgett / vesicle fusion method. The relatively cost-effective and highly reproducible fabrication method lead to bare and nano structured cavity arrays formed at the electrode surface with high plasmonic properties. Reduced variability both in electroactive surface area between electrodes and in SERS / MEF results among a single substrate or between different batches proved the great potential of this multimodal microfluidic device that needs to be further explored.

6.2 Future work

From the successes and challenges described in this thesis the following future work might be considered.

Firstly, if the microfluidic device in its most updated format presented in chapter 5 is applied to biophysical studies, verification of the reliable formation of homogeneous lipid membranes suspended at the cavity arrays will be important, particularly for arrays with NPs in cavities. Based on recent data from our group using the improved method described in chapter 3 to build the cavity array, it appears that the gold substrates outside of the microfluidic platform readily and reproducibly support lipid bilayers.¹⁻⁴ Issues can arise if the electrode or underlying polymer exhibit hydrophobicity or nanoroughness, as such nano-substructures perturbate the lipid membrane assembly. Even though the success of spanning a bilayer at the array in the microfluidic device should be mostly dependent on the gold and not the surrounding polymer, improvement of PET wettability reported by Gotoh et al.⁵ will surely help for a successful spanning of a lipid bilayer at the SERS / electroactive gold arrays.

Trying to adapt the method developed in chapter 2 to form a cavity array at the PET surface for FCS study would not be useful, due to the autofluorescence reported for this material.^{6,7} However, further investigations focussed on surface chemistry toward improving hydrophilicity of the PMMA substrate might be useful as such material could be easily implemented in the most updated format of the microfluidic device. An alternative route to air plasma treatment to render the PMMA surface hydrophilic to implement would be use of a cushion polymer to form a polymer cushioned supported bilayer. Despite drawbacks reported for lipid membrane models on flat surfaces in terms of interactions between the bilayer and the polymer cushion, this route could be suitable to our arrays as the polymer cushion thickness should be minimal in comparison to the cavity volume. The void should thus remain sufficiently filled with buffer to support a suspended lipid bilayer and decoupling it from the substrate and/or the polymer cushion.

Further electrochemical and SERS characterisation of the overall four working electrodes device could also be conducted to give an idea of the variability expected among a single device. Likewise work described in chapter 3, the electroactive area of the different cavity arrays delimited by the microfluidic channel could be assessed. In similar conditions as discussed in chapter 4, SERS properties of the arrays could be evaluated. Reducing the sensing area is expected to give better reproducibility of result intra sample. As well, inter sample reproducibility among the same device should be at least as good as described in chapter 4, given the nano sub-structured will be formed this time along the same etching batch.

Finally, the application of the platforms developed here for use with simultaneous analytical methods is the next step particularly for the study of lipid membranes. Indeed, combining SERS and electrochemical sensing onto a single sensor to enable a dual sensing approach from both techniques could help the device to move progressively from proof-of-concept towards a viable commercial product intended for the investigation of the effect of pharmaceuticals on the lipid bilayer or as a method for rapid analysis of new drugs' ability to bind to a membrane receptor.

6.3 References

1. Berselli, G. B., Sarangi, N. K., Ramadurai, S., Murphy, P. V. & Keyes, T. E. Microcavity-Supported Lipid Membranes: Versatile Platforms for Building Asymmetric Lipid Bilayers and for Protein Recognition. *ACS Applied Bio Materials* **2**, 3404–3417 (2019).
2. Steplewska, A. Plasmonic Assay for Molecular-Lipid Membrane binding, Permeation and dynamics of permeation (PhD thesis submitted 2019). (Dublin City University).
3. Steplewska, A., Kho, K. W., Gimenez, A. V. & Keyes, T. E. A Plasmonic Fluorescent Assay for molecular Lipid membrane binding and dynamics of permeation (Manuscript in preparation). (2020).
4. Berselli, G., Sarangi, N. K., Gimenez, A. V., Murphy, P. V. & Keyes, T. E. Microcavity Array Supported Lipid Bilayer Models of Ganglioside - Influenza Hemagglutinin1 Binding. *Chem. Commun.* (2020) doi:10.1039/D0CC04276E.
5. Gotoh, K., Yasukawa, A. & Kobayashi, Y. Wettability characteristics of poly(ethylene terephthalate) films treated by atmospheric pressure plasma and ultraviolet excimer light. *Polymer Journal* **43**, 545–551 (2011).
6. Features of Fluorescence Spectra of Polyethylene Terephthalate Films. *Jpn. J. Appl. Phys.* **43**, 8107 (2004).
7. Kihara, N. *et al.* Low-autofluorescence fluoropolymer membrane filters for cell filtration. *Japanese Journal of Applied Physics* **57**, 06JF03 (2018).

Appendices

Appendix A. Hardness optimisation of the silicone based embossing master - Study of the curing temperature - Hardness Shore A measurements

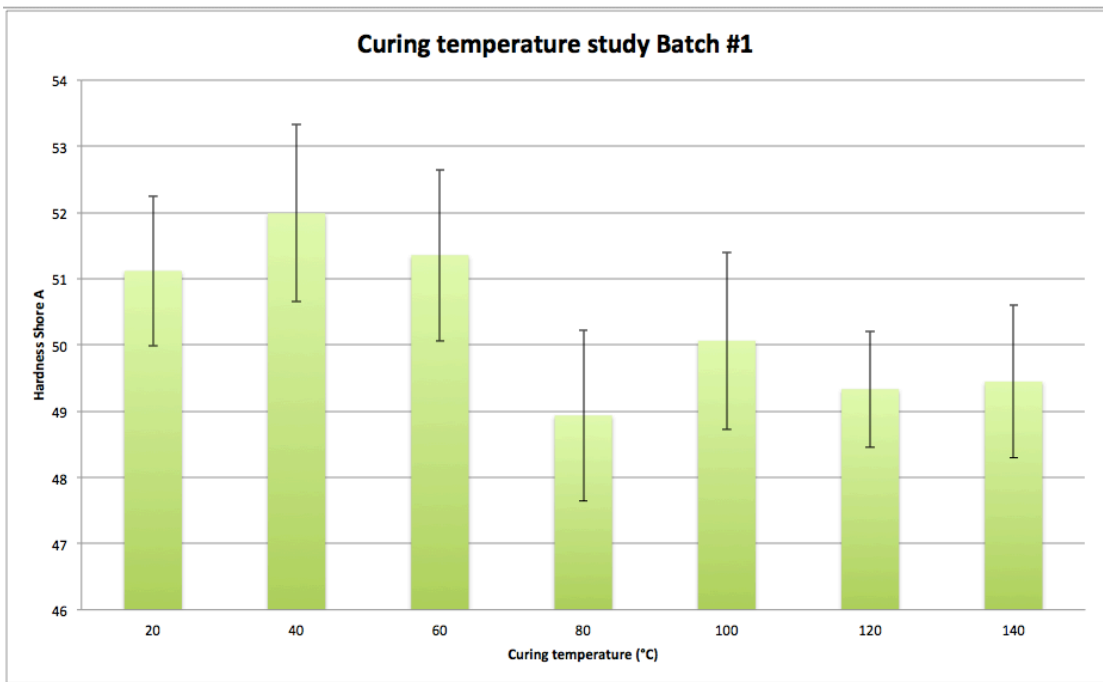


Figure A1: Results of Hardness shore A measurements done on a first batch of Elastosil® RT607 samples (3 samples per temperature tested with a minimum of 31 measurement per sample after statistical treatment). Samples have been prepared in a 9 :1 ratio (elastomer : curing agent) and cured at different temperature.

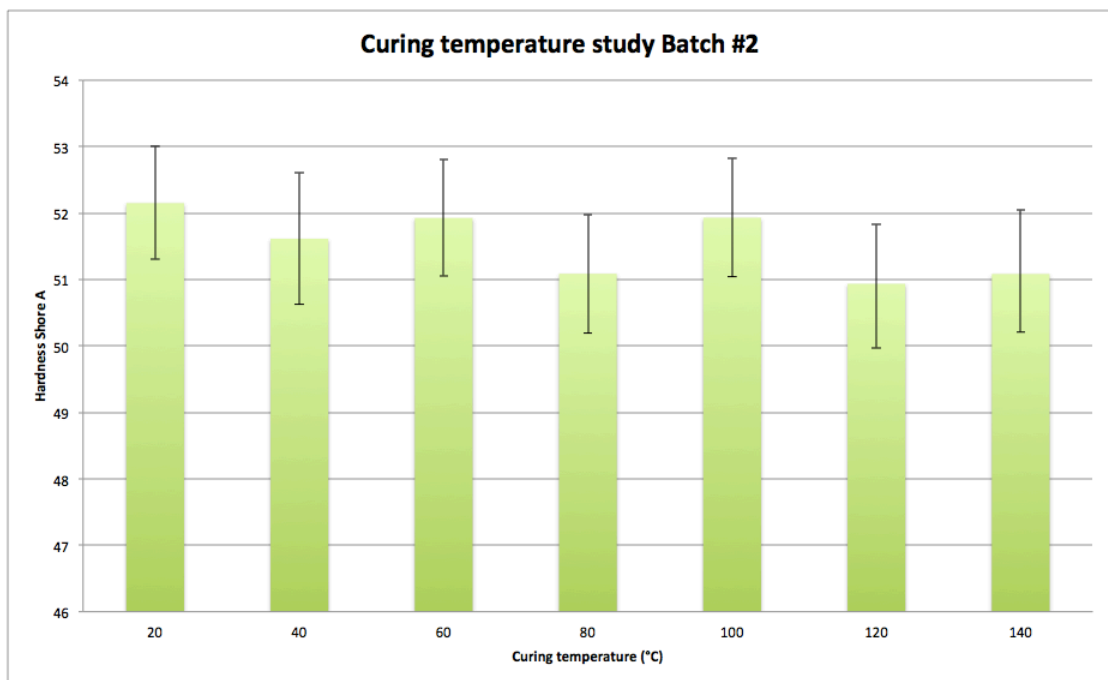


Figure A2: Results of Hardness shore A measurements done on a second batch of Elastosil® RT607 samples (3 samples per temperature tested with a minimum of 31 measurement per sample after statistical treatment). Samples have been prepared in a 9 :1 ratio (elastomer : curing agent) and cured at different temperature.

Appendix B. Hardness optimisation of the silicone based embossing master - Study of the impact of the ratio silicone elastomer base vs. curing agent on Elastosil® RT607 – Hardness Shore A measurements

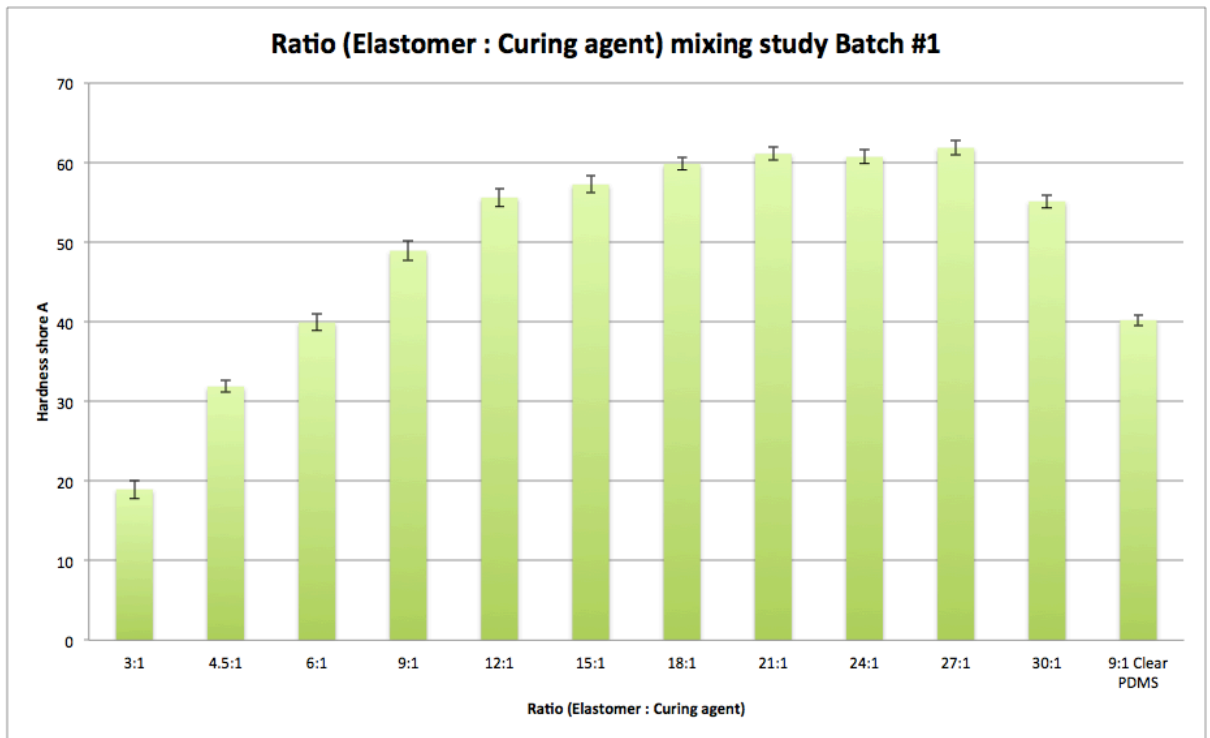


Figure B1: Results of Hardness shore A measurements done on a first batch of Elastosil® RT607 samples. Samples have been prepared in different ratio (elastomer : curing agent). Sample named « 9 : 1 Clear PDMS » has been made using another reference of silicon (Sylgard® 184).

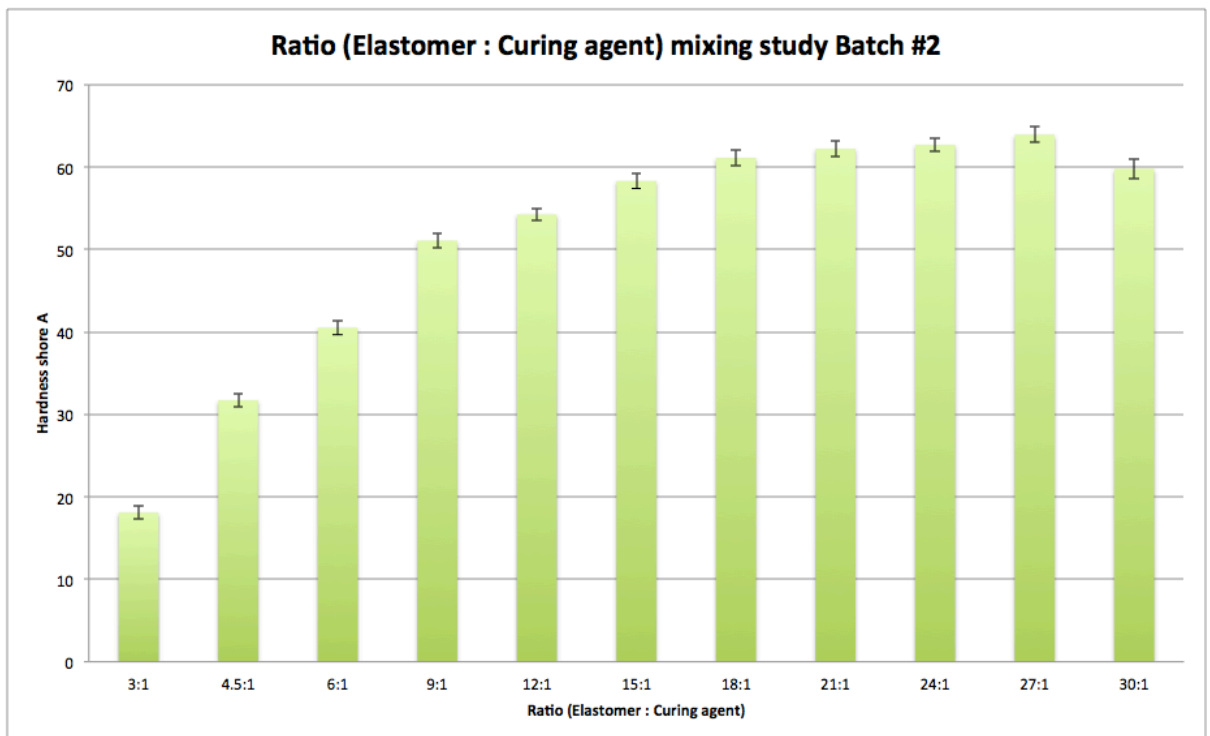


Figure B2: Results of Hardness shore A measurements done on a second batch of Elastosil® RT607 samples. Samples have been prepared in different ratio (elastomer : curing agent).

Appendix C. Hardness optimisation of the silicone based embossing master - Study of the impact of the ratio silicone elastomer base vs. curing agent on Elastosil® RT607 – Compressive strength measurements

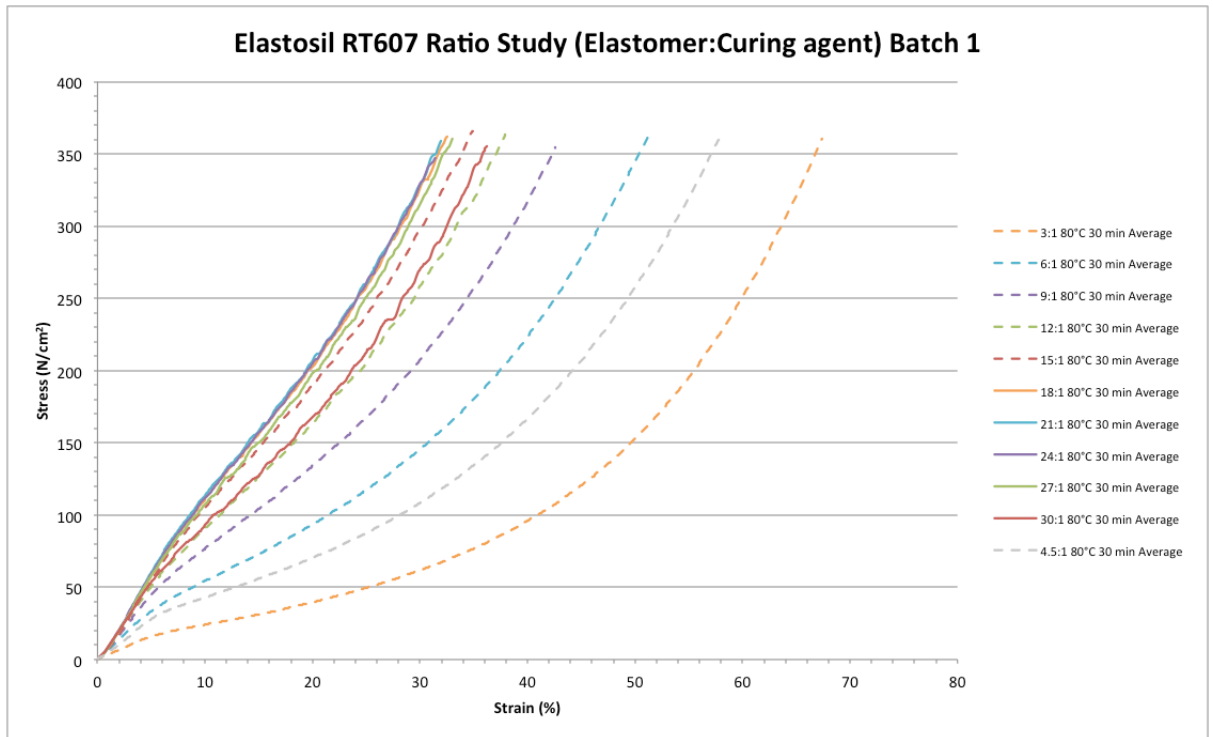


Figure C1: Compressive strength measurements done on a first batch of Elastosil® RT607 samples. Samples have been prepared in different ratio (elastomer : curing agent) and analysed the same day.

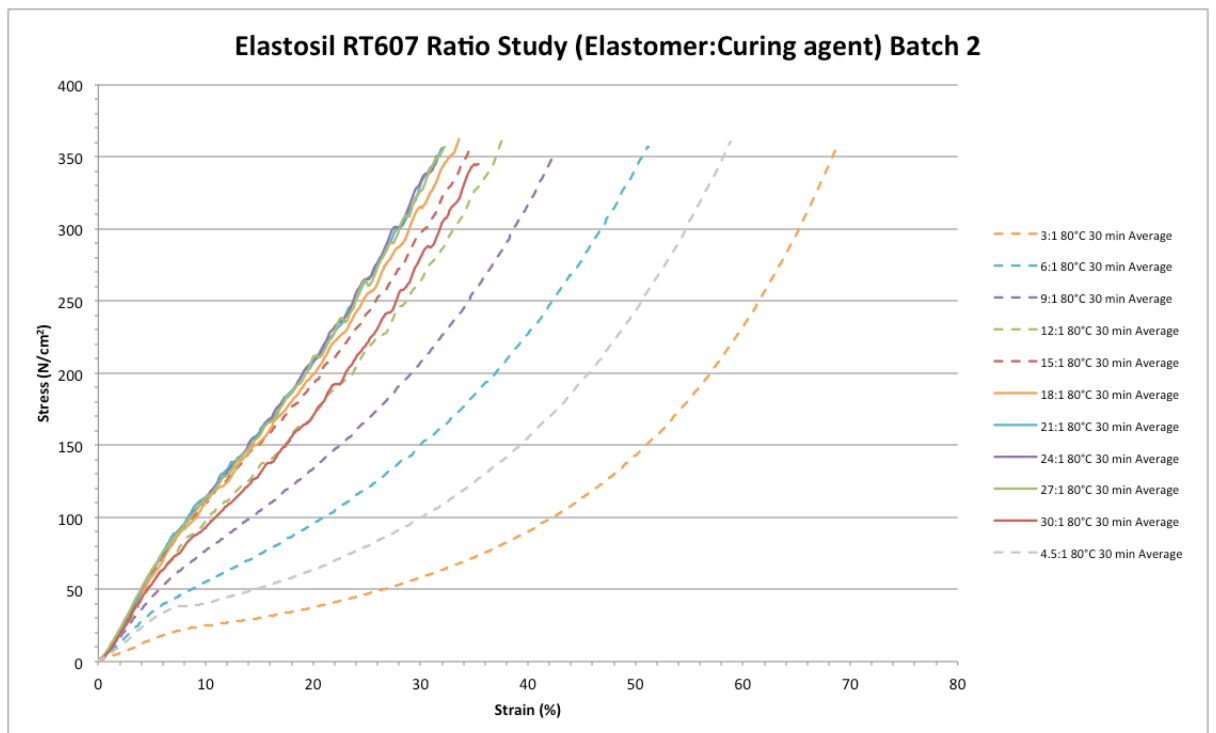


Figure C2: Compressive strength measurements done on a second batch of Elastosil® RT607 samples. Samples have been prepared in different ratio (elastomer : curing agent) and analysed the same day.

Appendix D. Thesis Outputs: Publications and Conferences

Elements of the work of this thesis have been disseminated elsewhere as follows:

IDF co-contributor:

« A method and device for assaying the interaction and dynamics of permeation of a molecule and a lipid bilayer » (submitted 11th June 2019, PCT/EP2019/065044)

Publications:

- ✓ Gimenez, A. V., Kho, K. W. & Keyes, T. E. Nano-substructured Plasmonic Pore Arrays: A robust, low cost route to reproducible hierarchical structures extended across macroscopic dimensions. *Nanoscale Adv.* (2020), DOI:10.1039/D0NA00527D (Accepted Manuscript)
- ✓ Berselli, G. B., Sarangi, N. K., Gimenez, A. V., Murphy, P. V. & Keyes, T. E. Microcavity Array Supported Lipid Bilayer Models of Ganglioside - Influenza Hemagglutinin1 Binding. *Chem. Commun.* (2020), DOI:10.1039/D0CC04276E (Accepted Manuscript)
- ✓ Steplewska, A., Kho, K. W., Gimenez, A. & Keyes, T. E. A Plasmonic Fluorescent Assay for molecular Lipid membrane binding and dynamics of permeation (Manuscript in preparation). (2020)
- ✓ Berselli, G. B., Gimenez, A. V., O'Connor, A. & Keyes, T. E. Light sensible photo-activated biosensor mounted at microcavities supported lipid bilayers (Manuscript in preparation). (2020)

Work published in the group following the fabrication method:

Berselli, G. B., Sarangi, N. K., Ramadurai, S., Murphy, P. V. & Keyes, T. E. Microcavity-Supported Lipid Membranes: Versatile Platforms for Building Asymmetric Lipid Bilayers and for Protein Recognition. *ACS Applied Bio Materials* 2, 3404–3417 (2019).

Conferences:

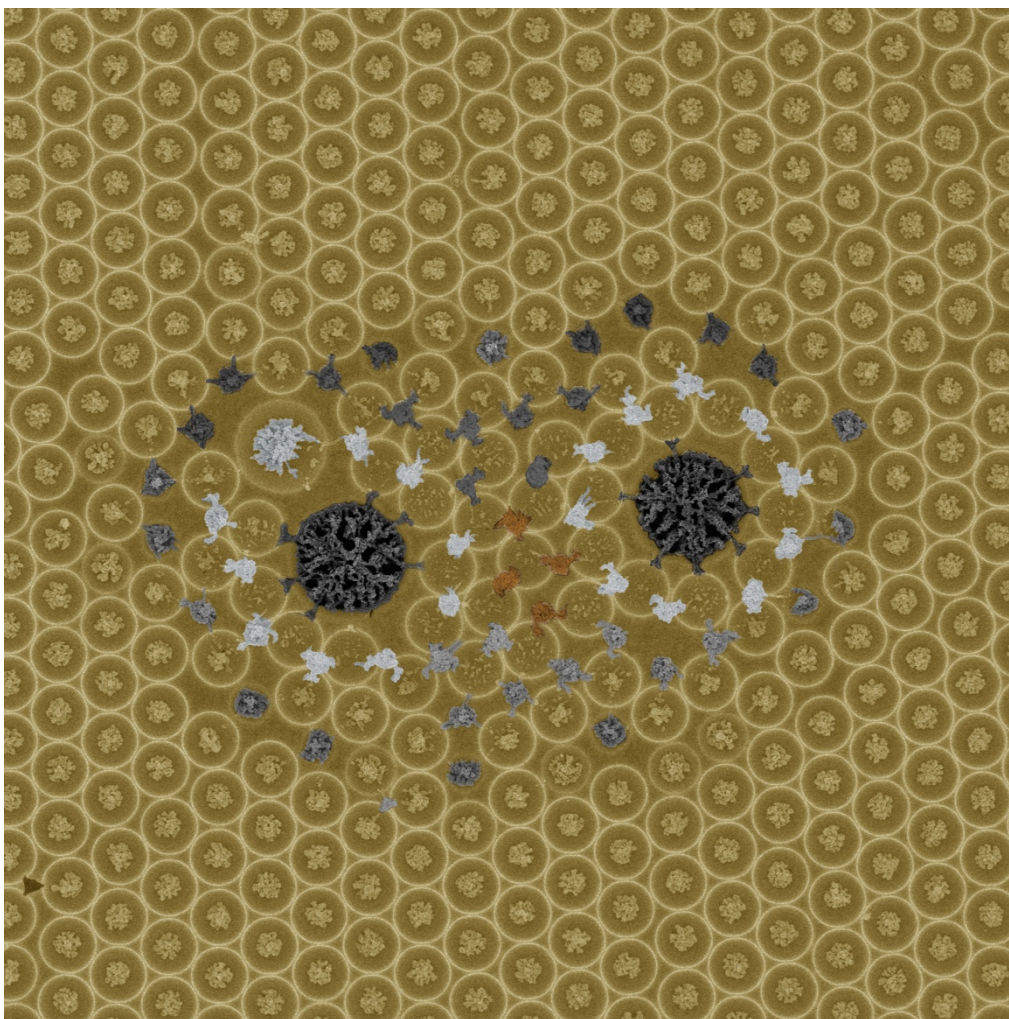
18th IEEE International Conference on Nanotechnology, Cork, Ireland, July 2018

- ✓ Best student poster contribution award

Nano-substructured periodic gold nanoarrays for Surface Enhanced Raman Spectroscopy (SERS) / Metal Enhanced Fluorescence (MEF) applications - Aurélien Gimenez, Kiang Wei Kho and Tia E. Keyes

- ✓ IEEE NanoArt competition winner

3 days exhibition of 15 best images of Nanoscience and Nanotechnology at the Crawford/CIT gallery in Cork



Don't put OWL your eggs in one basket.

Two anomalously large plasma-etched polystyrene spheres in a sea of otherwise uniform close-packed gold nanocavities containing gold sub-nanostructuring causes the smaller surrounding particles to assemble as multi layers in a concentric circles pattern around the spheres. These arrays have been designed for use as platforms for Surface Enhanced Raman Spectroscopy and Metal Enhanced Fluorescence applications.

PhD Graduate Training Elements

I have successfully completed 20 ECTS credits of Graduate Training Elements as follows:

PS408	Microfluidics	5 credits
BDI503	Advances in Diagnostics and Nanobiotechnology	7.5 credits
BE525	Introduction to Animal Cell Culture and Theory	2.5 credits
CS507A	Advanced Data Processing using Microsoft Excel	5 credits